# DYNAMIC IMPACT RESPONSE AND CORROSION BEHAVIOR OF COARSE- AND ULTRAFINE-GRAINED AISI 321 AUSTENITIC STAINLESS STEEL

A Thesis Submitted to the College of
Graduate and Postdoctoral Studies
In Partial Fulfillment of the Requirements
For the Degree of Doctor of Philosophy
In the Department of Mechanical Engineering
University of Saskatchewan
Saskatoon

By
Ahmed Alade Tiamiyu

## Permission to Use

In presenting this thesis in partial fulfillment of the requirements for a Postgraduate degree from the University of Saskatchewan, I agree that the Libraries of this University may make it freely available for inspection. I further agree that permission for copying of this thesis in any manner, in whole or in part, for scholarly purposes may be granted by Prof. Akindele Odeshi and Prof. Jerzy Szpunar, the professors who supervised my thesis work or in their absence, by the Head of the Department or the Dean of the College in which my thesis work was done. It is understood that any copying or publication or use of this thesis or parts thereof for financial gain shall not be allowed without my written permission. It is also understood that due recognition shall be given to me and to the University of Saskatchewan in any scholarly use which may be made of any material in my thesis.

Requests for permission to copy or to make other uses of materials in this thesis in whole or part should be addressed to:

Head of the Department of Mechanical Engineering
University of Saskatchewan
57 Campus Drive
Saskatoon, Saskatchewan S7N 5A9
Canada.
OR

Dean
College of Graduate and Postdoctoral Studies
University of Saskatchewan
116 Thorvaldson Building, 110 Science Place
Saskatoon, Saskatchewan S7N 5C9 Canada

## Abstract

The excellent corrosion-resistance of metastable AISI 321 austenitic stainless steel makes it a choice material in the fabrication of nuclear and chemical plants, pressure vessels, automobile and aircraft components, etc. However, AISI 321 is characterized by low-yield strength and poor tribological properties that hinder its widespread application. Therefore, it is important to improve its yield-strength to expand its structural applications without compromising its excellent corrosion resistance.

In this study, the effect of grain refinement via cryo-rolling followed by annealing on the strength and corrosion resistance of AISI 321 austenitic stainless steel is investigated. The mechanical behavior of the as-received coarse-grain and refined alloy (fine-grain and ultrafine-grain) were investigated at high (dynamic impact) and low (quasi-static compression) strain rates using the split Hopkinson pressure bar and Instron R5500 mechanical testing machine, respectively. The corrosion resistance of coarse-grained (CG), fine-grained (FG), and ultrafine-grained (UFG) specimens were also investigated using electrochemical methods. Scanning and transmission electron microscopy (SEM, TEM), X-ray diffraction (XRD), and electron-backscattered diffraction (EBSD) were used for the microstructural and textural characterization of various specimens of the alloy before and after plastic deformation.

The optimum thermomechanical process conditions for developing UFG structure in the AISI 321 steel is cryo-rolling to 50 % reduction of plate thickness followed by process annealing at 1023 K (750 ℃) for 600 s (10 minutes). The hardness of the UFG steel specimens is determined to be ~195 % higher than that of the as-received (CG) AISI 321 steel. The developed UFG specimens have strong intensity of ζ-fibre ({110}<uvw>) texture, which is attributed to pseudo-texture memory effect in AISI 321 steel. The mechanism for pseudo-texture memory in AISI 321 steel is proposed.

The yield strength of the UFG AISI 321 steel is ~400 and ~200% higher than those of the CG specimens under both quasi-static and dynamic deformation conditions, respectively. Slip and twinning are the active deformation mechanisms in CG specimens. Both are highly suppressed in the UFG specimens due to spatial restriction effect. During plastic deformation, γ-FCC to martensite (α′-BCC) phase transformation occurred, which is more favored in the UFG specimens and at low strain rates. The co-existence of martensitic phase transformation paths with and

without an intermediate phase (HCP ε-martensite) is confirmed in AISI 321 steel during plastic deformation under both quasi-static and dynamic loading conditions. Irrespective of grain size, Shoji-Nishiyama, Kurdjumov-Sachs and Burgers orientation relationships exist between the γ and ε, γ and α′, and ε and α′ phases, respectively. Thus, the phase transformation sequence follows both FCC γ → BCC α′ and FCC γ → HCP ε → BCC α′ path. The stable end-orientation of the austenite phase in compression is [110]||CD texture while that of the martensitic phase is [100]||CD with spread towards [111]||CD texture.

Under dynamic impact load, UFG specimens exhibit lower critical strain and strain rate at which shear strain localization (adiabatic shear bands) occurs. EBSD analysis revealed the development of equiaxed ultrafine-grained structure (average grain sizes of ~0.17 μm in CG and ~0.14 μm in UFG specimens) inside transformed shear bands by rotational dynamic recrystallization mechanism. The five strengthening sources that contribute to strain hardening in AISI 321 steel are determined to be: (a) grain boundary strengthening, (b) deformation-induced martensite transformation, (c) deformation twinning acting as a barrier to dislocation motion (d) dislocation-dislocation interactions, and (e) dislocation interaction with titanium carbides. On the stability of the austenite phase in AISI 321 steel, EBSD analyses confirmed the evolution of both thermally- and deformation-induced martensite that is grain size and orientation-dependent. The results of corrosion studies show that the excellent corrosion resistance of AISI 321 steel is not compromised by strength enhancement through grain refinement. Although the presence of TiC particles in AISI 321 is not detrimental to its corrosion resistance, that of TiN particles is.

## Acknowledgment

In all sincerity, my journey towards completing my PhD program has taught me how important people can be in one's life. To this end, I have many people to appreciate. However, I am restrained for the lack of space and for the fear of omitting someone's name unintentionally. Whether or not you are mentioned, you are highly appreciated!

My immeasurable gratitude goes to my supervisors, Prof. Akindele Odeshi and Prof. Jerzy Szpunar for their constant guidance and support towards the successful completion of my PhD program. The contributions (advice, insightful and valuable comments) of my advisory committee members, Prof. H. Guo, Prof. I. N. A. Oguocha, Prof. Q. Yang and Prof. M. Boulfiza are greatly appreciated.

My appreciation also goes to Mr. Nan Fang Zhao and Mr. Rob Peace for their time, advice and patience in training me on some of the equipment used in the course of my PhD program. To members of our research groups, colleagues and friends (in school and Church); your understanding, contributions and moral support towards the completion of this thesis are indeed needful and helpful. Many thanks to Prof. Marc Meyers and members of his research group at the University of California, San Diego, USA, for giving me access to use their focused ion beam equipment and transmission electron microscope for the analysis of some of my samples.

Gratitude for financial supports also goes to the University of Saskatchewan for the international Dean's scholarship, Natural Sciences and Engineering Research Council of Canada (NSERC) for Vanier Canada Graduate Scholarship, College of Engineering award committee for the Toyota Automotive Engineering and Safety Scholarship and Douglas Patton Hogg Memorial Award. I am also grateful to ACUREN Group Inc., Saskatoon, for the use of Fischer Feritscope MP30E.

To my parents (Mr & Mrs Tiamiyu) and siblings, thanks for your prayers and understanding. Profound and unreserved gratitude to my wife, Raliat Abiodun Tiamiyu. Your submission towards my aspirations and visions cannot go unnoticed. I'm grateful! May our "wine" never turn sour!

## Dedication

**To God,**

"Now unto him that is able to do exceeding abundantly above all that we ask or think, according to the power that worketh in us"

**To my lovely wife,**

whose immeasurable love and support at all times made this work possible

**To my kids,**

although I started this journey with my wife, you came in, to be part of this success story. Your smiles alone are powerful drive!

## Table of Contents

## List of Tables

## List of Figures

## List of Abbreviations and Symbols

### Abbreviations

| | |
|---|---|
| ASS | Austenitic stainless steel |
| FCC | Face-centred cubic |
| BCC | Body-centred cubic |
| HCP | Hexagonal close-packed |
| CG | Coarse grain |
| UFG | Ultrafine grain |
| FG | Fine grain |
| DIM | Deformation-induced martensite |
| TWIP | Twinning-induced plasticity |
| TRIP | Transformation-induced plasticity |
| ASB | Adiabatic shear band |
| DSB | Deformed shear band |
| TSB | Transformed shear band |
| OM | Optical microscopy |
| SHPB | Split Hopkinson pressure bar |
| FP | Firing pressure |
| SEM | Scanning electron microscope/microscopy |
| TEM | Transmission electron microscope/microscopy |
| ECAP | Equal-channel angular processing |
| EDS | Energy dispersive X-ray spectroscopy |
| EBSD | Electron backscattered diffraction |
| XRD | X-ray diffraction |
| VPSC | Visco-plastic self-consistent |
| AISI | American iron and steel institute |
| SFE | Stacking fault energy |
| LAGB | Low angle grain boundary |
| HAGB | High angle grain boundaries |
| KAM | Kernel average misorientation |
| DRX | Dynamic recrystallization |

| | |
|---|---|
| RDRX | Rotational dynamic recrystallization |
| DRV | Dynamic recovery |
| EIS | Electrochemical impedance spectroscopy |
| HV | Vickers hardness |
| IPF | Inverse pole figure |
| ODF | Orientation distribution function |
| CD | Compression direction |
| MSR | martensitic shear reversion |
| DR | Diffusional reversion |
| SRS | Strain rate sensitivity |
| TSA | Thermal stability of austenite |
| MSA | Mechanical stability of austenite |

## Symbols

| | |
|---|---|
| $\gamma$ | FCC-austenite |
| $\alpha'$ | BCC-martensite |
| $\varepsilon$ | HCP-martensite/Strain |
| $M_s$ | Martensite start temperature |
| $M_f$ | Martensite finish temperature |
| $M_{d30/50}$ | Temperature (in $^{o}$C) at which 50% of $\gamma$ transform to $\alpha'$ due to 30% imposed strain |
| $C_v$ | Heat capacity, J/kg K |
| $W_p$ | Specific work of deformation, J/m$^3$ |
| $\sigma$ | Stress, MPa |
| $\dot{\varepsilon}$ | Strain rate |
| $\rho$ | Density, kg/m$^3$ |
| $\Delta G^{(\alpha\rightarrow\gamma)}$ | Free energy change for BCC transformation to FCC phase |
| $\beta$ | Taylor-Quinney parameter |
| $m$ | Strain rate sensitivity |
| $\vartheta^*$ | Activation volume |
| $k$ | Boltzmann constant |
| $E_{oc}$ | Open circuit potential |

# Chapter 1

# Introduction

This chapter focuses on the motivation behind this study. It also documents the existing problem with the structural use of AISI 321 austenitic stainless steel and the need to address it. The research questions to answer, the overall and specific objectives of this study are presented. An overview of the content of this thesis is also presented.

## 1.1 Motivation

Over the years, many countries have experienced some major nuclear/chemical plant explosions. Examples of such explosions in Canada include the boiler explosion at the Cliff Central Heating and Cooling Plant in Ottawa in 2009 and the Neptune Technologies and Bio Resources factory explosion (Sherbrooke, Quebec) in 2012. Canada is one of the world's leading uranium producer with nuclear power as one of her sources of energy. The energy industries in Canada and the rest of the world, therefore, require high-performance materials to generate, transport and store energy. Metastable AISI 321 austenitic stainless steel is a choice material in the energy, automotive, aerospace, and chemical process industries, where it can be subjected to extreme service conditions. The extreme conditions include highly corrosive environments, high temperature and cryogenic environments, and environments where engineering materials are exposed to external loading conditions at high and low strain-rate regimes.

Since the austenite phase in AISI 321 steel is metastable, it can be affected by extreme service conditions. For instance, in a cryogenic environment, thermally induced α'-martensite may form from the austenitic phase. Under external load, deformation-induced martensitic phase transformation could also occur at a strain level greater than a critical strain. The stability of the austenite phase in deformed AISI 321 will be different under quasi-static compression (low strain rate) and dynamic impact loading (high strain rate) conditions. Furthermore, the selection of AISI 321 steel for application is corrosion-driven with less attention paid to improvement of its inherent low yield strength and poor tribological properties. To this end, it will be of interest to investigate the prospect of improving its yield strength by grain refinement.

The condition under which metastable austenite phase in AISI 321 stainless steel becomes unstable (e.g. through phase transformation) is not well understood. The question of how this will affect the established excellent corrosion resistance of the alloy needs to be addressed. Besides deformation-induced martensitic phase transformation, what other strengthening mechanisms occur when AISI 321 steel is subjected to mechnnical loading? What is the role of strain, strain rate, crystallographic texture, and grain size on the stability of the austenite phase and, by extension, the mechanical, and corrosion behavior of the AISI 321 steel? These are some of the research questions that are addressed in this PhD work since, to the best of the author's knowledge, not much research has been done to answer these questions for AISI 321 steel. The microstructural and mechanical data generated from this study can be used for future alloy development to enhance failure resistance under different service conditions.

## 1.2 Research objectives

The overall goal of this research is to expand the structural application of AISI 321 stainless steel through grain refinement to UFG structure to areas where low yield strength hinders its application. To realize this goal, the following specific objectives were pursued;

I. Determine the dynamic mechanical behavior and texture evolution across the thickness of as-received hot-rolled AISI 321 steel.

II. Develop ultrafine-grained (UFG) structure in AISI 321 stainless steel via cryogenic rolling and annealing and characterize the refined alloy.

III. Determine the effect of grain size on the mechanical response of AISI 321 stainless steel over a wide range of strain rates.

IV. Determine the effect of grain size and prior deformation on the corrosion behavior of AISI 321 steel in saline environment.

## 1.3 Research contributions

The combined improvement of the yield strength and corrosion resistance of AISI 321 stainless steel by grain refinement was accomplished. The optimum thermo-mechanical processing conditions for developing UFG structure of ~0.31 μm grain size were determined. For the first

time, AISI 321 stainless steel was determined to be a texture memory alloy with associated mechanism proposed. Results obtained in this study indicate that the operational deformation mechanisms in AISI 321 steel under mechanical load are complex (i.e. slip and twinning occur concurrently, alongside deformation-induced phase transformation). It is also established that strain, strain-rate, grain size, and crystallographic texture influences which of the three mechanisms dominate. The possible co-existence of martensitic phase transformation paths with and without an intermediate phase (HCP $\varepsilon$-martensite) during plastic deformation is established. Five strengthening sources that contribute to strain hardening in the AISI 321 steel are identified. They are: grain boundary strengthening, deformation-induced martensite transformation, deformation twinning acting as barrier to dislocation motion, dislocation-dislocation interactions, and dislocation interaction with titanium carbides. This work also revealed that the evolution of both thermally- and deformation-induced martensite is orientation-dependent in both fine- and coarse-grained specimens, while the austenite phase in UFG specimens is highly stable in cryogenic environment. The thermal and mechanical instability of the austenite phase was observed to be highest in the RD/CD||[100]-oriented grains (RD and CD are rolling and compression directions, respectively), followed by grains oriented near RD/CD||[110] and RD/CD||[111], in that order. In conclusion, the results have demostrated that the strength of AISI 321 steel can be significantly improved without compromising the excellent corrosion resistance of this alloy. The list of publications that reports all the research contributions from this study is presented in APPENDIX A

## 1.4 Thesis organization

The thesis contains twelve chapters. Chapter 1 contains the overview, motivation, and objectives of the research while the review of literature is presented in Chapter 2. Chapter 3 contains the details of the material and methodology used in this study. The experimental results from various aspects of this study have been published in reputable peer review journals. They are presented in Chapter 4 (Objective #I), Chapters 5 and 6 (Objective #II), Chapters 7, 8, 9 and 10 (Objective #III) and Chapter 11 (Objective #IV).

In Chapter 4, the dynamic mechanical behavior and high-resolution EBSD investigation of the microstructural evolution in deformed AISI 321 stainless are presented. The emphasis is on the variation in the dynamic impact response of the as-received steel across the thickness of the steel

plate in comparison with the mechanical response under quasi-static lading condition. This work has been published in *Materials Science & Engineering A.* In Chapter 5, the optimum thermo-mechanical process conditions required to develop UFG structure in AISI 321 austenitic stainless steel is presented. The α'-martensite to γ-austenite reversion behavior and the associated texture development are discussed. The content of this chapter was published in *Metallurgical and Materials Transactions A.* In Chapter 6, the observed texture memory effect in this alloy is reported and the mechanism for its occurrence is proposed. To the best of my knowledge, this is the first time that this effect is being reported for AISI 321 steel. This work was published in the IOP Conference Series *Materials Science and Engineering (ICOTOM 2017).*

In Chapter 7, the dynamic impact responses of coarse (37 μm) and ultrafine-grained (0.24 μm) AISI 321 austenitic stainless steel are presented and discussed. The dynamic failure, along with the underlying deformation and strengthening mechanisms in both coarse and ultrafine-grained specimens, is explored. The content of this chapter was published in the *Materialia* journal. Based on the findings in Chapter 7, it became necessary to study the behaviour of the steel under low strain rate condition. This is because the results in Chapter 7 cannot be generalized for all strain rate regimes. Hence, the effects of grain refinement on the behavior of AISI 321 steel when compressed in the low strain rate regime was investigated, the results of which are presented in Chapter 8. FCC-austenite to BCC-martensite transformation paths in the investigated AISI 321 austenitic stainless steel are also discussed**.** This work was published in the *International Journal of Plasticity.*

In Chapter 9, the effect of grain size on the strain rate sensitivity and activation volume of metastable AISI 321 austenitic stainless steel at high strain rate regime is discussed. The content of this chapter has been published in the *Materials Characterization* journal. In Chapter 10, the roles of grain size, texture, strain and strain rate on the thermal and mechanical stability of austenite in AISI 321 metastable austenitic stainless steel is discussed. These findings could open a new window for engineering the initial texture of metastable austenitic stainless steel to either suppress or promote both isothermal and deformation-induced martensitic phase transformation. This work was published in the *Metallurgical and Materials Transactions A* journal. The role of grain size and prior deformation (and deformation rate) on the corrosion behavior of AISI 321 austenitic stainless steel in 3.5 wt.%-NaCl solution is discussed in Chapter 11. This work was published in

the *Scientific Report* journal. Finally, highlights of research findings and the major conclusions drawn from this research work are presented in Chapter 12. This chapter also includes some recommendations for future work.

# Chapter 2

## Literature Review

A comprehensive review of previous studies on stainless steels and their applications is provided in this chapter. The plausible conditions that can result in the instability of the austenite phase in austenitic stainless steel are highlighted. Previous works on plastic deformation of stainless steel at different strain rates and the associated failure mechanisms are also reviewed.

### 2.1 Stainless steels: composition, microstructure and properties

Generally, stainless steels are corrosion resistant iron-based alloys with a minimum of 12 wt.% chromium (Cr) content. In terms of composition, microstructure and mechanical properties, they are the most complex among all steel types [1]. Stainless steels resist corrosion by the formation of a thin passive film of $Cr_2O_3$; the corrosion resistance increases with Cr content [2]. They find applications in chemical, pharmaceutical, oil industries etc. [3]. Alloying elements in stainless steels can be divided into two major groups. The first group promotes the formation of austenite (called *austenite former*) during hot rolling or solution treatment at elevated temperatures while the second promotes the formation of δ-ferrite (called *ferrite former*). While Cr, the principal alloying element promotes δ-ferrite formation at high temperatures, Fe can accommodate about 13 wt.% Cr at a temperature of about 1050 ℃ and still remains completely austenite. An increase of Cr from ~12 to 17 wt.% could stimulate a progressive change from an austenitic structure to δ-ferrite at elevated temperatures with the ferrite remaining as the stable phase on cooling to room temperature [1]. This can be observed in the Fe-Cr equilibrium diagram (Fig. 2.1a) that is also characterized by the presence of both sigma phase at about 50 wt.% Cr and the constrained austenite phase fields (called gamma-loop). As Cr content increases beyond 13 wt.%, duplex austenite and ferrite phase field evolves at the expense of a single-phase austenite at 1050 $^{o}$C. It is necessary to mention that while FCC austenitic structure within the gamma-loop transforms to martensite on cooling to ambient temperature, ferrite formed at elevated temperature undergoes no phase change on cooling. Stainless steel becomes completely ferritic when the Cr is increased above 18 wt.% for carbon content of about 0.1 wt.% C [1]. Low volume fraction of ferrite is considered beneficial under certain conditions such as in welds, while high volume fraction can promote cracking and decrease corrosion resistance [4]. The nomenclature δ-ferrite is used to differentiate the high temperature BCC ferrite phase from α-ferrite (a transformed product from

austenite). Sigma phase is a hard and brittle intermetallic compound produced in alloys containing less than 50 wt.% Cr. Formation of the sigma phase retards corrosion resistance. As such, the temperature range (about 750-820$^{o}$C) that promotes its formation in Fe-Cr alloys should be avoided in service.

Nickel is a strong austenite-former that is usually added to steel to preserve austenite in the presence of high ferrite-forming Cr content [5]. Its addition to the Fe-Cr alloy helps negate the restriction imposed by Cr content on the formation of austenite. Figure 2.1b shows an expanded austenite phase in Fe-Ni equilibrium phase diagram. Therefore, in a high Cr steel with substantial ferritic microstructure, it is possible to reverse the process and re-establish an austenitic structure by the addition of a large amount of Ni. Steels containing 17 wt.% Cr and 0.1 wt.% C have a microstructure comprising 65% δ-ferrite and 35% austenite at a solution treatment temperature (Fig. 2.2a). At 1050 $^{o}$C, stainless steels become fully austenitic with the addition of 5 wt.% Ni as shown in Fig. 2.2b where the percentage of δ-ferrite is near zero.

Ni addition depresses $M_s$-$M_f$ transformation range. However, Ni content above 4 wt.% depresses the $M_f$ temperature below room temperature. Therefore, the addition of larger amount of Ni will result in a drop in hardness owing to an incomplete transformation to martensite and a large amount of retained austenite (Fig. 2.2b). This implies that a 18 wt.% Cr 9 wt.% Ni will be fully austenitic at 1050$^{o}$C but with a depressed $M_s$-$M_f$ temperature range to sub-zero temperatures. This is due to the high Ni addition and influence of other alloying elements. Hence, this steel retains its austenitic structure when cooled to room temperature and has a low strength but high formability.

Other δ-ferrite forming elements include silicon (Si), molybdenum (Mo) and titanium (Ti) at high temperature whereas carbon (C), nitrogen (N), manganese (Mn) and copper (Cu) promotes austenite formation. Both ferrite- and austenite-forming elements will lower the $M_s$-$M_f$ temperature range, thereby influencing the evolved microstructure on cooling to room temperature. Therefore, the composition of stainless steel is governed by [1]:

a. the balance between ferrite- and austenite-forming elements that eventually controls the structure of a hot rolled and solution treated stainless steels,

b. the overall content of alloying elements which controls the $M_s$-$M_f$ temperature range and the eventual structure and properties at room temperature.

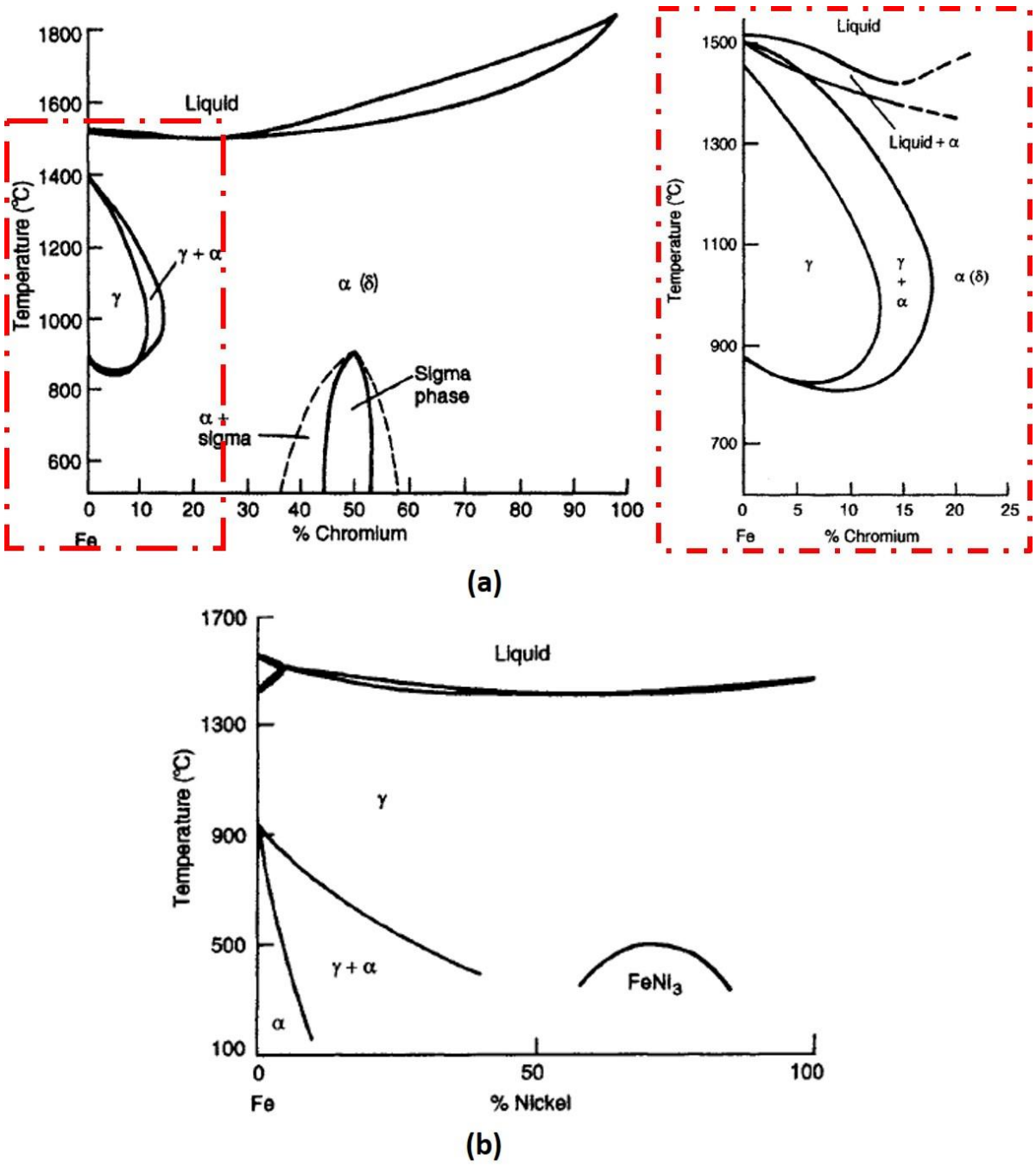


Fig. 2.1. (a) Fe-Cr and (b) Fe-Ni equilibrium diagrams. Exploded view in (a) is a simplified illustration of the marked region for Fe-Cr alloys containing 0.1% C [1].

For the various classes of stainless steels, there exists a compromise between corrosion resistance and other properties such as mechanical strength, formability etc. [1]. For example, Abreu *et al.*

[6] observed that as the volume fraction of martensite increases, pitting and general corrosion resistance decrease.

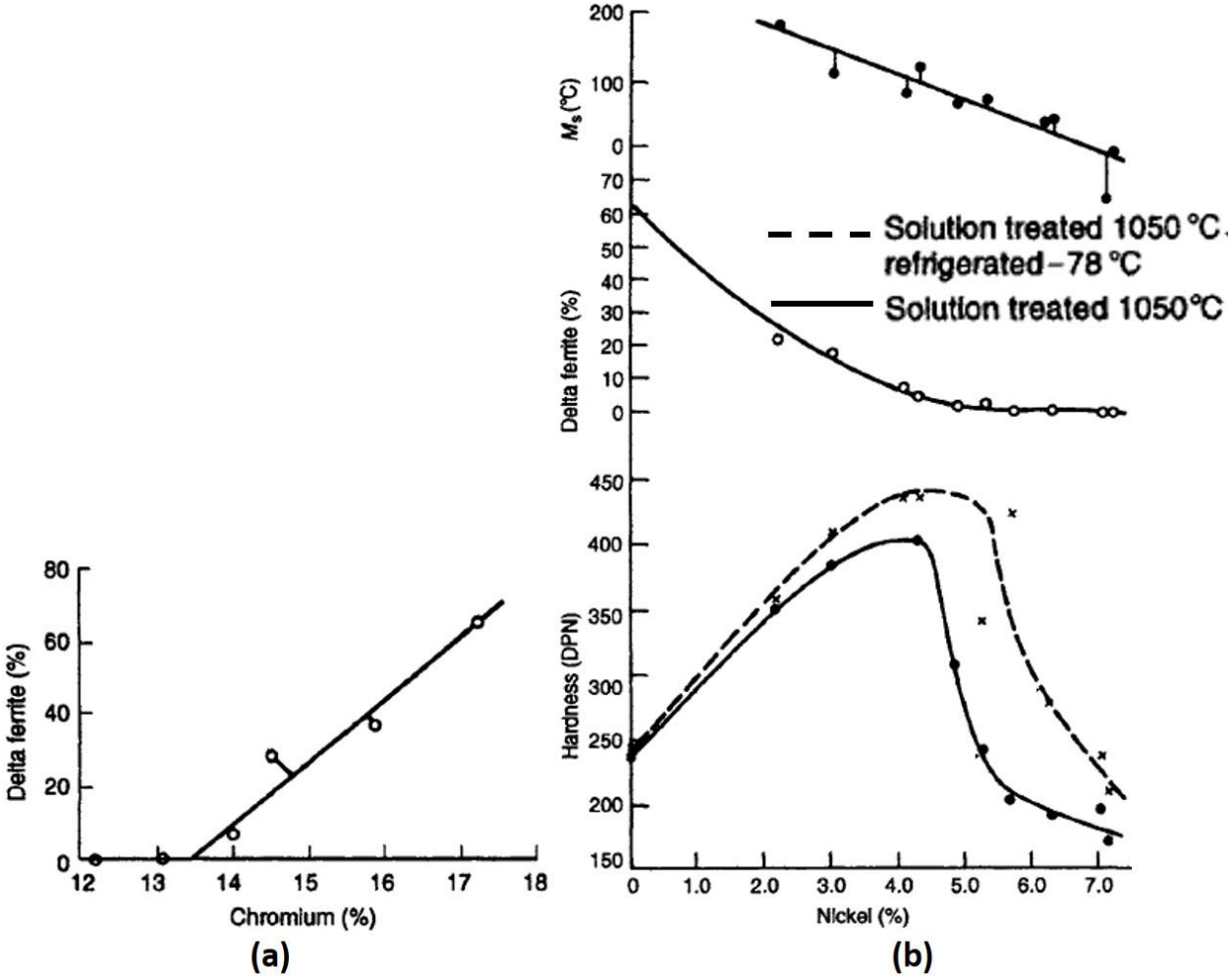


Fig. 2.2. (a) Percentage of δ-ferrite with respect to Cr content in 0.1 wt.% Carbon steels solution-treated at 1050 ℃ and (b) effect of Ni content on the Ms temperature, % δ-ferrite and hardness of 0.1 wt.% C 17 wt.% Cr steels [1].

Depending on its chemistry, the microstructure of stainless steel constitutes mainly of ferrite, austenite, and martensite. Based on these microstructures, stainless steels are classified as ferritic, austenitic, martensitic, duplex or precipitation hardening (PH) stainless steels [7-9]. While the ferritic and martensitic stainless steels are ferromagnetic, austenitic stainless steels are non-magnetic [9]. The 200 series contains Cr, Ni and Mn as major alloying elements while the alloys belonging to the 300 series contains mainly Cr and Ni, and are both (200 and 300 series) austenitic [10,11]. The alloys in the 400 series that cannot be hardened by heat treatment are ferritic, the

hardenable 400 series type is martensitic [11]. Duplex steels mainly belong to the 2000 series. Meanwhile, the PH stainless steels, which contains Cr, Ni and small amounts of various additions of Cu, Co, Al, P, Ti, Mo and Nb belongs to the 600 series [12,13]. As useful as equilibrium phase diagrams are, they are sometimes not sufficient to predict the dominant microstructure after solidification [5]. To this end, Schaeffler [14] developed an empirical equation, termed chromium equivalent and Nickel equivalent, that constitutes some of the ferrite and austenite formers listed above. These are used to plot a constitution diagram called Schaeffler's diagram. Although Shaeffler's approach did not take into account the cooling rate and aging heat treatments, it permits the prediction of microstructure as a function of composition [5,15]. Schneider [16], however, developed a modified-Schaeffler's diagram (Fig. 2.3a) using Cr equivalent (Eqn. 2.1) and Ni equivalent (Eqn. 2.2) that considers a wider range of compositions. The modification of Schaeffler's diagram is a continuous effort as new grades of stainless steel are being developed. For instance, Klueh et al. [17] reported that Shaeffler's diagram that was established to predict phases in Fe-Cr-Ni-C stainless steels could not predict the phases in Fe-Cr-Mn-C stainless steels. The authors observed that Mn has lower austenite-stabilizing effect against the formation of δ-ferrite than Ni (i.e. Ni is a stronger austenite former than Mn). Hence, they propose a modified diagram that is superimposed on the Schaeffler's diagram as shown in Fig. 2.3b.

$$Cr\ equivalent = (Cr) + (2Si) + (1.5Mo) + (5V) + (5.5Al) + (1.75Nb) + (1.5Ti) + (0.75W) \quad \ldots 2.1$$

$$Ni\ equivalent = (Ni) + (Co) + (0.5Mn) + (0.3Cu) + (25N) + (30C) \quad \ldots 2.2$$

### 2.1.1 The 300 series austenitic stainless steel

The AISI 321 selected for investigation in this PhD work belongs to the 300 series (Fe–Cr–Ni) of austenitic stainless steels which have good ductility and excellent overall corrosion resistance [3]. However, they possess relatively low yield strength (250 to 350 MPa) [18] which limits their use in structural applications [18]. Some examples of alloys in this series are indicated in Fig. 2.3a. Another major disadvantage of stainless steels belonging to the 300 series is their low hardness, which leads to very poor tribological properties [3]. They have a face-centred cubic (fcc) structure [19] with low stacking fault energy (SFE) [20]. Austenitic stainless steels (ASS) are produced on solidification by peritectic reaction [21]. One of the major problems of cast and welded ASSs is hot cracking which is usually induced by severe microsegregation of trace elements such as

phosphorus and sulfur when austenite dendrites form instead of ferrite dendrites. Regulating the content and morphology of ferrites in austenitic stainless steels becomes a problem [21].

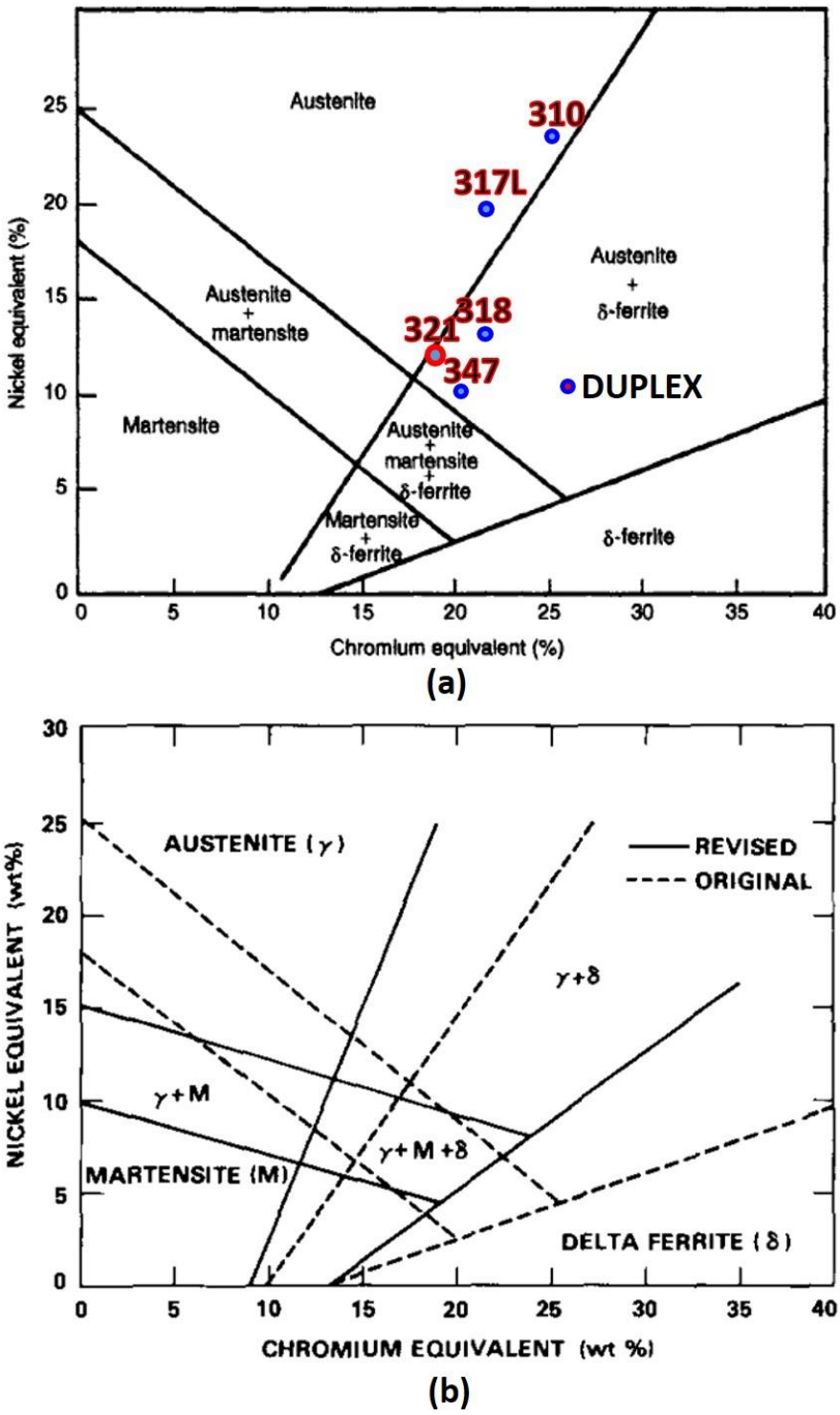


Fig. 2.3. Schaeffler diagram modified by (a) Schneider [1] and (b) Klueh et al. [17]; (b) also shows the original Schaeffler diagram superimposed on the diagram modified by Klueh et al.

### 2.1.2 AISI 321 austenitic stainless steel and applications

An age-long problem associated with ASSs is the frequent occurrence of sensitization. Sensitization is a phenomenon in which intergranular corrosion occurs when ASSs are exposed to heat at a temperature between 500 and 800 °C [22]. It is caused by the depletion of Cr in the vicinity of the grain boundaries due to the precipitation of $Cr_{23}C_6$ [5,22]. To circumvent this problem, metallurgist proposed the use of carbon content below 0.03 wt.% to suppress the formation of $Cr_{23}C_6$ [23]. This led to the development of L-type austenitic stainless steels such as AISI 304L and 316L type [5]. The grain boundary engineering of austenitic stainless steel to induce 'special' coincidence site lattice boundaries of Σ3 and Σ9 by cold rolling has also been reported to be an effective way to prevent sensitization and intergranular corrosion [24]. Another approach is to add elements which have stronger affinity for carbon than Cr, i.e. the addition of carbide formers such as Nb and Ti, to the alloy's system [5,23,25]. This is also to avoid the formation of $Cr_{23}C_6$ through preferential formation of non-detrimental NbC and TiC, respectively, leaving Cr in the solid solution at high temperature [26,27]. While the Nb-rich stainless steel is named the AISI 347 alloy, AISI 321 is the Ti-rich stainless steel. The chemical composition of AISI 321 austenitic stainless steel is presented in Table 2.1 while the influence of the alloying elements in stainless steel is presented in Table 2.2. Using the Eqns. 2.1 and 2.2, the Cr and Ni equivalents for AISI 321 and some other ASS are estimated and indicated in Fig. 2.3a. AISI 321 austenitic stainless steel has excellent corrosion resistance [3], and find application in components design for aircraft exhaust stacks and exhaust manifolds, pressure vessels, nuclear power and chemical reactors, automobile exhaust systems, mufflers for engines, carburetors, expansion bellows, stack liners, etc. [28,29]. Due to the presence of nitrogen in AISI 321 ASS, TiN can form in this steel, which has been reported to act as passive film breakdown sites for pit initiation in an acyl chloride environment [30]. AISI 321 austenitic stainless steel is essentially non-magnetic, and can only be hardened by cold working [30,31].

Table 2.1. Chemical composition of the AISI 321 austenitic stainless steel (wt. %).

| C | Si | Mn | P | S | Cr | Ni | Cu | Mo | Co | N | Nb | Ti | Fe |
|---|---|---|---|---|---|---|---|---|---|---|---|---|---|
| 0.044 | 0.40 | 1.56 | 0.04 | 0.001 | 17.61 | 9.17 | 0.3 | 0.42 | 0.15 | 0.0117 | 0.008 | 0.36 | Bal. |

Table 2.2. Role of alloying elements in stainless steels [32]

| Element | Description |
|---|---|
| C | It contributes to the strengthening of stainless steel. Content is deliberately low to obtain desired properties (such as prevention of sensitization) and mechanical characteristics. |
| Si | Improves oxidation resistance. It also confers hardenability on steel when present in small amount. |
| Mn | Prevents the formation of iron sulphide inclusions that cause hot cracking. It also promotes deoxidation of steel. |
| Cr | Promotes the corrosion-resistance of stainless steels through the formation of adherent, passive film that shields the steel from uniform and localized attack. |
| Ni | Promotes the corrosion-resistance of stainless steels especially in sulphuric acid environments and when passive layer is absent or damaged. It also imparts strength to stainless steel. |
| Mo | Improves resistance to pitting and crevice in chloride environments. It also decreases the breakdown tendencies of previously formed passive films. |
| N | Increases the resistance to pitting or intergranular corrosion due to the evolution of $Cr_2N$ instead of $Cr_{23}C_6$. |
| Nb | Prevents intergranular corrosion and contributes to strengthening due to the precipitation of fine NbC. |
| Ti | Used to stabilize stainless steel to promote the formation of TiC at the expense of $Cr_{23}C_6$. It also forms TiN in the presence of Nitrogen. |

## 2.2 Martensitic phase transformation in stainless steels

Most of the austenitic stainless steels, including AISI 321, are metastable. This means that martensitic phase transformation could occur on exposure to any conditions that could result in the instability of its austenite phase. Some of these stability-deteriorating conditions include exposure to cryogenic environment and external load, either at low or high strain rates. This section, therefore, focused on the development of martensitic phase transformation in austenitic stainless steels that is thermally- or mechanically-induced.

### 2.2.1 Thermally-induced phase transformation

Without an external load, the α′-martensite start temperature ($M_s$) of AISI 300-series austenitic stainless steels strongly depends on the alloy content. Among other empirical equations, Eqn. 2.3 proposed by Eichelman and Hull [33] is most widely used;

$$M_s(℃) = 1302 - 42(\%Cr) - 61(\%Ni) - 33(\%Mn) - 28(\%Si) - 1667(\%C + \%N) \quad \ldots 2.3$$

where compositions are in wt.%. Using Eqn. 2.3, the estimated $M_s$ for AISI 321 is $-153$ ℃. This suggests that the FCC γ-austenite phase in AISI 321 (and other austenitic stainless steels) will transform to α′-martensite when exposed to cryogenic environment. Unlike pearlite or ferrite formation, α′ evolve due to the deformation of the γ lattice without atomic diffusion. This deformation induces a change in shape of the transformed region that now consists of a large shear and a volume change [34]. Austenite in metastable stainless steels can transform into two different types of martensite; the hexagonal close-packed (HCP) ε-martensite and the body-centered cubic (BCC) α′–martensite [6]. Both martensitic phases tend to induce volume changes in comparison with the parent austenite. While the formation of α′-martensite generates a volume expansion of 1-4 %, the ε-martensite generates a volume contraction. Similarly, while the α′-martensite nucleates from austenites through dislocation reactions (at dislocation pile-ups) [6], ε-martensite is formed at stacking faults [35]. Between the ε- and α′-martensite phases, the transformation of the latter is of substantial interest, as it increases the work-hardening capacity and affects the ductility of the steels [19]. Apart from the chemical composition of the alloy, the occurrence of sensitization in stainless steel prior to exposure to cryogenic environment may also influence the amount of phase transformation [5]. This is because the formation of $M_{23}C_6$ carbide at the grain boundaries results in the depletion of chromium, carbon, and other alloying elements in the grain boundary area, which in-turn, leads to a higher $M_s$ temperature. This makes the material more susceptible to the formation of α′-martensite close to grain boundaries during cooling than the unsensitized alloy [36]. Grain size can also affect the extent of phase transformation in stainless steel as reported by Matsuoka et al. [37]. The authors observed that the volume fraction of thermally-induced martensite decreased with a decrease in grain size in Fe–16%Cr–10%Ni metastable stainless steel.

Generally, martensitic transformation would occur athermally in steels, although an isothermal transformation is also possible depending on the transformation kinetics [38,39]. In athermal transformation, the amount of martensite formed depends only on temperature while that formed through isothermal transformation process is function of both temperature and time [40]. Although isothermal transformation has no definite $M_s$ temperature, it occurs at an incubation time during isothermal holding. It is well documented that thermal activation is not necessary for athermal transformation to start and proceed [41]. This implies that only the thermodynamic driving force (that must overcome the elastic energy that opposes martensite initiation at specific sites at and below the $M_s$) obtained by lowering temperature is sufficient for athermal martensitic transformation. The Koistenen and Marburger [42] equation (Eqn. 2.4) that describes the transformation progress below $M_s$ also affirm that the extent of transformation is independent of time.

$$1 - V_{\alpha'} = exp[-0.011(M_s - T_q)] \quad \ldots 2.4$$

$V_{\alpha'}$ represents the volume fraction of α′-martensite and $T_q$ represents the quenching temperature that is below $M_s$. The athermal character deduced from this expression (time independent) is a result of very rapid nucleation and growth of martensite that permits the time taken for growth completion to be negligible. The rate at which a martensite plate grows was determined to be 1100 $ms^{-1}$, a significant fraction of speed of sound in steel [34,43]. Apart from the fact that the composition of the product phase (martensite) is identical to that of the parent phase (austenite), the aforementioned observation also lends support to the general knowledge that martensitic phase transformation is diffusionless since the fastest diffusion process occur at about 800 $ms^{-1}$ in pure Ni [34]. Based on the thermal activation model for the transformation kinetics, it has been predicted that isothermal transformation will occur when athermal transformation is suppressed [40,44]. However, the occurrence of both transformations in the same material has been reported [45,46].

### 2.2.2 Mechanically-induced phase transformation

The metastable austenite phase in austenitic stainless steels is known to undergo partial transformation to a martensitic microstructure during cold deformation [18,30]. This plastic deformation provides the required energy to promote martensitic transformation, thereby

increasing the martensite formation temperature to $M_d$. $M_d$ is the temperature higher than $M_s$, below which martensite will evolve on application of an external load. The martensite produced via plastic deformation is called deformation-induced martensite (DIM) and the phenomenon is termed transformation-induced plasticity (TRIP) [47]. The empirical equations, for $M_{d30/50}$ (i.e. the temperature (in $^{o}$C) at which 50% of austenite will transform to α′-martensite due to 30% imposed true strain) is given by Nohara et al. [48] in Eqn. 2.5.

$$Md_{30/50}(℃) = 551 - 462(\%C + \%N) - 9.2(\%Si) - 8.1(\%Mn) - 13.7(\%Cr) - 29(\%Cu + \%Ni) - 18.5(\%Mo) - 68(\%Nb) - 1.42(G - 8) \quad \ldots 2.5$$

where $G$ is the ASTM grain size number of the investigated steel. With an ASTM grain size number of 6, the $M_{d30/50}$ for AISI 321 steel is $-12$ ℃, a significant rise from the $M_s$ ($-153$ ℃). During deformation, the debate on whether the martensitic transformation followed FCC γ-austenite → BCC α′-martensite or FCC γ-austenite → HCP ε-martensite → BCC α′-martensite sequence exists. Processing parameters such as the temperature, state of stress, chemical composition, stacking fault energy (SFE) and rate of deformation are reported to influence the amount of ε and α′–martensite formed [6,18]. SFE tends to play an important role in the stability of austenite since it controls the formation of shear bands and other DIM nucleation sites [19,49]. SFE ($\gamma$) itself depends on factors such as chemical composition and temperature [50] and can be estimated using Eqn. 2.6 (Brofman and Ansell [51]), Eqn. 2.7 (Schramm and Reed [52]), and Eqn. 2.8 (Rhodes and Thompson [53]).

$$\gamma = 16.7 + 2.1(\%Ni) - 0.9(\%Cr) + 26(\%C) \quad \ldots 2.6$$

$$\gamma = -53 + 6.2(\%Ni) + 0.7(\%Cr) + 3.2(\%Mn) + 9.3(\%Mo) \quad \ldots 2.7$$

$$\gamma = 1.2 + 1.4(\%Ni) + 0.6(\%Cr) + 17.7(\%Mn) - 44.7(\%Si) \quad \ldots 2.8$$

Generally, TRIP becomes the dominant operative deformation mechanisms in stainless steels when the SFE is below 18 mJm$^{-2}$ [54]. The decrease in temperature can cause a drop in SFE, which in turn, raises the chemical driving force (i.e. variation in the chemical free-energy difference between the austenite and α′-martensite phases) for the phase transformation. Similarly, increasing the temperature leads to an increase in SFE and thus nucleation sites for the α′ -martensite decrease

[49]. Other relevant parameters to consider for the deformation-induced martensitic transformation are the deformation mode and the strain rate. Patel and Cohen [55] found uniaxial tension to be more beneficial for martensite formation than uniaxial compression or hydrostatic compression. Similarly, martensitic transformation is more favored at low strain rates than at high strain rates since the later will heat the sample and hinder martensitic transformation [43]. Eskandari *et al.* [18] observed that cross-rolling increased the volume fraction of martensite formed in cold rolled plates than the conventional unidirectional rolling since the former results in increase of intersections of shear bands that are preferential sites for martensite nucleation [18].

In a previous study, the initial α′-martensite nucleus was reported to be coherent with the parent austenite [56], but there exited loss of coherency as the α′-martensite plate grew. On the other hand, ε-martensite remained coherent with the parent austenite. With enough driving force (i.e. decrease in Gibbs free energy), α′-martensite nucleus will rapidly grow as plates, which terminate at high angle grain boundaries or at other martensite plates. Therefore, prior austenite grain size is a factor that affects the growth of martensite plates. It should be noted that sometimes the martensite/austenite interface is not strong enough to prevent the growth of martensite, hence, the martensite continues to grow to form the martensite intersections [57]. Deformation-induced phase transformation occurs by two mechanisms: strain-induced and stress-assisted/induced phase transformation. Strain-induced martensite is known to occur at the intersection of shear bands [58]. This is because shear strains imposed by these intersections promote atomic arrangement that favors the nucleation of α′ [59]. Shear band in this context is a collective term for the planar defects that form due to the overlapping of stacking faults (formed by the dissociation of perfect dislocations into Shockley partial dislocations during plastic deformation) on austenite {111} planes during plastic deformation [19]. This shear band could be an intersecting ε-martensite or twin band depending on the overlapping process of stacking faults. An ε-martensite is formed if the intrinsic stacking faults overlap regularly on every second {111} plane, while mechanical twin will develop by overlapping three stacking faults on successive {111} plane [60]. The formation of ε-martensite and twin and their respective bands are schematically shown in Fig. 2.4. Figure 2.4a shows an isolated stacking fault of width, $r_i$, that forms on a {111} plane from the dissociation of a perfect dislocation under an applied stress. The size of the stacking fault increases with applied stress until a critical width, $r_i^*$, is reached as shown in Fig. 2.4b. A number of stacking faults, $n_i$ [n is 1 and 3 for ε (Fig. 2.4b) and twin (Fig. 2.4c), respectively], overlap in adjacent {111} planes

to form an embryo with a critical width $r_i^*$ and length $l_i^*$. The length of the embryo, $l_i$, then increases and propagates through the grain interiors by subsequent overlapping of stacking faults in adjacent planes (Fig. 2.4d). Once the structure is fully formed, its width $w_i$ increases by forming adjacent embryos of constant width, $r_i^*$ [$w_i$=$r_i^*\hat{N}_\iota$, where $\hat{N}_\iota$ is the number of embro in a band] as shown in Fig. 2.4e. Finally, the increase in ε/twinning volume fraction increases by the formation and overlapping of new embryos in various locations of a grain, leading to the formation of micro-bands (Fig. 2.4f).

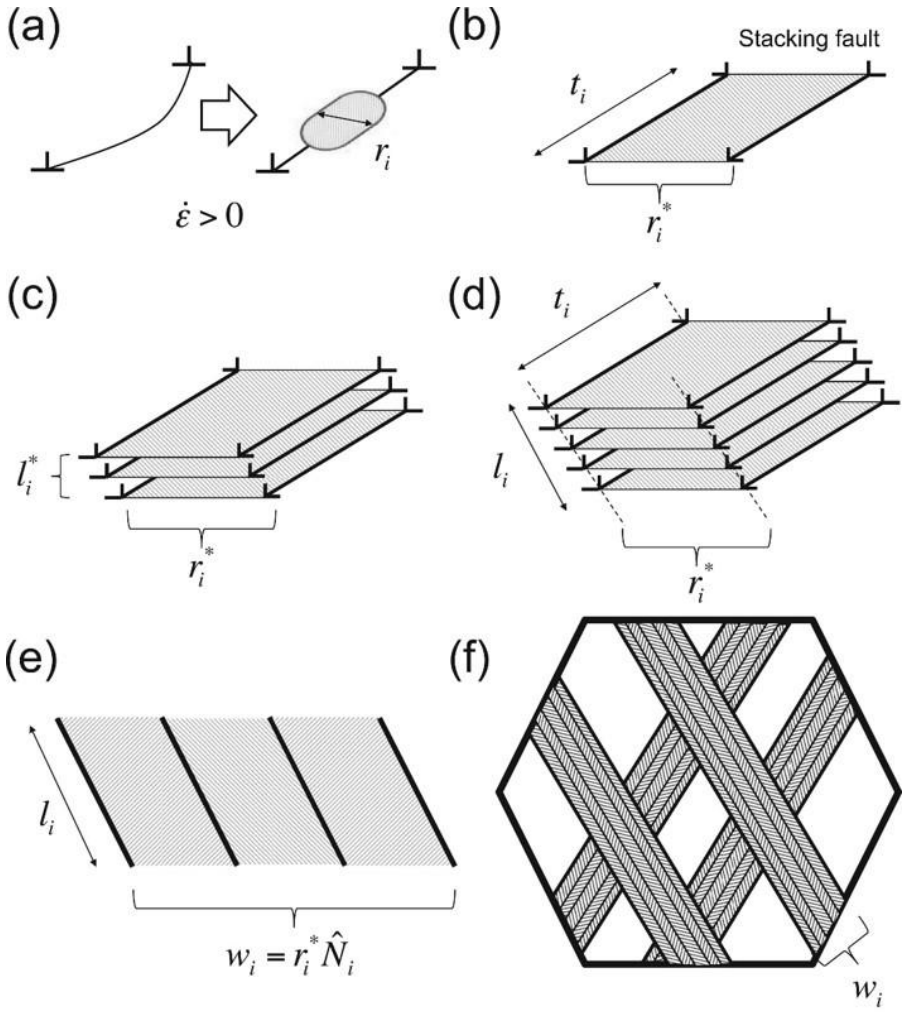


Fig. 2.4. Schematic diagrams of the mechanism of ε and twin formation and the formation of their respective band [60].

Stress-assisted phase transformation nucleation occurs predominantly at γ grain boundaries [59]. In summary, while the nucleation of strain-induced α′ need the creation of new embryos such as the intersection of ε bands or the intersection of an ε band with a twin in the parent austenite by

plastic deformation, the nucleation of stress-assisted α′ occurs at the grain boundaries with no need for new nucleation sites [58] as shown in Fig. 2.4. The result in Fig. 2.5 [61] also shows that α′ developed via both strain-induced and stress-assisted mechanisms in coarse-grained stainless steel while stress-assisted was the dominant mechanism in UFG specimen.

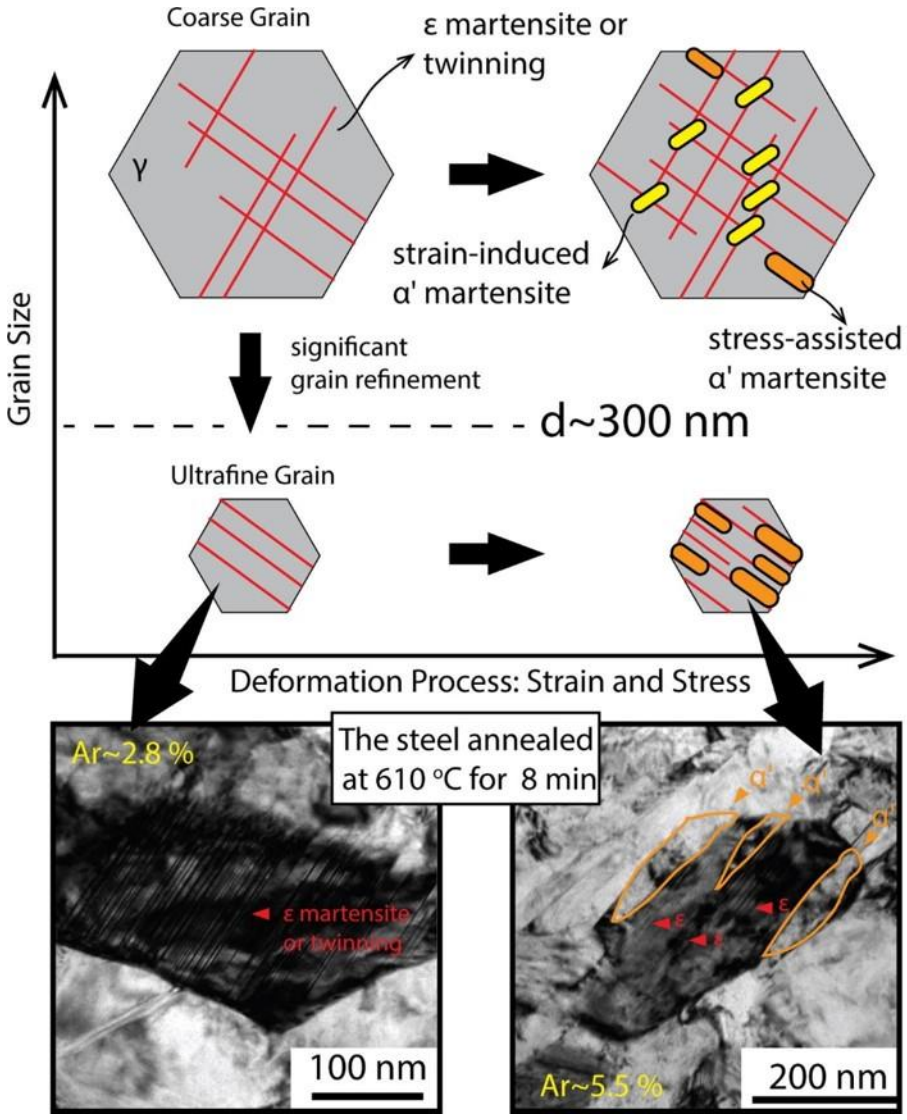


Fig. 2.5. Schematic diagram and TEM micrographs of deformed stainless steel showing the relationship between grain size and mechanism of deformation-induced martensite [61].

## 2.3 Deformation twinning in stainless steels

Deformation twinning occurs in most austenitic stainless steels during plastic deformation. This leads to a phenomenon termed twinning-induced plasticity (TWIP). Apart from the 300 series ASS, special type of austenitic stainless steel that exhibits TWIP effect is the high Mn TWIP steels

that contain up to 25-35 wt% Mn with a minor addition of Al and Si [62]. They are attractive material for structural applications due to their unique ability to offer combine strength (up to 800 MPa) and ductility (up to 95%) [63]. Although different mechanisms have been proposed, as they are well documented by Cooman *et al.* [64], the development of deformation twins is generally a process that proceeds by dislocation mechanism [65]. One of the accepted formation mechanisms of deformation twinning is already discussed in Section 2.2.2 since it is quite similar to that of HCP ε-martensite [63] as shown in Fig. 2.4. As previously indicated, the operative deformation mechanisms in metals are strongly influenced by their SFE [66]. It is reported that deformation twinning will dominate at a SFE in the 18 - 35 $mJm^{-2}$ range while slip occurs above 35 $mJm^{-2}$ [54]. Regardless of the dominant deformation mechanisms, be it phase transformation or twinning, plastic deformation by slip of dislocations will still occur [67]. Deformation twins act as sub-boundary-like obstacles to dislocation motion; leading to Hall–Petch-type strengthening of the twinned-metal [68]. This phenomenon is termed dynamic Hall–Petch effect [69] since twins nucleate as deformation proceeds and simultaneously resulting in a continuous grain refinement. Hence, the dislocation mean-free path is reduced and significant hardening rate is generated.

Twinning stress, which is a combination of stresses required to nucleate and grow twins, is a necessary requirement to generate deformation twinning. The determination of the stress to nucleate a deformation twin is experimentally difficult [70]. As such, it is considered that the twinning stress determined experimentally is the stress required for twin growth. The assumption is that twin nuclei already exist within the metal, e.g. stacking faults [65]. Despite the experimental difficulty involved in determining twin nucleation stress, Rahman [65] determined the critical twin nucleation stress for an infinite grain size in a TWIP steel to be ~50 MPa, which increases with decrease in grain size (i.e. twinning becomes more difficult in fine grains). However, Bouaziz et al. [71] reported that twin nucleation stress is independent of grain size (in the grain size range of 1.3-25 $\mu m$ though). Classical twinning theories for determining the critical stress for twinning have been proposed and documented [64]. The $\sigma_{twin}$ proposed by Byun [72] in terms of uniaxial stress is expressed in Eqn. 2.9 as a function of SFE and Burgers vector.

$$\sigma_{twin} = 6.14\ (\Gamma/b) \qquad \ldots 2.9$$

where $\Gamma$ is the SFE and $b$ is the Burgers vector of the Shockley partials. Therefore, it implies that high SFE and/or low $b$ will result in high critical true stress for mechanical twinning (i.e. nucleation of twins become more difficult). Other factors that may influence the evolution of deformation twinning are temperature, strain rate, level of pre-strain, specimen and/or grain size, specimen crystallographic texture, alloy composition, precipitates, etc. [70]. Some of these factors are interdependent and difficult to separate.

## 2.4 Mechanical behaviour of austenitic stainless steels

One of the very important factors that influence the mechanical behavior of metals, including the austenitic stainless steels, is the strain rate at which they are deformed. By classification, strain rates below $10^{-6}$ $s^{-1}$ are in the *creep* domain while those at or below $10^{-3}$ $s^{-1}$ represent *quasi-static* deformation conditions. Strain rates above $10^{2}$ $s^{-1}$ are classified as *high strain rates*, above $10^{4}$ $s^{-1}$ are called *very high strain rates*, and strain rates above $10^{6}$ $s^{-1}$ are called *ultra high strain rates* deformation conditions [73]. For the purpose of this thesis, only the mechanical behavior of austenitic stainless steel under *quasi-static* and *high strain rates* deformation conditions are discussed further in Sections 2.4.1 and 2.4.2, respectively. Unlike the behavior under quasi-static condition where strain hardening dominates, plastic deformation in metals under dynamic impact loading is a complex phenomenon that is characterized by the competition between strain hardening and thermal softening. The thermal softening results from the conversion of impact energy to thermal energy, leading to a temperature rise in the impacted specimens [74]. It was suggested that 90 % of the kinetic energy of the striking projectile is converted to thermal energy [75]. The extent of thermal softening in a deformed specimen is influenced by this temperature rise, which can be estimated from the stress-strain data using Eqns. 2.6 [76].

$$T - T_o = \Delta T = \frac{\beta W_p}{\rho . C_v} \qquad \ldots 2.6$$

where $T_o$ and T are the temperatures of the specimen before and after high strain-rate deformation, $\beta$ is the fraction of plastic work that is converted into heat (assumed to be 0.9) and it is referred to as the Taylor-Quinney parameter (Eqn. 2.7-a), $C_v$ is the specific heat capacity, $\rho$ is the density and $W_p$ is the plastic work of deformation which is expressed in Eqn. 2.7-b.

$$\beta = \frac{Q_p}{W_p} \quad \ldots 2.7\text{-a}$$

$$W_p = \int \sigma \, . \, d\varepsilon \quad \ldots 2.7\text{-b}$$

where $Q_p$, σ and ε are the heat converted from plastic work, stress and strain, respectively. The general description of deformation behavior in metals under different loading condition is illustrated in Fig. 2.6 [77]. Under quasi-static loading conditions where the temperature rise in specimen is negligible, deformed specimen exhibits continuous hardening to large strain in the stress-strain curve until the material fractures as shown in Fig. 2.6. Under dynamic loading conditions where the plastic work heats up the deformed metal, the flow stress first hardens up to a peak value $\gamma_{\text{max stress}}$, followed by strain softening (the "adiabatic" curve on Fig. 2.6). Still under the dynamic loading condition, a localized thermal softening may become extreme resulting in stress collapse that culminates to strain localization (the "localization" curve in Fig. 2.6).

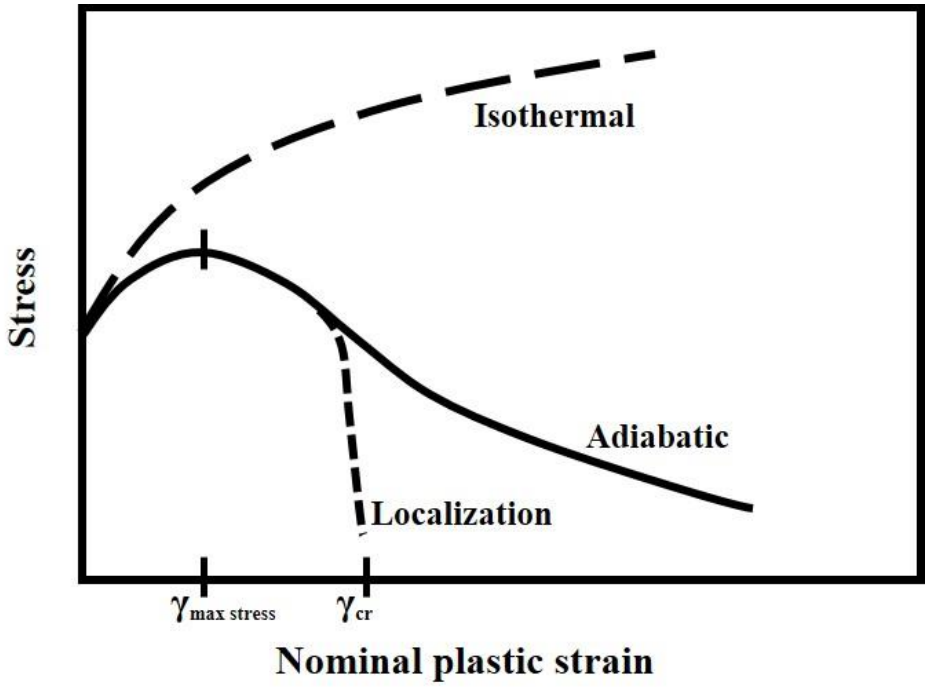


Fig. 2.6. Shear stress-nominal shear strain plot for a typical work-hardening material [77].

### 2.4.1 Under quasi-static condition

As previously mentioned, the temperature rise in a specimen under quasi-static loading conditions is negligible. The implication of this for austenitic stainless steels is that the transformation of the

metastable austenite phase to martensite during plastic deformation can be spontaneous without being influenced by temperature rise within the specimen. It has been reported that martensitic phase transformation occurred in AISI 304 stainless steel under tensile load at room temperature, but was suppressed at 75 ℃ [78]. The authors concluded that the presence of martensite increased the hardening rate in the specimens deformed at room temperature. The tensile deformation of selected stainless steel grades showed a decrease in deformation-induced martensite with increase in alloying content, temperature, strain rate (within the low strain rate regime) and SFE [19]. At room to cryogenic temperatures and at different strain rates also within the low strain rate regime, selected 300 series stainless steel showed an increase in yield strength and a decrease in fracture strain as the deformation temperature decreased [79]. Meanwhile, yield strength and fracture strain increased and decreased with increased strain rate, respectively. The evolution of deformation twinning in a high Mn austenitic TWIP steel under tensile load became more difficult as the grain size decreases [80]. Similarly, finite element simulation of AISI 304 ASS under uniaxial tension shows the activation and suppression of twinning in coarse and ultrafine-grained structures, respectively, while experimental results confirm the suppression of both the deformation twinning and martensitic phase transformation by grain refinement [81]. The EBSD analysis of the same selected area provided evidence of de-twinning during an interrupted reverse tension-compression loading of a TWIP steel [62]. It was reported that all deformation twins formed during forward tension loading were removed upon subsequent reverse compression loading. On the role of texture [82], deformation twinning occurred in grains oriented near [111]||TD (tensile direction) where the twinning stress is larger than the slip stress.

### 2.4.2 Under dynamic condition

Unlike the quasi-static deformation condition, adiabatic heating in the specimen during dynamic deformation can influence the microstructure of the metal and by extension, its mechanical response during high strain-rate deformation. For instance, most austenitic stainless steels undergo martensitic phase transformation, and the fraction of transformed martensite can be different compared to those deformed under quasi-static condition. Under a compressive load, Sahu [83] also determined that the stability of austenite in austenitic stainless TWIP steels was low at lower strain rates, but phase transformation was suppressed during high-strain-rate deformation. The ease of α′-martensite formation and its suppression when adiabatic heating is not significant and

substantial, respectively, have also been reported during the dynamic deformation of AISI 304 steel [84]. The value of temperature rise in austenitic stainless steels calculated using Eqn. 2.6 is believed to be underestimated due to the generally-assumed value of β (0.9). In fact, there exists a variability of the value of β for austenitic steels that undergo deformation-induced martensitic transformation at high strain rates [85]. It is believed that latent heat released due to the exothermic nature of the martensitic transformation and the heat dissipated during the co-deformation of γ and α′ contributes to the source of heat that results in the temperature rise in impacted specimens [85]. This can influence the value of β.

The implication of the aforementioned sources of heat is that the temperature rise is tied to the austenite grain straining alone at the onset of loading (since no phase transformation will occur at this time). When martensitic transformation is activated as deformation continues, latent heat associated with the martensite transformation and the straining of α′ comes into play. Hence, $Q_p$ in Eqn. 2.7-a is the summation of heat converted from plastic work and the heat due to phase transformation. Therefore, the use of a constant value of 0.9 for β may lead to underestimation of the temperature rise in specimen. The temperature rise in a Fe-Cr-Ni austenitic stainless steel that was deformed under high strain rate condition (~5.8 x $10^5$ $s^{-1}$) was ~943 K [86]. For austenitic steels of different SFEs deformed in tension at strain rates ranging from the quasi-static to dynamic regime, Curtze [68] reported an upsurge in SFE at high strain rate due to adiabatic heating, which resulted in a drop in the suppression of deformation twin evolution. Other authors [87] have also reported the important role adiabatic heating play on the SFE of austenitic stainless steels. The dynamic mechanical behavior of high-Mn austenitic stainless steel specimens is different from those deformed under quasi-static condition. While strain-hardening that is followed by a strain softening is characteristic of the stress-strain curves of the specimens deformed under dynamic condition, curves of specimens deformed under quasi-static condition only show strain hardening due to negligible rise in specimen's temperature [88].

## 2.5 Dynamic failure mode in metals

Usually, the mode of deformation in metals exposed to high strain-rate loading condition is associated with formation of a thermally-assisted shear strain localization called adiabatic shear band (ASB). ASB is a narrow shear zone which is a preferential site for dynamic failure/fracture [89,90]. The intense shear strain localization is due to loss of load carrying-capacity from thermal

softening in the region of intense adiabatic heating. Zener and Hollomon [91] ascribed their occurrence to a competition between strain hardening and thermal softening. ASBs develop rapidly in impacted specimen due to lack of time for thermal diffusion such that the specimen which undergoes localized instantaneous heating is rapidly cooled by the relatively cool matrix around the ASB [92]. This suppresses work hardening and promotes localized softening [93]. Examples of dynamic loading conditions that metals can be exposed to are, ballistic or hypervelocity impact, friction stir welding, forging [90], high speed machining/cutting [94], dynamic punch test, explosive loading, shaped charge jet, torsion rolling, explosive welding, etc. [95,96].

### 2.5.1 Initiation and propagation mechanisms of adiabatic shear band

Several mechanisms for the initiation of ASB have been proposed, some of which are summarized in Fig. 2.7. These are grain-scale microstructural initiation mechanisms in single-phase homogeneous materials [97]. Figure 2.7a suggests that large grains in materials containing varying grain sizes will plastically deform at the expense of the small grains such that the large grains become initiation sites for shear bands. This is because the large grain exhibits low yield stress ($\sigma_1$) while the small grain possesses high yield stress ($\sigma_2$) in agreement with the Hall-Petch equation. The second possible mechanism (Fig. 2.7b) is related to the tendency for ASBs to initiate from localized softened grains that are caused by grain rotation. The increase in Schmid factor of a plastically deformed grain can also cause localized softening that have the propensity to initiate shear band. This mechanism suggests that localized deformation of one grain can propagate along a band as shown in Fig. 2.7c. Pierce et al. [98] and Anand and Kalidindi [99] modelled the mechanism of localization through cooperative plastic deformation between participating grains that supports model presented in Fig. 2.7c. Armstrong and Zerilli [100] also proposed another mechanism that is shown in Fig. 2.7d. The mechanism suggests that local temperature rise and necessary plastic deformation can be generated to initiate ASB when dislocation pile-up bursts through a grain boundary. In all, the initiation of shear band is an inherent and natural outcome of large deformation processes which is related to the concurrent evolution of crystallographic texture [99]. Due to these complexities of ASB being more of a physical phenomenon than most other failure modes in engineering materials, numerical simulations have been proposed to be the most efficient way to study shear band propagation [101].

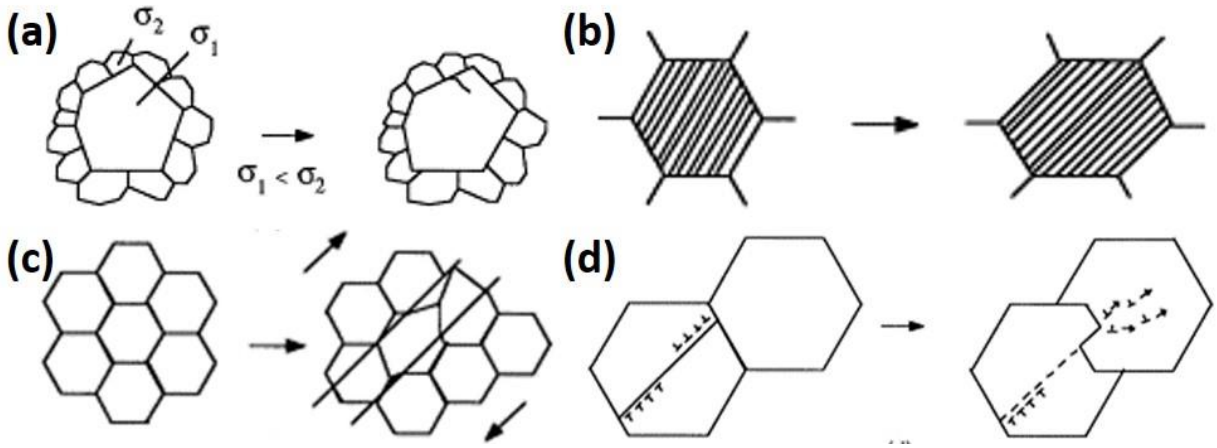


Fig. 2.7. Possible shear-band initiation mechanisms in single-phase homogeneous materials. (a) grain-size inhomogeneity, (b) geometrical softening, (c) Peirce–Asaro–Needleman textural localization and (d) dislocation pile-up release [97].

### 2.5.2 Types of ASB and their microstructural features

It has been established that the formation of ASBs, which are characteristics of high strain rate deformation in a metal, is a precursor to the dynamic fracture of the metal. There are two type ASB: the deformed shear band (DSB) and transformed shear band (TSB) [95,102]. The onset of DSB and TSB in a metal depends on the critical strain and strain rates at which it is deformed [56]. The DSB contains elongated and distorted grains that develop at a lower critical strain and strain rates than the critical values at which TSB is formed [92,102]. This implies that TSBs are transformed DSBs and, in most cases, TSBs are flanked by DSBs; a hint that DSB is a precursor to TSB. TSBs on the other hand, are characterized by ultra-fine equiaxed grains formed as a result of dynamic recovery (DRV) or dynamic recrystallization (DRX) [92,96,102]. The hardness profile across a TSB showed higher microhardness values in the TSB than the matrix [103,104], which is attributed to grain refinement. Besides DRV and DRX, other microstructural changes such as phase transformations [105,106], melting and amorphization [93,107] and carbide fragmentation and redistribution [108] have been reported to occur within the TSB.

### 2.5.3 Dynamic recovery and dynamic recrystallization

It has been postulated that the formation and propagation of ASB (in this case, the TSB-type) is directly related to and dictated by the occurrence of DRX inside the TSB [101]. In fact, the formation and propagation of TSB are sometimes described by the onset conditions of DRX inside the TSB. To this end, it becomes necessary to understand the mechanism of DRX inside the TSB.

The occurrence of DRX is usually preceded by DRV. DRV is a microstructural softening process that is characterized by the presence of lamellar boundaries and are usually observed at the interface between the inside and outside TSB region [109]. It involves the rearrangement of dislocation into a more energetically favorable configuration referred to as subgrain or cell structure. The cells are characterized by heavily dislocated boundaries with comparable orientation as the parent grains. As strain rate increases, subgrain size decreases but the misorientation between them increases [110]. The mechanism of recovery as schematically shown in Fig. 2.8a includes the annihilation of point defects such as vacancies and interstitials by diffusion to sinks (dislocations). This is followed by dislocation annihilation by attraction of mobile dislocations of opposite sign; a process promoted by temperature rise in specimen during deformation (Fig. 2.8a1 and a2). The next is the polygonization stage that involves the coordination of free, random dislocations into dislocation walls/sub-boundaries (Fig. 2.8a3). The sub-boundary walls eventually coalesce as subgrain grows (Fig. 2.8a4).

Over the years, researchers have proposed several mechanisms of DRX in TSB. However, Derby [111] classified the mechanism of DRX into migrational and rotational. While the migrational DRX (MDRX) mechanism involves diffusion and develops by nucleation and growth of recrystallized grains, rotational DRX (RDRX) is completed through self-rotation of subgrains [94]. Since the time of formation of TSB is extremely short, MDRX mechanism is not capable of explaining the equiaxed ultrafine grain (UFG) structure in TSB. The most accepted RDRX mechanism (that involves concurrent plastic deformation) model for explaining equiaxed UFG structure in TSB is proposed by Nesterenko *et al.* [112] as schematically shown in Fig. 2.8b. The first stage (Fig. 2.8b1) is the accumulation of random and homogenously distributed dislocations. This dislocation re-arranges to elongated dislocation cells as shown in Fig. 2.8b2. The elongated dislocation cells transform into elongated subgrains of fine boundaries (Fig. 2.8b3) as deformation proceeds. Figures 2.8b1-b3 completes a dynamic recovery process that is synonymous to the description in Fig. 2.8a. As deformation proceeds further, subgrains disintegrate into equiaxed subgrains because of the interfacial energy minimization (Fig. 2.8b4). The equiaxed subgrains are then rotated to complete the evolution of DRXed UFGs (Fig. 2.8b5). Using crystal plasticity theory, some authors have proposed another feasible model called the progressive subgrain misorientation recrystallization whose detailed description can be found in Ref. [110].

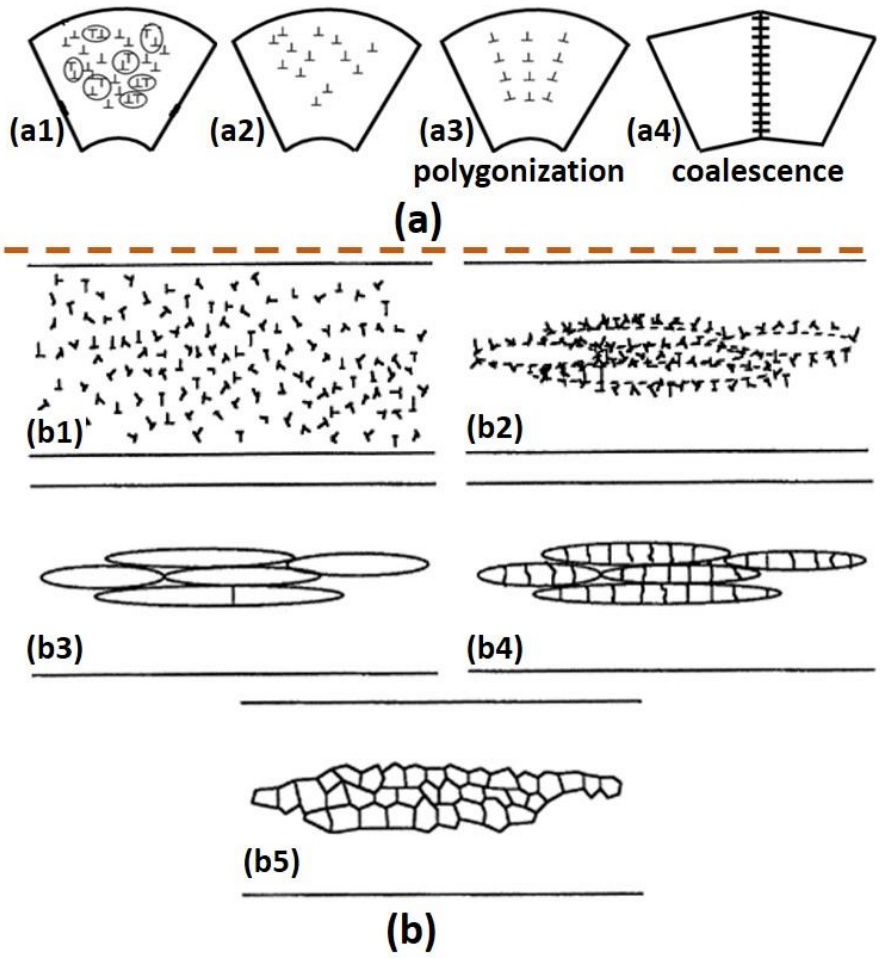


Fig. 2.8. Schematic diagrams of (a) dynamic recovery (successive dislocation annihilation mechanism) [113] and (b) dynamic recrystallization [112] mechanisms.

## 2.6 Dynamic fracture mechanism in impacted metals

The formation of ASBs in shock-loaded specimens is often precursors to ductile fracture i.e. ASBs serve as potential sites for crack initiation and propagation [90,114,115]. Due to the condition for formation, DSB is usually first formed in an impacted specimen, followed by the TSB as previously described. As shear strain localization becomes intense, crack is then initiated and propagated through the TSB [116,117]. A typical micrograph showing the two types of shear bands are presented in Fig. 2.9 [118]. The mechanism of crack initiation and propagation in TSB that leads to dynamic fracture of impacted metals is generally reported to proceeds in five sequential steps [119,120]. As shown in Fig. 2.10, these steps includes; (i) the formation of micro-voids in TSB, (ii) amalgamation of the micro-voids to form elongated void-clusters, (iii) initiation of fine micro- cracks from opposite ends of the elongated void-clusters, (iv) growth and interconnection

of adjacent micro-cracks, and (v) crack propagation to dynamic failure. Several mechanisms have been reported to play a role in the nucleation of micro-voids in TSB. They include the presence of second phase particles [118,121], the existence of stress gradient between the inside and outside TSB that tends to generate tensile stresses, the vacancy accumulation at a high-stress region, void nucleation at the head of dislocation pile-ups and grain boundary sliding [119].

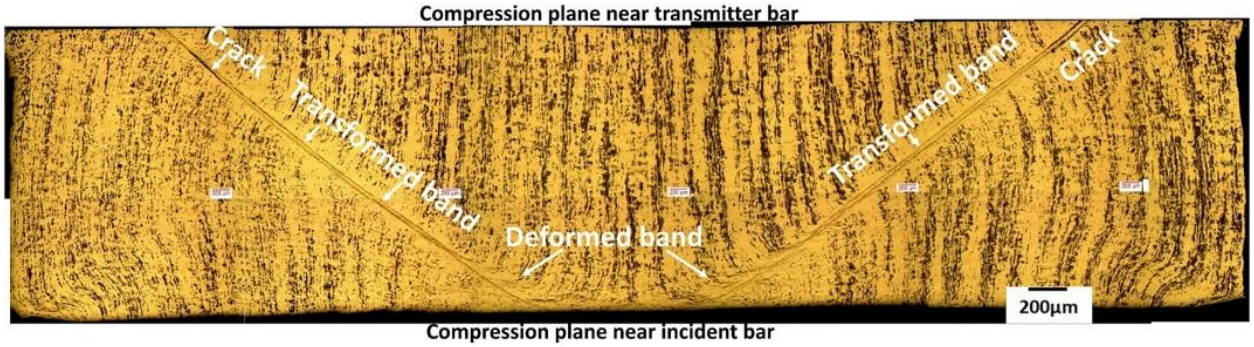


Fig. 2.9. Optical micrograph showing crack initiated and propagated along a transformed shear band on the longitudinal section of an impacted AA 2017-T451 specimen [118].

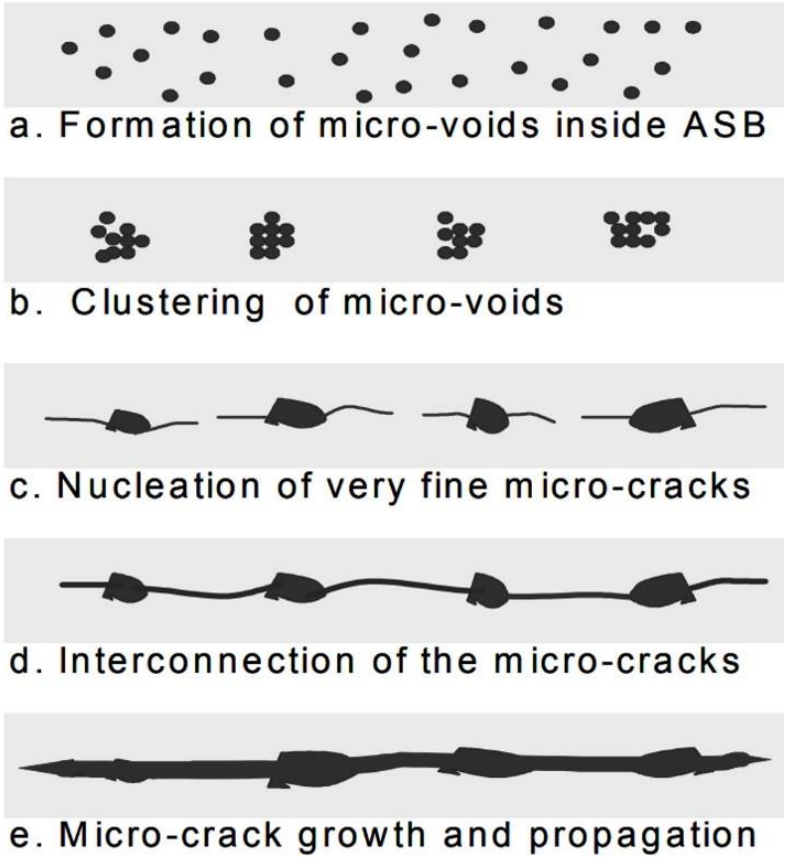


Fig. 2.10. Microstructural model for crack initiation and propagation inside TSB [120].

## 2.7 Summary

This chapter is a comprehensive review of previous studies on stainless steels and their applications. It highlights the composition of stainless steels and specifically, the composition of AISI 321 stainless steel, its intended applications, and the current hindrances to its widespread applications. The review of the literature affirms that AISI 321 stainless steel is not well-studied, neither is its response to external loadings well-understood. There is a need to improve the mechanical strength of AISI 321 steel to expand its use to other structural applications, where low mechanical strength hinders their use. It is very important that whatever strengthening method is adopted for AISI 321 steel, it must not adversely affect the excellent corrosion resistance of the steel. It is, therefore, not clear in the literature how strengthening by grain refinement will affect both the mechanical and corrosion properties of AISI 321 steel. That is the focus of this PhD research study.

# Chapter 3

## Materials and Methodology

In this chapter, the material and methods used for developing ultrafine grain (UFG) structure and microstructural characterization are presented. The procedure for determining the mechanical properties of the as-received and refined alloy using hardness test, quasi-static compressive and dynamic impact tests are discussed. This chapter also contains detailed information on the materials' characterization using optical and scanning electron microscopy, transmission electron microscopy (TEM), energy dispersive spectroscopy (EDS), electron-backscattered diffractometry (EBSD), X-ray diffractometry (XRD) and Feritscope. The procedure for electrochemical corrosion tests is also discussed in details.

### 3.1 Materials

The nominal composition of the AISI 321 austenitic stainless steel used in this study is presented in Table 2.1. The investigated alloy was received from SANDMEYER steel company, PA, USA, in the form of a hot-rolled plate, 25.4 mm thick, as schematically shown in Fig. 3.1. The mechanical data are presented in Table 3.1 while the packing list and certified material test report can be found in APPENDIX B. The average grain size of the as-received steel is 37 μm on the ND-TD plane. The optical micrographs in Fig. 3.1 shows the as-received alloy is characterized by microstructural inhomogeneity across sample thickness; forming banding at mid-thickness.

Table 3.1. Mechanical data of AISI 321 austenitic stainless steel provided by supplier.

| Yield strength | Tensile strength | %Elongation | Hardness |
|---|---|---|---|
| 242 MPa | 554 | 47% in 51 mm | RB 80 |

### 3.2 Solution heat treatment and cryo-rolling procedures

Before rolling, the alloy was solution treated by soaking at 1373 K (1100 ℃) for 30 minutes in a benchtop Muffle furnace (Fig. 3.2a), followed by quenching to room temperature in water to achieve chemical homogeneity. In a previous study [122], no additional formation of martensite was observed when a cold-formed austenitic stainless steel specimen was exposed to a cryogenic temperature, whereas prior exposure to cryogenic temperature before rolling led to a substantial

formation of martensite. Therefore, the solution treated sample was initially soaked in liquid nitrogen for 25 minutes, followed by multi-pass unidirectional rolling using a STANAT rolling

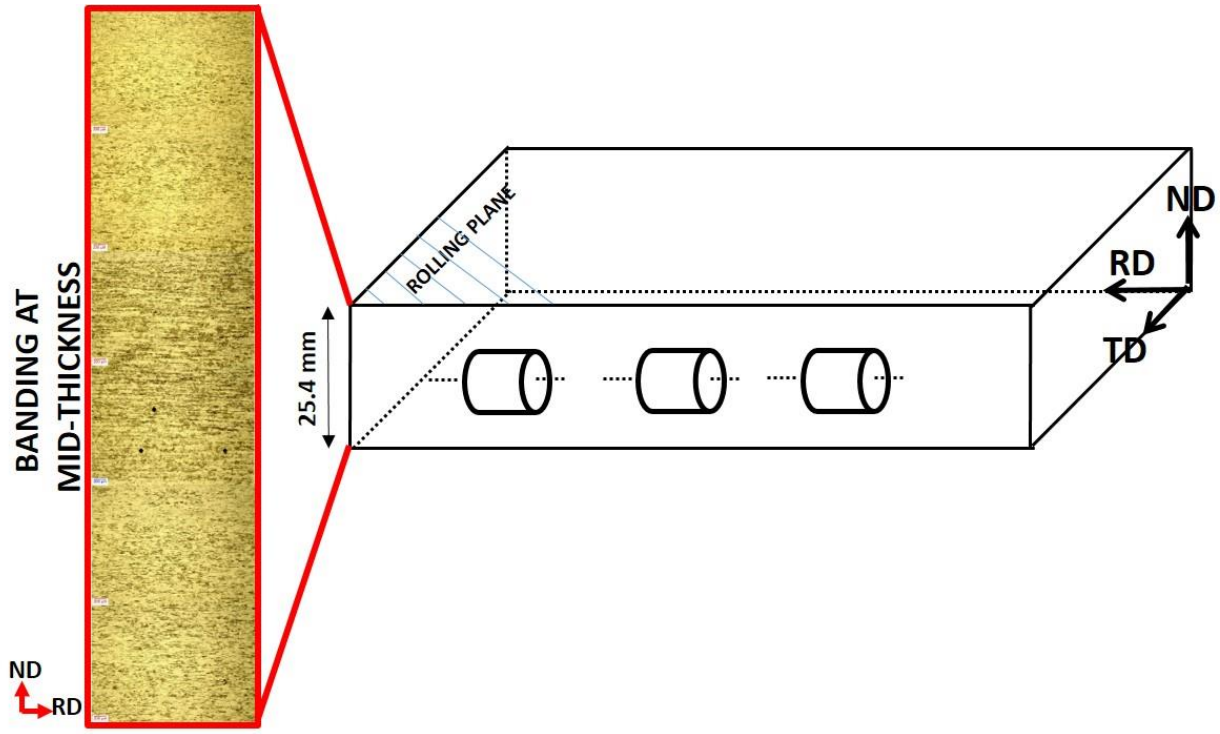


Fig. 3.1. Schematic drawing showing AISI 321 austenitic stainless steel plate whose rolling direction (RD) is parallel to the axis of the cylindrical compression test specimen. The exploded view is the optical micrographs showing microstructural inhomogeneity across sample thickness (i.e. banding at mid-thickness).

mill (Fig. 3.2b). The steel specimen was intermittently re-soaked to avoid temperature rise during the multiple pass rolling. A previous work [123] on AISI 301 stainless steel showed that rolling at 77 K to 20% thickness reduction resulted in the saturation of BCC martensitic phase in the steel. Therefore, it is expected that the cryo-rolling of AISI 321 steel at 77 K will nearly or completely transform the FCC-austenitic phase (γ) to BCC-martensite (α′) at 20% thickness reduction (r20). To obtain complete transformation and crushing of α′-martensite, cryo-rolling of up to 50% thickness reduction (r50) was conducted on 105 mm x 33 mm x 11 mm plates till a final thickness of 5.5 mm was reached. The r50 cryo-rolled samples with saturated and crushed α′-martensite were reversed to austenite (γr) by annealing at 923 K (650 ℃), 973 K (700 ℃), 1023 K (750 ℃) and 1073 K (800 ℃) for 60-28800 s, 60-1800 s, 30-1200 s and 30-1800 s, respectively. Both benchtop Muffle furnace and the STANAT rolling mill are located in the material science lab, Engineering Building, University of Saskatchewan, Canada.

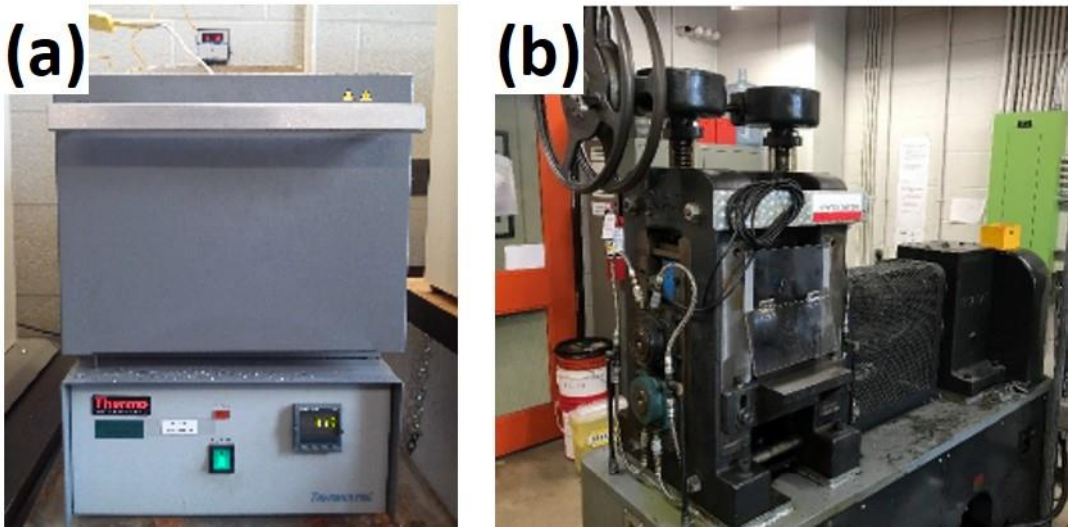

Fig. 3.2. Images of (a) benchtop Muffle furnace and (b) STANAT rolling mill.

## 3.3 Mechanical test

### 3.3.1 Hardness test

Microhardness tests were carried out using a Mitutoyo Micro Vickers hardness testing machine (MVK-H1). The specimens were subjected to a load of 1 kgf for 10 s. The test was repeated four more times in a sample. Common errors such as indenting close to the edge of specimens and/or to previous indents were avoided. The average values of five hardness measurements are reported for each specimen.

### 3.3.2 Quasi-static compression test

An Instron R5500 mechanical testing machine with a 150 kN load cell (Fig. 3.3) was used to determine the mechanical behaviour of the AISI 321 steel under low strain-rate compressive loading. Cylindrical specimens were deformed using a cross-head speed of 1 mm/min. The dimension of the specimens and the orientation of machining with respect the RD, TD, and ND of the alloy plate are specified in each of the chapters, where necessary. This cross-head speed generated an engineering strain rate of $4.2 \times 10^{-3}$ /s in the specimens. The tests were repeated under the same condition to ensure reproducibility of test data. All tests were carried out at room temperature. The contact surfaces between the test specimens and the platens of the testing machine were lubricated with Vaseline to minimize barreling caused by friction during compression.


Fig. 3.3. The Instron R5500 mechanical testing machine.

### 3.3.3 Dynamic Impact test

The dynamic impact test was conducted on the cylindrical specimens of the alloys using a split Hopkinson pressure bar (SHPB) system. The dimension of the specimens and the orientation of machining with respect the RD, TD, and ND of the alloy plate are specified in each of the chapters, where necessary. A schematic illustration of the SHPB system is presented in Fig. 3.4a. The equipment was designed and constructed by the College of Engineering machine shop at the University of Saskatchewan. The standard operating procedure (SOP) of the SHPB, can be found in Appendix A of Ref. [124]. The SHPB, as shown in Fig. 3.4b, consists of an incident and a transmitter bar of the same length (1500 mm, each). Strain gages are installed at the mid-length of each of the bars. Specimens are usually sandwiched between the two bars while a 2.04 kg striker, 38 mm in diameter and 225 mm long, fired by a light gun impact the incident bar. This process generates stress waves that propagate through the incident bar and captured as incident waves by strain gauge 1. Some portion of these waves is used to deform the specimen while part of the waves is reflected and captured as the reflected waves by the same strain gauge 1. The remaining waves propagate through the specimens to the transmitter bar and are captured as transmitted waves by the strain gage 2 mounted on the transmitter bar. The projectile, incident, and transmitted bars are

made of maraging steel (Mar C300). Further details on the working principles of SHPB system and the stress waves equations (Eqn. 3.1-3.3) used in generating engineering stress, strain, and strain rate data can be found in Ref. [125].

$$\sigma = \left(\frac{A_B}{A_S}\right) E_B \varepsilon_T \quad \ldots 3.1$$

$$\varepsilon = -2 \left(\frac{C_B}{L_S}\right) \int_0^t \varepsilon_R \, dt \quad \ldots 3.2$$

$$\dot{\varepsilon} = -2 \left(\frac{C_B}{L_S}\right) \varepsilon_R \quad \ldots 3.3$$

where $A_B$ and $A_S$ are cross-sectional areas of the bars and specimen respectively; $\varepsilon_T$ and $\varepsilon_R$ are transmitted and reflected strain pulses, respectively. $C_B$, $E_B$, $L_S$ and $t$ are the velocity of elastic waves in the bars, elastic modulus of the bar material, the initial length of specimen and deformation time, respectively. $C_B$ can be calculated using Eqn. 3.4.

$$C_B = \sqrt{E_B/\rho} \quad \ldots 3.4$$

where elastic modulus ($E_B$) for maraging steel is given as 180 GPa and density ($\rho$) is given as 7960 kg m$^{-3}$. $C_B$, when calculated, was approximately 4750 ms$^{-1}$. Alternatively, $C_B$ can be determined experimentally by striking the incident bar in contact with transmitted bar with no specimen in between them. $C_B$ is, therefore, determined using Eqn. 3.5 [125].

$$C_B = 2l/\Delta t \quad \ldots 3.5$$

where $l$ is half the length of the incident or transmitter bar; and $\Delta t$ is the time interval between the incident and reflected pulses when the bars are impacted by the striker. The $\sigma_T$, true strain ($\varepsilon_T$), and $\dot{\varepsilon}_T$ data were obtained using Eqns. 3.6-3.8 [126], respectively;

$$\sigma_T = \sigma[1 - \varepsilon] \quad \ldots 3.6$$

$$\varepsilon_T = -ln[1 - \varepsilon] \quad \ldots 3.7$$

$$\dot{\varepsilon}_T = \frac{\dot{\varepsilon}}{1-\varepsilon} \quad \ldots 3.8$$

However, average values of true strain rate were reported using $\dot{\varepsilon}_{Tavg} = \left(\int_{\varepsilon_{T1}}^{\varepsilon_{T2}} \dot{\varepsilon}_T d\varepsilon_T\right) / \varepsilon_{T2} - \varepsilon_{T1}$.

All tests were carried out at room temperature. The contact surfaces between the test specimens and bars of the SHPB system were lubricated with Vaseline to minimize barreling caused by friction during compression.

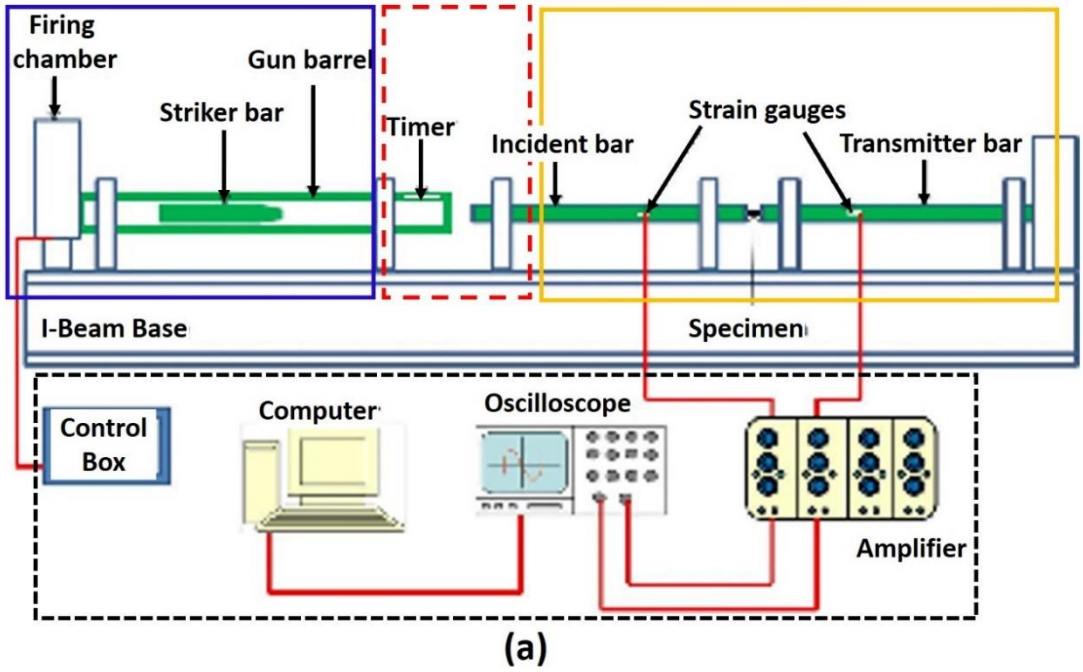


(a)

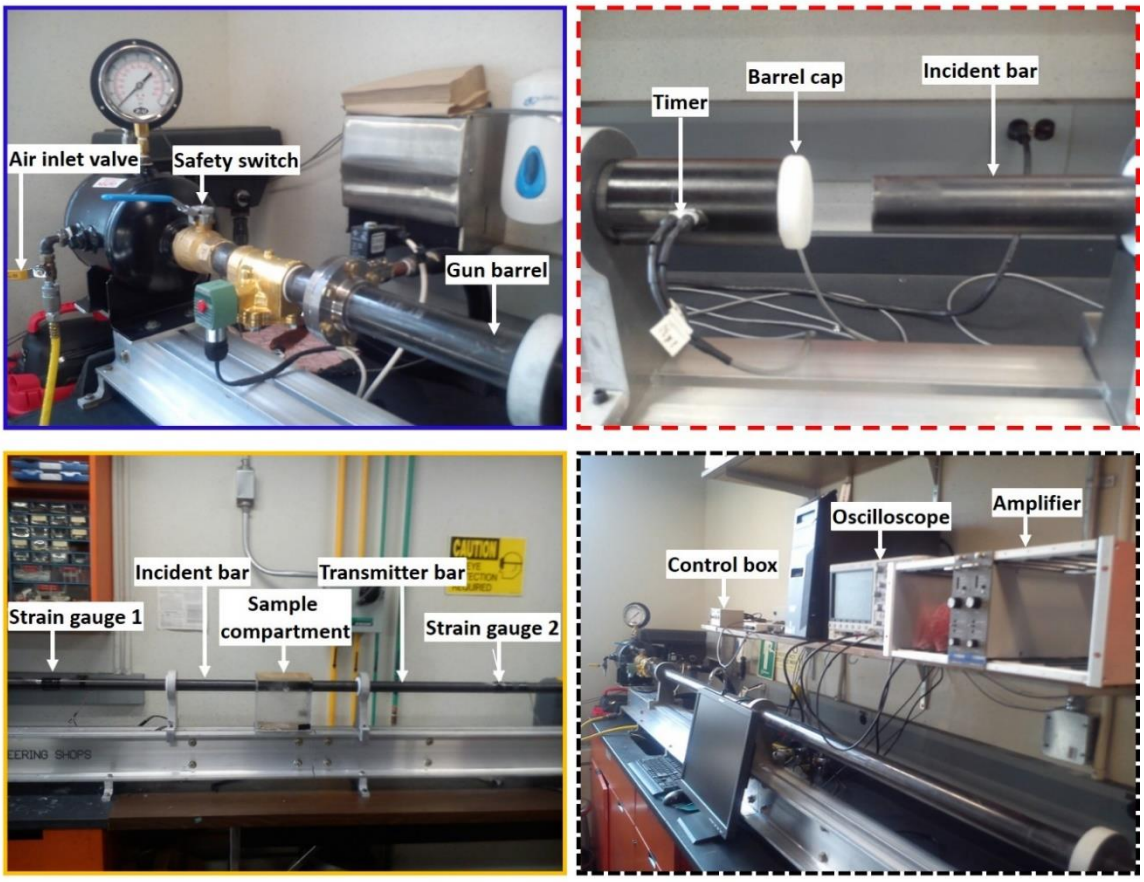


(b)

Fig. 3.4. (a) Schematic and (b) images of the split Hopkinson pressure bar system used in this study.

### 3.4 Electrochemical corrosion tests

All electrochemical corrosion tests in this study were conducted using an Interface 1000 potentiostat made by Gamry Instruments. Measurements were carried out in the order: open circuit potential ($E_{oc}$), electrochemical impedance spectroscopy (EIS) and Tafel polarization, using a three-electrode system as shown in Fig. 3.5. A graphite rod was utilized as the counter electrode while an Ag/AgCl (sat. KCl) reference electrode measured the magnitudes of electrical potentials within this work. These electrodes were connected to the potentiostat with a deformed or an undeformed specimen as the working electrodes. Before the test, a 30-minute equilibration time was allowed for each metal coupons exposed to the aerated corrosive solution (3.5 wt.% NaCl) at a defined exposed area (0.35 $cm^2$). EIS measurements were conducted by applying a 10-mV sinusoidal alternate low-voltage perturbation (peak-to-peak) with the frequency ranging from $10^4$ to 10 mHz, 10 points per decade at $E_{oc}$. The Tafel polarization test was conducted after the impedance measurements by applying an overpotential of ±250 mV from $E_{oc}$ at a scan rate of 0.5 mV $s^{-1}$. All the electrochemical measurements presented in this study are reproducible; results are representative of the multiple measurements.

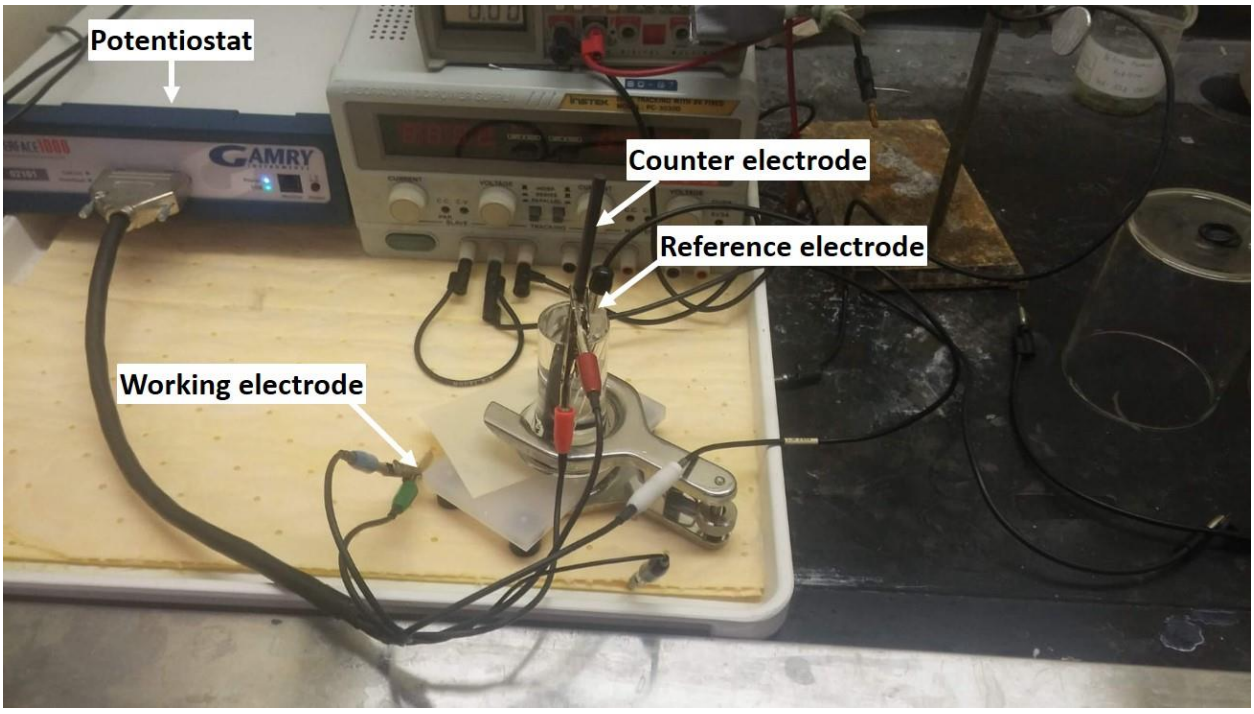


Fig. 3.5. Electrochemical corrosion test set-up.

## 3.5 Microstructural evaluation

### 3.5.1 Metallographic sample preparation

#### 3.5.1.1 Mechanical grinding and polishing

Microstructural evaluation of the alloy specimens before and after mechanical loading was preceded with metallographic sample preparation, which begins with cold-mounting of the specimens using acrylic resin (a mixture of VersoCit-2 powder and liquid in ratio 2:1) in a LECOMAT® pressure vessel. This was followed by pre-grinding, fine grinding and polishing (diamond and oxide) of the compression plane of the specimens to obtain a mirror surface finish. The 320 and 800 grade SiC emery papers were used for the pre-grinding stage while 9 µm MD-Largo cloth with 9 µm MD-Largo suspension were used for fine grinding. Diamond polishing was done using 3 µm MD-Mol with 3 µm MD-Mol suspension and 1 µm MD-Nap clothes with 1 µm MD-Nap suspension.

#### 3.5.1.2 Electrolytic polishing

Electrolytic polishing (electropolishing) was also used in metallographic sample preparation in this study. This technique is the reverse of electroplating. Electropolishing process involves ion by ion removal of metal from the surface of a work-piece through an electrochemical process [127]. It was conducted at room temperature by applying a potential of 32 V. The negative terminal (cathode) of a DC power supply was connected to a platinum wire while its positive terminal (anode) was connected to the work-piece (AISI 321 specimen). Both the platinum wire and the specimen to be polished were then submerged in an electrolyte as shown in the experimental set-up presented in Fig. 3.6a. The electrolyte used in this study was a mixture of 35% sulfuric acid, 45% orthophosphoric acid and 20% de-ionized water [127]. The EBSD phase maps of solution heat-treated AISI 321 stainless steel sample that was prepared by mechanical grinding and polishing (described in Section 3.5.1.1) and electropolishing are presented in Figs. 3.6b and c, respectively. The results show mechanically-ground and polished specimens experienced tremendous strain-induced martensitic phase transformation (Fig. 3.6b). In view of this, a combination of mechanical grinding with SiC papers (320, 800 and 1200 grits) and electropolishing for a minimum of 20 s was used in this study for metallographic sample preparation. The purpose of the electropolishing step was to eliminate roughness, residual strain,

and formation of strain-induced α′- or ε-martensite introduced on the surface of the specimen by mechanical grinding. The mechanical grinding of specimens using SiC paper up to 600 grits was sufficient for initial sample preparation prior to electropolishing [128].

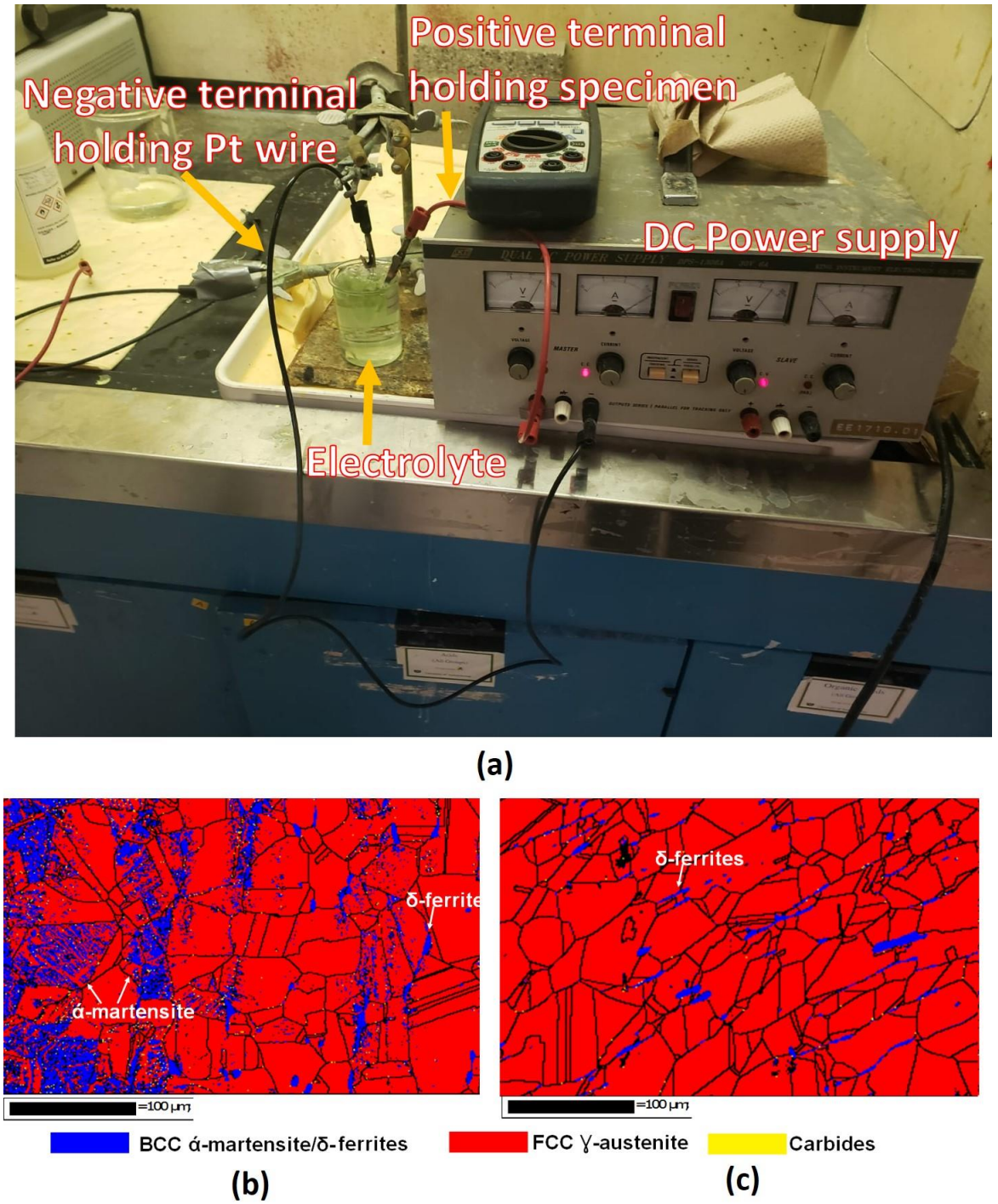


Fig. 3.6. (a) Electrolytic polishing set-up; EBSD phase maps of solution heat treated AISI 321 stainless steel sample that was (b) mechanically- and (c) electro-polished.

### 3.5.2 Optical microscopy

Polished specimens were etched using a mixture of 45 ml HCl, 15 ml $HNO_3$, 20 ml methanol for 45 s. Optical microscopy provided an overview of the microstructure of the specimens before investigating finer microstructural features using electron microscopy. Nikon MA100 inverted metallographic microscope with Pax-it! image analysis software (Fig. 3.7a) was used in this study.


Fig. 3.7. (a) Nikon MA100 inverted metallographic optical microscope and (b) SU 6600 Hitachi Field Emission scanning electron microscope that is coupled with EDS (Oxford X-Max Silicon Drift) and EBSD (Oxford Instruments Nordlys Nano EBSD) detectors.

### 3.5.3 Scanning Electron Microscopy (SEM), Energy Dispersive Spectroscopy (EDS) and Electron Backscattered Diffractometry (EBSD)

A Hitachi field emission SEM (model SU 6600) operating at an accelerating voltage of 20 keV was used in this study (Fig. 3.7b). This SEM is coupled with both Oxford X-Max Silicon Drift EDS and Oxford Instruments Nordlys Nano EBSD detectors. The EDS analytical technique was used for the elemental analyses of phases in the specimens. For microtexture evaluation of deformed and undeformed specimens, AZTEC 2.0 EBSD data acquisition software was used to acquire electron diffraction patterns with a binning of 4 × 4 pixels and step size of 30 - 400 nm. Raw data were post-processed using the Oxford Instrument's Channel 5 post processing software. This software helped to determine the grain orientation, grain boundary misorientations, Kernel average misorientation (KAM), Schmid factor (SF) and recrystallization fraction. Grain boundaries (GB) were defined as continuous regions of misorientation for misorientation angle ($\theta$) >5°. In this study, GBs with $5° < \theta < 15°$ are considered as low angle grain boundaries (LAGB) and $\theta > 15°$ as high angle grain boundaries (HAGB). In the recrystallization fraction analysis, $1^o <$

$\theta$ < 7.5° was the misorientation angle (θ) considered to separate subgrains while $\theta$ > 7.5° was considered to separate grains.

The KAM, which is a measure of local misorientation that indicates strain distribution in the specimen, is estimated as the average misorientation between each measured point in the EBSD scan and its neighbors. This is based on the condition that misorientations do not exceed 5° so as to exclude the effect of large misorientations related to the presence of grain boundaries [67]. The higher the local misorientation in a microstructure, the higher the accumulated strain. EBSD SF map associated with different grain orientations is plotted using active slip systems {111}<1-10>, {110}<-111> and {0001}<11-20>, for FCC γ, BCC α′ and HCP ε phases, respectively, along the z-compression direction of the test specimens. The Schmid factor indicates which of the grains or crystallographic orientation experiences higher or lower resolved shear stress during compression [129]. To avoid misinterpretation of results, post-processed EBSD data with no noise reduction was reported in this study since nano-sized titanium carbides (TiC) precipitates were removed after noise reduction. The average grain size of a phase was measured as the average of the diameter of all the grains of that phase in the map. The grain size diameter was obtained from the diameter of a circle that has the same area of the grain. The area of a grain was obtained from the number of data points in the grain multiplied by their pixel size.

### 3.5.4 X-ray diffractometry (XRD) and Feritscope

Figure 3.8 shows the Bruker D8 Discover diffractometer with Cr Kα radiation that was used to carry out X-ray phase identification and macrotexture measurements. The diffraction pattern was collected between 10° and 110° for 2θ. This is to ensure that all available peaks in the range of the detector's geometric limits are captured. For processing the raw XRD texture data, (111) and (200) incomplete pole figures were collected for the austenitic phase, and (110) and (200) for martensitic phase. The orientation distribution functions (ODFs) were then constructed from the obtained incomplete pole figures using Resmat software. The quantitative volume fraction of BCC α′ phase was obtained using a Feritscope MP30E. This device was originally designed to measure δ-ferrite content in austenitic stainless steel weldments. Since both δ-ferrite and α′ phase are BCC in structure, the actual α′ content can be determined by multiplying the feritscope reading by a correction factor of 1.7. The correction factor was experimentally determined by Talonen et al.

[130]. The advantage this device has is in its ability to measure α′ *in situ* and it is a non-destructive technique.

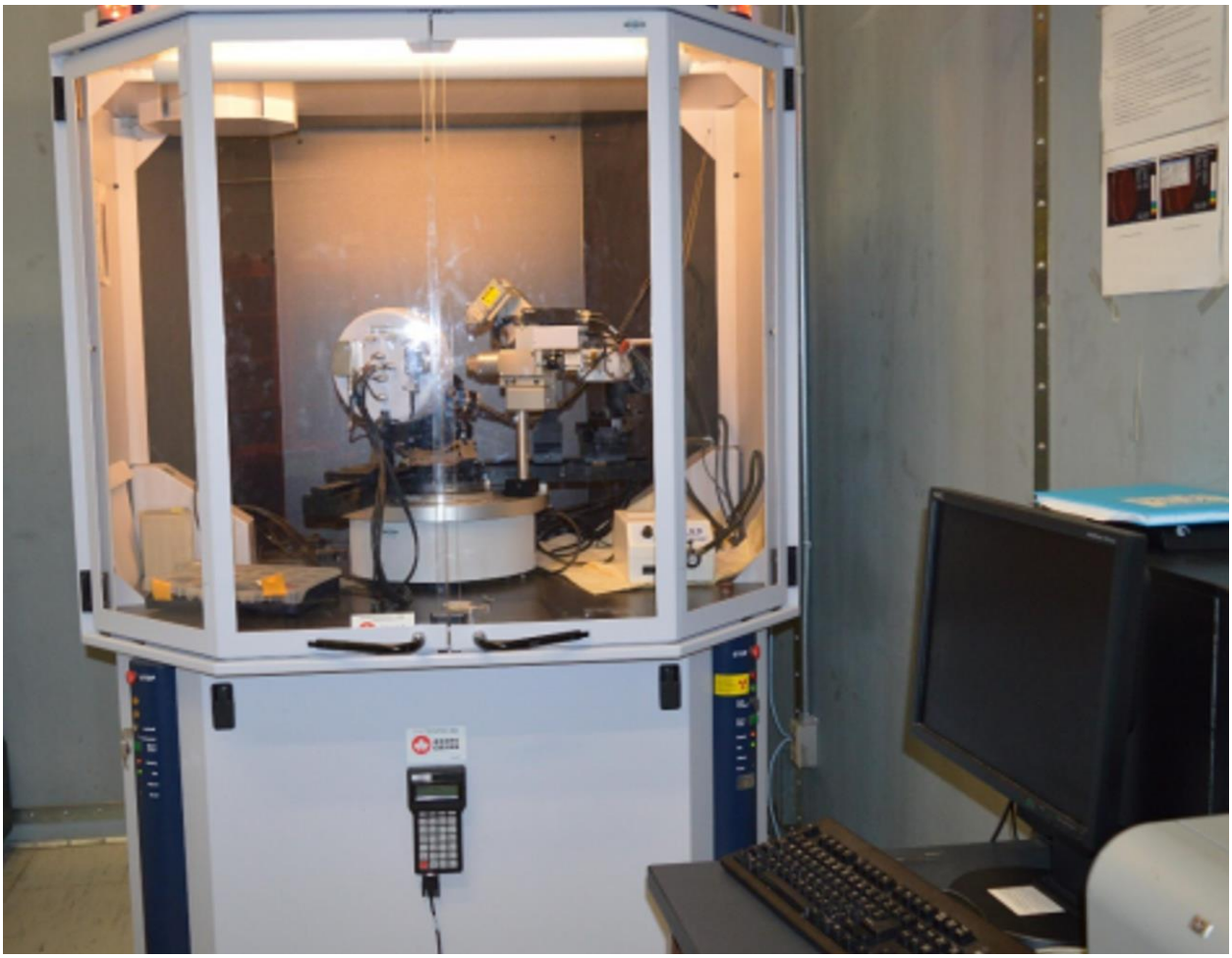

Fig. 3.8. X-ray diffractometer (Bruker D8 Discover diffractometer) with Cr Kα radiation source.

### 3.5.5 Transmission Electron Microscopy (TEM)

Transmission electron microscopy (TEM) and scanning transmission electron microscopy (STEM) analyses were performed on deformed and undeformed specimens using a FEI-Talos F200X microscope coupled with a Super-X$^{TM}$ EDS detector operating at a voltage of 200 kV (Figs. 3.9a and b). The thickness of specimens was initially reduced to 0.1 mm by mechanical grinding and polishing techniques. Disks of 3 mm in diameter were punched from the 0.1 mm thick specimens using a manual punching machine in Fig. 3.9c. Electron transparent disks for TEM/STEM analysis were prepared using a Struers TenuPol-3 twin-jet electro-polisher. The electrolyte containing a mixture of 93% methanol, 2% nitric acid and 5% perchloric acid (vol.%)

was used at –30 °C and at a voltage of 20 V. The focused ion beam (FIB) facilty at the University of California, San Diego, USA, was used prior to the TEM analysis of specimens used in Chapter 11.

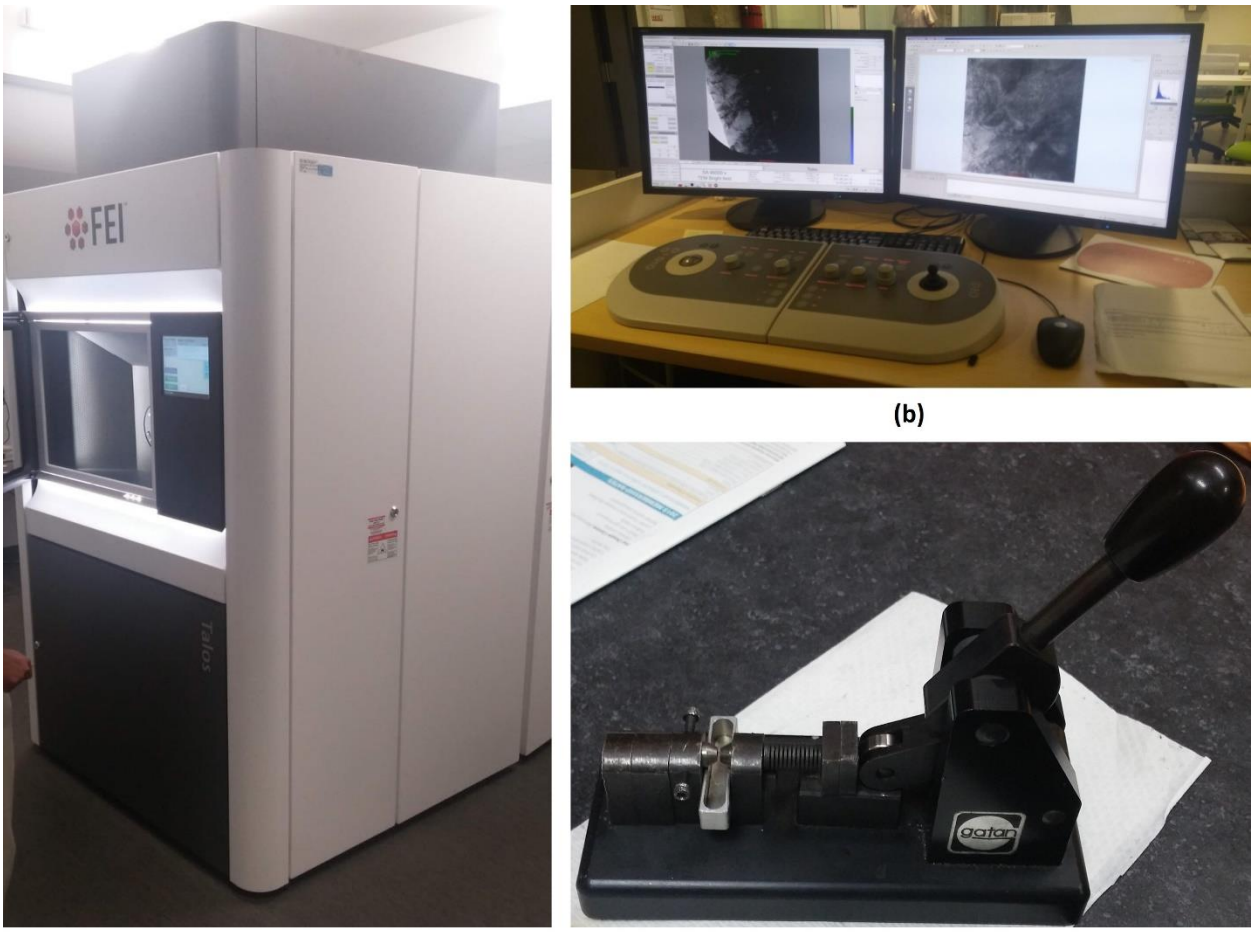


Fig. 3.9. (a, b) Set-up of FEI-Talos F200X microscope coupled with a Super-X$^{TM}$ EDS detector and (c) manual punching machine.

# Chapter 4

## Mechanical Behavior and High-Resolution EBSD Investigation of the Microstructural Evolution in Aisi 321 Stainless Steel under Dynamic Loading Condition

In this chapter, the experimental results of the investigations carried out to determine the variation in the mechanical behaviour of specimens cut from different locations (top, middle and centre) across the thickness of the as-received AISI 321 steel plate are discussed. The mechanical responses of these specimens under dynamic impact and quasi-static loading conditions are compared. The microstructural evolution in the deformed stainless steel specimens under both loading conditions was investigated using EBSD, and the results are also discussed in this chapter. This chapter has been published in "*Materials Science & Engineering A"* as follows:

A. A. Tiamiyu, M. Eskandari, M. Sanayei, A. G. Odeshi, and J. A. Szpunar, "Mechanical behavior and high-resolution EBSD investigation of the microstructural evolution in AISI 321 stainless steel under dynamic loading condition," *Mater. Sci. Eng. A*, vol. 673, pp. 400–416, 2016.

My contributions to this paper include a review of relevant literature, design and carrying out of the required experiments, analysis of test results and preparation of the manuscript. My supervisors, Professors Akindele Odeshi and Jerzy Szpunar, reviewed the paper and made suggestions which were implemented before it was submitted for publication. The present manuscript is a modified version of the published paper. Detailed information about materials and experimental procedure provided in Chapter 3 are removed to avoid repetition. The copyright permission for manuscript reuse was obtained, and it is provided in APPENDIX C.

### Abstract

The impact response of three regions (top, mid and center) across the thickness of AISI 321 austenitic stainless steel plate at high strain rates (> 6000 $s^{-1}$) was studied using the split Hopkinson pressure bar system. The result shows that texture and stored energy heterogeneity across plate thickness influenced the mechanical responses of the investigated steel in these regions. Microstructural evaluation using high-resolution electron backscattered diffraction (HR-EBSD) analysis showed that strengthening in AISI 321 steel originates from the evolution of strain-induced martensite and formation of nano-carbides in addition to plastic deformation by

mechanical twinning and slip. This resulted in a desirable combination of high strength and good ductility (approx. 2000 MPa at 0.42 true strain). Phase transformation, dynamic recrystallization, and formation of nano-carbides were confirmed within the adiabatic shear band (ASB) region. The average dynamic recrystallized (DRX) grain size in the shear band region is 0.28 μm in comparison to grain size of 15 μm outside the shear bands. The nano-sized grain inside the shear bands is proposed to form by rotational dynamic recrystallization. A comparative study of the alloy's behavior under dynamic and quasi-static compression shows that the stability of austenite is higher at high strain rates and lower at a low strain rate. The strength in the dynamically impacted specimen is compromised as a result of the suppressed evolution of strain-induced martensite and mechanical twin. Martensitic transformation under both loading conditions follows the FCC γ-austenite → BCC α′-martensite kinetic path and both phases obey the Kurdjumov-Sachs' $\{(111)_{\gamma}||(110)_{\alpha'}$ and $<-101>_{\gamma}||<1-11>_{\alpha'}\}$ orientation relationship.

**Keywords:** *AISI 321 austenitic stainless steel; EBSD; adiabatic shear bands; mechanical twinning; strain-induced phase transformation; nano-carbides*.

### 4.1 Introduction

AISI 321 is an austenitic stainless steel (ASS) stabilized with titanium to reduce sensitization. Although the widespread structural application of austenitic stainless steels is hindered by their relatively low strength and poor tribological properties, AISI 321 ASS is a choice material for high-temperature applications due to its relatively good mechanical properties at high temperature coupled with good resistance to intergranular corrosion [131]. It is an attractive material for load-bearing applications in nuclear power reactors, boilers, chemical reactors, aircraft's engine and automobile exhaust systems [28].

The use of ASS in strength-critical aerospace/automotive applications is prohibitive owing to its high cost and insufficient simulation models; however, the increasing demand for safe lightweight vehicles along with lifespan cost concerns increases the competitiveness of austenitic steel for selected crash-prone components [132]. Though the choice applications of AISI 321 ASS are corrosion-driven, their exposure to both quasi-static and dynamic impact loading conditions in service can occur. It is therefore important to study its behavior under both loading conditions. The results of a previous study [83] showed that the mechanisms of plastic deformation in steels varies

with loading conditions. Typically, in high strain rate loading conditions, the microstructures of deformed specimens are characterized by the presence of adiabatic shear bands (ASB). ASBs are paths of intense shear strain localization due to loss of load carrying capacity from excessive thermal softening in a region of intense adiabatic heating [118]. They are known to develop within a short time frame such that the region undergoes localized instantaneous heating and rapid cooling by the relatively cold matrix around them [92]. Although the investigation of evolution of shear bands was first observed and interpreted by Tresca in the 19$^{th}$ century [97], its mechanistic model was first proposed by Zener and Hollomon [91,133], who attributed the occurrence of ASB to a competition between strain-rate hardening and thermal softening. Localized deformation occurs when thermal softening dominates strain-hardening. ASBs consist of either elongated and distorted grains (deformed band) or ultra-fine equiaxed grains (transformed band). The ultra-fine grains form as a result of dynamic recovery or dynamic recrystallization [134,135]. The transformed band in steels exhibits white-etching characteristics under an optical microscope, which some researchers attributed to phase transformation [102].

The dynamic responses of several steels have been studied [107,108,109,119,134,136,137]. The characterization of AISI 304L stainless steel after exposure to dynamic shock loading conditions by Meyers et al. [107] using a transmission electron microscope (TEM) revealed two distinct regions within the shear band. The first consists of grains having sizes ranging between 0.1 and 0.2 μm with well-defined grain boundaries while the second indicated glassy structure (suggesting amorphization) within the shear band. This work also reported that the deformation of AISI 304L stainless steel is accompanied by martensitic transformation, stacking faults and twinning outside the shear band region. Lins et al. [109] investigated the occurrence of ASBs in a hot-rolled interstitial free (IF) steel under high strain rate loading conditions and observed equiaxed grain structure within the shear band irrespective of the test temperature. During dynamic shear loading of an ultra-fine-grained (UFG) iron with a grain size of approximately 500 nm, adiabatic shear bands (ASBs) formed while cracks nucleated and propagated along the shear bands [136]. TEM observations indicated that grains in the shear bands were further refined compared to the grains in the UFG iron. Recent high resolution-electron backscatter diffraction (EBSD) study [137] on the dynamic mechanical response of Mn-steel confirms the evolution of both ε (hcp) and α′ (bcc)-martensitic transformations within the shear band region and the neighboring grains. The aforementioned phases obey Shoji-Nishiyama and Burger crystallographic relationship

respectively, with the parent austenite phase. While studying the role of carbides on ASBs, Boakye-Yiadom *et al.* [108] observed that extensive carbide fragmentation during plastic deformation produces fine residual carbide particles which are redistributed within the ASBs. The authors also concluded that dislocation motion within the shear bands was hindered by residual carbide particles, thereby contributing to increased local hardening. The results of other studies [134,135] suggested that carbide particles in steels can be a dominant source of strengthening such that the finer the particles, the smaller the inter-particle spacing, and the higher will be the strengthening effect.

With the growing applications of AISI 321 stainless steel in load-bearing structures in a corrosive or high-temperature environment, previous studies [27,30,138,139] on this grade of stainless steel focused majorly on its response to corrosive or high-temperature environments. Little or no work has been done to understand the deformation mechanism in AISI 321 stainless steel under dynamic shock loading condition. The objectives of this work is to characterize, using high-resolution EBSD, the microstructural evolution in AISI 321 austenitic stainless steel subjected to dynamic impact load in comparison with those deformed under quasi-static compressive loading condition. The mechanical response of this alloy across the sample thickness was also studied and reported in this paper.

## 4.2 Material and Methodology

The thickness of the as-received AISI 321 stainless steel plate is 25.4 mm. In order to study the mechanical response and texture evolution in this alloy across the sample thickness under both dynamic and quasi-static loading conditions in compression, cylindrical test specimens, 4 mm in diameter and 4 mm long, were machined from the as-received plate. The axis of the cylindrical test specimen is parallel to the normal direction (ND) of the plate. Three sets of samples were machined as shown in Fig. 4.1. The first set was machined close to the rolling plane of the plate (hereafter referred to the Top samples). The second set was machined just at the mid region between the rolling plane and the center line of the as-received plate (hereafter referred to Mid samples) and the third set was machined at the center line of the plate (hereafter referred to the Center samples). The dynamic impact and quasi-static compressive tests and microstructural analyses such as the optical/SEM microscopic examinations, EBSD and X-ray diffractometry measurements were carried out as described in Chapter three.

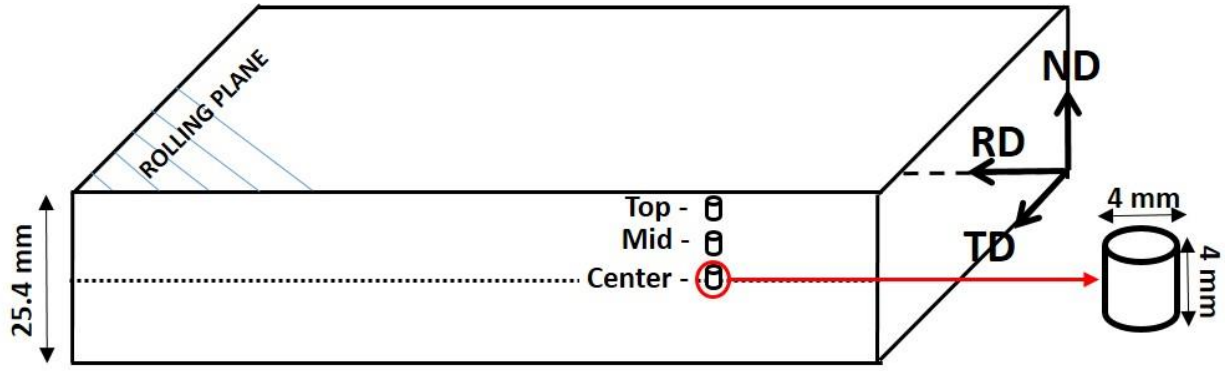


Fig. 4.1. Schematic of sample geometry.

## 4.3 Results

The SEM micrograph of the as-received (undeformed) AISI 321 ASS indicate a microstructure containing more than 98% austenitic phase (Fig. 4.2a). The average grain diameter is 45±5 μm (ASTM 06). The X-ray diffractogram in Fig. 4.2b indicates highest and lowest peak intensities at (111) and (200) plane respectively in the center specimen, suggesting a change in the texture of the austenite grains from the top (rolling plane) to the center of the as-rolled plate. Macrotexture measurement (Fig. 4.2c) also shows the volume fraction of ND||<100> fibre at the center differs strongly from other regions of the plate. The kernel average misorientation (KAM) of undeformed samples at the three regions of the plate was obtained to be less than 0.3$^o$ as shown in Fig. 4.2d. Though the low KAM is a signature of an annealed sample, the misorientation of the center sample shows a shift in the distribution towards higher local misorientations with a KAM (0.29$^o$) that is almost double of that obtained in the top and mid (0.17$^o$) regions. This suggests more stored energy at the center than any other region across the plate thickness.

### 4.3.1 Dynamic mechanical behavior

The results of the dynamic impact test conducted with the projectile striking the incident bar at a momentum of 22 kg.m/s are presented in Fig. 4.3. The corresponding strain rates generated in the top, mid and center specimens by this impact load are 6500, 6600 and 6100 $s^{-1}$ respectively; suggesting variations in the mechanical response across the sample thickness (Fig. 4.3a). The true stress-true strain curves show a clear competition between thermal softening and strain hardening. True yield stresses ($\sigma_{YS}$) defined by the first peak were 681, 514 and 452 MPa for the top, mid and

center specimen respectively. Moreover, the investigated steel exhibits an excellent combination of high strength and ductility (approx. 2000 MPa at 0.42 true strain). The inset in Fig. 4.3a is the true stress-true strain curve of an impacted mid specimen repeated to show the consistency, reliability, and repeatability of the dynamic impact test data. As deformation proceeds beyond the yield point, top and mid specimen shows similar strain hardening behavior before thermal softening dominates the deformation process at about 0.35 true strain. The strain hardening capability of the center specimen is higher than those of the top and mid specimens which resulted in higher peak flow stress before the onset of thermal softening dominance at much higher true strain (0.42). Though the final true strain values of the three sets of the specimens are quite close (0.44), there was 7 μs delay in the total completion time required for the deformation process of center specimen in comparison with both the top and mid specimens that lasted 135 μs as shown in Fig. 4.3b.

Optical micrograph (Fig. 4.4a) reveals the development of ASB in the impacted specimen, a microstructural feature typical of all the three sets of samples. The X-ray diffractograms (Fig. 4.4b) shows that deformation-induced transformation occurred with center specimen showing higher BCC α′-martensite peaks, the first peak [α′(110)] appearing as a shoulder to an FCC γ-austenite peak [γ(111)] and the second peak, α′(200). Although the sequence of martensitic transformation in some stainless steels follows FCC γ-austenite → HCP ε-martensite → BCC α′-martensite [19,50], no ε-martensite was observed in the deformed specimens. Figure 4.4b also shows a new peak on (111) plane of the X-ray diffractogram of center specimen which is identified as TiC.

4.3.1.1 Microstructure evaluations inside adiabatic shear band and neighboring grains after dynamic impact

A. Strain-induced phase transformation inside and outside adiabatic shear band

EBSD maps of regions inside and outside the ASB in the impacted top (Fig. 4.5), mid (Fig. 4.6a-b) and center (Fig. 4.6c-d) specimens depict the microstructural changes accompanying strain localization and formation of ASB in the steel under dynamic impact loading. Although phase maps revealed that austenitic phase transformation to martensite occurred inside and outside the ASB region in all the three sets of specimens, center specimen (Fig. 4.6d) tends to have a larger

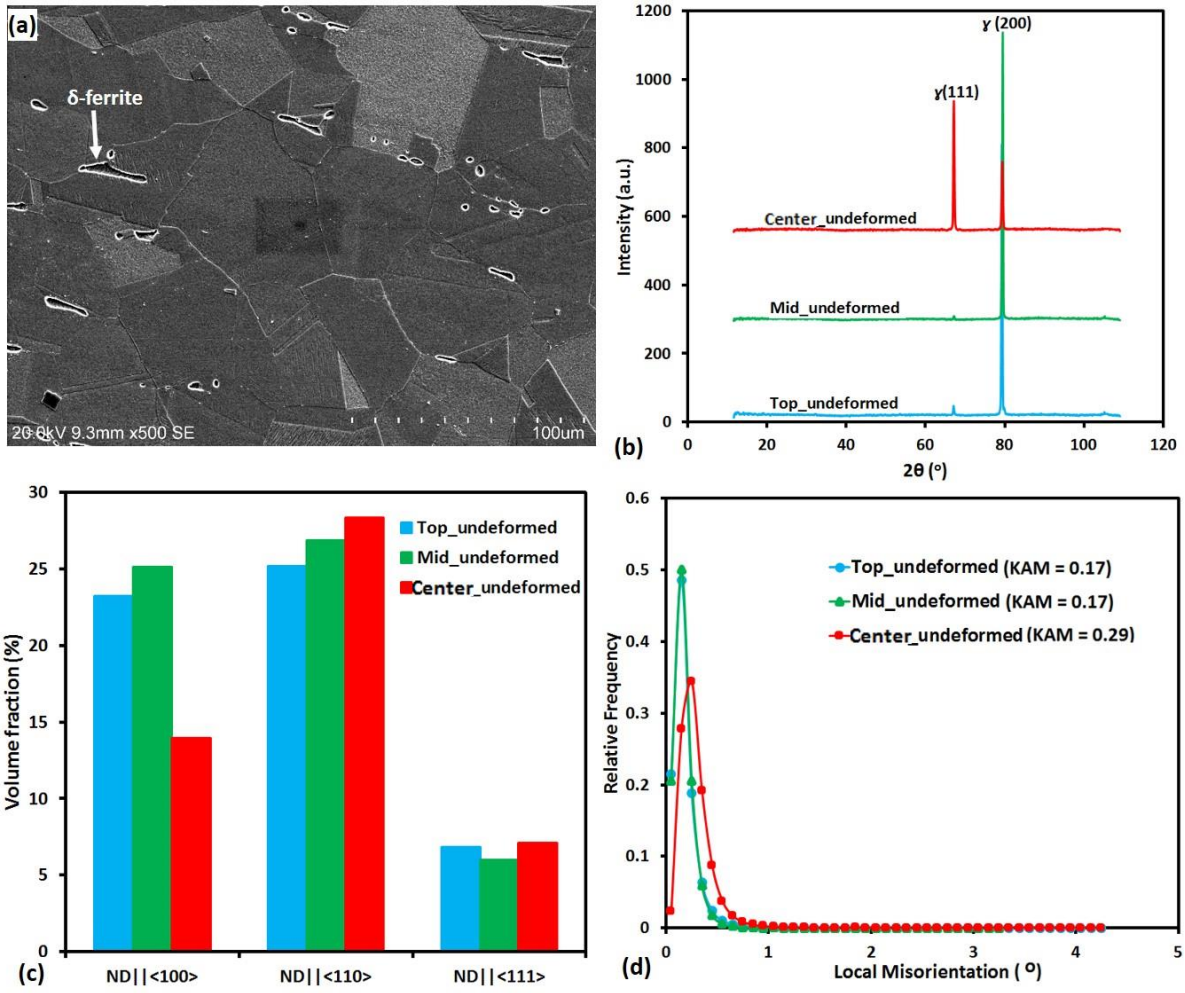


Fig. 4.2. (a) SEM micrograph (b) X-ray diffractogram (c) volume fraction of selected fiber (NDs) and (d) Local misorientation distribution in undeformed samples.

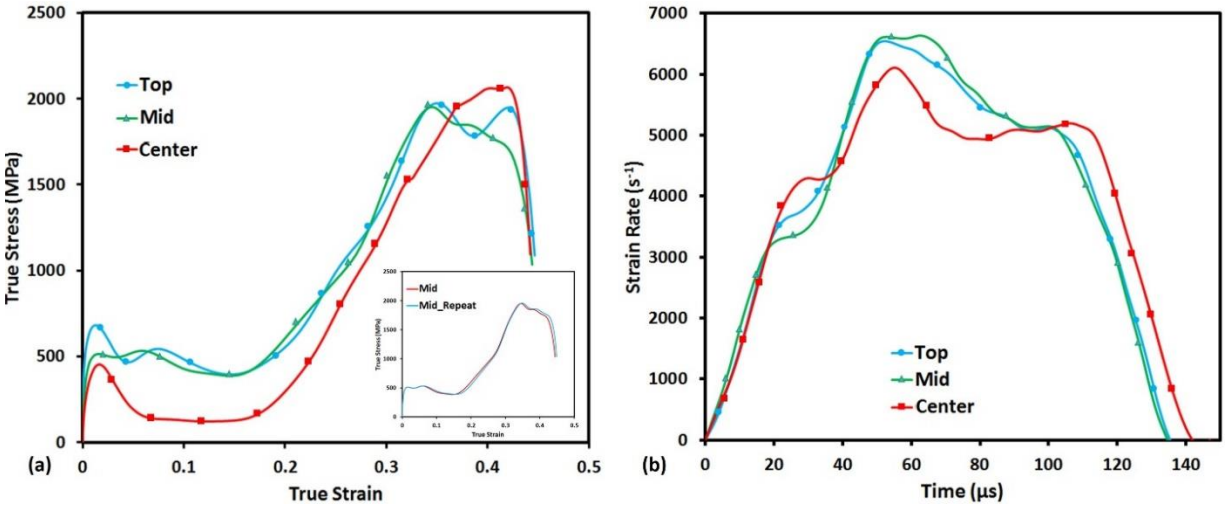


Fig. 4.3. (a) True stress-true strain and (b) strain rates-time curves of shock loaded top, mid and center specimens at a common impact momentum of 22 kg m/s.

area fraction of BCC α′-martensite compared to top and mid specimens. This is in agreement with the result of the X-ray diffractograms in Fig. 4.4b. While the IPF color maps indicate that both austenite and martensite grains outside ASB are of Z||<110> and Z||<111> orientations in the top, mid and center specimens, ASB region comprises of grains with Z||<100>, Z||<110> and Z||<111>

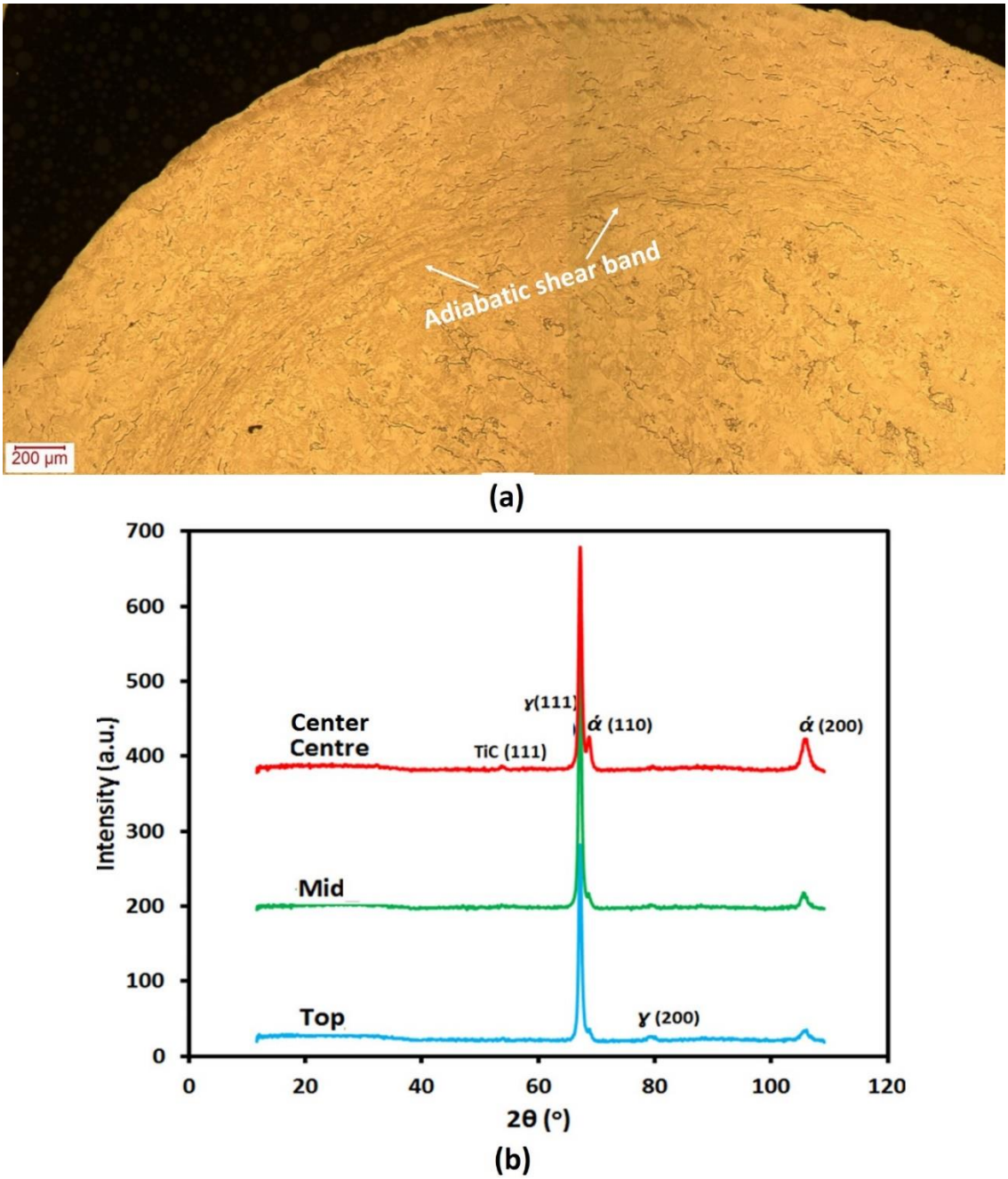


Fig. 4.4. (a) Optical micrographs showing adiabatic shear band geometry on compression plane (b) X-ray diffractograms of the three set of specimen impacted at a common impact momentum of 22 kg m/s.

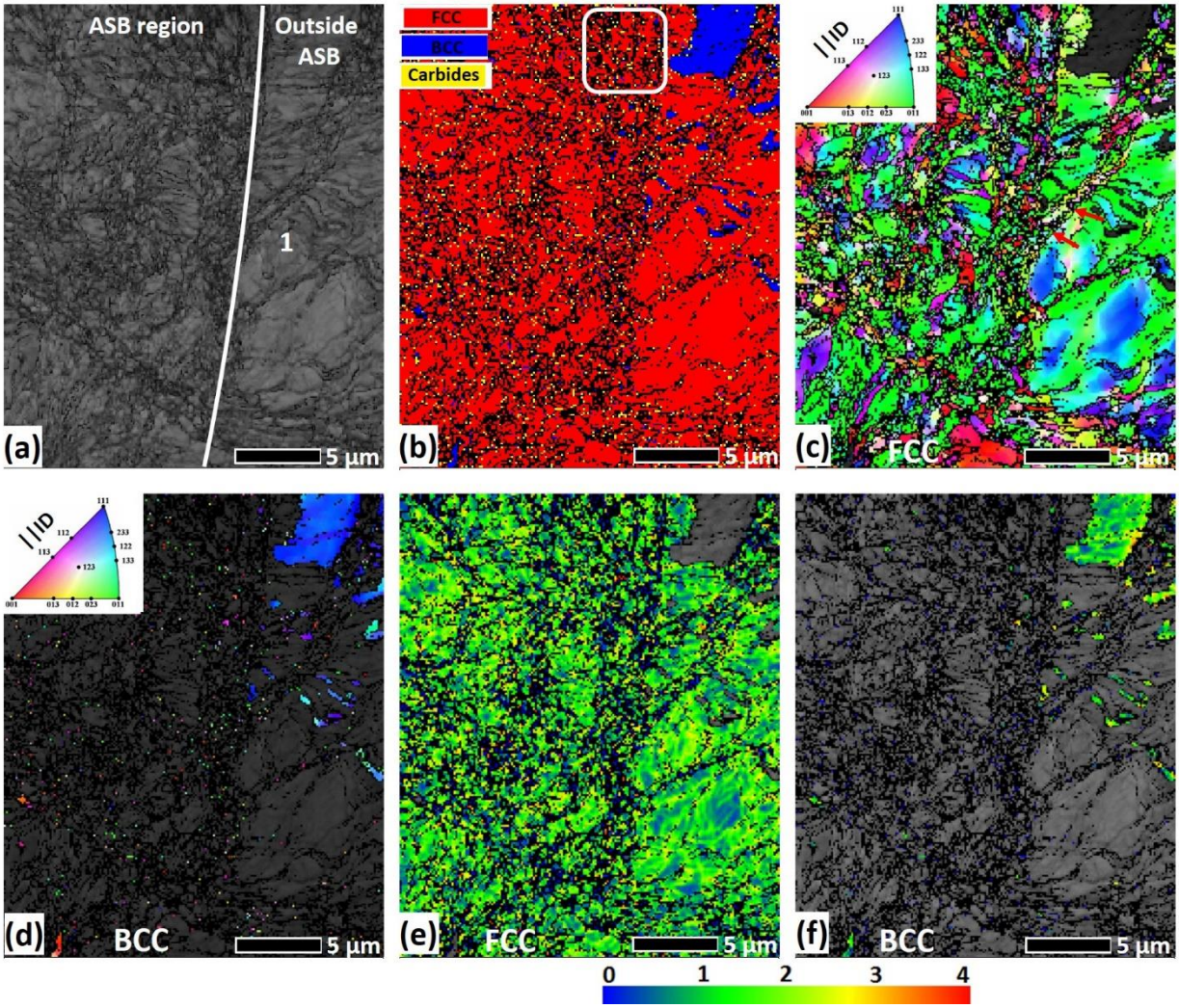


Fig. 4.5. EBSD maps of top specimen showing the shear band and neighbor grains region: (a) band contrast map, (b) phase map showing FCC γ-austenite, BCC α′-martensite and TiC as red, blue and yellow respectively, (c) Inverse pole figure map (IPF-Z) of FCC γ-austenite, (d) Inverse pole figure map (IPF-Z) of BCC α′-martensite, (e) kernel average misorientation map of FCC γ-austenite (f) kernel average misorientation map of BCC α′-martensite.

orientations. The KAM of both phases at the three regions of the plate was observed to be above 1.4$^{o}$ which is high enough to serve as a signature for a plastically deformed metal. This indicates that slip is the main plastic deformation mechanism in the investigated stainless steel. The center specimen possesses the highest KAM, indicating more stored energy compared to other regions across the plate thickness. In addition to phase transformation, the other pronounced microstructural change within the shear band is grain refinement, which will be discussed in the next section.

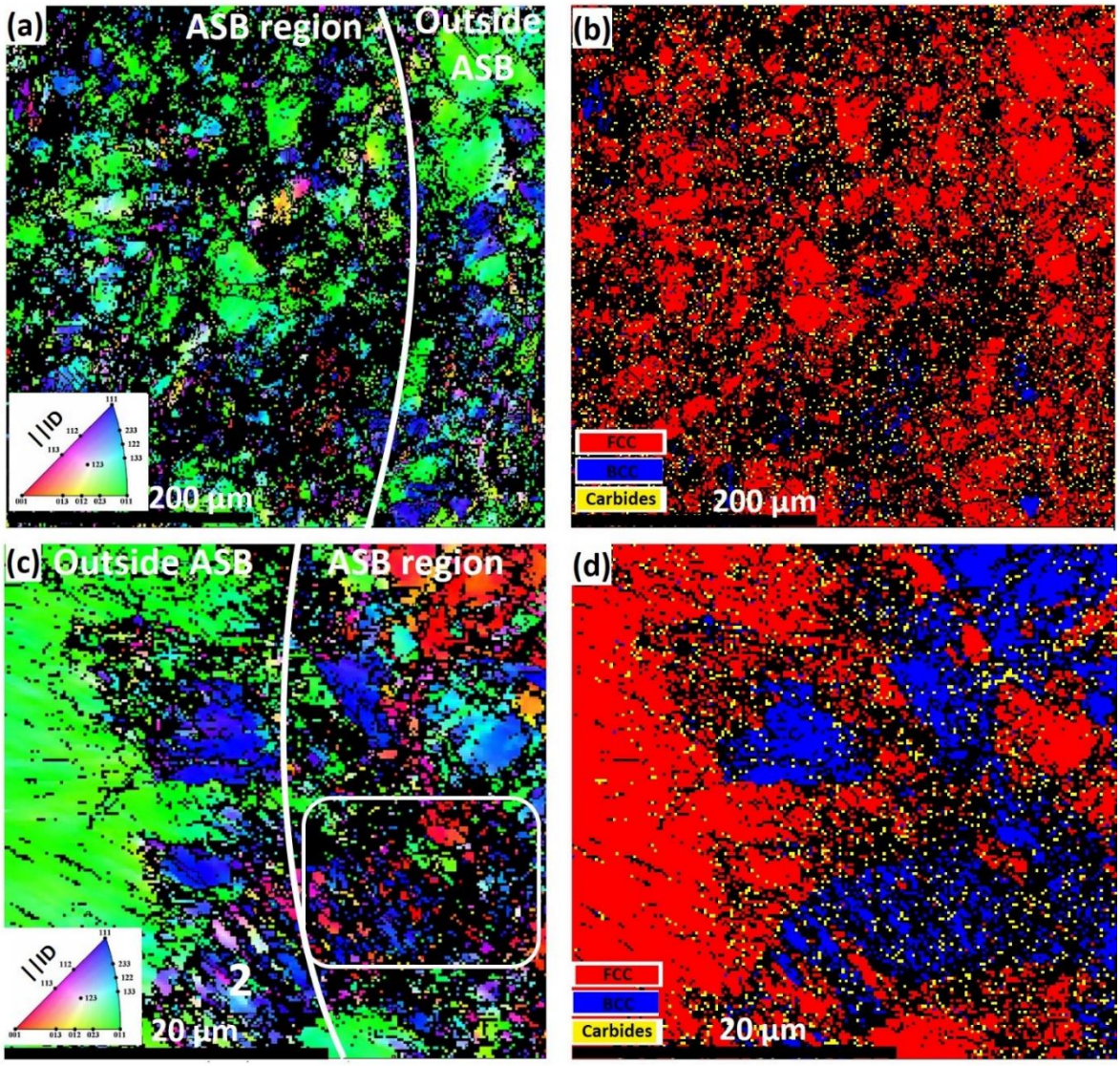


Fig. 4.6. EBSD maps for (a-b) mid and (c-d) center specimens showing the shear band and neighbor grains region: (a) Inverse pole figure map (IPF-Z) of mid specimen, (b) phase map of mid specimen showing FCC γ-austenite, BCC α′-martensite and TiC as red, blue and yellow respectively, (c) Inverse pole figure map (IPF-Z) of center specimen and (d) phase map of center specimen showing FCC γ-austenite, BCC α′-martensite and TiC as red, blue and yellow respectively.

B. Dynamic recrystallization inside adiabatic shear band

The higher magnification HR-EBSD maps (step size of 60 nm) of the regions marked with white rectangles in Figs. 4.5b and 4.6c are presented in Figs. 4.7 and 4.8 respectively. These regions showed evidence of dynamic recrystallized grains inside ASB. Since dynamic recrystallized (DRX) grains were observed in all the three sets of specimens, only maps from the top (Fig. 4.7)

and center (Fig. 4.8) specimens are reported to avoid data duplication. The average DRX grain size in the shear band region is 0.28 μm. It is worth noting that martensite took a morphology different from the two typical morphologies of martensite in steels (i.e. lath and plate).

IPF maps (Fig. 4.7a and d) and pole figures (Fig. 4.7g and h) for both phases in the top specimen show grains with different crystallographic orientations. Grains with a near $0^o$ misorientation angle in the KAM map (blue color) are predominant in the FCC γ-austenite phase which is an evidence of DRX grains. In addition to the DRX grains, substructured and deformed grains (Figs. 4.7(c) and (f)) were observed. Figure 4.7(d-f) shows less evidence of DRX in the martensitic phase. It, therefore, implies that dynamic recrystallization tends to reduce the driving force for strain-induced transformation and stabilizes the austenite [83] in the top specimen. Figure 4.7(g) and (h) are the pole figures ({100}, {110}, {111}) and orientation distribution functions ($0^o$ and $45^o$ sections) for FCC γ-austenite and BCC α′-martensite phases respectively. While the orientation distribution function (ODF) of austenitic phase has Cube, Goss, Brass and Z({111}<110>) texture components as shown in Fig. 4.7(g), texture components of martensitic phase are Cube and Z({111}<110>) as in Fig. 4.7(h).

The IPF map (Fig. 4.8a) and pole figure (Fig. 4.8g) for the austenitic phase in the center specimen show grains with Z||<110> and Z||<111> orientations. BCC α′-martensitic grains are of Z||<100> and Z||<111> orientations as shown in Fig. 4.8d and h. In addition to substructured and deformed grains (Figs. 4.8(b) and (e)), grains with a near $0^o$ misorientation angle on the KAM map (blue color) are present in both phases which are evidence of DRX grains. Figure 4.8(d-f) shows more evidence of martensitic DRX grains, which imply that the stability of austenite is less in the center region; promoting the driving force for strain-induced phase transformation. Figure 4.8(g) and (h) are the pole figures and ODF ($0^o$ and $45^o$ sections) for FCC γ-austenite and BCC α′-martensite phases respectively. While the ODF of the austenitic phase has Goss, Brass and Z({111}<110>) texture components as shown in Fig. 4.8(g), texture components of martensitic phase are Cube, Y({111}<112>) and Z({111}<110>) as in Fig. 4.8(h). Comparing the pole figures of FCC γ-austenite (Fig. 4.8g) and BCC α′-martensite (Fig. 4.8h) phases, the existing orientation relationship between them can be obtained. It can be observed that common orientation relationship; Kurdjumov-Sachs $\{(111)_\gamma||(110)_{\alpha'}$ and $<-101>_\gamma||<1\text{-}11>_{\alpha'}\}$ exists between the phases.

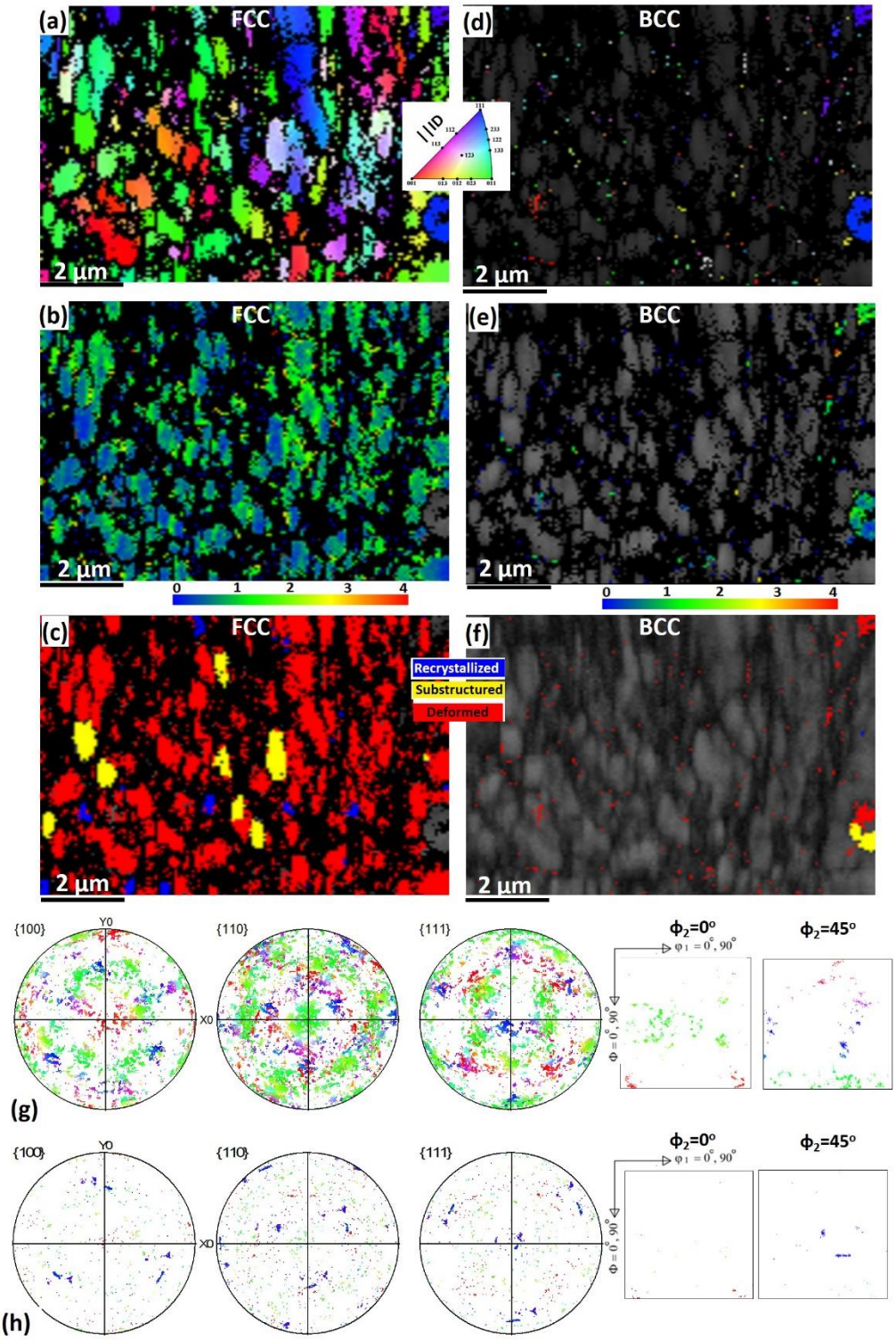


Fig. 4.7. HR-EBSD maps showing DRX grains inside the shear band region for top specimen: Inverse pole figure maps (IPF-Z) of (a) FCC γ-austenite and (d) BCC α′-martensite, Kernel average misorientation maps of (b) FCC γ-austenite and (e) BCC α′-martensite, Recrystallization fraction maps of (c) FCC γ-austenite and (f) BCC α′-martensite and pole figures and ODFs of (g) FCC γ-austenite and (h) BCC α′-martensite.

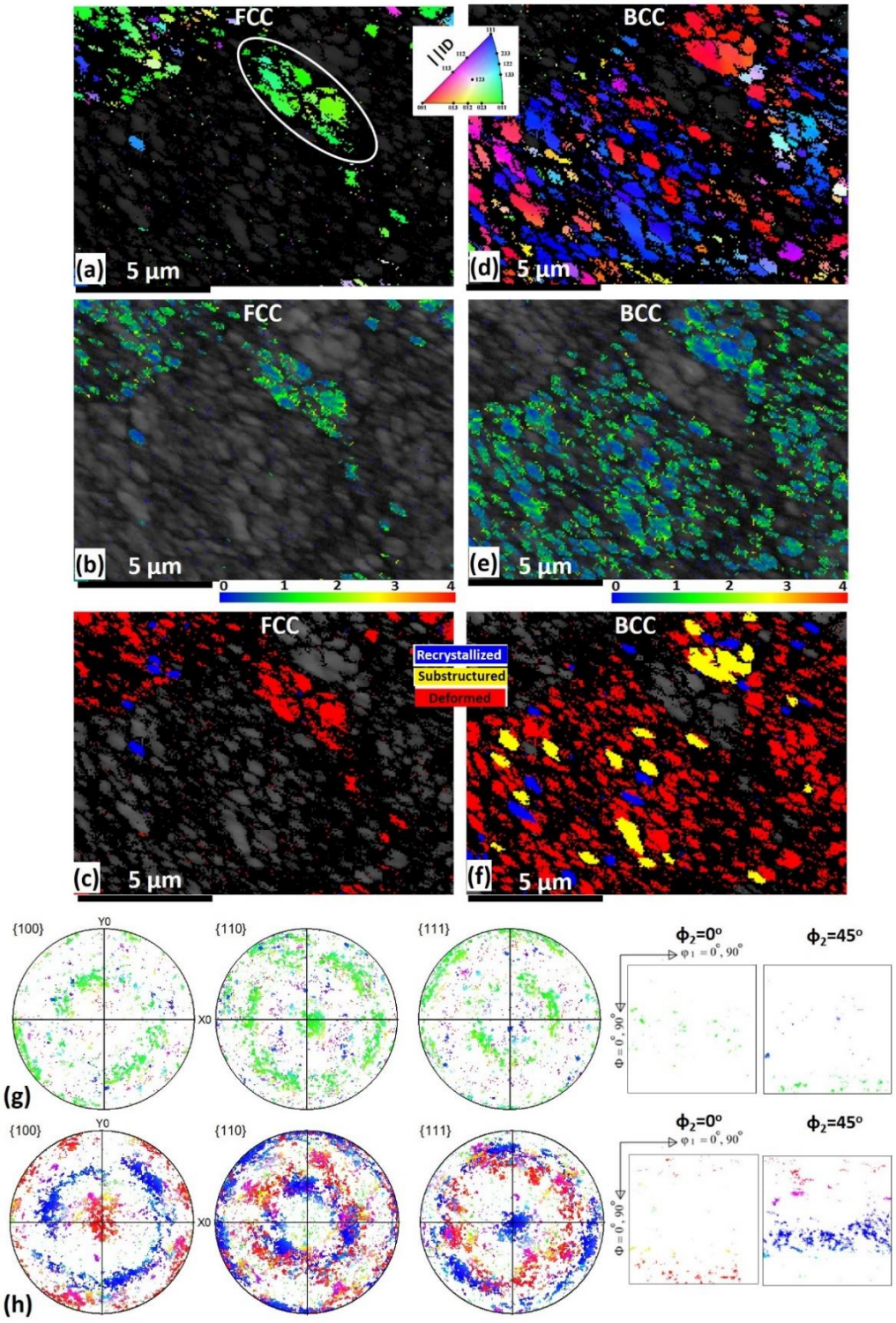


Fig. 4.8. HR-EBSD maps showing DRX grains inside the shear band region for center specimen: Inverse pole figure maps (IPF-Z) of (a) FCC γ-austenite and (d) BCC α′-martensite, Kernel average misorientation maps of (b) FCC γ-austenite and (e) BCC α′-martensite, Recrystallization fraction maps of (c) FCC γ-austenite and (f) BCC α′-martensite and Pole figures and ODFs of (g) FCC γ-austenite and (h) BCC α′-martensite.

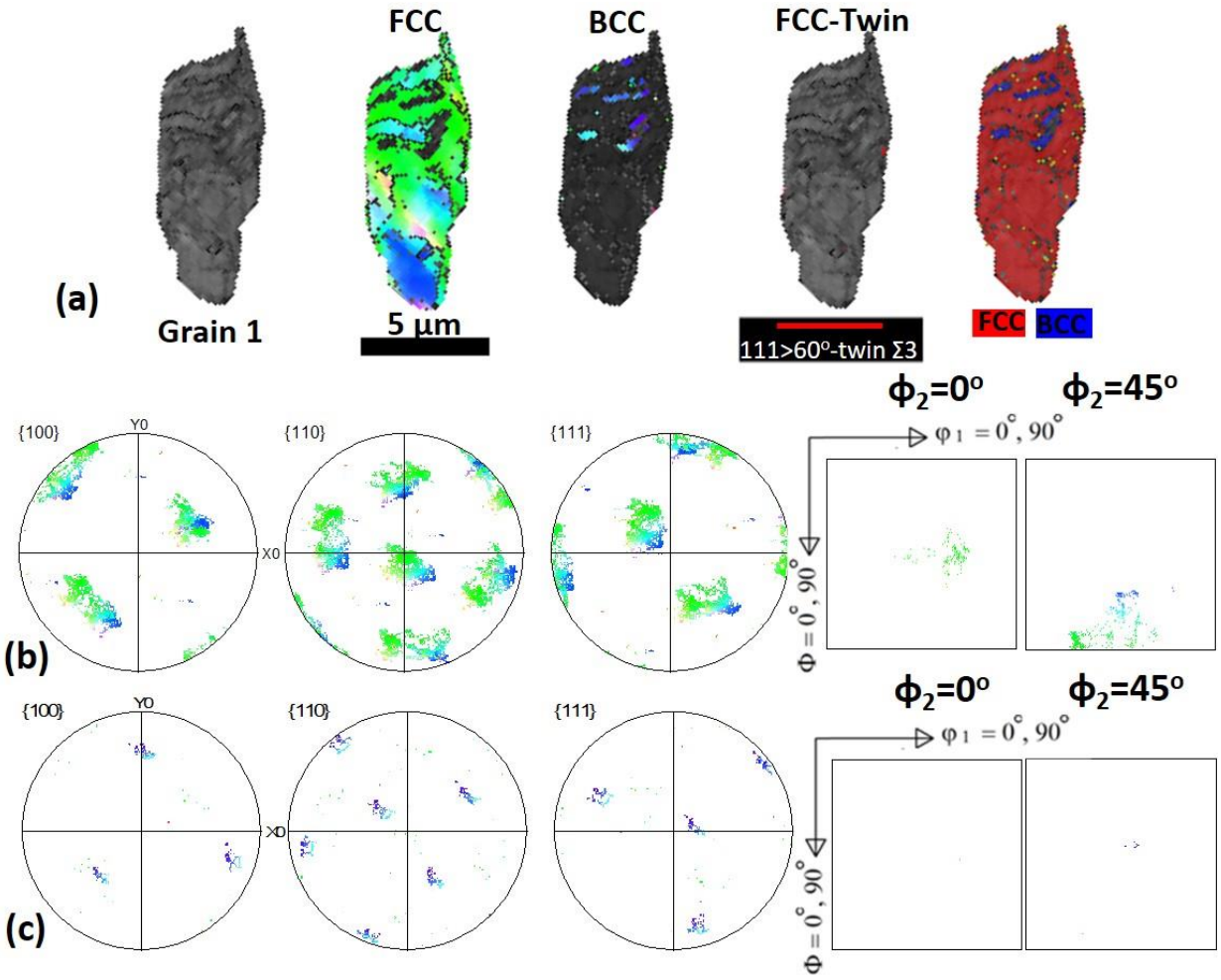


Fig. 4.9. EBSD maps analysis of neighbor grain 1 from the top specimen in Fig. 4.5a showing (a) Band contrast map, IPF-Z map γ-austenite phase, IPF-Z map α′-martensite, Coincidence site lattice (CSL) among FCC variants ($60^{o}$<111> Σ3 red), Phase color map showing γ-austenite and α′-martensite as red and blue respectively. Pole figures and ODFs of (b) FCC γ-austenite and (c) BCC α′-martensite.

C. Characterization of grains near adiabatic shear band (neighbor grains)

Figures 4.9 and 4.10 provide results of detailed EBSD analysis of marked shear band neighbor grain 1 in Fig. 4.5a and grain 2 in Fig. 4.6c, respectively. The IPF-Z maps, pole figures and ODFs of the two grains outside the ASB shows that irrespective of the phases, grains are of or near Z||<110> and Z||<111> orientations. Notable differences in the two grains arose from the volume fraction α′-martensite present and the extent of plastic deformation by twinning. A lower fraction of BCC α′-martensite and mechanical twins in grain 1 (Fig. 4.9a) in comparison with grain 2 (Fig. 4.10a) suggests that phase transformation and twinning are more pronounced in the center

specimens. Comparing the pole figures of FCC γ-austenite and BCC α′-martensite phases in both grains (Fig 4.9b-c and Fig. 4.10b-c) shows that both phases follows Kurdjumov-Sachs $\{(111)_{\gamma}||(110)_{\alpha'}$ and $<-101>_{\gamma}||<1\text{-}11>_{\alpha'}\}$ orientation relationship.

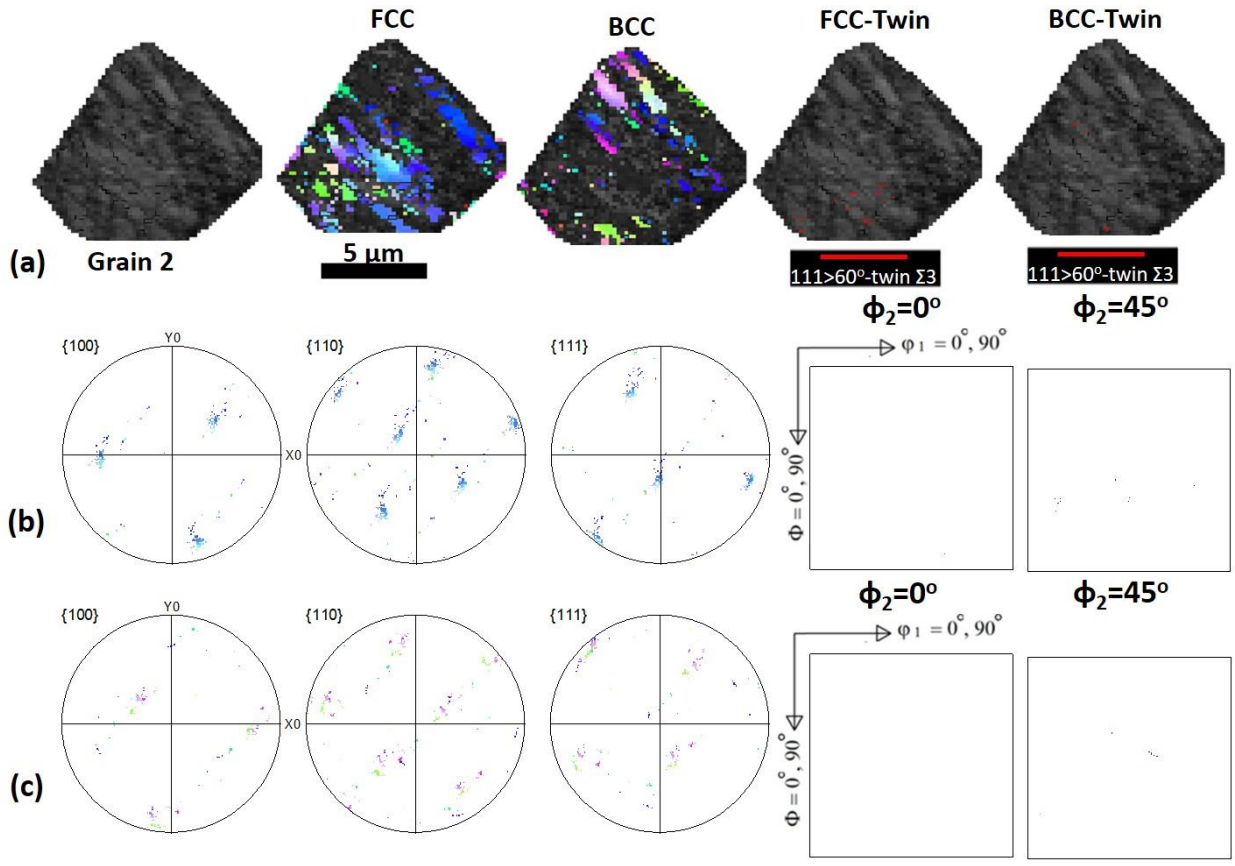


Fig. 4.10. EBSD maps analysis of neighbor grain 2 from the center specimen in Fig. 4.6c showing (a) Band contrast map, IPF-Z map γ-austenite phase, IPF-Z map α′-martensite, Coincidence site lattice (CSL) among FCC variants ($60^{o}<111>$ Σ3 red), Coincidence site lattice (CSL) among BCC variants ($60^{o}<111>$ Σ3 red).

D. Carbide precipitation

Another notable observation, common to all regions (though more pronounced in the center specimen) across the thickness of the investigated AISI 321 ASS plate is the increase in volume fraction of TiC precipitate. EBSD analysis revealed that the fraction of TiC particles in all undeformed samples as indicated in Fig. 4.11a, is less than 0.4%. Large deformation ($\varepsilon_T = 0.44$, $\dot{\varepsilon} > 6000\ s^{-1}$) used in this study resulted in an increase in volume fraction of TiC to 5.8% (Figs. 4.5b, 4.6b and d). TiC particles were observed to precipitate inside and outside ASB, predominantly in the dark (un-indexed) areas suspected to be regions of high dislocation densities. HR-EBSD study

(Fig. 4.11b) shows that the TiC particles have size in the range of 65-70 nm. The contribution of nano-sized TiCs to strengthening as reported by other authors [140,141] can be ascertained if the carbides were precipitated during and not after deformation is complete. To solve the aforementioned problem, the impact of the center specimen was repeated under the same condition, but this time, the sample chamber of the SHPB was filled with water at room temperature to allow rapid quenching of the specimen after impact. Nano-sized TiC particles were still precipitated (Fig. 4.11c) after rapid quenching of the deformed specimen. The quenched specimen have the same volume fraction of TiC particles as that obtained in the unquenched deformed specimen. This is confirmed by the X-ray diffractogram in Fig. 4.11d

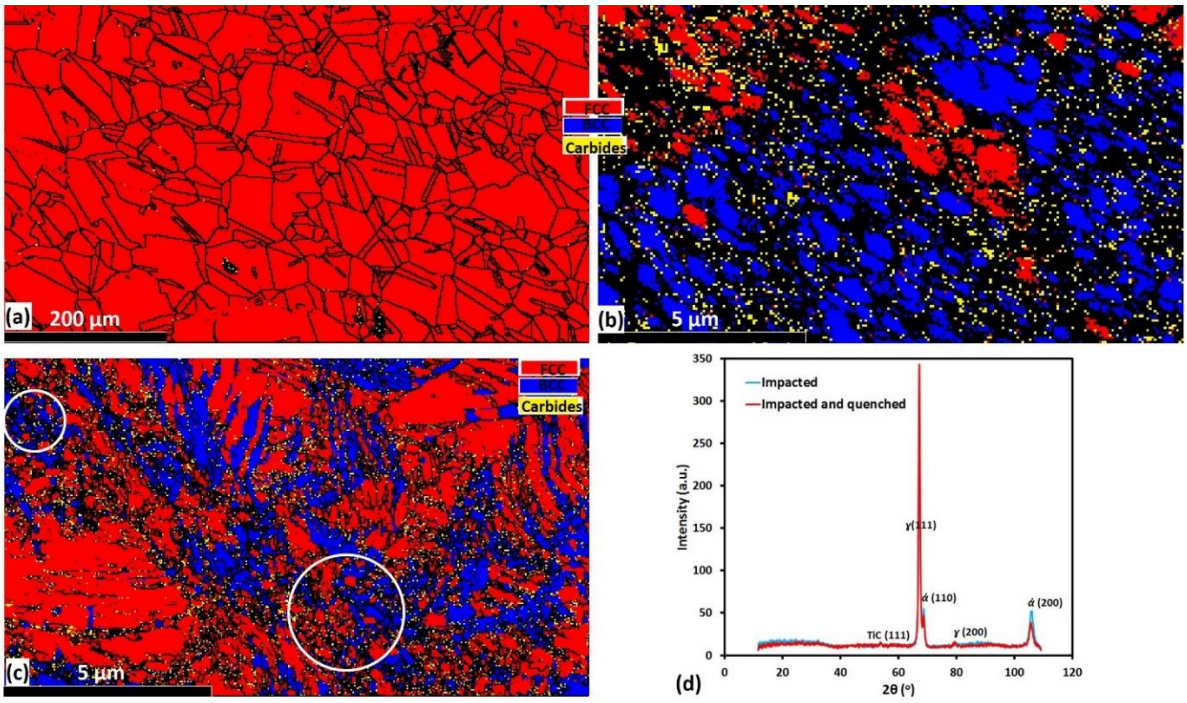


Fig. 4.11. EBSD phase maps of (a) undeformed, (b) impacted, (c) impacted and rapidly quenched center specimens and (d) X-ray diffractograms of (b) and (c).

which shows equal peak intensities for TiC. Observation of recrystallized grains (white circles in Fig. 4.11c) in the quenched specimen could also confirm the occurrence of dynamic recrystallization and not static recrystallization. Similarly, the reduction in the BCC α′-martensite peaks (Fig. 4.11d) of impacted and quenched specimen also confirm that the rapid quenching resulted in lower austenite to martensite phase transformation. This also suggests that the phase transformation continues when specimen is allowed to cool slowly after impact. Therefore, the observation of nano-sized carbides alongside BCC martensite, DRX grains after rapid quenching

suggests that the nano-sized carbide precipitates at about the same time FCC austenite transform to BCC martensite and not during the slow cooling of the specimen.

4.3.1.2 Macrotexture evolution away from ASB

Figure 4.12 shows the results of macrotexture measurement in a region far away from ASB. Comparison of pole figures (Fig. 4.12a) confirmed that the orientation relationships between the FCC γ-austenite and BCC α′-martensite phases as indicated by black arrows follow Kurdjumov-Sachs' $\{(111)_{\gamma}||(110)_{\alpha'}$ and $<-101>_{\gamma}||<1-11>_{\alpha'}\}$. While the volume fraction of Cube and R-cube texture components in FCC γ-austenite phase reduced in all the three sets of specimens under dynamic loading conditions, Goss, Brass, S and Copper components were significantly developed with top specimen showing the lowest fraction of the texture components mentioned above (Fig. 4.12b and c). The crystallographic texture of BCC α′-martensite with strong S component remains relatively unchanged across the thickness of the sample plate (Fig. 4.12d).

### 4.3.2 Quasi-static compression

A comparative study on the effect of strain rate on the mechanical response and microstructural evolution of AISI 321 austenitic stainless steel was conducted on the mid specimen only. The true yield stress of AISI 321 ASS under quasi-static compression is 280 MPa, about 45% lower than that obtained under dynamic impact (Fig. 4.13a). The stress-strain curve under quasi-static loading shows the dominance of strain hardening as deformation proceeds towards the maximum stress (6280 MPa). Unlike dynamic loading condition where strain hardening competes with thermal softening, little or no trace of such competition was observed under quasi-static loading. Macro-texture analysis (Fig. 4.13b) shows that similar crystallographic texture (ID/CD||<110>) evolves in retained austenite under both loading conditions, athough lower maximum intensity is recorded in the specimen subjected to quasi-static compression. Meanwhile, the crystallographic texture of BCC α′-martensite phase in both loading conditions is different: ID||<001> & <111> for specimen subjected to dynamic impact and CD||<001> & <110> for specimen subjected to quasi-static compressive loading. A lower maximum intensity was recorded for BCC α′-martensite phase in the specimens subjected to dynamic impact loading. This implies that the texture of the retained FCC γ-austenite phase is not strain-rate dependent.

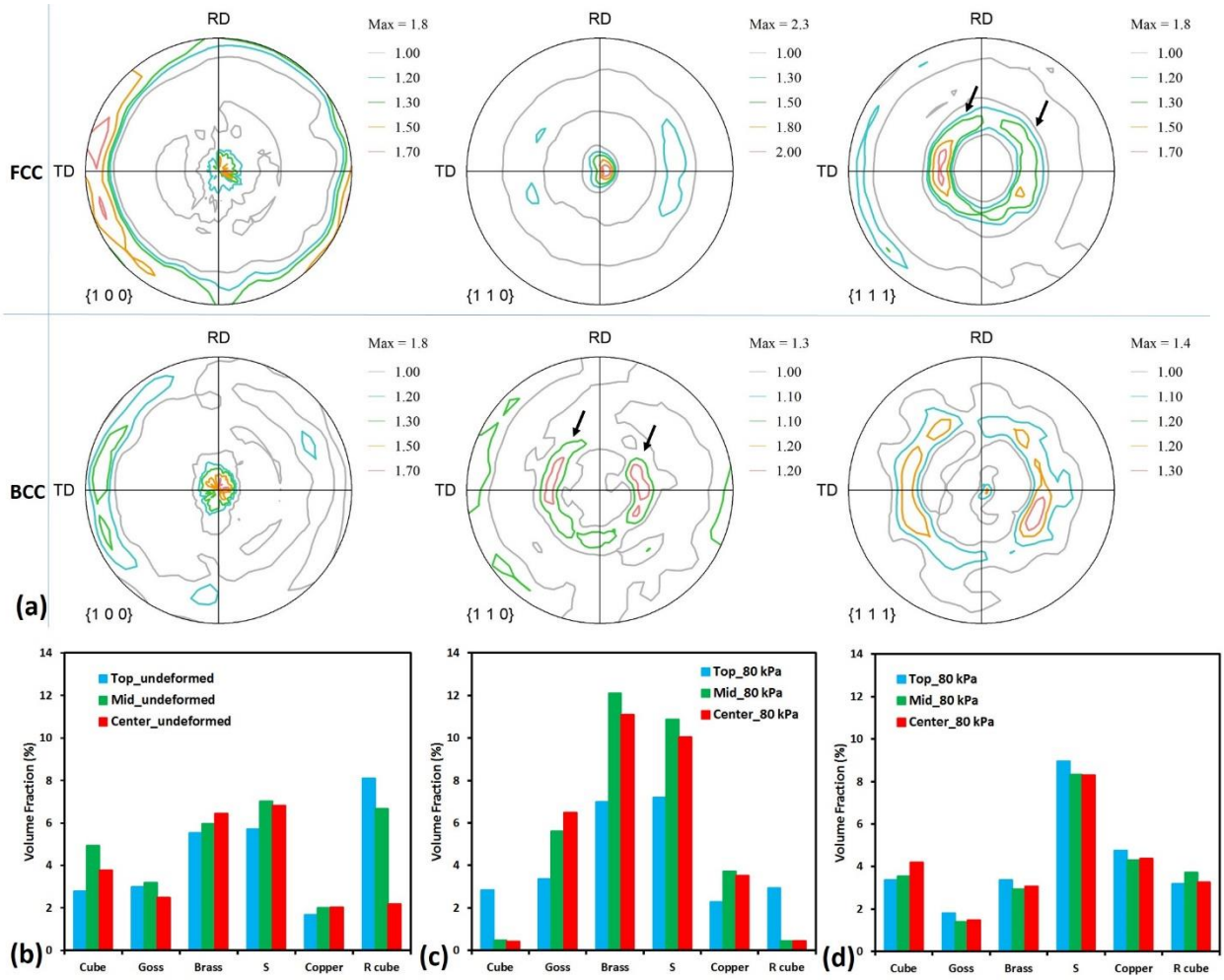


Fig. 4.12. Macrotexture measurement away from ASB: (a) FCC and BCC pole figures ({100}, {110}, {111}) for top specimen and volume fraction of selected texture component in (b) undeformed specimens, (c) deformed FCC γ-austenitic phase and (d) deformed BCC γ-austenitic phase.

Figure 14 shows the results of the microstructural evaluation of a specimen compressed under quasi-static load using EBSD. A large scan area was taken from the center toward the edge of the compressed cylindrical specimen (Fig. 4.14a) in order to observe if any region of intense strain localization exists. FCC (CD||<110>) and BCC (CD||<001>) compression textures in Figs. 4.14(b) and (c) were predominant, which is in agreement with compression textures of FCC and BCC metals, respectively [142]. When compared to impacted specimens, higher kernel average misorientations (Fig. 4.14e and f) were observed in the specimen subjected to quasi-static loading for both parent (austenite) and product (martensite) phases, which are about 2.2$^{o}$ and 1.9$^{o}$, respectively. HR-EBSD analysis (Fig. 4.15) of the white rectangular region in Fig. 4.14a shows

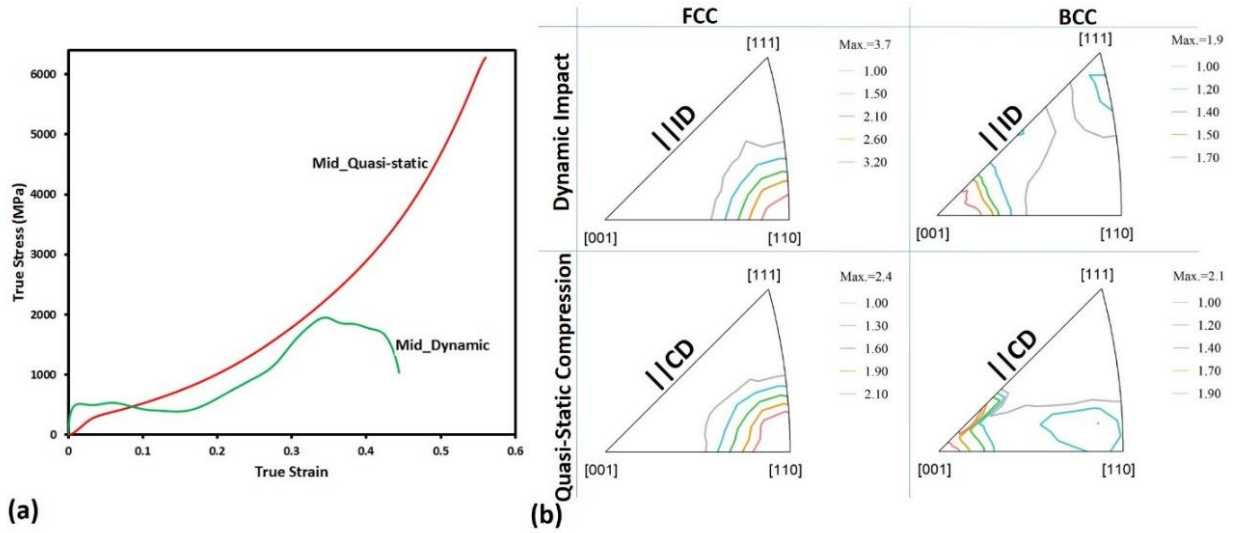


Fig. 4.13. (a) Co-plot of quasi-static and dynamic true stress-true strain curves and (b) Macro-texture IPF-Z of deformed mid specimens: ID and CD are impact and compression directions parallel to the normal direction.

that the deformed shear band characterized by elongated grains of both the parent and product phases exists alongside nano-sized TiC particles. Fig. 4.15a shows that more than 50% of austenites transformed into α′-martensite during deformation. This was confirmed using XRD for phase identification (Fig. 4.15b). An EBSD analysis of the marked grain 3 far away from the deformed band region in Fig. 4.14a is presented in Fig. 4.16. Evaluation of the IPF-Z maps, pole figures and ODFs of the grain indicates that it is of or near Z||<110> and Z||<111> orientations for FCC γ-austenite phase. Meanwhile, BCC α′-martensitic phase has strong Z||<100> orientation with traces of Z||<110> and Z||<111> orientations. Figure 4.16(b) and (c) are the pole figures and ODFs for FCC γ-austenite and BCC α′-martensite phases respectively. While the ODF of the austenite phase has Goss, Brass, Y({111}<112>) and Twin-Copper ({255}<511>) texture components as shown in Fig. 4.16(b), texture components of the martensite phase is predominantly Cube as indicated in Fig. 4.16(c).

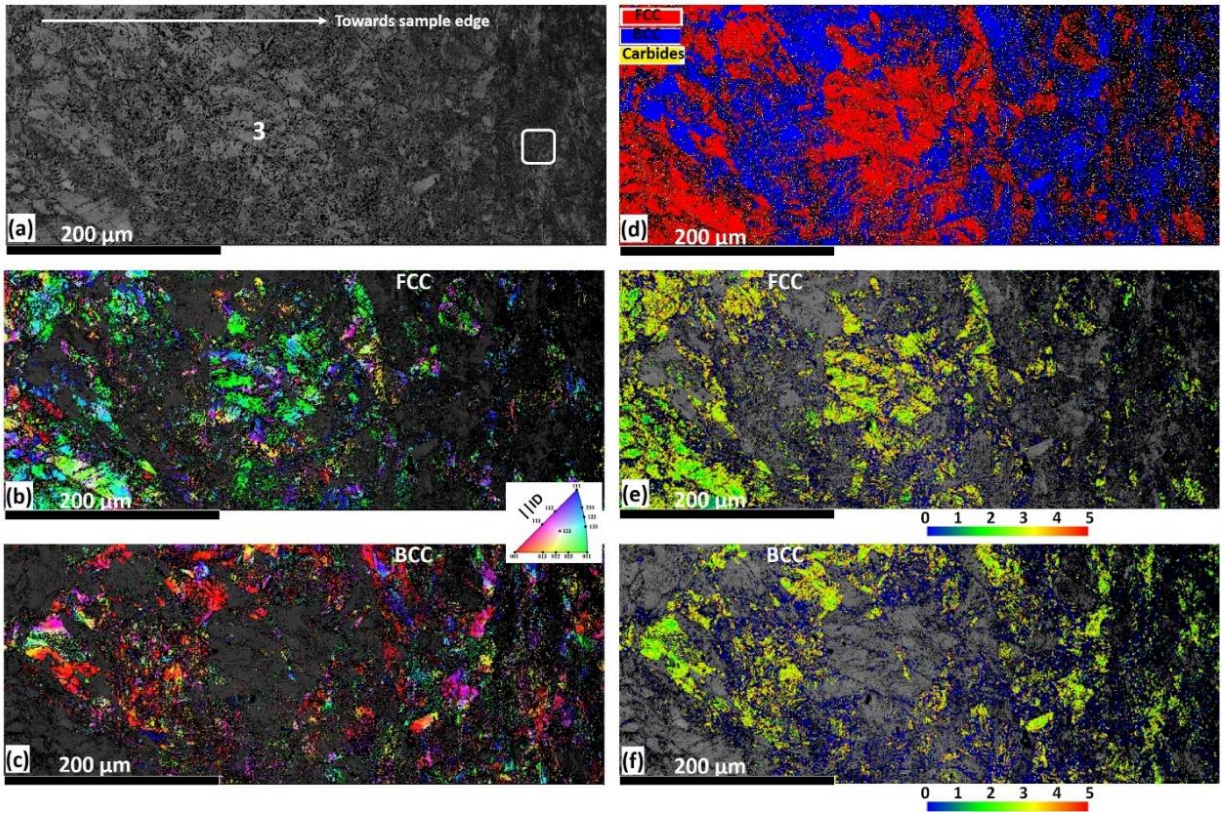


Fig. 4.14. EBSD maps of mid specimen subjected to quasi-static compression showing microstructure from the center of compression plane towards specimen edge: (a) band contrast map, (b) and (c) Inverse pole figure map (IPF-Z) maps of FCC γ-austenite and BCC α′-martensite respectively (d) phase map showing FCC γ-austenite, BCC α′-martensite and TiC as red, blue and yellow respectively, (e) and (f) kernel average misorientation map of FCC γ-austenite and BCC α′-martensite respectively.

## 4.4 Discussion

### 4.4.1 Mechanical Response

Characterization of three regions, top, mid and center, along the thickness of the as-received AISI 321 plate shows heterogeneity in the texture and stored energy (Fig. 4.2) which can trigger different mechanical behavior. The dynamic impact response of specimens from these regions is shown in Fig. 4.3. Lower yield strength, higher strain hardening capability and delay in the completion of deformation process in a specimen from the center region than any other regions across the plate thickness may not be unconnected with the low volume fraction of ND||<100> fibre and higher KAM (stored energy) at the center region. The high strain rate loading conditions led to the development of adiabatic shear bands (ASB) in Fig. 4.4 which are paths of intense shear strain localization due to loss of load carrying capacity from excessive thermal softening in the

region of intense adiabatic heating [118]. Temperature rise, leading to thermal softening and occurrence of ASB during dynamic shock loading condition has been reported to be as high as 1409K in β-Ti alloy [96], 943K in Fe–Cr–Ni austenitic stainless steel [86] and $0.5T_m$ ($T_m$ melting point of steel) in 304L ASS [107]. While the flow stress in metallic materials can generally depict microstructural changes during deformation, Nkhoma *et al.* [29] suggested that the majority of the flow curves that showed the occurrence of dynamic recrystallization (DRX) exhibited a single peak. The authors also reported that the appearance of multiple peaks is only feasible when the deformation is carried out at a high temperature and low strain rate, and when $d_o > 2d_{DRX}$. In this case, $d_{DRX}$ is the dynamically recrystallized grain size and $d_o$ is the initial grain size. Therefore, the appearance of multiple peaks in flow stress of specimen deformed at high strain rates (that resulted in temperature rise) in Fig.3 suggests the occurrence of DRX since $d_o >>> 2d_{DRX}$. The result of quasi-static compression test in Fig. 4.13a shows that the mechanical response of AISI 321 ASS is strongly dependent on strain rate. Specimens subjected to quasi-static compression shows lower yield strength but higher strain hardening rate than impacted specimens. The little or no trace of competition between strain hardening and thermal softening in quasi-static true stress-true strain curve is an indication of little or no temperature rise in the test specimen during quasi-static compression.

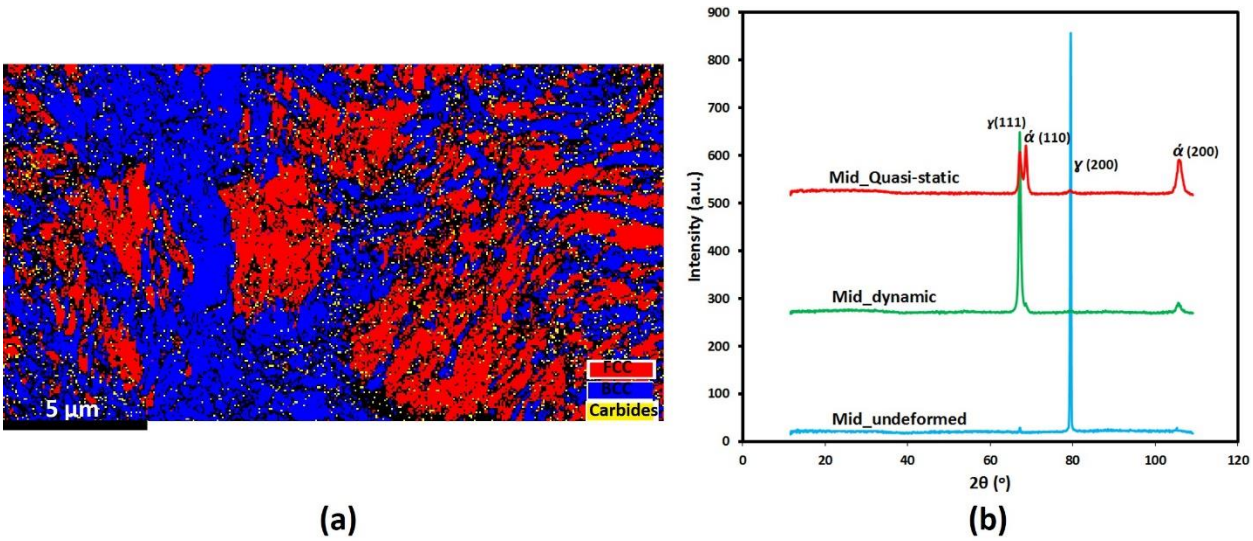


Fig. 4.15. (a) HR-EBSD phase map of the mid specimen in the region indicated by the white rectangle in Fig. 4.14a and (b) X-ray diffractograms of undeformed and deformed mid specimens.

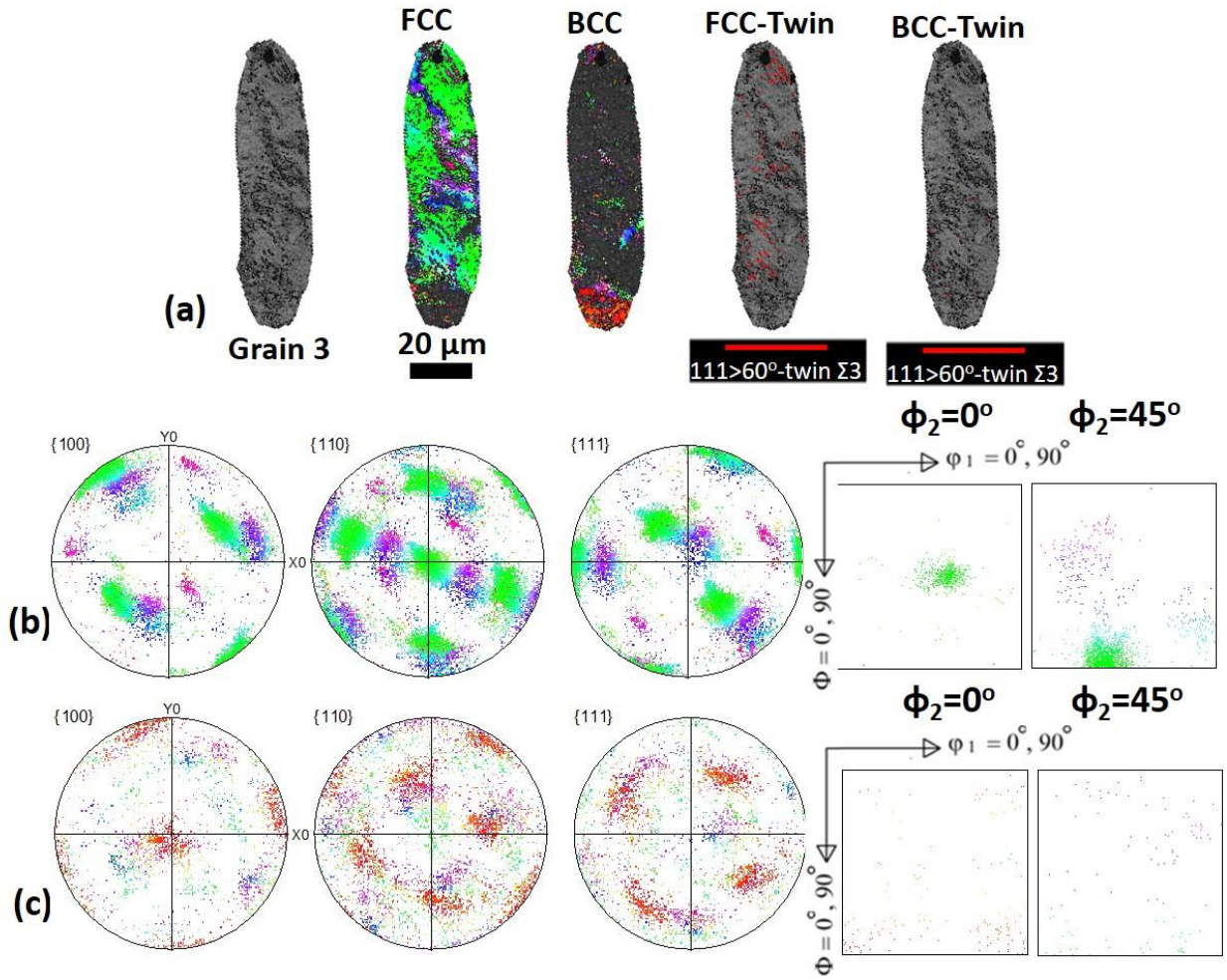


Fig. 4.16. EBSD maps analysis of grain 3 in Fig. 4.14a showing (a) Band contrast map, IPF-Z map γ-austenite phase, IPF-Z map α′-martensite, Coincidence site lattice (CSL) among FCC variants ($60^o$<111> Σ3 red), Coincidence site lattice (CSL) among BCC variants ($60^o$<111> Σ3 red). Pole figures and ODFs of (b) FCC γ-austenite and (c) BCC α′-martensite.

### 4.4.2 Microstructural Evaluation

#### 4.4.2.1 Phase Transformation

Figure 4.4b confirmed martensitic transformation of parent austenite with a higher volume fraction of martensite in the center specimen under dynamic impact load. This could imply that the stability of austenitic phase decreases from the top of the plate to the center of the plate. Austenitic phase transformation to martensite has been reported to be influenced by austenite stability and stacking fault energy (SFE), both of which depend on the chemical composition, temperature and orientation of the austenite grains (texture) [50]. The lower stability of austenite in the center specimen promoted more martensitic phase transformation which in turn contributed to the higher

strain hardening capability as shown in Fig. 4.3. EBSD maps (Figs. 4.5 and 4.6) confirms phase transformation inside ASB. The co-existence of both austenite and martensite phases were confirmed in the ASB region. The study of ASB by XRD techniques in Ni-Cr steel under dynamic shock loading conditions confirmed that both the austenite and martensite phases co-exist with the former likely to be retained austenite [56]. Phase transformation has been confirmed in the ASB region of other metals such as β-Ti alloy [96] and Titanium alloy [104] under high strain rate loading conditions.

The volume fraction of martensite in a mid specimen subjected to quasi-static compression (Figs. 4.14 and 4.15) is more than 50%. This contributed to higher strain hardening in this specimen in comparison with an impacted specimen. The low temperature rise in the quasi-statically compressed specimen is considered to be the most beneficial condition for martensitic transformation [79]. Similarly, Wang *et al.* [78] did not observe any significant phase transformation in 304 stainless steel deformed at 75 °C but a substantial phase transformation at room temperature. The result of their modeling work is also in agreement with the conclusion that the presence of the martensitic phase increases the hardening rate substantively. Phase transformations are results of combined shear and dilatational volume expansion which promotes additional plasticity in the neighboring matrix by imposing locally concentrated stress field [78]. The transformation of austenite to martensite during plastic deformation leads to a phenomenon termed transformation induced plasticity (TRIP) [47]. Therefore, the higher work hardening in low strain-rate compression can be attributed to the higher TRIP effect which enhances the excellent combination of strength and ductility [132].

The lower volume fraction of deformation induced martensite in dynamic impacted specimen could be due to two reasons: The first is the possibility that the temperature rise suppressed the transformation of austenite to martensite during the deformation process. The second possibility is that a higher percentage of martensites was originally formed from austenite at a certain stage of deformation but some reverted to austenite (due to temperature rise in the specimen) before deformation was completed. The latter was suspected owing to the observed austenitic grains (white circle in Fig. 4.8a) with z||<110> orientation in the packet of martensitic grains (z||<100> and z||<111> orientations) in Fig. 4.8d. Nakada et al. [143] studied the reversion of austenite in a

13%Cr–6%Ni stainless steel and concluded that most of the reverted austenite had the same orientation as the original austenite matrix before martensitic transformation. They also suggested that reverted austenite retained a Kurdjmov–Sachs relationship with martensite. During annealing of formed martensite, reverted austenite from α′-martensite may or may not have the same orientation as the remaining austenite. When athermal reversion occurs such that the martensite involves coordinated movements of atoms and atomic relationship between the parent and product lattices exist, reversion will most likely not affect orientation in this condition. Similarly, if diffusional reversion occurs, the order of the atomic arrangement in the product lattice differs from the parent lattice due to the long-range movement of atoms during reversion, such that the atomic relationship ceases to exist, the orientation of the reverted austenite may not be the same as the remaining austenite [144]. Therefore, it could be concluded that martensite in the shear band region had undergone athermal reversion, since the reverted austenite grains in Fig. 4.8a have similar near z||<110> orientation with the remaining austenite in Fig. 4.6c. In addition to the similar orientation observed, the time required for the completion of the deformation process (135 μs) in this study is too short to permit reversion by diffusion.

In the current study, martensitic transformation in both loading conditions tends to follow the kinetic path; FCC γ-austenite → BCC α′-martensite. Some authors [6,145] could also not detect the presence of ε-martensite in the martensitic transformation of stainless steels, while other authors [19,50] did. The difference in observation could be as a result of different test conditions adopted [6]. It is, therefore, possible that ε-martensite is only a step in the austenite-martensite transformation process such that the reaction γ → ε → α′ is already completed. Sahu et al. [83] reported the occurrence of dynamic recrystallization due to adiabatic heating instead of ε-martensite transformation in twinning induced plasticity (TWIP) steels. They explained that strain softening due to dynamic recrystallization consumed the driving force for ε-martensite transformation.

#### 4.4.2.2 Twinning

The observation of deformation twinning by EBSD analysis of selected grains (Figs. 4.9, 4.10 and 4.16) under both loading conditions confirmed their contribution to strengthening since they act as barriers to dislocation glide. Therefore, a larger fraction of deformation twin reduces dislocation mean free path, which results in a higher strain-hardening rate. More TWIP effect in specimens

subjected to quasi-static compression (Fig. 4.16a) is justified by lower or negligible temperature rise during compression that increases the instability of theaustenite phase. A study on the stability of austenite in TWIP steels [83] shows that austenite stability is low at lower strain rates, but high during high strain-rate deformation. The stability at high strain rates was attributed to the temperature rise during such deformation leading to dynamic recrystallization in the material. The extent of twinning in AISI 321 ASS subjected to both high and low strain rate can be explained by the expression of the critical true stress for mechanical twinning presented in Eqn. 2.9. This expression implies that the higher the SFE, the higher is the critical true stress for mechanical twinning. An increase in temperature at a fixed composition would result in an increase in SFE. Hence, a temperature rise due to adiabatic heating during high strain rate deformation is sufficient enough to increase the SFE of the deformed metal [146] which in turn suppresses mechanical twinning. Therefore, the driving force for TWIP effect during quasi-static compression tends to be higher than during high strain rate of deformation. Both twinning and martensitic transformation during deformation are promoted by a decrease in SFE of the austenitic phase [50]. Lower SFE in quasi-statically compressed specimen therefore permits stronger TWIP and TRIP effect that contribute to higher strain hardening rate than specimen deformed under high strain-rate loading conditions. Besides from the effect of SFE, previous work [147] showed that low Mn content stimulates both TWIP and TRIP effects while higher Mn content resulted in only TWIP effect during deformation of low carbon steels. This is also in agreement with the current study as AISI 321 ASS exhibits both TWIP and TRIP effect since this alloy contains less than 2 wt. % of Mn (Table 2.1).

#### 4.4.2.3 Slip

The (111) FCC pole figure measurement within the austenite grain (marked 1) adjacent to shear band in Fig. 4.9, indicates the gradual lattice rotation by the splitting of blue color to green, which is a good indication of intensive deformation by slip . According to this observation, the main plastic deformation mechanism during impact, of an austenite grain away from shear band is slip. In addition to that, the KAM map of the austenite grains in Fig. 4.14 suggests deformation was mainly by slip mechanism during quasi static compression. Hence, during low and high strain rate deformation, slip mechanism is also a dominant plastic deformation mechanism.

#### 4.4.2.4 Carbide precipitation

EBSD phase maps of specimens deformed at high (Figs. 4.5b, 4.6b and d) and low (Figs. 4.14d and 4.15a) strain rates show the precipitation of nano-sized TiC paricles at grain boundaries and dark regions in parent and product phases as another possible source of strengthening. The indexing of TiCs around the dark regions indicates that they are surrounded by arrays of dislocations. Dark regions whose measure of orientations in deformed specimen cannot be resolved are signature attributed to high dislocation density due to large deformation [148]. While TiCs were observed within grains (intragranular) and along grain boundaries (intergranular) outside shear band region in Figs. 4.5(b), 4.6(b and d), they were only observed at the grain boundaries of DRX grains within the transformed band (Fig. 4.11b). Intragranular TiC particles in AISI 321 ASS have been reported to precipitate on dislocations and thereby contribute to the strengthening of the grains serving as barriers to motion of dislocations [149]. The presence of TiC as a fine dispersion in matrices and grain boundaries improve tensile and creep strength significantly over a wide range of temperatures [140]. A previous research finding reports high strength inside the shear band formed in severely deformed Fe-C steels [135]. These authors attributed the observation to the formation of ultra-fine ferrite grains containing nano-sized carbides upon rapid re-transformation of austenite at the end of the shear band evolution process.

#### 4.4.2.5 Dynamic recrystallization

HR-EBSD study indicates formation of 0.28 μm-sized dynamic recrystallized grains in regions of intense strain localization in the specimens subjected to dynamic impact loading (Figs. 4.7 and 4.8). DRX grains of both FCC γ-austenite and BCC α′-martensite phases were observed with the morphology of α′-martensite different from the two typical lath and plate morphologies observed in steels. Kitahara et. al [150] had also observed fine-grained martensites in Fe-Ni alloy. Recently, a high-resolution EBSD technique was used to observe ultrafine equiaxed DRX grains with diameter 0.1–0.3 μm in adiabatic shear bands that developed in AISI 304 ASS [86]. The TEM characterization of AISI 304L stainless steel after exposure to dynamic shock loading conditions also revealed grains having sizes ranging between 0.1 and 0.2 μm inside shear bands [107]. DRX is the result of the gradual rotation of subgrains coupled with dislocation annihilation [112]. The initiation of DRX is preceded by growing fluctuations of grain boundary shape (i.e. serrations) prior to the new grains forming along these grain boundaries [29]. Serrated grains are

characteristics of dynamic recovery, which are observed in grains adjacent to ASBs (indicated by red arrows in Fig. 4.5c). There has been controversy over the effects of recovery on recrystallization, and it is generally believed that these two processes are competing [110]. Derby [111] classified dynamic recrystallization mechanisms into migrational (MDRX) and rotational (RDRX). The migrational dynamic recrystallization mechanism is ruled out in explaining the fine grain structure observed in ASB because the formation time of ASB is extremely short. The RDRX mechanism which involves concurrent plastic deformation was suggested by Nesterenko *et al.* [112] and the model became one of the most accepted mechanisms to explain ultrafine grain structure inside transformed ASBs. The results of a study on the microstructural evolution in copper during high strain rate deformation by Tang *et al.* [151] indicated elongated ultrafine grains rather than equiaxed ultrafine grains in ASBs. The mechanism of formation of the elongated ultrafine grains was reported to be similar to the RDRX mechanism but the equiaxed micrograins at the final stage of the recrystalization process are re-elongated due to effective shear deformation. This is in agreement with the morphology of the ultra-fine grains observed in this study as the grains were slightly elongated along the shear direction (Figs. 4.7 and 4.8). Therefore, a rotational dynamic recrystallization mechanism is proposed for the evolution of nano-sized grains in ASB regions in this study.

### 4.4.3 Texture Evolution

It has been established that metallic materials under high strain rate loading conditions exhibit microstructural features, including ASBs, that depend on the initial texture of the material before mechanical loading [152,153]. During the process of recrystallization, new grains are formed within the parent matrix. These grains, which usually have a different orientation from the original grains, contains sharp-faceted boundaries characterized by low dislocation density in its interior [110,148,154]. In the current study, grain orientation inside and outside the adiabatic shear band are quite different in γ-austenite and α′-martensite phases. While grains outside the ASB irrespective of phases are of Z||<110> and Z||<111> orientations, ASB regions are comprised of grains with Z||<100>, Z||<110> and Z||<111> orientations. Low strain rate compression led to strong CD||<110> and CD||<001> orientations of FCC and BCC phases respectively in Figs. 4.14(b) and (c) which are in agreement with compression textures of metals [142]. Texture analysis on the 304 steel after dynamic shock loading conditions revealed that there was reorientation of

grains with <110> in a path along shear direction, and {111} plane aligning with the shear plane near the shear band. The work of Paul *et al.* [155] suggested that crystal lattice rotates to the point where {111} slip planes become nearly parallel to the maximum shear direction in an FCC metal (Al-0.23%wt.Zr) at a low rate of deformation. They observed that the continuity of slip direction is responsible for shear bands occurring across grain boundaries.

## 4.5 Conclusions

The dynamic mechanical response of hot rolled AISI 321 austenitic stainless steel plate across the plate's thickness was investigated under both dynamic impact and qiasis-static loading. A comparison of the mechanical responses under both loading condirions is made. The following major conclusions are drawn from the results obtained from this study:

1. The texture and the amount of stored energy at the center are different from those in any other region across the thickness of the as-received plate. The stored energy is higher in the centre of the plate.
2. The specimen cut in the center of the as-received plate exhibits the lowest yield strength and highest strain hardening capacity than any other region under the dynamic impact loading condition. However, quasi-statically compressed specimens exhibit lowest yield strength and highest strain hardening capability than the dynamic impacted specimens.
3. Although the stability of austenite is high at high strain rates and low at a low strain rate, strength at high strain rates is compromised as a result of suppression of the evolution of strain-induced martensite and mechanical twinning. Martensitic transformation in both loading conditions follows the FCC γ-austenite → BCC α′-martensite kinetic path.
4. The orientation relationships between the FCC γ-austenite and BCC α′-martensite phases in deformed AISI 321 ASS follow Kurdjumov-Sachs' $\{(111)_{\gamma}||(110)_{\alpha'}$ and $<-101>_{\gamma}||<1-11>_{\alpha'}\}$.
5. Microstructural evaluation of this work showed that a number of strengthening mechanisms might have contributed to the mechanical properties of the AISI 321 ASS. They include austenitic phase transformation to martensite and formation of nano-carbides, which in combination with twinning and slip resulted in a desirable combination of high strength and good ductility.

6. High resolution EBSD confirmed phase transformation, dynamic recrystallization and formation of nano-carbides within the ASB region.
7. The average DRX grain size in the transformed band region is 0.28 μm, which is proposed to form by rotational dynamic recrystallization.

# Chapter 5

## Development of Ultra-Fine-Grained Structure in AISI 321 Austenitic Stainless Steel

The overall goal of this research is to improve the mechanical properties of AISI 321 stainless steel through grain refinement of the existing coarse grain structure to ultrafine grain (UFG) structure. In this chapter, the optimum thermo-mechanical process conditions required to develop UFG structure in AISI 321 austenitic stainless steel are reported. The α′-martensite to γ-austenite reversion behavior and the associated texture development are also discussed. The most economical steps in achieving the optimum conditions for UFG development can be incorporated at the later stage of the existing production line in Canadian steel-producing companies. This chapter is published in "*Metallurgical and Materials Transactions A*" as follows:

A. A. Tiamiyu, J. A. Szpunar, A. G. Odeshi, I. Oguocha, and M. Eskandari, "Development of Ultra-Fine-Grained Structure in AISI 321 Austenitic Stainless Steel," *Metall. Mater. Trans. A Phys. Metall. Mater. Sci.*, vol. 48A, pp. 5990–6012, 2017.

My contributions to this paper include a review of the relevant literature, design and conduction of experiments, analysis and discussion of test results and preparation of the manuscript. The manuscript was reviewed by my supervisors (Professors Akindele Odeshi and Jerzy Szpunar) and their comments were addressed before submission for publication. The present manuscript is a modified version of the published paper: information provided in material and methodology (Chapter 3) are removed to avoid repetition. The copyright permission for manuscript reuse was obtained and provided in APPENDIX C.


### Abstract

Ultra-fine-grained (UFG) structure was developed in AISI 321 austenitic stainless steel (ASS) using cryogenic rolling followed by annealing treatments at 923 K (650 ℃), 973 K (700 ℃), 1023 K (750 ℃) and 1073 K (800 ℃) for different lengths of time. The α′-martensite to γ-austenite reversion behavior and the associated texture development were analyzed in the cryo-rolled specimens after annealing. The activation energy, Q, required for the reversion of α′-martensite to γ-austenite in the steel is estimated to be $80\ \mathrm{kJmol^{-1}}$. TiC precipitates and unreversed triple junction α′-martensite played major roles in the development of UFG structure through the Zener

pinning of grain boundaries. The optimum annealing temperature and time for the development of UFG structure in the cryo-rolled AISI 321 steel are (a) 923 K (650 ℃) for approximately 28800 s (8 h) and (b) 1023 K (750 ℃) for 600 s (10 min), with average grain sizes of 0.22 μm and 0.31 μm, respectively. Annealing at 1023 K (750 ℃) is considered a better alternative since the volume fraction of precipitated carbides in specimens annealed at 1023 K (750 ℃) are less than those annealed at 923 K (650 ℃). More so, the energy consumption during prolonged annealing time to achieve an UFG structure at 923 K (650 ℃) is higher due to low phase reversion rate. The hardness of the UFG specimens is 195% greater than that of the as-received steel. The higher volume fraction of TiC precipitates in the UFG structure may be an additional source of hardening. Micro and macrotexture analysis indicated {110}<uvw> as the major texture component of the austenite grains in the UFG structure. Its intensity is stronger in the specimen annealed at low temperatures.

**Keywords:** *AISI 321 austenitic stainless steel; Texture; Strain-induced martensite; Ultra-fine-grain; Activation energy*

## 5.1 Introduction

AISI 321 is a titanium (Ti)-stabilized austenitic stainless steel (ASS) that is used widely in chemical process plants [3] and fabrication of pressure vessels [1] where excellent corrosion resistance and good mechanical strength are important considerations in materials selection. Ti in the steel reacts with carbon to form titanium carbide (TiC) precipitates thereby preventing the precipitation of chromium carbides along the grain boundaries (sensitization) at elevated temperatures [27]. Despite its attractive corrosion resistance, AISI 321 steel is characterized by low yield strength and low hardness, which leads to very poor tribological properties [3,18]. This has, therefore, led to the interest in the development of nano-/ultra-fine-grained (UFG) structure in stainless steels in order to obtain high strength and good ductility [18].

Several severe plastic deformation (SPD) techniques such as high-pressure torsion (HPT), equal channel angular pressing (ECAP), and cyclic extrusion compression [156-158] are used to develop ultrafine grained structure in metallic alloys. However, repetitive application of conventional thermo-mechanical processing is reported to be very suitable for developing UFG structure in steels [159]. This process involves conventional cold or cryogenic rolling (cryo-rolling) followed by annealing at an appropriate temperature [156,159]. The relatively low accumulated strain

required in this process (about 1-3.6 in comparison to 3-6 required in SPD) is an advantage over other SPD techniques. This suggests that the thermo-mechanical process of developing UFG structure is amenable to large-scale production and the process parameters can easily be optimized, while combined benefits of phase transformation and controlled cooling are exploited [159].

The α′-martensite start temperature ($M_s$) of AISI 300-series austenitic stainless steels depends on the alloy content as expressed in Eqn. 2.3. However, plastic deformation can introduce the necessary energy for martensitic transformation, which increases the martensite formation temperature to $M_d$. $M_d$ is the temperature, below which martensite will evolve during deformation. The martensite produced via plastic deformation is called strain-induced martensite (SIM). Angel [160] studied the effect of chemical composition on the stability of austenite in steels and established an expression for $M_{d30/50}$, which is the temperature (in $^{o}$C) at which 50% of austenite will transform to α′-martensite at 30% true strain. The expression was subsequently modified by Nohara et al. [48] to incorporate the effect of austenite grain size as stated in Eqn. 2.5. The transformation of metastable FCC austenitic (γ) to a BCC martensite (α′) during the cold rolling of ASS below the $M_d$ temperature is exploited in the development of ultra-fine-grain (UFG) structure, which in-turn, improves the yield strength of the steel [18]. The strain-induced martensite (α′) reverts to γ upon annealing at a carefully-selected temperature and time, to develop UFG structure in the austenitic phase. This completes the thermo-mechanical process.

During the repetitive cryo-rolling of austenitic stainless steel, there exists a critical strain called saturation strain (εs), at which the austenite phase (γ) is completely transformed to α′-martensite. The strain value (ε) is estimated using the expression: $\ln[1/(1-r)]$, where $r$ is the thickness reduction. A low value of εs, obtainable by cryo-rolling is advantageous in the grain refinement process. This is due to the extensive crushing of martensite that will occur at strains higher than the εs [18]. Saturation strain was reported to be 0.7 for the cold rolling of AISI 301 at 273 K (0 ℃), and 0.2 for cryo-rolling at 77 K [161]. A prerequisite for the development of UFG structure is to ensure the saturation and break-up (via additional heavy cold/cryo-rolling) of α′-martensite prior to austenite reversion [162]. It has been suggested that the break-up of individual martensite grains may lead to carbon redistribution in the ASS, interfering with the shear process in such a way that martensite grains possess enough stored energy that favors the evolution of ultra-fine strain-free austenite grains [163]. The cold/cryo-rolling of an ASS leads to the development of transformed

α′-martensite with two types of morphologies; lath and dislocation-cell type [158,163,164]. If the α′-martensite is lath-type, the austenite grains will nucleate and grow at the lath boundaries and intersections into the martensite lath. Equiaxed ultrafine austenite grains will nucleate at martensite grain boundaries if the α′-martensite morphology is of the dislocation-cell-type that consist of dislocation forests and ultra-fine lath martensite [164]. The distortion of martensite within the matrix at high intensity of plastic deformation during cold rolling results in morphology change from lath to dislocation cell-type (the preferred type for the development of UFG structure) martensite [158,163]. The dislocation cell-type martensite is expected to provide a high density of austenite nucleation sites.

The sequence of martensitic transformation (γ (parent phase) → α′) during the cryo-rolling process is still a subject of debate among researchers [6,165,166]. There is a dispute about whether the martensitic transformation followed the sequence: FCC γ-austenite → BCC α′-martensite or the sequence: FCC γ-austenite → HCP ε-martensite → BCC α′-martensite. Processing parameters such as the temperature, state of stress, chemical composition, stacking fault energy (SFE) and rate of deformation have been reported to influence the amount of ε and α′–martensite that form [6,18]. Meanwhile, the mechanisms of austenitic reversion (α′ → γ [product phase]) in the final stage of the thermo-mechanical process is of two type; martensitic shear reversion (MSR) and diffusional reversion (DR) [162,167]. MSR results in the alteration of atomic arrangement by homogeneously deforming the BCC α′-martensite into FCC γ-austenite structure without the diffusion of atoms, while austenite grains developed by DR mechanism nucleate and grow by diffusion of Cr, Ni and Fe atoms [168]. Since diffusion is time-dependent, martensite-to-austenite reversion takes longer time to complete in specimen subjected to DR than specimen subjected to MSR. The morphology of the FCC γ-austenite grains developed from the lath BCC α′-martensite by MSR mechanism are lath-like, and in addition, the grains are characterized by the presence of high dislocation densities that developed during prior deformation. On the other hand, austenite grains via DR mechanism are equiaxed and are randomly nucleated in α′ lath boundaries [163,167,169]. The main factors affecting reversion kinetics includes chemical composition of the steel, the amount of cold work, annealing temperature and time [158,170]. Thermodynamic analysis is used to explain the effect of chemical compositions on the dominant reversion mechanism. This is usually done by plotting the temperature dependence of free energy change for BCC transformation to FCC phase ($\Delta G^{(\alpha\rightarrow\gamma)}$) using a solution model expressed in Eqn. 5.1 [167]. From this plot, the annealing temperature that

will result in the DR and MSR of BCC-martensite to FCC-austenite of ternary Fe-Cr-Ni system steels can be estimated.

$$\Delta G^{(\alpha\rightarrow\gamma)}\left(\frac{J}{mol}\right) = 10^{-2}\Delta G_{Fe}^{(\alpha\rightarrow\gamma)}(100 - \%Cr - \%Ni) - 97.5(\%Cr) + 2.02(\%Cr)^2 - 108.8(\%Ni) + 0.52(\%Ni)^2 - 0.05(\%Cr)(\%Ni) + 10^{-3}T[73.3(\%Cr) - 0.67(\%Cr)^2 + 50.2(\%Ni) - 0.84(\%Ni)^2 - 1.51(\%Cr)(\%Ni)] \quad \ldots 5.1$$

where T is a selected temperature (K) and $\Delta G_{Fe}^{(\alpha\rightarrow\gamma)}$ is the free energy difference for pure iron obtained from the thermodynamic data published by Kaufman et al. [171]. Tomimura et al. [167] reported that a free energy of -500 J/mol provides the minimum driving force for complete martensitic shear reversion. In the present paper, the term "transformation" is reserved for the γ (parent phase) → α′ transformation reaction while the term "reversion" is used for the α′ → γ (product phase) transformation.

So far, there has been a remarkable success in the development of UFG structure in various steel grades via the thermo-mechanical process. Grain sizes in the range of ∼200–600 nm was developed and observed with transmission electron microscope (TEM) in strips of ∼1.5 mm steels (Fe–16Cr–10Ni alloy, AISI 301LN and 301 ASSs) cold rolled to 73.5% reduction with subsequent annealing in the temperature range of 700–925 °C for 1–100 s [163]. Whereas the austenitic UFGs in the Fe–16Cr–10Ni and AISI 301 ASS occurred by MSR process, the austenite grains in the AISI 301LN ASS were reported to develop by DR mechanism. This affirms the role of chemical composition in the type of reversion mechanism that occurs during subsequent annealing of cold-rolled austenitic stainless steel. A 75% thickness reduction of an ultra-low carbon (ULC) austenitic steel at room temperature and subsequent annealing at 575 °C, 605 °C and 665 °C, led to an average austenite grain size of 0.3, 0.6 and 2.0 μm, respectively [172]. An average grain size of 130 nm with an approximately 83% volume fraction of austenite was reported in AISI 321 austenitic stainless steel after cold rolling at -20 °C to a 90% thickness reduction and annealing at 750 °C for 5 minutes [49]. Only few authors have reported the development of crystallographic texture during the reversion of α′-martensite to γ-austenite. The orientation relationship between γ and α′ is the Kurdjumov–Sachs (K–S) relation, {111}γ||{110}α and <110>γ||<111>α, which has about 24 crystallographic variants [173]. Somani et al. [169] observed strong Brass {110}<112> and Goss {110}<100> orientations with minor Copper {112}<111> and S {123}<634> orientations for

reversed austenite in cold-rolled and annealed AISI 301LN. Similar texture was reported for other austenitic stainless steels [145,174].

In general, the development of UFG structure and the accompanying crystallographic texture in AISI 321 austenitic stainless steel has not been well addressed to the best of the authors' knowledge. The objective of this study is to determine the optimum thermo-mechanical process parameters for developing ultra-fine-grained structure in AISI 321 austenitic stainless steel. In addition, a systematic and detailed study of the texture development at each stage of the austenite reversion process during annealing was carried out.

## 5.2 Material and Methodology

### 5.2.1 Material

An AISI 321 austenitic stainless steel plate described in Section 3.1 was used in this study.

### 5.2.2 Cryo-rolling process and annealing treatments

The cryo-rolling process and annealing treatment procedure are as described in Section 3.2.

### 5.2.3 Material characterization

Material characterization techniques are as described in Sections 3.3.1 (hardness tests) and 3.5 (electrolytic polishing, EBSD, X-ray diffractometry and Feritscope measurements). All microstructural analysis and measurements in this study were conducted on the RD-TD plane, otherwise referred to as the ND plane.

## 5.3 Results and Discussion

### 5.3.1 As-received and cryo-rolled samples

The results of the X-ray phase ID measurement that confirms the complete martensitic transformation of the austenite phase in the as-received sample after cryo-rolling at 77 K are presented in Fig. 5.1. It can be observed that the austenitic structure of the as-received steel has completely transformed to α′-martensite at 20% thickness reduction. However, a higher percentage thickness reduction (r = 50%) was carried out so that the martensite grains can accumulate enough stored energy that promotes the development of ultra-fine strain-free austenite grains during

subsequent annealing. X-ray diffraction patterns also show that the martensitic peak with the highest intensity (preferred orientation) changed from (110)α′ to (200)α′ as the percentage thickness reduction increased from 20 to 50%. The EBSD inverse pole figure (IPF) maps in the inset of Fig. 5.1 shows a near-random texture of the austenitic phase and the presence of annealing twins in the as-received alloy. The maps confirmed that the austenitic structure of the as-received steel did not only completely transform to α′-martensite, significant texturing also occurred in both cryo-rolled samples. While the orientation of martensite grains in cryo-rolled samples are predominantly ND||{100} and ND||{111}, the orientation of few grains are ND||{123}, {133} and

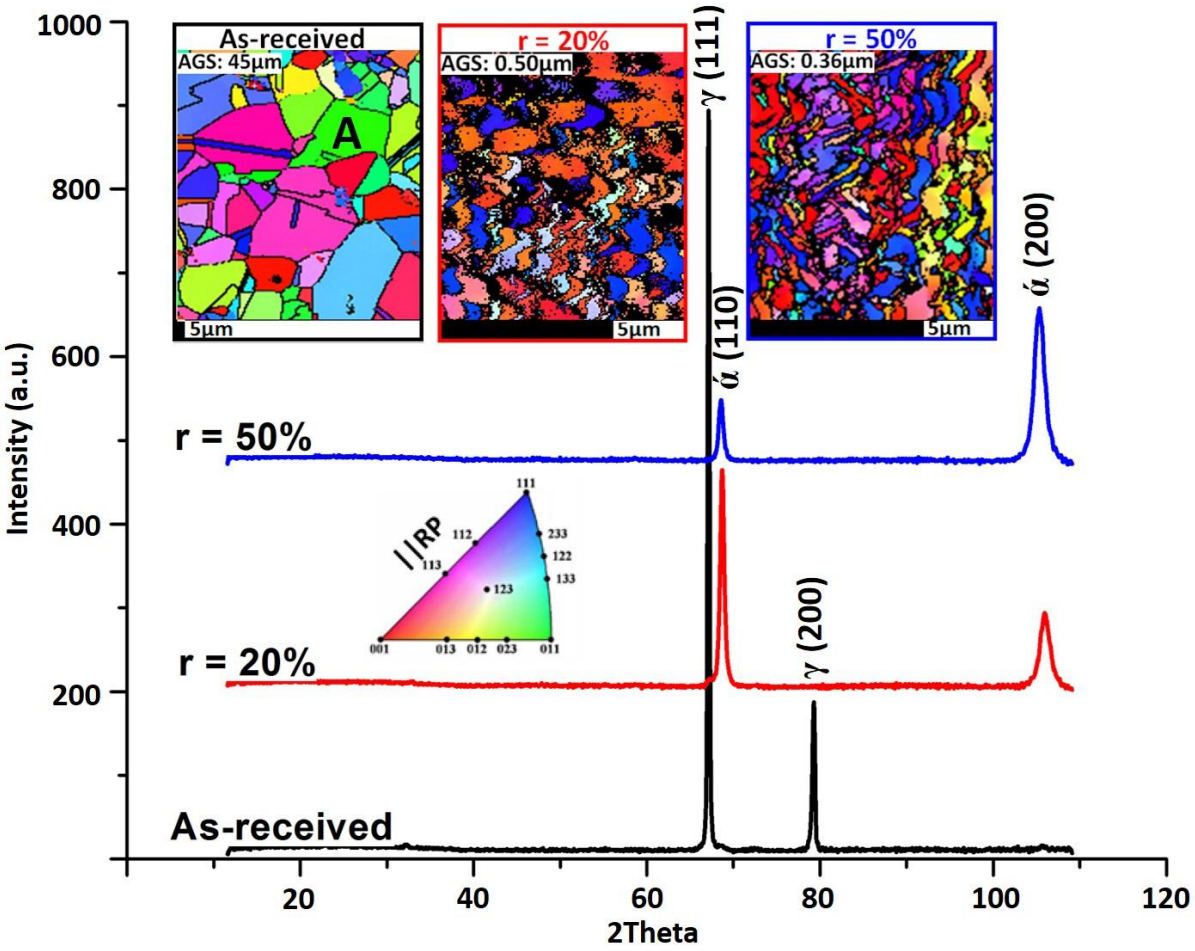


Fig. 5.1. X-ray diffraction patterns of the as-received sample and cryo-rolled specimens reduced by 20% and 50% of its original thickness. Inset is the associated EBSD inverse pole figure (IPF-Z) colour maps of both the FCC-austenitic phase of the as-received and the BCC-martensitic phase of the cryo-rolled specimens.

ND‖{013}, {012}, {023} in r20 and r50 samples, respectively. Furthermore, the EBSD maps confirm the further crushing of martensite grains and the development of dislocation-cell type α′-martensite with an average grain size of 0.36 μm as the percentage thickness reduction increased from 20 to 50%. Three ϕ2 sections of the calculated ODF in Fig. 5.2a confirm the randomness of texture in the austenitic phase of the as-received sample. Similarly, an increase in thickness reduction to 50% led to the replacement of strong Cube {001}<100> in r20 sample with R-Cube {001}<110> component as shown in Fig. 5.2b and c. The intensities of Z {111}<110> and R-Cu {112}<110> texture was also increased by the increase in the degree of cryo-rolling. Fig. 5.2d is used in the interpretation of the major texture components and fibres in the three ϕ2 sections of the calculated ODF. Further analysis in this study will henceforth center on the r50 sample since it has the necessary characteristics that favours the development of UFG structure.

### 5.3.2 Annealing at 923 K, 973 K, 1023 K and 1073 K

#### 5.3.2.1 Reversion kinetics and hardness profile

The X-ray diffraction patterns that show the reversion behaviour of BCC α′-martensite to FCC γ-austenite after annealing at 923 K (650 ℃), 973 K (700 ℃), 1023 K (750 ℃) and 1073 K (800 ℃) are presented in Fig. 5.3. No new peak(s) were observed for 60 s annealing at 923 K (650 ℃), 973 K (700 ℃) and 1023 K (750 ℃) and 30 s annealing at 1073 K (800 ℃). These suggest there is no evidence of the commencement of austenitic reversion since only the BCC peaks were still present at these times. This behavior may be peculiar to the investigated steel. In a separate study [49], the 90% rolling reduction of an AISI 321 austenitic stainless steel at 253 K with subsequent annealing at 973 K (700 ℃), 1023 K (750 ℃), 1073 K (800 ℃) and 1123 K (850 ℃) for 240, 180, 120 and 60 s, respectively, shows no austenitic reversion. As annealing time increased, (111)γ and (200)γ peaks appeared and their intensities increased at two 2θ positions (67.1° and 79.3°) at the expense of the (110)α′ and (200)α′ peaks. However, at certain annealing temperature and specific time range, the intensities of martensite peaks remain either unchanged or increased with time, signaling the formation of thermally-induced martensite. For instance, (110)α′ and (200)α′ peaks remain nearly unchanged or increased between 3600-14400 s, 600-1200 s and 600-1200 s when cryo-rolled samples were annealed at 923 K (650 ℃), 973 K (700 ℃) and 1023 K (750 ℃), respectively.

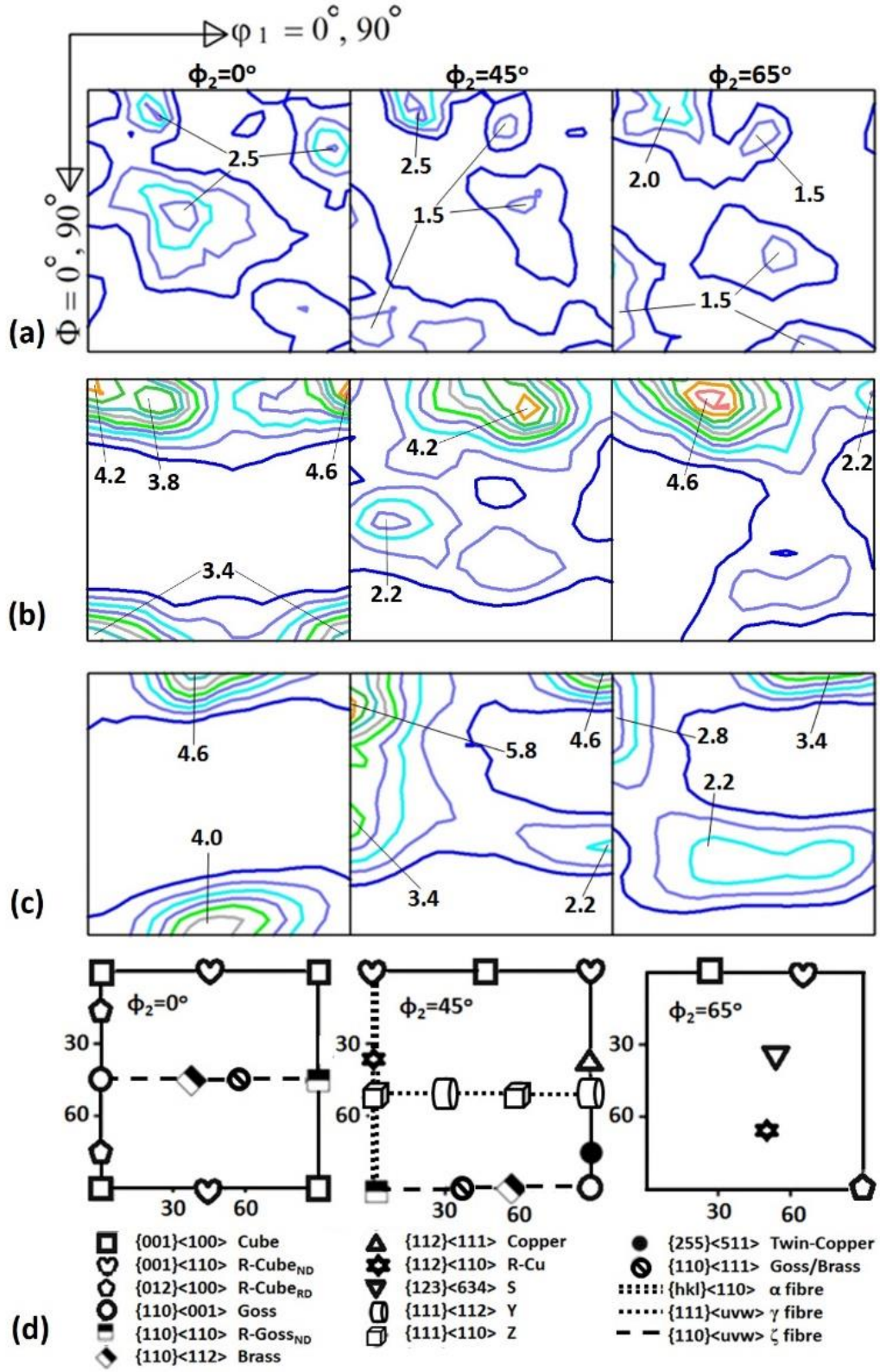


Fig. 5.2. Selected ODF ϕ2 sections from the XRD measurement of the (a) austenitic phase in as-received specimen and martensitic phase in (b) r = 20% and (c) r = 50% cryo-rolled specimen (d) ideal texture components observed in steels. r is the percentage thickness reduction.

The reverse was observed to be the case for the specimen annealed at 1073 K (800 ℃) as the intensities of the martensite peaks consistently decreased with time. Similarly, Fig. 5.3a-c shows the presence of a new TiC (111) peak in the X-ray diffraction patterns of specimens annealed at 923 K (650 ℃), 973 K (700 ℃) and 1023 K (750 ℃), which is nearly absent in the specimen annealed at 1073 K (800 ℃) (Fig. 5.3d).

Notable similarities also exist among the specimens subjected to the four reversion temperatures used in this study, as it relates to peaks and the preferred orientation. Between the two martensitic planes, (200)α′ is the preferred orientation with intensity higher than that for (110)α′, for all reversion temperatures, irrespective of the annealing time. However, austenite peaks show a switch of preferred orientation from (200)γ to (111)γ when the reversion of α′-martensite to γ-austenite is near completion, as observed in the maximum annealing times of 28800 s and 1800 s for specimens annealed at 923 K (650 ℃) and 1073 K (800 ℃), respectively (Figs. 5.3a and d). At

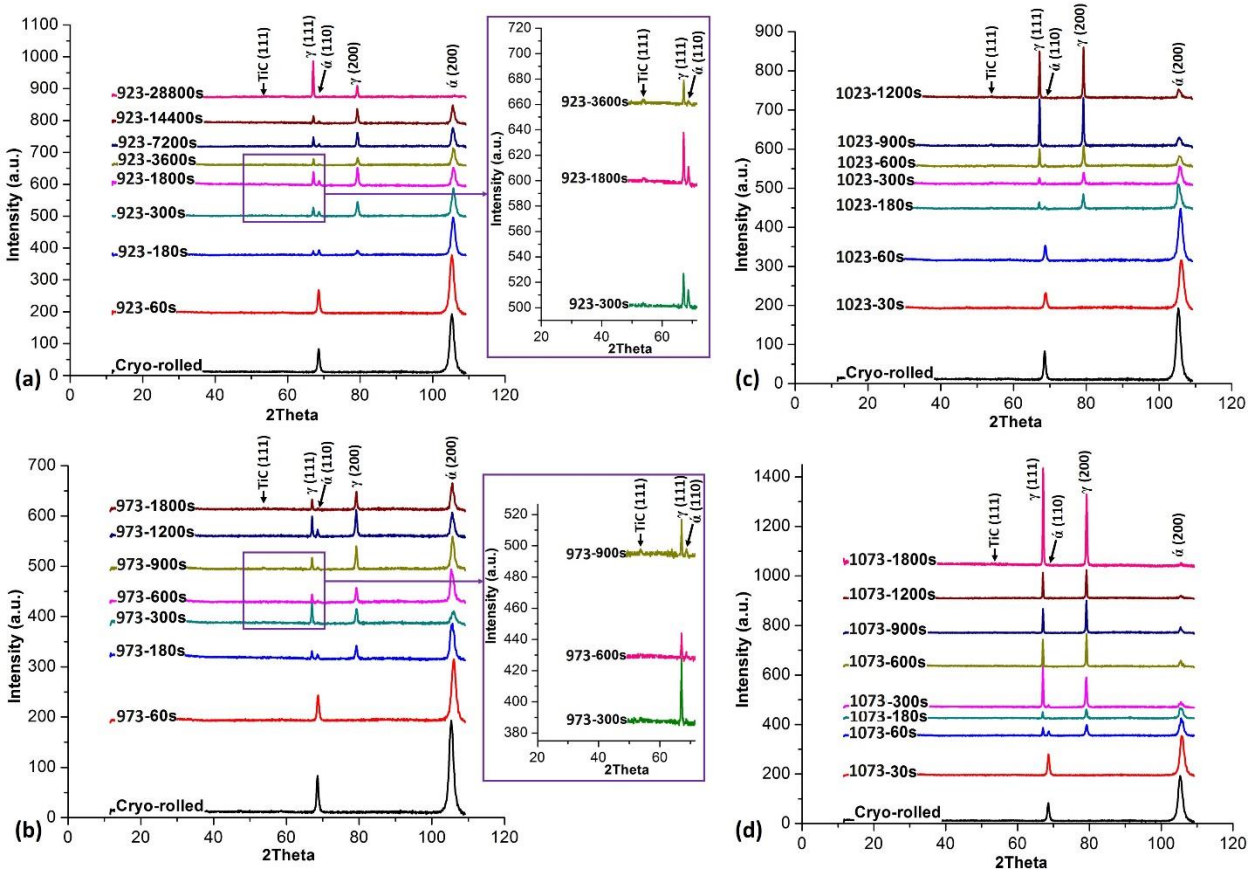


Fig. 5.3. X-ray diffraction patterns showing the pattern of phase transformation at an annealing temperature of (a) 923 K (650 ℃), (b) 973 K (700 ℃), (c) 1023 K (750 ℃) and (d) 1073 K (800 ℃). Enlargement in (a) and (b) shows more clearly the TiC peaks in selected annealing times.

annealing temperature of 973 K (700 ℃) and 1023 K (750 ℃) (Figs. 5.3b and c) where the maximum annealing time does not result in the completion of the reversion process, it is observed that (200)γ plane is the preferred orientation. A shift in the preferred orientation of martensitic planes had also been observed during the isochronal annealing of a cold rolled AISI 301 austenitic stainless steel [158].

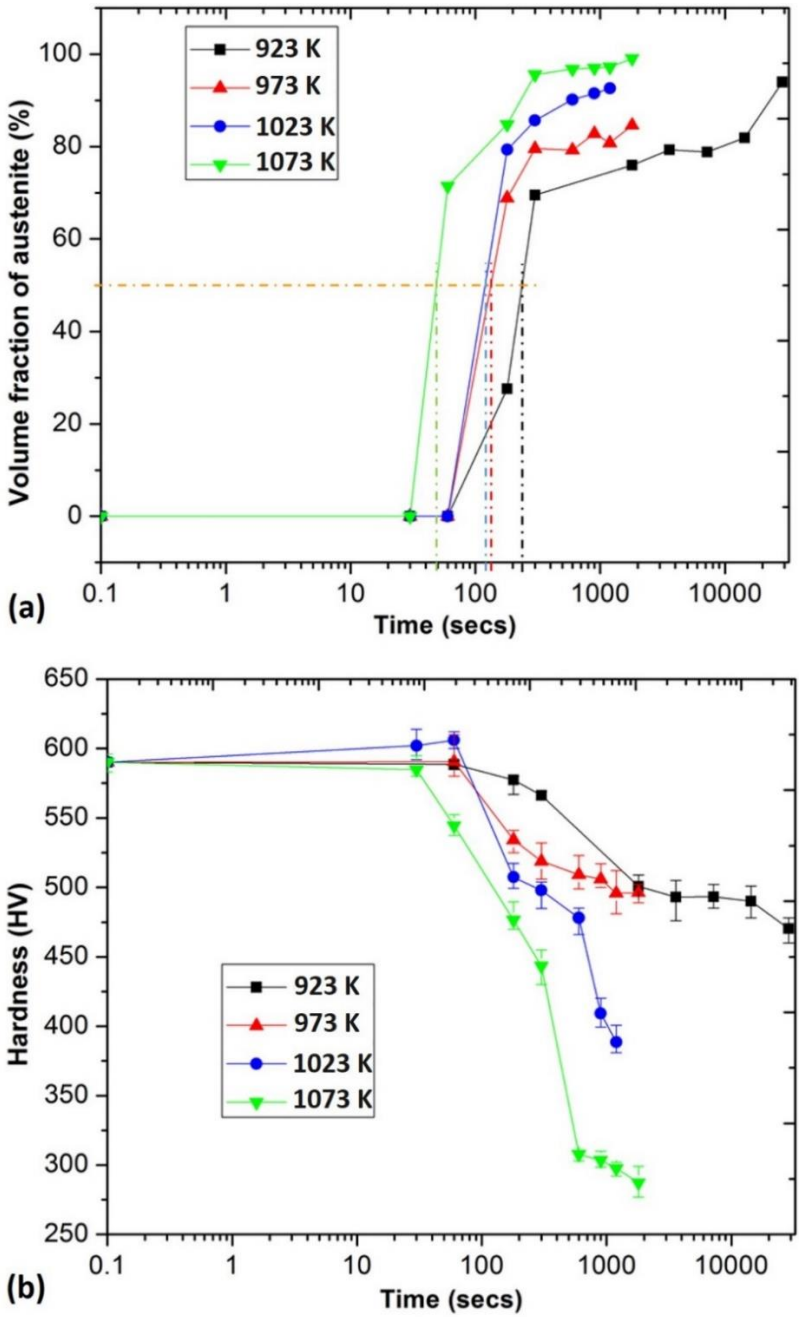


Fig. 5.4. (a) Volume fraction of reversed austenite and (b) corresponding hardness profile during reversion.

Once the reversion commences as shown in Fig. 5.4, the volume fraction of austenite increases with time, while the hardness decreases until a near-asymptotic behaviour is observed. The reason for asymptotic behavior of the austenite fraction is under debate. However, a previous study indicated that the depletion of carbon (an austenite former) in the $\gamma_r$ as a result of the precipitation of carbides during reversion can increase the $M_s$ temperature above the room temperature in AISI 301 steel [169]. The increase in $M_s$ temperature implies that the $\gamma_r$ may transform back to martensite (thermally-induced martensite) on cooling from the annealing temperature to room temperature. This may result in asymptotic behaviour or increased martensite fraction at higher annealing times. In this study, the $M_s$ temperature of AISI 321 austenitic stainless steel was re-estimated to be -79 $^{o}$C (194 K) using Eqn. 2.3 without carbon.

Therefore, the cooling of the reverted austenite to room temperature in AISI 321 steel may not be responsible for the transformation of austenite back to martensite. It is obvious from this study that the observation of asymptotic behaviour and evidence of TiC during reversion at 923 K (650 ℃), 973 K (700 ℃) and 1023 K (750 ℃) may suggest that TiC precipitates (and not the depletion of carbon itself) inhibit austenitic reversion rate to keep the volume fraction of the martensite constant or increased it at higher annealing times. It has been suggested that the asymptotic behavior can indicate an upper limit to the prospect of increasing the mechanical properties of the austenitic steel via grain refining process [157]. This is true and could be validated by considering, for instance, sample annealed at 923 K (650 ℃) in Fig. 5.4. At an annealing time beyond the asymptotic region (28800 s), austenite fraction increased, hardness value decreased and grain growth (confirmed and presented in the next section) had begun.

The effect of annealing temperature on the percentage volume fraction of reversed austenite ($\gamma_r$) follows a typical sigmoidal shape as shown in Fig. 5.4a. The sigmoidal shape implies that at the commencement of annealing, nucleation of the austenite grains occurs slowly. However, nucleation and growth rate reached its peak and reversion rate slows down again near completion due to the impingement and exhaustion of nucleation sites [175]. As earlier observed in the X-ray diffraction patterns presented in Fig. 5.3, Feritscope measurements also confirmed that austenitic reversion had barely occurred for samples annealed at 923 K (650 ℃), 973 K (700 ℃) and 1023 K (750 ℃) for 60 s and at 1073 K (800 ℃) samples for 30 s. As annealing time increased, specimens showed a relative increase in austenite fraction, though a near-asymptotic behavior was observed

after certain annealing times towards the completion of reversion. From the isothermal reversion plot in Fig. 5.4a, the rate of reversion during the annealing at 923 K (650 ℃), 973 K (700 ℃), 1023 K (750 ℃) and 1073 K (800 ℃) are estimated to be 4.17 x $10^{-3}$, 6.99 x $10^{-3}$, 8.00 x $10^{-3}$ and 20.41 x $10^{-3}$ $s^{-1}$, respectively, using Eqn. 5.2 [176]. These values confirmed that the rate of reversion increases with annealing temperature.

Table 5.1. Variation of α′-martensite and γ-austenite grain size with annealing temperature and time.

| | **Grain size, μm** | | | | | | | |
|---|---|---|---|---|---|---|---|---|
| **Temp., K** | **923 K** | | **973 K** | | **1023 K** | | **1073 K** | |
| **Phases** | **α′** | **γ** | **α′** | **γ** | **α′** | **γ** | **α′** | **γ** |
| **Time, s** | | | | | | | | |
| 60 | 0.36 | - | 0.36 | - | 0.36 | - | 0.21 | 0.21 |
| 180 | 0.23 | 0.16 | 0.13 | 0.16 | 0.19 | 0.21 | 0.18 | 0.24 |
| 300 | 0.20 | 0.22 | 0.15 | 0.18 | 0.18 | 0.25 | 0.16 | 0.12-2.73 |
| 600 | 0.20 | 0.22 | 0.17 | 0.22 | 0.17 | 0.31 | 0.10 | 0.9-5.6 |
| 900 | 0.20 | 0.22 | 0.17 | 0.22 | 0.16 | 0.12-2.32 | 0.10 | 1.2-8.6 |
| 1200 | 0.20 | 0.25 | 0.16 | 0.28 | 0.15 | 0.93-5.32 | 0.10 | 2.8-10.6 |
| 1800 | 0.20 | 0.25 | 0.16 | 0.32 | - | - | 0.10 | 4.2-14.6 |
| 3600 | 0.20 | 0.26 | - | - | - | - | - | - |
| 14400 | 0.19 | 0.33 | - | - | - | - | - | - |
| 28800 | 0.18 | 0.12-1.7 | - | - | - | - | - | - |

$$Rate = 1/t_{0.5} \quad \ldots 5.2$$

where $t_{0.5}$ is the time required for the reversion to proceed half way to completion as obtained from Fig. 5.4a.

Figure 5.4b shows the hardness profile of the cryo-rolled AISI 321 sample as the annealing time increases. The Vickers hardness value of the as-received austenitic steel had increased from 166 $\pm$ 8 to 590 $\pm$ 5 HV upon cryo-rolling at 77 K. The complete transformation of γ-austenite to α′-martensite and the crushing of the martensitic grains to ultra-fine size via 50% thickness reduction would have resulted in the 255% rise in the hardness value. However, low annealing times (60 s at 923 K [650 ℃], 973 K [700 ℃] and 1023 K [750 ℃] and 30 s of annealing at 1073 K [800 ℃]) that shows no trace of commencement of austenite reversion, the hardness remained relatively unchanged, in comparison with the hardness value of the cryo-rolled sample. As annealing time was further increased, hardness values dropped till an asymptotic behavior is reached at approx. 490 HV for lower annealing temperature (923 K [650 ℃] and 973 K [700 ℃]) It is suspected that a further drop in the hardness value below the asymptotic region signalled the onset of grain growth

which will be analyzed in the subsequent section. The hardness values were observed to be higher in specimens subjected to lower annealing temperatures (923 K [650 ℃] and 973 K [700 ℃]) than those subjected to higher annealing temperatures (1023 K [750 ℃] and 1073 K [800 ℃]). A higher fraction of TiC particles in the specimens annealed at low temperature may have been an additional source of hardening. So far, there exists a striking correlation between the evolution pattern of thermally-induced martensite, TiCs and the asymptotic behavior in the hardness profile during austenite reversion. This pattern is observed more in a wider range of time at low annealing temperatures. The effect of annealing temperature and time on the α′-martensite and γ-austenite grain size is presented in Table 5.1. Increase in annealing temperature and time results in a relative increase in γ grain size at the expense of the α′ grains.

5.3.2.2 Microstructural evaluation

5.3.2.2.1 Microtexture analysis

The results of the high resolution (HR) EBSD measurement on the cryo-rolled and annealed AISI 321 ASS specimens are presented in Figs. 5.5-5.11. Measurement on the specimens annealed at 923 K (650 ℃), 973 K (700 ℃) and 1023 K (750 ℃) for 60 s and 1073 K (800 ℃) for 30 s also suggest no evidence of austenite reversion as previously noted in Figs. 5.3 and 5.4. Therefore, EBSD maps of these specimens are not included in this article for brevity.

Annealing at 923 K

Figure 5.5 shows the EBSD maps of a specimen annealed for 180 s at 923 K (650 ℃), indicating an early stage of reversion. Phase colour map in Fig. 5.5a clearly shows that fairly equiaxed austenite grains with an average size of 0.16 μm randomly nucleated in the α′-martensite lath boundaries. The α′-martensite lath boundaries and its vicinity are the dark regions and are indications of accumulation of stored energy with high Kernel average misorientation (KAM) values (KAM map not included in the figure) that promote the evolution of new austenite grains and TiC particles. The IPF color map and BCC ODFs in Figs. 5.5b and d showed five possible α′-martensite variants ({001}<100>, {111}<2-31>, {110}<-331>, {112}<-2-33> and {123}<-2-33>), with {001}<100>, {111}<2-31> and {112}<-2-33> as the predominant variants. On the other hand, four possible γ-austenite variants ({001}<201>, {110}<110>, {113}<3-16> and {212}<1-51>) were observed in Fig. 5.5c and d, with {110}<110> as the predominant variants

(preferred orientation). It is worth noting that α′-{110}<-331> (green color) was observed to be finely dispersed at the lath boundaries (Fig. 5.5b); the same region where equiaxed γ-{110}<110> grains nucleates (Fig. 5.5c). α′-{110}<-331> and γ-{110}<110> are close in orientation and the former (finely dispersed in Fig. 5.5b) could be thought to influence the latter. The superimposition of {111}γ and {110}α′ pole figures in Fig. 5.5e shows the poles from all variants are in coincidence. A {100} oriented-α′ and {110} oriented-γ grains adjacent to one another were randomly selected and further analyzed in Fig. 5.5f. It can also be seen (black circles) that one of the poles of {111}γ is parallel to one of the poles of {110}α′. Similarly, one of the <110>γ directions is parallel to one of the <111>α′ directions. These confirm that the nucleated γ-austenite follows K-S orientation relationship with the α′-martensite.

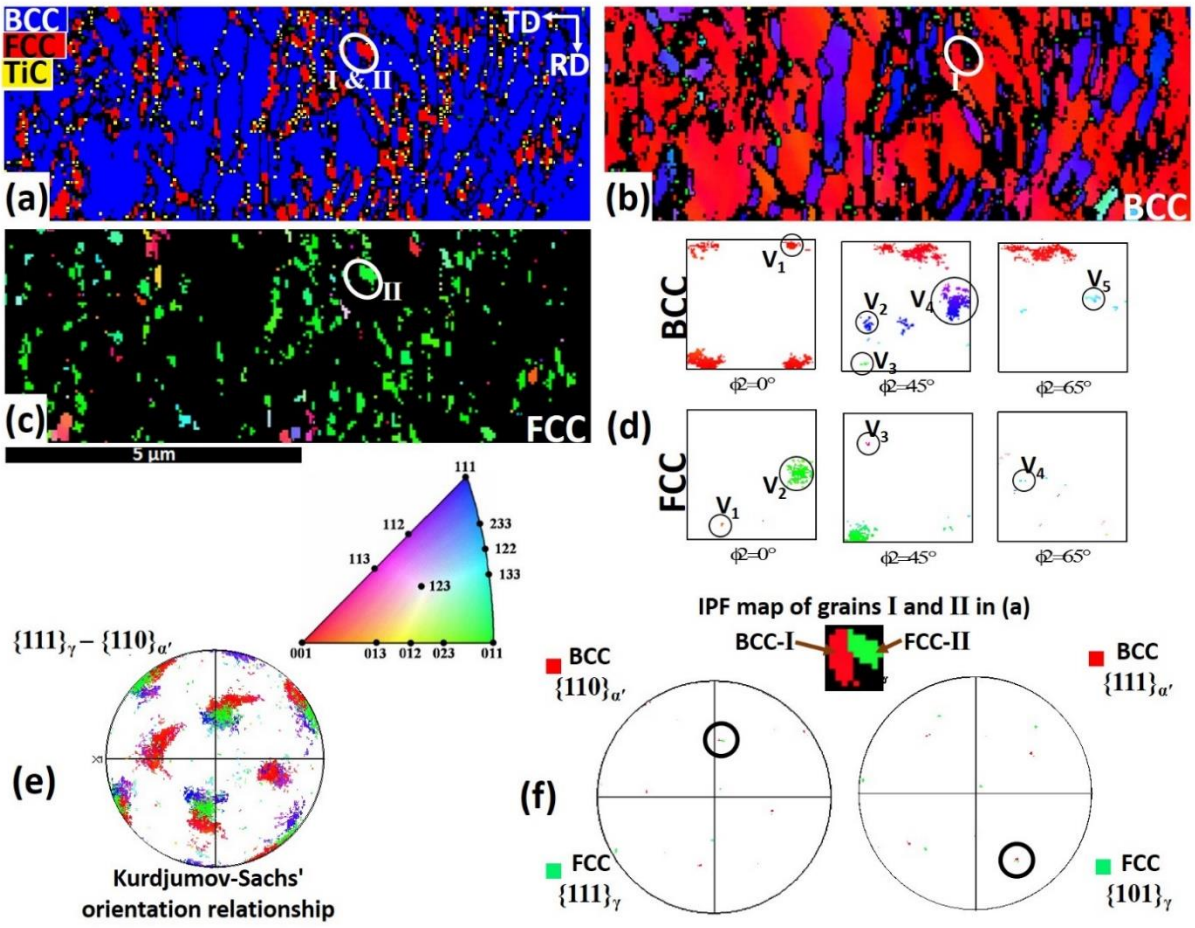


Fig. 5.5. HR-EBSD maps of specimen annealed at 923 K (650 ℃) for 180s: (a) phase color map. IPF color maps of (b) BCC α′-martensite and (c) FCC γ-austenite, (d) 0o, 45o, 65o ϕ2 ODF sections of the BCC α′-martensite and FCC γ-austenite. Superimposed {111} and {110} pole figures for (e) all grains and (f) selected α′-γ grains.

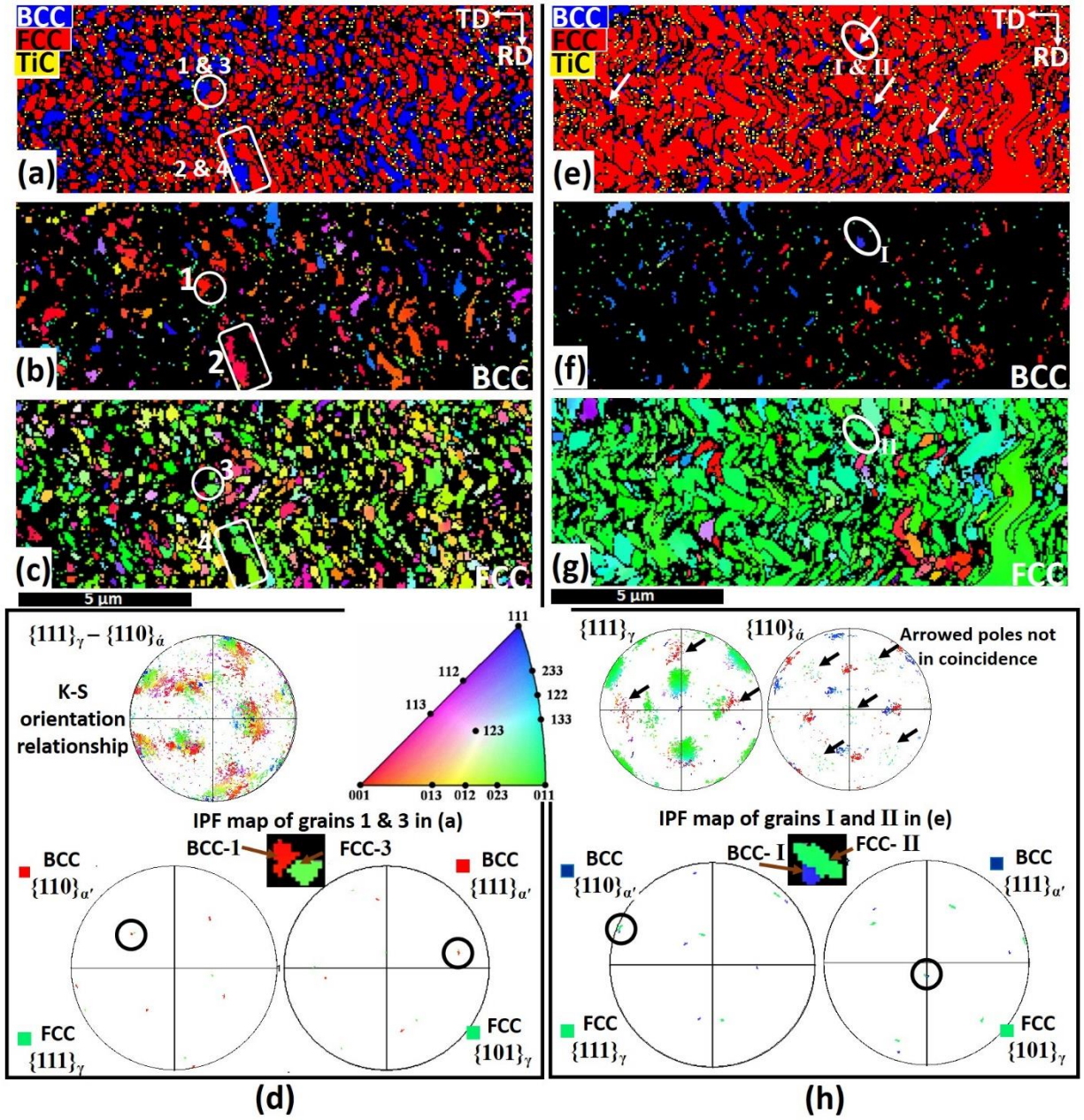


Fig. 5.6. HR-EBSD maps of specimen annealed at 923 K (650 ℃) for (a-d) 300s and (e-h) 28800s: (a, e) phase color maps, (b, f) IPF color maps of BCC α′-martensite, (c, g) IPF color maps of FCC γ-austenite, (d) superimposed {111} and {110} pole figures for all grains and selected α′-γ grains in 300s-annealed specimen, (h) unstratified and superimposed {111} and {110} pole figures for all grains and selected α′-γ grains in 28800s-annealed specimen.

At the annealing time of 300 s, a change in the area fraction and texture of the phases, and significant change in the morphology of the α′-martensite can be observed (Fig. 5.6a-d). Unlike at the nucleation stage of austenite grains, where the martensite grains are lath-like as shown in Fig. 5.5, the shape of the α′-martensite grains gradually changed from lath to near equiaxed as annealing

time increased to 300 s. The change in morphology of the martensite was also accompanied by a decrease in grain size to an average of 0.20 μm. Similarly, the austenite average size had increased to 0.22 μm while maintaining its equiaxed morphology. It is evident that the morphology of the growing austenite grains is influenced by the morphology of their neighboring martensite grains. This can be explained by considering four grains (1, 2, 3 & 4) in Fig. 5.6a. Grains 1 and 2 are martensitic (Fig. 5.6b) while grains 3 and 4 are austenitic (Fig. 5.6c). The equiaxed martensite grain 1 in Fig. 5.6a has a corresponding equiaxed austenite grain 3 as its neighbour. Similarly, the elongated martensite grain 2, that is an exception to the equiaxed structure in Fig. 5.6a, have an elongated austenite grain 4 as its neighbour. This suggests that a growing austenite boundary is hindered by the boundaries of their neighbour grains; thereby forcing the austenite grain to take the morphology of the martensite or surrounding grain. In a separate study [158,167], the morphology of transformed martensite (α′) has been reported to influence the shape of the $\gamma_r$. On the crystallographic orientation of grains, five variants each were present in both BCC ({001}<201>, {110}<2-11>, {111}<-1-21>, {113}<1-41> and {213}<1-30>) and FCC ({110}<3-11>, {001}<201>, {113}<2-51>, {112}<0-21>, {111}<-1-23> and {213}<-1-32>) phases. It can also be clearly observed that the orientation of the γ-variants is close to those of the α′-variants, again suggesting that the orientation of austenite grains is affected by those of the martensite. The comparison of {111}γ and {110}α′ pole figures in Fig. 5.6d also confirms the coincidence of poles from all variants and those of the selected grains of both phases; affirming that the K-S orientation relationship still exists between γ-austenite and α′-martensite. At this stage of annealing, it is worth mentioning that grain growth is yet to commence and the preferred orientation of the austenite UFG is still near {110}||ND, though not as strong as observed in the early stage of nucleation (Fig. 5.5c and e). However, the specimen at this stage still contains approximately 30.5% volume fraction of martensite.

As already documented in Figs. 5.3a and 5.4a, the reversion rate at the annealing temperature of 923 K (650 ℃) is low such that microstructural (EBSD) analysis indicate no evidence of grain growth until annealing time was increased to 28800 s (Fig. 5.6 e-h). Though majority of the austenite grains are still ultra-fine at annealing time of 28800 s, grain size is now in the range of 0.12 - 1.70 μm as shown in the EBSD phase color map (Fig. 5.6e). Most of the unreversed α′-martensite (up to about 6% volume fraction as observed in Fig. 5.4a) were located at the austenite triple junctions. These are marked by white arrows in the phase color map. Fewer variants were

observed with significant texturing of the austenite grains near {110}||ND. Unlike the observations in Figs. 5.5 and 5.6a-d, comparison of {111}γ and {110}α′ pole figures of all variants in Fig. 5.6h shows no coincidence of some variants (black arrowed poles) and could indicate the loss of the K-S orientation relationship between γ-austenite and α′-martensite of these variants. Meanwhile, the non-arrowed poles or variants (green in {111}γ pole figure, and red and blue in {110}α′ pole figure) are in coincidence, obeying K-S orientation relationship. This is also confirmed by the coincidence of poles from the variants of the selected BCC-I and FCC-II grains. It is expected that the annealing temperature at 923 K (650 ℃) promotes the evolution of carbide precipitates as confirmed in phase color maps (Figs 5.5a, 5.6a, and 5.6e). Both the TiCs and α′-martensite at triple junctions contribute to the stability of the equiaxed UFG structure.

Annealing at 973 K

In comparison with Fig. 5.5a which shows approx. 28% volume fraction of reversed γ-austenite, about 69% of α′-martensite has been reversed to γ-austenite when the cryo-rolled AISI 321 steel was annealed at 973 K (700 ℃) for 180 s. The average martensite and austenite grain sizes are 0.13 and 0.16 μm, respectively. Increasing the annealing time from 180 s to 900 s (Fig. 5.7) led to an increase in the area fraction and the average grain size (approx. 31% increase) of α′-martensite as shown in Fig. 5.7b. Fig. 5.7b indicates a mixture of equiaxed and lath-like α′-martensite grains that could signal a change in the mechanism of reversion at this annealing temperature. Consequently, the $\gamma_r$ also shows a mixture of these morphologies (Fig. 5.7c). However, significant texturing of the austenite grains near {110}||ND occurred. The comparison of {111}γ and {110}α′ pole figures confirm the coincidence of poles from all grain variants (Fig. 5.7e) and those of the selected grains (Fig. 5.7f) of both phases. These confirm that the nucleated γ-austenite grains at this annealing temperature and time follow K-S orientation relationship with the α′-martensite.

Annealing at 1023 K

The results of the microtexture analysis of specimens annealed at 1023 K (750 ℃) are presented in Figs. 5.8 and 5.9. The development of UFG structure with an average austenite grain size of 0.21 μm was only met after annealing for 180 s (Fig. 5.8a). Meanwhile, 21% volume fraction of the α′-martensite is yet to revert to γ-austenite. The IPF color maps, pole figures, and ODFs in Fig. 5.8b-e shows four possible variants in both BCC ({023}<1-32>, {113}<-1-21>, {012}<2-41>,

{014}<-1-71>) and FCC ({110}<-331>, {113}<1-10>, {012}<1-33>, {015}<-4-31>) phases. Unlike the previously analyzed data where the preferred orientation of austenite grains is near {110}||ND, Fig. 5.8b and c shows that the preferred orientations of both BCC and FCC grains are near {112} and {113}||ND. However, it is possible that small EBSD scan area is from a block of a parent grain such that the aforementioned preferred orientation is not a representative of the entire specimen. In this case, the result of the XRD macrotexture analysis will be more reliable to ascertain if {112} and {113}||ND orientations are the preferred orientations. The coincidence of poles of all possible variants when {111}γ and {110}α′ pole figures are superimposed (Fig. 5.8e) indicates that the reversed γ-austenite follows K-S orientation relationship with the α′-martensite. This is further confirmed by the analysis of selected reversed austenite and transformed martensite grains (Fig. 5.8f); one of the poles of {111}γ is parallel to one of the poles of {110}α′ and one of the <110>γ directions is parallel to one of the <111>α′ directions.

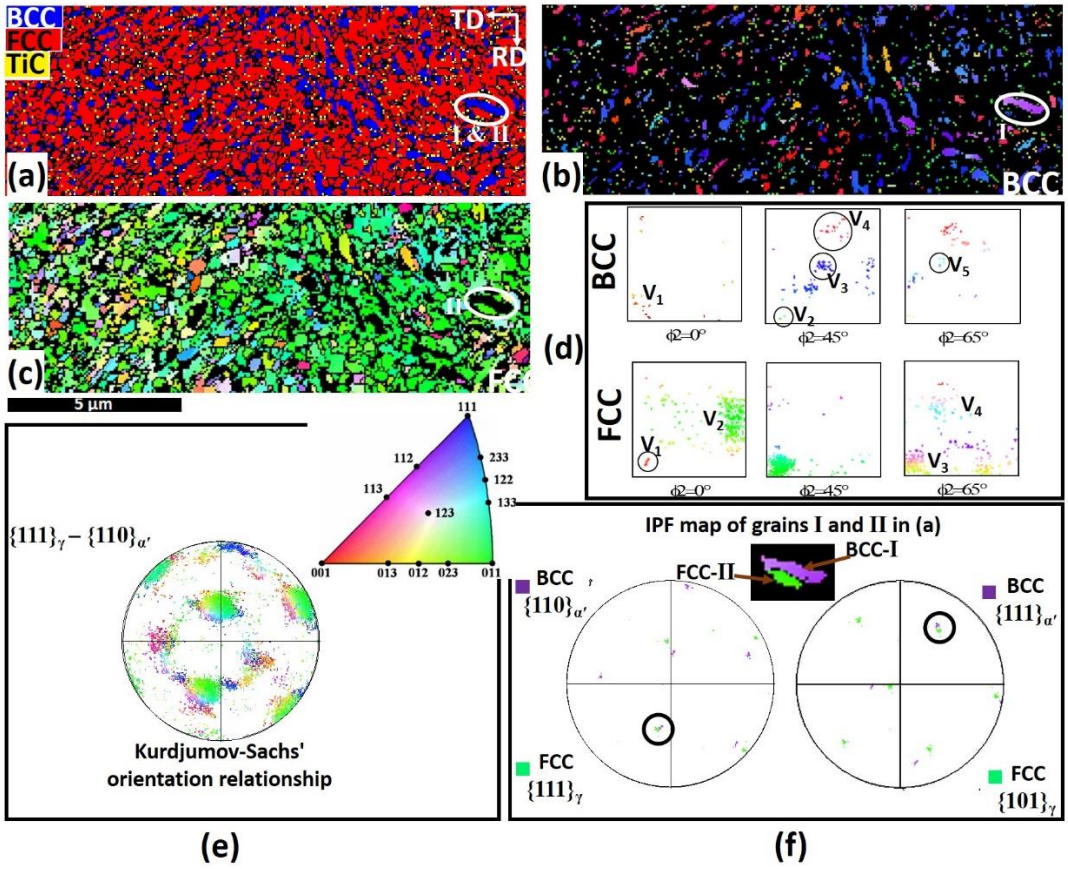


Fig. 5.7. HR-EBSD maps of specimen annealed at 973 K (700 ℃) for 900s: (a) phase color map. IPF color maps of (b) BCC α′-martensite and (c) FCC γ-austenite, (d) 0º, 45º, 65º ϕ2 ODF sections of the BCC α′-martensite and FCC γ-austenite. Superimposed {111} and {110} pole figures for (e) all grains and (f) selected α′-γ grains.

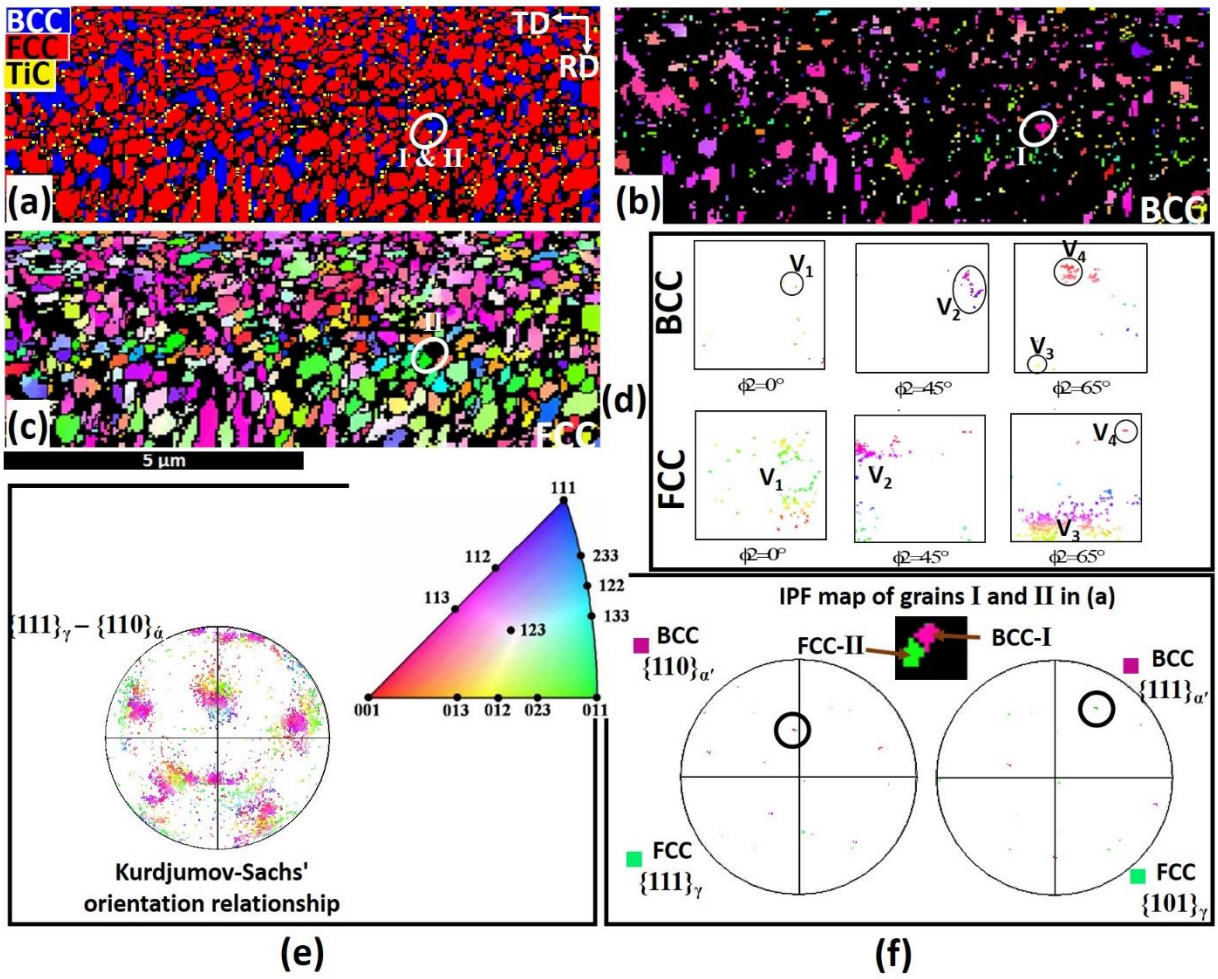


Fig. 5.8. HR-EBSD maps of specimen annealed at 1023 K (750 ℃) for 180s: (a) phase color map, IPF color maps of (b) BCC α′-martensite and (c) FCC γ-austenite, (d) 0º, 45º, 65º ϕ2 ODF sections of the BCC α′-martensite and FCC γ-austenite. Superimposed {111} and {110} pole figures for (e) all grains and (f) selected α′-γ grains.

Annealing for 600 s (Fig. 5.9a-d) shows the development of UFG structure with an average austenite grain size of 0.31 µm. The volume fraction of the unreversed α′-martensite is approximately 8%. Most of the unreversed α′-martensite with an average grain size of 0.17 µm are observed at the austenite triple junctions with few located at the austenite boundaries. Three variants were observed in each of the martensite ({001}<100>, {111}<3-41>, {213}<0-41>) and austenite ({011}<0-11>, {114}<1-10>, {213}<0-41>) phases. The preferred orientation in the austenite grains is near {110}||ND (γr-{011}<0-11>), while martensite grains are near {100}||ND ({001}<100>) and {111}||ND (α′-{111}<3-41>). So far, the comparison of {111}γ and {110}α′ pole figures of specimens with a negligible fraction of unreversed α′-martensite do not show the

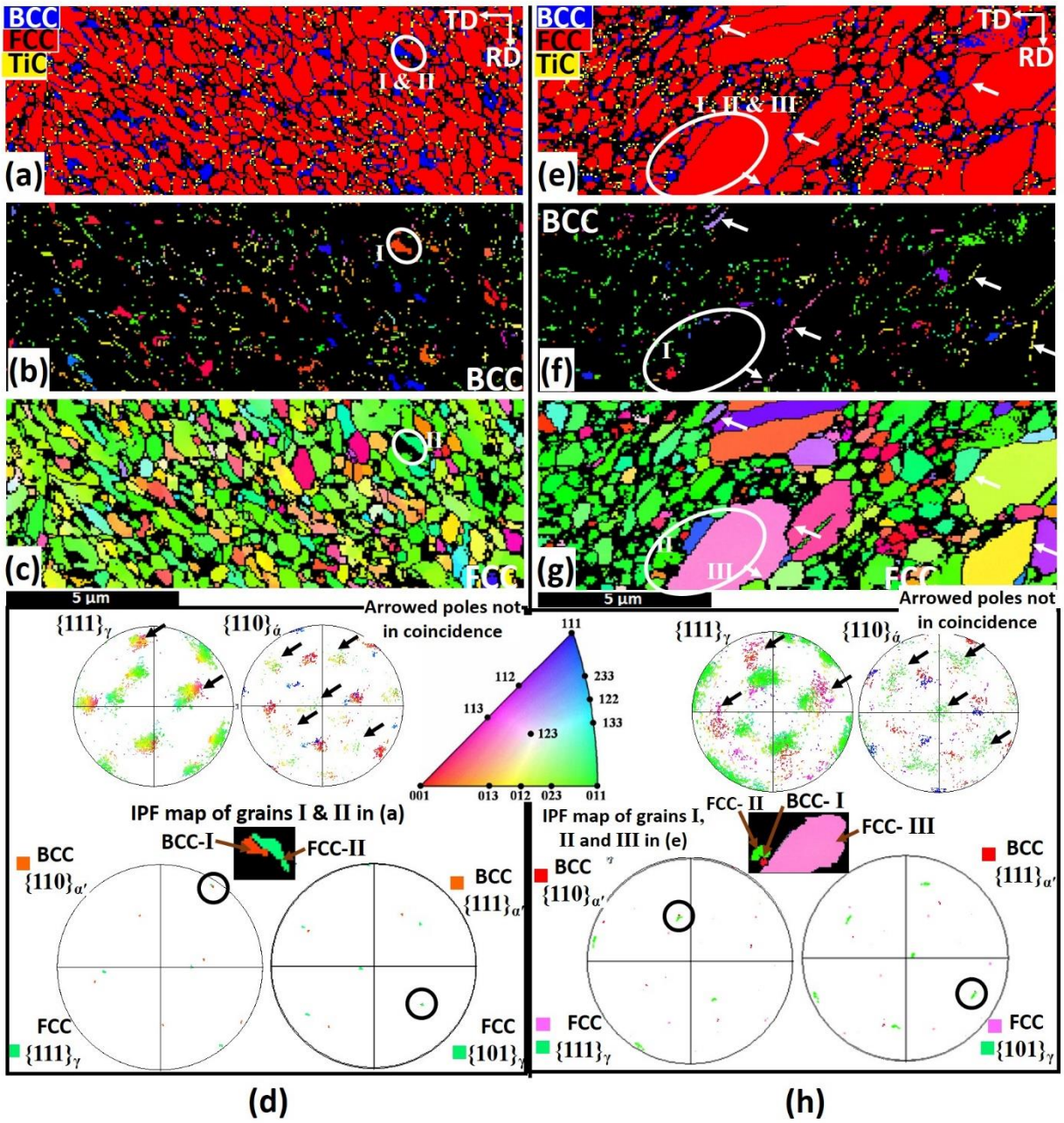


Fig. 5.9. HR-EBSD maps of specimen annealed at 1023 K (750 ℃) for (a-d) 600s and (e-h) 900s: (a, e) phase color maps, (b, f) IPF color maps of BCC α′-martensite, (c, g) IPF color maps of FCC γ-austenite. Unstratified and superimposed {111} and {110} pole figures for all grains and selected α′-γ grains in specimens annealed for (d) 600s and (h) 900s.

coincidence of black-harrowed poles in Fig. 5.9d. This indicates loss of the K-S orientation relationship between the arrowed variants in both phases. The non-arrowed poles or variants (green in {111}γ pole figure and red in {110}α′ pole figure) are in coincidence, obeying K-S orientation relationship. This is further confirmed by the coincidence of poles from the variants of the selected

BCC-I and FCC-II grains. The negligible fraction of α′ suggests this annealing condition could be acceptable for the development of UFG structure.

At 900 s (Fig. 5.9e-h), the volume fraction of unreversed α′-martensite is less than 7%. However, discontinuous or abnormal grain growth of the austenite grains had occurred. The phase map in Fig. 5.9e shows two distinct regions of the FCC phase; UFG and abnormal grain growth. There are unique features in the phase map that distinguishes these regions. The UFG regions are characterized by the presence of triple junction martensite, finely dispersed martensite, and TiC precipitates at the grain boundaries. Abnormal grain growth regions, which show little or no TiC, are mainly characterized by finely arranged martensite (white-arrowed in Fig. 5.9e-h) at grain boundaries. A comparison of Figs. 5.9b, c and 5.9f, g shows that finely dispersed martensite of the same crystallographic orientation is orderly arranged at (or "pushed" towards) austenite boundaries during grain growth; forming a grain boundary α′ allotriomorph. While the preferred orientation near {110}||ND is maintained in the FCC UFG region, grown grains which are accompanied by annealing twins, are characterized by random orientations. It is worth noting that the orientations of the grain boundary α′ allotriomorph (white-arrowed in Fig. 5.9f) have the same crystallographic variant with only one of its γ-austenite neighbor (white-arrowed in Fig. 5.9g) and not with the other γ grain. This is attributed to the K-S orientation relationship that exists between the grain boundary α′ allotriomorph and only one of its γ-austenite neighbor [177]. However, the comparison of {111}γ and {110}α′ pole figures in Fig. 5.9h also shows that unreversed ultrafine α′-martensite (BCC-I) only obeyed a K-S orientation relationship with a neighboring ultrafine γ-grain (FCC-II) and not with the γ abnormal (large) grain (FCC-III). This is confirmed by the coincidence of only variants of BCC-I and FCC-II (black circles).

Annealing at 1073 K

EBSD maps of specimen annealed at 1073 K (800 ℃) show features that are quite different from those observed in specimens annealed at 923 K (650 ℃), 973 K (700 ℃) and 1023 K (750 ℃). This could largely be due to the higher rate of reversion (as estimated from Fig. 5.4a) obtainable at 1073 K (800 ℃) annealing temperature. Unlike annealing at a lower temperature, maps in Fig. 5.10 shows reversion had gone beyond half-way (about 71% volume fraction of $\gamma_r$) after annealing at 1073 K (800 ℃) for 60 s. Both martensite and austenite grains have an average size of 0.21 μm. The phase color map in Fig. 5.10a shows the area fractions of lath-like γr and α′ that are inclined

at 45$^{o}$ to the rolling direction. Again, a careful observation of Fig. 5.10 a, b and c revealed that the morphology (lath) of the γr took after those of the neighbouring α′-martensite. Figure 5.10b-e shows five possible orientation variants in each of the martensite ({011}<1-33>, {111}<-1-23>, {113}<-3-32>, {210}<1-31>, {212}<-2-33>) and austenite ({011}<0-11>, {111}<1-42>, {531}<1-20>, {311}<1-53>, {212}<-3-23>) phases. At this annealing temperature and time, K-S orientation relationship is obeyed between the $\gamma_r$ and α′ grains (Fig. 5.10e and f).

Annealing at 1073 K (800 ℃) for 180 s (Fig. 5.11a-d) shows the onset of grain growth with few annealing twins, and yet a substantial percentage volume fraction (15%) of the α′-martensite is present in the specimen. The observation of grown grains with some fractions of unreversed martensite is a clear indication that both phase reversion and grain growth occur simultaneously during annealing. The orientation relationship between the $\gamma_r$-austenite and α′-martensite followed K-S (Fig. 5.11d). At a shorter time (in comparison with specimens annealed at 923 K [650 ℃], 973 K [700 ℃], 1023 K [750 ℃]), abnormal grain growth was observed in the specimen annealed at 1073 K for 300 s (Fig. 5.11e-h). UFG and abnormal grain growth regions of the FCC phase with features such as the grain boundary α′ allotriomorph in Fig. 5.9e-g were also observed in Fig. 5.11e-h. At this annealing condition, the lath-like morphology of grains is lost. The K-S orientation relationship is not obeyed between the unreversed ultrafine α′-martensite (BCC-I) and two neighbor γ abnormal grains (FCC-II and III) as shown in Fig. 5.11h. None of the poles of {111}γ is parallel to the poles of {110}α′, and none of the <110>γ directions is parallel to the <111>α′ directions.

5.3.2.2.2 Macrotexture analysis

XRD texture measurements on the cryo-rolled and annealed AISI 321 ASS specimens are presented in Figs. 5.12-5.15. All the XRD ODFs are compared with Fig. 5.2d for ease of interpretation. The ODFs of martensite and austenite phases at specific annealing times in Figs. 5.12-5.15 are omitted due to the very low or negligible fraction of the phases. As earlier observed, specimens annealed at 923 K (650 ℃), 973 K (700 ℃), 1023 K (750 ℃) for 60 s and 1073 K (800 ℃) for 30 s suggest no evidence of austenite reversion. However, the intensities of Y {111}<112> and Z {111}<110> components of the BCC phase in these specimens increased at the expense of R-Cube {001}<110> in comparison with the cryo-rolled sample (Figs. 5.12-5.15).

Irrespective of the annealing temperature and time, R-Cube {001}<110>, Y {111}<112>, Z {111}<110> and R-Cu {112}<110> are the major texture components of unreversed α′-martensite. Similarly, Brass {110}<112> and Goss {110}<100> with minor spread in R-CubeRD {012}<100>, Copper {112}<111> and S {123}<634> are the major crystallographic orientations of $\gamma_r$ grains. Similar observations in other austenitic stainless steels have been reported [145,169,173]. The intensities of these texture components did not follow a specific pattern with annealing times in specimens subjected to lower reversion temperature (Figs. 5.12 and 5.13). However, at higher reversion temperature (Figs. 5.14 and 5.15), the orientation intensities in the

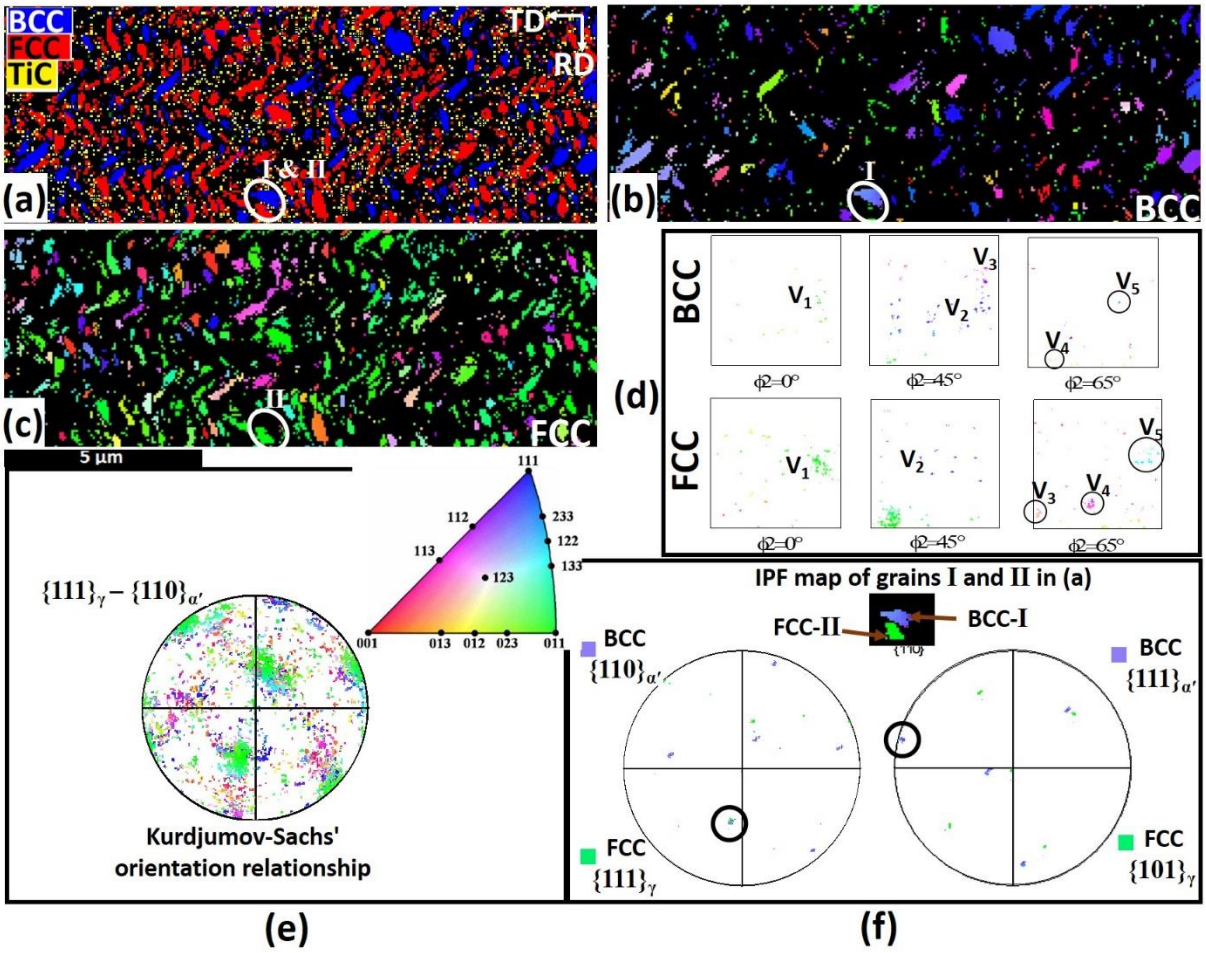


Fig. 5.10. HR-EBSD maps of specimen annealed at 1073 K (800 ℃) for 60s: (a) phase color map, IPF color maps of (b) BCC α′-martensite and (c) FCC γ-austenite, (d) 0º, 45º, 65º ϕ2 ODF sections of the BCC α′-martensite and FCC γ-austenite. Superimposed {111} and {110} pole figures for (e) all grains and (f) selected α′-γ grains.

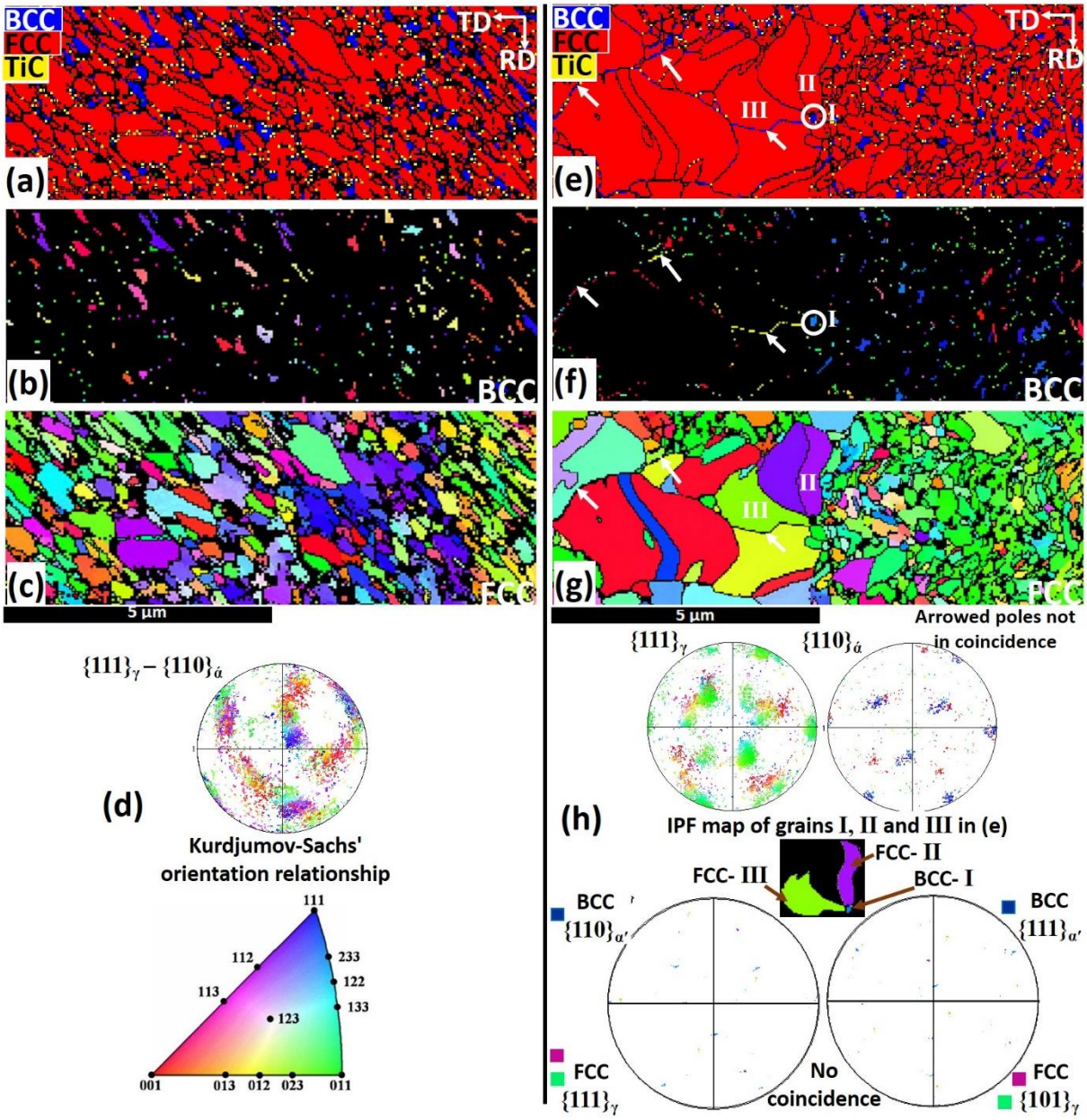


Fig. 5.11. HR-EBSD maps of specimen annealed at 1073 K (800 ℃) for (a-d) 180s and (e-h) 300s: (a, e) phase color maps, (b, f) IPF color maps of BCC α′-martensite, (c, g) IPF color maps of FCC γ-austenite. (d) Superimposed {111} and {110} pole figures for all grains in specimens annealed for 180s. (h). Unstratified and superimposed {111} and {110} pole figures for all grains and selected α′-γ grains in specimens annealed for 300s.

FCC ODFs shows a distinct pattern with annealing time. The intensities of Brass {110}<112> and Goss {110}<100> remain unchanged upon annealing for 600 s and 180 s in specimens annealed at 1023 K (750 ℃) and 1073 K (800 ℃), respectively. Beyond these annealing times, the intensities of Brass {110}<112> and Goss {110}<100> dropped. This could be attributed to the onset of

randomly-oriented grain growth as earlier confirmed by the HR-EBSD maps in Figs. 5.9 e-h and 5.11.

### 5.3.3 Role of TiC and unreversed martensite

From the results of XRD and EBSD investigations, the evolution of TiC particles during the martensite to austenite reversion of a cryo-rolled AISI 321 steel is obvious. These particles are more stable at lower reversion temperature, i.e. 923 K (650 ℃) and are less stable at a higher temperature of 1073 K (800 ℃). TiC particles were observed to precipitate within the γ-γ, γ-α′ and α′-α′ grain boundaries and none were observed inside the grains. It is, therefore, logical to have higher volume fraction of TiC in UFG samples since they have higher grain boundary area per unit volume than samples with larger grain size. Similarly, large grains with some fractions of unreversed martensite were observed at a higher annealing time, which is an indication that simultaneous phase reversion and grain growth occurred at a certain stage of reversion [158]. To develop an UFG structure without abnormal grain growth, it may therefore be impractical to completely revert the α′-martensite to γ-austenite without retaining some negligible fraction of the α′-martensite in the alloy. Two types of unreversed martensite were observed in this study. The first is the finely dispersed martensite with random orientation, i.e. grain boundary α′ allotriomorph, while the second is the equiaxed, ultrafine and textured (preferred orientation near {100} or {111}||ND) martensite that is predominantly found at the triple junctions.

Both the TiCs and the triple junction martensite are observed to be important in obtaining an UFG structure through the Zener pinning of grain boundaries. The growth of the austenite grains involves the migration of high angle boundaries whose motion is effectively hindered by second phase particles such as TiC particles and the unreversed triple junction martensite; contributing to the stability of the equiaxed UFG structure. Celada-casero *et al.* [170] also reported pinning of the austenite grain boundaries (which in-turn prevents grain growth) by χ-phase and nanometric Ni3(Ti, Al) precipitates during diffusional reversion in a metastable austenitic stainless steel. However, the TiC particles were observed to dissolve when reversion is either prolonged at low annealing temperature or done at an elevated temperature. The implication of this is that some high angle boundaries can break away before others, paving the way for the occurrence of abnormal grain growth [178] and loss of texture [164]. The finely dispersed martensite (grain boundary α′ allotriomorph) is observed to be neatly arranged at the grain boundaries according to their crystal

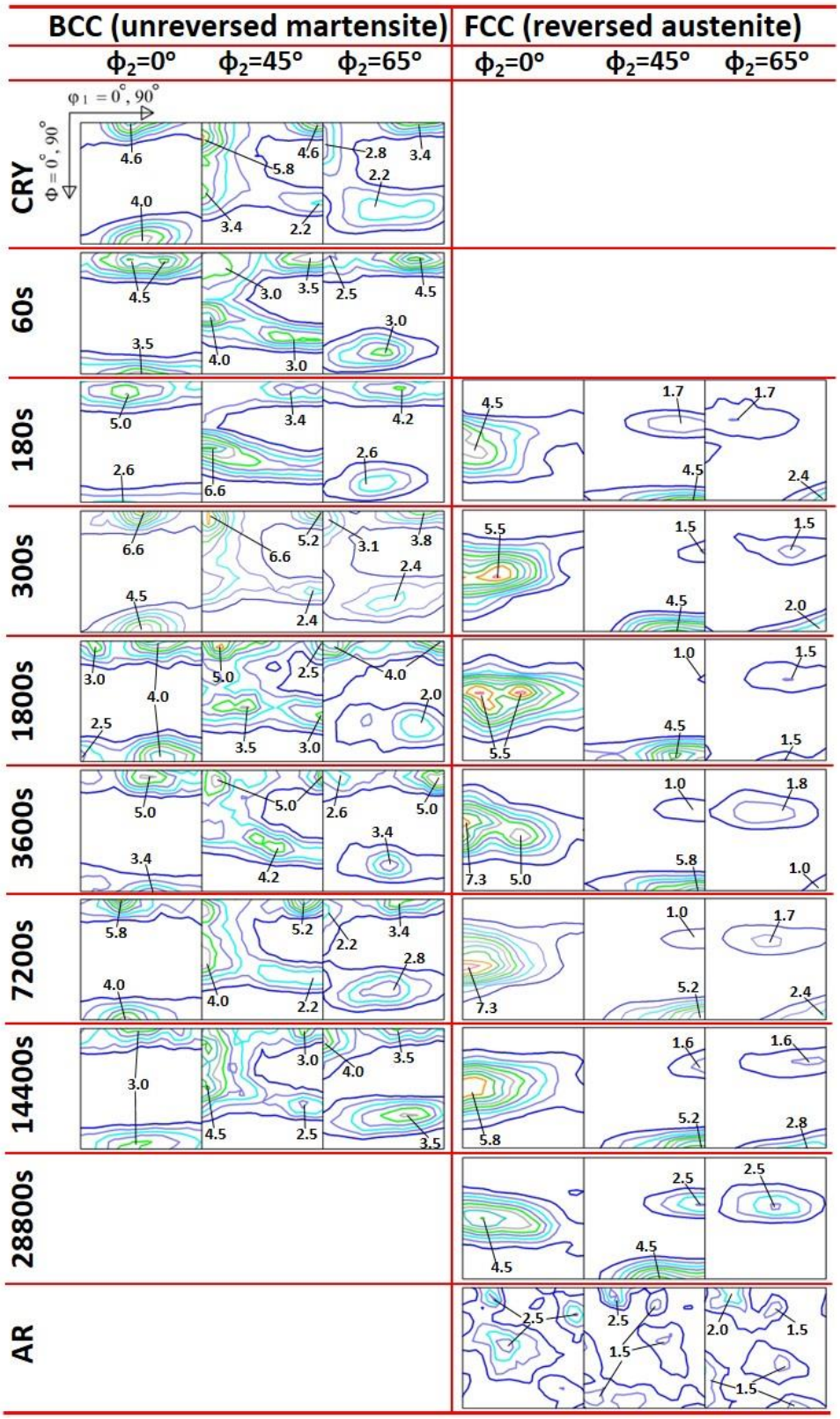


Fig. 5.12. 0º, 45º, 65º ϕ2 ODF sections of the BCC α′-martensite and FCC γ -austenite phases obtained from the XRD measurement on the specimens annealed at 923 K (650 ℃).

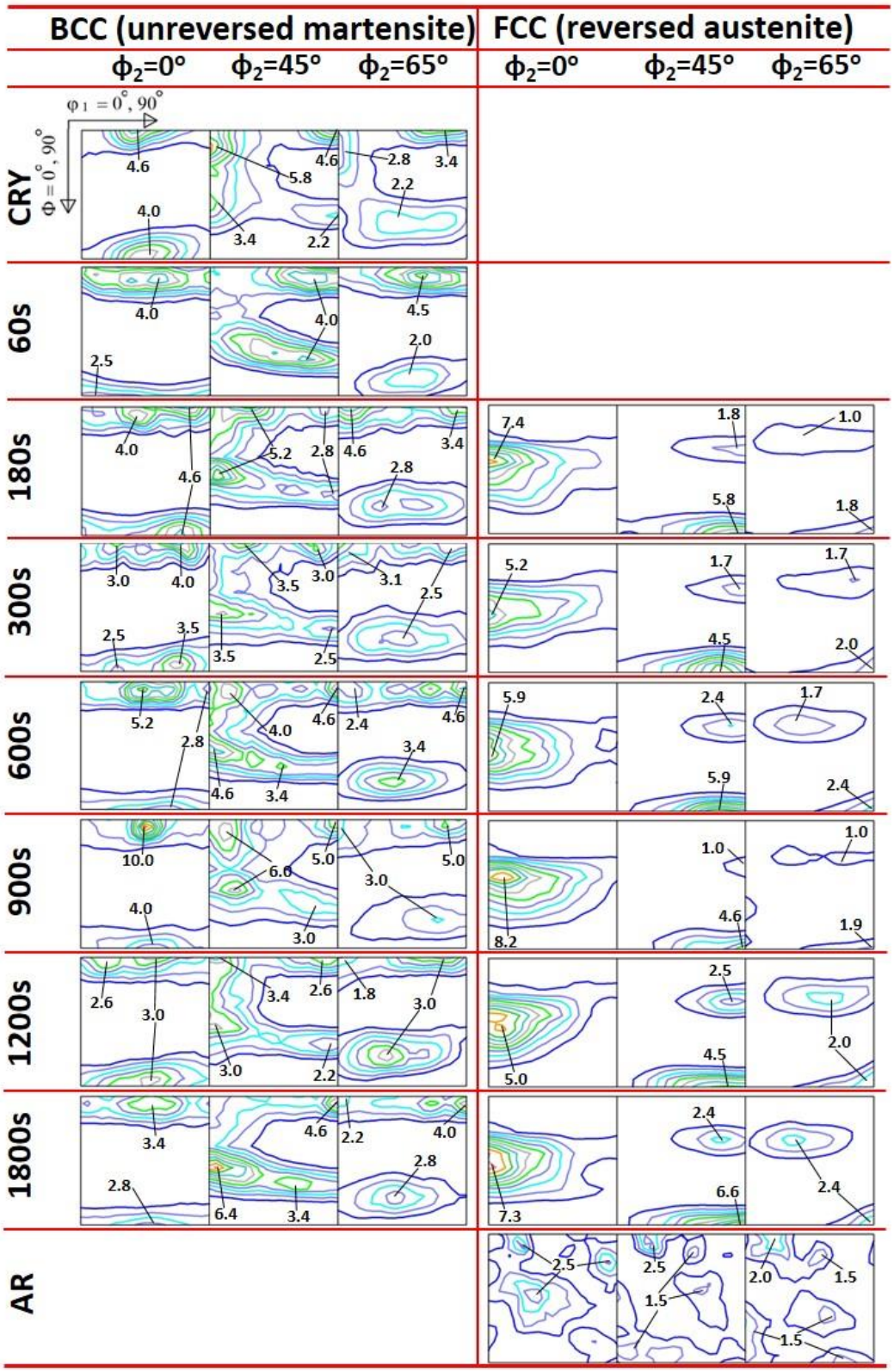


Fig. 5.13. 0°, 45°, 65° ϕ2 ODF sections of the BCC α′-martensite and FCC γ -austenite phases obtained from the XRD measurement on the specimens annealed at 973 K (700 ℃).

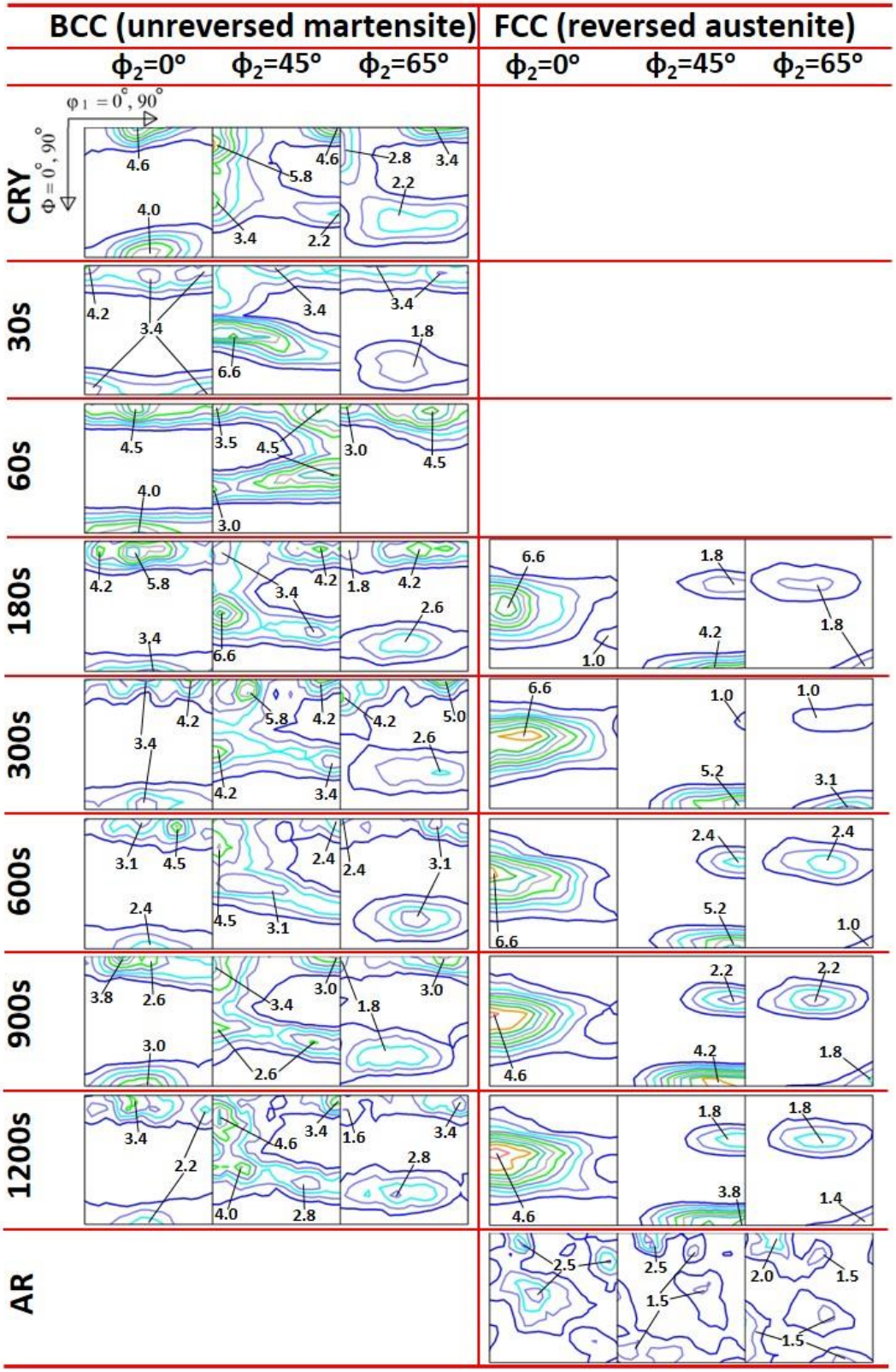


Fig. 5.14. 0º, 45º, 65º ϕ2 ODF sections of the BCC α′-martensite and FCC γ -austenite phases obtained from the XRD measurement on the specimens annealed at 1023 K (750 ℃).

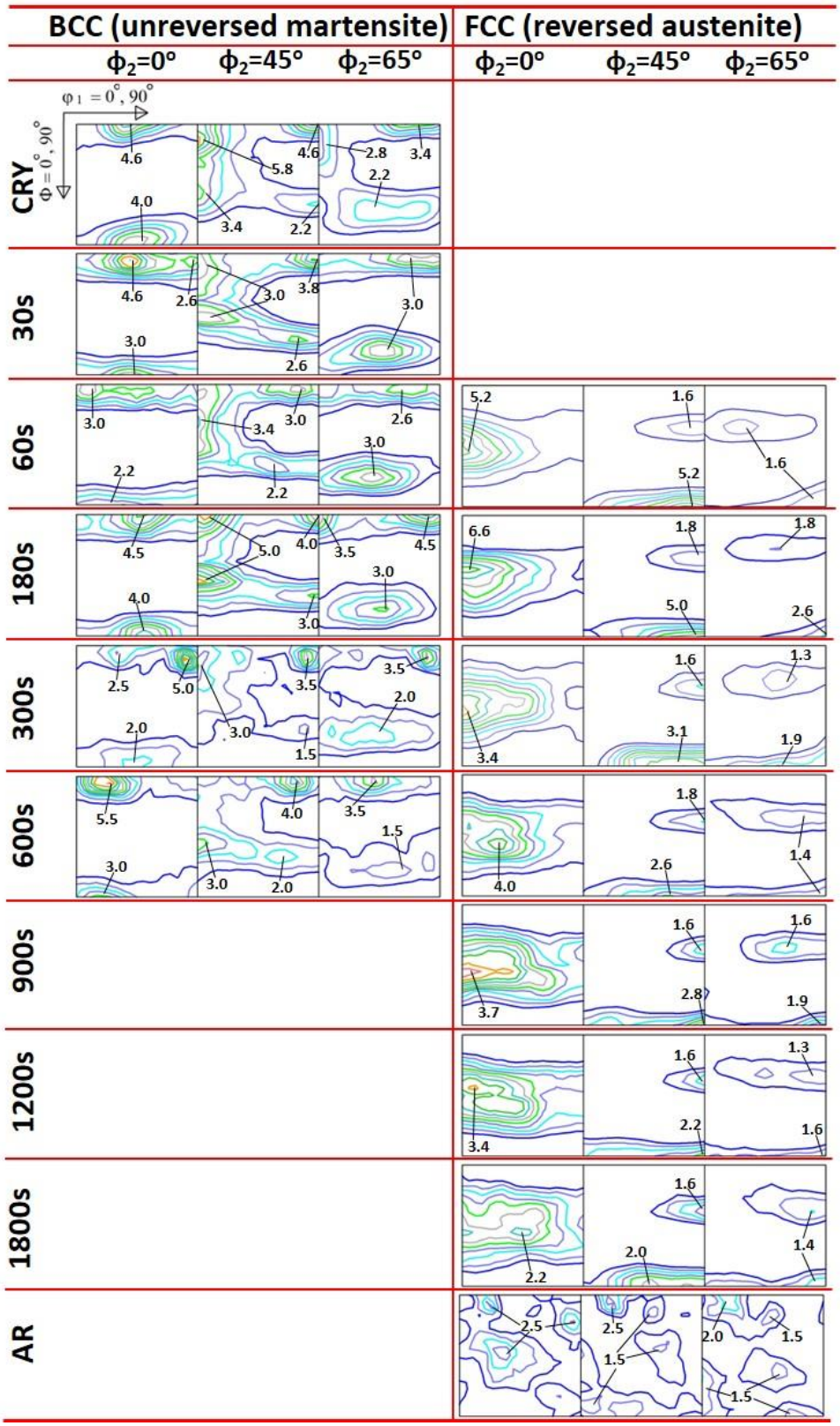


Fig. 5.15. 0º, 45º, 65º ϕ2 ODF sections of the BCC α′-martensite and FCC γ -austenite phases obtained from the XRD measurement on the specimens annealed at 1073 K (800 ℃).

orientations as shown in Figs. 5.9f and 5.11f. It is the orientation of this finely arranged martensite that influences the texture of grown grains and in-turn leads to the loss of significant texturing in the sample. Other authors [168,179] have reported that very small fraction of unreversed α′-martensite is also effective in suppressing austenitic grain growth through grain boundary (Zener) pinning during the deformation of ultrafine grained austenitic stainless steel.

The stages of austenitic reversion in the development of UFG structure at low/medium reversion rate such as those obtained in samples annealed at 923 K (650 ℃), 973 K (700 ℃) and 1023 K (750 ℃) therefore follows; (a) austenitic reversion and carbide precipitation, (b) austenitic reversion, carbide precipitation and limited grain growth, (c) carbide precipitation and limited grain growth and (d) carbide dissolution and abnormal grain growth. Similarly, the stages of

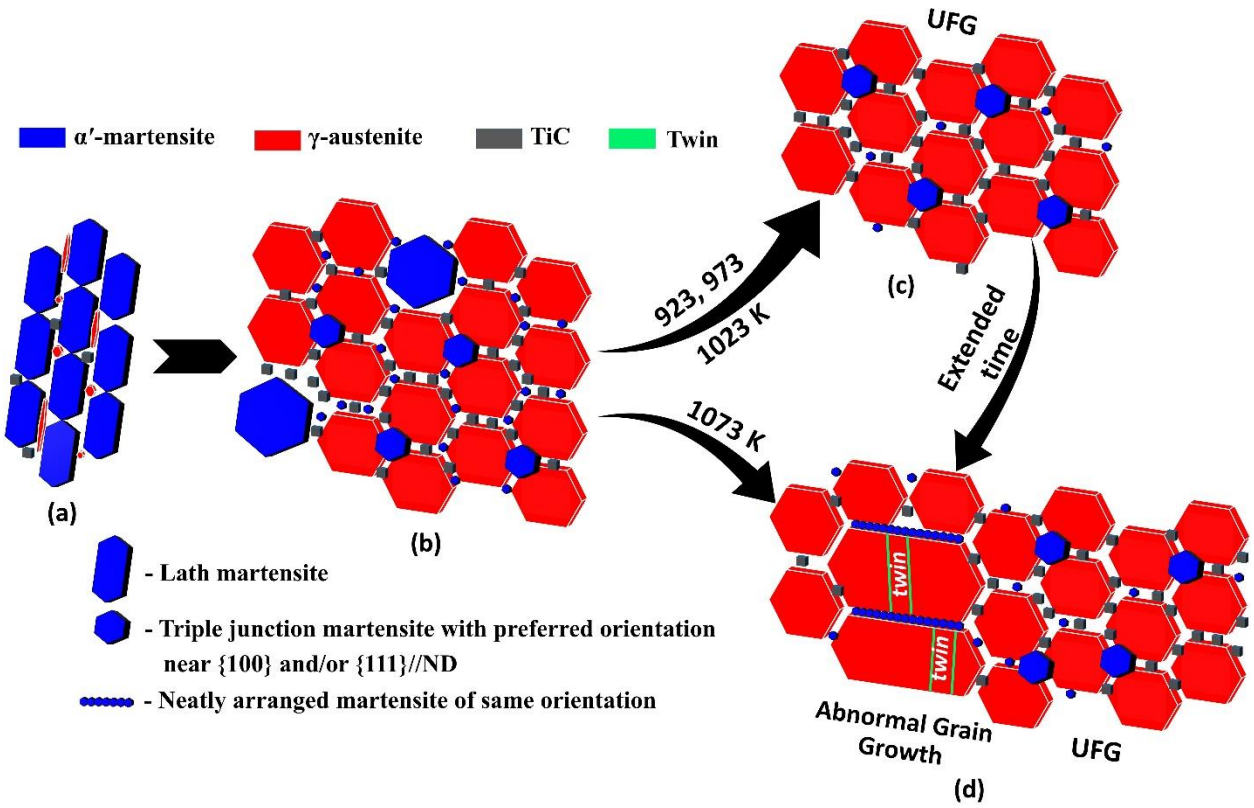


Fig. 5.16. Schematic of the stages of austenitic reversion: (a) onset of austenite reversion; nucleation of austenite grains within martensite lath boundaries, (b) austenite reversion and TiCs evolution in progress, (c) development of UFG structure with TiC and negligible amount unreversed martensite at austenite triple junctions, (d) possible development of abnormal grain growth (AGG) within UFG structure at an extended period of time or high reversion/annealing temperature; dissolution of TiCs also occurred at this stage. *Shape and size of grains and particles are exaggerated to show the sequence of UFG development*.

reversion at a higher reversion rate obtained by 1073 K (800 ℃) follows; (a) austenitic reversion, carbide precipitation, (b) austenitic reversion, carbide precipitation and limited grain growth and (c) carbide dissolution and abnormal grain growth. These stages are schematically shown in Fig. 5.16.

### 5.3.4 Reversion Mechanisms

Figure 5.4a shows that the percentage volume fraction of austenite in the specimen annealed for 180 s at 923 K (650 ℃) is below 50%. This suggests the possibility of a different mechanism of reversion in the specimen annealed at 923 K (650 ℃) in comparison with those annealed at 973 K (700 ℃), 1023 K (750 ℃) and 1073 K (800 ℃) whose austenite volume fraction is higher than 50% for 180 s. The equiaxed morphology of the reversed austenite in the specimen annealed at 923 K (650 ℃) (Figs. 5.5 and 5.6) are characteristics of diffusional reversion (DR) mechanism as described in section 5.1. On the other hand, the lath-like austenite grains, which are features of martensitic shear reversion (MSR) mechanism, were observed in specimens annealed at higher temperatures and became more pronounced at 1073 K (800 ℃) (Figs. 5.10 and 5.11a-d). Apple and Krauss [180] observed differences in the morphology of $\gamma_r$ in a quenched Fe-Ni-C (0.05–0.3 wt.%) alloy when the heating rate was varied between 3 °C/s and 1500 °C/s. The authors detected that slow heating rates enabled adequate time for short-range diffusion, resulting in equiaxed grains by DR mechanism while higher heating rates resulted in limited diffusion, culminating in the formation of lath-like austenite morphologies by MSR mechanism. To elucidate more on this, Eqn. 5.1 was used to plot the $\Delta G^{(\alpha\rightarrow\gamma)}$ versus temperature curve as shown in Fig. 5.17. Using the free energy of -500 J/mol as the minimum driving force criterion required for a complete MSR [167], it was indeed confirmed that DR occurred in the specimen annealed at 923 K (650 ℃) and MSR for specimens annealed at 973 K (700 ℃), 1023 K (750 ℃) and 1073 K (800 ℃).

### 5.3.5 Estimation of Activation energy and rate of reversion

The Arrhenius relationship in Eqn. 5.3 [175] was used to estimate the activation energy (Q) required for the reversion of α′-martensite to γ-austenite in AISI 321 ASS in this study. Taking the $log$ of both sides of the Eqn. 5.3, Eqn. 5.4 is obtained. It therefore follows that the slope of a $ln\,1/t_{0.5}\;vs\;1/T$ plot can be used to obtain the value of $-Q/R$. Although other methods such as the *rate constant* and *change of slope* techniques can also be used to estimate Q, the adopted technique

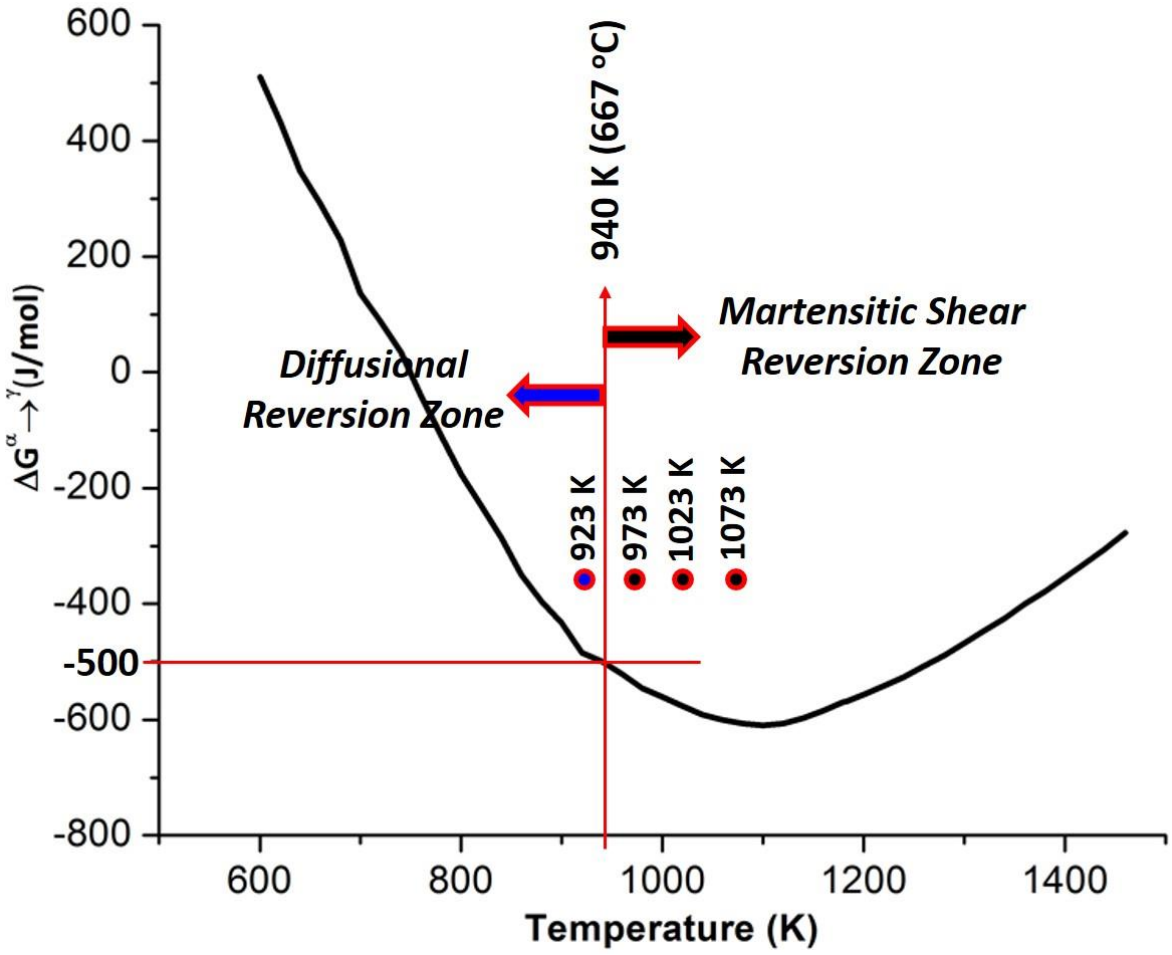


Fig. 5.17. $\Delta G^{(\alpha \rightarrow \gamma)}$-Temperature (K) curve for AISI 321 austenitic stainless steel.

in this study is termed *time for constant fraction* [181].

$$k = 1/t_{0.5} = A \exp(-\frac{Q}{RT}) \quad \ldots 5.3$$

$$ln\, 1/t_{0.5} = \left(-\frac{Q}{R}\right)\frac{1}{T} + \ln A \quad \ldots 5.4$$

where $k, A, Q, R$ and $T$ are the reaction rate coefficient ($s^{-1}$), frequency factor ($s^{-1}$), activation energy (J/mol), the universal gas constant ($8.314\ Jmol^{-1}K^{-1}$) and absolute temperature ($K$), respectively. The $ln\, 1/t_{0.5}\ vs\ 1/T$ plot is shown in Fig. 5.18a with Q estimated to be 80 $kJmol^{-1}$ using regression analysis. The dependence of $1/t_{0.5}$ on any reversion temperature is shown in Fig. 5.18b which is obtained by substituting $131\ s^{-1}$ and 80 $kJmol^{-1}$ for $A$ and $Q$, respectively, in Eqn. 5.3. Figure 5.18b provides useful information about the reversion kinetics of a cryo-rolled AISI 321 ASS subjected to different reversion temperature. For example, the reversion rate at 1173 K

(900 ℃) is about 17 times greater than the reversion rate at 873 K (600 ℃). This also indicates the influence of annealing temperature on reversion rate; the reversion kinetics at a lower temperature (e.g. 923 K [650 ℃]) is slow compared to that at a higher temperature (e.g. 1073 K [800 ℃]). The inset in Fig. 5.18b is the expanded plot of the reversion temperature range used in this study.

### 5.3.6 Preferred annealing temperature and time for the development of UFG structure

Results of the current investigations indicate that equiaxed UFG structure containing negligible volume fraction of unreversed α′-martensite can be obtained through the (a) DR route at 923 K (650 ℃) for approximately 28800 s (8 h) as shown in Fig. 5.6e-h and (b) MSR route at 1023 K (750 ℃) for 600 s (10 min) as shown in Fig. 5.9a-d. The average grain size is 0.22 and 0.31 μm in the specimens processed at these temperatures using DR and MSR routes, respectively. However, the DR route may not be the best choice for two reasons. The first is the precipitation of TiC at the grain boundaries which are more stable and of higher density at the annealing temperature of 923 K (650 ℃) than 1023 K (750 ℃). Qualitative characterization of a specimen reversed via DR route has been reported to be prone to the formation of secondary phase precipitates [182]. These carbides serve as a barrier to grain growth on one hand [158,182] but have been reported to be detrimental, especially in providing preferential sites for cavity nucleation in austenitic stainless steels exposed to creep–fatigue interaction during structural application [183]. In a study on fatigue behaviour of 316Ti stainless steel in high-temperature water, Xu et al. [184] reported Ti-bearing precipitates as the preferential initiation site for cracking. Secondly, the time required for DR to retain an acceptable volume fraction of unreversed α′-martensite while at the same time maintaining its ultra-fine structure is too high (Fig. 5.4a). Hence, the achievement of an UFG structure via DR mechanism will not be as economical (in terms of the energy consumption during prolonged annealing) as those obtained via the MSR mechanism. Martensitic shear reversion is not only rapid, the amounts of the deleterious TiC particles produced during reversion is very low compared to diffusion reversion.

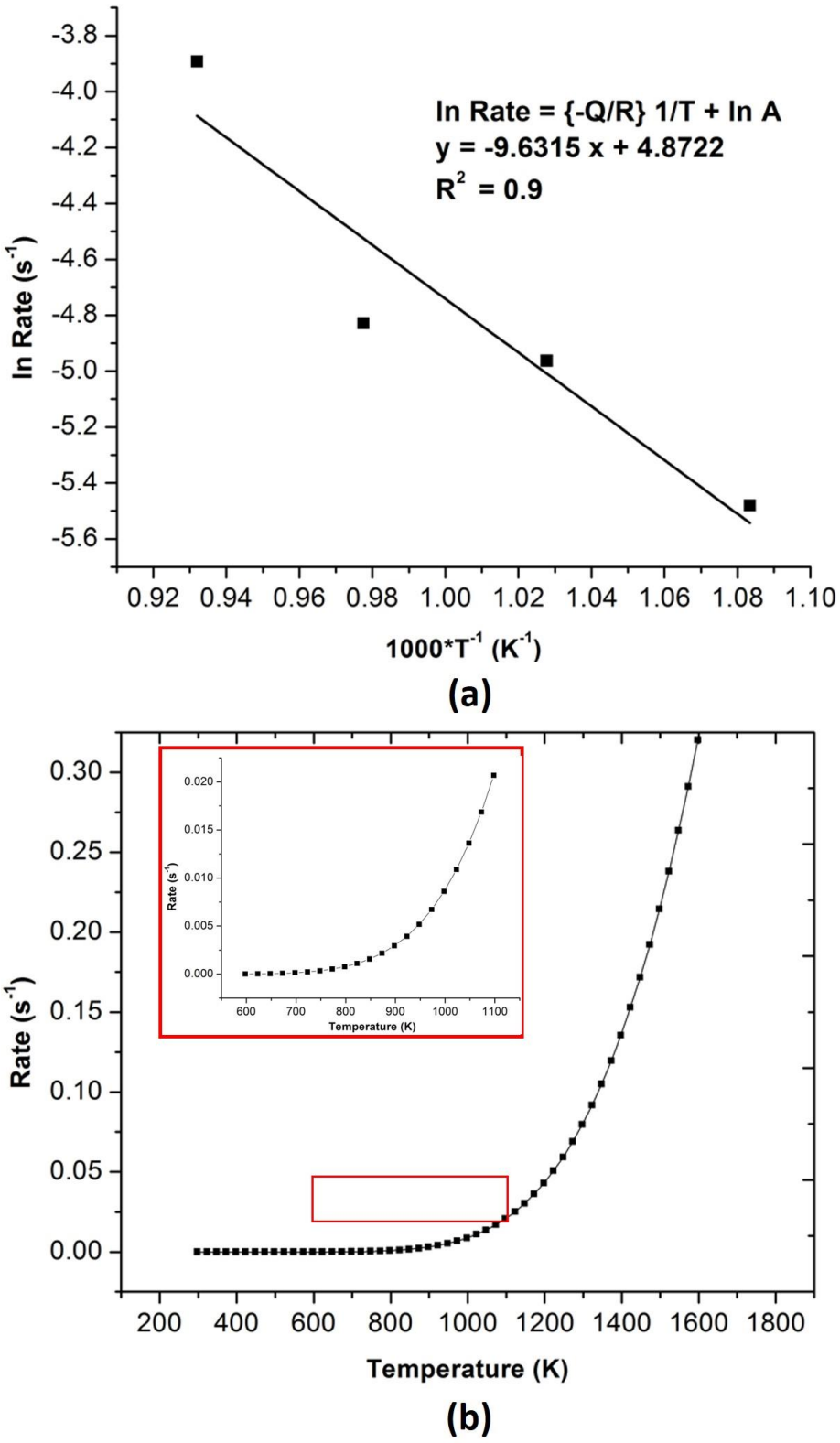


Fig. 5.18. (a) $ln\,1/t_{0.5} - 1/T$ plot for the estimation of activation energy, (b) reversion rate as a function of temperature for AISI 321 ASS. Inset in (b) is the expanded plot of the reversion temperature range used in this study.

## 5.4 Summary and Conclusions

In this article, the optimum thermo-mechanical processing conditions required to develop UFG structure in AISI 321 austenitic stainless steel were experimentally determined. The reversion behavior and the associated texture development was studied in the cryo-rolled steel specimens annealed at 923 K (650 ℃), 973 K (700 ℃), 1023 K (750 ℃) and 1073 K (800 ℃) for varying times. The following are the major conclusions drawn from this work:

1. The minimum annealing temperature at which martensitic shear reversion will occur in AISI 321 steel is 940 K (667 ℃). Hence, the dominant reversion mechanism is diffusion reversion (DR) at annealing temperature of 923 K (650 ℃) while martensitic shear reversion (MSR) dominates at 973 K (700 ℃), 1023 K (750 ℃) and 1073 K (800 ℃).
2. TiC precipitates and unreversed triple junction α′-martensite played a major role in obtaining an UFG structure by Zener pinning of grain boundaries. The carbides are more stable in DR specimens. Consequently, a more stable UFG structure is obtainable in DR specimens at higher annealing time than in the MSR specimens.
3. The sequence of austenitic reversion in the development of UFG structure at low/medium reversion rate such as those obtained in samples annealed at 923 K (650 ℃), 973 K (700 ℃) and 1023 K (750 ℃) follows; (a) austenitic reversion and carbide precipitation, (b) austenitic reversion, carbide precipitation and limited grain growth, (c) carbide precipitation and limited grain growth and (d) carbide dissolution and abnormal grain growth. On the other hand, the sequence of reversion for a higher reversion rate at 1073 K (800 ℃) K follows; (a) austenitic reversion, carbide precipitation, (b) austenitic reversion, carbide precipitation and limited grain growth and (c) carbide dissolution and abnormal grain growth.
4. The activation energy, Q, required for the reversion of α′ to γ in AISI 321 ASS is 80 $kJmol^{-1}$.
5. UFG size of 0.22 μm can be obtained through the DR route at 923 K (650 ℃) for approximately 28800 s (8 h) and 0.31 μm through the MSR route at 1023 K for 600 s (10 s). However, the MSR route at 1023 K (750 ℃) may be the best choice since the volume fraction of carbides are less than those in DR specimen, and perhaps, the energy

consumption required to achieve an UFG structure via DR mechanism is higher due to low reversion rate.

6. About 195% increase in hardness value was observed for UFG specimens in comparison with the hardness value of the as-received specimen, though a higher fraction of TiC precipitates in the UFG structure may be an additional source of hardening.
7. At any annealing temperature, the elapsed annealing time (30-60 s) with no reversion showed that the crystallographic orientation of the martensitic grains changed. The intensity of Y {111}<112> and Z {111}<110> components increased at the expense of R-Cube {001}<110> in comparison with the cryo-rolled sample. This suggests that α′-martensite grains first, attain an orientation at the early stage of annealing that favors the nucleation of new austenite grains.
8. The {110}<uvw> is the major texture component of austenite grains in the UFG structure. It is stronger at a lower temperature where DR is the mechanism of reversion and weaker at a higher annealing temperature when MSR is the dominating reversion mechanism.

# Chapter 6

## Pseudo-Texture Memory in AISI 321 Austenitic Stainless Steel

In this chapter, the research findings on texture memory effect in the investigated AISI 321 austenitic stainless steel is presented and discussed. To the best of my knowledge, this is the first time that this alloy is being reported to exhibit texture memory effect. A mechanism of this effect is proposed to validate AISI 321 as a texture memory alloy. This chapter is published in "*IOP Conference series: Materials Science and Engineering*" as follows:

Tiamiyu, A. A., Szpunar, J. A., and Odeshi, A. G. (2017). Pseudo-texture memory in AISI 321 austenitic stainless steel. *IOP Conference series: Materials Science and Engineering*. ICOTOM 2017, 5-10 November, St George, Utah, U.S.A.

My contributions to this paper include review of the relevant literature, design and implementation of experimental procedures, analysis of test results and preparation of the manuscript which was reviewed by my supervisors; Professors Akindele Odeshi and Jerzy Szpunar. Their comments and suggestions were addressed before the manuscript was submitted for publication. The present manuscript is a modified version of the published paper. Detailed information on experimental procedures, which are covered in Chapter three, is removed to avoid repetition. This manuscript is used under the terms of the Creative Commons Attribution 3.0 licence. Hence, no copyright permission is required.

### Abstract

In this study, AISI 321 austenitic stainless steel with a grain size of 45 μm was cryo-rolled at -196 ℃ to 50 % thickness reduction to completely transform the γ-austenite phase to α′-martensite. The cryo-rolled sample was subsequently annealed in the temperature range of 923 – 1073 K for 30-28800s (0.5 – 480 mins) to reverse the α′-martensite back to γ-austenite and develop ultrafine grain (UFG) structure at optimum annealing condition. Average austenite grain sizes of 0.22 and 0.31 μm were obtained at an optimum annealing conditions of 923 K for less than 480 minutes and 1023 K for 10 minutes, respectively. High-resolution EBSD and XRD texture analyses show that ζ-fibre ({110}<uvw>) is the major texture component of the austenite grains in the UFG structure and it is stronger in specimen annealed at 923 K than those of the higher temperatures (973, 1023

and 1073 K) used in this study. The strong intensity of ζ-fibre in UFG is attributed to pseudo-texture memory in AISI 321, i.e. the ability of the steel to memorize the crystallographic orientation of the deformed austenite, rather than that of the conventional as-received austenite phase that is random.

## 6.1 Introduction

Texture memory effect (TME) is a phenomenon which occurs when the texture of material strengthens or remains unchanged after the phase transformation cycle from one phase to another and back to the initial phase [185,186]. TME has mainly been observed after the α′ (bcc) → γ (fcc) → α′ (bcc) transformation in BCC metals [186,187] and α (hcp) → β (bcc) → α (hcp) transformation in HCP metals [188,189] during a heating and cooling cycle. On the completion of transformation cycle in 0.1% C-1% Mn steel [186], a BCC metal, {100}<011>, {311}<011> and {332}<113> texture components reappeared with little decrease in intensity. Other alloys in which TME has been reported include interstitial free (IF) steel [187], Ti–6Al–4V [188] and zirconium [189]. The orientation relationship (OR) between γ and α′ in steels is the Kurdjumov–Sachs (K–S) relation, $\{111\}_{\gamma}\|\{110\}_{\alpha'}$ and $<110>_{\gamma}\|<111>_{\alpha'}$, or the Nishiyama–Wasserman (N–W) relation, $\{111\}_{\gamma}\|\{110\}_{\alpha'}$ and $<112>_{\gamma}\|<110>_{\alpha'}$. There are about 24 and 12 crystallographic variants in K–S and N–W relations, respectively. In those metals that exhibit TME, crystallographic OR is obeyed between parent and product phases. Thus, implying that out of the dozens of the equivalent crystallographic orientations allowed under the OR, only specific ones are selected after the completion of the phase transformation cycle. This phenomenon is termed variant selection [186] and its description can be found elsewhere [143,190]. Although the mechanism behind TME is still not very clear, mechanisms related to transformation strain, role of precipitates, and development of special boundaries during heating have been proposed [185,186].

In the present study, UFG structure was developed in AISI 321 austenitic stainless steel (ASS) to improve its mechanical properties. AISI 321 is a titanium (Ti)-stabilized austenitic stainless steel that is widely used in chemical process plants [3] and fabrication of pressure vessels [1]. To the best of the authors' knowledge, the development of UFG structure and the accompanying crystallographic texture in AISI 321 austenitic stainless steel has not been well addressed. The objective of this study is to investigate texture evolution during the development of UFG structure in AISI 321 steel. For the first time, the mechanism of texture memory in AISI 321 is addressed.

## 6.2 Material and methods

An AISI 321 austenitic stainless steel plate described in Section 3.1 was used. The cryo-rolling process and annealing treatment procedure are as described in Section 3.2. Material characterization techniques are as described in Sections 3.3.1 (hardness tests) and 3.5 (electrolytic polishing, EBSD, X-ray diffractometry and Feritscope measurements). All microstructural analysis and measurements in this study were conducted on the rolling plane (RP).

## 6.3 Results and discussion

Figure 6.1a shows a random texture in the γ-austenite phase of the as-received AISI 321 ASS. The as-received AISI 321 sample was slightly deformed (early stage of rolling) to avoid the start of martensitic transformation and the resulting deformed structure is hereafter referred to as the deformed austenite ($\gamma_d$). The EBSD IPF map of the $\gamma_d$ grains (Fig. 6.1b) showed a significant texturing near the ζ-fibre ({110}<uvw>). The strong development of {110}<uvw> could be explained using grain B in Fig. 6.1b. This grain shows a possible orientation interplay between {110}||ND and {111}||ND i.e. the gradual rotation of {111}||ND grains during deformation to {110}||ND, which is the most stable end-orientation. Schmid factor (SF) map using {111}[1-10] as the active slip system was plotted to establish the correlation between plastic deformation mechanism (slip) and the orientation of $\gamma_d$ (Fig. 6.1c). The SF varies with orientations in the following order: {100}||ND (highest) > {110}||ND > {111}||ND. This indicates that the ease at which slip will occur on {111}[1-10] slip system for the grains with {111}||ND orientation is lowest and as a matter of fact, these set of grains are near hard orientation. The {111}||ND oriented-grains are then "forced" to rotate during deformation to a more stable orientation ({110}||ND orientation with higher SF) [112]. Comparing the spread of orientation in the inverse pole figure (IPF) of undeformed γ (grain A) and deformed $\gamma_d$ (grains B and C) in Fig. 6.1d shows that the $\gamma_d$ has undergone plastic deformation by slip. The orientation of grain A converges to a point in the IPF triangle; suggesting a strain-free grain. The grains B and C show the widest orientation spread, which is an indication of large plastic deformation by slip. The IPF triangle could also be a useful tool in showing the gradual rotation of {111}||ND to {110}||ND as in grain B (a spread of blue color towards green) and C (rotation nearly complete as confirmed by the predominant green color). Upon 15% thickness reduction during cryo-rolling, 80% of the γ phase is transformed to α′-martensite (Fig. 6.1e). While the BCC IPF map in Fig. 6.1e shows a significant texturing of α′-

phase around {100}||ND, the remaining $\gamma_d$ is textured around {110}||ND. To validate the existing OR between the $\gamma_d$ and $\alpha'$ phases, grains i and ii in Fig. 6.1e are selected and analyzed in Fig. 6.1f. The comparison of $\{110\}_{\alpha'}$ and $\{111\}_{\gamma}$ pole figures for grains i and ii, respectively, in Fig. 6.1f shows the coincidence of poles (circled). These confirms that K-S orientation relationship exists between the $\gamma_d$ and $\alpha'$ and not $\gamma$ and $\alpha'$. Hence, the $\gamma \rightarrow \alpha'$ sequence is revised to $\gamma \rightarrow \gamma_d \rightarrow \alpha'$ as also expressed in Fig. 6.1g.

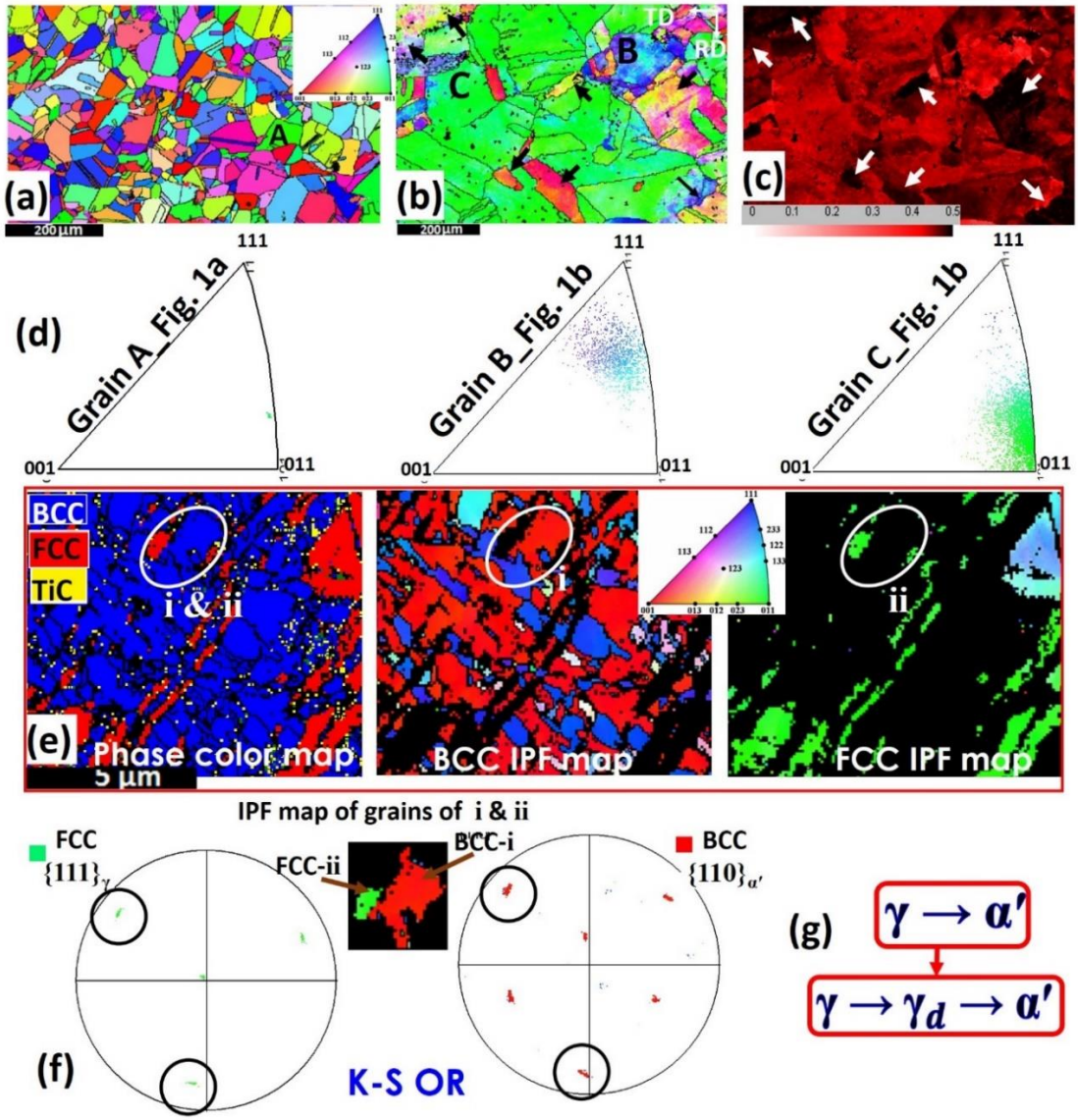


Fig. 6.1. (a) EBSD-IPF map of the as-received sample, (b) IPF and (c) Schmid factor maps of deformed austenite ($\gamma_d$), (d) inverse pole figures of selected undeformed and deformed austenite grains. (e) EBSD-phase color, BCC and FCC IPF color maps of $\gamma_d$ and $\alpha'$, (f) $\{111\}_{\gamma}$ and $\{110\}_{\alpha'}$ pole figures of selected grains in (e), (g) revised sequence of strain-induced martensitic transformation.

The results of the X-ray measurement that confirms the complete martensitic transformation of the austenite phase in the as-received sample after cryo-rolling at 77 K are presented in Fig. 5.1. Although γ-austenite of the as-received steel was transformed completely to α′-martensite at 20% thickness reduction, it was increased to 50% to generate finer martensite grains (insets in Fig. 5.1) that accumulate enough stored energy. This promotes the development of ultra-fine strain-free austenite grains during subsequent annealing. The sigmoidal isothermal reversion curves and associated hardness profiles at two annealing temperatures are presented in Fig. 6.2. Feritscope reading showed that austenitic reversion had barely occurred for samples annealed at 923 K and 1023 K for 60 s. As annealing time increases, specimens showed an increase in austenite fraction and a corresponding decrease in hardness values with annealing time. A notable observation in Fig. 6.2 is the sharp drop in hardness value of specimens annealed beyond 600s at 1023K. This is suspected to signal the onset of grain growth. Therefore, annealing at 1023 K for 600s may be the optimum reversion condition to develop UFG structure via the martensitic shear reversion mechanism. Similarly, annealing at 923 K for 28800s may be the optimum reversion condition via the diffusional reversion mechanism since the volume fraction of the unreversed martensite is approximately 6%.

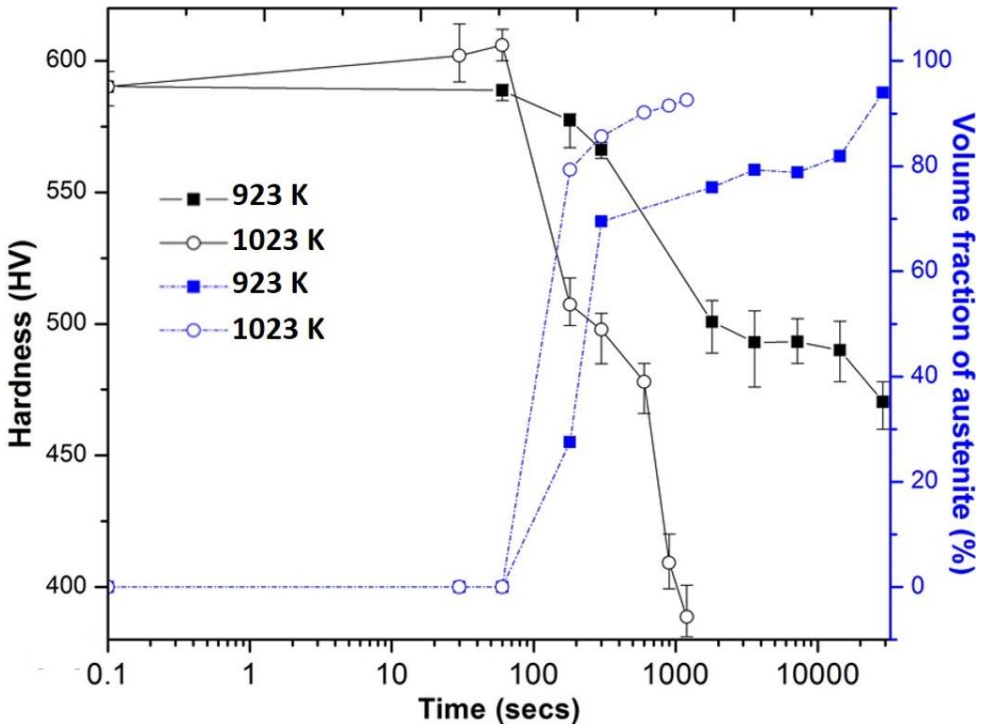


Fig. 6.2. Volume fraction of reversed austenite and corresponding hardness profile during reversion.

The results of macrotexture analyses show that the UFG structure is significantly textured with strong Brass {110}<112>, Goss {110}<100> and Copper {112}<111> components (Fig. 6.3a). Specimen annealed at 923 K for 28800s (8 h) developed stronger texture than the specimen annealed at 1023 K for 600s (10 min). The EBSD maps of a specimen annealed for 180s at 923 K are presented in Fig. 6.3b-d, which indicate an early stage of reversion. Fairly equiaxed austenite grains with an average size of 0.16 μm randomly nucleated in the α′-martensite lath boundaries (Fig. 6.3b). At the annealing time of 300s, the area fraction, morphology and texture of the phases significantly changed (Fig. 6.3e-g). The shape of the α′-martensite grains had changed from lath to near equiaxed after annealing for 300s. It is apparent in Fig. 6.3e-g that the morphology of the growing austenite grains is influenced by the morphology of their neighboring martensite grains.

To expatiate on this, four grains (1, 2, 3 & 4) in Fig. 6.3e-g are considered. The equiaxed martensite grain 1 has a corresponding equiaxed austenite grain 3 as its neighbour. Similarly, grains 2 and 4 are neighbours and both elongated. This shows that a growing austenite grain boundary may be hindered by the boundaries of their neighbour grains; forcing the austenite grain to take the morphology of the martensite. Elsewhere, the morphology of transformed α′ have been reported to influence the shape of the reversed austenite ($\gamma_r$) [167]. On the crystallographic orientation of grains, few variants are present in both BCC and FCC phases (Fig. 6.3h and i). All the variants, V, developed during reversion in this study are presented in Table 6.1. The comparison of $\{111\}_{\gamma}$ and $\{110\}_{\alpha'}$ pole figures for all grains in Fig. 6.3j and k confirms the coincidence of poles. Grains 5

Table 6.1. The {hkl}<uvw> of all identified variants in the EBSD pole figures and ODFs.

| **Variants** | **α′-martensite** | **$\gamma_r$-austenite** | **α′-martensite** | **$\gamma_r$-austenite** | **α′-martensite** | **$\gamma_r$-austenite** |
|---|---|---|---|---|---|---|
| | **923 K / 180s** | | **923 K / 300s** | | **923 K / 28800s** | |
| **$V_1$** | {001}<100> | {001}<201> | {001}<201> | {110}<3-11><br>{001}<201> | {001}<100> | {110}<100> |
| **$V_2$** | {111}<2-31> | {110}<110> | {110}<2-11> | {113}<2-51> | {110}<1-10> | {001}<101> |
| **$V_3$** | {110}<-331> | {113}<3-16> | {111}<-1-21> | {112}<0-21> | {332}<1-22> | {111}<-1-34> |
| **$V_4$** | {112}<-2-33> | {212}<1-51> | {113}<1-41> | {111}<-1-23> | - | {211}<0-32> |
| **$V_5$** | {123}<-2-33> | - | {213}<1-30> | {213}<-1-32> | - | - |
| | **1023 K / 180s** | | **1023 K / 600s** | | **1023 K / 900s** | |
| **$V_1$** | {023}<1-32> | {110}<-331><br>{001}<102> | {011}<0-11><br>{001}<100> | {011}<0-11><br>{031}<0-13> | {011}<1-11> | {011}<0-11> |
| **$V_2$** | {112}<111><br>{113}<-1-21> | {113}<1-10> | {111}<3-41> | {114}<1-10> | {001}<102> | {001}<3-10> |
| **$V_3$** | {012}<2-41> | {112}<110><br>{012}<1-33> | {213}<0-41> | {213}<0-41> | {111}<1-21> | {223}<3-41> |
| **$V_4$** | {014}<-1-71> | {015}<-4-31> | - | - | {210}<2-41> | {210}<1-34> |
| **$V_5$** | - | - | - | - | {213}<0-21> | {213}<0-21> |

({100} oriented-α′) and 6 ({110} oriented-γ) are selected and further analyzed as presented in Fig. 6.3l. One of the poles of $\{111\}_{\gamma}$ is parallel to one of the poles of $\{110\}_{\alpha'}$. This confirms that K-S orientation relationship exists between the reversed γ-austenite and α′-martensite.

The EBSD maps of specimens annealed at 923 K for 28800s (Fig. 6.4a-c) and at 1023 K for 600s (Fig. 6.4d-f) show the development of UFG structure with very low and acceptable fraction of α′-martensite. The average austenite grain sizes are 0.22 µm and 0.31 µm in the specimens annealed at 923 K and 1023 K, respectively. Although the orientation of $\gamma_r$ grains are close to {110}<uvw> (ζ-fibre), texture is stronger in the specimen annealed at 923 K (Fig. 6.4c) than in the specimen annealed at 1023 K (Fig. 6.4f). This agrees with the result of the macrotexture measurement in Fig. 6.3a. It is worth noting that most of the unreversed α′-martensite and TiC particles are located at the austenite triple junctions. These contribute to the stability of the UFG structure via Zener pinning of grain boundaries [191]. At higher annealing temperature and times, the larger fraction of the TiC particles dissolve and the volume fraction of α′-martensite was near-zero. This leads to abnormal grain growth by the breaking away of high angle boundaries and loss of texture [164]. To develop an UFG structure without abnormal grain growth, it may, therefore, be impractical to completely reverse the α′ to γ without retaining some negligible fraction of the α′.

While the texture of the γ-phase (parent) in the as-received AISI 321 ASS is random (Fig. 6.1a), it is apparent that the ζ-fibre texture of the $\gamma_r$ (product) in the UFG structure memorizes the texture of the deformed austenite ($\gamma_d$) on the completion of γ (parent) → α′ → $\gamma_r$ (product) transformation cycle. Since $\gamma_d$ is intermediated between γ (parent) → α′ and conventional texture memory like those observed in BCC and HCP metals require that the texture of the product phase 'remembers' that of the initial parent phase, the phenomenon in AISI 321 steel is hereby referred to as Pseudo-texture memory. Hence, the transformation cycle is revised to γ → $\gamma_d$ → α′ → $\gamma_r$ as shown in Fig. 6.4g. The mechanism behind the pseudo-texture memory involves microstructural sites such as special grain boundaries. The variant that acted on the first transformation ($\gamma_d$ → α′) in the special grain boundary is memorized and the same path becomes more accessible than the others for the α′ → $\gamma_r$ reversion during annealing. This is schematically shown in Fig. 6.4h-l. At the early stage of cryogenic rolling of AISI 321 ASS, the austenite grains will first be deformed (Fig. 6.4h). As cryogenic rolling proceeds, two α′ grains, for instance, nucleate along the same $\gamma_d$ boundary (Fig. 6.4i).

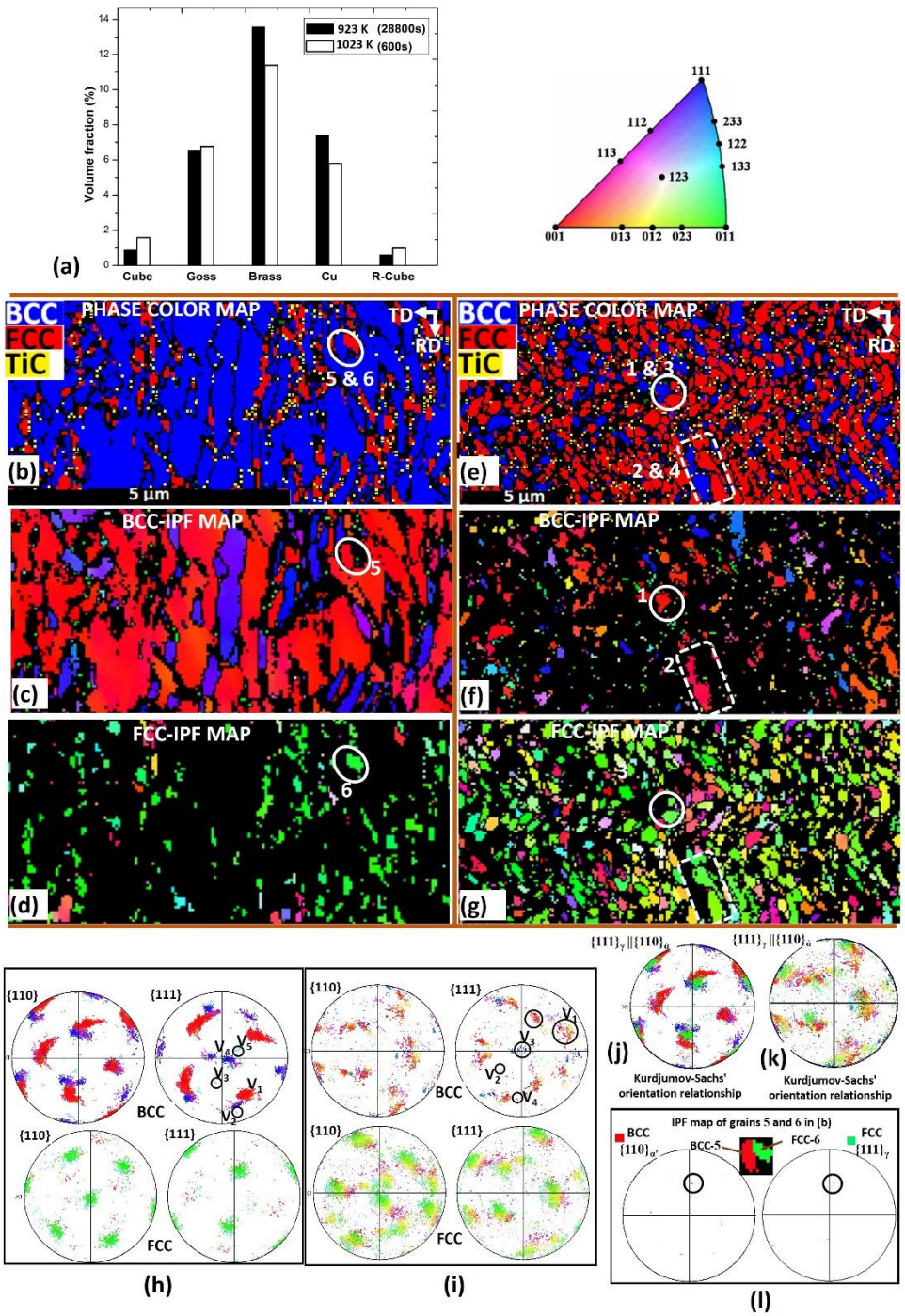


Fig. 6.3. (a) Volume fraction of selected texture components. (b-g) EBSD maps of specimen annealed at 923 K (650 ℃) for (b-d) 180s and (e-g) 300s: (b and e) phase color maps, (c, d, f, g) IPF color maps. {110} and {111} pole figures of specimens annealed at (h) 180s and (i) 300s. Superimposed $\{111\}_{\gamma}$ and $\{110\}_{\alpha'}$ pole figures of all grains in specimen annealed for (j) 180s and (k) 300s, (l) $\{111\}_{\gamma}$ and $\{110\}_{\alpha'}$ pole figures of selected grains in specimen annealed for 180s.

These two α′ grains obey the K-S orientation relationship with $\gamma_{d2}$, but exhibiting different variants of the 24 possible K-S conditions. As the percentage thickness reduction increases, both grains

should grow into the neighbor $\gamma_{d1}$ grain and then merge to establish a 'special grain boundary' in the new α′ grain structure (Fig. 6.4j). When the new α′ grain structure is annealed, the special grain boundary will be highly favored for the nucleation of $\gamma_r$ grains that possess the same orientation as the $\gamma_{d2}$ since it is the orientation that fulfills the K-S condition (Fig. 6.4k), as indicated in the experimental results presented in Fig. 6.3b-d, h-l. The available special grain boundaries in the specimen therefore act as crystallographic orientation memory sites during austenitic reversion. This process is more pronounced at lower annealing temperature (923 K) where TiC precipitates

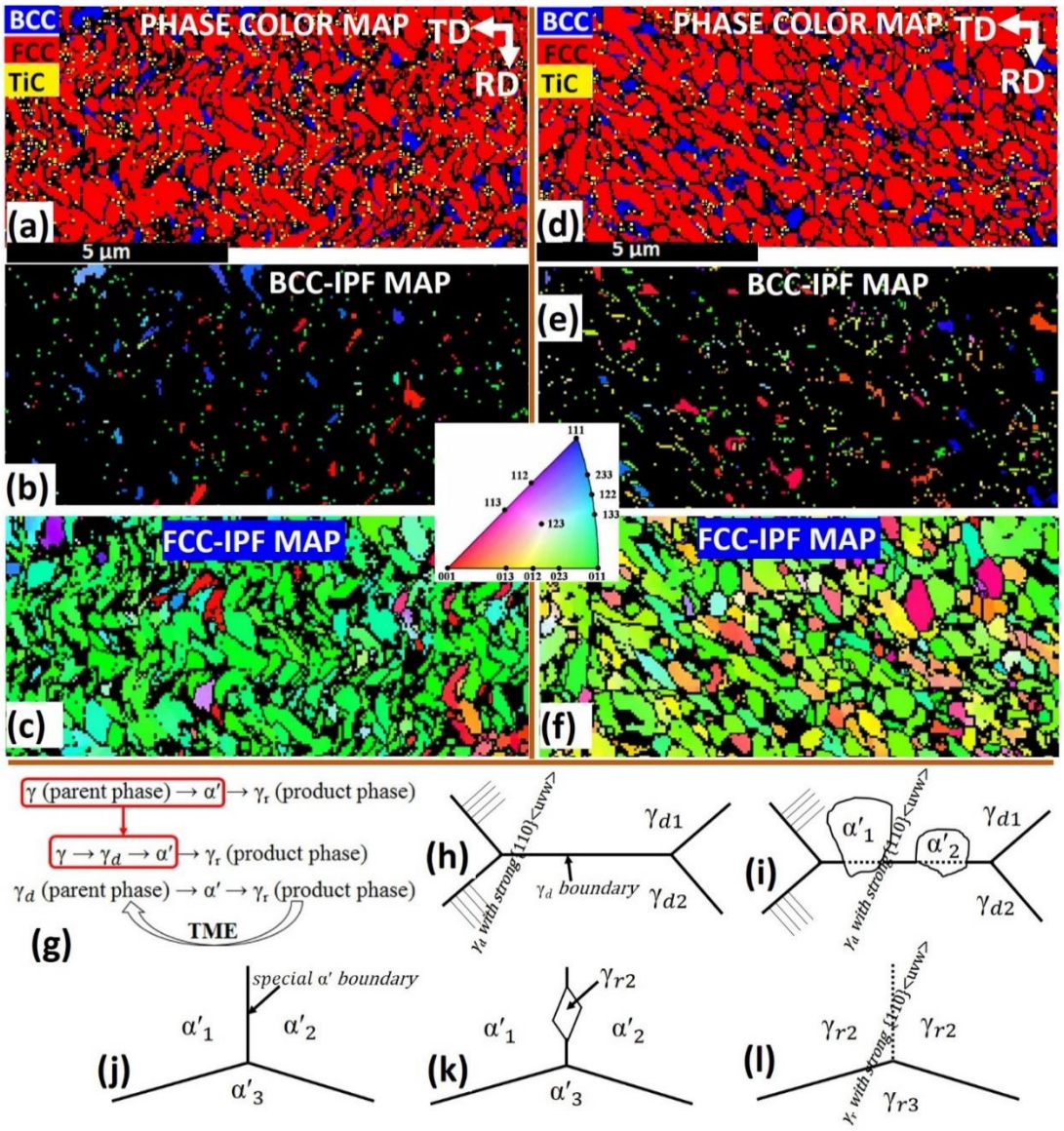


Fig. 6.4. EBSD maps of specimen cryo-rolled and subsequently annealed at (a-c) 923 K (650 ℃) for 28800s and (d-f) 1023 K (750 ℃) for 600s. (g) sequence of transformation/reversion, (h-l) schematic of the pseudo-texture memory process adapted from Ref. [185].

are more stable than at higher annealing temperature (1023 K). This explains why the intensity of ζ-fibre is stronger at lower temperature (Figs. 6.3a and 6.4c) and weaker at higher annealing temperature (Figs. 6.3a and 6.4f). TME in Mn-IF steel has been attributed to the formation of TiC precipitates [185]. It can therefore be concluded that TiC precipitates played a significant role in the TME exhibited by AISI 321 steel. The schematic of pseudo-texture memory and stages of martensitic transformation and austenitic reversion during the development of UFG structure is shown in Fig. 6.5.

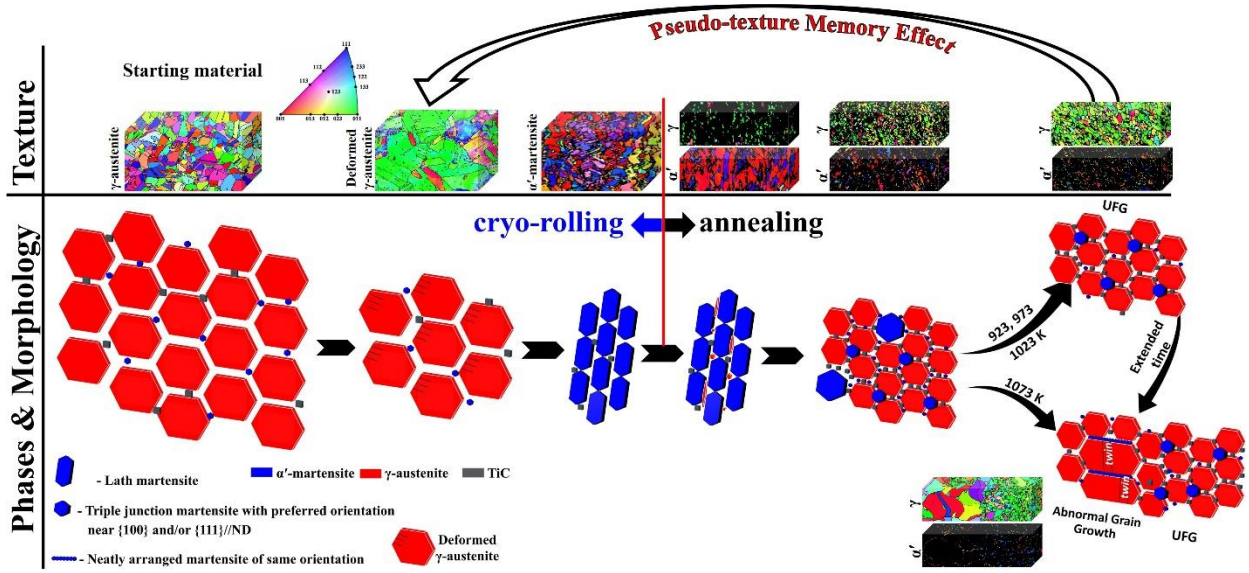


Fig. 6.5. Schematic of texture memory and stages of martensitic transformation and austenitic reversion. Shape and size of grains and particles are exaggerated to show the sequence of UFG development

## 6.4 Conclusion

The strong ζ-fibre ({110}<uvw>) observed in the austenite phase of the UFG structure can be traced to AISI 321 ASS's ability to memorize the orientation of the deformed austenite.

# Chapter 7

## Characterization of Coarse and Ultrafine-Grained Austenitic Stainless Steel Subjected to Dynamic Impact Load: XRD, SEM, TEM and EBSD Analyses

Upon the successful development of ultrafine grain (UFG) structure, it became necessary to determine how the dynamic impact responses of AISI 321 austenitic stainless steel has been influenced by grain refinement to UFG structures. In this chapter, the results of the investigations on the dynamic impact responses of UFG specimens in comparison with those of the as-received coarse-grained (CG) AISI 321 austenitic stainless steel are reported. The mechanical test was conducted using split Hopkinson pressure bar while transmission electron microscopy (TEM), electron backscatters diffraction (EBSD) and x-ray diffraction (XRD) were used in identifying deformation and strengthening mechanisms in both coarse- and ultrafine-grained specimens. This chapter is published in "*Materialia*" as follows:

A. A. Tiamiyu, A. G. Odeshi, and J. A. Szpunar. "Characterization of coarse and ultrafine-grained austenitic stainless steel subjected to dynamic impact load: XRD, SEM, TEM and EBSD analyses" *Materialia*, vol. 4, pp. 81-98, 2018.

My contributions to this paper include review of the relevant literature, design and implementation of the experimental procedures, analysis of test results and preparation of the manuscript, which was reviewed by my supervisors; Professors Akindele Odeshi and Jerzy Szpunar. Their comments were addressed before submission for publication. The information already provided in Chapter 3 (material and methodology) of this thesis have been removed to avoid repetitions. The copyright permission for manuscript reuse was obtained and provided in APPENDIX C.

### Abstract

A comparative study of the dynamic impact responses of coarse- (37 μm) and ultrafine-grained (0.24 μm) AISI 321 austenitic stainless steel was conducted using a split Hopkinson pressure bar system. An increase in firing pressure of the system's projectile results in the corresponding increase in impact momentum, strain rate, total strain, and maximum flow stress of the specimens. Although ultrafine-grained (UFG) specimens show higher compressive strength, coarse-grained (CG) specimens possess higher strain hardenability than the UFG specimens under the same

impact loading conditions. UFG specimens exhibit lower critical strain and strain rate at which adiabatic shear bands (ASBs) developed when subjected to high strain-rate loading; hence, UFG specimens are more susceptible to ASB formation than CG specimens. Using the XRD, SEM, TEM and EBSD characterization techniques, the underlying deformation and strengthening mechanisms were studied. Slip and twinning are the active deformation mechanisms in CG specimens, and they are highly suppressed in UFG specimens due to spatial restriction effect. At higher strain rates, CG specimens are only susceptible to the formation of multiple transformed shear band (MTSB), while UFG specimens are susceptible to both MTSB and TSB bifurcation. Although the mechanism behind the formation of MTSB is not completely clear, bifurcation of TSB was geometrically necessary, and the presence of precipitate at the bifurcation point could play a major role. EBSD analysis of inside, interface and outside the TSB revealed the development of equiaxed ultra-fine grain structure (~0.17 μm in CG and ~0.14 μm in UFG specimens) inside the TSB by rotational dynamic recrystallization mechanism.

**Keywords:** *AISI 321 austenitic stainless steel; SHPB; EBSD; Strain-induced martensitic transformation; Adiabatic shear band.*

## 7.1 Introduction

Studies on the dynamic impact response of materials under high strain-rate loading conditions have received increased interest. This is largely due to the ability of dynamic impact test to simulate the behavior of materials under ballistic impact, crash or explosive events. An important mode of deformation in materials subjected to dynamic impact load is the formation of adiabatic shear bands (ASB), which is a consequence of thermally-assisted shear strain localization. This band is a narrow shear zone that eventually becomes preferential sites for dynamic failure/fracture [89,90]. Localized shear deformation, for decades, has been of great interest since the pioneering work of Zener and Hollomon [91], who ascribed the occurrence of ASB to a competition between strain hardening and thermal softening.

Deformed shear band (DSB) consisting of elongated/distorted grains and transformed shear band (TSB) consisting of equiaxed ultrafine grains formed by dynamic recovery or dynamic recrystallization are the two types of ASB that develop in impacted specimens. The TSB is a metamorphosed DSB upon an increase in strain and/or strain rate [192]. Other possible structural

alterations such as phase transformation [105,106], amorphization [107] and carbide fragmentation and redistribution [108] have been reported to occur within the TSB. Factors affecting ASB formation includes strain and strain rate [192], strain rate sensitivity [193], specimen geometry and dimension, presence of local defects [194,195], notches [196], pre-heat treatment [197,198], stacking fault energy [199], temperature of deformation and grain size [200].

High strain rate deformation and the associated microstructural evolution in different metals have enjoyed substantial number of both experimental [35,89,106-108,201-205] and theoretical [110,154,206] research investigations. Xue and Gray [201] used transmission electron microscope (TEM) to observe equiaxed grain substructures (< 100 nm) that developed by both dynamic recovery and recrystallization within ASB in AISI 316L stainless steel. In another study [202], sintered AISI 316L steel was subjected to a wide range of strain-rates ($10^{-3}$ to 7.5 x $10^{3}$ $s^{-1}$) using MTS 810 Material Testing System and split Hopkinson pressure bar (SHPB) system at low and high strain-rate regimes, respectively. The flow stress, rate of work hardening, and strain rate sensitivity of the sintered steel were observed to be dependent on strain rate. ASB formation was recorded at strain rate above 5.6 x $10^{3}$ $s^{-1}$. In the study of the dynamic deformation and failure of ultrafine-grained (~120 nm) pure titanium using a SHPB system, Li et al. [203] observed equiaxed nanograins (~40 nm) that developed via rotational dynamic recrystallization mechanism within ASB. They reported that the developed ASB in the alloy served as the eventual crack initiation site and crack propagation path leading to a combination of brittle and ductile fracture [203]. Using the electron backscattered diffraction (EBSD) technique, Wang *et al.* [86] observed ultrafine grains (0.1 - 0.3 μm) in the ASB region that developed in an impacted Fe-Cr-Ni austenitic stainless steel. The exposure of AISI 304L stainless steel to dynamic shock loading conditions was also studied by Meyers *et al.* [107], who used TEM to reveal two distinct regions within the adiabatic shear band. While the first region consisted of refined grains with sizes ranging between 0.1 and 0.2 μm, glassy structure (amorphization) was observed in other regions of the band. It was also reported that martensitic transformation, stacking faults and twinning occurred outside the ASB region of the deformed AISI 304L steel. In a recent high resolution-EBSD study [137], the dynamic impact response of Mn-steel confirms both ε (HCP) and α′ (BCC)-martensitic transformations inside and outside the ASB region, which obey the Shoji-Nishiyama and Burger crystallographic relationship, respectively, with the parent austenite (FCC) phase.

The aim of this study is to investigate the dynamic impact response of AISI 321 steel, an austenitic stainless steel that is stabilized with titanium (Ti) to reduce sensitization in elevated-temperature applications. AISI 321 steel has an FCC structure with low stacking fault energy [20], and its γ-austenite phase can transform to martensite during plastic deformation. Due to its corrosion resistance [3], AISI 321 finds application in components designed for nuclear power and chemical reactors, automobile exhaust systems, aircraft exhaust stacks and exhaust manifolds, pressure vessels, mufflers for engines, carburetors, expansion bellows, stack liners, etc. In some of these applications, the alloy can be exposed to explosive or impact loading. A major limitation of AISI 321 stainless steel is its relatively low yield strength. To expand its structural applications to areas where low yield strength is a limitation, an ultrafine-grained (UFG) structure was developed from the commercial as-received coarse-grained (CG) alloy via thermo-mechanical processing [207]. A comparative study of the deformation behavior of the coarse and ultrafine-grained AISI 321 stainless steel under dynamic impact load is conducted using a SHPB system. The goal is to understand the mechanical response and microstructural evolution in this steel under loading conditions that simulate explosive or impact loading. X-ray diffraction (XRD), optical and electron microscopy (SEM, EBSD, and TEM) techniques were used to investigate the microstructural evolution in the steel during high strain-rate deformation.

## 7.2 Materials and methodology

The commercial coarse-grained AISI 321 with a grain size of 37 μm was subjected to cryorollimg and subsequent annealing treatments to obtain ultrafine grains, 0.24 μm in size, as discussed in Chapter 3, Section 3.1. High strain-rate test using a split Hopkinson pressure bar (SHPB) system was conducted on cylindrical test specimens (4mm x 4mm) machined along the rolling direction (RD). The compression direction (CD) is parallel to the RD. Both the CG and UFG specimens were deformed using projectile's firing pressures that ranged between 50 and 130 kPa (at 10 kPa interval). These generated strain rates between 1300 and 8800 $s^{-1}$ in the specimens. The dynamic impact tests and microstructural analyses using SEM, TEM, EBSD, XRD and Feritscope are described in detail in Chapter 3.

## 7.3 Result and discussion

TEM micrographs of the CG and UFG samples, respectively, before dynamic impact are provided in Figs. 7.1a and b. Stacking faults (Fig. 7.1[a1]) and annealing twins can be observed in the CG alloy, which are absent in the UFG alloy. The absence of twinning in UFG alloy (Fig. 7.1b) could imply that the grain size (0.24 μm) is below the critical grain size at which annealing twin can occur in AISI 321 steel. The presence of nanosized (~100 nm) carbide identified as TiC particle by the EDS spectra can be observed in Fig. 7.1(a2 and a3). The results of the XRD bulk texture measurement (Fig. 7.1c) indicate R-Cube ({001}<110>) as the major crystallographic orientation in the CG alloy, with a spread around Goss orientation ({110}<001>). However, the UFG alloy is significantly textured around Cube orientation ({001}<100>). Both undeformed CG and UFG alloy samples contain less than 10% BCC α′ and their Vickers hardness values are 186 and 490 HV, respectively.

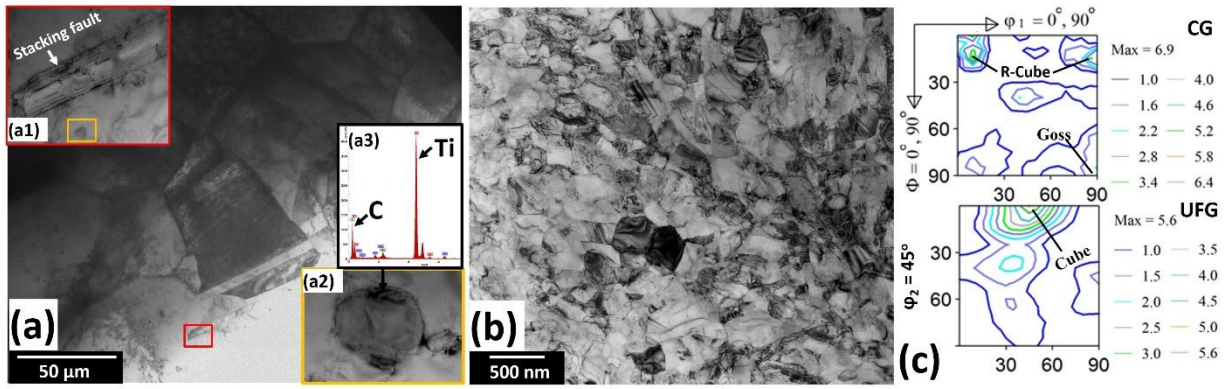


Fig. 7.1. TEM bright field micrographs of undeformed (a) CG and (b) UFG samples. (c) ODF 45°-$\phi_2$ sections from the XRD texture measurement of the undeformed samples. Insets in (a); a1, a2 and a3, are the stacking fault, TiC particle and EDS spectra of the TiC particle.

### 7.3.1 Dynamic mechanical behaviour

The dynamic engineering stress-strain curves of the CG and UFG specimens deformed using various firing pressures (FP) are presented in Fig. 7.2. As FP increases, the impact momentum, strain rate (lower in UFG), final deformation strain (lower in UFG) and maximum flow stress (higher in UFG) increases, as also summarized in Table 7.1. The stress-strain curves typically show two major peaks. The first peak occurs near the yield point after a drop in flow stress. This is followed by a steady rise in flow stress that leads to the second peak (i.e., the maximum flow stress) at the later stage of the deformation process. The corresponding strain at the maximum flow

stress (MFS) is referred to as the instability strain. The 'rising and falling' of the stress-strain curve is attributed to the competition between strain hardening (rising) and thermal softening (falling) which are characteristics of specimens under dynamic loading conditions. Hardening in metastable AISI 321 stainless steel has been attributed to multiple strengthening sources during plastic deformation [208]. Whereas, thermal softening leading to thermo-mechanical instability and eventual loss of load-carrying capability, occurs when the impact energy of projectile converts to thermal energy. About 90 % of the kinetic energy of projectile has been estimated to convert to thermal energy during high strain rate deformation [75]. It has been reported that a variation in stress-strain curves could be related to variation in the microstructural evolution in the material during mechanical loading [209]. Therefore, the steepness of the drop in flow stress beyond the instability strain, which increases with increasing firing pressure could signal a differing microstructural changes in the deforming specimen.

Table 7.1. Experimental data sheet from the dynamic impact test of AISI 321 steel specimens.

| Grain structure | FP, kPa | IM, $kg.ms^{-1}$ | Strain rate, $s^{-1}$ | Total strain | MFS, MPa | Type of ASB | ASB Bifurcation | Deformation time (μs) | Temperature inside ASB, K |
|---|---|---|---|---|---|---|---|---|---|
| **CG** | 50 | 10 | **2600** | **0.24** | **790** | **NO** | **NO** | **170** | **-** |
| UFG | | | 1300 | 0.12 | 1490 | NO | NO | 168 | - |
| **CG** | 60 | 14 | **4000** | **0.36** | **1010** | **NO** | **NO** | **167** | **-** |
| UFG | | | 2700 | 0.24 | 1700 | NO | NO | 158 | - |
| **CG** | 70 | 18 | **5400** | **0.48** | **1030** | **NO** | **NO** | **149** | **-** |
| UFG | | | 3800 | 0.33 | 1780 | DSB | NO | 148 | - |
| **CG** | 80 | 20 | **6400** | **0.57** | **1300** | **DSB** | **NO** | **145** | **-** |
| UFG | | | 5100 | 0.45 | 1900 | DSB+TSB | NO | 147 | - |
| **CG** | 90 | 21 | **7100** | **0.63** | **1430** | **DSB** | **NO** | **145** | **-** |
| UFG | | | 6100 | 0.54 | 2040 | TSB | NO | 143 | 985 |
| **CG** | 100 | 23 | **7600** | **0.68** | **1460** | **MTSB** | **NO** | **145** | **680** |
| UFG | | | 6700 | 0.60 | 2020 | TSB | NO | 143 | 999 |
| **CG** | 110 | 26 | **8200** | **0.73** | **1710** | **MTSB** | **NO** | **140** | **688** |
| UFG | | | 7600 | 0.67 | 2180 | TSB | YES | 141 | 1015 |
| **CG** | 120 | 31 | **8700** | **0.76** | **1970** | **MTSB** | **NO** | **148** | **696** |
| UFG | | | 7900 | 0.70 | 2400 | MTSB | YES | 143 | 1021 |
| **CG** | 130 | 36 | **8800** | **0.81** | **2120** | **MTSB** | **NO** | **151** | **702** |
| UFG | | | 8400 | 0.74 | 2480 | MTSB | YES | 144 | 1029 |

FP- Firing pressure, IM- Impact momentum, MFS- Maximum flow stress

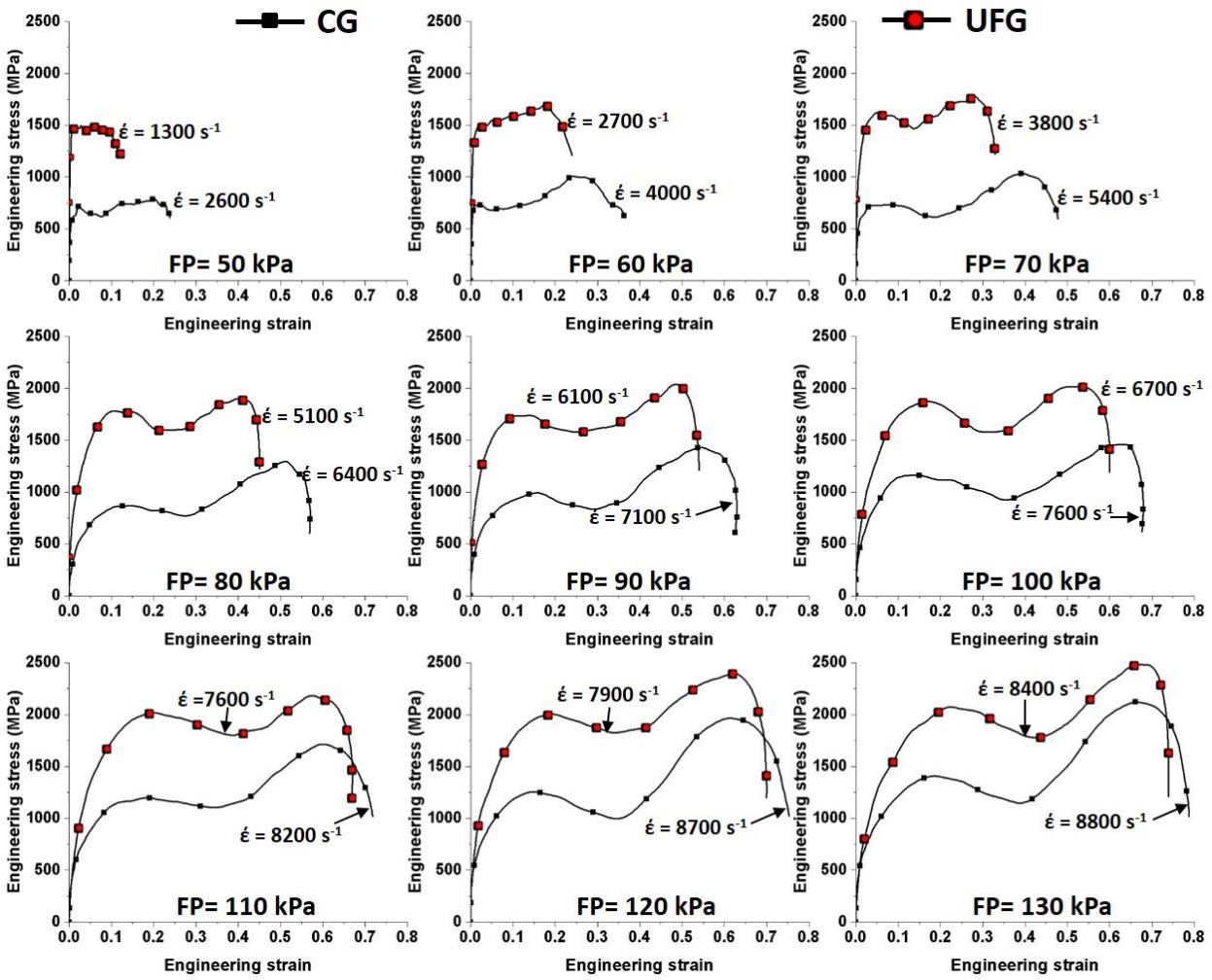


Fig. 7.2. Dynamic stress-strain curves of deformed CG and UFG specimens.

The UFG specimens show higher compressive strength than the CG specimens, thereby obeying the Hall [210]-Petch [211] relation. However, CG specimens possess higher strain hardenability than the UFG specimens. This is corroborated by the plot of hardening diagrams in Fig. 7.3 that corresponds to the stress-strain curve in Fig. 7.2. Complete dominance of thermal softening occurs at strain where strain hardening rate consistently drops below zero. This is the same as instability strain indicated in Fig. 7.2. The instability strain increases with FP/strain rate, and it is higher in CG specimen, which suggests a higher strain hardenability in CG specimen. However, at FP above 100 kPa (or $\dot{\varepsilon} \geq 7600\ s^{-1}$), the strain hardenability of both CG and UFG becomes relatively comparable (Fig. 7.3).

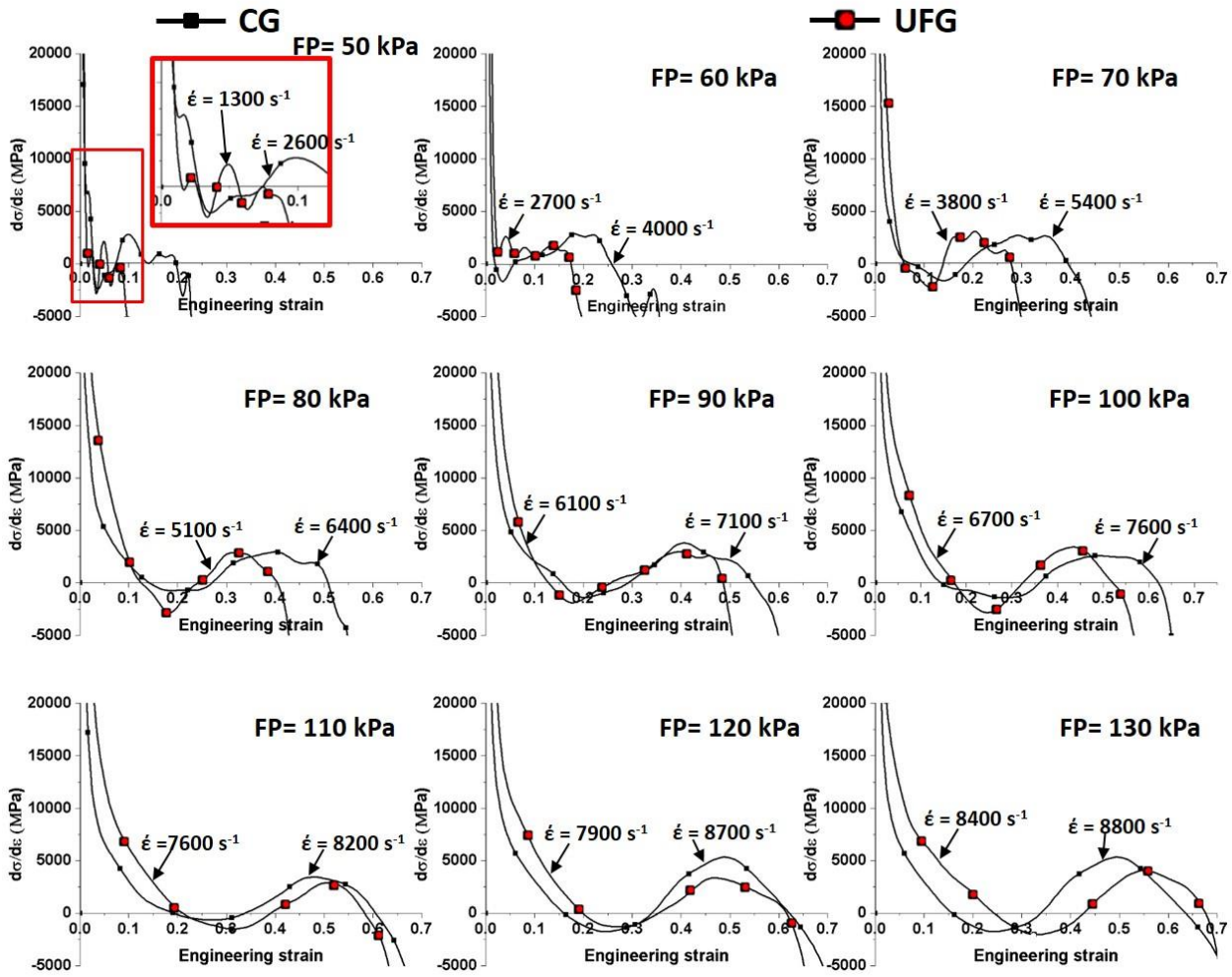


Fig. 7.3. Dynamic strain hardening curves of deformed CG and UFG specimens.

### 7.3.2 Microstructural characterization of deformed specimens

Due to the complexities associated with the very short deformation time involved in investigating the deformation behavior of materials under dynamic loadings, it is difficult to analyze the dynamic deformation process in real-time without a high-speed camera. A viable alternative to revealing deformation mechanisms and damage evolution in a material during such rapid and massive deformation is to examine the microstructure of the materials after the deformation. This is because there is usually a strong correlation between the post-deformation microstructure and the deformation process [212]. Hence, highlights of the observed microstructural changes in CG and UFG specimens under dynamic impact load are provided in this section.

7.3.2.1 Optical microscopic (OM) analysis: Effect of strain rate and grain size on the onset of adiabatic shear band

Optical micrographs showing the onset of adiabatic shear band (DSB and TSB) in CG and UFG specimens, respectively are presented in Figs. 7.4 and 7.5. These bands form a conical shape in the specimen. When observed on the compression plane in contact with the transmitter bar, the bands are observed to be circular. The circular shape of the shear band on the compression plane might be due to the cylindrical shape of the test samples [193]. Systematic observation of the deformed specimens showed that there's a critical FP or strain rate at which DSB and TSB forms. Strain rate at which TSBs formed is higher than that of DSBs, which affirm that TSB is a metamorphosed DSB at high strain rates [192]. However, grain size plays a significant role in the onset and type of ASB that formed in the AISI 321 steel. Both DSB and TSB first formed at higher strain and strain rate in CG specimen (Fig. 7.4) than in the UFG specimen (Fig. 7.5a-d) as presented in Table 7.1. For instance, the strain and strain rate at which DSB is formed in CG specimen are 0.57 and 6400 $s^{-1}$ (FP = 80 kPa), respectively, compared to 0.33 and 3800 $s^{-1}$ (FP = 70 kPa) for UFG specimen. These critical conditions for the onset of DSB accurately correspond to the same conditions (in CG and UFG, respectively) at which the drop in flow stress beyond the MFS first becomes steeper (Fig. 7.2). Thus, the susceptibility of metals to adiabatic shear banding can be predicted from the stress-strain curves [213].

Similarly, the strain and strain rate at which TSB formed in the CG specimen is 0.68 and 7600 $s^{-1}$ (FP = 100 kPa), respectively, compared to 0.45 and 5100 $s^{-1}$ (FP = 80 kPa) for the UFG specimen. This implies that UFG samples, which are characterized by lower strain and strain hardening rate (favourable factors for shear strain localisation [214]) as described in Section 7.3.1, are more susceptible to ASB formation than CG samples. At higher FP/strain rate, the formation of multiple TSB (MTSB) and bifurcation of TSB is observed. While multiple TSBs were observed in the CG specimen (Fig. 7.4c and d), TSB bifurcation was observed in addition to MTSB in UFG specimen (Fig. 7.5e-h) as summarized in Table 7.1. Although grain size, strain and strain rate played key roles in the evolution of these band type, the mechanism of their formation is not well understood. In the study of the adiabatic shear failure of AA 2024 aluminum alloy deformed at high strain rate using the SHPB system, temper condition and strain rate were reported to influence the susceptibility of the alloy to the formation of both MTSB and TSB bifurcation [198]. As a result

of the development of ASB near the circumference of the impacted cylindrical specimens, it is expected that the microstructure at the centre of the specimen will differ from that in the region of shear strain localization.

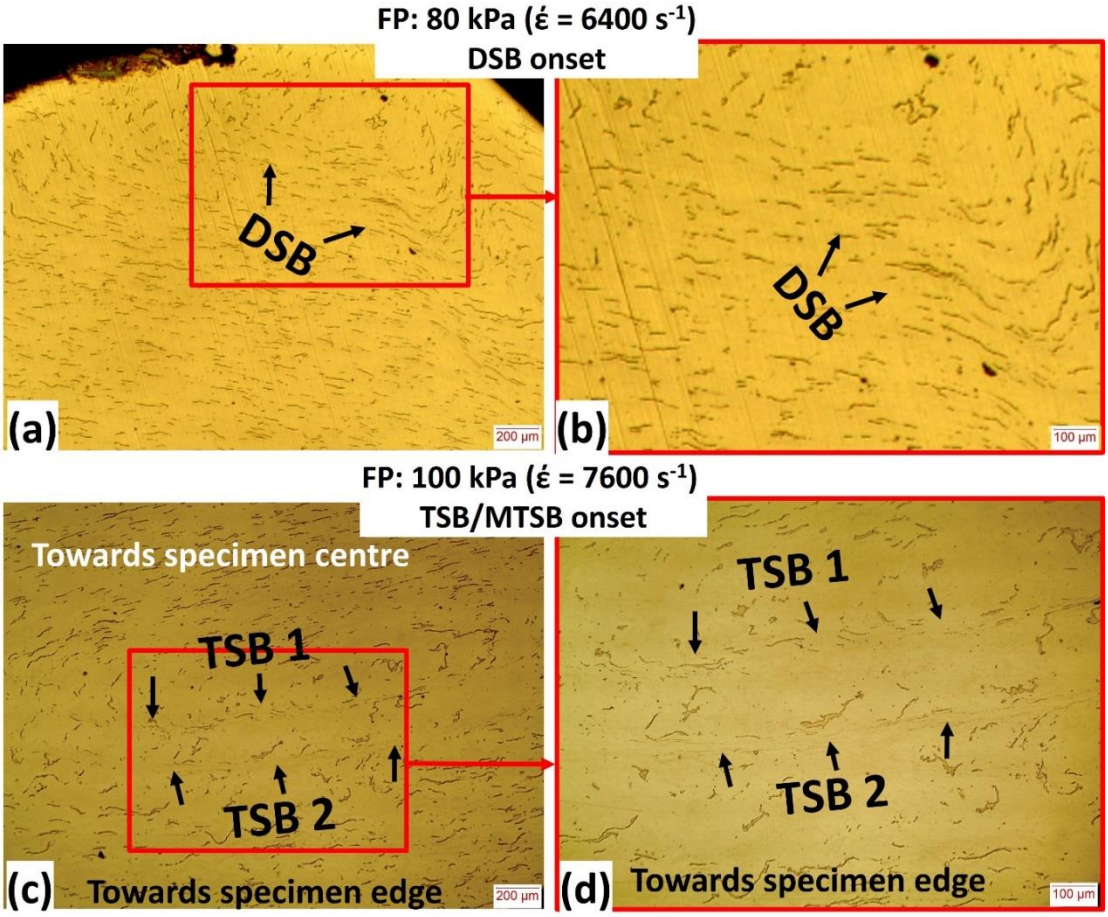


Fig. 7.4. Optical micrographs showing the onset of ASB in deformed CG specimens.

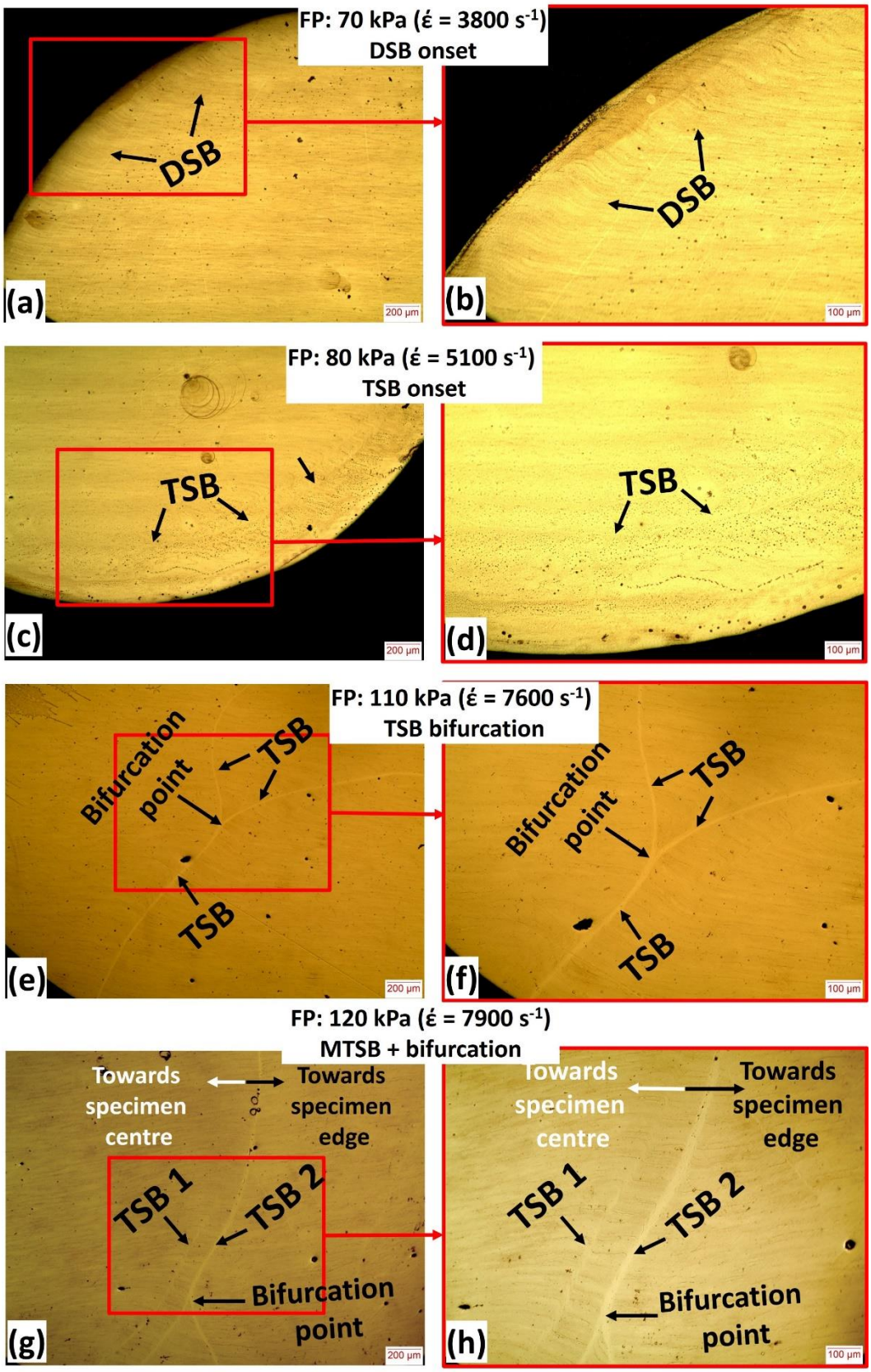


Fig. 7.5. Optical micrographs showing the onset of ASB in deformed UFG specimens.

7.3.2.2 XRD, EBSD and TEM analyses at the specimens' centre

7.3.2.2.1 XRD analysis (macrotexture and phase identification) and Hardness profile

The result of the X-ray diffraction measurements (Fig. 7.6) shows evidence of strain-induced martensitic phase transformation as indicated by the appearance of α′-martensite peaks at two 2θ positions [$(110)_{\alpha'}$ and $(200)_{\alpha'}$]. This phenomenon is termed transformation-induced plasticity (TRIP) effect. It is observed that the stability of the austenite phase is lower in impacted UFG specimens (Fig. 7.6b) than in the CG specimens (Fig. 7.6a). It can be observed from the diffraction patterns for both CG and UFG specimens that the α′ peaks initially increases as the firing pressure increases. At a critical FP, the intensity of α′ peaks starts to decrease with further increase in FP. This trend was also confirmed during the quantitative measurement of α′-martensite using Feristcope. Although the martensitic phase transformation is more suppressed in the CG specimens (Fig. 7.7), the volume of α′ in both CG and UFG specimens increased to ~10 (at FP = 70 kPa) and ~43 % (at FP = 80 kPa), respectively. Beyond these critical firing pressures, the volume percent of α′-martensite decreased with increase in strain rate. The drop in the volume percent of α′ at higher FP/strain rate may be due to the temperature rise in the material as impact energy was converted the heat energy.

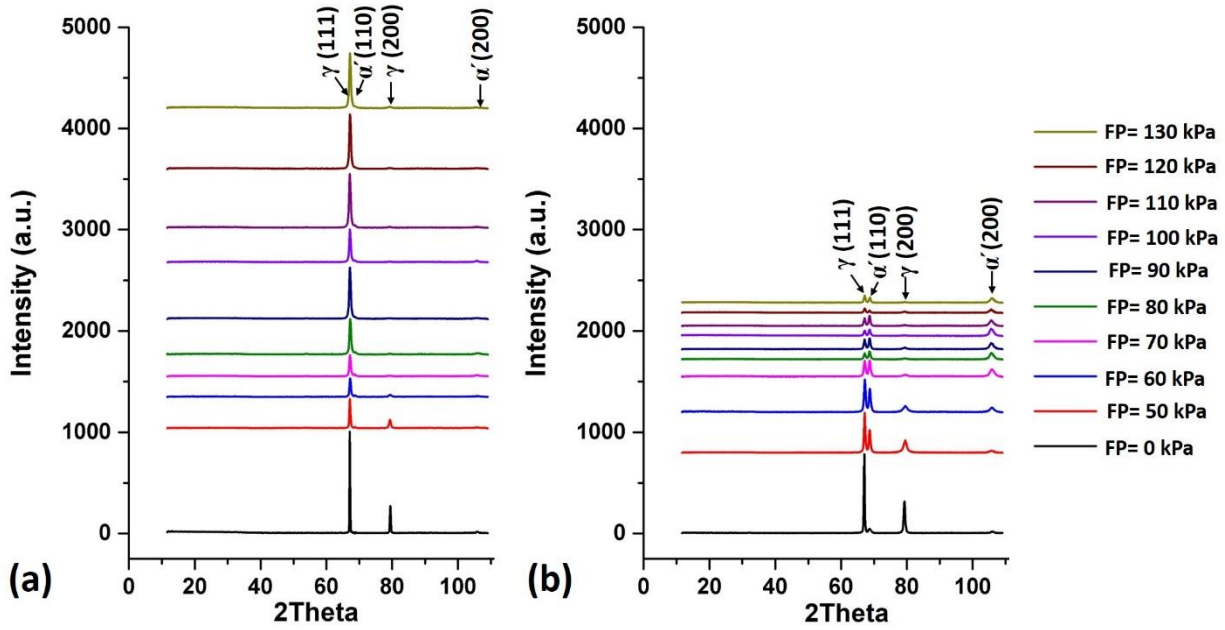


Fig. 7.6. X-ray diffraction patterns showing the trend of phase transformation in deformed (a) CG and (b) UFG specimens.

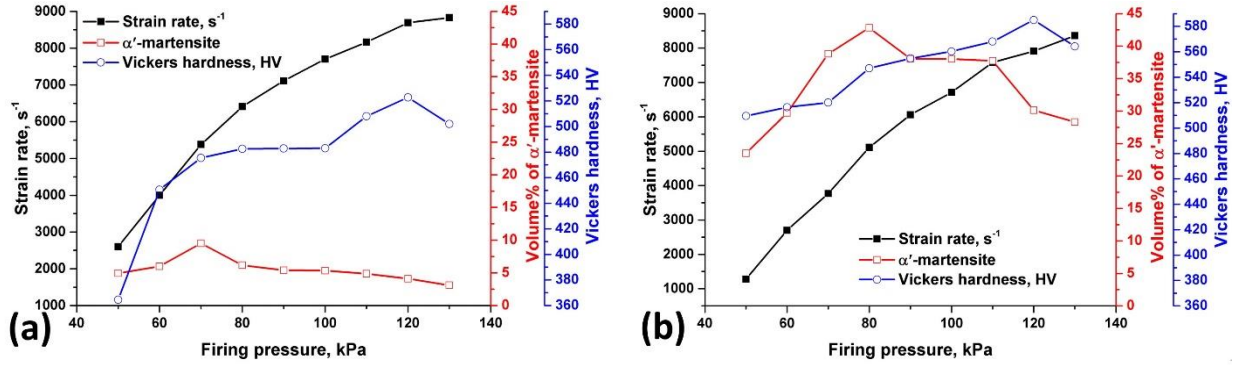


Fig. 7.7. Strain rate, volume percent of α′-martensite and Vickers hardness at region outside the ASB as a function of firing pressure for (a) CG and (b) UFG specimens.

These findings are consistent with those of Hecker et al. [215] who reported the ease of α′-martensite formation in AISI 304 stainless steel under low-strain dynamic loading, but their (α′) suppression during high-strain dynamic loading due to adiabatic heating. There are two possible reasons for the 'rise and fall' (Fig. 7.7) of the final volume fraction of α′-martensite in a dynamic impacted metastable stainless steel. The first possibility is that the temperature rise suppressed strain-induced martensitic phase transformation during the deformation process. Alternatively, it is also possible that a higher percentage of martensite was originally formed at an early stage of deformation, and some were reversed back to austenite due to temperature rise in the material before deformation was completed. Because the formation of strain-induced martensite during deformation (TRIP effect) improves materials' strength [216], it is thought that a drop in volume fraction of martensite should be accompanied by a corresponding drop in strength or hardness. This is not the case, as the hardness values (and yield stress/MFS) of the impacted specimens increased with an increase in firing pressure/strain rate (Fig. 7.7). The increase in hardness beyond the FP at which the volume percent of α′ drops suggest other plausible strengthening sources in the AISI 321 stainless steel which will be discussed later in this article.

The results of macrotexture analysis using XRD (Fig. 7.8) indicate the volume percent of [100], [110] and [111]||CD fibres as a function of the firing pressure. Although a higher volume percent of [110]||CD fibre is recorded in coarse-grained specimens, however, the stable end-orientation of the γ-austenite phase is [110]||CD fibre at the expense of [100] and [111]||CD fibres irrespective of the grain size. This agrees well with the earlier reported end-orientation in compressed FCC

metals [142]. The strengthening of [111]||CD texture in the CG specimens at higher firing pressures coincides with the slight drop in [110]||CD texture (Fig. 7.8a). This is not noticeable in UFG specimens, and it may be due to different active deformation mechanism(s) in the CG and UFG specimens.

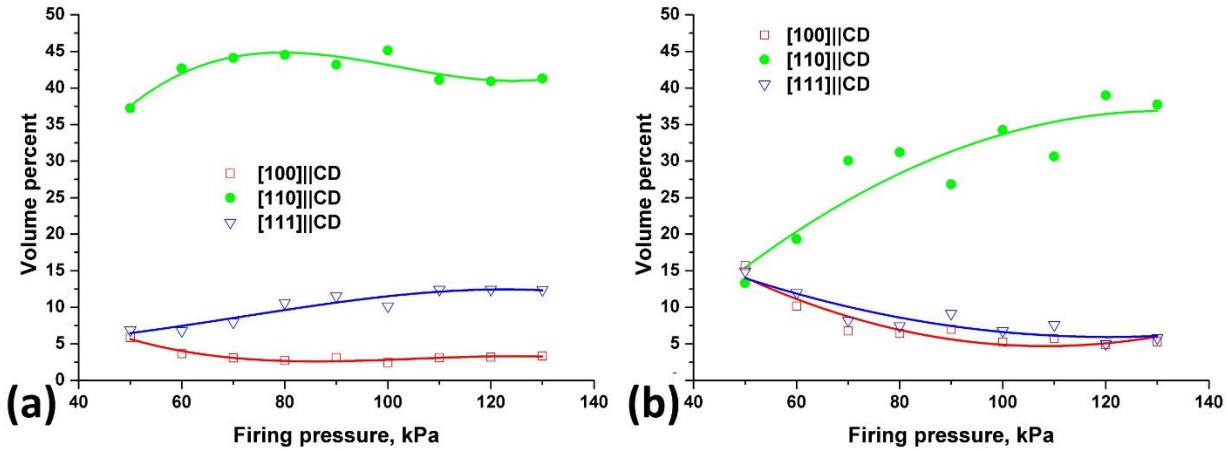


Fig. 7.8. Volume percent of selected fibre texture of the γ-austenite phase as a function of firing pressure: (a) CG and (b) UFG specimens.

7.3.2.2.2 EBSD analysis

The result of the microtexture (EBSD) analysis of the CG (Figs. 7.9-7.11) and UFG (Fig. 7.12) specimens deformed at FPs of 60 and 80 kPa are highlighted in this section.

*Coarse-grained structure*

For CG specimen deformed at 60 kPa (Fig. 7.9a-d), the band contrast map (low image quality) shows a signature of strained region while the phase map shows a significantly low area fraction of the BCC phase as also observed in Fig. 7.7a. The IPF map in Fig. 7.9c confirms [110]||CD texture as the predominant crystallographic orientation. A notable observation is the orientation interplay mainly between [110]||CD-green color and [111]||CD-blue color within an austenite grain. This indicates gradual lattice rotation and slip as the dominant plastic deformation mechanism. It is therefore suggested that the slight drop and increase in the volume percent of [110]||CD and [111]||CD textures, respectively, at higher FP (Fig. 7.8a) may be due to intense and dominant slip deformation mechanism. Dominant slip mechanism in CG specimen is also supported by the high KAM value (>1.0$^{o}$), which was recorded in the largely austenitic phase in Fig. 7.9d. High KAM value is a signature of large stored energy and plastic deformation by slip.

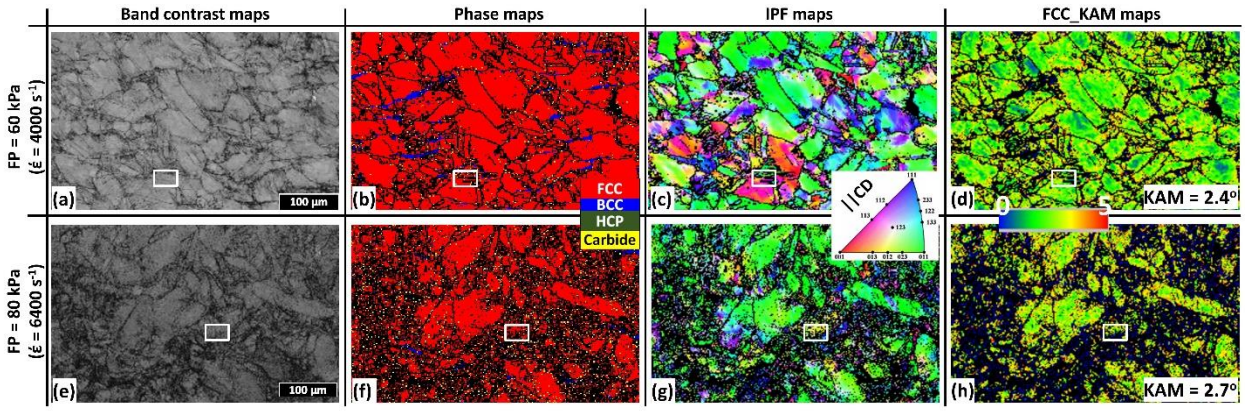


Fig. 7.9. EBSD maps of CG specimens deformed at FP of (a-d) 60 and (e-h) 80 kPa.

The high magnification and low step size scan of the marked region in Fig. 7.9a-d is presented in Fig. 7.10. BCC α′-martensite with mainly [100]||CD texture (few with spread near [111]||CD texture) were observed to nucleate at grain boundaries with higher KAM values or defects (circled region). In two separate studies [50,217], the nucleation of martensite embryo at grain boundaries that are characterized by dislocation pile-ups has been reported. Other α′-martensite nucleation sites observed in Fig. 7.10 (arrowed regions) includes dislocation bands (region of higher KAM) and {110} austenite twin plane. Localized dislocation bands and twinned austenite grains were also reported in Refs. [218] and [219], respectively, as favorable nucleation sites for martensitic transformation in steels. In Fig. 7.10a, the presence (circled region) and absence (arrowed) of HCP ε-martensite are observed, which can suggest the sequence of γ - α′ transformation (either γ → α′ or γ → ε → α′) during impact. Using the XRD, SEM and TEM techniques, Grassel et al. [220] studied the effect of aluminum (Al) and silicon (Si) contents on the martensitic phase transformation in an austenitic Mn-steel under both tensile and compressive loads. They observed the suppression of γ → ε phase transformation as the Al fraction increases. Meanwhile, the increase in the fraction of Si promotes γ → ε transformation. While overlapping stacking faults are widely accepted as the origin of the ε-phase in steels [145], parameters such as the state of stress, temperature, chemical composition, SFE, and deformation rate have been reported to influence the amount of ε and α′–martensite that form [6,19].

Although the area fraction of the HCP ε-martensite is very low (justifying the absence of ε-peak on the X-ray diffraction patterns in Fig. 7.6), their presence in the circled region in Fig. 7.10a could imply a possible FCC γ-austenite → HCP ε-martensite → BCC α′-martensite transformation path

during plastic deformation. This path has also been reported for AISI 304 austenitic stainless steel [19]. Similarly, two inferences could be drawn from the absence of ε-martensite in the arrowed

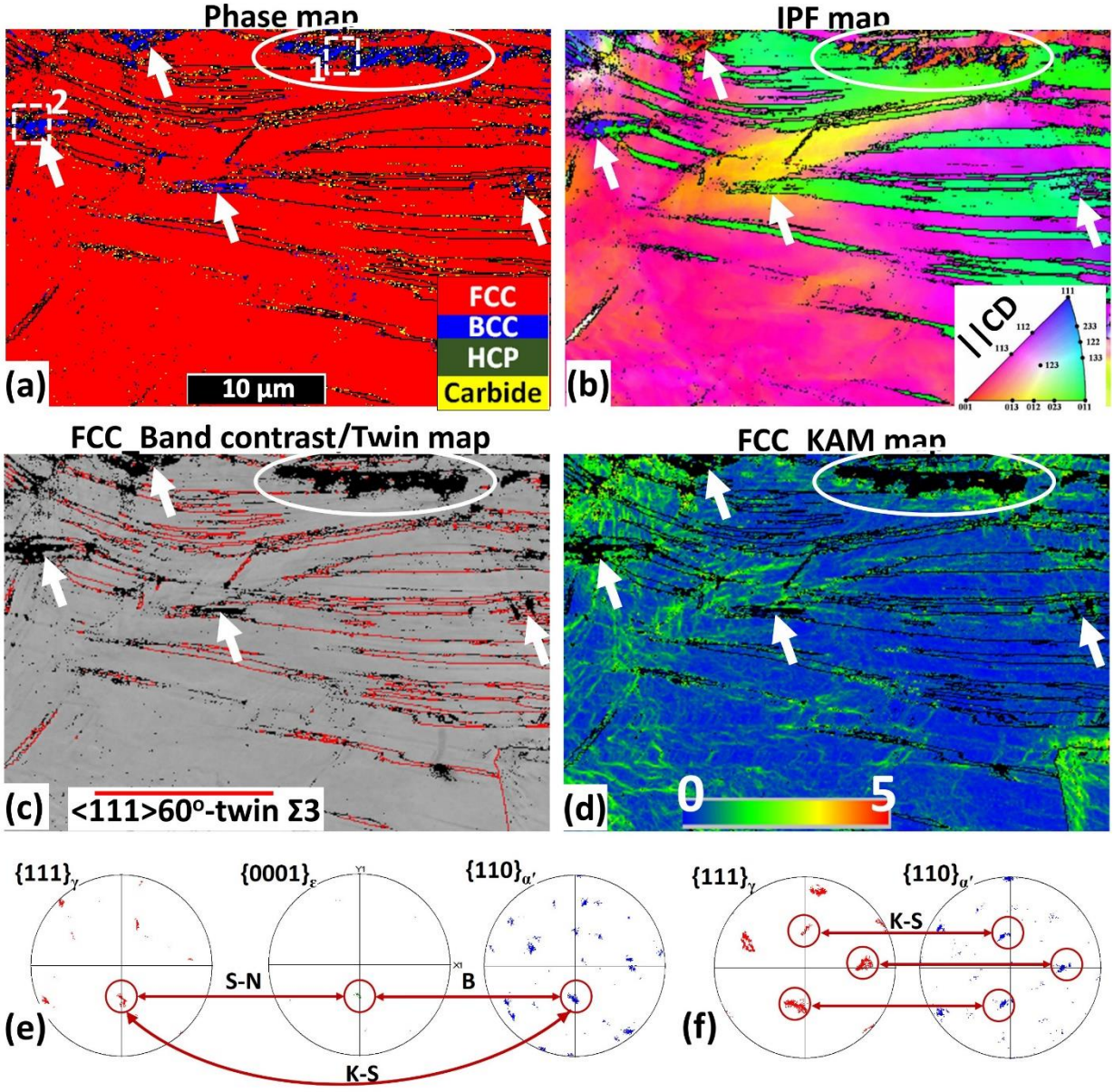


Fig. 7.10. (a-d) EBSD maps of the marked region in Fig. 7.9(a-d). (e and f) are the $\{111\}_{\gamma}$, $\{0001\}_{\varepsilon}$ and $\{110\}_{\alpha'}$ pole figures showing existing Shoji-Nishiyama, Kurdjumov-Sachs and Burgers' orientation relationships between the γ & ε, γ & α′ and ε & α′ phases, respectively, in regions (e) 1 and (f) 2 on Fig. 7.10a.

regions (Fig. 7.10a). The first could be that a $\gamma \rightarrow \varepsilon \rightarrow \alpha'$ is already completed. The second explanation could be that ε phase is completely suppressed or by-passed, thereby favoring the direct $\gamma \rightarrow \alpha'$ transformation sequence. The singular transformation path ($\gamma \rightarrow \alpha'$) has also been

reported in AISI 301L [221] austenitic stainless steels. Therefore, the co-existence of transformation paths with and without the ε-phase is possible in AISI 321 steel as also observed during the plastic deformation of austenitic Mn-steel [222] and duplex stainless steel [223]. This aformentioned observation is further confirmed by analyzing the rectangular regions 1 and 2 in Fig. 7.10a for possible orientation relationships that may exist between the γ, ε and α′ phases. The $\{111\}_{\gamma}$, $\{0001\}_{\varepsilon}$ and $\{110\}_{\alpha'}$ pole figures of region 1 (Fig. 7.10e) confirms the existence of Shoji-Nishiyama (S-N) $\{111\}_{\gamma}\|\{0001\}_{\varepsilon}$, Kurdjumov-Sachs (K-S) $\{111\}_{\gamma}\|\{110\}_{\alpha'}$ and Burgers (B) $\{0001\}_{\varepsilon}\|\{110\}_{\alpha'}$ orientation relationships between the γ & ε, γ & α′ and ε & α′ phases, respectively. The $\gamma \rightarrow \varepsilon \rightarrow \alpha'$ transformation path is therefore, a good possibility. Similarly, Fig. 7.10f confirms the feasibility of $\gamma \rightarrow \alpha'$ transformation path by the K-S orientation relationship that exists between γ and α′ phases.

Figure 7.10c also shows the development of deformation twinning; a phenomenon termed twinning-induced plasticity (TWIP) effect. Among several proposed mechanisms, the development of deformation twins is generally a process that proceeds via a dislocation mechanism [224]. Both critical dislocation density and stress concentration at grain boundaries [225] were reported to be required for initiation of deformation twin. Hence, KAM value as high as $2.4^{o}$ (Fig. 7.9d) can promote TWIP effect in AISI 321 steel. The extent of twinning in AISI 321 ASS subjected to high impact load can be explained using the expression (Eqn. 2.9) for the critical stress required for mechanical twinning. Because an increase in temperature of metal of fixed composition would increase the SFE, temperature rise due to adiabatic heating during high strain rate deformation is sufficient to increase the SFE of the deformed metal [146]. This should in-turn suppress mechanical twinning. It is therefore expected that similar to TRIP effect, TWIP effect is also suppressed by the temperature rise in the specimen during high strain rate deformation. The suppression of both twinning and martensitic transformation due to an increase in SFE of an austenitic phase has also been reported [50]. However, the comparison of Fig. 7.10a and c show more stability of TWIP effect in deformed CG specimen than the TRIP effect. A larger fraction of deformation twin reduces dislocation mean free path. This results in high strain hardening (Fig. 7.3) in CG specimens since twins are strong obstacles to dislocation glides, even in specimens deformed at higher strain rates [83].

The residual strain in the austenite matrix of the CG specimen deformed at FP of 80 kPa (Fig. 7.9e-h) is higher than those of the specimens deformed using FP of 60 kPa (Fig. 7.9a-d). This is indicated by the lower image quality in the band contrast map and increased KAM value to 2.7$^{o}$ for the specimen deformed at 80 kPa. Whereas the phase color map in Fig. 7.9f shows more suppressed martesitic phase transformation, the area fraction of [110]||CD texture increased in

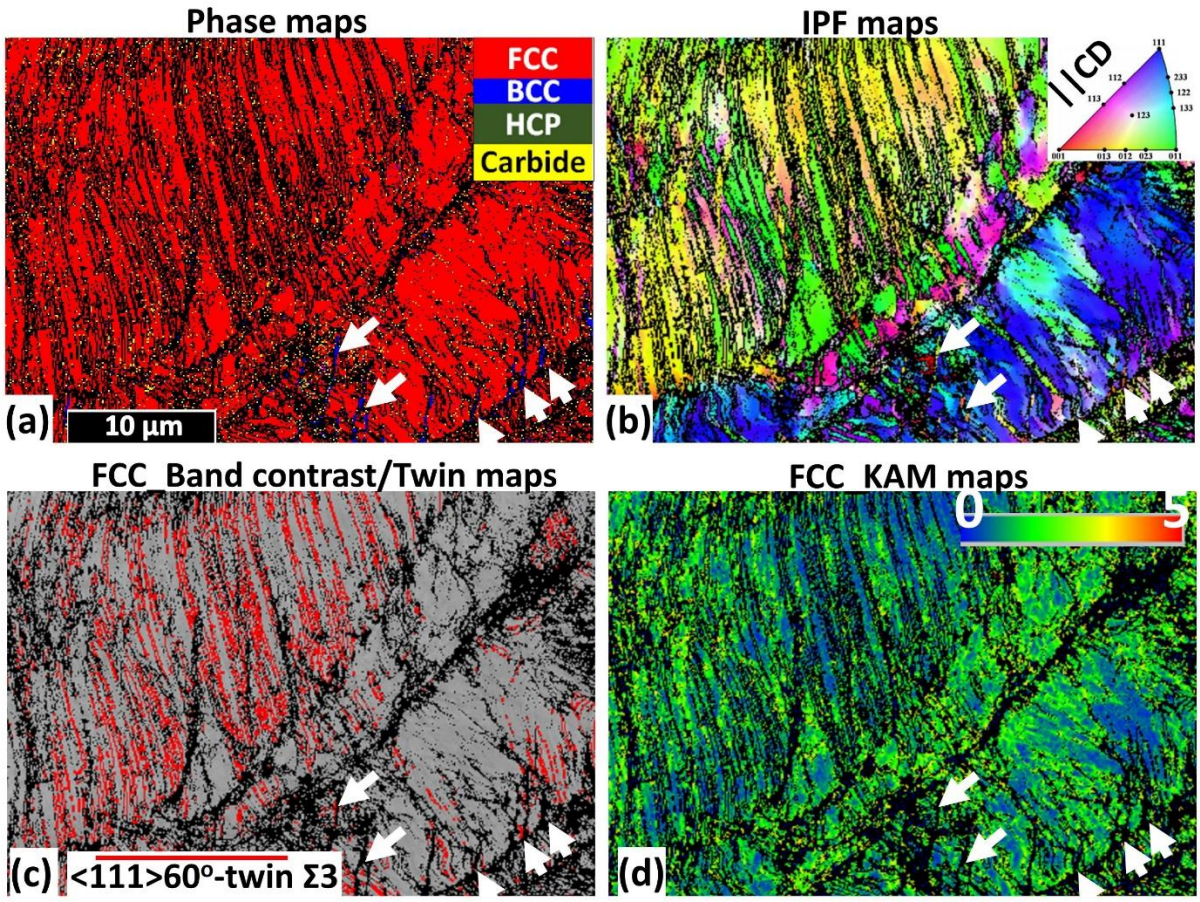


Fig. 7.11. EBSD maps of the marked region in Fig. 7.9(e-h).

agreement with the XRD texture result in Fig. 7.8a. The high magnification and low step size scan of the marked region in Fig. 7.9e-h are presented in Fig. 7.11. Very low fraction of BCC α′-martensite (arrowed) is observed to nucleate from the grain boundaries. Hence, the TRIP's contribution to strain-hardening will be significantly low. Recall, that the increase in FP from 60 to 80 kPa resulted in an increase in strain rate and an increase in temperature rise within the specimen. It is, therefore, possible that the absence of HCP ε-martensite in Fig. 7.11a translates to the rapid completion of $\gamma \rightarrow \varepsilon \rightarrow \alpha'$ or the complete suppression of ε-martensite in the transformation sequence.

On twin development, the area fraction of {110} twin plane in Fig. 7.11b and c increases (in comparison with the specimen impacted at an FP of 60 kPa) despite higher temperature rise that is expected to suppress TWIP effect. Figures 7.11c and d show that twins nucleate at the grain boundaries and twin bands are surrounded by higher KAM value; an indication that twin is an effective barrier to dislocation glide. On a grain scale, the higher KAM value suggests slip (in addition to twinning) as a dominant deformation mechanism in AISI 321 stainless steel; hence, contributing significantly to strain-hardening in CG specimens.

*Ultrafine-grained grained structure*

The very major strengthening source in UFG specimen is via the grain boundary strengthening. On exposure to an external load, dislocations in polycrystalline material move within the grain. At a certain point, the mobile dislocations are hindered by the grain boundaries. Dislocation pileups start as more dislocations propagate towards these boundaries; hence, leading to repulsive stress fields. The smaller the grain size, the lower the stress at the tip of the pile-up; therefore, requiring larger applied stress to move dislocations across grain boundaries [226]. This culminates in improved mechanical properties of the UFG specimens as can be observed in Fig. 7.2.

Kocks [227] proposed a composite model of a polycrystal on the evidence that the grain boundary region deforms differently than the grain interior. The author argued that a rule-of-mixture based on an averaging procedure as expressed in Eqn. 7.1 should be used to obtain the yield strength ($\sigma_y$) of a polycrystal.

$$\sigma_y = \sigma_I A_I + \sigma_{GB} A_{GB} \quad \ldots 7.1$$

where $\sigma_I$ and $\sigma_{GB}$ are the flow stresses of a grain interior and a hard grain boundary region of constant width, respectively, $A_I$ and $A_{GB}$ are the area fractions of grain interior and grain boundary region. This implies that as the grain size of the polycrystal decreases, the $A_{GB}$ for the constant width grain boundary region increases (as $A_I \rightarrow 0$), resulting in an increase in the yield strength of the polycrystal since $\sigma_{GB} > \sigma_I$. This further justifies the high dynamic mechanical strength recorded in UFG specimen.

On the dynamic impact response of UFG specimens, no twinning (TWIP effect) was observed in the UFG structure deformed at a firing pressure of 60 kPa. Hence, for brevity, only the phase, IPF

and KAM maps are presented in Fig. 7.12a-e. The absence of deformation twin (i.e. suppression of TWIP effect) in UFG specimen is further discussed and verified using the TEM technique in the subsequent subsection. It, therefore, suggests that the twinning stress, i.e. stress required to develop deformation twinning in UFG structure is high compared to those of the CG structure. A study on the effect of grain refinement on deformation twinning in a high Mn austenitic TWIP steel under tensile load was conducted by Ueji et al. [80]. The authors observed that the evolution of deformation twinning becomes more difficult as the grain size decreases to a certain scale. In a finite element simulation of AISI 304 ASS under uniaxial tension, twinning activation and suppression were observed in coarse and ultrafine-grained structures, respectively [81]; reduced distance between the obstacles that suppresses twin growth was attributed to twinning suppression in the UFG structure.

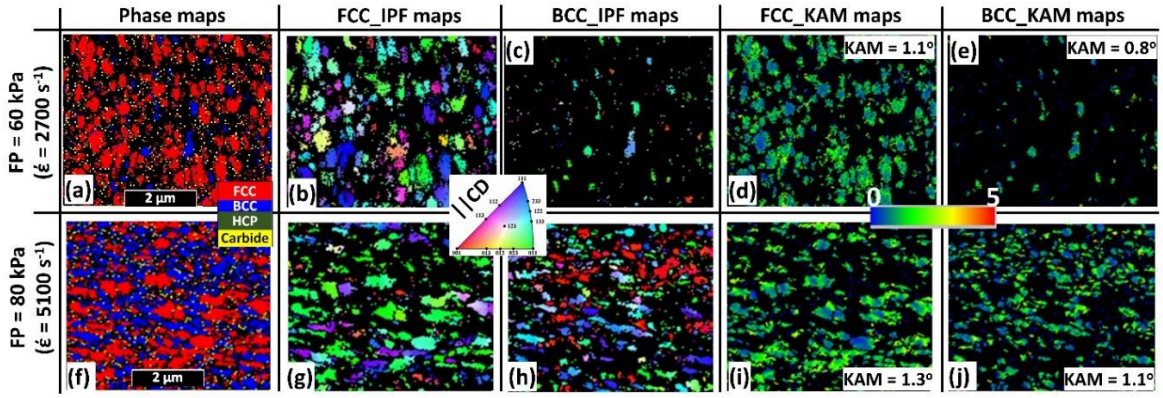


Fig. 7.12. EBSD maps of UFG specimens deformed at FP of (a-e) 60 and (f-j) 80 kPa.

However, the phase map in Fig. 7.12a shows the development of UFG strain-induced martensite (TRIP effect). A notable observation is the absence of ε-martensite in Fig. 7.12a; implying that only the FCC γ-austenite → BCC α′-martensite transformation path occurs in UFG specimen. Hence, grain size and temperature rise due to adiabatic heating (deformation mode) could also play a major role in strain-induced martensitic phase transformation path. Although the area fraction of [110]||CD texture in the deformed UFG austenite is slightly higher (Fig. 7.12b), it is not as significantly textured around [110]||CD in comparison with those observed in the deformed CG specimens (Fig. 7.9c); an agreement with the macrotexture results in Fig. 7.8. Similarly, the IPF map of the UFG strain-induced martensite (Fig. 7.12c) is of a single variant. The KAM values of the FCC (Fig. 7.12d) and BCC (Fig. 7.12e) grains are very low compared to those of CG specimen (Fig. 7.9d). This implies low dislocation density and less of slip activity in the UFG specimen.

Therefore, on the basis that deformation twins proceed via a dislocation mechanism such that both critical dislocation density and stress concentration are key requirements for its evolution, low KAM in UFG specimens justifies suppression of deformation twin.

An increase in FP to 80 kPa shows an increase in the area fractions of UFG α′-martensite, [110]||CD texture and KAM value (Fig. 7.12f-j). The UFG α′-martensite are mainly textured around [100]||CD with fairly equiaxed structure. Owing to the low slip activity due to low KAM (in comparison with that of the CG specimen in Fig. 7.9h) and absence of twinning in UFG specimen, it is expected that the other major strain-hardening source is the substantial increased fraction of UFG BCC α′-martensite (pronounced TRIP effect). Hence, the composite model in Eqn. 7.1 can be re-written to obtain Eqn. 7.2. This is to account for the stress contribution from α′-grains as in the case of AISI 321 steel that undergoes a deformation-induced martensitic transformation during plastic deformation.

$$\sigma_y = (\sigma_I A_I + \sigma_{GB} A_{GB})_\gamma + (\sigma_I A_I + \sigma_{GB} A_{GB})_{\alpha'} \quad \ldots 7.2$$

Under external load, α′-martensite can withstand a higher stress than the γ-austenite; this makes α′-martensite act as a more effective reinforcing phase than the γ-austenite phase [228]. Hence, $\sigma_I$ and $\sigma_{GB}$ of martensitic grains are higher than those of the austenite.

7.3.2.2.3. TEM analysis

This is a complimentary post-mortem analysis that verifies the results of the XRD and EBSD analyses and gives more information on the strengthening sources in the deformed specimens. The TEM bright field micrographs of the CG and UFG specimens deformed at 90 kPa are presented in Fig. 7.13. The micrographs of the CG specimen in Fig. 7.13a and b show multiple strengthening sources that justify higher strain hardening rate in CG specimens than those of the UFG specimens. Twin intersection and their effective barrier to dislocation glide are observed in Fig. 7.13a; as pile-ups of dislocations are noticeable at the intersection of the twins and around them. A plausible source of strengthening during high strain rate deformation is from the TiC-dislocation interaction. The inset in Fig. 7.13a shows an in-grain nano-sized TiC precipitate acting as a barrier to an on-coming dislocation forest. Elsewhere [149], intragranular TiCs have been reported to contribute to the strain hardening capability of AISI 321 ASS by serving as effective barriers to dislocation motion [149]. Other strengthening sources in the CG specimen could be from dislocation-

dislocation interaction and dislocation multiplication during slip activity. This is confirmed by the presence of high dislocation-forming networks observed in Fig. 7.13a. Fig. 7.13b shows a dense dislocation pile-up at the grain boundary and nucleation of nano-twin around it. This validates the earlier observation (by EBSD technique) on the nucleation of twins at the grain boundary of high KAM value in Fig. 7.11.

The absence of deformation twin was confirmed in the TEM micrographs of the UFG grain specimen (Fig. 7.11c). Only the martensitic phase (TRIP effect) with moderate dislocation density was noticeable under TEM; an agreement with the EBSD results in Fig. 7.12. Hence, the higher strain hardening rate in CG specimens than those of UFG specimens in Figs. 7.2 and 7.3 are because of the combined contribution of TWIP effect (twinning, twin intersection and their interaction with dislocations), slip (dislocation multiplication and dislocation-dislocation interactions) and carbide precipitation (carbide interaction with dislocation) in CG specimen. Although grain boundary strengthening and TRIP effect contribute to strengthening, their contribution to strain-hardening is minimal in CG specimens but more effective in UFG specimens.

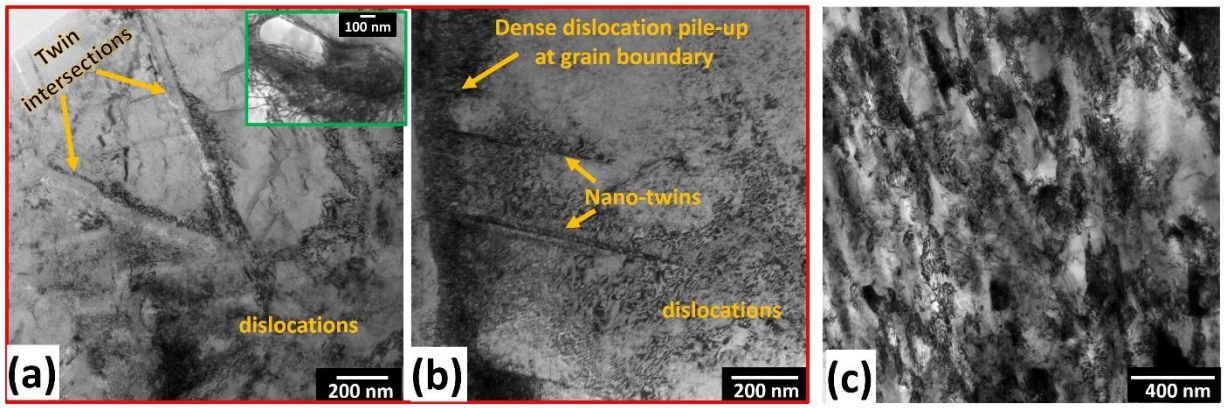


Fig. 7.13. TEM bright field micrographs of (a and b) CG and (c) UFG specimens deformed at 90 kPa. Inset in (a) is dense dislocation pile-up around a TiC particle.

7.3.2.3 EBSD investigation of the ASB region

It will be recalled from section 7.3.2.1 (OM analysis) that at higher FP/strain rate, CG specimen is only susceptible to the formation of MTSB while UFG specimen is susceptible to both MTSB and TSB bifurcation. This section, therefore, reports the possible mechanism of microstructural evolution inside the ASB (Figs. 7.14 a-d and 7.15). Furthermore, the mechanism of MTSB (Fig.

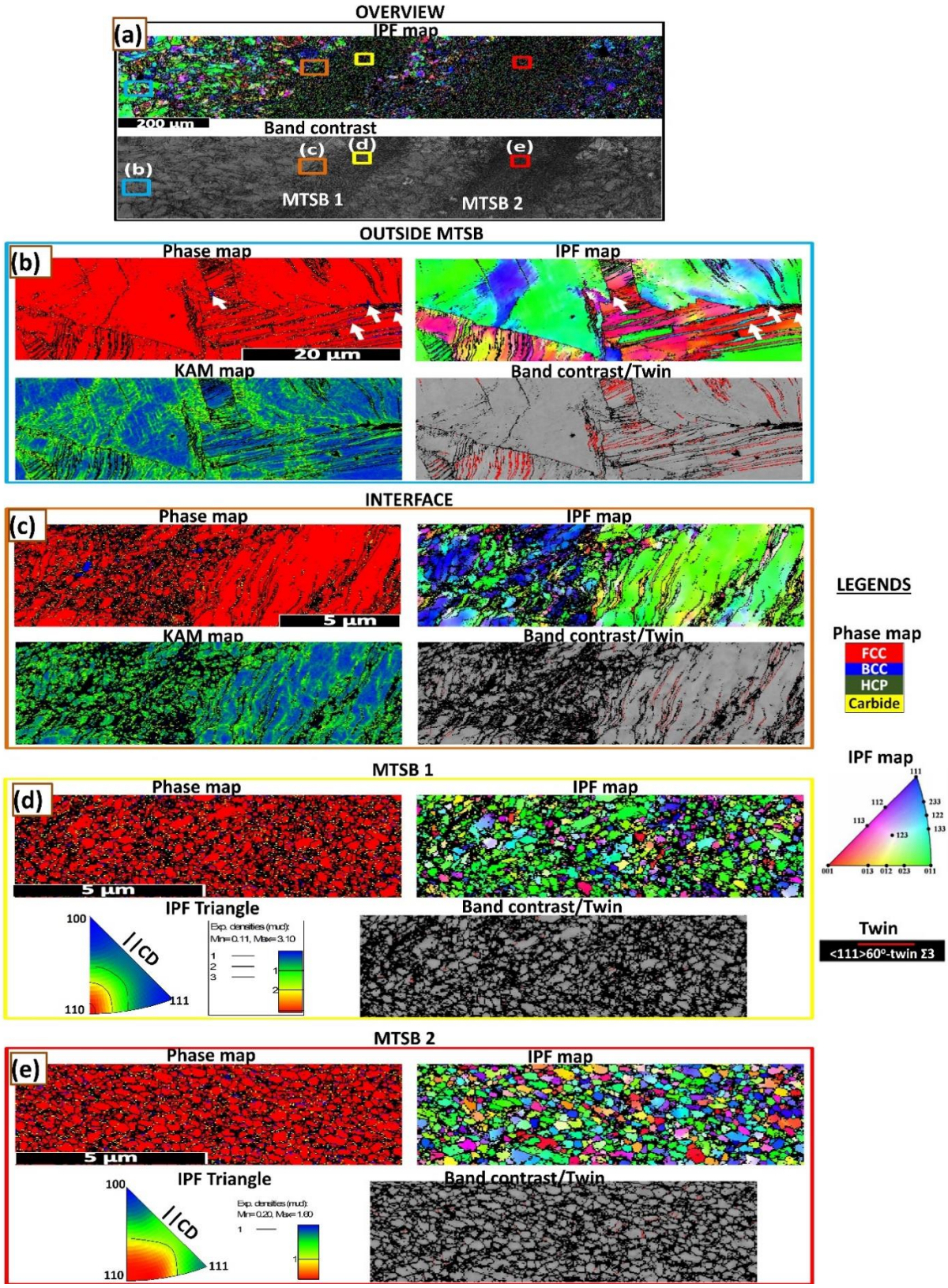


Fig. 7.14**.** EBSD maps showing the development of multiple transformed shear band (MTSB) in CG specimen deformed at a FP of 110 kPa.

7.14) and bifurcated TSB (Figs. 7.16 and 7.17) formation are discussed. For brevity, and on the assumption that the mechanism of MTSB formation is the same in AISI 321 irrespective of grain size, only the characterization of the MTSB in CG specimen is discussed.

#### 7.3.2.3.1 Dynamic recrystallization mechanism and temperature rise inside TSB

The IPF map in Fig 14a shows inhomogeneous texture distribution across the compression plane; the dominant crystallographic orientation of the austenite grains changes from the [110]||CD fibre at the specimen centre to [111]||CD fibre towards the edge of the cylindrical specimen). Meanwhile, the band contrast map (Fig. 7.14a) shows shear strain localized regions of lower image quality. In agreement with earlier observation in Figs. 7.9-7.11, Fig. 7.14b, confirm a very low fraction of α′-martensite nucleated at the high dislocation density grain boundary (indicated by white arrows in the phase map), and pronounced slip (IPF and KAM maps) and twinning (BC/twin map) mechanisms in the region outside the transformed shear band. On approaching the MTSB 1, a clear mixture of ultrafine grains and lamellar grains (with twin boundaries) that are elongated along the shear direction are observed in the interface region (Fig. 7.14c). The microstructural feature in this region gives vital information on the mechanism of ASB formation. The equiaxed grains with near weak texture are thought to have their origin closely associated with the nearly [110]||CD oriented lamellar grains in the IPF map of Fig. 7.14c. This is confirmed in the KAM map by the presence of higher KAM network (dislocation cells) within the lamellar grains.

With an increase in deformation, the lamellar grain breaks up to minimize interfacial energy leading to the development of equiaxed subgrains. The coexistence of some near weak-textured ultrafine grains and subgrains within lamellar boundaries in Fig. 7.14c suggests that the interface between the inside and outside ASB region underwent dynamic recovery [109]. Ahead of the dynamic recovery front (interface) is the presence of UFG grain structure within the TSB (Fig. 7.14d). A comparison of the IPF maps in Fig. 7.14 c (interface) and d (MTSB 1) shows a stronger texture of [110]||CD oriented UFG grains in the MTSB 1 than the interface. This suggests a further rotation of the ultrafine subgrain to accommodate further imposed strain leading to the development of ultrafine grain (~0.17 μm in size) in the TSB region. This mechanism of ultrafine grain development in the TSB region in this study is in agreement with the rotational dynamic recrystallization (RDRX) mechanism proposed by Nesterenko *et al.* [112]. RDRX mechanism occurs concurrently during plastic deformation, and it is one of the most accepted mechanisms to

explain ultrafine grain structure inside TSB. The other mechanism, migrational dynamic recrystallization (MDRX), as classified by Derby [111], cannot explain the ultrafine grain structure observed in ASB. This is because MDRX is governed by diffusion and recrystallized grains develop by nucleation and growth. The time for ASB formation (Table 7.1) is too short for the required diffusion process to occur. It is expected that the proposed RDRX mechanism for the development of UFG structure in CG specimen (Fig 7.14) holds for those developed in UFG specimens, although some stages of the mechanism may be hastened or retarded due to the size of the grain.

According to the RDRX mechanism, fragmented subgrains as observed in Fig. 7.14c should make about ~30$^o$ rotation to form the final recrystallized grains in Fig. 7.14d. The required time, *t*, for the rotation process can be estimated using [107]:

$$t = \frac{L_1 kT f(\theta)}{4\delta\eta D_{ob}\exp(-Q_b/RT)} \qquad \ldots 7.3$$

where $L_1$ is the average size of the fragmented subgrains; $\delta$ is the grain boundary thickness; $\eta$ is the grain boundary energy; $D_{ob}$ is a constant related to grain boundary diffusion, $Q_b$ represents the activation energy of the grain boundary diffusion. $\theta$ is the degree of grain rotation and $f(\theta)$ is expressed as:

$$f(\theta) = \frac{3tan(\theta)-2\cos(\theta)}{3-6\sin(\theta)} - \frac{4\sqrt{3}}{9} ln \frac{2+\sqrt{3}}{2-\sqrt{3}} + \frac{4\sqrt{3}}{9} ln \frac{\tan(\theta/2)-2-\sqrt{3}}{tan(\theta/2)-2+\sqrt{3}} + \frac{2}{3} \qquad \ldots 7.4$$

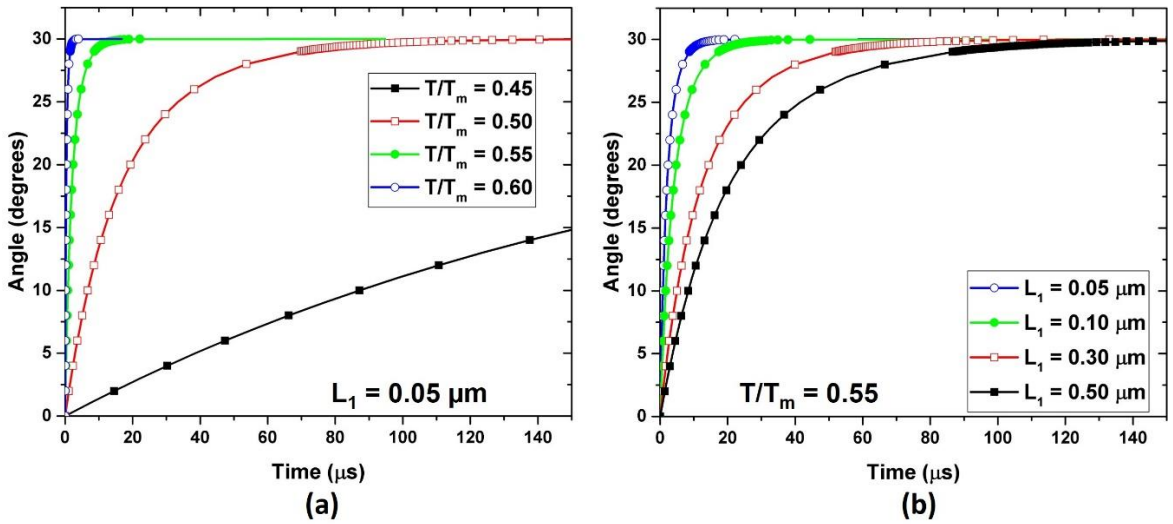


Fig. 7.15. Angle of rotation of subgrain boundaries as a function of time for: (a) different temperatures for $L_1$ = 0.05 μm `and (b) different grains size at 0.55$T_m$.

For AISI 304 stainless steel, $k$ = 1.38 x$10^{-23}$ $JK^{-1}$, $\delta$ = 0.5 nm, $\eta$ = 0.625 $Jm^{-2}$, $\delta D_{ob}$ = $2.0\times10^{-13}$ $m^3s^{-1}$, $Q_b$ = 167 $KJmol^{-1}$ and $R$ = 8.314 $J(K.mol)^{-1}$ [229]. AISI 321 is a derivative of AISI 304 and hence, these values are acceptable parameters that can be used in this study. With ~1673 K as the melting temperature ($T_m$) of AISI 321 stainless steel, the kinetic curve that predicts the RDRX mechanism within the ASB are constructed using Eqns. 7.3 and 7.4, and presented in Fig.15. The homologous temperature ($T/T_m$) within the ASB was varied from 0.45 to 0.60 at a fixed subgrain size of 0.05 μm in Fig. 7.15a. Similarly, the subgrain size was varied from 0.05 to 0.5 μm at a fixed $T/T_m$ of 0.55 (Fig. 7.15b). At both instances, the rate of rotation decreases with the increasing angle and asymptotically approaches 30° as $t\rightarrow\infty$. The deformation time as presented in Table 7.1 is ~145 μs at the higher firing pressures (FP), where ASBs are formed. Therefore, the calculations accurately predict the rotation of the subgrain boundaries (within the deformation time of 145 μs) at a temperature of $0.5T_m$ and above, for subgrain size of 0.05 μm (Fig. 7.15a). From Fig. 7.15b, it can be concluded that subgrain sizes in the range 0.05 to 0.5 μm can form via RDRX mechanisms at $T/T_m$ of 0.55. Hence, the higher the temperature inside ASB and the smaller the subgrain size, the lower the time required for subgrain rotation.

If an adiabatic condition is assumed, the temperature inside the ASB of the investigated steel can be estimated by the integration of Eqn. 7.5 and substituting the Zerilli-Armstrong constitutive equation (Eqn. 7.6) for $\sigma$:

$$dT = \left(\frac{\beta}{\rho \cdot C_v}\right)\sigma d\varepsilon \qquad \ldots 7.5$$

where $T$ and $\sigma$ are the temperature and flow stress, $\beta$ (0.9 assumed) is the fraction of plastic work that is converted into heat and it is referred to as the Taylor-Quinney parameter, $C_v$ and ρ are the specific heat capacity (475 J/kg-$^oC$) and density (7920 $kg/m^3$) of AISI 321 stainless steel.

$$\sigma = C_o + K_1 d^{-1/2} + C_2 \varepsilon^{C_n} \exp(-C_3 T + C_4 T ln\dot{\varepsilon}) \qquad \ldots 7.6$$

where $C_o$, $C_2$, $C_3$, $C_4$, $C_n$ *and* $K_1$ are -76.9 MPa, 2340 MPa, 0.0016 $K^{-1}$, 0.00008 $K^{-1}$, 0.36 and 0.75 $MNm^{1/2}$ [107]. The result (Table 7.1) shows that temperature inside the ASB is higher in UFG specimens than those of the CG specimens; hence, promoting the earlier formation of ASB in the former as observed in Figs. 7.4 and 7.5.

Whether thermal softening or DRX-induced softening is the potential trigger for the ASB initiation has remained a subject of debate amount different researchers. Meanwhile, both thermal softening and DRX are expected to play a role in ASB initiation. On their respective role, Longere [230] observed that ASB initiation is controlled by thermal softening when the onset of DRX is late. Alternatively, DRX softening mainly control ASB initiation when the onset of DRX is early. Based on the experimental findings in the current study, it can be safely proposed that thermal softening (and not DRX softening) played a major role in the initiation of ASB in AISI 321 stainless steel. This is because the temperature rise that results in thermal softening increases with FP/strain rate and no DRX was observed at lower FP/strain rate (Figs. 7.9-7.13). DRX was only observed at a higher FP/strain rate.

#### 7.3.2.3.2 Multiple and Bifurcated adiabatic shear band

Only the formation of MTSB and TSB bifurcation in specimen deformed using an explosive testing technique has been extensively studied so far. This technique uses thick-walled hollw cylindrical specimens rather than the solid cylindrical specimens conventionally used in the SHPB technique [112]. The explosive testing induces multiple and bifurcated shear bands in the thick-walled cylinder specimens in which features of self-organization and spacing of bands were of major interest as investigated in AISI 304L stainless steel [231] and other alloys [232-236]. In the current study, multiple and bifurcated adiabatic shear bands developed in solid cylindrical specimens that were rapidly deformed using the SHPB system.

The EBSD maps showing the overview of the developed MTSB in CG specimen are presented in Fig. 7.14a. The maps with higher magnifications and lower step size scan of the first TSB, MTSB 1 (closer to specimen interior), and the second, MTSB 2 (closer to specimen edge) are presented in Fig. 7.14d and e, respectively. The spacing between these bands is ~200 μm and ~100 μm in CG (Figs. 7.4d and 7.14a) and UFG (Fig. 7.5h) specimens, respectively. This confirms the role of grain size on ASB spacing, which has been earlier reported to decrease with increasing strain rate [237]. The mechanism of formation of MTSB is not completely clear; although different mechanical and physical properties of materials could result in different adiabatic shearing energy barrier (i.e. energy required to nucleate and propagate of ASB) that promotes multiple ASBs [236]. Liu et al. [238] experimentally and numerically determined the response of Ti-6Al-4V alloy to impact from a 12.7-mm armor-piercing projectile. They observed that the periodic loading–

unloading cycle of hydrostatic pressure of the target elements leads to the formation of multiple periodic ASBs. During multiple bands formation, Zhou et al. [237] also suggest that bands adjust their spacing for the fastest localization that results in the least energy dissipation.

It is very important to know which TSB in Fig. 7.14a formed first. This may clarify the direction of the "loading–unloading cycle" that leads to the formation of MTSB. For instance, if MTSB 1 is first formed, it implies the direction of loading–unloading cycle is to the right of Fig. 7.14a (towards specimen edge), and vice-versa if MTSB 2 formed first. The quantitative summary of the salient microstructural characteristics (estimated from larger EBSD scan area than those presented) of the MTSB 1 and 2 are shown in Table 7.2. Although the size of DRXed UFG in MTSB 1 (~0.17 μm) is smaller than that in MTSB 2 (~0.21 μm), both MTSBs show the absence of twinning as observed in the band contrast/twin maps in Fig. 7.14d and e. The IPF maps and triangles show that the DRXed UFG are more textured around [110]||CD in MTSB 1 (Fig. 7.14d) than MTSB 2 (Fig. 7.14e), suggesting that more DRXed UFGs in the later rotated than in the former. The IPF maps also indicate that DRXed UFGs in MTSB 2 have well-defined high angle grain boundaries (i.e. complete RDRX) while those of MTSB 1 are signature of the penultimate stage (subgrain structure with not well-defined boundaries) of the RDRX phenomenon described in section 7.3.2.3.1. Although the LAM values of both MTSBs (Table 7.1) are characteristics of DRXed grains, MTSB 1 in addition to the lower recrystallized fraction of UFG grains, has higher LAM value than that of MTSB 2. On the strength of these observations, it can be concluded that MTSB 2 first developed since it possesses features of DRXed UFGs that underwent a complete rotational dynamic recrystallization. Hence, the direction of "loading–unloading cycle" is to the left of Fig. 7.14a (towards specimen centre).

The EBSD maps showing the overview of the developed bifurcated TSB in UFG specimen are shown in Fig. 7.16a. Figure 7.16b shows high area fraction of mainly [100]||CD-oriented α′-martensite outside the TSB, which is in agreement with the volume fraction estimated using Feritscope (Fig. 7.7b). The 'mother' TSB was observed to split at a bifurcation point into two 'child' bands (Child 1 and 2). Higher magnification and lower step size scan of these regions are presented in Fig. 7.16c-f, respectively. From the mother band to the bifurcation point and subsequently to the two-child bands, there is no specific pattern in the microstructural characteristics other than a slightly larger grain size in child 2 TSB (0.15 μm) than other regions

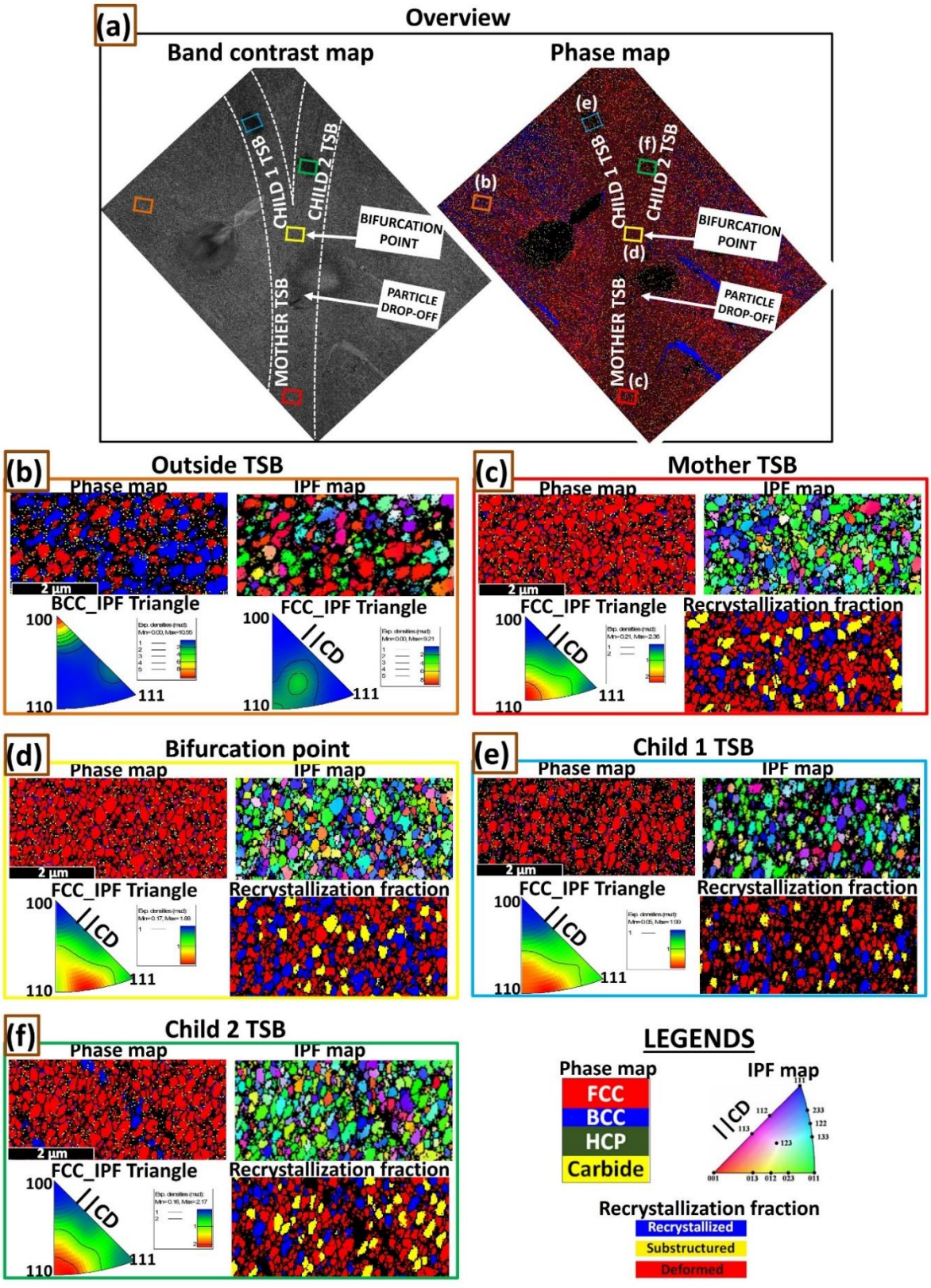


Fig. 7.16. EBSD maps showing bifurcation of transformed shear band in UFG specimen deformed at a FP of 110 kPa.

Table 7.2. Quantitative summary of the salient microstructural characteristics in MTSBs 1 and 2 formed in CG specimen (Fig. 7.14).

| FP, kPa | MTSB | Grain size in TSB, μm | Recrystallization (%) | | | LAM ,° | FCC_Area percent of | | | Grain size ratio ($G_r$) |
|---|---|---|---|---|---|---|---|---|---|---|
| | | | Recryst allized | Substru ctured | Defor med | | [100]\|\| CD | [110]\|\| CD | [111]\|\| CD | |
| 110 | **1** | **0.17** | **9.9** | **6.5** | **83.6** | **1.08** | **2.2** | **31.8** | **4.69** | **0.005** |
| | 2 | 0.21 | 22.4 | 16.6 | 61.0 | 0.85 | 4.3 | 31.7 | 12.4 | 0.006 |

Table 7.3. Quantitative summary of the salient microstructural characteristics in bifurcated TSB formed in UFG specimen (Fig. 7.16).

| FP, kPa | Bifurcate d TSB | Grain size in TSB, μm | Recrystallization (%) | | | LAM ,° | FCC_Area percent of | | | Grain size ratio ($G_r$) |
|---|---|---|---|---|---|---|---|---|---|---|
| | | | Recryst allized | Substru ctured | Defor med | | [100]\|\| CD | [110]\|\| CD | [111]\|\| CD | |
| 110 | **Mother** | **0.14** | **26.2** | **13.2** | **60.6** | **0.80** | **3.3** | **33.5** | **12.8** | **0.583** |
| | Bif. point | 0.14 | 31.0 | 13.0 | 56.0 | 0.79 | 3.8 | 31.1 | 15.4 | 0.583 |
| | **Child 1** | **0.14** | **17.7** | **13.6** | **68.7** | **0.89** | **1.1** | **20.8** | **9.0** | **0.583** |
| | Child 2 | 0.15 | 25.9 | 16.5 | 57.6 | 0.80 | 3.5 | 34.9 | 10.8 | 0.625 |

(0.14 μm) as summarized in Table 7.3. This implies that the UFG specimens are further refined inside the TSB by rotational dynamic recrystallization described in section 7.3.2.3.1. Although ASB developed earlier in impacted UFG specimens than in CG specimens, the extent of grain refinement in the TSB of the UFG specimens is lower largely due to the spatial restriction effect (very small size of grains), i.e., the size of grains in the UFG specimen did not permit enough accumulation of random, but yet homogeneously distributed dislocations. Hence, subsequent re-arrangement to elongated dislocation cells that produce the subgrains are minimized. This is further validated by observing the higher grain size ratio ($G_r$) in UFG specimens (Table 7.3) than in CG specimens (Table 7.2). Grain size ratio ($G_r$) is defined by;

$$G_r = \frac{G_{asb}}{G_i} \quad \ldots 7.7$$

where $G_{asb}$ and $G_i$ are grain sizes inside the adiabatic shear band and in the initial microstructure before impact, respectively. The lower the $G_r$, the more the occurrence of an extensive grain refinement within the ASB and vice-versa.

The mechanism of the TSB bifurcation in UFG specimens is not well understood. However, bifurcation of TSB is reported to be geometrically necessary during the explosive testing of thick-walled cylindrical Ti alloy specimen [232]. This geometrically-necessary bifurcation was attributed to the spiral trajectory of the band and the need to keep similar band spacing. On the damage and failure mechanism of aluminum alloy (thick-walled cylindrical specimen) subjected

to radial collapse, Yang et al. [239] report that barriers such as precipitates, impurity and other defects could resist the propagation of a band along its original direction. Consequently, the band is forced to part along the region of maximum shear stress with low resistance and a new band is

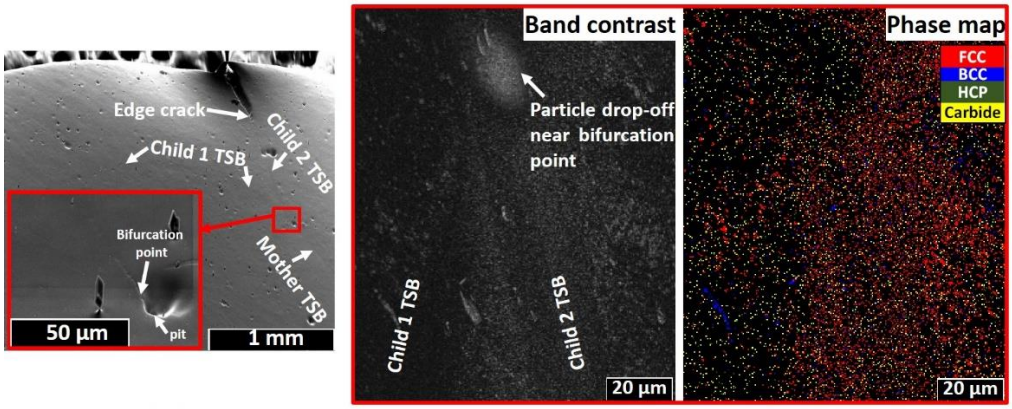


Fig. 7.17. (a) SEM micrograph showing edge crack-child 2 TSB link and particle drop-off region, (b) EBSD band contrast maps showing bifurcation of transformed shear band at another region other than the region presented in Fig. 7.16.

formed. The previously provided reasons for bifurcation in Refs. [232] (geometrically necessary) and [239] (barrier-providing precipitates) could play major roles in the bifurcation of TSB in this study. The SEM micrograph showing an edge crack-child 2 TSB link is suggestive of a geometrically necessary bifurcated TSB. It is possible that at this imposed firing pressure, the specimen has exceeded the maximum allowable strain at which no crack initiates. In accommodating further imposed strain, the formation of child 2 TSB is necessitated in advance along which edge crack can nucleate and propagate. On the other hand, cavities suggesting plausible TiN particle drop-off point (that may occur during electrolytic polishing) are observed near bifurcation points in Fig. 7.16a and inset in Fig. 7.17a, which may support the idea relating to the role of barriers on bifurcation. The low-magnification EBSD scan of another bifurcation region was taken to validate this observation; again, suspected particle drop-off point can be observed as shown in Fig. 7.17b.

## 7.4. Conclusion

A comparative study on the deformation behavior of coarse (37 µm) and ultrafine-grained (0.24 µm) AISI 321 stainless steel under dynamic impact load was conducted using a SHPB system. XRD, OM, SEM, EBSD and TEM characterization techniques were used for microstructural

analyses of the alloy before and after deformation under impact load. The following conclusions are drawn from this study:

1. An increase in firing pressure of the projectile results in a corresponding increase in impact momentum, strain rate, final deformation strain, and maximum flow stress of the specimens.
2. Although ultrafine-grained (UFG) specimens show higher compressive strength than the coarse-grained (CG) specimens, CG specimens possess higher strain hardenability than the UFG specimens at the same firing pressure.
3. Multiple strengthening sources such as the development of strain-induced martensite (little contribution), twin/twin intersection-dislocation, TiC-dislocation, dislocation-dislocation and dislocation-grain boundary interactions contributed to higher strain hardening rate in CG specimens. Meanwhile, only strain-induced martensite and grain boundary strengthening contributed to hardening of the UFG specimens under impact load.
4. Slip and twinning are the active deformation mechanisms in CG specimens and they are highly suppressed in UFG specimens due to spatial restriction effect. While the TRIP effect was suppressed and TWIP effect occurs readily in CG specimens, the reverse was observed to be the case for the UFG specimens.
5. The co-existence of martensitic phase transformation paths with and without an intermediate phase (HCP ε-martensite) during plastic deformation is confirmed in AISI 321 stee. The temperature rise in specimen and grain size influences the transformation path.
6. The stable end-orientation of the austenite phase in compression is [110]||CD texture while that of the martensitic phase is [100]||CD with spread towards [111]||CD texture.
7. UFG specimens exhibit lower critical strain and strain rate at which localized shear strain regions develop. They are therefore more susceptible to ASB formation than CG specimens.
8. While multiple TSB (MTSB) developed in the CG specimen, both the MTSB and TSB bifurcation develop in the UFG specimens. Although the mechanism behind the formation of MTSB is not completely clear, bifurcation of TSB was geometrically necessary, and the presence of precipitate at the bifurcation point could play a major role.

9. EBSD analysis of inside, interface and outside the TSB revealed the development of equiaxed ultra-fine grain structure (~0.17 μm in CG and ~0.14 μm in UFG specimens) inside the TSB by rotational dynamic recrystallization mechanism.

# Chapter 8

## Effects of Grain Refinement on the Quasi-Static Compressive Behavior of AISI 321 Austenitic Stainless Steel: EBSD, TEM, and XRD Studies

The results discussed in Chapter 7 made it necessary to study AISI 321 steel's behaviour under low strain rate condition, more so that the findings in Chapter 7 cannot be generalized for all strain rate regimes. In Chapter 8, the results of investigations on the effects of grain refinement on the behavior of AISI 321 steel when compressed at low strain rate regime are presented and discussed. The co-existence of both FCC $\gamma \rightarrow$ BCC $\alpha'$ and FCC $\gamma \rightarrow$ HCP $\varepsilon \rightarrow$ BCC $\alpha'$ transformation paths in AISI 321 steel, which is a subject of debate in the literature is confirmed**.** Visco-plastic self-consistent (VPSC) modeling was employed to validate the experimental results. This manuscript is published in "*International Journal of Plasticity"* as follows:

A. A. Tiamiyu, V. Tari, J. A. Szpunar, A. G. Odeshi, and A. K. Khan, "Effects of grain refinement on the quasi-static compressive behavior of AISI 321 austenitic stainless steel: EBSD, TEM, and XRD studies," *International Journal of Plasticity*, vol. 107, pp. 79–99, 2018.

My contributions to this paper are as follows: I reviewed the relevant literature, designed and conducted the experiments, analyzed test results and prepared the manuscript, which was reviewed by my supervisors (Prof. Akindele Odeshi and Prof. Jerzy Szpunar) before submitting it to the International Journal of Plasticity for publication. This chapter contains a modified version of the published paper. General information such as detailed experimental procedure has been moved to Chapter 3. The copyright permission to use the manuscript in this thesis was obtained form the publishers and it is provided in APPENDIX C.

### Abstract

The effects of grain refinement on the quasi-static compressive behavior of AISI 321 austenitic stainless steel (ASS) were studied. The effect of strain on the final microstructure after compressive deformation was also investigated. The compression tests on steel specimens were conducted at a strain rate of $4.2 \times 10^{-3}$ $s^{-1}$. Ultrafine-grained (UFG) specimen with the grain size of 0.24 μm exhibits an excellent combination of high yield strength (~1 GPa) and good strain hardenability. Meanwhile, the coarse-grained (CG) specimen with the grain size of 37 μm exhibits

yield strength of ~0.2 GPa. At 0.53 true strain, UFG and CG specimens exhibit compressive strengths of 5.95 and 4.80 GPa, respectively. The Hall-Petch relation constants, $\sigma_o$, and *K*, for the AISI 321 ASS were estimated to be 128 MPa and 478 MPa $\mu m^{-0.5}$, respectively. The strain hardening process in both UFG and CG specimens occured in three distinctive stages. The CG specimens exhibit a higher strain-hardening rate than the UFG specimens up to a critical true strain of 0.4, above which strain-hardening rate in UFG becomes greater. X-ray diffraction (XRD), electron backscatter diffraction (EBSD) and transmission electron microscope (TEM) techniques were used for microstructural analyses to understand the underlying mechanisms behind the strain hardening behavior of the alloy under quasi-static compressive load. Texture evolution during deformation, orientation relationship between phases and the sequence of martensitic phase transformation were also studied and are discussed in this paper. Visco-plastic self-consistent (VPSC) modeling was employed to determine the role of various deformation mechanisms in the macroscopic stress-strain response, and also in texture evolution during uniaxial compression loading.

**Keywords:** *AISI 321 austenitic stainless steel; C. Electron microscopy; A. Twinning; A. Phase transformation; A. strengthening mechanisms; VPSC*

## 8.1 Introduction

Conventional coarse-grained (CG) austenitic stainless steels are characterized by relatively low yield strength. This is a challenge in high load-bearing applications, where their excellent corrosion resistance is desired. To overcome this challenge, the alloy is commonly strengthened via grain refinement. Grain refinement of metallic alloys has been a subject of widespread research in recent years [240,241]. Amongst different strengthening mechanisms, only strengthening by grain refinement simultaneously improves the strength and toughness of a polycrystalline material. Hence, ultra-fine-grained (UFG) austenitic stainless steels (ASS) exhibit the good potential of replacing the conventional coarse-grained alloys for structural applications that require high mechanical strength and good toughness. ASS has a face-centered cubic (FCC) crystal structure, and it possesses low stacking fault energy (SFE) [19][20]. Partial transformation of the thermodynamically-metastable austenitic phase to a martensitic phase (strain-induced martensite) can occur in ASS during deformation [30]. The resulting martensite is harder than the prior austenite phase, resulting in a composite strengthening and a high strain hardening capability. This

is the phenomenon that promotes an excellent combination of high strength and ductility during deformation of ASS [218]. This phenomenon is called Transformation-Induced Plasticity (TRIP). The kinetics of evolution of martensitic phase and other phenomena such as twinning and slip during plastic deformation may differ for both CG and UFG structures due to the spatial restriction effect in the UFG materials [37].

In a study on the relationship between grain size, martensitic phase transformation and ductility of ultralow-carbon austenitic steel during deformation under tensile loading, Yoo et al. [172] observed that the UFG specimens exhibit a slower (in comparison with the CG specimen) martensitic transformation kinetics due to higher critical stored energy required for martensitic formation. In another study [37], it was reported that the mechanical stability of austenite in a Fe-Ni-Cr alloy with a wide range of grain sizes (1 - 80 μm) and subjected to a quasi-static tensile loading at $5.6 \times 10^{-4}$ $s^{-1}$ is independent of grain size. Shen et al. [81] reported UFG AISI 304 ASS with an average grain size of ~270 nm to exhibit high yield and tensile strength of 1890 ± 50 MPa and 2050 ± 30 MPa, respectively. The high strength was reported to originate mainly from grain boundary strengthening effect. The authors concluded that the volume fraction of twins and martensite phase increases with an increase in grain size.

A comprehensive understanding of the deformation behavior of UFG steels under different loading conditions is very important, more so that the few available publications focus on their behavior under tensile load. In this study, an ultrafine-grain structure was developed in the as-received coarse-grain AISI 321 ASS using thermo-mechanical processing. The process involved cryogenic rolling, followed by annealing at an appropriate temperature and time. This study, therefore, focuses on the effects of grain refinement on the quasi-static compressive behavior of AISI 321 austenitic stainless steel. X-ray diffraction (XRD), electron backscatter diffraction (EBSD) and transmission electron microscope (TEM) techniques were used to investigate the microstructure and texture of the alloy deformed to different strain values. Results of the XRD and microscopic analyses will provide information on the mechanism of deformation in the alloy under quasi-static compressive loading conditions. The sequence of phase transformation during the deformation of stainless steel remains a subject of debate among various researchers. While some authors [6] reported FCC γ-austenite → BCC α′-martensite transformation sequence, others [19] reported FCC γ-austenite → HCP ε-martensite → BCC α′-martensite transformation sequence. The formation of

these phases depends on several conditions that are material- and/or test condition-dependent. The effects of aluminum (Al) and silicon (Si) on deformation twinning and martensitic phase transformation in an austenitic Fe-(15-30) wt.% Mn steels under tensile and compressive loads were studied by Grassel et al. [220]. Using the XRD, SEM and TEM techniques, they reported the suppression and promotion of γ-austenite → ε-martensite phase transformation by the increase in the fraction of Al and Si in the steel, respectively. In a duplex TRIP-assisted stainless steels, the coexistence of both phase transformation sequences (FCC γ-austenite → BCC α′-martensite and FCC γ-austenite → HCP ε-martensite → BCC α′-martensite) were reported [223]. On the role of austenite grain size, all transformation paths including via deformation twin (FCC γ-austenite → twinning → BCC α′-martensite) were observed in a coarse-grained AISI 304L steel subjected to quasi-static tensile loading [242]. On the other hand, Yen et al. [61] reported stress-assisted α′-martensite rather than the strain-induced α′-martensite (α′ formed at the intersection of ε-martensite or twin bands) in UFG duplex steels. These researchers also presented both experimental and theoretical evidence on the effect of compositional differences to support the deformation-induced microstructure and mechanical properties of steels. To provide further clarification on the reported variations in the phase transformation path, the role of grain size on the phase transformation sequence in AISI 321 ASS under quasi-static compressive loading is addressed in this study.

## 8.2 Material and methods

Coarse (37 μm) and ultrafine (0.24 μm) grained AISI 321 austenitic stainless steel plate described in Section 3.1 were used in this study. The details on the development of UFG structure in AISI 321 ASS are provided in Chapter 5, while detailed information of the quasi-static compression test is discussed in Section 3.3.2. Cylindrical test specimens, 4 mm in diameter and 4 mm long, (Length/Diameter = 1) were machined with the axis of the specimen parallel to the rolling direction (RD). The compression direction (CD) is parallel to the RD and all compression tests were conducted at room temperature. Samples of 0.24 μm (UFG) and 37 μm (CG) grain sizes were compressed to the same true strain value of 0.22, 0.30, 0.37, 0.47 and 0.53. Material characterization techniques are as described in detail in Sections 3.3.1 (hardness tests) and 3.5 (electrolytic polishing, TEM, EBSD, X-ray diffractometry, and Feritscope measurements). All microstructural analysis and measurements in this study were conducted on the compression plane.

Visco-plastic self-consistent (VPSC) modeling was employed to identify the role of deformation mechanisms in the macroscopic stress-strain response and texture evolution in the alloy during the uniaxial compression test. The formulation of VPSC is extensively described elsewhere [243] and only a brief description of the hardening in a single crystal is provided in this manuscript. The plastic response of each grain is described by activating the deformation system(s) at predetermined values of critical resolved shear stress (CRSS), and the value of CRSS during plastic deformation is given by extended Voce hardening rule [244]:

$$\tau_{cr}^{s} = \tau_0^s + (\tau_1^s + \theta_1^s \Gamma)\left[1 - exp\left(-\frac{\theta_0^s \Gamma}{\tau_1^s}\right)\right] \quad \ldots 8.1$$

where $\tau_0^s$ and $\tau_1^s$ are the initial and back extrapolated critical resolved shear stresses, $\theta_0^s$ and $\theta_1^s$ are the initial and final asymptotic hardening rates associated with the slip or twin system(s). With respect to latent hardening effects, the activities on the various slip and twinning systems harden each other to:

$$\dot{\tau}^s = \frac{d\tau_{cr}^s}{d\Gamma} \sum_{\acute{s}} h^{s\acute{s}} \dot{\gamma}^{\acute{s}} \quad \ldots 8.2$$

where $h^{s\acute{s}}$ is the latent hardening matrix which empirically considers the effect of obstacles to slip or twinning in the system.

### 8.3 Results and discussion

The reference ideal texture components used to interpret all the orientation distribution functions (ODF) presented in this article are shown in Fig. 8.1a. Meanwhile, the EBSD IPF color maps for the undeformed CG (37 μm) and UFG (0.24 μm) samples are presented in Fig. 8.1b and c, respectively. The IPF maps show a fairly random orientation of grain in CG sample and significantly textured grains near Y, Copper and Cube orientations. The microtexture result is not statistically reliable owing to the small EBSD scan area. Their corresponding selected ODF $\phi_2$ sections (from a more statistically-reliable bulk texture measurement) shows that R-Cube is the major crystallographic orientation in the CG sample, with a minor spread near Cube, Copper, and Goss orientations (Fig. 8.1b). Meanwhile, UFG sample is significantly textured around Cube orientation with a minor spread near Y and Copper orientations (Fig. 8.1c). The microstructure of both CG and UFG samples contain less than 10% retained BCC α′. The Vickers hardness values of undeformed CG and UFG samples are 186 and 490 HV, respectively.

### 8.3.1 Mechanical response during compression

The true stress-true strain curve of the specimens compressed to a strain of 0.53 is presented in Fig. 8.2a. For clarity and to prevent data clumsiness, curves of the specimens compressed to 0.22, 0.30, 0.37 and 0.47 true strains are not presented. This is because all the curves generated from the compressed specimens perfectly superimpose on one another, and are hard to distinguish. Figure 8.2a shows an increase in true yield strength ($\sigma_y$) from 207 to 1104 MPa (433% increase) when the austenite grain size was reduced from 37 (CG) to 0.24 μm (UFG). At strain 0.22, 0.30,

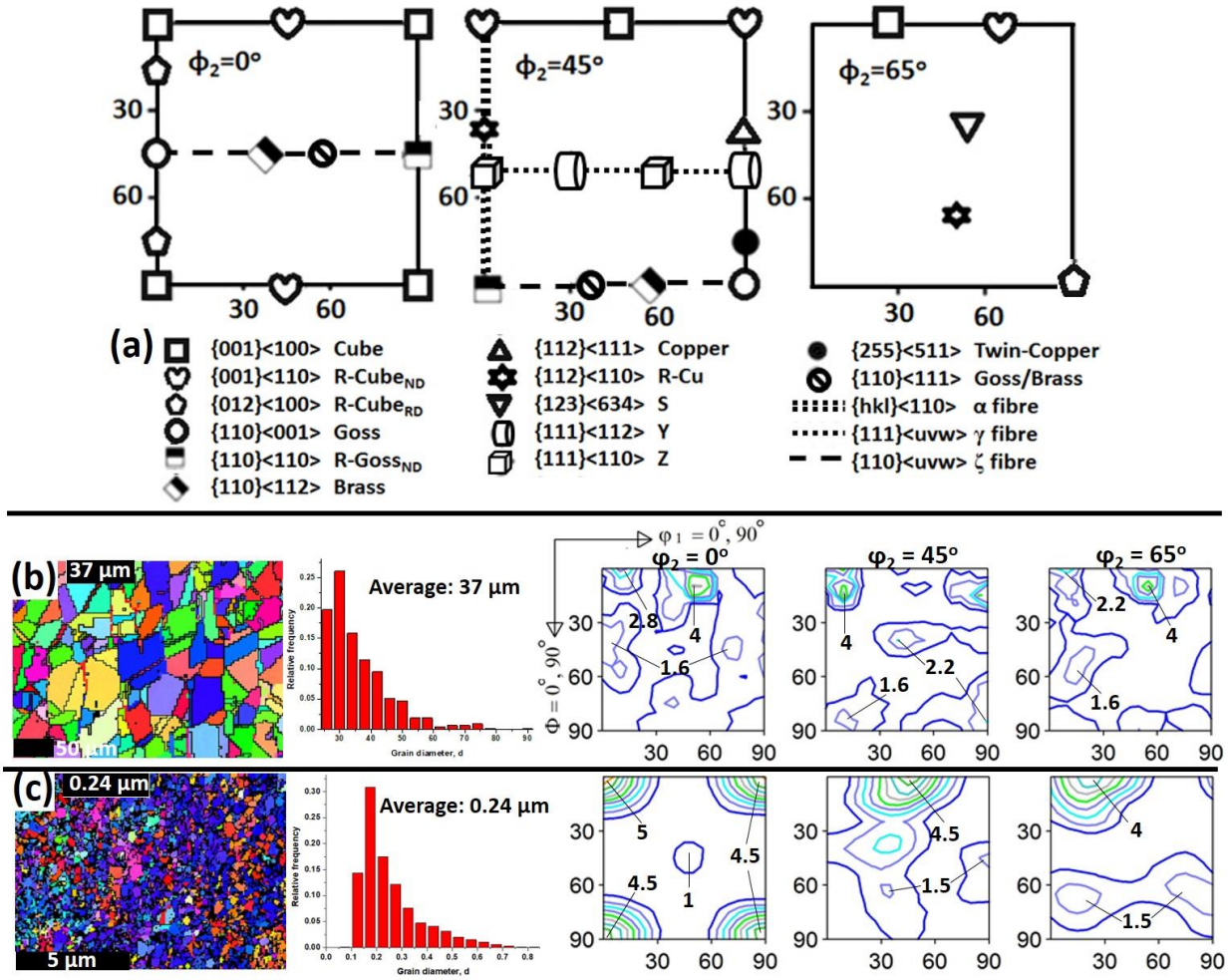


Fig. 8.1. (a) Ideal texture components observed in steels. (b and c) EBSD IPF color maps, grain size distribution estimated from larger scan area and the corresponding selected ODF $\phi_2$ sections from the XRD measurement of the undeformed samples.

0.37, 0.47 and 0.53, the corresponding compressive true stresses are 995, 1570, 2240, 3570 and 4790 MPa, respectively, for CG specimens. Similarly, the compressive true stresses at the selected

strain levels are 1810, 2380, 3030, 4460 and 5950 MPa, respectively, for UFG specimens. The increase in yield strength by grain size reduction conforms with the Hall [210]-Petch [211] relation (Eqn. 8.3).

$$\sigma_y = \sigma_o + Kd^{-0.5} \quad \ldots 8.3$$

where $\sigma_y$ is the true stress corresponding to the 0.2% true strain, $\sigma_o$ is the lattice friction stress required to move individual dislocation, *K* is a constant that measures the relative hardening contribution of grain boundaries, and d is the average grain diameter. The estimated values of $\sigma_o$ (128 MPa) and *K* (478 MPa $\mu m^{-0.5}$) are obtained for AISI 321 ASS by solving the two simultaneous equations obtained by substituting the grain sizes of CG and UFG specimens and their corresponding yield strengths in Eqn. 8.3. Figure 8.2b provides a plot of the estimated yield strength of AISI 321 ASS at any grain size, d, > 0.1 μm. The plot is obtained by using the values of $\sigma_o$ and *K* and varying the values of the grain diameter (d) in Eqn. 8.3. To validate the correctness of the values of $\sigma_o$ and *K* and the reliability of Fig. 8.2b, an AISI 321 ASS sample with an average grain size of 3 μm was compressed under the same loading condition. A true yield strength of ~388 MPa was obtained as shown in Fig. 8.2c. This is comparable to the value of $\sigma_y$ (~400 MPa) obtained from Fig. 8.2b.

The higher yield strength of the UFG specimen also agrees with Kocks' composite model [227] for a polycrystal. The author showed that grain interior deforms differently than the grain boundary region, such that the $\sigma_y$ of the polycrystal is obtained by a rule-of-mixture based on an averaging procedure expressed in Eqn. 8.4.

$$\sigma_y = \sigma_I A_I + \sigma_{GB} A_{GB} \quad \ldots 8.4$$

where $\sigma_I$ and $\sigma_{GB}$ are the flow stresses of a grain interior and grain boundary region of constant width, respectively, $A_I$ and $A_{GB}$ are the area fractions of grain interior and grain boundary region. This implies that as the grain size of AISI 321 ASS decreases, the $A_{GB}$ for the constant width grain boundary region increases, resulting in an increase in the $\sigma_y$ (since $\sigma_{GB} > \sigma_I$) as can be observed in Fig 8.2a.

Figure 8.2d shows the variation of strain hardening rate ($d\sigma_T/d\varepsilon_T$) with true strain for both UFG and CG specimens. Three distinct stages of hardening are observed. Stage I is a regime

characterized by a drop in strain hardening rate, which is similar to the dynamic recovery process such as cross-slip and annihilation of dislocations of opposite signs [245]. This stage is also related to the elastic-plastic transition behavior of the alloy during compression [246]. As strain increases, the hardening rate increases steadily till a 0.4 true strain is reached (stage II), above which an accelerated hardening rate occurred (stage III). Although stage I occurs at a lower strain for CG specimen (in comparison to UFG specimen), hardening in stage II is slightly higher for CG specimen until a critical true strain of 0.4. Hardening rate in UFG specimen became higher than that observed in CG specimen above the critical strain (stage III). This suggests that the activation and slowdown of deformation and/or strengthening mechanisms in both specimens can be different at certain strain level. The repeat of the compression test confirms that these behaviors occur at the same strain range and are repeatable.

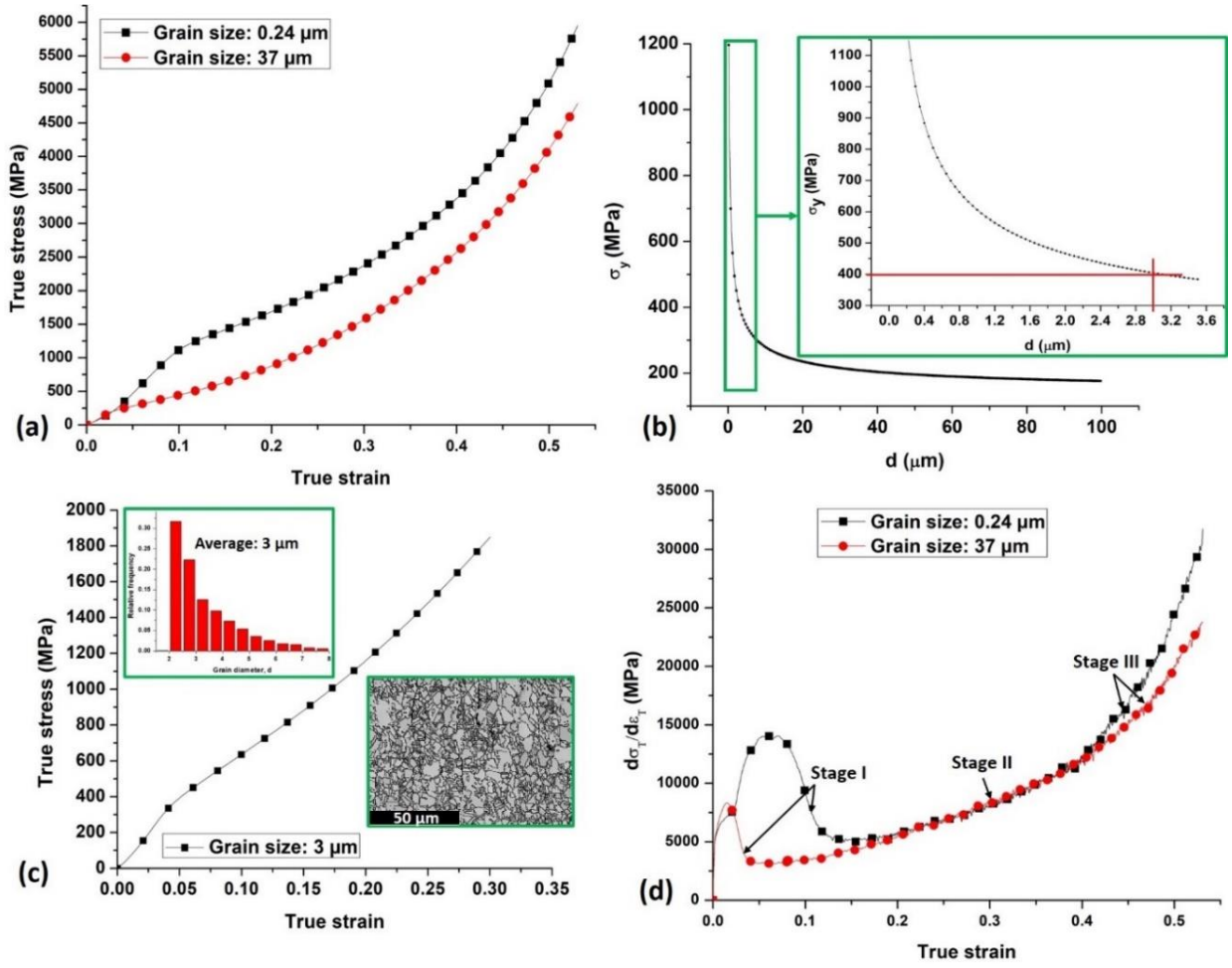


Fig. 8.2. (a and c) True stress-true strain, (b) yield stress-grain diameter curves, (d) strain hardening rate-true strain (hardening diagram).

### 8.3.2 Microstructural evaluation after compression

To understand the microstructural changes responsible for the hardening behavior in Fig. 8.2d, the specimens compressed to 0.30, 0.37, 0.47 and 0.53 true strains were investigated using EBSD, TEM, and XRD techniques.

#### 8.3.2.1 EBSD (microtexture) and TEM analyses

##### 8.3.2.1.1 *At $\varepsilon_T$ = 0.30: In the region of hardening stage II*

Figure 8.3 shows the EBSD maps of CG (Fig. 8.3a-d) and UFG (Fig. 8.3e-j) specimens deformed to 0.30 strain. For the CG specimen, a very low fraction of martensite is observed in the phase map (Fig. 8.3a). The presence of both deformation and annealing twins (4.6% - area percent) in the austenite phase (Fig. 8.3c). The distribution of KAM value in Fig. 8.3d is non-uniform; a higher misorientation in the 3-4$^o$ range was observed near the grain and twin boundaries than in the grain interior. This, coupled with the reduction of the dislocation mean free path that occurs as a result of nucleation of deformation twins, suggests that these boundaries are effective barriers to dislocation motion leading to hardening. The high magnification-low step size scan of the marked region in Fig. 8.3a is presented in Fig. 8.4. The map shows dark slip bands (an unresolvable measure of orientations) which are regions of high dislocation densities, as also evident by higher KAM values around them (Fig. 8.4d). Similar slip bands were observed using high-resolution digital image correlation and EBSD techniques in a recent study on the polycrystalline plasticity of AISI 304L subjected to quasi-static tensile load [247]. Figures 8.4a and b show the evolution of <0013>||CD-oriented HCP ε in <110>||CD-oriented austenite grain in grain 1. Grain 2 also reveals the evolution of BCC α′ in the band and close to the grain boundaries, say, the boundary between grains 2 and 3, where higher dislocation exists. Similarly, ε- and α′-martensite are observed to coexist along the bands in grain 4 and its boundaries are observed. This agrees with previous findings on the nucleation of martensite embryo on slip bands [218] and grain boundaries [217] that are characterized by dislocation pile-ups. A notable observation in Fig. 8.4c is also the evolution of nano-twins along the bands and grain boundaries in grains 3, 4 and 5. These nano-twins which are thought to also contribute to strain hardening, are not observed at a lower magnification and lower step size scan in Fig. 8.3a-d. Despite the several mechanisms proposed to

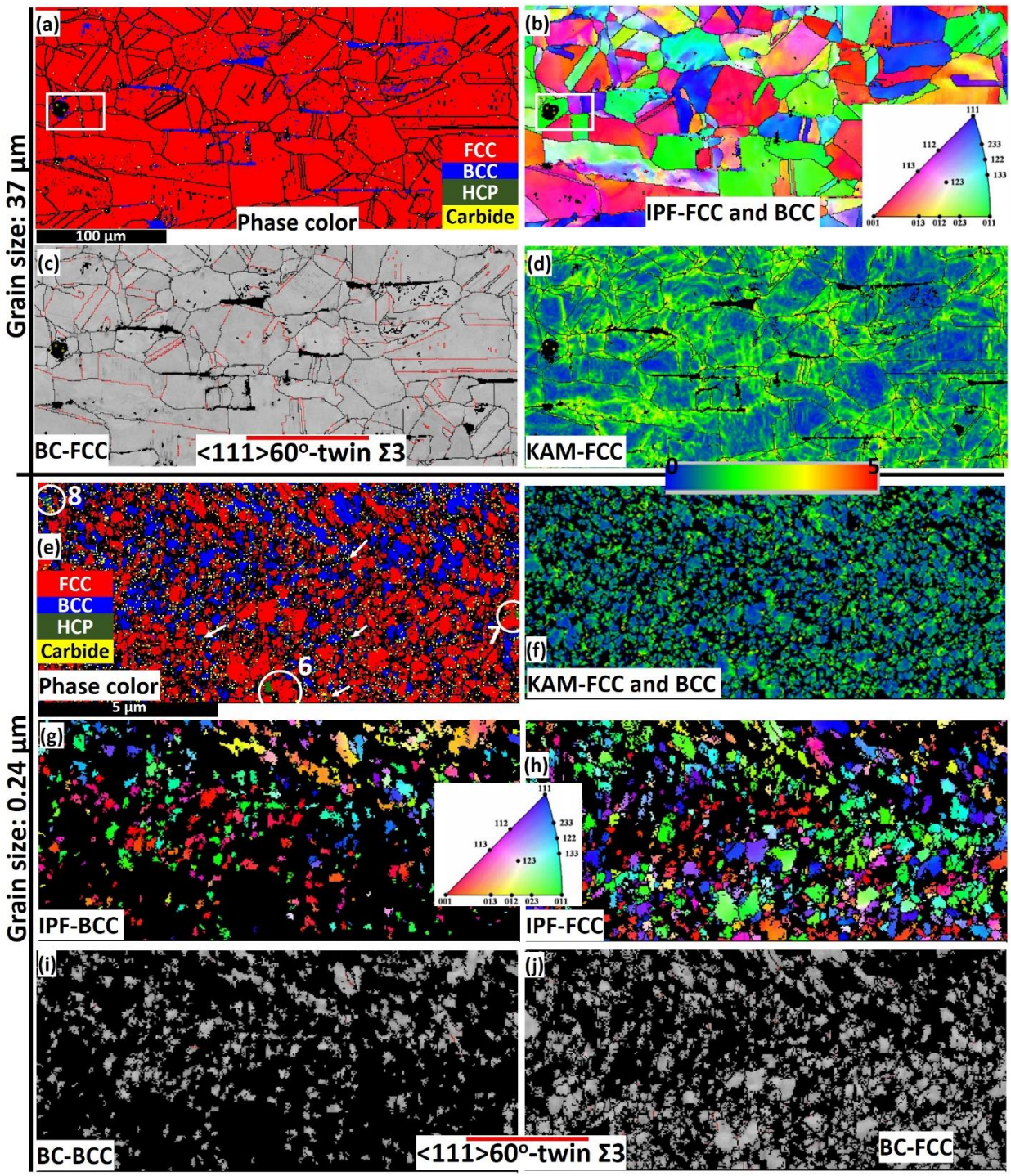


Fig. 8.3. EBSD maps of (a-d) 37 and (e-j) 0.24 µm grain-sized specimens deformed at 0.30 true strain. Phase color, KAM, IPF and BC maps are (a and e), (d and f), (b, g, h) and (c, i, j), respectively.

explain the development of deformation twins; it is generally considered a process that proceeds via a dislocation mechanism [224]. A critical dislocation density, as well as stress concentration at grain boundaries [225], have been reported to be required for initiation of deformation twins.

A higher fraction of martensite is observed in UFG specimen (Fig. 8.3e) at 0.30 true strain than in the CG specimen (Fig. 8.3a), which is attributed to the presence of other nucleation sites such as the triple junctions in UFG specimens. This observation is contrary to the findings reported in the study of a UFG austenitic steels subjected to tensile load [172]. The authors reported a decrease in the critical stored energy for the formation of BCC α′ with increasing austenite grain size i.e. higher stability of the austenite phase in the UFG samples. The variability of their findings in comparison with the current study could be due to the difference in the studied material and the test methods (compression test in this study, tensile test in [172]) and experimental conditions. Although, the distribution of KAM value in Fig. 8.3f shows higher misorientation near the grain boundaries than the grain interior, it is in the 2-3$^{o}$ range; lower than misorientation observed in CG specimens. As in the case with CG specimen, HCP ε is observed in grains 6 and 7 and other sites (white arrows) near the higher KAM grain boundaries. In grain 8, the coexistence of ε- and α′-martensite in austenite grain is also observed. This suggests that the phase transformation sequence in AISI 321 ASS under the above-described deformation conditions can follow both FCC γ→ BCC α′ and FCC γ → HCP ε → BCC α′; irrespective of the grain size. The absence of bands of high dislocation density and near-absence of twins (< 1% in each of α′ and γ phases) are observed in UFG specimen, largely due to space shortage (very small size of grains). This might be responsible for lower hardening rate in UFG specimen in stage II of Fig. 8.2d. The near absence of twins in UFG specimen suggests that the twinning stress (stress required to develop twinning) is high in UFG structure compared to those of the CG specimen. This also agrees with the findings of Gutierrez-Urrutia et al. [82] that grain refinement makes the nucleation of deformation twinning difficult. These authors also reported a good correlation between the Hall–Petch relation and grain size effect on the twinning stress; suggesting that as the yield strength of metal increases with a decrease in grain size, so does the twinning stress increases. Finite element simulation of AISI 304 ASS under uniaxial tension shows the activation of twinning in specimens with an average grain size of 35 μm and suppression of twinning in specimens with grain sizes of 800 nm and 270 nm [81]; the authors attributed the behavior in the latter to the reduced distance between the obstacles that suppressed twin growth.

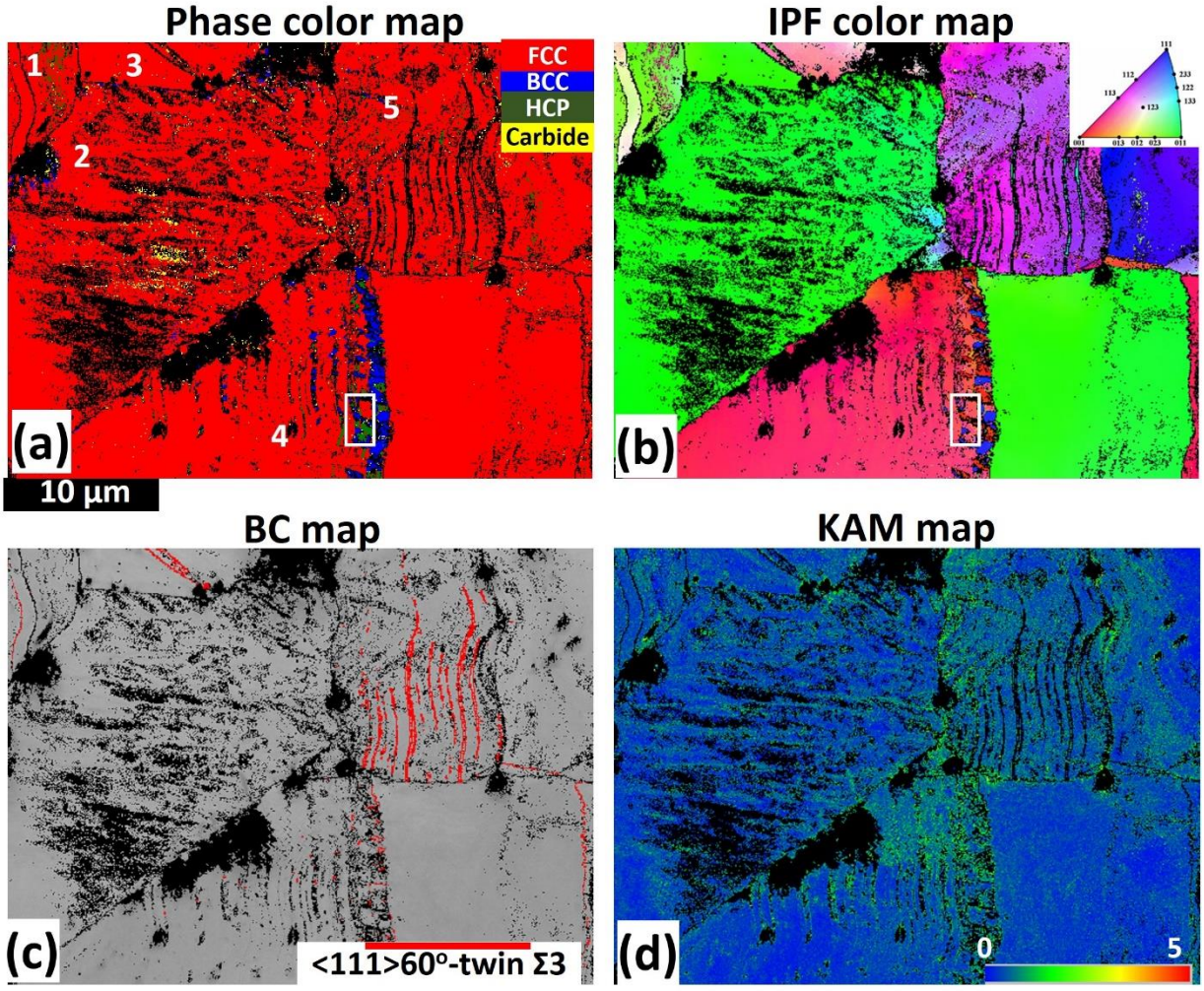


Fig. 8.4. EBSD maps of marked region in Fig. 8.3a: (a) Phase color, (b) IPF, (c) BC and (d) KAM maps.

8.3.2.1.2 *At $\varepsilon_T$ = 0.37: Still in the region of hardening stage II*

As strain was increased to 0.37, the fraction of BCC α′ increased to ~35% of the scanned area in the CG specimen, while the fraction of HCP ε decreased as shown in Fig. 8.5a-e. Meanwhile, the area percent of BCC α′ in UFG specimen increased to ~72% with a near absence of HCP ε (Fig. 8.5f-j). It is thought that HCP ε transformed to BCC α′ upon an increase in strain. In a previous study on the deformation behavior of AISI 304 steel under tension at $10^{-4}$ $s^{-1}$ [218], continuous transformation of HCP ε to BCC α′ was reported to occur with increased strain. Analyzing the crystallographic orientation of the deformed austenite and martensite phase, the area fraction of grains with near-<100> and <111>||CD textures is observed to increase (compared to those at 0.30 true strain) in the BCC α′ phase. Similarly, the area fraction of austenite grains with near-<110>

and <111>||CD textures increased with strain. With twin formation nearly absent in UFG specimen (Fig. 8.5i and j), the total area percent of twins in the CG specimen (Fig. 8.5d and e) is now shared between the austenite (2.3 %) and α′-martensite (5.6 %) phases.

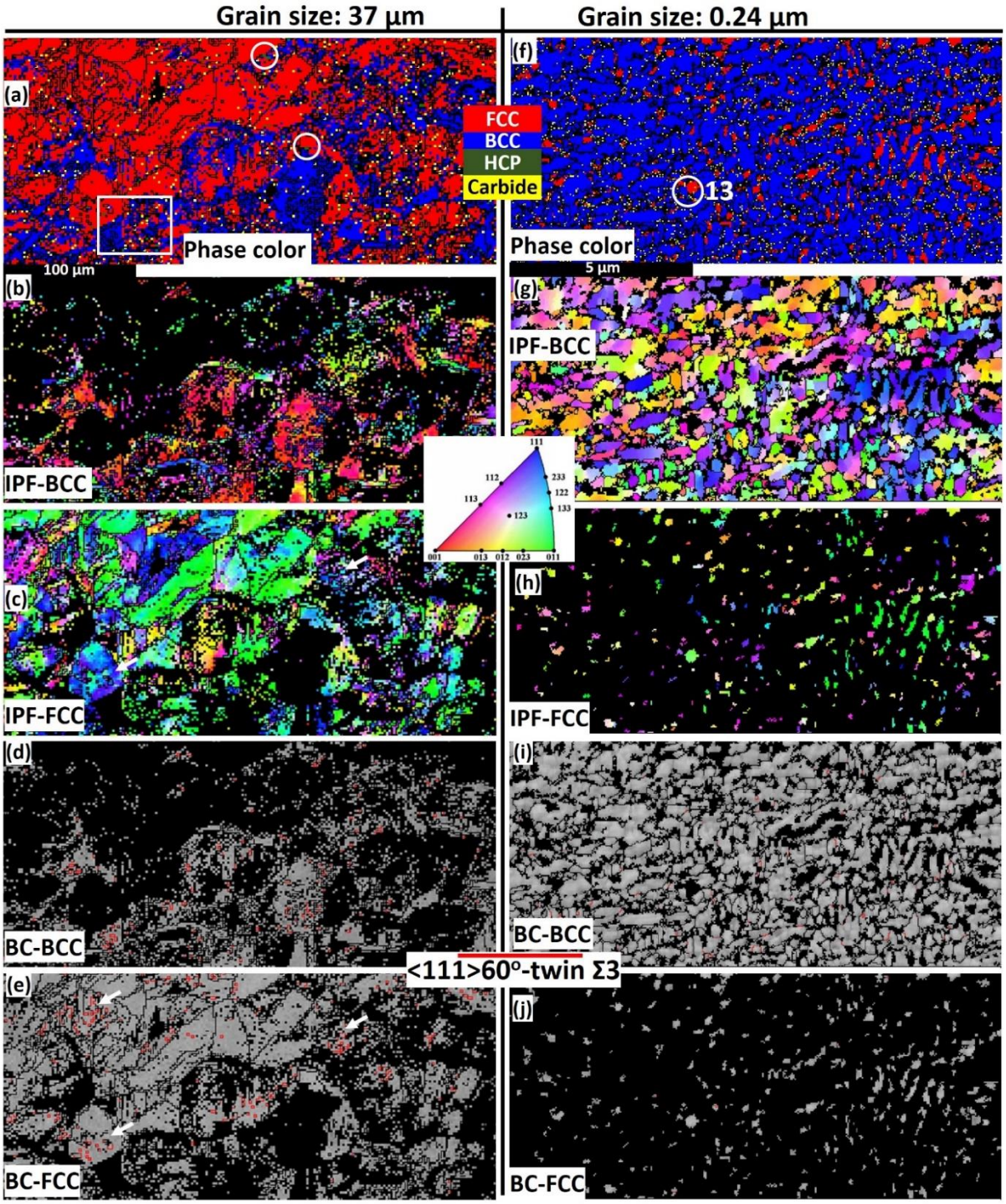


Fig. 8.5. EBSD maps of (a-e) 37 and (f-j) 0.24 µm grain-sized specimens deformed at 0.37 true strain. Phase color, IPF and BC maps are (a and f), (b, c, g, h) and (d, e, i, j), respectively.

A high magnification-low step size scan of the rectangular-marked region in the CG specimen (Fig. 8.5a) is presented in Fig. 8.6. At this strain, it can be observed that all bands with high-density dislocations are now fully-formed shear bands, saturated with mostly BCC α′ as observed in grains 10 and 11 on Fig. 8.6a. These bands (in Fig. 8.6a) are hereafter referred to as austenite-martensite bands (A-M band). Austenite phase in grain 9 with the lowest Schmid factor and KAM value (in comparison with those of grains 10 and 11) shows the lowest fraction of BCC α′ as seen in Figs. 8.6 and 8.7. It can also be observed from grain 9 that twinned austenite

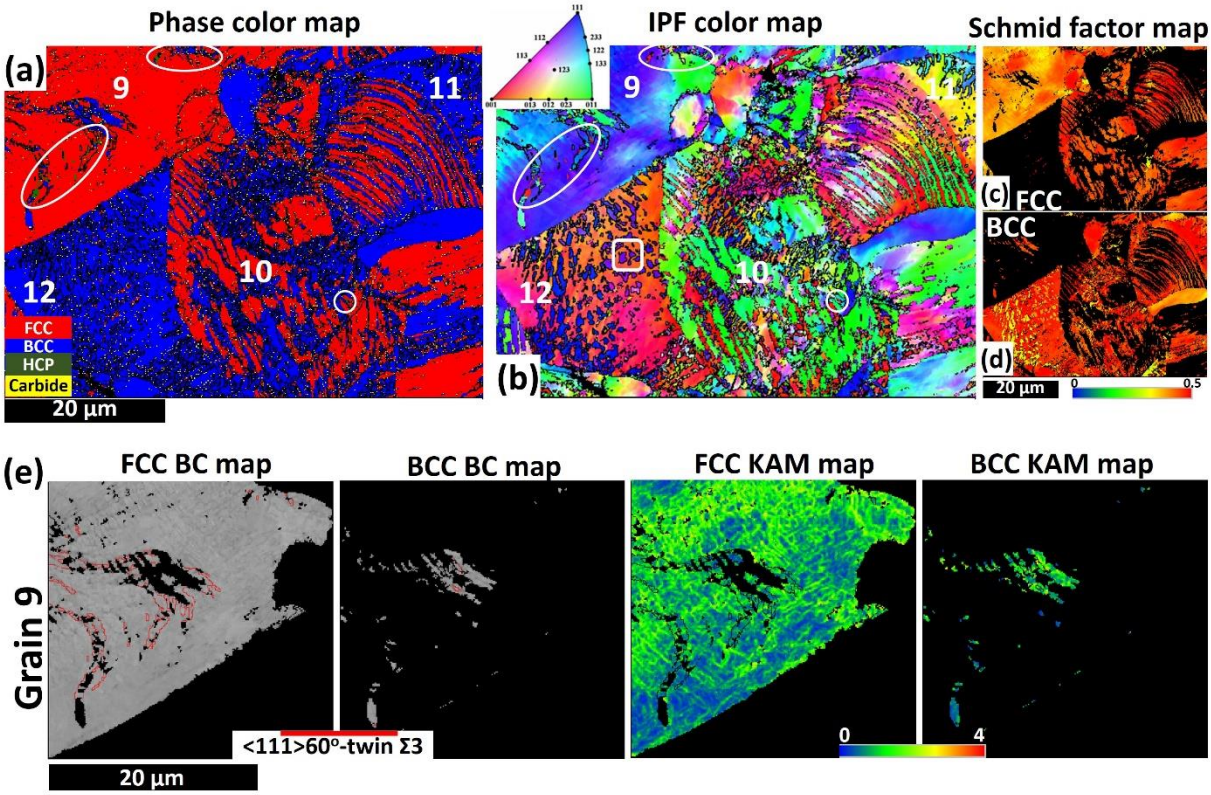


Fig. 8.6. EBSD maps of the rectangular-marked region in Fig. 8.5a: (a) Phase color, (b) IPF and (c and d) Schmid factor maps; (e) BC and KAM maps of grain 9 in Fig. 8.6a

grains with <111>||CD orientation are effective martensite nucleation sites as also reported elsewhere [219,242]. The formation of martensite at deformation twin interiors, slip bands and near grain boundaries in this study is an indication that martensite transformation was induced by stress concentration. This kind of martensite is referred to as stress-assisted α′-martensite [242]. Whereas, neither shear band (ε-martensite or twin bands) intersection nor martensite nucleation at these intersections were observed, irrespective of grain size. These band intersections are reported to be predominant sites for the nucleation of strain-induced martensite [59]. It, therefore, implies

that the martensite formed in AISI 321 ASS under compression is stress-assisted. Moving from grains 9 to 10 and to 11 (Figs. 8.6 and 8.7), A-M bands, the area fraction of martensite, Schmid factor (SF) and KAM increases. Meanwhile, grain 12 is completely transformed to BCC α′. The FCC and BCC KAM maps of grains 9 (Fig. 8.6e), 10 (Fig. 8.7a) and 11 (Fig. 8.7c) shows that the evolved α′-martensite inherit the KAM value (in the 3-4$^{o}$ range) or stored defects of their surrounding austenite phase. Once, the bands are saturated by α′-martensite, continuous grain refinement of the martensite strip in the A-M bands by deformation twinning occur to accommodate further strain as shown in the FCC and BCC BC maps for grain 10 (Fig. 8.7a) and 11 (Fig. 8.7c). This contributes to strain hardening in steels, and it is attributed to a dynamic Hall–Petch effect [224]. This mechanism is also noticeable in a non-banded martensite grain such as grain 12. The $\{111\}_{\alpha'}$ pole figure that corresponds to the marked region in grain 12 (Fig. 8.6b) shows a pole common to both α′-martensite and twins in Fig. 8.7d. The twin exhibits a 60° rotation around {111} axis such that the rotation leads to three common poles in $\{110\}_{\alpha'}$ pole figure. The refinement of austenite strips by twinning in the A-M bands are absent in the austenite strips as shown in Fig. 8.7. A notable observation in this study is the effect of austenite grain size on the morphology of martensite and the number of crystallographic orientation variants they (α′) possess. While the martensite grains in CG specimen are lath-like and multi-variant (for example, four variants (Fig. 8.7b) in the circled region in grain 10), the martensite grains in the UFG specimen are mostly single variants, and they maintain the equiaxed morphology of their neighboring grains as shown in Figs. 8.3h and 8.5g. A change in the morphology of martensite as a result of grain size reduction in steels has also been reported [248].

#### 8.3.2.1.3 *At $\varepsilon_T$ = 0.47: In the region of hardening stage III*

Transmission electron microscopy was used for the microstructural analysis of the specimen compressed to 0.47 true strain. Although no quantitative result was obtained for comparison with other specimens compressed to different strain levels, the TEM micrographs in Fig. 8.8 provide evidence of phase transformation, nano-twins, dislocations and the presence of TiC particles. Figure 8.8a shows the austenitic phase with the absence of twins and dislocations in the undeformed UFG sample. After compression (Fig. 8.8c), martensitic phase with high dislocation density was observed. This implies that UFG AISI 321 is dominated mainly by martensitic phase

transformation and slip of partial dislocations. No twin was observed in the UFG specimen even after compression to 0.47 true strain.

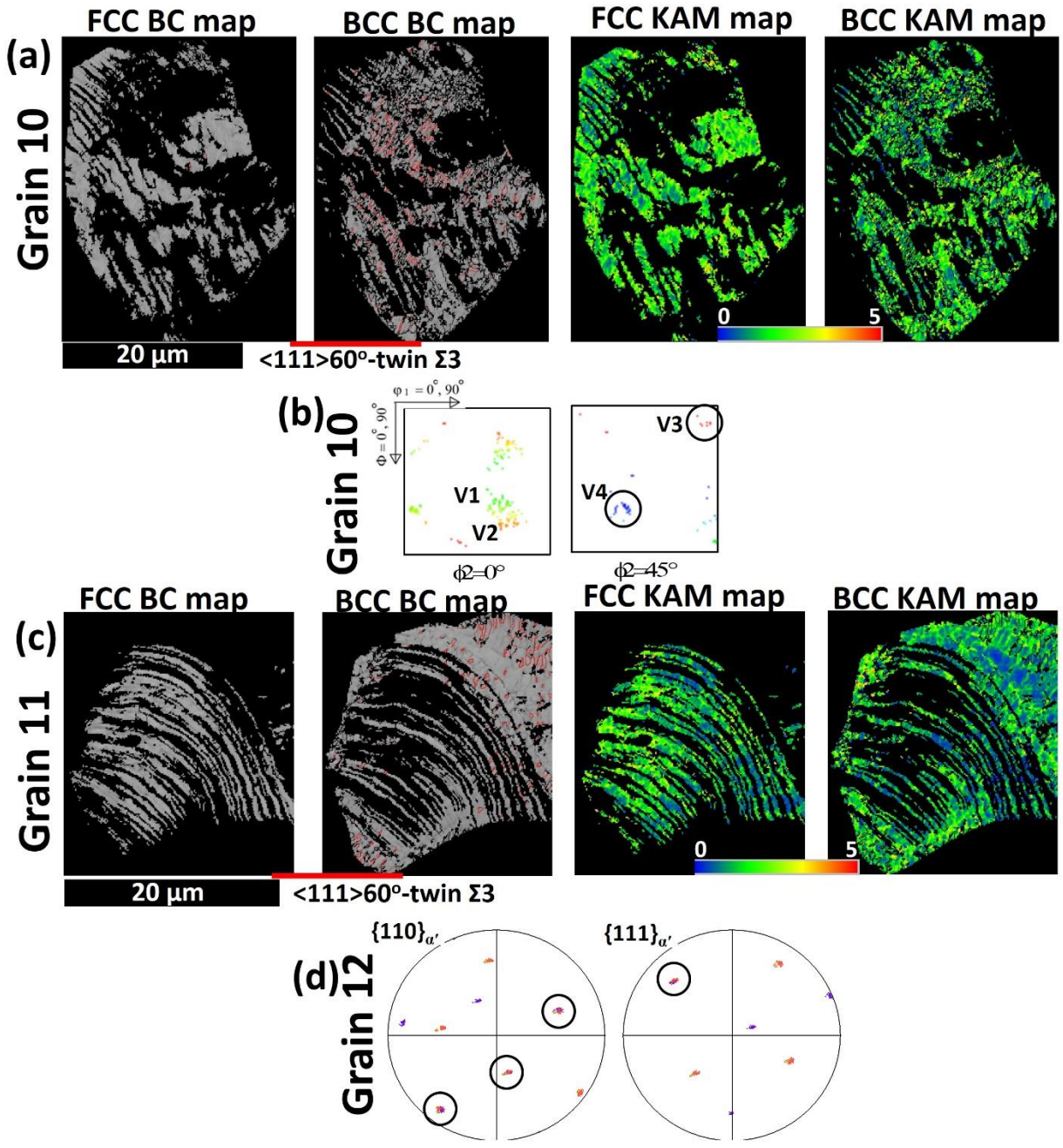


Fig. 8.7. EBSD maps of grains 10, 11 and 12 in Fig. 8.6a: (a and c) BC and KAM maps; (b) selected 0° and 45° ϕ2 ODF sections of the BCC α′-martensite in grain 10; (d) Pole figures of $\{110\}_{\alpha'}$ and $\{111\}_{\alpha'}$ of marked region in grain 12 (Fig. 8.6b).

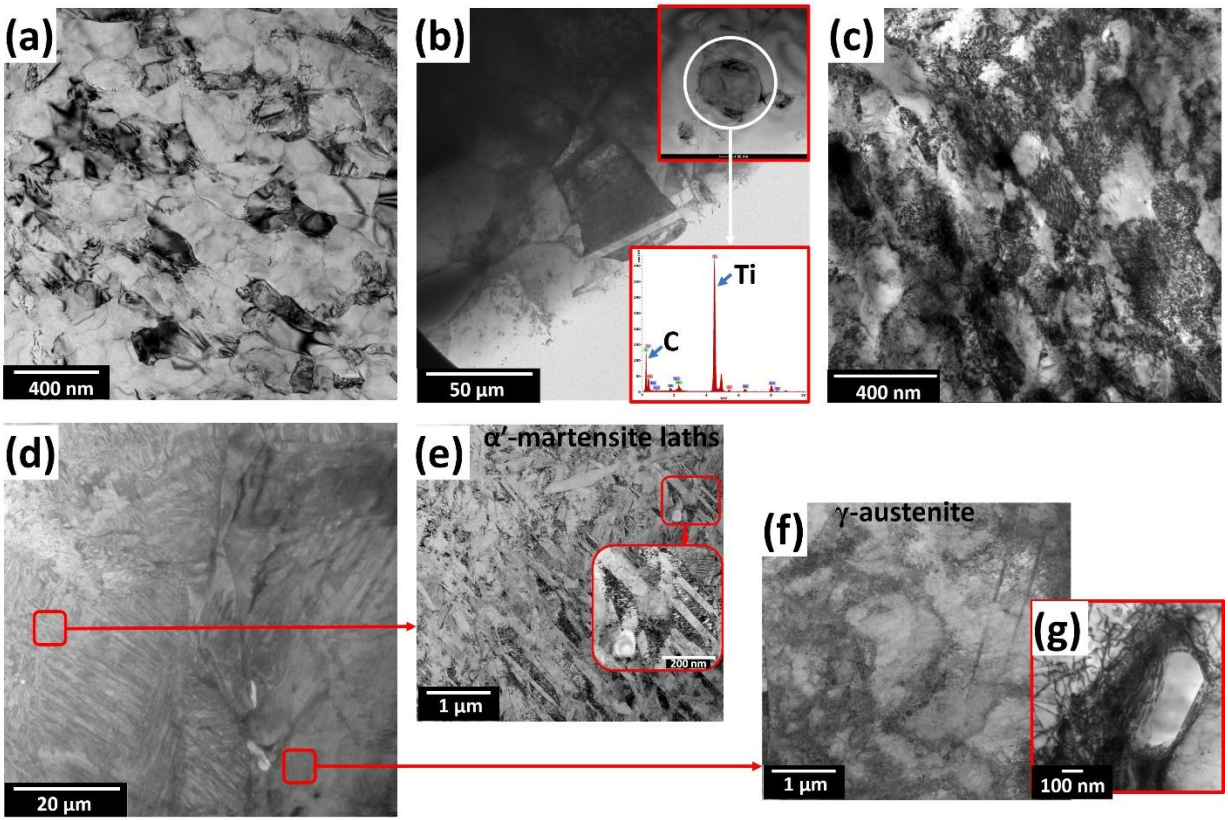


Fig. 8.8. TEM bright field micrographs of (a and b) undeformed and (c-g) deformed specimens at 0.47 true strain: (a and c) 0.24 and (b, d-g) 37 µm grain-sized specimens. TiC particle identified by STEM technique before (inset in (b)) and after (g) deformation.

This affirms the role of grain size on the activation of deformation twin. On the other hand, the TEM micrograph affirms the presence of annealing twins in the CG specimen before compression (Fig. 8.8b). After compression, the coexistence of austenite, lath-like α′-martensite, dislocation, deformation twin and TiCs were observed (Figs. 8.8d-g). Deformed austenite (Fig. 8.8f) shows high dislocations forming-networks and their interaction with nano-twins. The TEM results, therefore, confirm five plausible strengthening sources in this steel. These are grain boundary strengthening (most beneficial to UFG specimen), deformation-induced martensite formation (most beneficial to UFG specimen), deformation twin acting as barrier to dislocation motion (only beneficial to CG specimen), dislocation-dislocation interactions and multiplication during slip (most beneficial to CG specimen) and dislocation interaction with titanium carbides as shown in inset Fig. 8.8b-before and Fig. 8.8g-after compression (most beneficial to CG specimen).

8.3.2.1.4 *At $\varepsilon_T$ = 0.53: Still in the region of hardening stage III*

At 0.53 true strain, the area percent of α′-martensite had increased (50% in CG, 96% in UFG) and significant texturing (<110>||CD for γ, <100>||CD and <111>||CD for α′ in both CG and UFG specimens) had occurred as shown in Fig. 8.9. While ε-martensite might be observed in the CG specimen since there is a substantial fraction of austenite phase (Fig. 8.9a), no fraction of ε-martensite were observed in UFG specimen (Fig. 8.9f). With twin formation nearly absent in UFG specimen (Fig. 8.9i and j), the area percent of twins in the CG specimen (Fig. 8.9d and e) is now drastically reduced in the austenite phase (0.4 %). Meanwhile, the twin fraction in the martensite phase slightly increased (6.7 %) in comparison with the twin fraction in specimen compressed to 0.37 strain. The increase in phase transformation in CG structure may slow down the twinning process in the austenite phase. A high magnification-low step size scan of an area with less α′-martensite (marked in Fig. 8.9a) is presented in Fig. 8.10. The phase map in Fig. 8.10a affirm that slip bands of high dislocation density (e.g., grain 14) and grain boundaries (e.g., grains 15-17) are martensite nucleation sites. Some α′ lath with multiple crystallographic variants are observed to nucleate at one end of a grain boundary, and then their growth is either impinged at the other end of the grain boundary due to steeper stress gradient at the boundary [225] or by another α′ lath as observed for example in grain 17. The ε-martensite is observed in the CG specimen as seen in grains 15 and 17 since there is still a substantial fraction of deformed austenite phase in these grains. In agreement with earlier observation, from grains 14 to 15 (Fig. 8.10), the formation of A-M bands from slip bands, the area fraction of martensite and Schmid factor (SF) increases, while α′-martensite saturates in grain 18. Again, grains 16 and 17 show some bands saturated by α′ lath and these laths are further segmented by twins to accommodate strain as shown in the BCC BC map in Fig. 8.10e. No such behavior is observed in the austenite phase.

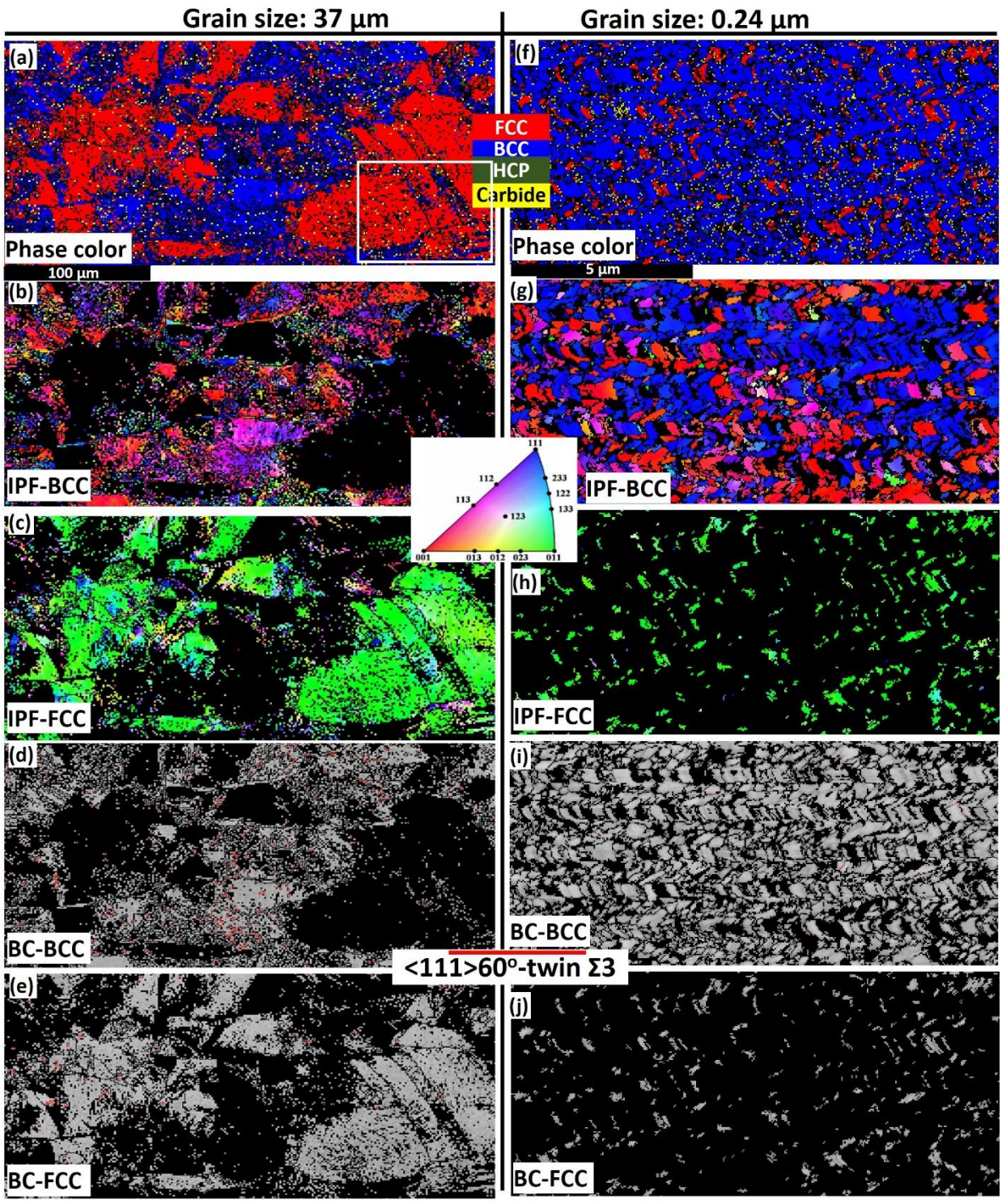


Fig. 8.9. EBSD maps of (a-e) 37 and (f-j) 0.24 µm grain-sized specimens deformed at 0.53 true strain. Phase color, IPF and BC maps are (a and f), (b, c, g, h) and (d, e, i, j), respectively.

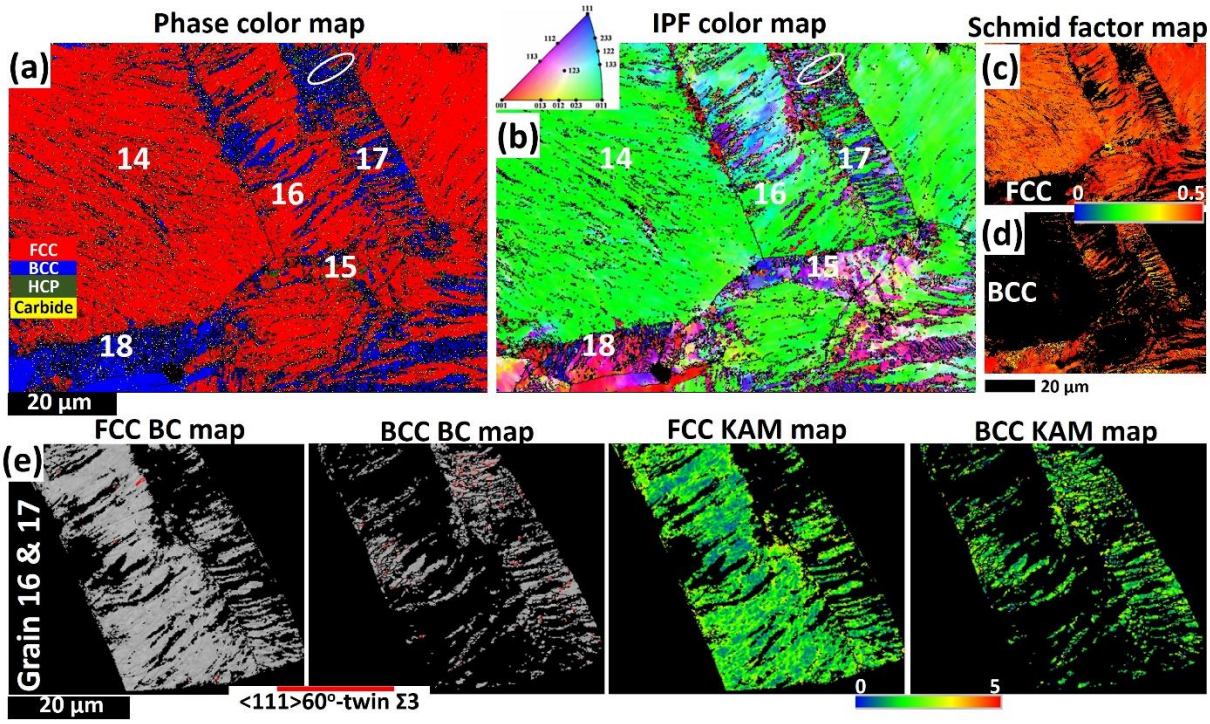


Fig. 8.10. EBSD maps of the rectangular-marked region in Fig. 8.9a: (a) Phase color, (b) IPF and (c and d) Schmid factor maps; (e) BC and KAM maps of grains 11 and 12 in Fig. 8.10a.

8.3.2.2 XRD, Feritscope and hardness measurement

8.3.2.2.1 *Phase identification (ID) and hardness result*

The result of the XRD phase ID measurement (Fig. 8.11a and b) corroborate the EBSD results. For both CG and UFG specimens, the intensity of the martensitic phase transformation increases with strain. That is, the intensities of $(110)_{\alpha'}$ and $(200)_{\alpha'}$ martensitic peaks increase with strain at the expense of the $(111)_{\gamma}$ and $(200)_{\gamma}$ austenitic diffraction peaks. However, the mechanical stability of the austenite phase in the UFG specimen is lower; for instance, 50 volume percent of α′-martensite was obtained at 0.53 and 0.30 true strain in CG and UFG specimens, respectively. This is confirmed by the measurements obtained from the use of Feritscope (Fig. 8.11c); a higher volume percent α′-martensite was recorded in the UFG specimen than in the CG specimen. A careful look at the diffraction patterns of the CG specimens shows the presence of a $(110)_{\varepsilon}$ peak (HCP ε-martensite) at 0.30 and 0.37 true strain levels. The absence of the $(110)_{\varepsilon}$ diffraction peak at other strain levels does not necessarily imply the absence ε-martensite phase, it would rather mean that the volume percent of ε-martensite is too low to show the $(110)_{\varepsilon}$ peak on the diffraction pattern. Hence, at 0.22 true strain, the ε-martensite might just be evolving while their fraction may

have reduced at 0.47 and 0.53 true strains, due to the possible occurrence of HCP ε→ BCC α′ at these strains. Although EBSD phase maps (Figs. 8.3e and 8.5f) show a very low fraction of ε-martensite in the UFG specimen at low strain, the $(110)_{\varepsilon}$ peak is not observed in the diffraction patterns of the UFG specimens at all strain. This implies that the mechanical stability of ε-martensite is higher in CG than in UFG specimens. The Vickers hardness value of compressed specimens shows a near-linear increase with the increase in strain, with the UFG specimens possessing higher values (Fig. 8.11d). Comparison of Figs. 8.11c and d indicate the possible contribution of α′-martensite to the hardness value of AISI 321 ASS as the curves tend to follow a similar pattern.

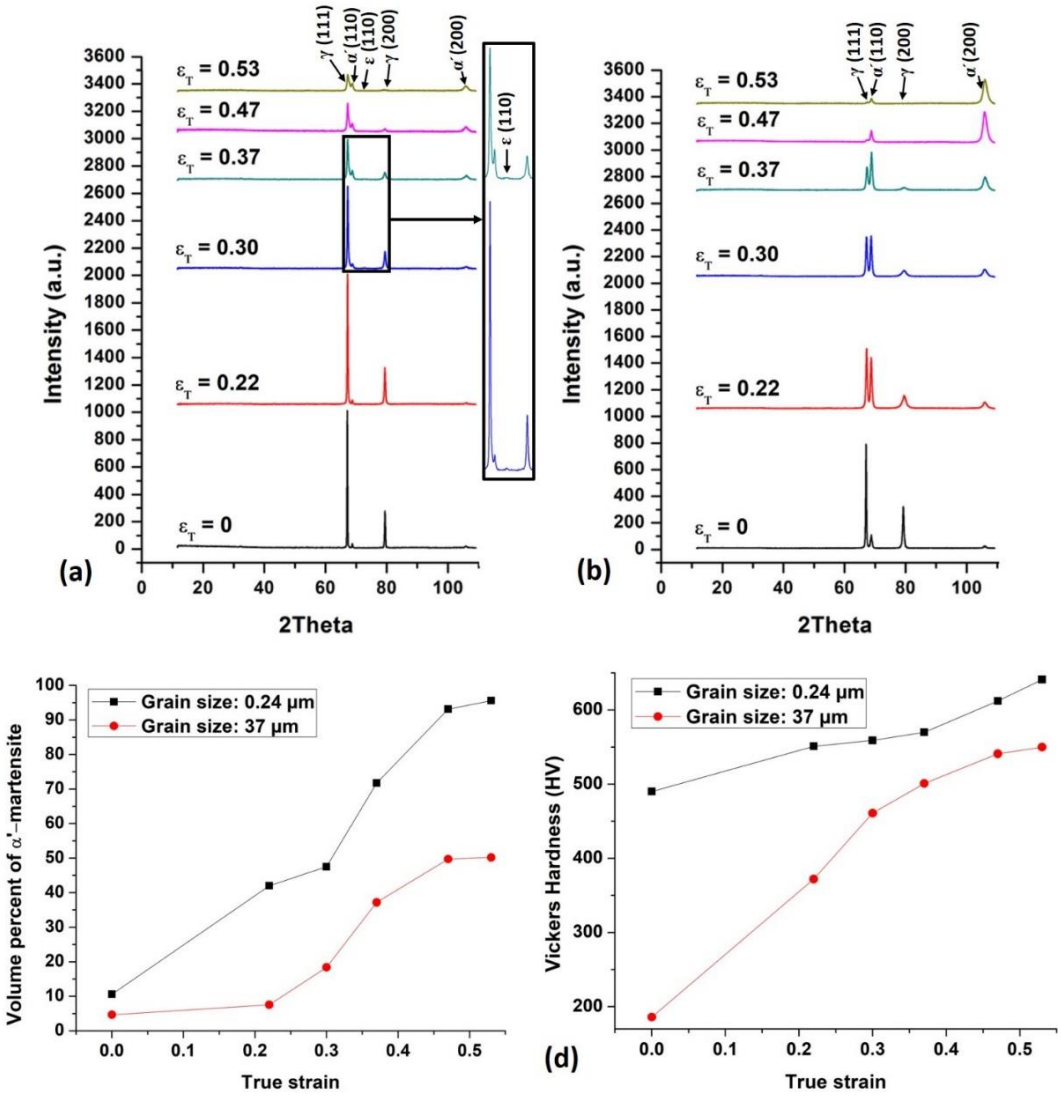


Fig. 8.11. X-ray diffraction patterns of (a) 37 and (b) 0.24 μm grain-sized specimens, (c) volume percent of α′-martensite (d) Vickers hardness profile.

#### 8.3.2.2.2 *Macrotexture analysis*

Figures 8.12 and 8.13 indicate the effect of grain refinement and strain on the deformation texture in both γ-austenite and α′-martensite phases. For both CG and UFG specimens, the ODF of the austenite phase (Fig. 8.12) shows that the Goss and Brass (ζ fibre) strengthens as strain increase at the expense of R-Cube, Cu, and R-Cu textures. However, CG and UFG specimens show a significant and complete dominance of ζ fibre at ~0.30 and 0.47 true strains, respectively. This indicates grain size affects the bulk deformation texture of AISI 321 ASS. Similarly, the ODF of the martensite phase (Fig. 8.13) shows the strengthening of Y and Z (γ fibre) and Cube as strain increases at the expense of R-Cube and Brass textures. While CG specimens show significant and complete dominance of γ fibre and Cube texture at ~0.53 true strain, UFG specimens show the dominance of the same textures at ~0.47 true strain. The critical true strain at which the textures above (i.e., <110>||CD fibre in austenite and <100> and <111>||CD fibres in martensite) become dominant is also confirmed by the calculated inverse pole figure (IPF) triangles in Fig. 8.14. A notable observation in the ODFs (Figs. 8.12 and 8.13) and IPFs (Figs. 8.14) is the variation in texture intensities. While there is no large variation in the austenite texture intensity of both CG and UFG specimens, martensite texture intensity in CG specimens are lower than those in UFG specimens. The reason for this behavior is not completely understood, but phase transformation certainly plays no role in the variability of the intensities of these textures [78]. Meanwhile, earlier observations (Figs. 8.6a-d and 8.10a-d) suggests the role of texture in phase transformation. The <100>||CD fiber grains of highest Schmid factor tends to promote phase transformation more often than the <110> and <111>||CD fibre grains of lower Schmid factor. It could, therefore, imply that the initial texture plays a significant role in phase transformation. For instance, the initial texture of UFG specimen is strongly <100>||CD fibre; hence, promoting earlier and more martensitic phase transformation in UFG specimen than those of CG specimens, whose initial texture deviates from <100>||CD texture as shown in Fig. 8.1.

To make a quantitative comparison of the texture components, the volume fraction of <100>, <110> and <111>||CD fibres as a function of strain was calculated for γ and α′ phases in both CG and UFG specimens (Fig. 8.15). While the volume percent of <100> and <111>||CD fibres decreased with an increase in strain in the γ phase of both set of samples, the volume percent of the <110>||CD fibre increased (Fig. 8.15a-c). A similar trend is observed in copper and 70/30 brass,

which have low and medium SFE, respectively [249]. The reverse of this behavior is observed in the α′ phase (Fig. 8.15d-e). The observed crystallographic orientations in both γ and α′ phases agree with those of the EBSD results and those reported in the literature. The volume percent of <110>||CD fibre texture, which is the stable end-orientations in compression for the γ phase, is clearly higher in CG specimens at all strains.

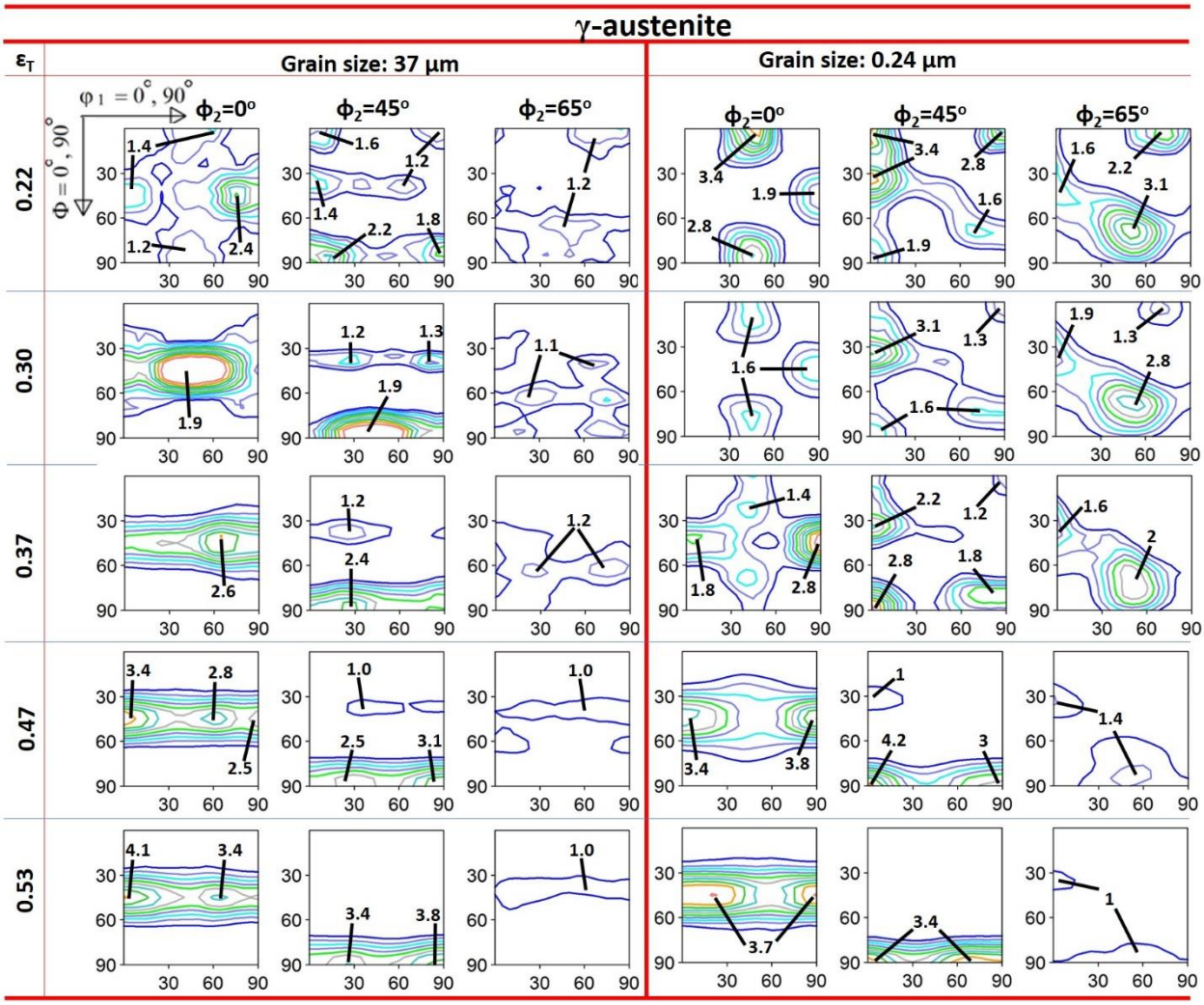


Fig. 8.12. 0°, 45°, 65° ϕ2 ODF sections of the FCC γ -austenite in deformed specimens.

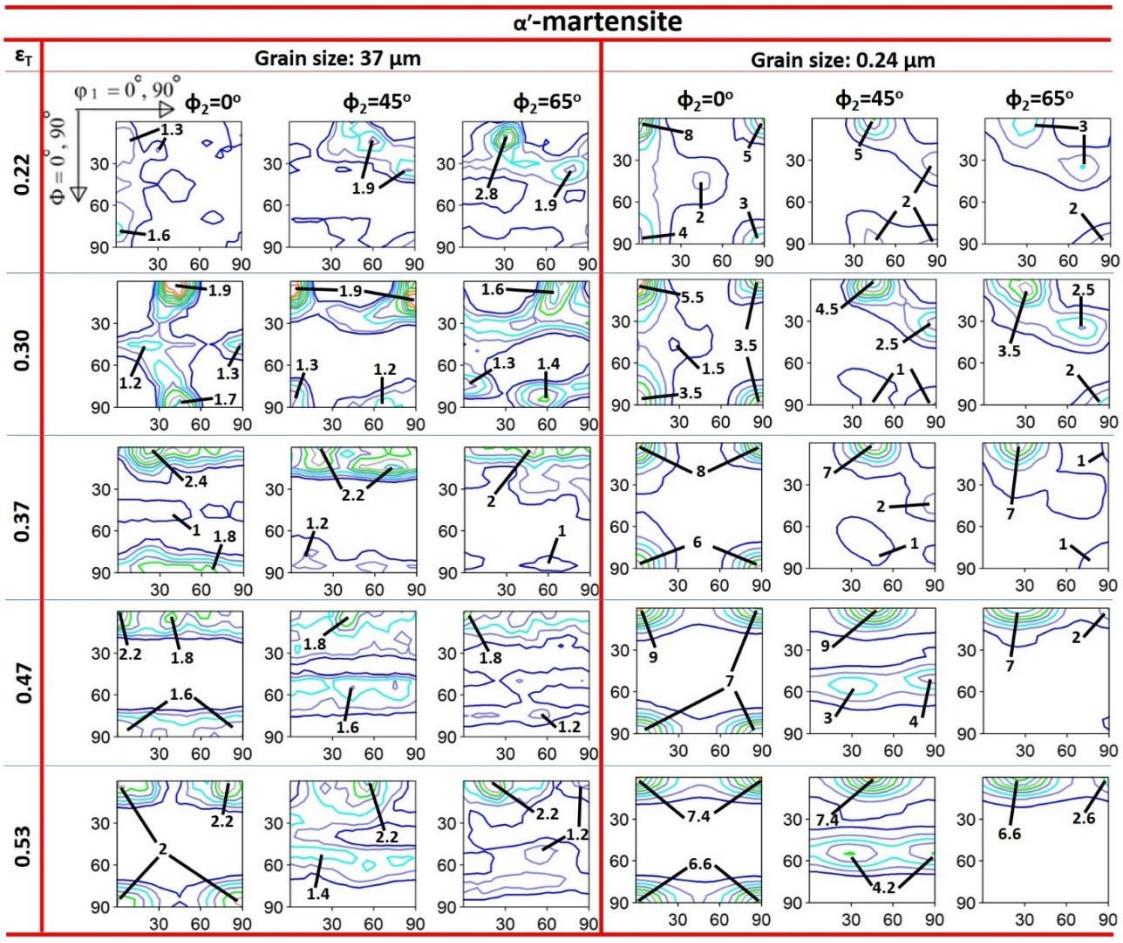


Fig. 8.13. 0º, 45º, 65º ϕ2 ODF sections of the BCC α′-martensite in deformed specimens.

8.3.2.3 Microstructure-strain hardening rate correlation

It has been reported that the deformation mechanisms in metals with UFG structure can be very different from those operational in metals with CG structure [250]. The summary of the findings in the current study is presented in Table 8.1. The presented data affirms the dependence of deformation and strengthening mechanisms on grain size. In this study, the compressive strain hardening behavior of CG and UFG AISI 321 ASS specimen seems to be quite different in comparison with those reported in the literature. While some authors observed a higher strain hardening rate in CG austenitic stainless steel specimen (in comparison with the UFG sample) [81], this behavior occurred up to a critical true strain of 0.4 in AISI 321 steel. Above 0.4 true strain, strain hardening in UFG specimen becomes higher (Fig. 8.2d). As reported in the previous subsections, the strength-contributing sources in AISI 321 steel under compression are dislocation multiplication and interaction, twinning and their interaction with dislocations (negligible effect

in UFG specimen), martensitic phase transformation, and precipitation of carbides. The onsets of these sources correlate to the start in the rise of strain hardening rate. At mid strain range (Fig. 8.2d), the slightly higher hardening curve for CG specimen could be attributed to twinning activity as also reported in other FCC [251] and hexagonal closed-packed (HCP) [252] low SFE alloys.

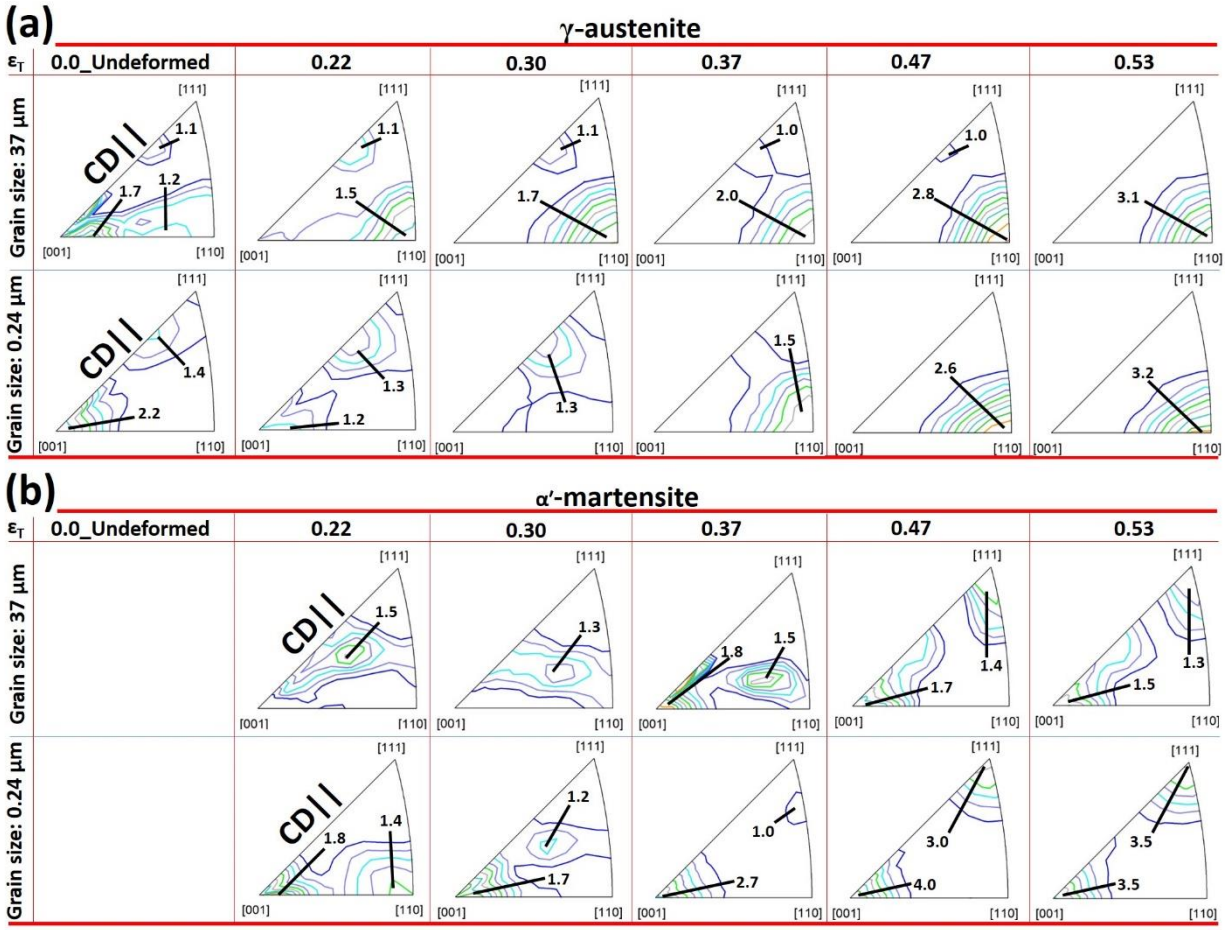


Fig. 8.14. IPF triangles showing crystallographic fibre texture in (a) FCC γ -austenite and (b) BCC α′-martensite phases of the deformed specimens.

The strain hardening behavior beyond 0.4 true strain (stage III of the hardening diagram) could also be attributed to either deceleration or acceleration of specific deformation and strengthening mechanisms. Although both specimens show accelerated hardening rate beyond 0.4 true strain, hardening in UFG specimen is higher and it is attributed to higher martensitic phase transformation rate and α′ grain boundary strengthening. The α′-martensite acting as a reinforcing phase in stainless steels has been reported by [228]. This is due to the ability of α′ to withstand a higher stress than the austenite phase under external load. Hence, α′-martensite will act as a more effective

reinforcing phase than the austenite phase; contributing significantly to the strain hardening rate of UFG specimen beyond 0.4 true strain.

Table 8.1. A comparison table of observations from the CG and UFG specimens subjected to same deformation conditions.

| True Strain | True Yield (MPa) | | Compressive true strength, MPa | | Hardness, HV | | BCC α′ (vol. %) | | Twin in FCC γ (area %) | | Twin in BCC α′ (area %) | |
|---|---|---|---|---|---|---|---|---|---|---|---|---|
| | 37 µm (CG) | 0.24 µm (UFG) | 37 µm (CG) | 0.24 µm (UFG) | 37 µm (CG) | 0.24 µm (UFG) | 37 µm (CG) | 0.24 µm (UFG) | 37 µm (CG) | 0.24 µm (UFG) | 37 µm (CG) | 0.24 µm (UFG) |
| 0.00 | | | 0 | 0 | 186 | 490 | 5.0 | 9.6 | - | - | - | - |
| 0.22 | | | 995 | 1810 | 372 | 551 | 7.6 | 42.0 | 4.4 | 0.0 | 0.0 | 0.4 |
| 0.30 | 207 | 1104 | 1570 | 2380 | 461 | 559 | 18.4 | 47.5 | 4.6 | 0.2 | 3.7 | 0.5 |
| 0.37 | | | 2240 | 3030 | 501 | 570 | 37.2 | 71.7 | 2.3 | 0.2 | 5.6 | 0.5 |
| 0.47 | | | 3570 | 4460 | 541 | 612 | 49.7 | 93.2 | * | * | * | * |
| 0.53 | | | 4790 | 5950 | 550 | 641 | 50.2 | 95.6 | 0.4 | 0.1 | 6.7 | 0.5 |

* No quantitative data at this strain level

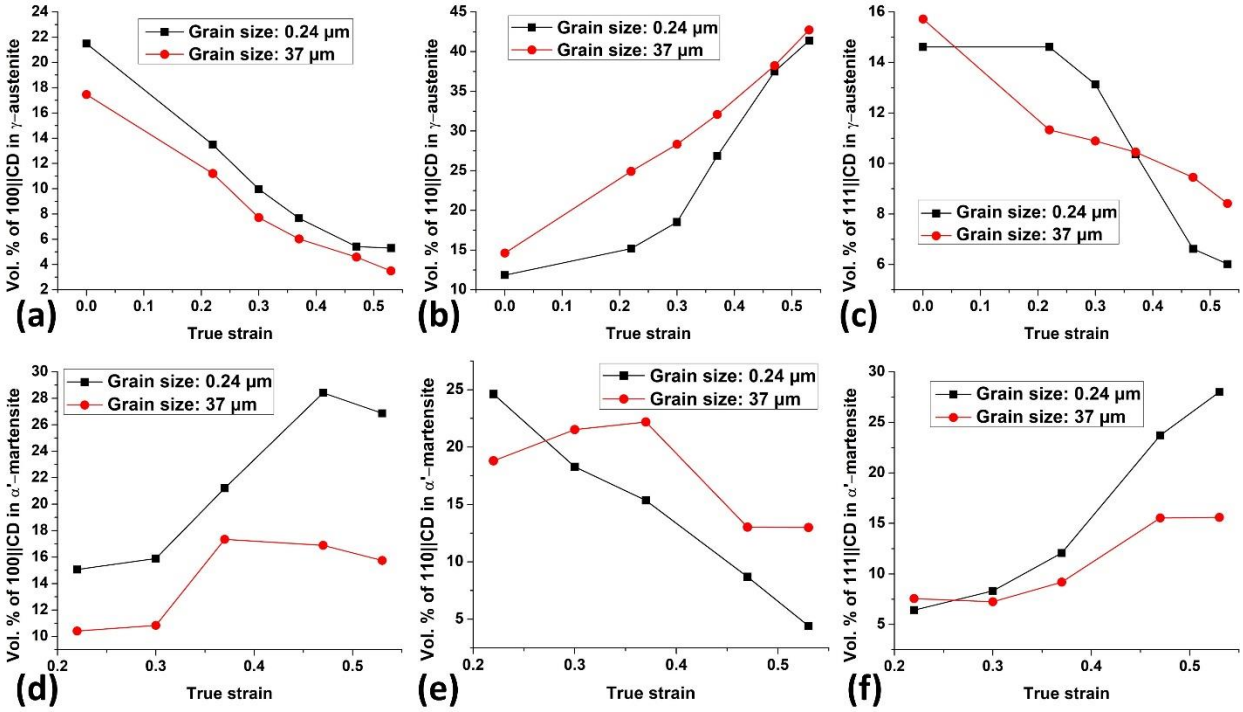


Fig. 8.15. Volume percent of selected texture fibres in (a-c) FCC γ -austenite and (d-f) BCC α′-martensite phases of the deformed specimens.

8.3.2.4 Phase transformation path for α′-martensite and orientation relationships between phases

In the present study, it is established that ε-martensite is a transition phase that acts as a precursor to the formation of α′-martensite in a compressed AISI 321 austenitic stainless steel specimen (Figs. 8.3, 8.4, 8.6, 8.10 and 8.11). However, the phase transformation sequence can follow both

FCC γ → BCC α′ and FCC γ → HCP ε→ BCC α′; irrespective of grain size. This is confirmed by the analysis of selected grains in both the UFG (Fig. 8.16) and CG (Fig. 8.17) specimens. At 0.30 strain (for UFG specimen), grain 6 (Fig. 8.16a) shows the evolution of ε-martensite phase in an austenite grain. Both the ε-martensite and the austenite phases have Shoji-Nishiyama's (S-N) orientation relationship $\{111\}_{\gamma}\|\{0001\}_{\varepsilon}$ obeyed between them. Meanwhile, grain 8 (Fig. 8.16b) shows the coexistence of the martensite (ε and α′) and austenite phases with S-N, Kurdjumov-Sachs (K-S) $\{111\}_{\gamma}\|\{110\}_{\alpha'}$ and Burgers (B) $\{0001\}_{\varepsilon}\|\{110\}_{\alpha'}$ orientation relationships existing between the γ & ε, γ & α′ and ε & α′ phases, respectively.

At 0.37 true strain, where there is near-absence of ε-martensite in UFG specimen, grain 13 (Fig. 8.16c) shows α′ transform from γ without a transiting phase (ε-martensite). Hence, the parent (γ) and product (α′) phases obey the K-S orientation relationship as shown by the coincidence of $\{111\}_{\gamma}$ and $\{110\}_{\alpha'}$ poles. The band contrast, Schmid factor and Kernel misorientation maps in Fig. 8.16 shows that the product phases inherit the microstructural features of the parent phase. The observations that confirm the existence of FCC γ → HCP ε → BCC α′ transformation also occured in the selected grains from EBSD maps of the CG specimens in Fig. 8.17. The two-phase transformation paths (FCC γ → BCC α′ and FCC γ → HCP ε→ BCC α′) were also reported in Fe-Mn-Al alloys in a previous study [253]. The development of ε-martensite as a transition phase, however, depends on the chemical composition of the material, test temperature and the amount of strain [220].

### 8.3.3 VPSC modeling

The Voce hardening parameters used in this study were adjusted to achieve a good agreement between the measured stress-strain curve and the VPSC simulated one, as shown in Fig. 8.18. The fitted Voce parameters for each modeling case are listed in Table 8.2. The negative $\tau_1$ on Table 8.2 for CG sample means both slip and twin softens during uniaxial compression. Based on the experimental evidence presented in this work, martensitic phase transformation, slip, and mechanical twinning are activated in the CG specimen during compression test while the operation of slip systems and martensitic phase transformation occurred in UFG specimen. All of these (mechanical twinning, slip, and phase transformation) play important roles in strain hardening and texture evolution during compression. However, VPSC only uses slip and twinning as the active deformation mechanisms for predicting stress-strain curves. Therefore, as shown in Table 8.2, slip

and twinning were considered in VPSC modeling as the active systems in the CG specimen, and only slip system in the UFG specimen.

Figure 8.18 shows that VPSC successfully predicted stress-strain curves for both CG and UFG specimens until the plastic strains of 0.16 and 0.23, respectively, are attained. The deviations of VPSC simulated curves from experimental curves in CG and UFG specimens are related to the

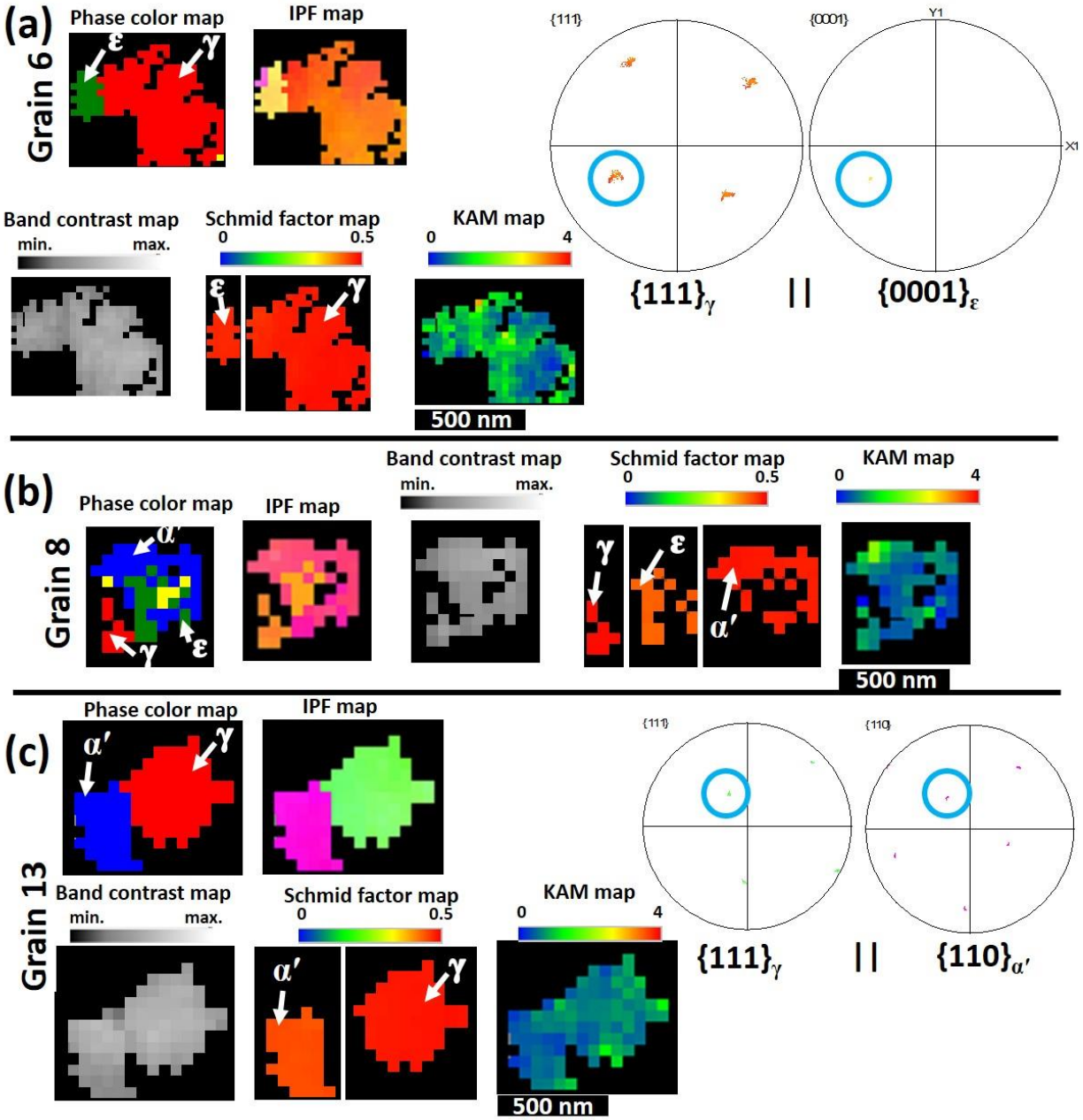


Fig. 8.16. EBSD analysis of (a) grains 6 and 8 in Fig. 8.3e; (c) grain 13 in Fig. 8.5f.

occurrence of martensitic phase transformation during compression. This is because VPSC only uses slip and twinning as the active deformation mechanisms for predicting the stress-strain curves. The same deviation has been reported in another previous study [78]. The variation between the experimental and simulated curves occurs in UFG specimen at lower plastic strain, which affirms an earlier onset of martensitic phase transformation in UFG than in CG specimens. This also agrees well with the experimental results presented in Figs. 8.3, 8.4 and 8.11c, which suggest possible earlier onset of phase transformation in the UFG specimen under compression. Hence, further VPSC simulated results focus on the operating mechanisms in the austenitic phase.

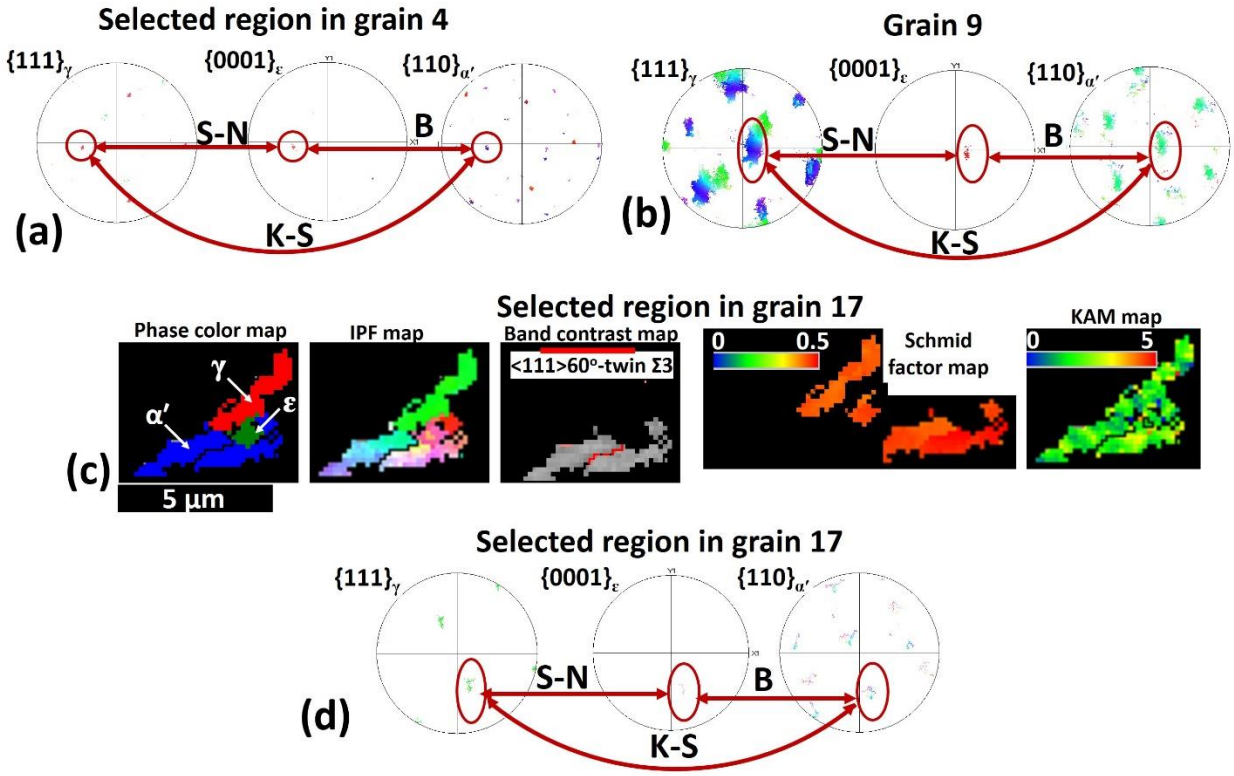


Fig. 8.17. Pole figures of $\{111\}_{\gamma}$, $\{0001\}_{\varepsilon}$ and $\{110\}_{\alpha'}$ for selected region in (a) grain 4 of Fig. 8.4b, (b) grain 9 of Fig. 8.6b and (d) grain 17 of Fig. 8.10; (c) EBSD maps of selected region in grain 17 of Fig. 8.10.

Table 8.2. Voce hardening parameters used in the VPSC model for slip and twining in CG and UFG specimens.

| Sample | Deformation mechanism | $\tau_o$ (MPa) | $\tau_1$ (MPa) | $\theta_o$ (MPa) | $\theta_1$ (MPa) |
|---|---|---|---|---|---|
| CG | Slip {111}<110> | 107 | -70 | 600 | 900 |
| | Twin {111}<112> | 118 | -111.2 | 794 | 1140 |
| UFG | Slip {111}<110> | 410 | 30 | 320 | 830 |

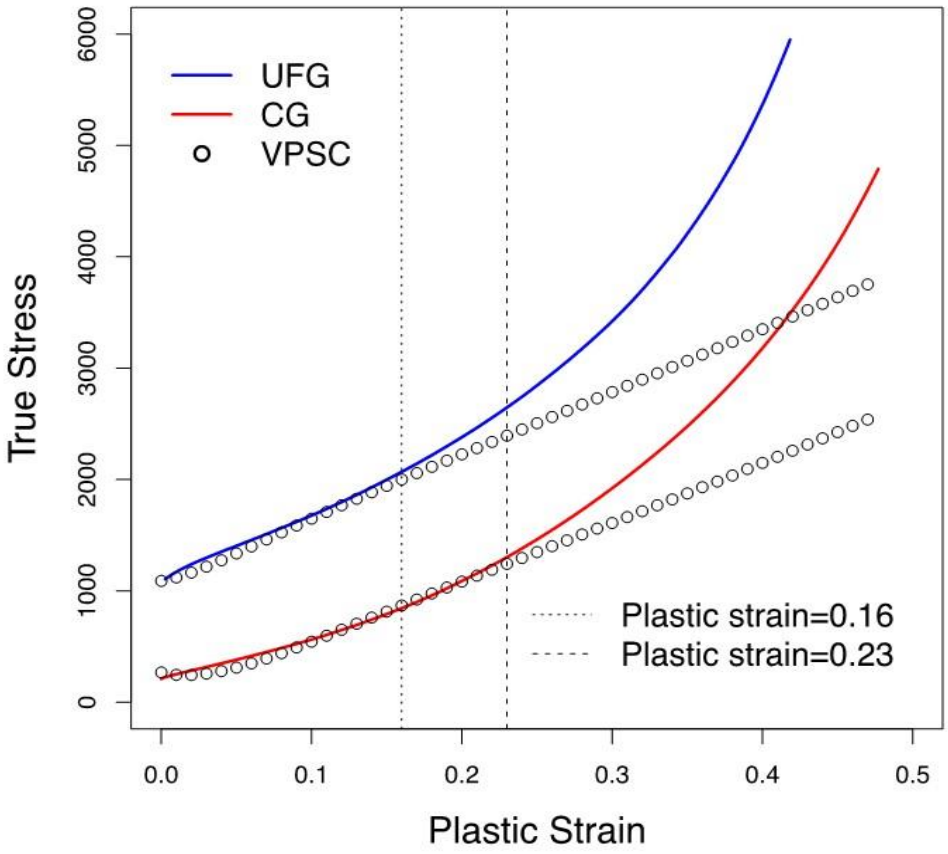


Fig. 8.18. True stress vs. plastic strain curves, the experimental and VPSC simulated curves for ultra fine grains (UFG) and coarse grains (CG). The deviation of experimental curves from simulated ones is related to the onset of the martensitic phase transformation that occurs at different strain levels.

Figure 8.19 shows the variations in relative activities of slip/twinning and slip in the austenite phase as a function of plastic strain during the compression of CG and UFG specimens, respectively. The results show that twinning decreases during straining, which agrees with the relative activities reported in other publications [254]. Slip deformation is significantly more active than twinning in CG specimen that is related to higher hardening parameters assigned to the twinning mode. Some grains deform by twinning in CG steels due to activation of the twin system during deformation. Figure 8.20 shows measured and calculated twin volume fraction. As also deduced from activation of the twin system in Fig. 8.19a, twin volume fraction increases with plastic strain until ~0.15 and remains constant with increasing plastic strain (Fig. 8.20). Figure 8.21 shows the simulated IPF in CG and UFG steel, which are in good agreement with the experimental ones in Fig. 8.14. The absence of a contour near-<112>||CD fiber in the simulated IPF triangle for the undeformed austenitic phase is the only difference in comparison with the

experimental IPF. The difference between the simulated texture of CG and UFG specimens can also be related to the difference in the initial texture of both sets of specimens. In addition, the occurrence of twinning in CG specimen decreases the intensity of <100>||CD fiber as shown in the IPFs (Fig. 8.21).

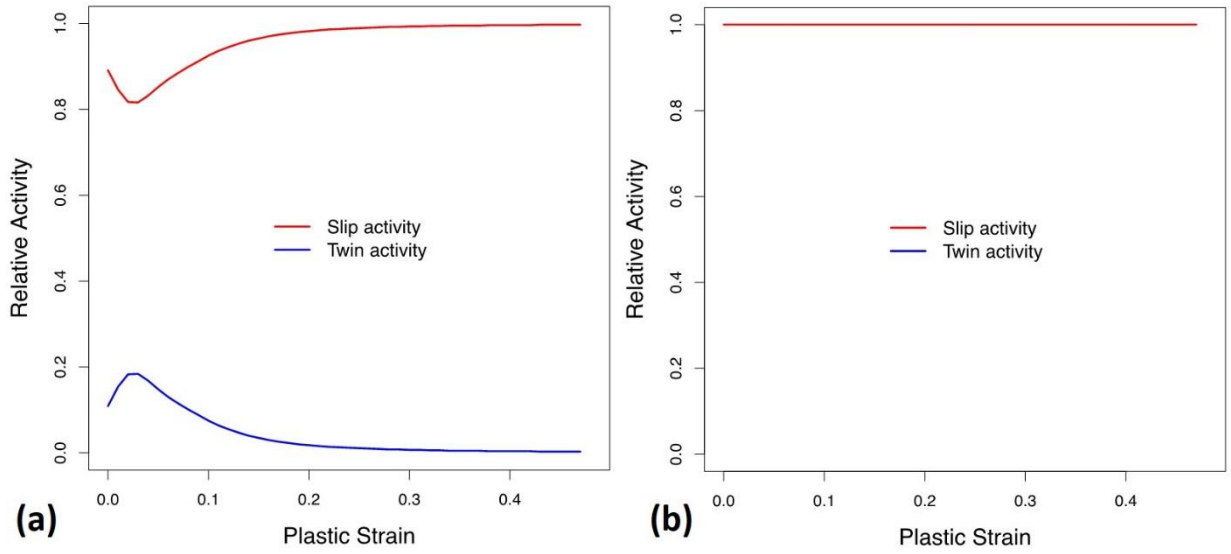


Fig. 8.19. Results of VPSC simulations showing the relative activity of slip and twinning during deformation in (a) CG and (b) UFG specimen.

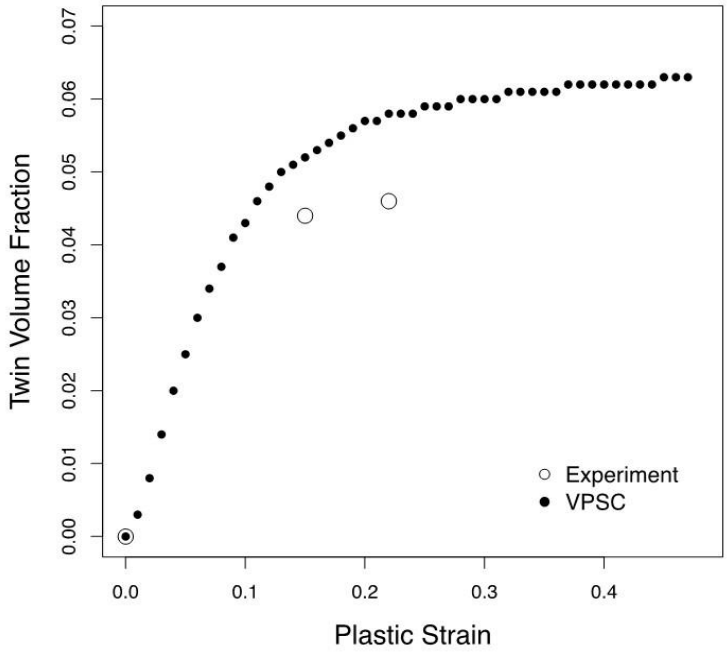


Fig. 8.20. The simulated evolution of the twin volume fraction compared to the measured ones.

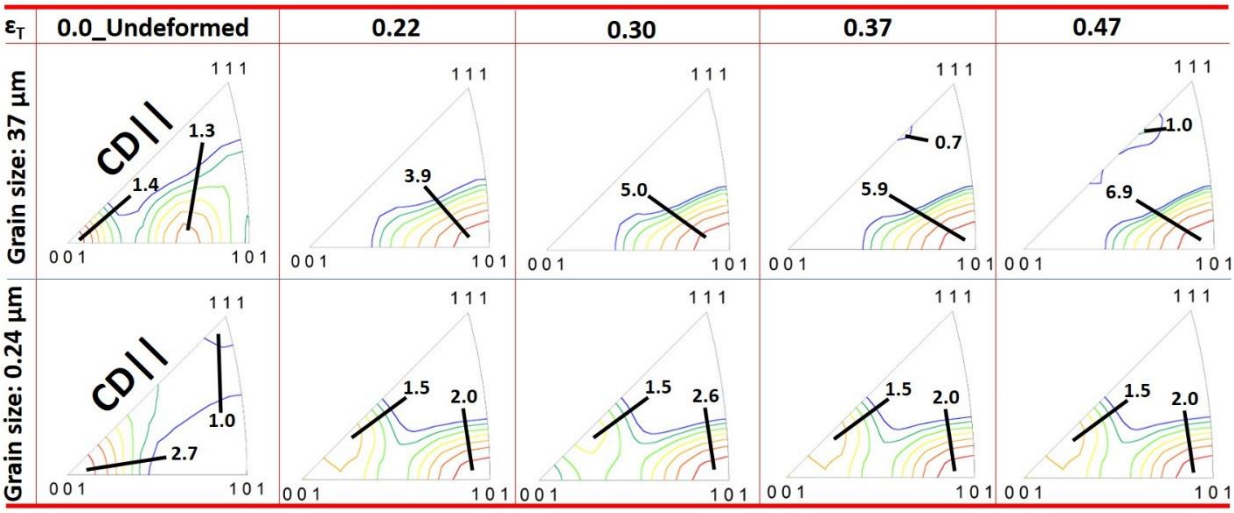


Fig. 8.21. Simulated IPF triangles showing crystallographic fibre texture in the γ-austenite phase of the deformed specimens.

## 8.4 Summary and Conclusions

The effects of grain refinement on the quasi-static compressive behavior of AISI 321 austenitic stainless steel were studied. The following are the conclusions drawn from experimental findings:

1. UFG sample exhibits an excellent combination of high yield strength (~1 GPa) and good strain hardenability, in comparison with the CG sample that shows yield strength ($\sigma_y$) of ~0.2 GPa and compressive strength of 4.8 GPa at 0.53 true strain.
2. The Hall-Petch relation constants, $\sigma_o$, and $K$, for AISI 321 ASS were estimated to be 128 MPa and 478 MPa $\mu m^{-0.5}$, respectively.
3. The strain hardening of both UFG and CG specimens occurs in three distinct stages.
4. Five strengthening sources contribute to hardening of the AISI 321 steel during compressive loading. They are: grain boundary strengthening (most beneficial to UFG specimen), deformation-induced martensite transformation (most beneficial to UFG specimen), deformation twinning acting as barrier to dislocation motion (only beneficial to CG specimen), dislocation-dislocation interactions and multiplication (most beneficial to CG specimen) and dislocation interaction with titanium carbides (most beneficial to CG specimen).
5. CG specimen exhibited a slightly higher strain hardening rate than the UFG specimen up to a critical true strain of 0.4. Above this value, strain hardening in UFG specimen became

higher. The higher hardening rate above 0.4 true strain in UFG specimen is attributed to higher martensitic phase transformation rate and α′ grain boundary strengthening.

6. Slip bands and grain boundary regions of high dislocation densities are observed to be nucleation sites for HCP ε-martensite, BCC α′ and deformation twin in the CG specimen. While grain boundaries and triple junctions are the nucleation sites for martensite in UFG specimen, twinning was not observed due to space restriction effect.
7. While <110>||CD fibre texture is the stable end-orientations in compression for the FCC γ phase, <100> and <111>||CD fibres are predominant for the BCC α′ phase.
8. Irrespective of grain size, Shoji-Nishiyama, Kurdjumov-Sachs and Burgers orientation relationships exist between the γ & ε, γ & α′, and ε & α′ phases, respectively. Hence, the phase transformation sequence follows both FCC γ → BCC α′ and FCC γ → HCP ε→ BCC α′ under the deformation condition used in this study.
9. Experimental results agree well with the VPSC simulation results. The latter confirms that the decrease in the intensity of <100>||CD fiber in CG specimen is due to twinning.
10. The deviations of VPSC simulated stress-strain curves from the experimental curves in coarse and ultra-fine grained specimens at plastic strains of 0.23 and 0.16, respectively, are due to martensitic phase transformation during the compression test. This is because VPSC only uses slip and twinning as the active deformation mechanisms for prediction of stress-strain curve.

# CHAPTER 9

## Strain Rate Sensitivity and Activation Volume of AISI 321 Stainless Steel under Dynamic Impact Loading: Grain Size Effect

A change in the strain rate sensitivity (SRS) upon an increase in strain rate could signal a transition in the dominant rate-controlling deformation mechanism(s). Therefore, it is necessary to understand the effects of grain size on the SRS and activation volume of metastable AISI 321 austenitic stainless steel (ASS) when deformed at high strain rates. The results of an investigation on the SRS and activation volume of three groups of the stainless steel specimens having grain sizes of 0.24 μm (ultrafine grain, UFG), 37 μm (fine grain, FG) and 37 μm (coarse grain, CG) under dynamic impact loading are presented and discussed in this chapter. Using the transmission electron microscopy (TEM) and electron backscattered diffractometry (EBSD) characterization techniques, the dominant deformation mechanism(s) in the UFG, FG and CG specimens are determined. This chapter has been published in "*Materials Characterization"* as follows:

A. A. Tiamiyu, J. A. Szpunar, and A. G. Odeshi, "Strain rate sensitivity and activation volume of AISI 321 stainless steel under dynamic impact loading: grain size effect," *Materials Characterization*, vol. 154, pp. 7-19, 2019.

My contributions to this paper include a review of the relevant literature, design and carrying out the experiments, analysis of test results and preparation of the manuscript. My supervisors (Prof. Akindele Odeshi and Prof. Jerzy Szpunar) reviewed the manuscript, and their comments and suggestions were adressed before the manuscript was submitted for publication. The present chapter is a modified version of the published paper. Repetition is avoided by removing the portions already covered in Chapter 3 (Materials and methodology). The copyright permission for manuscript reuse was obtained and provided in APPENDIX C.

### Abstract

The rapid change in strain rate sensitivity (SRS) of metals at a critical true strain rate ($\dot{\varepsilon}_{Tc}$) is commonly attributed to change in rate-controlling deformation mechanism from thermally-activated process to viscous drag. In this study, metastable AISI 321 stainless steel with grain sizes of 0.24 μm (ultrafine [G1]), 3 μm (fine [G2]) and 37 μm (coarse [G3]) was deformed under high

strain-rate loading regime. A change in SRS with increasing $\dot{\varepsilon}_T$ is observed only in G2 and G3 and it occurs at $\dot{\varepsilon}_{Tc}$ of ~5900 and 6800 $s^{-1}$, respectively; suggesting that grain size have an effect on the switch of rate-controlling deformation mechanisms. While the SRS of G1 is 0.101 and unchanged, those of G2 and G3 change from 0.094 to 0.326 and 0.091 to 0.634, respectively, once $\dot{\varepsilon}_{Tc}$ is reached. Similarly, the estimated activation volume in G1 specimen is ~$1.57b^3$, while those of G2 and G3 specimens change from ~$2.95b^3$ to ~$0.65b^3$ and from ~$4.10b^3$ to ~$0.45b^3$, respectively. Analysis of the deformed specimens using XRD, EBSD and TEM techniques revealed that the complexities in the deformation mechanisms in G2 and G3 specimens led to a change in $\dot{\varepsilon}_{Tc}$. Constant SRS in G1 specimen indicated no change in the operational deformation mechanisms.

*Keywords: AISI 321 austenitic stainless steel; Slip; Twinning; Phase transformation; Strain rate sensitivity; Activation volume*

## 9.1 Introduction

The strain rate sensitivity (SRS) of a metal describes the effect of strain rate on the plastic flow behaviour of that metal at constant strain and temperature [255]. Denoted by $m$ in Eqn. 9.1, SRS reflects the plastic behaviour by taking into account dislocation density, dislocation velocity and obstacles to dislocation motion. Some of these dislocation barriers may include grain boundaries, deformation twins, precipitates, etc. The implication of this is that an observable change in SRS upon an increase in strain rate could signal a transition in the dominant rate-controlling deformation mechanism [256]. Recently, Wang et al. [257] for the first time studied the effects of SRS on the mechanical behavior of Mg alloys at a wide range of strain-rates using an improved self-consistent polycrystal plasticity model. The strength of this work was hinged on the fact that Mg alloys exhibit multiple SRSs that are associated with different deformation mechanisms in operation during deformation. Hence, these authors used different SRSs for different deformation mechanisms to examine the strain-rate dependent behaviors of Mg alloys rather than a single SRS scheme commonly employed in numerical modelling. Amongst other use, SRS has been successfully used in the construction of phase diagram [258]. Activation volume, $\vartheta^*$, as expressed in Eqn. 9.2, can also be used to assess the rate-controlling deformation mechanism in metals. $\vartheta^*$ is based on thermal activation analysis and it is defined as the separation distance between points of dislocation intersection [259]. Hence, as plastic strain increases, the $\vartheta^*$ decreases due to the

multiplication of dislocations. The analysis of both $m$ and $\vartheta^*$ will, therefore, expatiate on the rate-controlling deformation mechanisms during the plastic deformation of metals [260].

$$m = \partial log\ \sigma_T / \partial log\ \dot{\varepsilon}_T \quad \ldots 9.1$$

where $\sigma_T$ and $\dot{\varepsilon}_T$ are true stress and true strain rate, respectively.

$$\vartheta^* = kT/m\sigma_T \quad \ldots 9.2$$

where $T$, and $k$ are temperature, and Boltzmann constant, respectively.

Revealing active deformation mechanisms by experimentally determining the mechanical response of materials to mechanical loading at different strain-rate regimes has been adopted in a number of studies. At both low and high strain rate regimes, alloys such as AISI 304L stainless steel [261,262], AISI 309 stainless steel [262], AA 2024-T351 aluminum alloy [259], Cu [260,263], Fe and Ta [260], AA 6061-T6 aluminum alloy [264], AA 1050 and AA 5052 aluminum alloys [265] etc., have been studied. Using a split Hopkinson pressure bar (SHPB) system, cylindrical test specimens of AISI 304L stainless steel (with or without prestrain) were subjected to compressive loads at strain rates ranging between 800 and 5000 $s^{-1}$ up to 0.1, 0.2 and 0.3 strain levels [261]. The authors observed increased work-hardening rate with increasing strain and strain rate while higher rate of hardening was observed in the prestrained specimens. In comparison with specimens subjected to quasi-static compressive loading, the authors also observed a rapid increase in SRS at strain rate above 1000 $s^{-1}$. This rapid change in SRS was attributed to the change in rate-controlling deformation mechanism from thermally-activated motion of dislocation during quasi-static compression to viscous drag during dynamic shock loading [266-269]. The strain rate ($\dot{\varepsilon}$) for thermally-activated process during plastic deformation can be described by the Arrhenius-type equation presented in Eqn. 9.3 [270]:

$$\dot{\varepsilon} = \dot{\varepsilon}_o \exp\left(\frac{-\Delta G(\sigma_a)}{k_B T}\right) \quad \ldots 9.3$$

where $\dot{\varepsilon}_o$, $\sigma_a$, $k_B$, $T$ and $\Delta G$ are the material pre-exponential constant, applied stress, Boltzmann constant, absolute temperature and the activation energy, respectively. In other previous studies [268,271], the thermally-activated motion of dislocation is reported to dominate up to a strain rate of ~3000 $s^{-1}$ before transition (i.e. before the steep rise in SRS) to viscosity drag mechanism. Strengthening due to twin-dislocation, precipitate-dislocation, dislocation-dislocation and

dislocation-grain boundary interactions, dominates at strain rates below ~3000 $s^{-1}$. On the other hand, viscous dislocation drag dominates the flow stress at strain rate beyond ~3000 $s^{-1}$. In both low and high strain rate regimes, the kinetics of generation and motion of dislocations govern plastic deformation. It is, therefore, the mechanism that results in the most rapid relaxation of the imposed elastic stress that will be the dominant plastic deformation mechanisms [272].

Investigating the role of temperature on the variability of SRS of AA 2024-T351 alloy deformed over a wide range of strain rate, Khan and Liu [259] reported that the specimens deformed at high strain rates showed a positive SRS. However, the effect of strain rate on strength was reported to be independent of temperature while the alloy specimens deformed under quasi-static loading regime exhibited a temperature-dependent SRS. Using coupled dislocation dynamics and diffusion kinetics simulations, Ahmed and Hartmaier [263] studied the mechanical behavior of metals whose material constants are similar to those of copper. The authors reported higher SRS for fine-grained material than for coarse-grained materials at a constant temperature. Meanwhile, SRS for fine- and coarse-grained materials were determined to be temperature-dependent and temperature–independent, respectively. Investigating the SRS and activation volume of FCC (Cu) and BCC (Fe and Ta) metals with ultrafine-grained (UFG) and/or nanocrystalline (NC) structure using tensile strain rate jump test, Wei et al. [260] observed higher SRS for UFG/NC FCC metals and lower SRS for UFG/NC BCC metals in comparison with specimens with coarse-grained structure. They reported lower activation volume for UFG FCC Cu, whereas those of UFG BCC Fe and Ta remained unchanged in comparison with coarse-grained specimens.

In this study, the strain rate sensitivity of AISI 321 austenitic stainless steel impacted only in the high strain rate regime is investigated. In addition to investigating the dynamic impact response of the steel, the following questions are intended to be answered in this manuscript: (a) How does grain size influence the SRS of AISI 321 steel? (b) Could there be a rapid change in SRS at a particular threshold of strain rate? (c) If the answer to question (b) is yes, what is the strain rate threshold at which rapid change in SRS occurs in AISI 321 steel and how does deformation mechanism (which is a function of grain size) influence it?

AISI 321 is a variant of AISI 304 stainless steel that is stabilized with titanium (Ti) to reduce sensitization during high-temperature applications. It has an FCC crystal structure with low

stacking fault energy [20]. Its FCC structure (γ-austenite phase) can transform to BCC structure (α'-martensite) during plastic deformation. Due to its corrosion resistance [3], AISI 321 finds application in components designed for nuclear power and chemical reactors, automobile exhaust systems, aircraft exhaust stacks and exhaust manifolds, pressure vessels, mufflers for engines, carburetors, expansion bellows, stack liners, etc. It is important to understand the mechanical response of this alloy to impact loading due to the possibility of its exposure to such an extreme loading condition in such applications. SHPB was used to deform the AISI 321 steel specimens (with varying grains sizes) at high strain rates. X-ray diffraction (XRD) and electron microscopic (SEM, EBSD and TEM) techniques were used to characterize impacted specimens to understand the underlying mechanism of deformation or strengthening in the alloy.

## 9.2 Materials and methodology

Ultrafine (0.24 μm), fine (3 μm) and coarse (37 μm) grained AISI 321 austenitic stainless steel plate whose nominal composition is presented in Table 2.1 were investigated in this study. The steel was received in hot-rolled condition with coarse grain structure (G3). Fine (G2) and ultrafine (G1) were obtained by annealing 50% cryo-rolled as-received (G3) sample at 800 ℃ (360 mins) and 750 ℃ (10 mins), respectively. The cryo-rolling process is described in Section 3.2.

High strain-rate test using the SHPB system was conducted on 4mm x 4mm cylindrical test specimens machined from the as-received and refined alloys. These specimens were machined along the rolling direction (RD) of the steel plate and compression direction (CD) is parallel to the RD. G1, G2 and G3 samples were subjected to common projectile's firing pressures (FP) at 50, 60, 70, 80, 90, 100, 110, 120 and 130 kPa. Upon generating the engineering stress, strain, and strain rate data from Eqns. 3.1-3.3, the $\sigma_T$, true strain ($\varepsilon_T$), and $\dot{\varepsilon}_T$ data were obtained using Eqns. 9.4-9.6 [73], respectively;

$$\sigma_T = \sigma[1 - \varepsilon] \quad \ldots 9.4$$

$$\varepsilon_T = -ln[1 - \varepsilon] \quad \ldots 9.5$$

$$\dot{\varepsilon}_T = \frac{\dot{\varepsilon}}{1-\varepsilon} \quad \ldots 9.6$$

The dynamic impact tests, hardness tests and microstructural analyses such as the optical microscopic examination, TEM, EBSD, X-ray diffractometry and Feritscope measurements were conducted as described in Chapter three.

## 9.3 Results and discussion

### 9.3.1 Microstructural evaluation before deformation

Figure 9.1 shows the EBSD band contrast maps and the TEM micrographs for the three starting microstructures (UFG-0.24 μm [G1], fine-3 μm [G2] and coarse-37 μm [G3]) of the investigated AISI 321 stainless steel. Besides revealing the morphology of the grain size, both EBSD and TEM techniques confirm the absence of annealing twins in UFG specimen and their (annealing twins) increase in fraction with an increase in grain size. The absence of annealing twins in UFG sample (Fig. 9.1a and d) suggests that 0.24 μm is below the critical grain size at which annealing twin can develop in AISI 321 stainless steel. A similar observation has also been reported in UFG AISI 304 stainless steel (~0.27 μm grain size) that was developed by accumulative rolling (up to 67% total reduction) followed by annealing at 823 K for 150 s [81]. The presence of nano-sized carbide precipitates identified by EDS technique as TiC was observed in the bulk of the investigated steel in the current study (insets [a2 and a3] in Fig. 7.1).

### 9.3.2 Dynamic mechanical behavior, martensitic phase transformation and hardness

Typical dynamic true stress-true strain curves and their corresponding strain hardening rate curves for G1, G2 and G3 specimens, deformed using the firing pressures of 50, 60 and 70 kPa are presented in Fig. 9.2. For brevity, other curves deformed at higher firing pressures are not included. The curves are uniquely characterized by yield, strain hardening and thermal softening regions. The summary of the mechanical data generated from the true stress-true strain curves is provided in Table 1. The competition between strain hardening and thermal softening are characteristics of the mechanical behaviour of metals under dynamic shock-loading conditions. This accounts for the rising (strain hardening) and falling (thermal softening) observed in the dynamic stress-strain curves. Although G1 specimens exhibit a higher yield strength, the strain hardening rate curves in Fig. 9.2d-f indicates the G1 specimen as the least strain-hardened specimen, compared to G2 and G3 specimens in the plastic zone. Unlike in stable alloys where hardening is solely attributed to dislocations, their multiplication, and their interaction with barriers [273], strain hardening in

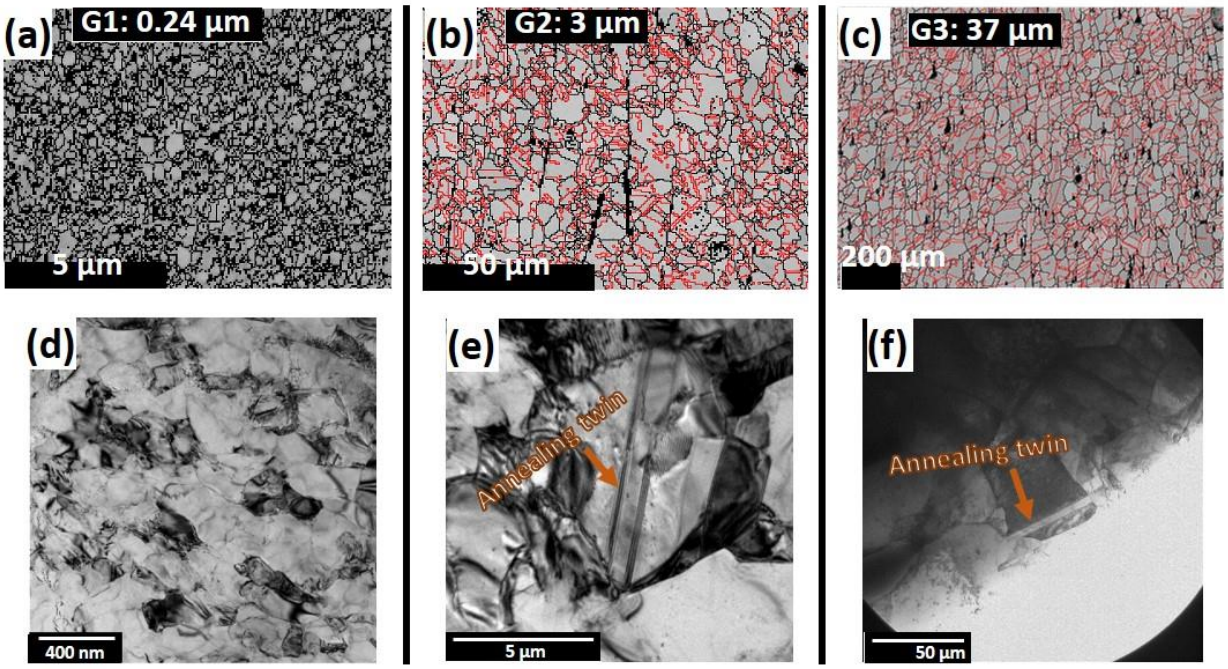


Fig. 9.1. (a-c) EBSD band contrast maps and (d-f) TEM bright field micrographs of undeformed (a, d) G1, (b, e) G2, and (c, f) G3 samples. Black and red lines in the EBSD maps are high angle grain boundaries and twin boundaries, respectively.

metastable AISI 321 stainless steel has been reported to be from multiple strengthening sources during plastic deformation [208]. Meanwhile, thermal softening occur when about 90 % of the kinetic energy of the projectile is converted to thermal energy during high strain-rate deformation [75]; leading subsequently to temperature rise in the specimen.

At a common firing pressure, say, 50 kPa, Fig. 9.2 shows that different strain rates (and strain) were generated in the G1 (1300 $s^{-1}$), G2 (2200 $s^{-1}$) and G3 (2900 $s^{-1}$) specimens. Consequently, at any firing pressure, highest and lowest strain rates (and strain) were recorded in G3 and G1 specimens, respectively. This affirms the effect of grain size on the dynamic impact response of the AISI 321 steel as G1 (UFG) specimens also show higher compressive strength than those of G2 (fine) and G3 (coarse) specimens; obeying the Hall-Petch relation [274]. X-ray diffraction patterns (Fig. 9.3(a-c)) confirms the evolution of deformation-induced martensitic phase transformation during high-strain-rate deformation. This is because the intensity of α'-peaks [$(110)_{\alpha'}$ and $(200)_{\alpha'}$] increases with increase in FP/strain rate at the expense of the γ-peaks [$(111)_{\gamma}$ and $(200)_{\gamma}$] of the starting microstructure. The intensity of α'-peaks are higher in G1 than G2 and G3 specimens; showing lower stability of austenite during dynamic deformation in G1 specimens.

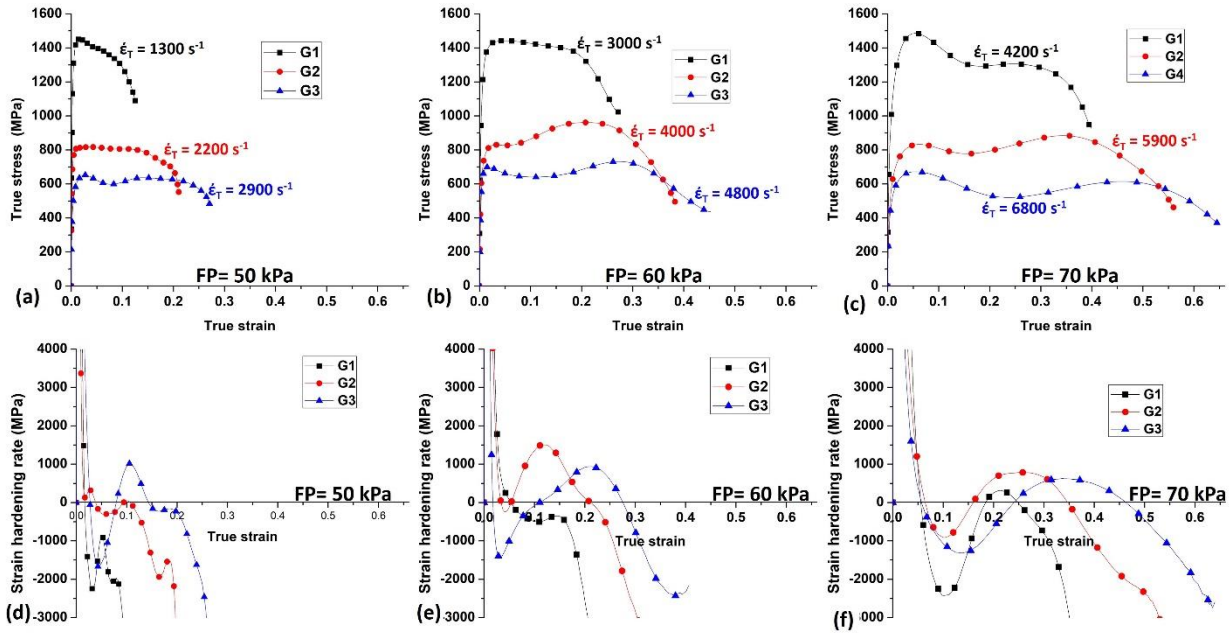


Fig. 9.2. Typical (a-c) true stress-true strain and (d-f) corresponding strain hardening rate curves of deformed G1, G2 and G3 specimens.

Meanwhile, the reverse hold for γ-peaks (i.e. higher intensity of γ-peaks in G3); implying higher stability of austenite in G3 specimens. However, increasing the FP/strain rate beyond a critical value, the intensity of α'-peaks drop again i.e. the development of α' is suppressed. This behavior is also confirmed in Fig. 9.3d that shows volume percent of α'-martensite, as measured using Feritscope, in the impacted specimens. The onset of the drop in the fraction of α' occurred at strain rates in the range 6000-8000 $s^{-1}$ (marked in Fig. 9.3d). The suppression of deformation-induced martensite above this strain-rate range is a result of the significant temperature rise (adiabatic heating) in the specimen which is associated with high strain rate testing conditions [255,262,275,276]. Among other factors such as alloy content, deformation temperature, pre-strain, stress state, deformation mechanism, and deformation methods, strain and strain rate are important factors reported to influence the fraction of deformation-induced martensite in stainless steel [19,66,105].

Table 9.1. Comparison table of observations from the dynamic impact responses of AISI 321 steel specimens.

| Grain structure | FP, kPa | IV, $ms^{-1}$ | IM, $kg.ms^{-1}$ | True strain rate, $s^{-1}$ | True strain | Type of ASB |
|---|---|---|---|---|---|---|
| G1 | 50 | 4.93 | 10 | 1300 | 0.13 | NO |
| G2 | | | | 2200 | 0.21 | No |
| **G3** | | | | **2900** | **0.27** | **NO** |
| G1 | 60 | 6.86 | 14 | 3000 | 0.27 | NO |
| G2 | | | | 4000 | 0.38 | No |
| **G3** | | | | **4800** | **0.45** | **NO** |
| G1 | 70 | 8.95 | 18 | 4200 | 0.40 | DSB |
| G2 | | | | 5900 | 0.56 | DSB |
| **G3** | | | | **6800** | **0.65** | **NO** |
| G1 | 80 | 9.44 | 20 | 6400 | 0.60 | DSB+TSB |
| G2 | | | | 8000 | 0.76 | DSB |
| **G3** | | | | **8800** | **0.84** | **DSB** |
| G1 | 90 | 10.38 | 21 | 8200 | 0.78 | TSB |
| G2 | | | | 9500 | 0.89 | TSB |
| **G3** | | | | **11500** | **0.99** | **DSB** |
| G1 | 100 | 11.51 | 23 | 9800 | 0.92 | TSB |
| G2 | | | | 11400 | 1.05 | TSB |
| **G3** | | | | **12000** | **1.14** | **TSB** |
| G1 | 110 | 12.88 | 26 | 11700 | 1.11 | TSB |
| G2 | | | | 13000 | 1.27 | TSB |
| **G3** | | | | **13400** | **1.30** | **TSB** |
| G1 | 120 | 15.47 | 31 | 12400 | 1.20 | TSB |
| G2 | | | | 14000 | 1.39 | TSB |
| **G3** | | | | **14500** | **1.43** | **TSB** |
| G1 | 130 | 17.71 | 36 | 13800 | 1.35 | TSB |
| G2 | | | | 14600 | 1.47 | TSB |
| **G3** | | | | **16000** | **1.56** | **TSB** |

G1, G2 and G3 are specimens with grain sizes of 0.24, 3 and 37 μm, resp., FP- Firing pressure, IM- Impact momentum, IV- impact velocity, ASB- Adiabatic shear band, DSB- Deformed shear band, TSB- Transformed shear band.

Besides adiabatic heating, grain size also plays a significant role in austenite stability during deformation. From Figs. 9.3c and d, the stability of austenite in the coarse-grained specimen (G3) is so high that phase transformation barely occurred. Hence, stronger austenite stability in G3 (without downplaying the effect of adiabatic heating within specimen) is more responsible for low α' fraction. This is because, from Eqn. 2.6, higher adiabatic heating is expected in G1 (UFG) specimens than in G2 and G3 specimens; as already confirmed elsewhere [277]. Based on this

observation, G1 logically should possess a lower fraction of martensite. However, the reverse is the case, which could be due to more α' nucleation sites such as grain boundaries and their triple junctions in ultrafine austenite grains [278]. Figure 9.3e shows the effect of grain size and strain rate on the Vickers hardness of the impacted G1, G2 and G3 specimens. While the hardness is inversely proportional to grain size, strain rate shows a direct relation to the hardness value of the investigated steel. Although hardening in metastable austenitic stainless steels is closely related to the fraction of α' [66], other hardening sources are found in AISI 321 stainless steel [277].

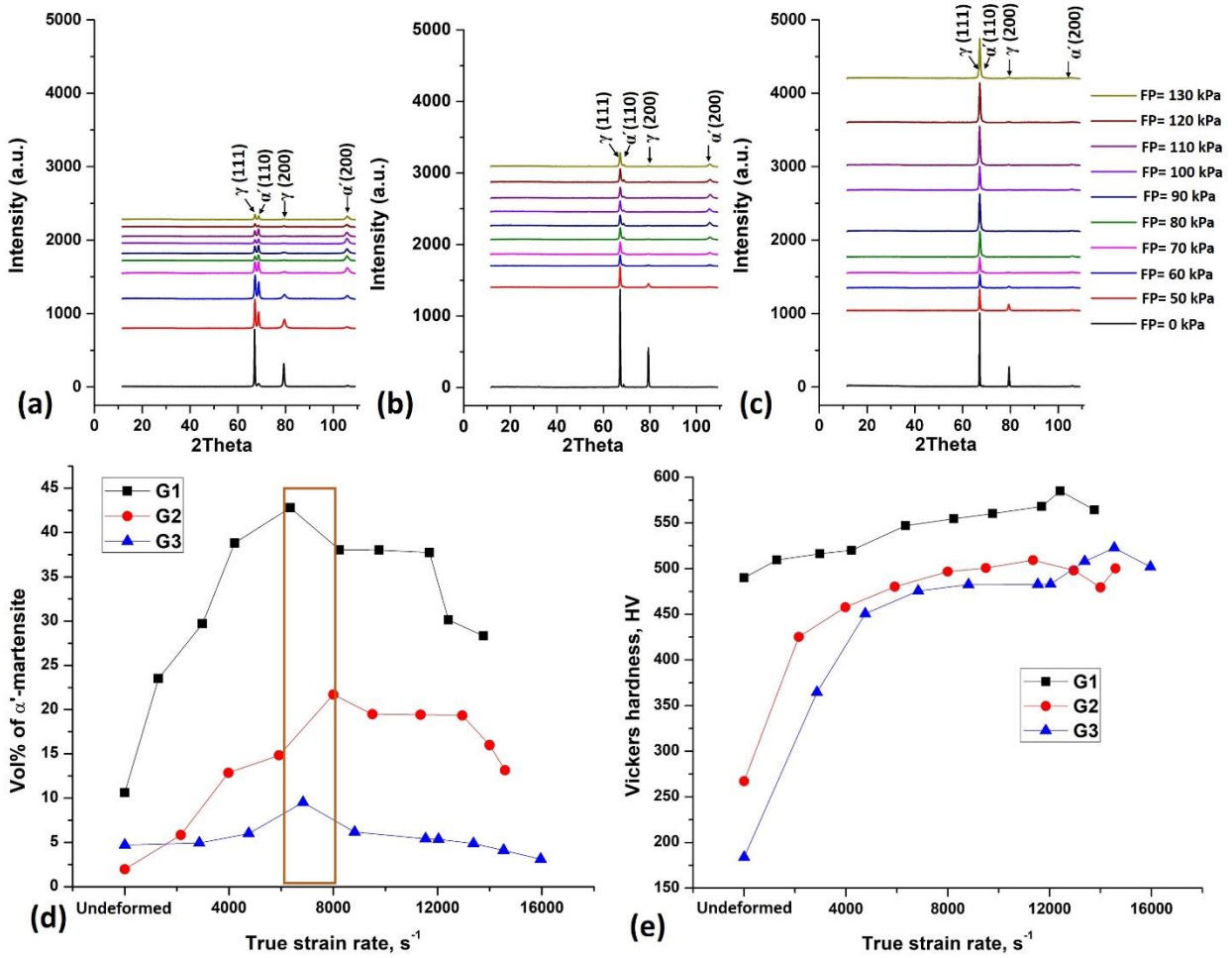


Fig. 9.3. X-ray diffraction patterns for (a) G1, (b) G2 and (c) G3 specimens; (d) α'-martensite vol%-true strain rate and (e) Vickers hardness-true strain rate plots.

### 9.3.3 Strain-rate sensitivity and activation volume

#### 9.3.3.1 Role of grain size

Figure 9.4 shows the effect of grain size on the strain rate sensitivity (*m)* of AISI 321 austenitic stainless steel. Positive *m* values are recorded at all investigated strain-rates which are characteristic of specimens subjected to dynamic impact loading condition [279]. While there is an observable rapid change in the value of *m* for G2 (fine) and G3 (coarse) specimens at the respective critical true strain rates, $\dot{\varepsilon}_{Tc}^{fg}$ and $\dot{\varepsilon}_{Tc}^{cg}$ that partition the curves into two stages, the value of *m* for G1 (UFG) specimen remains unchanged. However, at stage I, G1 specimens exhibit higher *m*-value than those of G2 and G3 specimens while higher value of *m* was recorded for G3 specimens at stage II (Fig. 9.4). The behavior in stage I (i.e. an increase in *m* with decreasing grain size) are general features in both FCC and BCC metals [263,280]. Higher *m*-value for G1 (UFG) samples in stage I could be due to low forest dislocation density in the UFG interior, yet, possessing higher grain boundary area [281]. The true strain rate thresholds at which the rapid change of *m* occurs are ~5900 and 6800 $s^{-1}$ for G2 and G3 specimens, respectively (Table 9.2). The steep change in *m*-value was reported to be at a strain rate threshold between 1800 and 4000 $s^{-1}$ [269] or above 3000 $s^{-1}$ [268] in FCC metals. This was suggested to be due to the transition in the rate-controlling mechanism of the dislocation motion from a thermally activated process to viscous drag [261,268]. Viscous drag is the slow down of dislocation motion due to the interaction of dislocations with lattice thermal vibrations during dislocation-phonon interaction. This observation is also corroborated by the results of a recent study by Tsai et al. [282] who studied the dynamic impact response of a high-entropy CoCrFeMnNi alloy and observed a rapid increase in *m*–value at a critical strain rate of 6000 $s^{-1}$. Hence, it is very likely that there was no change in the rate-controlling mechanism obstructing motions of dislocation in G1 specimens throughout the strain rate range used, while specimens of larger grain sizes (G2 and G3) shows a change in rate-controlling mechanism beyond the $\dot{\varepsilon}_{Tc}$ value [271].

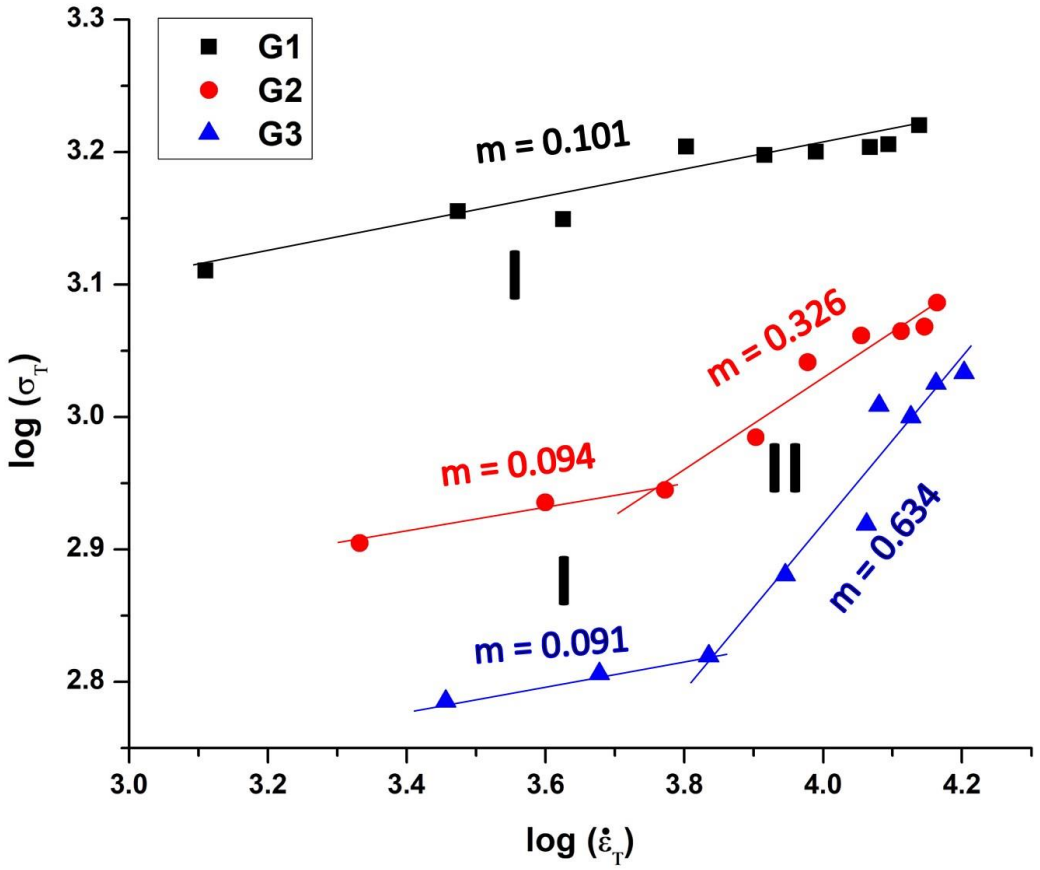


Fig. 9.4. A plot of log of true stress vs log of true strain rate: $\sigma_T$ at $\varepsilon_T = 0.1$.

**Table 9.2** Values of $m$ and $\vartheta^*$ at each stages for AISI 321 steel specimens.

| Grain structure | Stage | True strain rate range, $s^{-1}$ | Strain rate sensitivity, $m$ | Activation volume, $\vartheta^*$ |
|---|---|---|---|---|
| G1 | I | 1300 - 13800 | 0.101 | ~1.57$b^3$ |
| G2 | | ~ 2200 - 5900 | 0.094 | ~2.95$b^3$ |
| **G3** | | **~ 2900 - 6800** | **0.091** | **~4.10$b^3$** |
| G1 | II | - | - | - |
| G2 | | ~ 5900 - 14600 | 0.326 | ~0.65$b^3$ |
| **G3** | | **~ 6800 - 16000** | **0.634** | **~0.45$b^3$** |

To further expatiate on the rate-controlling mechanism in AISI 321 under high strain rate loading conditions, the activation volume, $\vartheta^*$, was estimated using Eqn. 9.2. The common practice is to express $\vartheta^*$ in terms of $b^3$ as presented in Table 9.2, where $b$ is the Burgers vector of the material under investigation. The $b$ (=0.258 nm [283]) in AISI 304 stainless steel was used since AISI 321 is a derivative of AISI 304. Hence, the activation volume ($\vartheta^*$) of G1, G2 and G3 specimens are determined to be ~1.57$b^3$, 2.95$b^3$ and 4.10$b^3$ in stage I, respectively. While the $\vartheta^*$ value for the G1 specimens remained nearly unchanged, 0.65$b^3$ and 0.45$b^3$ are the $\vartheta^*$ values for G2 and G3

specimens in stage II, respectively. The lower $\vartheta^*$ value recorded in G1 specimens at stage I could be due to the lower tendency for the occurrence of the cutting of forest dislocations in UFG materials [284]. These results also confirm that both grain size and strain rates influence the rate-controlling mechanism. From Eqn. 9.2, it can be inferred that $\vartheta^*$ is inversely proportional to $m$ and $\sigma$. Therefore, unlike $m$, $\vartheta^*$ increases with an increase in grain size in stage I, whereas it decreases with increase in grain size in stage II.

9.3.3.2 Role of Deformation and strengthening mechanisms

Strain rate sensitivity and/or activation volume has been successfully used in the previous sub-sections to determine a plausible change in the underlying deformation mechanism during the high strain rate deformation of AISI 321 stainless steel. However, it is necessary to understand which of these mechanisms are in operation at any strain-rate range and their influence on the critical strain rate ($\dot{\varepsilon}_c$). While the occurrence of α' phase transformation in the investigated steel is already discussed in section 3.2 and now verified by EBSD phase maps and TEM micrographs in Fig. 9.5-7, plastic deformation by slip and deformation twinning also occurred as observed in the EBSD and TEM results. It should be noted that the occurrence of slip, α' phase transformation (that leads to transformation-induced plasticity [TRIP]) and deformation twinning (resulting in twinning-induced plasticity [TWIP]) during dynamic shock loading are influenced by the stacking fault energy (SFE) of the deformed metal, which depends on the chemical composition and temperature [50,66,285]. While the main deformation mechanism in metals with SFE >35 mJ/m$^2$ is slip, TWIP will occur in steel with an SFE in the range 18-35 mJ/m$^2$ and TRIP dominates at SFE <18 mJ/m$^2$ [286]. Using Eqn. 2.7 [6], the SFE of AISI 321 is estimated to be 25.1 mJ/m$^2$. This value may be within an SFE range that permits the concurrent occurrence of slip, TRIP and TWIP in AISI 321 steel. Although the stability of α′ is favored in metals with low SFE (e.g. AISI 321 steel), a temperature rise due to adiabatic heating during high strain-rate deformation is sufficient to raise the SFE of the deformed metal [146]. This, therefore, could suppress the occurrence of TRIP as recorded in the specimens deformed at $\dot{\varepsilon}_c$ beyond ~7000 s$^{-1}$ (Fig. 9.3d).

The EBSD maps of the deformed specimen at stage I in Fig. 9.4 are provided in Fig. 9.5 while the results of the TEM and EBSD analyses on those specimens in the stage II region are provided in Figs. 9.6 and 9.7. At stage I, slip occurs in specimens for all investigated grain sizes. However, the extent of deformation due to slip decreases with a decrease in grain size (Fig. 9.5). This is validated

by the lowest (Fig. 9.5d) and highest (Fig. 9.5o) Kernel average misorientation (KAM) recorded for G1 and G3 specimens, respectively. KAM is a measure of local misorientation that indicates the extent of plastic deformation or elastic energy distribution in a specimen. It is estimated as the average misorientation between each measured point in the EBSD scan and its neighbors. In order to exclude the effect of large misorientations (grain boundaries), misorientations $\leq 5^{o}$ are only considered. Hence, high KAM translates to high accumulated strain or stored defects. Although the IPF maps of the austenite phase show significant texturing around [110]||CD fibre (stronger texture in G2 and G3), color gradient within a grain could also suggest the occurrence of slip. While the IPF maps (Figs. 9.5b and c) for G1 specimen shows a near-absence of in-grain color gradient, grains in G2 (Figs. 9.5h and i) and G3 (Figs. 9.5n) shows different color interplay or orientation spread especially between [111] and [110]||CD, and [113] and [110]||CD fibre textures. The pole figure of a fairly larger grain of ~0.7 μm in G1 specimen (marked in Fig. 9.5b) is presented in Fig. 9.5f. It shows a more clustered orientation pole than the widespread of orientation recorded in G3 specimen (Fig. 9.5q). The wider spread of orientation color in Fig. 9.5q does not depict a pole stemming from larger grain size in comparison with Fig. 9.5f, but rather, a pole of grain that has undergone larger plastic deformation by slip or larger lattice grain rotation from point 1 to 4. This lattice rotation is due to grain boundary-initiated intragrain plasticity [287]. On the other hand, deformation twinning occurred in G2 (Fig. 9.5l) and G3 (Fig. 9.5p) specimens only and their fraction increases with increase in grain size. The lower extent of slip and near absence of twin in G1 (UFG) specimens is attributed to spatial restriction effect. The near-absence of twins in UFG specimen suggests that the stress required to develop twinning (twinning stress) is high compared to those of the G2 and G3 specimens [80,82].

In stage II, the occurrence of slip and twinning are observed and qualitatively verified by the TEM results (Fig. 9.6). While dislocations and the absence of twins are observed in the G1 specimen (Fig. 9.6a), the intense slip in G3 specimen leads to grain boundary-dislocations (Fig. 9.6b), dislocation-dislocation (Fig. 9.6c), twin-dislocation (Fig. 9.6d and e) and carbide-dislocation (inset in Fig. 9.6e) interactions. These interactions hinder dislocation motion and hence, contributes to hardening during plastic deformation. Two notable deformation twin nucleation sites are observed in the steel under investigation; inside the grain interior via dislocation-dislocation interactions (Fig. 9.6e) and at the grain boundary via grain boundary-dislocation interactions (Fig. 9.6f). These twin nucleation sites have been reported using molecular-dynamics for the simulation of plasticity

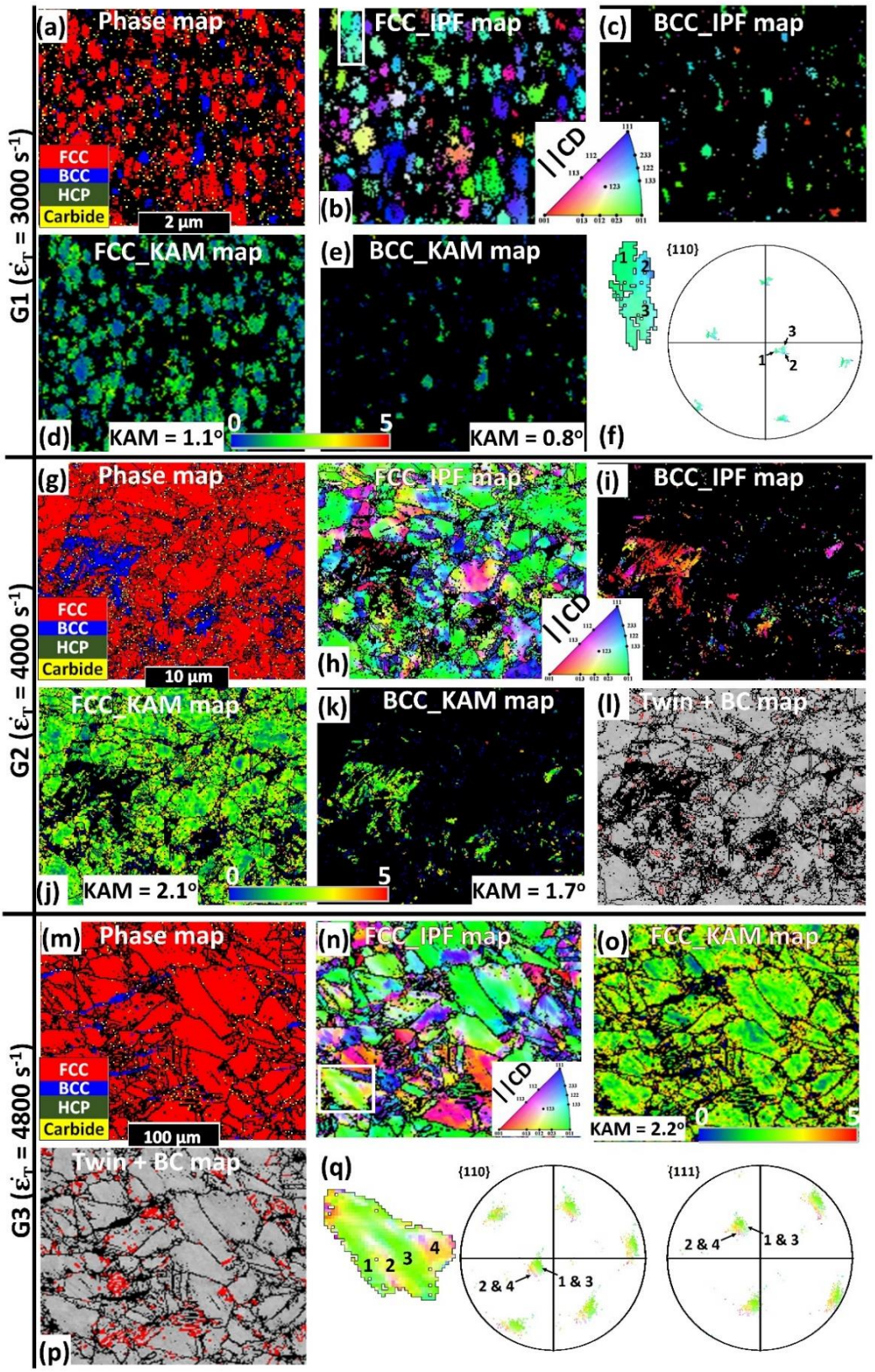


Fig. 9.5. EBSD maps of (a-f) G1, (g-l) G2 and (m-q) G3 specimens deformed at a firing pressure of 60 kPa: (f) and (q) are the pole figures of selected grains in (b) and (n), respectively.

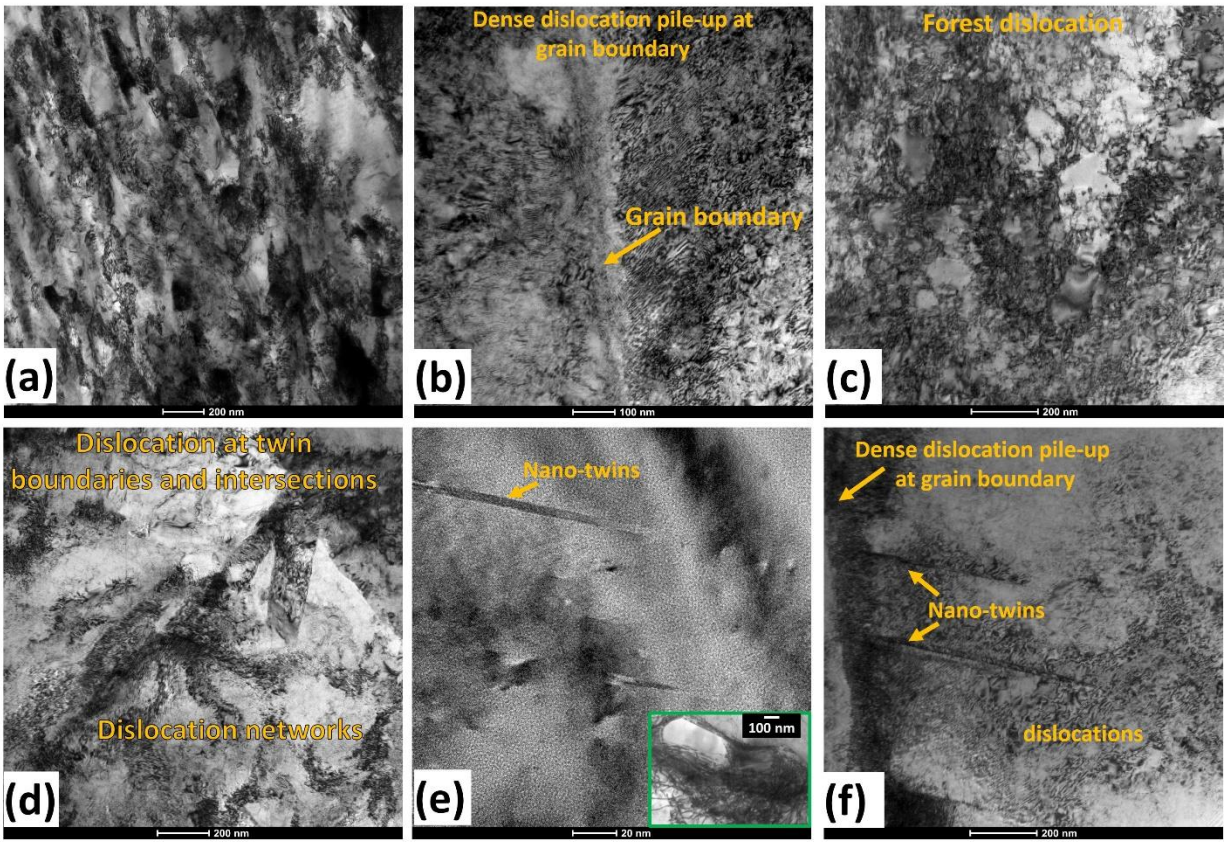


Fig. 9.6. TEM bright field micrographs of (a) G1 and (b-f) G3 specimens deformed using a firing pressure of 90 kPa. Inset in (e) is dislocation pile-up around a TiC particle.

of polycrystalline materials [288]. In a recent development [287], shock-induced deformation of a polycrystalline material using a molecular-dynamics-based simulation that is coupled with orientation mapping and selected area electron diffraction for microstructural analysis was investigated. In agreement with the current findings and previous works, the authors found that stacking faults and perfect dislocations emitted from grain boundaries are nucleating sites for deformation twins. These authors (Wang et. al. [287]) also concluded that intra-grain dislocation and twinning nucleated from grain boundaries, such as those observed in G3 specimen (Figs. 9.6c and 9.6f), could lead to partial grain rotation and eventual subgrain formation. At higher strain rate in stage II, the EBSD results in Fig. 9.7 shows a near-absence of α' in G3 specimen (Fig. 9.7l) and significant texturing of austenite grains around [110]||CD (Figs. 9.7g and 9.7m). A comparison of KAM maps and pole figures of selected grain in G1 and G3 specimens affirm the increase of slip activity with an increase in grain size. While the twin fraction in G1 specimen is still near zero (Fig. 9.7d), twin fraction increases as the grain size increases from fine (Fig. 9.7k) to coarse G3 (Fig. 9.7o) specimen. From Fig. 9.5 to 9.7, it can, therefore, be concluded that the increase in grain

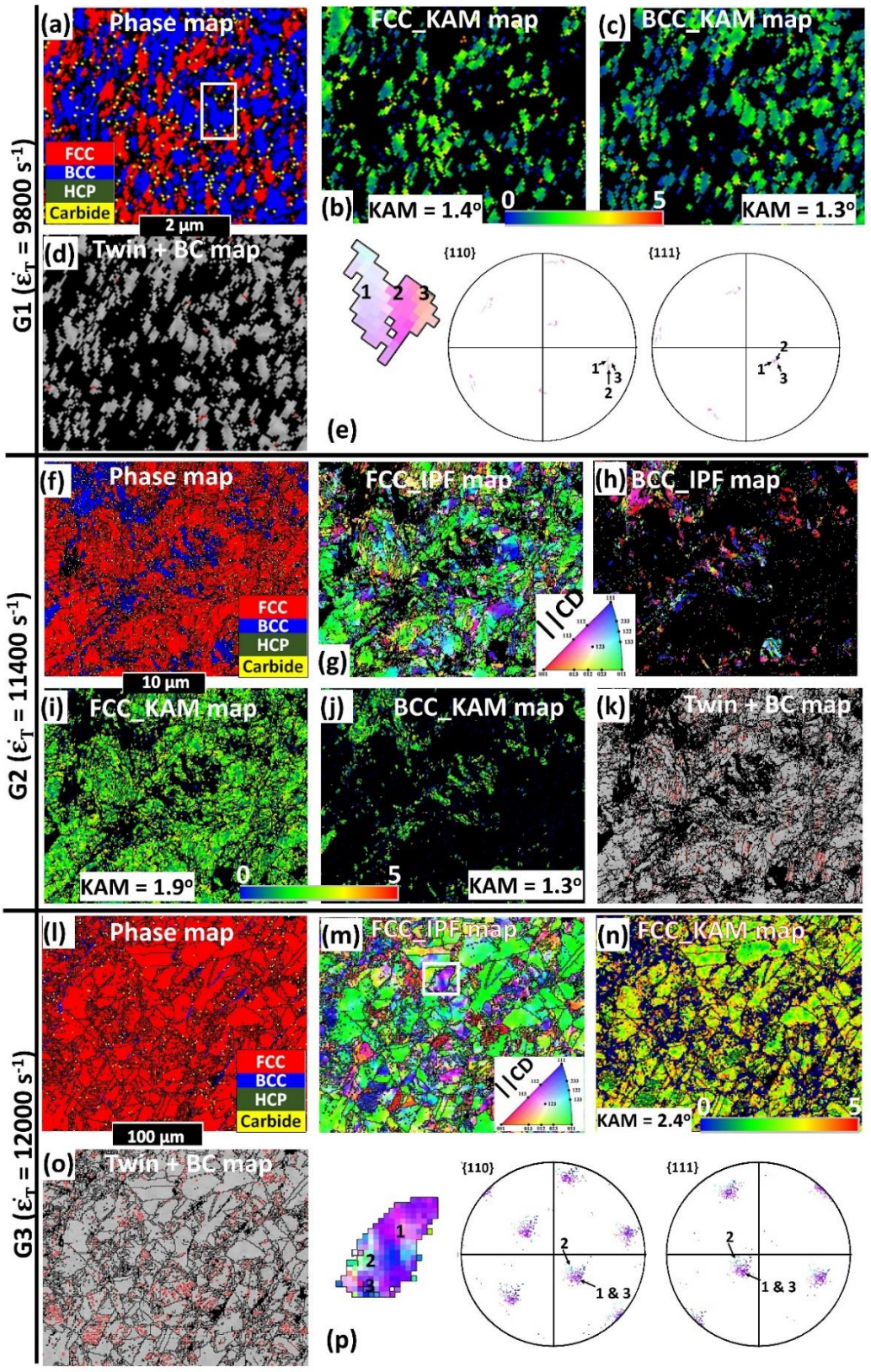


Fig. 9.7. EBSD maps of (a-e) G1, (f-k) G2 and (l-p) G3 specimens deformed at a FP of 100 kPa: (e) and (p) are the pole figures of selected grains in (a) and (m), respectively.

size and strain rate increases slip and twinning activities. On the contrary, an increase in grain size and strain rate suppresses α' phase transformation. It should be noted that the use of feritscope gave a close estimate of α'-martensite fraction with those of EBSD results. Although the X-ray diffraction patterns in Fig. 9.3a-c qualitatively agrees with the feritscope and EBSD results, the estimated α'-martensite fraction from XRD integrated intensity yielded an unreliable value that is off the EBSD and feritscope estimates. This could be due to the few peaks obtainable from the XRD machine equipped with Cr source used in this study.

Phase transformation sequence may either follow FCC γ-austenite → BCC α′-martensite or FCC γ-austenite → HCP ε-martensite → BCC α′-martensite sequence during the formation of deformation-induced martensite (DIM). Although under a quasi-static compressive condition, the coexistence of both phase transformation sequences has been reported in AISI 321 stainless steel (irrespective of grain size) [289], γ → α′ is observed in the current study. It is possible that after the dynamic impact of the investigated steel, the transformation sequence of γ → ε → α′ is already completed. The formation of a higher fraction of α′ in G1 specimens than in G2 and G3 specimens (Fig. 9.3d) could be attributed to the higher grain boundary area and triple junctions that are nucleation site for α′ transformation [290]. The γ grain boundaries have been reported as the dominant nucleation site for DIM in UFG austenite [59], and the process is commonly referred to stress-assisted nucleation process. On the other hand, strain-induced martensite occurs predominantly at two intersecting shear systems (i.e. ε-martensite bands) [58]. It is thought that the shear strains by the intersection of two ε-martensite variants result in an atomic arrangement that favors the nucleation of α′ [59]. Summarily, the nucleation of stress-assisted α′ depends on the same nucleation sites or embryos (such as grain boundaries), whereas the nucleation of strain-induced α′ require the creation of new sites or embryos (such as the intersection of ε bands or the intersection of an ε band with a twin in the parent austenite) by plastic deformation [58]. Therefore, the absence of ε-martensite and their intersections in AISI 321 stainless steel under dynamic loading condition can suggest that the observed α′ are stress-assisted α′. Subsequently, the higher density of stress-assisted α′ nucleation site (i.e. grain boundary area) in G1 samples is responsible for a higher fraction of martensite observed in Fig. 9.3d.

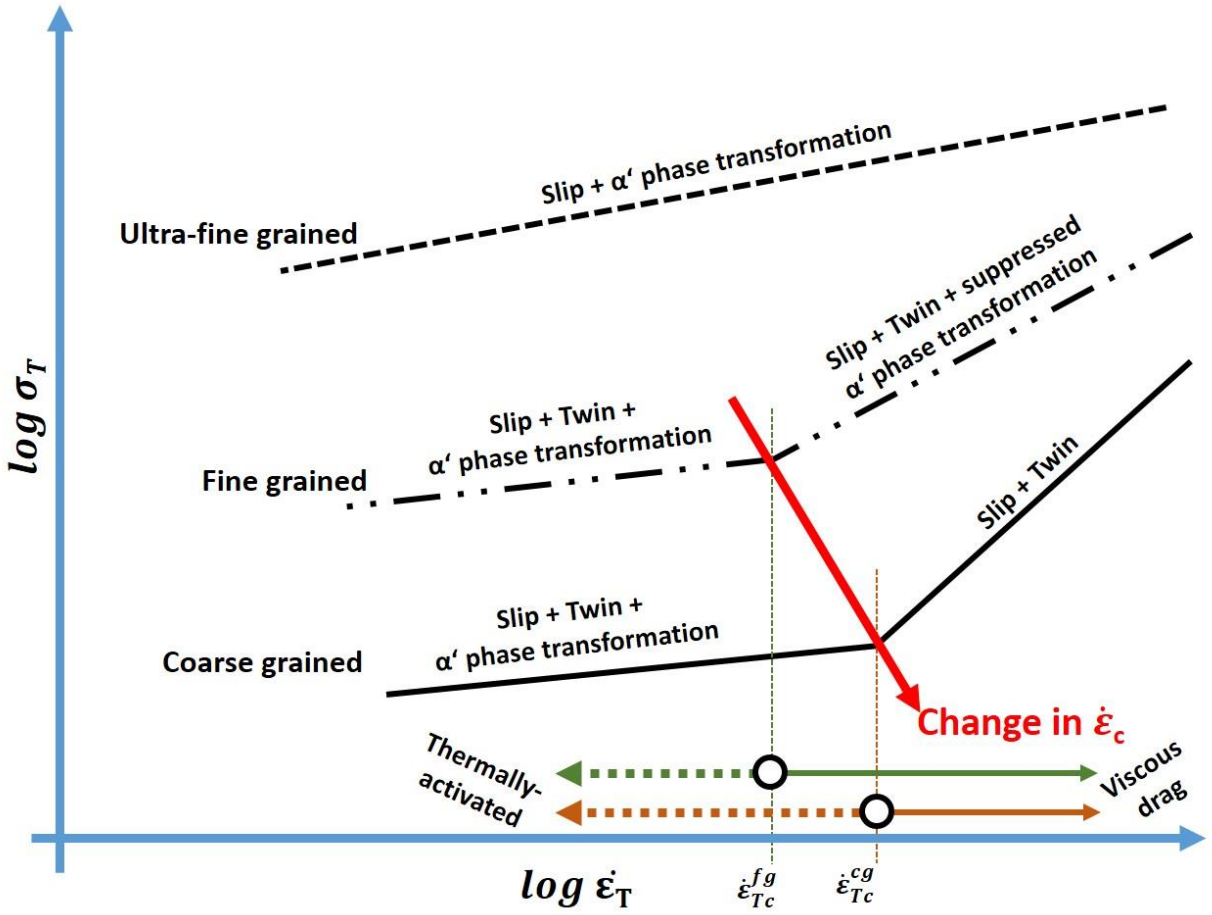


Fig. 9.8. Schematic representation of Fig. 9.4 and the activated deformation mechanisms at each stage.

Based on the observed activated deformation mechanisms at each of the stages in Fig. 9.4, a schematic diagram showing the role of deformation mechanism on the critical true strain rate ($\dot{\varepsilon}_{Tc}$) at which the rapid change of *m* occurs is presented in Fig. 9.8. Although it is widely accepted that a change in *m* at $\dot{\varepsilon}_c$ is due to the transition in the rate-controlling mechanism of the dislocation motion from a thermally activated process to viscous drag, it is concluded that difference in the value of $\dot{\varepsilon}_{Tc}$ for different grain sizes (Fig. 9.8) could be due to the complexities in the deformation mechanisms in metastable AISI 321 stainless steel. That is, the acceleration or the deceleration of any of the activated deformation mechanisms (slip, twinning and α' phase transformation) as the slope transit from stage I to II. Using the results from a direct impact Hopkinson pressure bar test to describe a change from a thermally activated process to a viscous regimes of stable (copper and nickel) and metastable (AISI 304L austenitic stainless steel) metallic materials, Couque [269] studied the effect of strain rate on transition in the rate-controlling mechanism. The author reported

no change in $\dot{\varepsilon}_c$ for the stable metals despite the change in grain size. However, $\dot{\varepsilon}_c$ changed with grain size for the metastable AISI 304L steel (of which AISI 321 is a derivative) [269]. There was no explanation for this behavior by Couque due to lack of microstructural analysis that might be beyond the scope of that work. Therefore, combining these previous findings with the current observation, it is thought that the constant value of $\dot{\varepsilon}_c$ irrespective of grain size for stable copper and nickel metals was due to a singular dislocation interaction activity as the dominant deformation mechanism. Whereas, complexities in the deformation mechanism such as the mechanisms involving dislocation (resulting in grain boundary-dislocations, dislocation-dislocation, twin-dislocation and carbide-dislocation interactions), twinning and α' phase transformation in fine and coarse-grained metastable AISI 321 (and in AISI 304L) could lead to a change in $\dot{\varepsilon}_c$. These observations could also suggest a possible role of grain size on the SFE of AISI 321 stainless steel. This is because, just as the grain size (as observed in this study), SFE is also partitioned in such a manner that favors specific operational deformation mechanisms as described above. Although SFE depends on factors such as chemical composition and temperature [50], the compositional equation (Eqn. 2.7) does not account for the role of grain size. Hence, the estimated SFE for AISI 321 from this equation (25.1 $mJm^{-2}$) could, therefore, be assumed for the undeformed G3 sample. The variation of dominant deformation mechanisms due to the effect of grain size in this study, therefore, suggests that the SFE of AISI 321 steel possibly deviates from the estimated value of 25.1 $mJm^{-2}$.

### 9.3.4 Macrotexture evaluation

During plastic deformation, defects such as dislocation and twinning impart local orientation changes by preferentially adjusting the orientation in soft grains [287,291]. Hence the need to identify the plausible stable end-orientations in the deformed specimens. Figure 9.9 shows the IPF triangles of both the austenite and martensitic phases. The result shows that the stable end-orientation in the austenitic phase is [110]||CD and its intensity increases with an increase in grain size and strain rate. The higher intensity of [110]||CD texture in G3 (coarse) could signify higher slip and twin activities in comparison with the lowest intensity of [110]||CD texture recorded in G1 (UFG) specimens due to low slip and near-absence of twinning. This could ultimately contribute to the higher hardening rate observed in the impacted G3 specimens (Fig. 9.2d-f).

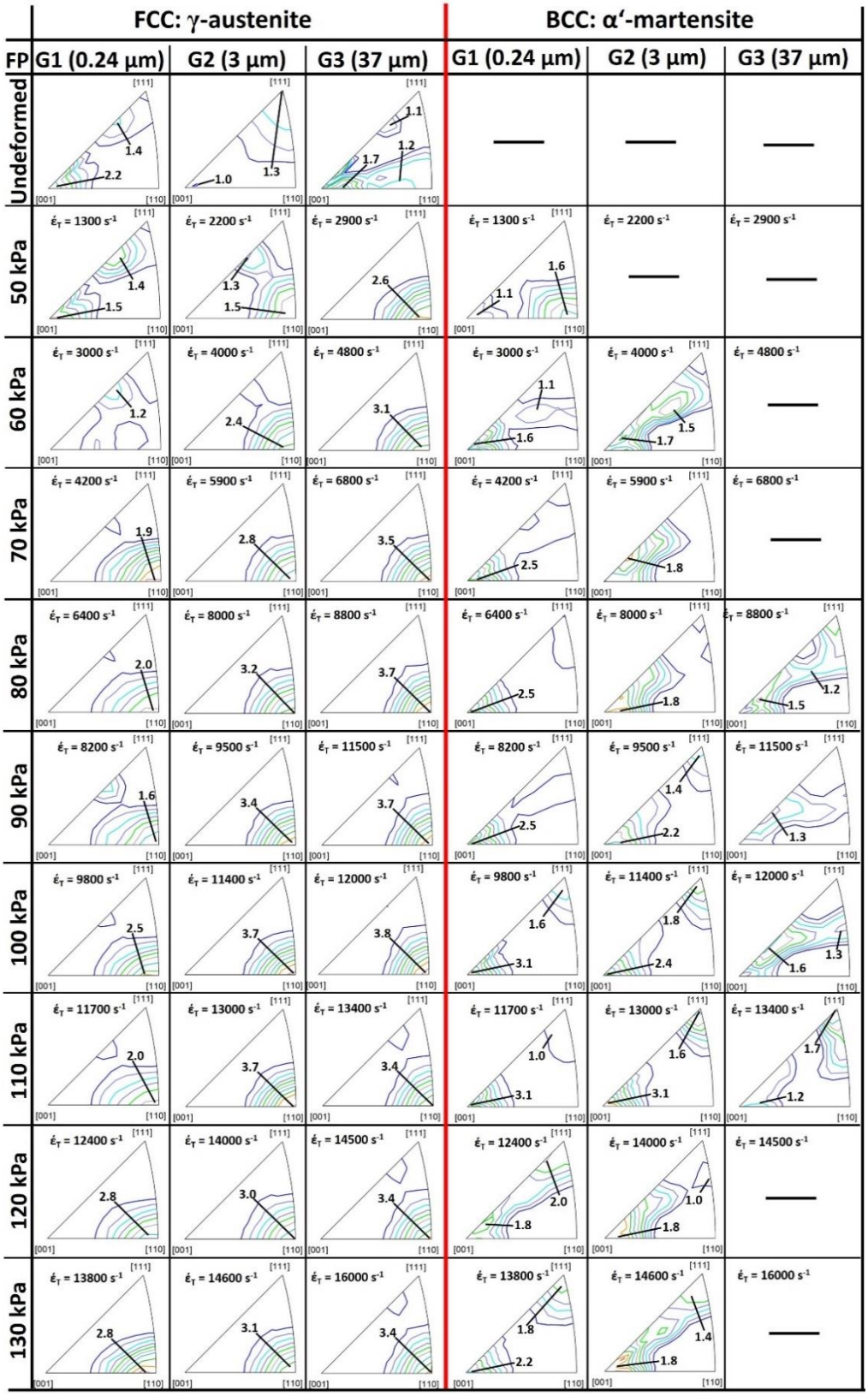


Fig. 9.9. IPF triangles of both the γ-austenite and α'-martensite phases in the impacted G1, G2 and G3 specimens.

Similarly, the stable end-orientations in the martensitic phase are [100] and [111]||CD and their intensities increases with decreasing grain size and increasing strain rate as shown in Fig. 9.9.

### 9.3.5 Formation of adiabatic shear band

A major deformation mode in metals subjected to dynamic impact load is the formation of adiabatic shear band (ASB). ASB is a region in a specimen subjected to dynamic impact loading, where intense shear strain localization occurs due to loss of load carrying capacity caused by extreme thermal softening from localized adiabatic heating [118]. Depending on the intensity of the localization, two types of ASB can develop; deformed and transformed shear bands. The deformed shear band (DSB) consists of elongated grains and transformed shear band (TSB) consists of equiaxed ultrafine grains [292]. Localized deformation usually starts with the formation of DSB, which then changes to TSB once a critical strain for formation of TSB is attained [192]. It is the formation of TSB that eventually initiates dynamic fracture of materials at high strain rates [293]. In this study, grain size plays a major role in the onset of ASB. As presented in Table 9.1, the onset of both DSB and TSB occur earlier (i.e. at a lower strain rate) in G1 specimens than in G2 and G3 specimens. The optical micrographs that show the formation of DSB and circular TSB on the compression plane of both G1 and G3 specimens are provided in Fig. 9.10. At the same firing pressure of 80 kPa, fully formed DSB was formed in both deformed G1 (Fig. 9.10a) and G3 (Fig. 9.10c) specimens; however, the onset of TSB is already noticeable in G1 (Fig. 9.10a) specimen. This confirms that G1 specimens are more susceptible to the formation of ASB compare to G2 and G3 specimens. Figure 9.10a also confirm that TSB is a metamorphosized DSB once a critical strain rate/strain for TSB-formation is reached. Fully-formed TSBs in both G1 and G3 specimens deformed at the same firing pressure of 120 kPa are presented in Figs. 9.10b and 9.10d, respectively. Detail analyses of these bands are beyond the scope of this paper. However, it was reported elsewhere that equiaxed dynamic recrystallized grains of sizes ~0.10, 0.18 and 0.24 μm developed inside the ASB formed in G1, G2 and G3 specimens, respectively, by rotational dynamic recrystallization mechanism [277].

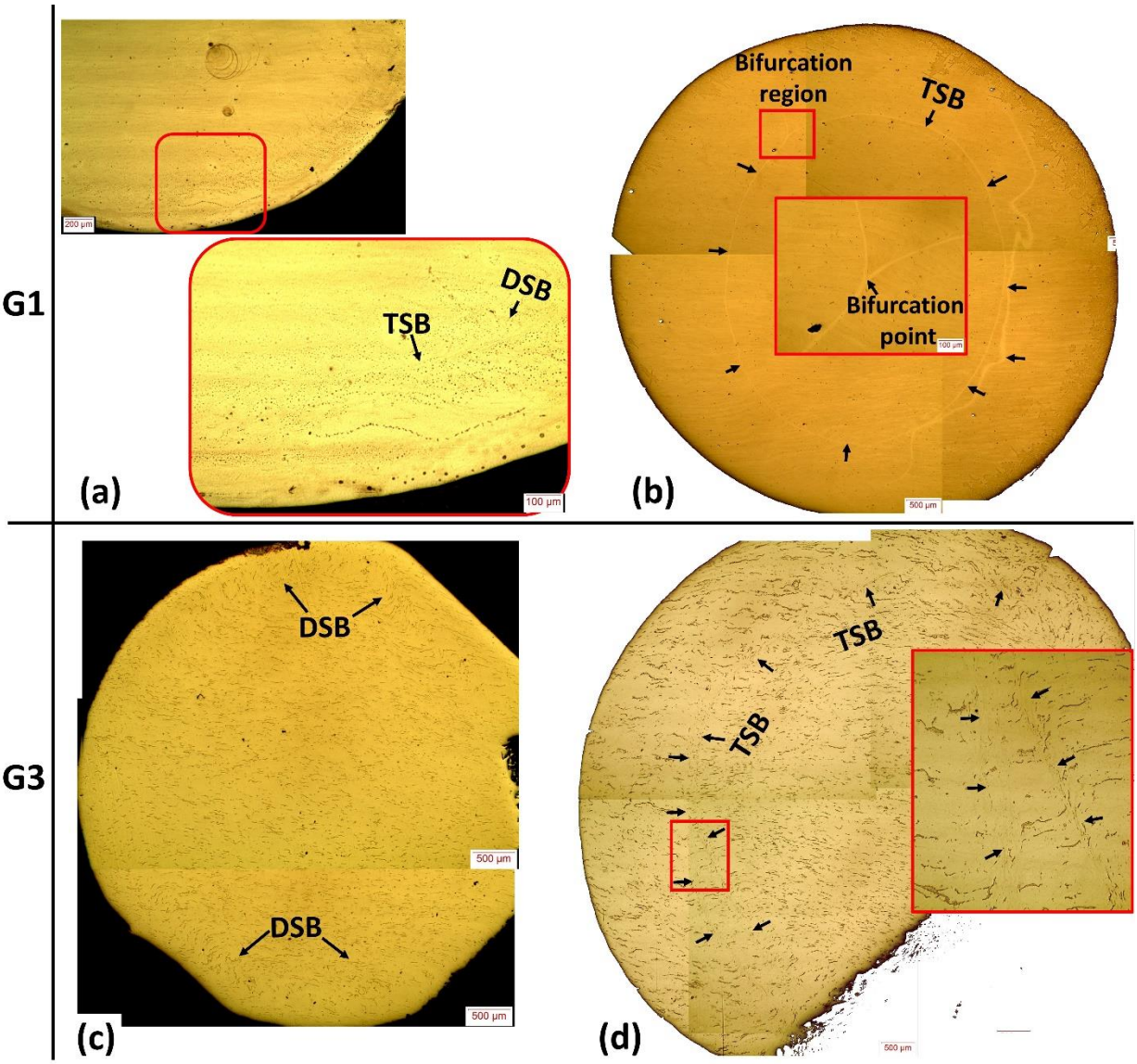


Fig. 9.10. Optical micrographs showing the deformed shear band at 80 kPa and fully-formed transformed shear band at 120 kPa in deformed (a) G1 and (b) G3 specimens.

## 9.4. Conclusion

The strain rate sensitivity and activation volume of metastable AISI 321 austenitic stainless steel with grain sizes of 0.24 µm (ultrafine [G1]), 3 µm (fine [G2]) and 37 µm (coarse [G3]) were investigated at high strain rate regime. The following conclusions are drawn from the experimental findings:

1. A change in strain rate sensitivity (SRS) with increasing true strain rate is observed only in G2 and G3 specimens and it occurs at a $\dot{\varepsilon}_{Tc}$ of ~5900 and 6800 $s^{-1}$, respectively.

2. While the SRS of ultrafine-grained (G1) specimen is 0.101 and remained unchanged as strain-rate increased, those of fine (G2) and coarse (G3) specimens changed from 0.094 to 0.326 and 0.091 to 0.634, respectively, once a critical true strain rate ($\dot{\varepsilon}_{Tc}$) is reached.
3. Similarly, the estimated activation volume in G1 specimen is ~1.57$b^3$, while those of G2 and G3 specimens changed, once $\dot{\varepsilon}_c$ is exceeded, from ~2.95$b^3$ to ~0.65$b^3$ and from ~4.10$b^3$ to ~0.45$b^3$, respectively.
4. The complexities in the deformation mechanisms such as the simultaneous occurrence of slip, twinning and α' phase transformation in fine and coarse-grained metastable AISI 321 stainless steel leads to a change in $\dot{\varepsilon}_c$. The constant SRS in G1 specimen suggests no change in operational deformation mechanisms (slip and α' phase transformation) at all investigated strain rates.
5. The stable end-orientation in the austenitic phase is [110]||CD and its intensity increase with an increase in grain size and strain rate. Higher slip and twin activities contribute to the higher intensity of [110]||CD texture in G3 (coarse) specimen.
6. The susceptibility of AISI 321 steel to the formation of adiabatic shear band increases with a decrease in grain size.

# CHAPTER 10

## Thermal and Mechanical Stability of Austenite in Metastable Austenitic Stainless Steel

In this chapter, the roles of grain size, texture, strain and strain rate on the thermal and mechanical stability of austenite in AISI 321 metastable austenitic stainless steel is discussed. The observations in this study could open a new window for engineering the initial texture of metastable austenitic stainless steel to either aid thermally and/or mechanically-stable austenite phase or promote both isothermal and deformation-induced martensitic phase transformation. These research findings are published in "*Metallurgical and Materials Transactions A"* as follows:

A. A. Tiamiyu, Shiteng Zhao, Zezhou Li, A.G. Odeshi, J.A. Szpunar, "Thermal and mechanical stability of austenite in metastable austenitic stainless steel", *Metall. Mater. Trans. A Phys. Metall. Mater. Sci.*, 2019. https://doi.org/10.1007/s11661-019-05362-2

My contributions to this paper include review of the relevant literature, design and carrying out of experiments, analysis of test results and preparation of the manuscript under the guidance of my supervisors (Prof. Akindele Odeshi and Jerzy Szpunar). Both supervisors' comments and suggestions were addressed before submitting the manuscript for publication. The content of this chapter is a modified version of the published paper. The modification involves removing material and methods already discussed in Chapter three to avoid repetition. The copyright permission for manuscript reuse was obtained and provided in APPENDIX C.

### Abstract

The roles of grain size, texture, strain, and strain rate on the thermal and mechanical stability of austenite in AISI 321 metastable austenitic stainless steel were studied. Ultrafine grain (UFG), fine grain (FG) and coarse grain (CG) specimens with average grain sizes of 0.24 μm, 3 μm and 37 μm sizes, respectively, were investigated. To determine the thermal stability of austenite (TSA), samples were soaked in liquid nitrogen (-196 $^{o}$C) for varying times between 0.5 to 24 h. On the other hand, the mechanical stability of austenite (MSA) was studied by subjecting cylindrical specimens to both quasi-static (4.4 x $10^{-3}$ $s^{-1}$) and dynamic loading conditions (between 1300 and 8800 $s^{-1}$). Thermally-induced α'-martensite was only observed at an incumbent time in AISI 321 to suggests an isothermal martensitic transformation occurred. Both Kurdjumov-Sachs ($\{111\}_{\gamma}\|\{110\}_{\alpha'}$ and $<\bar{1}01>_{\gamma}\|<1\bar{1}1>_{\alpha'}$) and Nishiyama–Wasserman ($\{111\}_{\gamma}\|\{110\}_{\alpha'}$ and

$<112>_{\gamma}||<011>_{\alpha'}$) orientation relationships existed between the untransformed γ and thin-plate α'-martensite. The thermally-induced phase transformation was highly suppressed in UFG specimens. While TSA decreased with an increase in grain size, MSA decreased with a decrease in grain size. While thin-plate α' predominantly formed in the thermally-treated AISI 321 steel (FG and CG specimens only), lath and irregularly-shaped α' formed in the specimens deformed under quasi-static and dynamic loading conditions, respectively. Irrespective of strain rate, deformation-induced α' in UFG specimens inherited the morphology of the deformed austenite grain that is equiaxed. Irrespective of grain size, MSA also decreased with increase in strain (up to a critical strain for specimens deformed under dynamic loading condition) and decrease in strain rate. In the event of adiabatic shear band (ASB) formation in a specimen deformed at high-strain rate, MSA increased as the ASB was approached due to the temperature rise in the ASB region. Electron backscattered diffractometry (EBSD) examination revealed that the evolution of both thermally- and deformation-induced martensite is orientation-dependent in FG and CG specimens. The instability (thermal and mechanical) of the austenite phase is highest in the RD/CD||[100]-oriented grains (RD and CD are rolling and compression directions, respectively), followed by grains oriented near RD/CD||[110] and RD/CD||[111], in that order. These findings could open a new window of engineering the initial texture of metastable austenitic stainless steel to either aid thermally and/or mechanically-stable austenite phase or promote both isothermal and deformation-induced martensitic phase transformation.

**Keywords:** *AISI 321 austenitic stainless steel; Texture; martensitic phase transformation; thermal stability of austenite; mechanical stability of austenite; SHPB*

## 10.1 Introduction

Metastable austenitic stainless steel (MASS) has a face-centered cubic (FCC) crystal structure and low stacking fault energy (SFE). It finds application in energy (chemical and nuclear) and transportation sectors. MASS could be exposed to various degree of conditions that could result in the instability of its austenite phase in service, i.e., martensitic phase transformation could occur. This could affect the properties of MASS, e.g., loss of non-magnetic property of the MASS when α'-martensite developed [294]. Some of these stability-deteriorating conditions include a cryogenic environment and exposure to an external load, either at low or high strain rates. In a cryogenic environment, the austenitic phase may become unstable, leading to the evolution of α'-martensite.

Generally, the martensitic transformation is displacive with definite crystallography [295], and they are categorized into athermal and isothermal transformations depending on the kinetics of transformation [38,39,296]. While the amount of martensites formed during athermal transformation depends solely on temperature, the amount of those that form during isothermal transformation is a function of both temperature and time [40]. For athermal transformation to occur and proceed, the thermal activation is not necessary [41]. In other words, only the thermodynamic driving force obtained by lowering temperature is adequate for athermal martensitic transformation. This thermodynamic driving force must overcome the elastic energy that opposes initiation at specific sites at and below the martensite start (Ms) temperature.

Athermal martensitic transformation involves two steps. The first step is "barrier-less", and it entails the evolution of martensite units, i.e., martensite unit starts to form without the need to overcome any form of barrier. The second step is the growth of the martensite units which involves the migration of a glissile interface without thermal activation [295]. Meanwhile, the isothermal transformation has no definite Ms temperature, but it occurs with time (incubation) during isothermal holding. The amount of the product phase (martensite) in athermal transformation does not depend on time, but on temperature due to its intrinsic nature [38]. This is because no diffusion is involved in athermal transformation, and the composition of the product is the same as that of the parent (austenite) phase. While thermal activation implies statistical probability (i.e. the same site will not always be the first to initiate the transformation process), the same site during a non-thermal activation process (athermal martensites) tends to repeatedly initiate the process of transformation. It, therefore, implies that the site with the lowest barrier is always the first one to initiate transformation during a non-thermal activation process.

Considering the thermal activation model for the transformation kinetics [40], it has been predicted that when an athermal martensitic transformation is suppressed, an isothermal transformation will occur after some incubation time [44]. However, earlier work has reported the possible occurrence of both transformations (athermal and isothermal) in the same material [45,46]. On the kinetic, morphology and magnetic characteristics of thermally-induced martensite in Fe–30%Ni–3.6%Mo alloy, Yasar et al. [39] observed the occurrence of both athermal and isothermal martensitic transformation in the alloy using a scanning and transmission electron microscope. Using the temperature dependence of magnetic susceptibility measurement and X-ray diffraction techniques,

Nam et al. [44] investigated the occurrence of martensitic transformation in micron-sized single and polycrystalline particles of an Fe–30.5 Ni (at.%) alloy. They observed a reduction in Ms temperature from 215 to 151 K when the grain size of the polycrystalline particles was reduced from 250 to 3.7 μm, which translates to lowering the tendency for athermal martensitic transformation. Similarly, a 4.6 μm-sized single crystal particle shows no Ms temperature, but instead, an isothermal martensitic transformation. On introducing grain boundaries and dislocation in the single crystal particle by sintering or deformation, Ms temperature appeared and athermal martensite developed. This affirms the role of lattice defects on athermal martensitic transformation.

Under external load, where the stability of the austenite phase in MASS could be lost, deformation-induced martensitic transformation could also evolve at a critical strain [30]. The induced martensitic phase is reported to be stronger and harder than the austenite phase; resulting in a composite strengthening and a high strain hardening. It has been reported that ά-martensite acts as a reinforcing phase since it can withstand higher stress than austenite [228]. However, it is thought that the stability of the austenite phase will be different in MASS under quasi-static compression and those exposed to dynamic impact loading condition. This is because unlike the case under quasi-static loading (where temperature rise is negligible), a temperature rise occurs in a specimen subjected to dynamic impact load, which may influence the stability of the austenite phase. Martensitic phase transformation (via both cryogenic environment and exposure to external load) does not start simultaneously in all austenite grains in a MASS [297]. Therefore, the main objective of this work is to determine the role of crystallographic texture and grain size on the stability of austenite grains in AISI 321 austenitic stainless steel subjected to; (a) cryogenic environment and (b) a uniaxial compressive loading conditions at low (quasi-static) and high (dynamic) strain rates.

## 10.2 Materials and methods

AISI 321 used in this study is a metastable austenitic stainless steel that is stabilized with titanium (Ti) to reduce sensitization during high-temperature application. Samples of three different grain sizes, 0.24 μm (ultrafine grain, UFG), 3 μm (fine grain, FG) and 37 μm (coarse grain, CG), were studied. The CG specimen was received in hot-rolled condition with a nominal composition (in weight %) of 17.61 Cr, 9.17 Ni, 1.56 Mn, 0.42 Mo, 0.40 Si, 0.36 Ti, 0.30 Cu, 0.15 Co and 0.044 C. The process of developing FG and UFG structures from the CG as-received sample is

schematically shown in Fig. 10.1a-d. The CG (as-received) sample was first cryo-rolled up to 50% thickness reduction. While some of the cryo-rolled specimens were annealed at 750 °C for 10 mins to develop UFG structure, others were annealed at 800 °C for 360 min to develop FG structure. More details on the thermo-mechanical process for developing UFG structure in the AISI 321 steel are provided in Ref. [207]. Investigation of thermal stability of austenite (TSA) involves soaking the steel samples in liquid nitrogen for varying times up to 24hrs (Fig. 10.1e). To determine the mechanical stability of austenite (MSA), 4 mm× 4 mm cylindrical test specimens of UFG, FG, and CG were machined with the axis of the specimen parallel to the rolling direction (RD) of the plate. Specimens were compressed under quasi-static and dynamic loading conditions (Fig. 10.1f). Compression direction is parallel to RD.

The dynamic impact and quasi-static compression tests, hardness tests and microstructural analyses such as the TEM, EBSD/EDS, X-ray diffractometry and Feritscope measurements were conducted as described in Chapter three. Meanwhile, focused ion beam (FIB) was used to accurately prepare TEM samples in the adiabatic shear band region formed in impacted specimens. All measurements and microstructural analysis were conducted on the ND-TD plane (for thermally-treated samples) and compression plane (for compressed specimens).

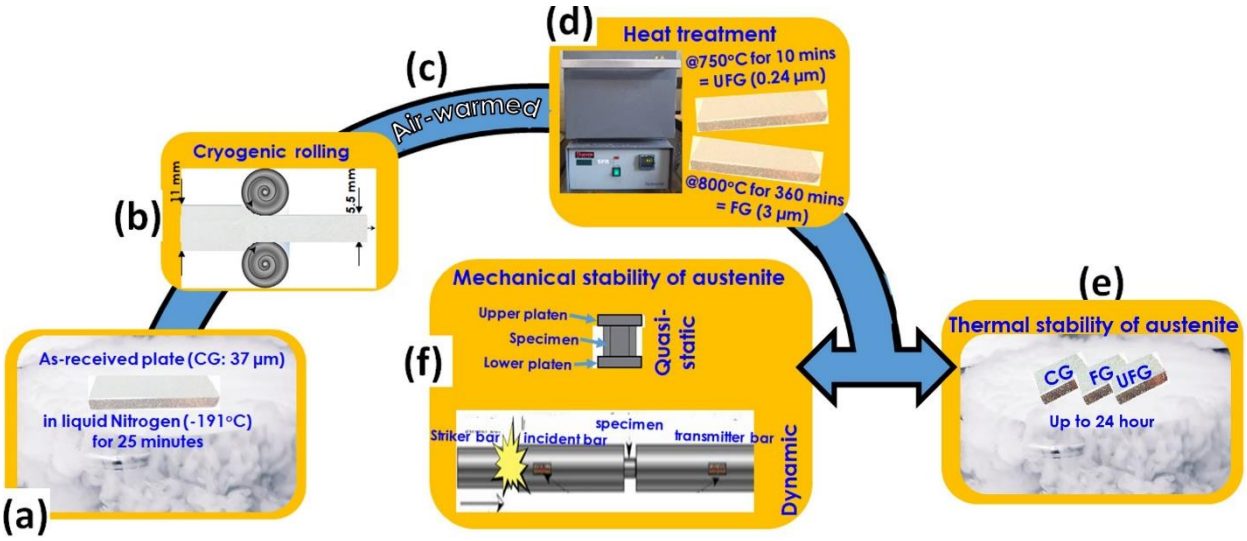


Fig. 10.1. Schematic drawing of the methodology: (a-d) development of UFG and FG structures, (e) samples in liquid nitrogen to investigate TSA and (f) compressed specimens under both quasi-static and dynamic shock loading to investigate MSA.

## 10.3 Results and discussion

### 10.3.1 Initial microstructure

Figure 10.2 shows the TEM micrographs of the UFG (Fig. 10.2a), FG (Fig. 10.2b) and CG (Fig. 10.2c-f) specimens without thermal or mechanical treatments. While the near-absence of annealing twins was observed in the UFG specimen, their (twins) presence was confirmed in the FG and CG specimens. Stacking faults (Fig. 10.2d) and near-absence of misfit around a particle that is confirmed to be TiC (Figs. 10.2e and f) are also present in CG specimen. This could, therefore, imply that 0.24 µm is near the critical grain size below which annealing twin cannot develop in AISI 321 stainless steel. A similar observation of twin suppression was observed in AISI 304 stainless steel (whose derivative is AISI 321) with a grain size of ~0.27 µm, developed by accumulative rolling that is followed by annealing at 550 ℃ for 150 s [81]. Figure 10.3 shows the bulk texture result of the starting microstructure for the three grain sizes. UFG is significantly textured with Cube orientation. Strong R-Cube and Cu orientations with spread around {112}<012>, {332}<123> and {123}<013> orientations are observed in FG specimens; the intensities of which decreases as the grain size increases to CG structure.

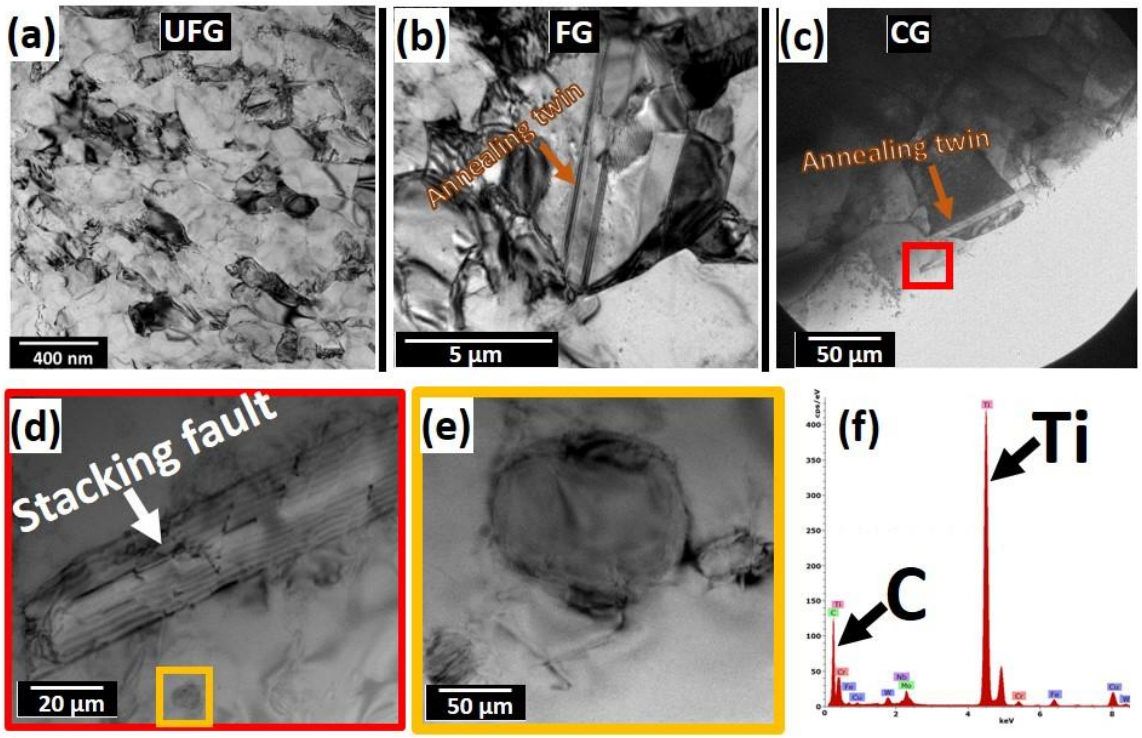


Fig. 10.2. TEM bright field micrographs of undeformed (a) UFG, (b) FG, and (c-e) CG samples. (f) is the EDS spectra of the TiC particle in (e).

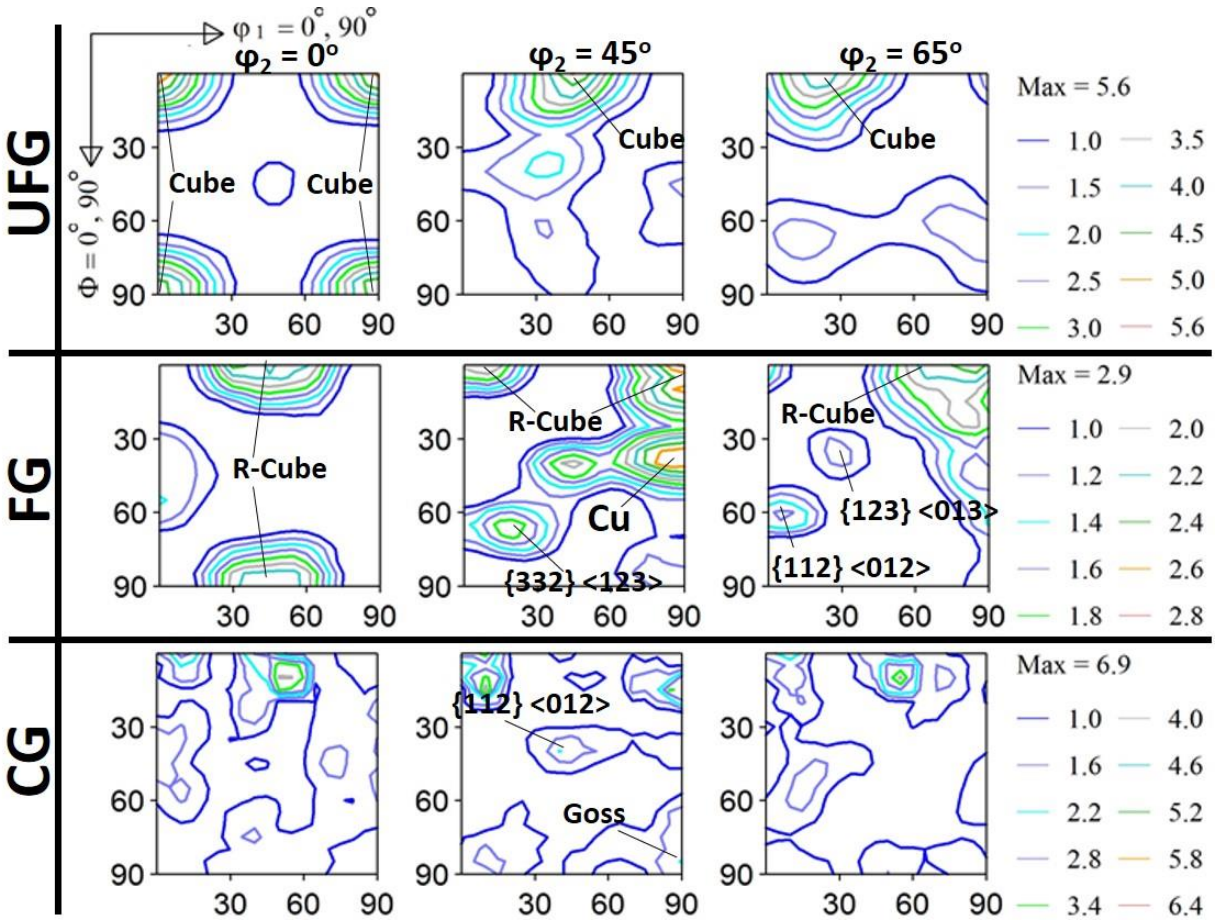


Fig. 10.3. Selected ODF ϕ2 sections from the XRD measurement of the undeformed UFG, FG, and CG samples.

### 10.3.2.1 Thermal stability of austenite (TSA)

Until now, the TSA in AISI 321 MASS has not been clearly clarified. It is certain that the γ phase becomes unstable in a cryogenic environment, thereby promoting the occurrence of martensitic phase transformation. However, it is not clear if phase transformation occurs athermally or isothermally, and by extension, how the role of grain size and crystallographic texture influences the evolution pattern.

The CG specimen was used to determine if martensitic phase transformation occurs athermally or isothermally by immersion in liquid nitrogen for different length of times until traces of α'-martensite was observed. Figure 10.4 shows the EBSD maps of the specimen in the same area, before (Fig. 10.4a-c) and after (Fig. 10.4d-f) thermal treatments. After 20 minutes of immersion, there was no evidence of phase transformation as observed in Fig. 10.4d. Traces of phase transformation was however observed after additional 1hour immersion (Fig. 10.4e) in liquid

nitrogen and the area fraction of the α'-martensite trace increases with time (Fig. 10.4f). The Kernel average misorientation (KAM) maps in Fig. 10.4 also confirm the occurrence of cryogenic-induced defects that accompanied phase transformation. These defects increases (higher KAM values) with an increase in the exposure time in a cryogenic environment. The annealing twin planes in Figs. 10.4e and f also show to be the least susceptible to martensitic phase transformation. Due to the observed kinetics, i.e., the onset of phase transformation after 1hr (a cumulative of 120 minutes) or suppression of transformation at and below 20 minutes, it is concluded that phase transformation in AISI 321 stainless steel occurs isothermally in cryogenic condition. Athermal martensitic transformation is ruled out because no martensite was observed in AISI 321 stainless steel until an incumbent time is reached despite being subjected to a cryogenic environment at -196 ℃. This temperature is below the Ms temperature of the steel, -152.5 ℃, estimated using Eqn. 2.3 [6].

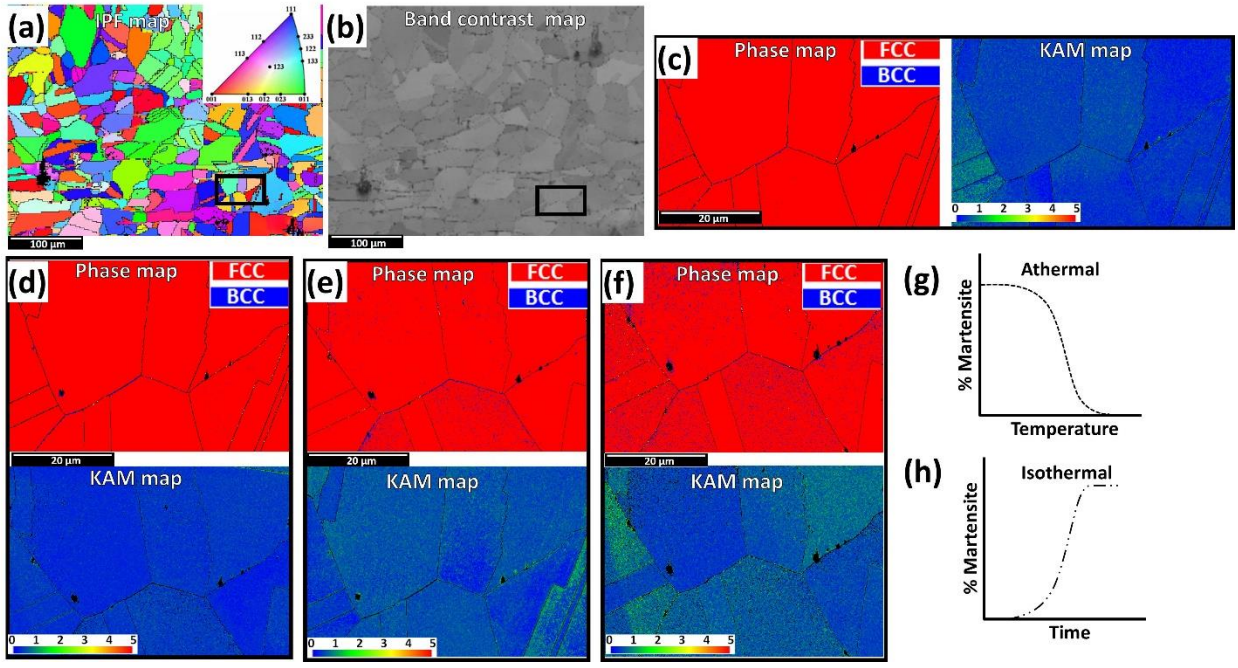


Fig. 10.4. EBSD maps (a-c) before thermal treatment and (d-f) successive increment of time in liquid nitrogen: (d) 20 minutes (e) 1hr 20mins and (f) 13 hrs 20mins. Sketch of kinetics of (g) athermal and (h) isothermal martensite formation.

The amount of athermal martensite that form depends on the degree of undercooling below Ms temperature and their character is a consequence of very rapid nucleation and growth such that the time taken (order of $10^{-7}$ s) can be ignored [34]. The sketch that represents the kinetics of athermal

and isothermal martensite transformations are presented in Figs. 10.4g and h, respectively. It is clear that the evolution of α' is formed isothermally, having required an incumbent time as shown in Fig. 10.4h.

Having observed that appreciable fraction of thermally-induced α' could form in AISI 321 steel after 12hrs in liquid nitrogen (Fig. 10.4), a new set of samples (UFG, FG, and CG specimens) were held in liquid nitrogen for 24 hrs to evaluate the role of grain size on isothermal martensitic transformation. EBSD (Figs. 10.5, 10.6, 10.8 and 10.9) and SEM (Fig. 10.7) analyses were conducted on a selected area, before and after thermal treatment, for each of the specimens with varying grain sizes. The EBSD band contrast maps of the selected area in UFG, FG and CG specimens before thermal treatment are presented in Figs. 10.5a, b, c, respectively. Figure 10.5d shows the EDS maps that confirm the presence of TiN particles in AISI 321 steel. In order to determine the role of grain orientations on phase transformation, the inverse pole figure (IPF) maps of grains with crystallographic orientations near RD‖[111], [110] and [100] were selected from Fig. 10.5 and presented in Fig. 10.6. The phase, band contrast (BC) and twin and KAM maps of the untreated selected grains are also presented. From Fig. 10.6, it can be deduced that annealing twins are only present in FG and CG specimens irrespective of the grain orientation.

The SEM micrographs showing the regions before and after 24 hours of thermal treatment are presented in Fig. 10.7. The figures show the evolution of plate-like martensite only occur in FG (Figs. 10.7e and 10.7h) and CG (Figs. 10.7f and 10.7i) as indicated by some arrows. The absence of α' plates in UFG specimen is possibly due to spatial restriction effect that resists the formation of isothermal martensite. This will subsequently restrict multi-variant transformation required to accommodate anisotropic transformation strain that occurred due to volume expansion. It can be concluded from these results that the area fraction of the thermally-induced α' increases with increasing grain size**.** This result establishes that grain refinement to UFG structure increased the thermal stability of the austenite phase in AISI 321 stainless steel. In a different study, Matsuoka [37] studied the thermal stability of Fe–16%Cr–10%Ni metastable stainless steel with grain sizes in the range of 1 to 80 μm. They observed that the TSA increased with decrease in grain size. Notably, the FG and CG specimens formed fine and coarse α' plates, respectively. This affirms the role of grain size on the size of thermally-induced α'. The limitation of α' plate by the prior γ grain size has been reported in another previous study [298].

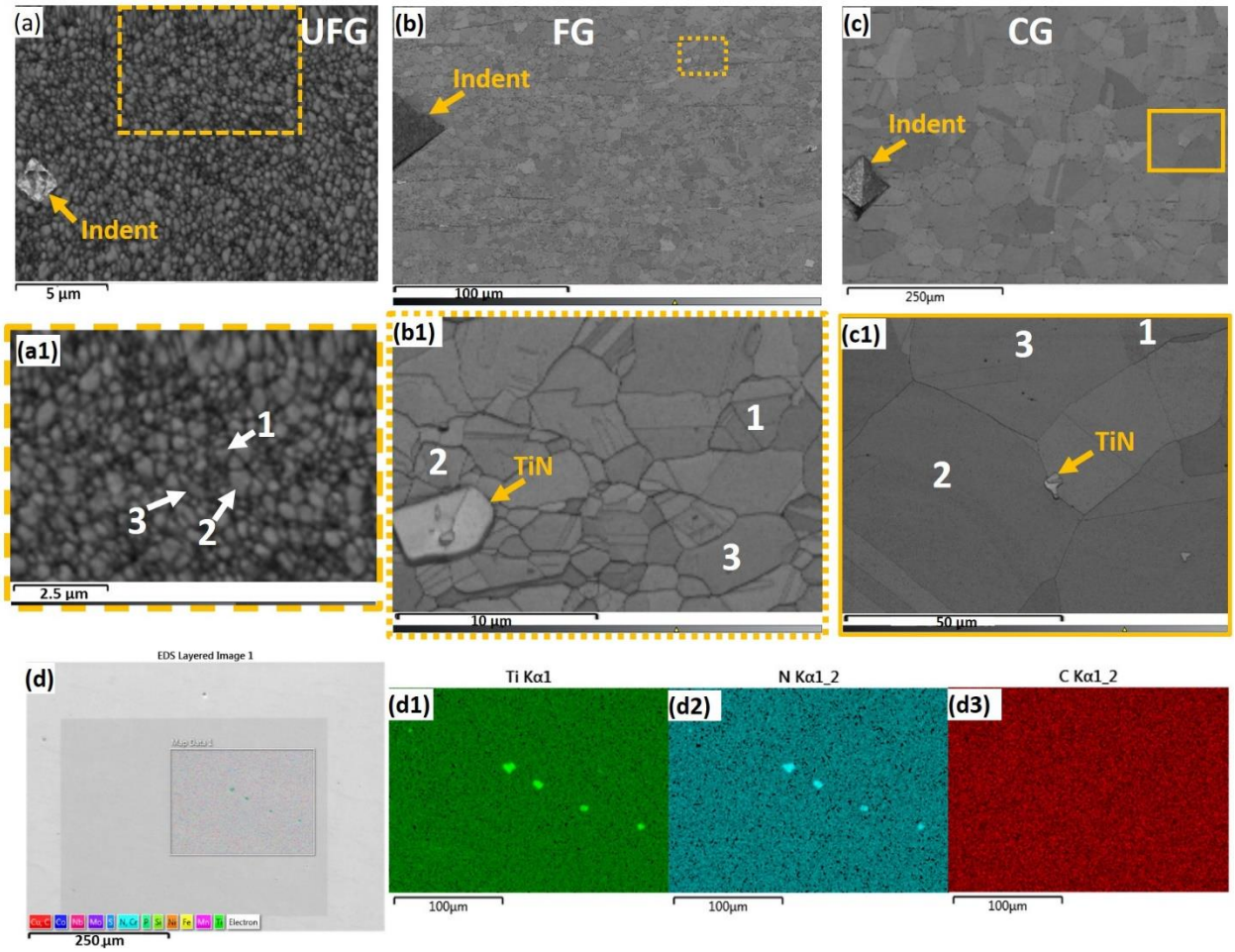


Fig. 10.5. Before thermal treatment: EBSD band contrast maps of (a) UFG, (b) FG, and (c) CG specimens. a1, b1 and c1 are the corresponding high magnification of scanned area. (d) is the EDS maps confirming the presence of TiN particles (d1, d2 and d3 are the corresponding EDS color maps for Ti, N and C, respectively).

### 10.3.2.2 **Role of crystallographic texture and annealing twins on thermal stability of austenite (TSA)**

Although Fig. 10.7 confirms that there is a critical grain size below which the nucleation of α' plates becomes difficult (as in the case of UFG specimen), the uneven distribution of the nucleated α' plates on the analyzed plane in FG and CG specimens hint that the nucleation of α' is texture-dependent. The EBSD maps of the selected grains in Fig. 10.6 after thermal treatment are now presented in Fig. 10.8 to justify the texture-dependent of the phase transformation. Figure 10.8 shows no phase transformation in the pre-selected grains from the earlier scanned area of FG specimen. However, EBSD measurement on another location confirms phase transformation in near RD||[100] oriented grain (Figs. 10.9a-d). Although α' nucleated in all (RD||[111], [110] and

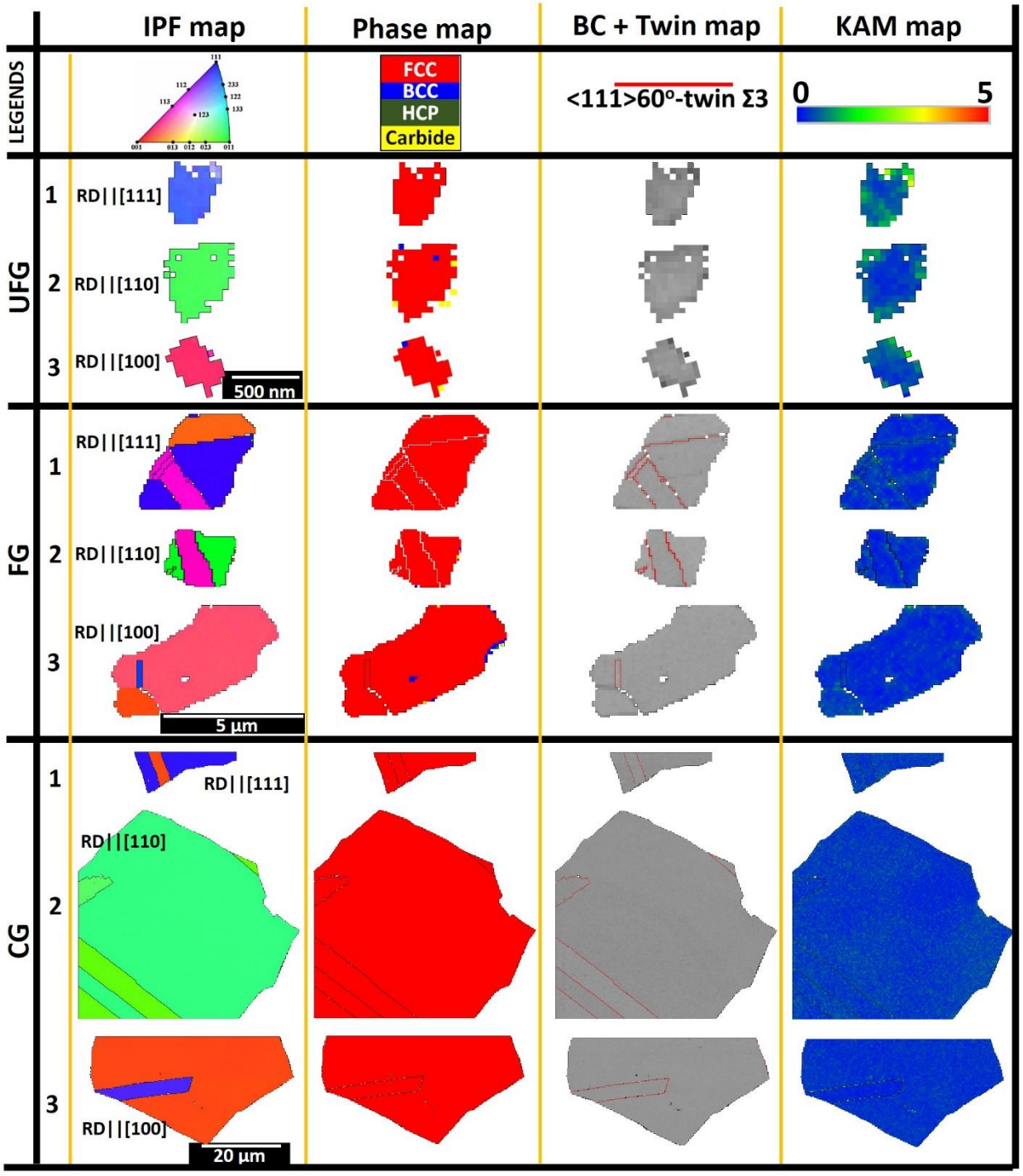


Fig. 10.6. Before thermal treatment: EBSD IPF, phase, BC/twin and KAM maps of selected grains in Figs. 10.5 a1, b1 and c1. Grains 1, 2 and 3 are RD||[111], RD||[110] and RD||[100]-oriented grains, respectively.

[100]) crystallographic-oriented grains for CG specimens, it is clear from the phase maps in Fig. 10.8 that RD||[100] grain is the least thermally-stable γ grain, followed by RD||[110] and [111]

grains in that order. The EBSD IPF (Figs. 10.9e and g) and phase maps (Figs. 10.9f and h) of another location in CG specimen show nucleation of α' in austenite grains oriented near RD||[100], which is in agreement with the earlier observation. In all scanned regions (including FG and CG specimens), a higher fraction of α' nucleated in RD||[100] oriented grains as indicated by white contours in the standard stereographic IPF triangle in Fig. 10.9i. These findings could open a new window of engineering the initial texture of metastable austenitic stainless steel to either aid thermally and/or mechanically-stable austenite phase (by developing [111]-oriented grains) or promote both isothermal and deformation-induced martensitic phase transformation (by developing [100]-oriented grains).

The BC and twin maps of CG specimen in Fig. 10.8 also confirmed the preferential nucleation of thermally-induced α' at the annealing twin boundaries; an important nucleation site. The near

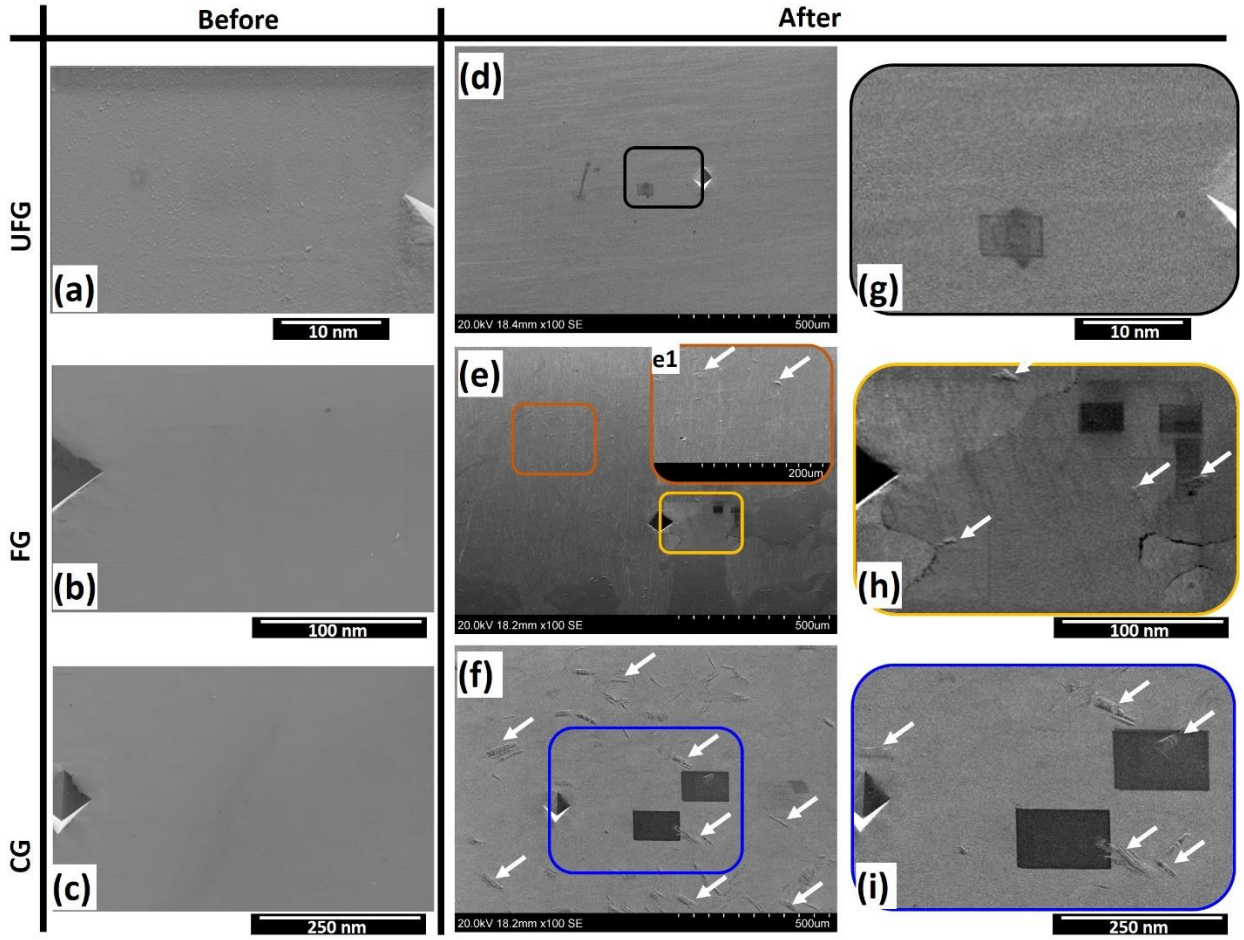


Fig. 10.7. SEM micrographs of the same region (a-c) before and (d-i) after thermal treatment. White arrows indicating some regions of thermally-induced martensite.

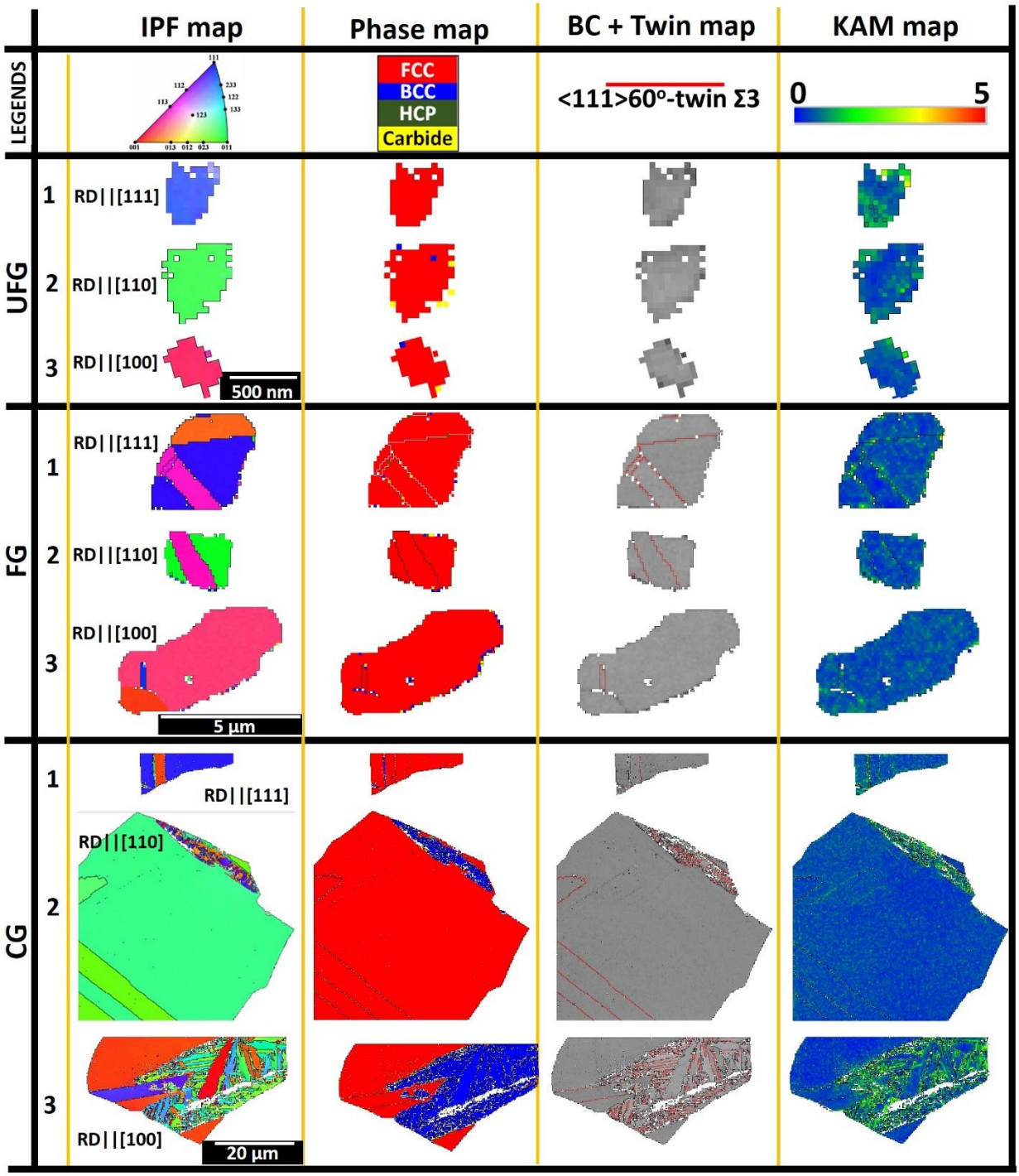


Fig. 10.8. After thermal treatment: EBSD IPF, phase, BC/twin and KAM maps of selected grains in Figs. 10.5 a1, b1 and c1. Grains 1, 2 and 3 are RD||[111], RD||[110] and RD||[100]-oriented grains, respectively.

absence of annealing twins in austenite phase of UFG specimen could, therefore, also justify its (UFG specimen) high resistance to isothermal martensitic phase transformation. Notably, the

nucleated α' are bounded by transformation twins. The comparison of the KAM maps in Figs. 10.6 and 10.8 shows an increase in the KAM value of the γ phase after thermal treatment. The KAM is a measure of local misorientation that indicates the strain distribution or stored elastic energy in the specimen. It is the average misorientation between each measured point and its neighbors which holds as long as the misorientation do not exceed 5° [67]. The higher the KAM value, the higher the stored energy and strain in the specimen. Therefore, thermally-induced strain occurred during thermal treatment due to higher KAM value in Fig. 10.8 than in Fig. 10.6. Specifically, high KAM values are recorded at the γ-α' and α'-α' boundaries in Fig. 10.8. The misorientation gradient could imply the occurrence of plastic deformation in the γ phase to accommodate the shape change (or shape strain) of α' during phase transformation [298]. Besides annealing twin boundaries, other authors have reported that carbide particles are potent nucleation site for

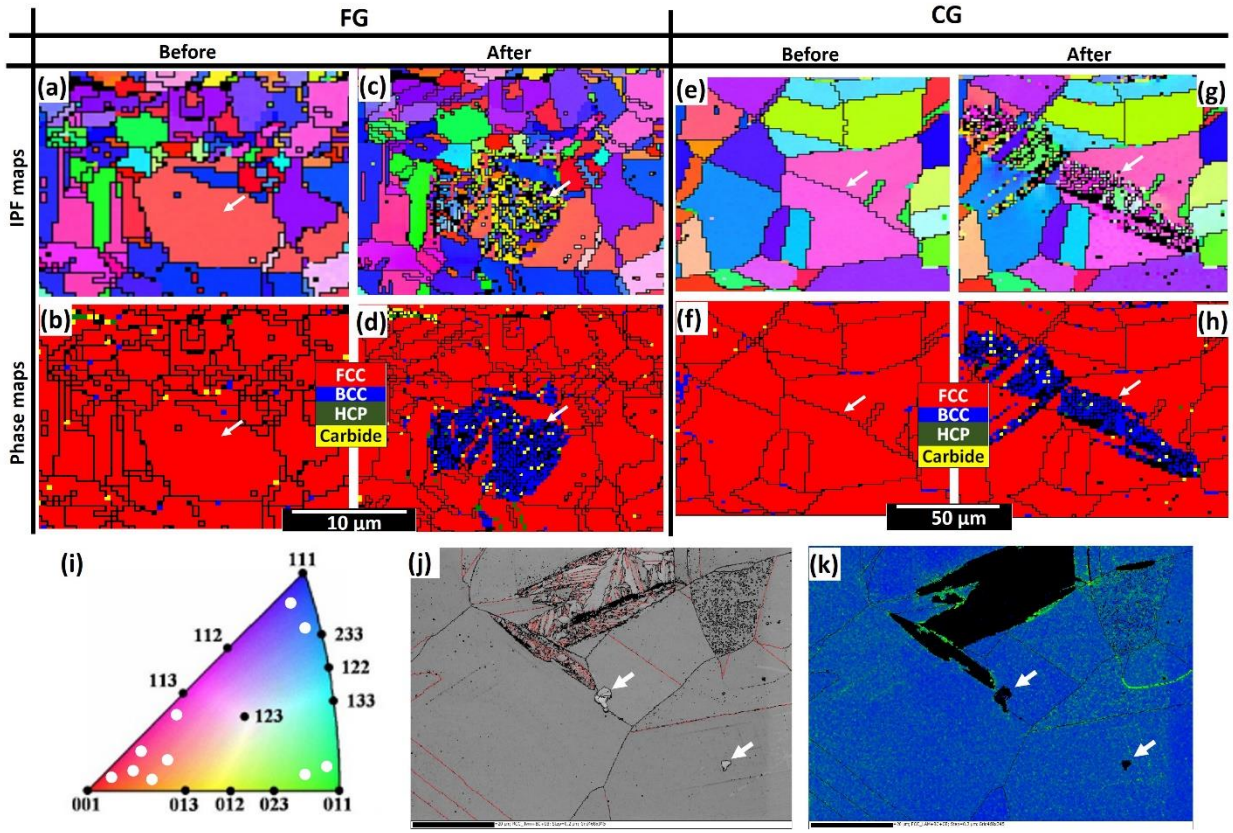


Fig. 10.9. Other regions in (a-d) FG and (e-h) CG specimens showing IPF and phase maps before and after thermal treatment; (i) contours in the standard stereographic IPF triangle showing the crystal orientation of austenite grains that developed martensite; (j) band contrast/twin and (k) KAM maps showing arrowed TiN particle site.

thermally-induced α' due to the misorientation that exists in the austenite phase at the particles' vicinity [34,298]. However, neither TiC nor TiN particles in AISI 321 stainless steel are found to be potential α' nucleation sites. This is because there was no α' observed to nucleate around the particles (white arrows in Fig. 10.9j), and the misorientation gradient in the austenite phase at the particles' vicinity is nearly absent (Fig. 10.9k).

#### 10.3.2.3 Morphology and structure of thermally-induced α'

There are primarily three different morphologies of martensite, namely, lath, thin plate, and lenticular. The evolution of these morphologies depends on the composition and the Ms temperature of the alloy [299]. Other factors (which can be related) such as the strength of parent (γ) and product (α') phases, critical resolved shear stress for slip and twinning in α' and SFE of γ have also been reported [300,301]. While lath α' forms in the highest temperature regime (especially in the low carbon steels and Fe-Ni alloys), thin plate α' forms in the lowest temperature range in high alloyed steels [302]. The lenticular α' however forms at an intermediate temperature regime between those of lath and thin plate α'. The formation range of α' as a function of Ms temperature and carbon concentration in Fe-Ni-C alloy systems is schematically shown in Fig. 10.10a [300]. Although, AISI 321 stainless steel is a Fe-Cr-Ni alloy system with 0.044 C wt%, Fig. 10.10a can still provide useful information on the plausible α' morphology with minimal deviation. Similarly, while lath α' is characterized by high dislocation density due to strain accommodation induced by phase transformation, thin plate α' is characterized by a set of uniformly spaced transformation twins crossing throughout the plate [298,299]. Lenticular α' has a lens-like morphology that contains three regions: the midrib (a region of highly dense and regularly spaced transformation twins), extended twinned region that emanates from the midrib and untwinned region (characterized by screw dislocations and a high density of tangled dislocations). It has been reported that the midrib of a lenticular α' is a thin plate α' since both (midrib and thin plate α') have similar morphology, substructure and crystallographic features [300]. Hence, the major difference between lenticular and thin plate α' is only in their growth behaviors; i.e., during growth, thin plate α' retains its deformation mode of twinning and midrib exhibits a combination of twinning and slip modes [34,298,300,302]. Shibata et al. [302] reported that midribs in lenticular α' could also be branched and kinked.

The higher magnification IPF and BC/twin maps for RD||[100] oriented coarse γ grain are presented in Figs 10.10b and c, respectively. The thermally-induced martensite grains are mainly oriented near [110] and characterized by pronounced transformation twins. This observation suggests the induced α' possess a thin-plate morphology. This is supported by tracing the AISI 321 carbon content and the thermal treatment temperature in Fig. 10.10a, although little deviation may exist. Relatively high austenite strength, low Ms temperature (as observed in Fig. 10.10a), high tetragonality of α' (i.e., small twin shear, low magnitude of shape strain and low twin boundary energy) are reported to favor the formation of thin plate α' [303]. Considering the different direction in which the α' grains are morphologically arranged, five possible growth directions are indicated in Fig. 10.10b. Martensite grains in 1, 2, 3 and 4 directions confirmed grain boundaries serve as a viable nucleation site. The nucleation of grains labeled, directions '3' and '4', from the grain boundaries are supported by considering Fig. 10.5c. There is the possible occurrence of 'burst' martensitic transformation phenomenon in which a martensite grain (such as the long [100] oriented α' grain indicates as direction '3' in Fig. 10.10b) nucleates a sequence of other plates (such

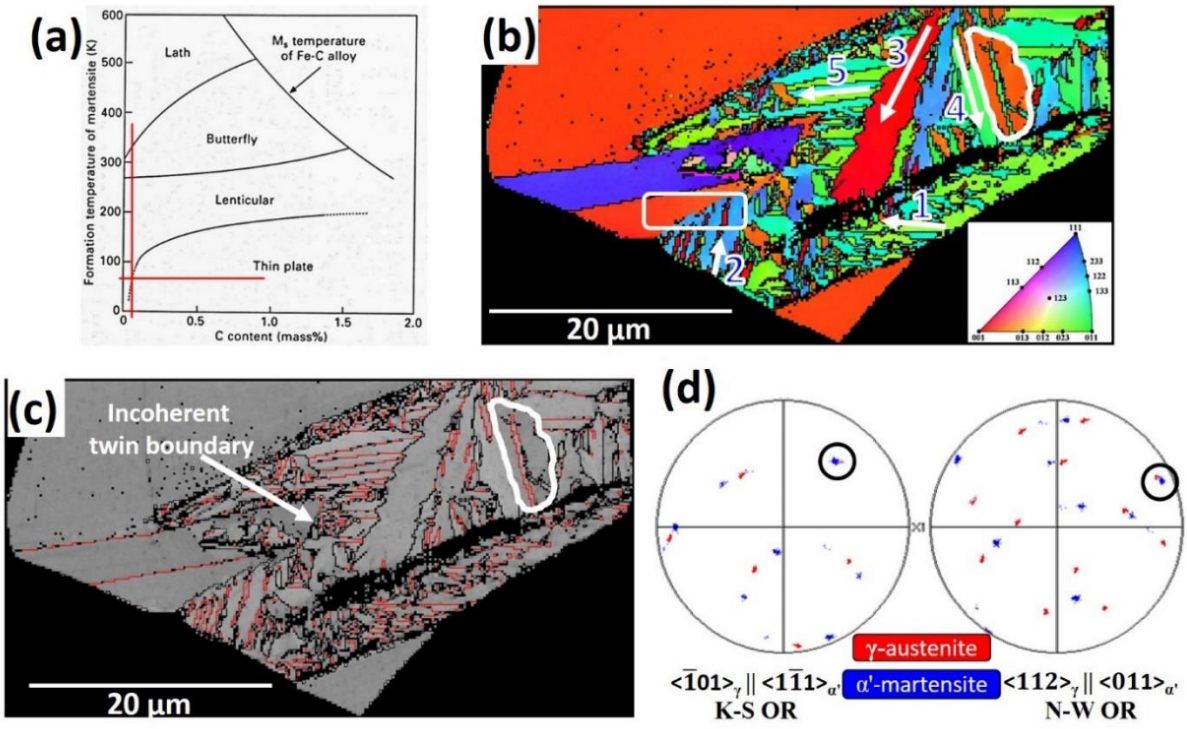


Fig. 10.10. (a) Schematic drawing showing the formation range of α' as a function of Ms temperature and carbon concentration in Fe-Ni-C alloy systems [300], (b) phase and (c) BC/twin maps of RD||[100] oriented austenite grain in Fig. 10.8, (d) co-plot of <1̄01>γ & <11̄1>α' and <112>γ & <011>α' pole figures of rectangular marked region in Fig. 10.10b.

as all the [110] oriented grain along direction ‘5’). These occur as a result of stress concentrations set up when the first plate reaches an obstruction such as grain boundary or another α' plate such as grains aligned in direction ‘1’ [34,298]. That is, the ‘bursting’ of grains aligned in direction ‘5’ could be due to the stress concentration set up during growth as a result of the collision of grain labeled direction ‘3’ on already isothermally nucleated grains in direction ‘1’. Figures 10.10b and c also shows that the growth of some ‘busted’ martensites (grains in direction ‘5’) are effectively hindered by the incoherent boundary of an existing annealing twin. Although incoherent twin boundaries could be likely sites for α' nucleation [34], it is confirmed that they can also actively hinder a growing α'. By qualitative kinetic classification, the bursting phenomenon and isothermal martensitic transformation are grouped together due to the absence of concurrent stabilization common to both [304]. This may justify their (bursting and isothermal behaviors) co-existence in Fig. 10.10.

Although the EBSD results suggest the isothermally-induced martensite have thin-plate morphology, it has been reported that this morphology could become lenticular under certain conditions. On the effect of deformation temperature on the stress-induced growth behavior of thin plate martensite, Shibata et al. [302] observed that thermally-transformed thin plate α' grows without a change in morphology when deformation is at a temperature close to the Ms temperature. A shape change into lenticular, however, occurs at a temperature above the Ms temperature, leading to the conclusion that midrib in lenticular α' was thin-plate α' at an earlier formation stage. During the isothermal holding of Fe–1.0C–17Cr (wt.%) stainless steel in liquid nitrogen (−196 °C), Lee et al. [299] observed that thin-plate martensite first formed, followed by the lenticular martensite after an extended period. This observation is contrary to the general opinion that lenticular α' forms at a higher temperature than the temperature at which thin-plate α' evolves. It is, therefore, possible that the thermally-induced thin-plate α' in AISI 321 steel will grow into lenticular α' at an extended time. This is validated by the presence of a RD||[100] oriented lenticular α' (lenticular white highlight in Fig. 10.10b and c) with a branched midrib. On the existing orientation relationship between the untransformed γ and thin-plate α', the coincidence of poles when $<\bar{1}01>_{\gamma}$ and $<1\bar{1}1>_{\alpha'}$ pole figures, and $<112>_{\gamma}$ and $<011>_{\alpha'}$ pole figures were superimposed in Fig. 10.10d confirmed the existence of both Kurdjumov-Sachs ($\{111\}_{\gamma}||\{110\}_{\alpha'}$ and

$<\bar{1}01>_{\gamma}||<1\bar{1}1>_{\alpha'}$) and Nishiyama–Wasserman ($\{111\}_{\gamma}||\{110\}_{\alpha'}$ and $<112>_{\gamma}||<011>_{\alpha'}$) orientation relationships, respectively.

### 10.3.3 Mechanical stability of austenite (MSA)

To determine the MSA in AISI 321 austenitic stainless steel, UFG, FG and CG specimens were deformed at different strain rate regimes i.e. under quasi-static and dynamic compressive loading conditions.

#### 10.3.3.1 True stress-strain curves and hardness profile

Typical true stress-strain curves of specimens deformed under quasi-static and dynamic loading conditions are presented in Fig. 10.11a and b, respectively. The mechanical strength of the alloy increases with a decrease in grain size under both deformation conditions. However, specimens compressed under quasi-static condition strain hardens up to the final deformation strain while those specimens subjected to dynamic loading conditions show strain hardening that is eventually

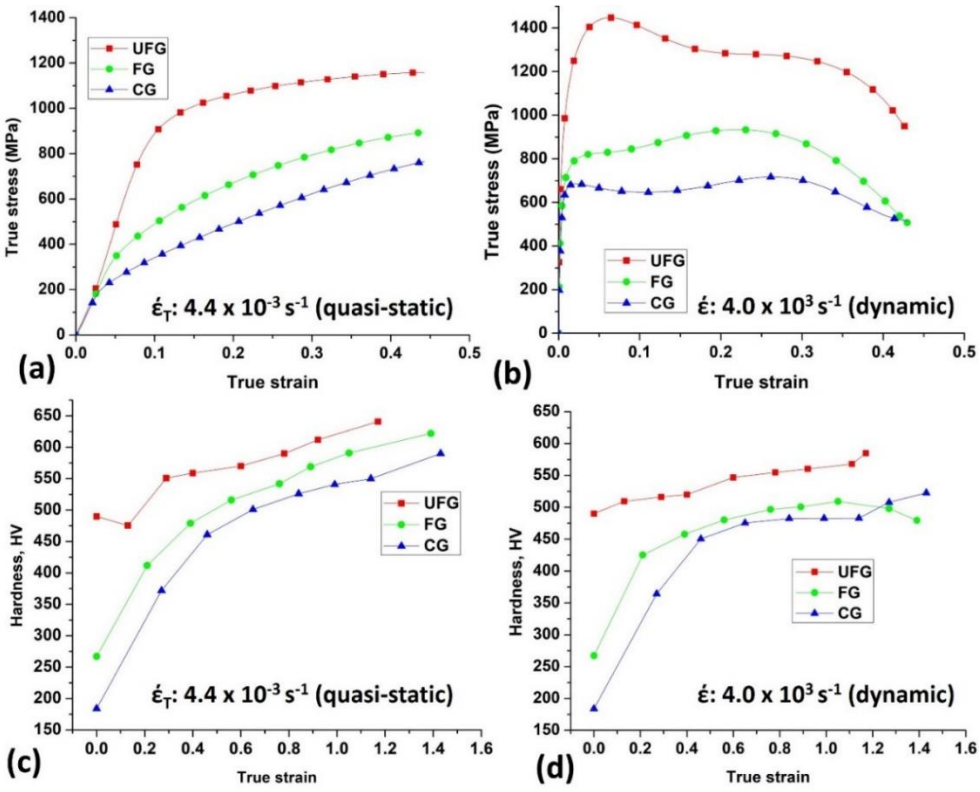


Fig. 10.11. (a, b) Typical true stress-strain and (c, d) hardness-true strain curves for specimens compressed under quasi-static and dynamic loading conditions. Standard deviations for (c) and (d) are 15 and 9, respectively.

overcome by thermal softening. The thermal softening leads to drop in flow stress and results in eventual loss of load-carrying capacity. Similarly, the hardness profile of specimens deformed under quasi-static and dynamic loading conditions are presented in Fig. 10.11c and d, respectively. Although the hardness value of the alloy increases with decrease in grain size and increase in strain under both deformation conditions, those deformed under quasi-static condition possesses higher hardness values. Hardening in AISI 321 steel has been attributed to multiple strengthening sources such as the simultaneous occurrence of slip, twinning and martensitic phase transformation [277]. Due to the scope of this work, subsequent sections are now focused on the evolution pattern of deformation-induced martensitic phase transformation in the investigated steel.

#### 10.3.3.3 Microstructural evaluation and morphology of deformation-induced martensite

Figure 10.12 shows the volume fraction of deformation-induced α' and its variation with grain size and strain in both low and high strain rate regimes. While the fraction of α' increases with strain (irrespective of grain size) in specimens deformed under the quasi-static loading condition (Fig. 10.12a), those of the specimens subjected to dynamic loading condition increased with strain up to a critical value above which the fraction of α' drops (Fig. 10.12b). The drop in α' (Fig. 10.12b) is attributed to the temperature rise (adiabatic heating) in the impacted specimen, which is a signature of high strain rate loading condition [255,262,275,276]. On the stability of the austenite phase under external compressive load, Fig. 10.12 shows that the mechanical stability of austenite in metastable AISI 321 austenitic stainless steel decreases with a decrease in grain size

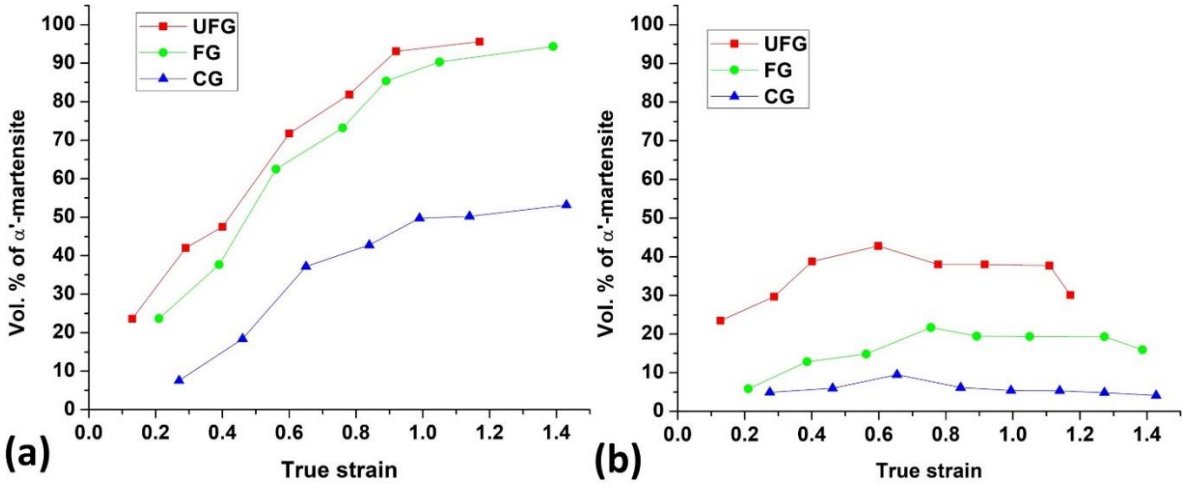


Fig. 10.12. Vol.% of α'-true strain curves for specimens compressed under (a) quasi-static and (b) dynamic loading conditions. Standard deviations for (a) and (b) are 0.93 and 0.22, respectively.

since the fraction of deformation-induced α' increases with a decrease in grain size. The reverse was observed to be the case for thermal stability of austenite (TSA) as discussed in the previous subsection.

The TEM micrographs of specimens compressed under the quasi-static condition (Figs. 10.13a-d) shows the morphology of deformation-induced α' that is distinctively different from that of the thermally-induced α'. Unlike the γ in UFG specimens that are perfectly stable in cryogenic environment, the γ in UFG specimen are very unstable under an external compressive load and the morphology of deformation-induced α' is equiaxed (Fig. 10.13a). The TEM micrographs of the CG specimen subjected to quasi-static compressive load are presented in Fig. 10.13b-d. It can be confirmed in Fig. 10.13b that high dislocation densities and nano-twins are present in the remaining austenite phase. Figure 10.13d shows that the morphology of deformation-induced α' in CG specimens is lath-like, which are ~70 nm thick and ~830 nm long. The size of the laths could justify why α' in UFG specimen retains the morphology of the γ (equiaxed); since α' laths are ~3.5 times longer than the γ grain size of UFG specimen. The evolution of lath-like α' in compressed CG specimens rather than thin-plate α', as in the case of thermally-treated CG specimen, could be due to the different temperature regimes at which thermal (-196 $^{o}$C) and mechanical (23 $^{o}$C) tests were conducted. It has been reported elsewhere [301] that the morphology of α' can be influenced by temperature as also shown in Fig. 10.10a. Qualitatively, the EBSD phase maps in Figs. 10.13e-h show the austenite phase in the UFG specimen to be more unstable than the CG specimen, and the instability increases with strain. This result agrees with the quantitative feritscope results in Fig. 10.12a. The formation of a higher fraction of α′ in UFG specimens is due to the higher grain boundary area and triple junctions that are nucleation sites for stress-induced α′ transformation [59,290].

On the role of texture on the mechanical stability of γ, the γ stability in AISI 321 increases from CD||[100] to CD||[110] and to CD||[111], in that order, for FG and CG specimens. In this case, CD is the compression direction. This observation is also reported else where [289]. This is affirmed by considering γ grains 1, 2, and 3 in the EBSD phase maps for a compressed CG specimen (Fig. 10.13i), which are oriented near CD||[100], CD||[110], and CD||[111], respectively (Fig. 10.13j). These grains underwent deformation-induced martensitic phase transformation with the highest mechanical instability of γ phase recorded in grain 1, followed by grains 2 and 3, in that order.

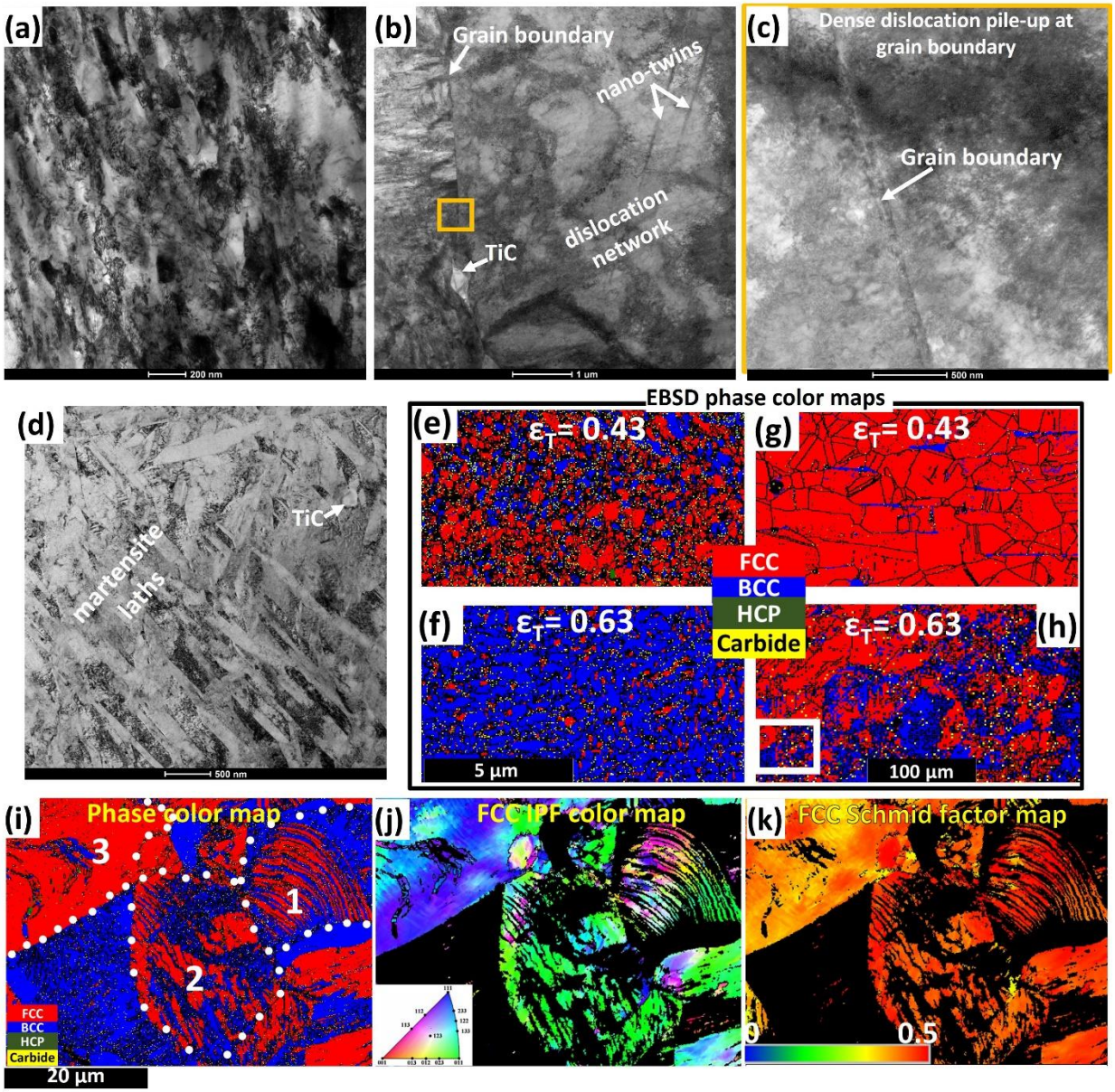


Fig. 10.13. (a-d) TEM micrographs: (a) UFG and (b-d) CG specimens; (e-h) EBSD phase maps: (e, f) UFG and (g, h) CG specimens compressed under quasi-static conditions; and (i-k) Higher magnification EBSD maps of marked region in (h): (i) phase color, (j) FCC IPF color, and (k) FCC Schmid factor maps.

Schmid factor map for the austenite phase (Fig. 10.13k) shows that the most mechanically-stable of γ, grain 3, possesses the lowest Schmid factor, while γ grain 1 is the least stable with highest Schmid factor. The Schmid factor, therefore, suggests that grain 1 (grain oriented near CD||[100]) demonstrate ease of slip system activation compared to grains of other orientations during compression [287,305,306].

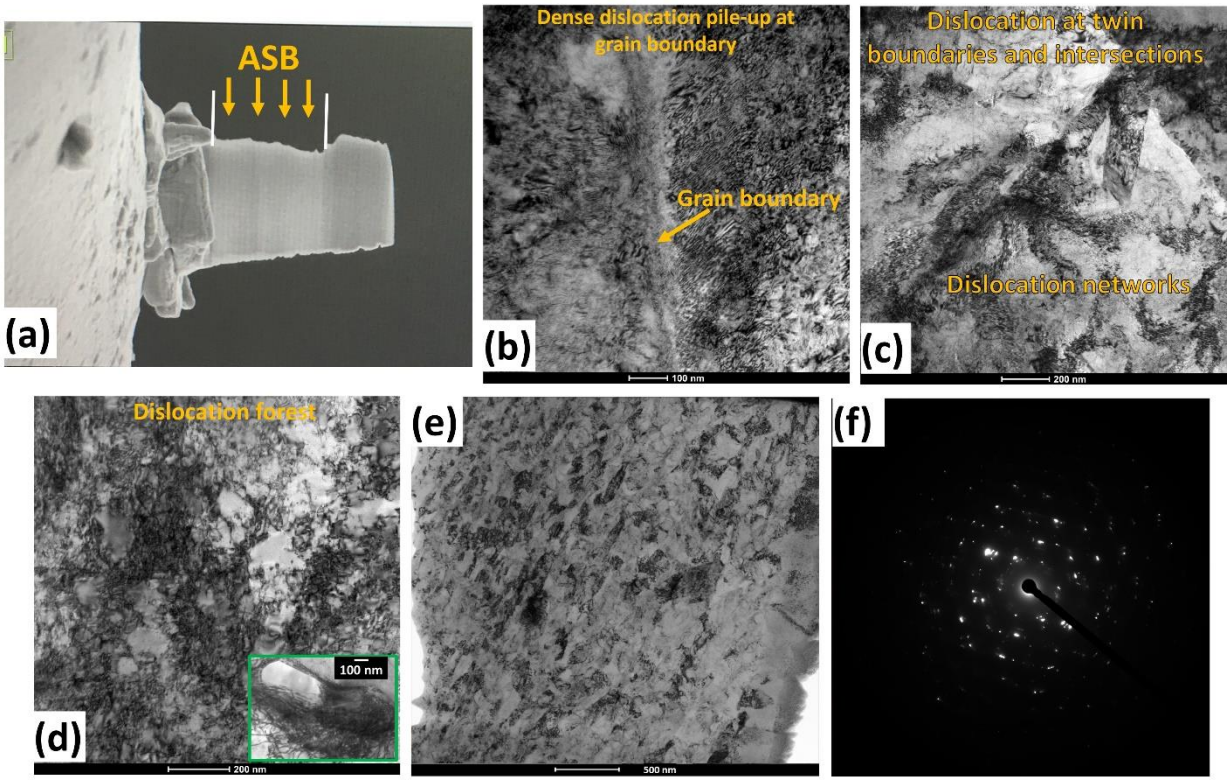


Fig. 10.14. TEM micrographs of dynamic-impacted specimens: (a) Fibbed specimen showing inside and outside regions of ASB, (b-d) outside ASB, (e) inside ASB, (f) selected area diffraction pattern for (e). Inset in (d) shows carbide-dislocations interaction.

TEM micrographs of CG specimen subjected to dynamic impact loading condition are presented in Fig. 10.14. A narrow shear zone, termed adiabatic shear band (ASB), that eventually become preferential dynamic failure/fracture sites is typically observed in the microstructure of materials subjected to dynamic impact load [89,90]. In a CG specimen that forms ASB (Fig. 10.14), the region outside the ASB shows grain boundary-dislocation interaction (Fig. 10.14b), twin boundary-dislocation interaction (Fig. 10.14c) and regions of dislocation forest in deformed austenite (Fig. 10.14c). The TEM micrographs of the region inside ASB (Figs. 10.14e and f) confirmed the occurrence of grain refinement which has been attributed to rotational dynamic recrystallization proposed by Nesterenko *et al.* [112]. The EBSD phase maps of inside and outside ASB of impacted UFG (Fig. 10.15a-c) and CG (Fig. 10.15d-e) specimens show that inhomogeneous deformation results in inhomogeneous phase distribution, i.e. the fraction of strain induced α' transformation is highest outside ASB and very low inside the ASB. The near-absence of α' in the ASB region (Figs. 10.15c and e) justifies that the temperature rise in these specimens are significantly high (to suppress phase transformation) and localized. Although the mechanical

stability of the γ phase is higher in specimens deformed under dynamic condition (Fig. 10.15) than those under quasi-static condition (Fig. 10.13), it can also be confirmed from Fig. 10.15 that the mechanical stability of the γ decreases with a decrease in grain size. On the morphology of

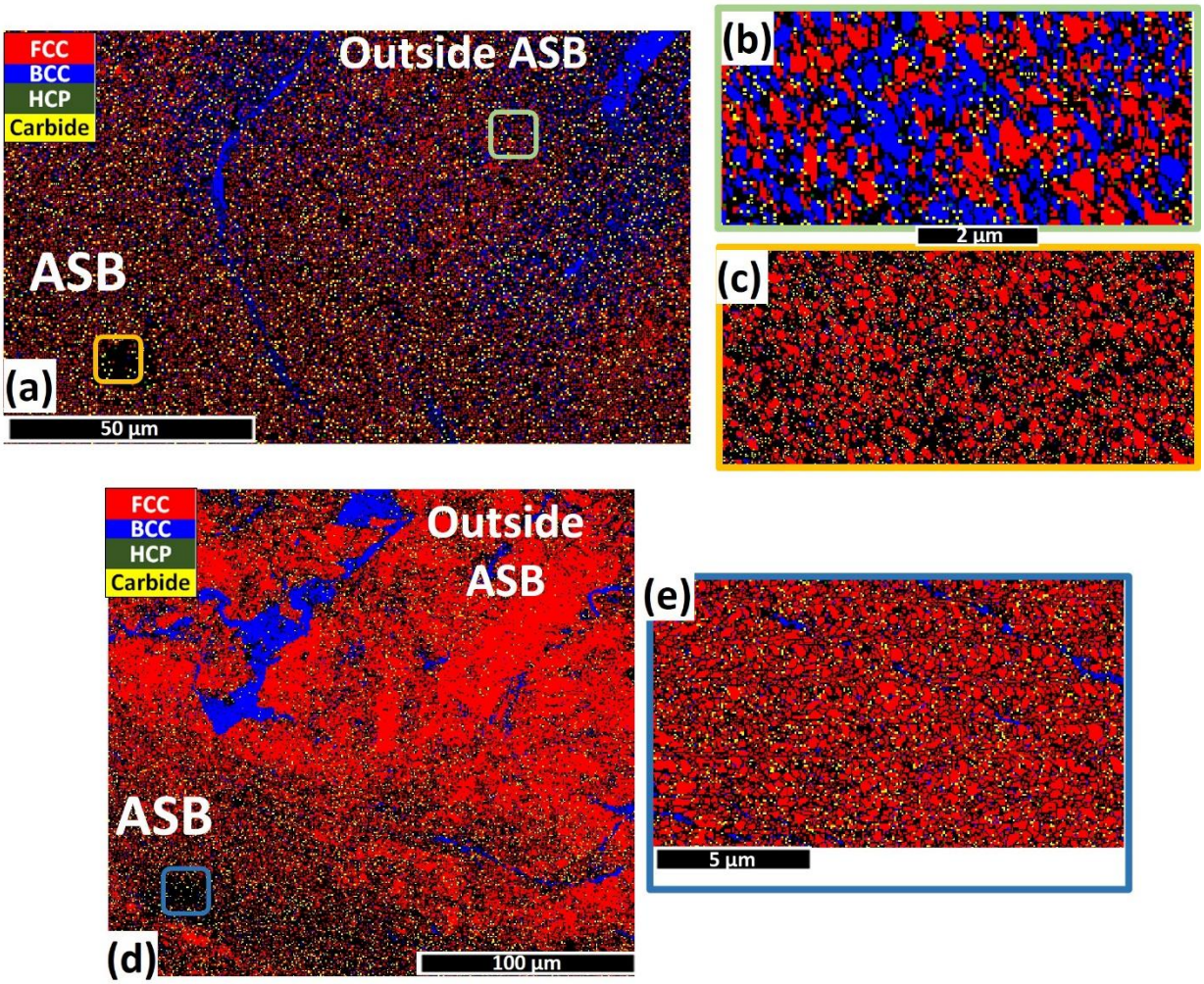


Fig. 10.15. EBSD phase maps of dynamic impacted specimens showing inside and outside ASB regions: (a-c) UFG and (d, e) CG specimens.

deformation-induced α' in specimens deformed under dynamic condition, the morphology of α' in UFG specimen are equiaxed (Fig. 10.15b) while those in CG specimen are irregular with no definite shape (Fig. 10.15d). Based on the above experimental data and discussion of results, the role of grain size, texture, strain, and strain rate on the thermal and the mechanical stability of austenite in AISI 321 stainless steel can be summarized in a schematic diagram as shown in Fig. 10.16.

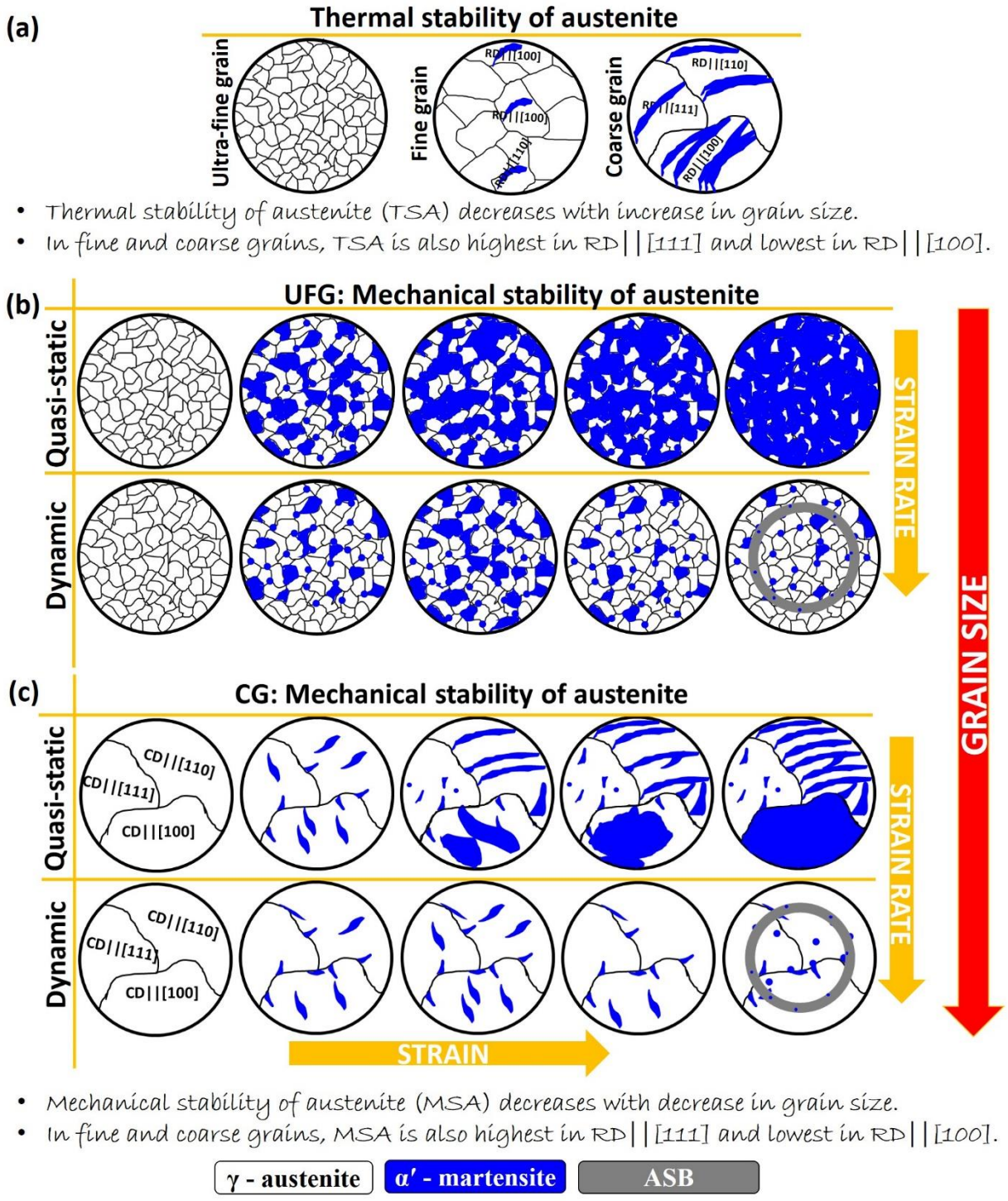


Fig. 10.16. Schematic drawing showing the role of grain size on (a) thermal and (b and c) mechanical stability of austenite in AISI 321 stainless steel.

## 10.4. Summary and conclusions

The roles of grain size, texture, strain and strain rate on the thermal and mechanical stability of austenite in AISI 321 metastable austenitic stainless steel were studied. Ultrafine grain (UFG), fine grain (FG) and coarse grain (CG) specimens with average grain sizes of 0.24, 3 and 37 μm sizes, respectively, were investigated. Samples were soaked in liquid nitrogen (-196 $^{o}$C) for 30 mins., 1 h, 12 h and 24 h to determine the thermal stability of austenite (TSA). On the other hand, the mechanical stability of austenite (MSA) was studied by subjecting cylindrical specimens to both quasi-static (4.4 x $10^{-3}$ $s^{-1}$) and dynamic loading conditions (between 1300 and 8800 $s^{-1}$). The following conclusions are drawn from the research findings;

1. Thermally-induced α'-martensite can only be observed at an incumbent time in AISI 321, suggesting the occurrence of an isothermal martensitic transformation. Both Kurdjumov-Sachs ($\{111\}_{\gamma}||\{110\}_{\alpha'}$ and $<\bar{1}01>_{\gamma}||<1\bar{1}1>_{\alpha'}$) and Nishiyama–Wasserman ($\{111\}_{\gamma}||\{110\}_{\alpha'}$ and $<112>_{\gamma}||<011>_{\alpha'}$) orientation relationships exist between the untransformed γ and thin-plate α'. The phase transformation is highly suppressed in UFG specimens.
2. While TSA decreases with an increase in grain size, MSA decreases with a decrease in grain size.
3. The higher mechanical instability of austenite in UFG specimen under compression is due to the presence of higher grain boundary area and triple junctions that promote stress-induced phase transformation. Meanwhile, the higher austenite stability of UFG specimen in cryogenic temperature is due to spatial restriction effect that resists the formation of isothermal martensite. This subsequently restricts multi-variant transformation required to accommodate anisotropic transformation strain.
4. While thin-plate α' is predominantly formed in thermally-treated AISI 321 steel (FG and CG specimens only), lath and irregularly-shaped α' are formed in specimens deformed under quasi-static and dynamic loading conditions, respectively. Irrespective of strain rate, deformation-induced α' in UFG specimens inherit the equiaxed morphology of the deformed austenite grain.
5. Irrespective of grain size, MSA also decreases with an increase in strain and decrease in strain rate. In the event of ASB formation in specimens deformed at high-strain rate, MSA

increases as the ASB is approached. This is due to the significant temperature rise inside the ASB region.

6. EBSD analysis revealed that the evolution of both thermally- and deformation-induced martensite is orientation-dependent in FG and CG specimens. The instability (both thermal and mechanical) of the austenite phase was observed to be highest in the RD/CD||[100]-oriented grains, followed by grains oriented near RD/CD||[110] and RD/CD||[111], in that order. These findings could open a new window of engineering the initial texture of metastable austenitic stainless steel to either aid thermally or mechanically-stable austenite phase or promote both isothermal and deformation-induced martensitic phase transformation.

# Chapter 11

## Corrosion Behavior of Metastable AISI 321 Austenitic Stainless Steel: The Effect of Grain Size and Prior Plastic Deformation on its Degradation Pattern in Saline Media

Having significantly improved the mechanical strength of AISI 321 stainless steel through the grain refinenment of the as-received coarse-grained (CG) alloy specimen to ultrafine grain (UFG) structure, it became necessary to determine if the improved mechanical strength is not at the expense of the excellent corrosion resistance of the alloy. Therefore, the role of grain size and prior plastic deformation (at high and low strain rates) on the corrosion behavior of AISI 321 austenitic stainless steel in 3.5 wt.%-NaCl solution is studied and discussed in this chapter. The mechanism of pitting in the AISI 321 steel in chloride solution is proposed. This manuscript is published in "*Scientific Report"* as follows:

A. A. Tiamiyu, Ubong Eduok, J. A. Szpunar, and A. G. Odeshi, "Corrosion behavior of metastable AISI 321 austenitic stainless steel: investigating the effect of grain size and prior plastic deformation on its degradation pattern in saline media", *Scientific Report,* 2019, https://doi.org/10.1038/s41598-019-48594-3.

My contributions to this paper include review of the relevant literature, design and carrying out of experiments, analysis of test results and preparation of the manuscript. My supervisors (Professors Akindele Odeshi and Jerzy Szpunar) reviewed it and their comments were addressed before submission for publication. The present manuscript is a modified version of the published paper. Materials covered in Chapter three are removed to avoid unnecessary repetition. 

### Abstract

The role of grain size and strain rate on the corrosion behavior of plastically deformed Ti-stabilized austenitic stainless steel (AISI 321) in saline media was investigated. The as-received coarse-grained alloy (CG: ~37 μm) was subjected to thermomechanical-processing to develop fine (FG: ~3 μm) and ultrafine (UFG: ~0.24 μm) grained structures. These samples were deformed under high (dynamic) and low (quasi-static) strain-rate conditions to a similar true strain of ~0.86.

Microstructural analyses on specimens after deformation prior to corrosion study suggests a shift from the estimated stacking fault energy value of the steel. Electrochemical tests confirm the highest corrosion resistance for UFG specimens due to the formation of the most stable adsorbed passive film. This is followed by FG and CG specimens in that order. For the three grain sizes, the corrosion resistance of specimen deformed under quasi-static loading condition is higher than that subjected to dynamic impact loading while the corrosion resistance of undeformed samples is the least. This work also confirms the non-detrimental effect of TiCs in AISI 321 austenitic stainless steel on its corrosion resistance. However, TiNs were observed to be detrimental by promoting pitting corrosion due to galvanic coupling of TiNs with their surrounding continuous phase. The mechanism of pitting in AISI 321 in chloride solution is proposed.

***Keywords:*** *AISI 321 austenitic stainless steel; Thermomechanical processing; Deformation-induced phase transformation; Corrosion; Microstructure*

## 11.1 Introduction

Corrosion resistance is an important criterion for selecting materials used in the fabrication of chemical and nuclear plants since the cost of materials degradation due to corrosion and the often associated environmental impact are quite substantial [307]. Generally, the composition of austenitic stainless steels (e.g. AISI 304 and other similar grades) is adjusted to meet service requirements in various corrosive environments. Their excellent corrosion resistance is usually hampered by the precipitation of chromium-rich $M_{23}C_6$ type carbide at the grain boundaries at elevated temperature, thereby promoting intergranular stress corrosion. To inhibit the undesired grain boundary segregation (sensitization), a Ti-stabilized AISI 321 austenitic stainless steel (a derivative of AISI 304) was developed to favor the preferential formation of TiC precipitates, thereby keeping chromium in solution for protection against corrosion [140]. AISI 321 steel is therefore widely used as choice material in the manufacture of heat exchangers for chemical process plants, high-pressure pipes, engine turbines for automobiles and aircraft, and also in nuclear reactors [28,29,140].

Several researchers have reported on the corrosion behavior of AISI 321 steel in selected environments that simulate service conditions. For instance, Lv and Luo [308] studied the effect of low-temperature sensitization (at 380 and 450 $^{o}$C) on the degree of sensitization (DOS) and

corrosion resistance of ultrafine-grained (UFG) AISI 321 steel. The authors observed lower DOS and improved corrosion resistance in the specimen annealed at 450 $^{o}$C than that annealed at 380 $^{o}$C. In a separate study [309], UFG structured AISI 321 steel developed via thermomechanical processing exhibited lower corrosion resistance than coarse grain (CG) specimens in 0.1 M NaCl solution at room temperature. However, the UFG specimen was more resistant to corrosion than the CG specimen in a 0.5 M $H_2SO_4$ solution at room temperature. Moura et al. [26] investigated the influence of stabilization heat treatments on the intergranular corrosion resistance of AISI 321 steel at high temperatures to promote TiC precipitation. Preservation of Cr in solid solution was observed before subsequent use for high temperature (600-800 $^{o}$C) applications. These researchers reported 950 $^{o}$C as the optimum stabilizing temperature that inhibits sensitization. Leban and Tisu [30] reported the deteriorating effect of TiN and deformation-induced martensite (DIM) on the corrosion behavior (pitting and stress corrosion cracking) of cold worked outer exhaust sleeve made of an AISI 321 steel. Other works on the corrosion behavior of AISI 321 and other stainless steels are reported in Refs. [139,310,311] and Refs. [312,313], respectively.

The role of grain size, prior deformation, and strain rate on the degradation pattern of AISI 321 stainless steel in corrosive environments is not well reported in the literature. This is the motivation for the present study. In this work, we have optimized the mechanical properties of the as-received coarse-grained AISI 321 austenitic stainless steel by developing fine and UFG structures in the steel via thermomechanical processing. It, therefore, becomes pertinent to investigate if the unique corrosion resistance of this steel has deteriorated as a result of the grain refinement process. Similarly, the AISI 321 steel with coarse, fine, and ultrafine grain structures were exposed to external loads using quasi-static and dynamic impact loading that can simulate the different loading conditions the steel can experience in service. The aim is also to ascertain how these loading conditions affect the corrosion behavior of AISI 321 steel.

## 11.2 Material and methods

AISI 321 metastable austenitic stainless steel (MASS) described in Section 3.1 was used in this study. Cylindrical specimens of 4 mm in diameter × 4 mm long were machined along the rolling direction (RD) for compression tests under both quasi-static and dynamic loading conditions. The quasi-static compression test was conducted at a true strain rate of $4.4 \times 10^{-3}$ $s^{-1}$. The high strain-rate test was conducted at a true strain rate of $8.8 \times 10^{3}$ $s^{-1}$. Specimens were compressed under both

dynamic and quasi-static loading conditions to a total true strain of approximately 0.86. The same true strain was accomplished by conducting, first, the dynamic impact test; the quasi-static test was interrupted once the true strain in specimen is the same as that obtained during the impact test. The average grain size of the as-received steel on the ND-TD plane is 37 μm (Fig. 11.1c). This is hereafter referred to as coarse-grained (CG). A thermo-mechanical process that involved annealing of 50% cryo-rolled as-received CG sample at 750 ℃ for 10 minutes, and 800 ℃ for 360 minutes, developed 0.24 (Fig. 11.1a) and 3 μm (Fig. 11.1b) grain sizes, respectively. These are hereafter referred to as ultrafine-grained (UFG) and fine grained (FG), respectively. The cryo-rolling process is described in Section 3.2. The Vickers hardness values of the undeformed UFG, FG and CG samples are 490, 267 and 186 HV, respectively.

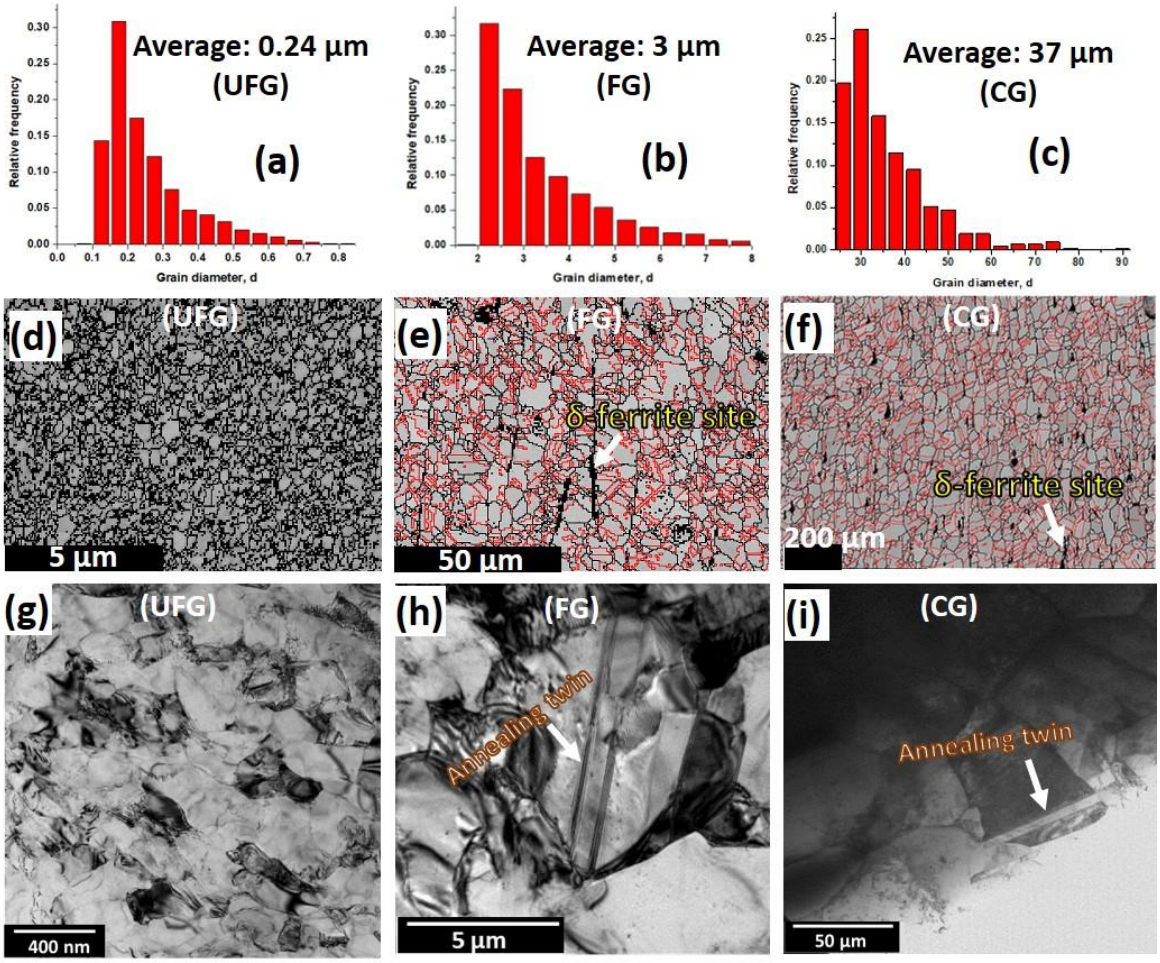


Fig. 11.1. (a-c) Grain size distribution estimated from large scan area, (d-f) EBSD band contrast maps with twins and (g-i) TEM micrographs of the undeformed specimens. Red lines in EBSD maps are annealing twins.

The EBSD maps (Fig. 11.1d-f) and TEM micrographs (Fig. 11.1g-i) show that the annealing twins are highly suppressed in UFG specimen, but the area fraction of annealing twin in the microstructure increases with an increase in grain size. This observation also suggests that deformation twinning will be difficult in UFG specimen on exposure to external load due to spatial restriction effect. Figures 11.1e and f also show the presence of intergrain δ-ferrite stringers. δ-ferrite is an intermetallic compound whose formation is promoted by high Cr content in alloys [1]. SEM micrographs also show the presence of the δ-ferrite in CG (Fig. 11.2a) and UFG specimens (Fig. 11.2b), and two variants of Ti precipitates, namely, TiN and TiC. While the EDS maps in Fig. 11.2c confirm the presence of TiN and Cr-rich stringers of δ-ferrite, Fig. 11.2d affirm the presence of nano-sized (~100 nm) TiC particle in the undeformed specimen. The TiC in austenitic stainless steels satisfy two purposes: first, their precipitation limits the formation of chromium-rich $M_{23}C_6$ type carbide at the grain boundaries and also prevents intergranular stress corrosion. Secondly, if TiC carbide precipitates as a fine dispersion in matrices and grain boundaries, they improve tensile and creep strength significantly at both high and low temperatures [140].

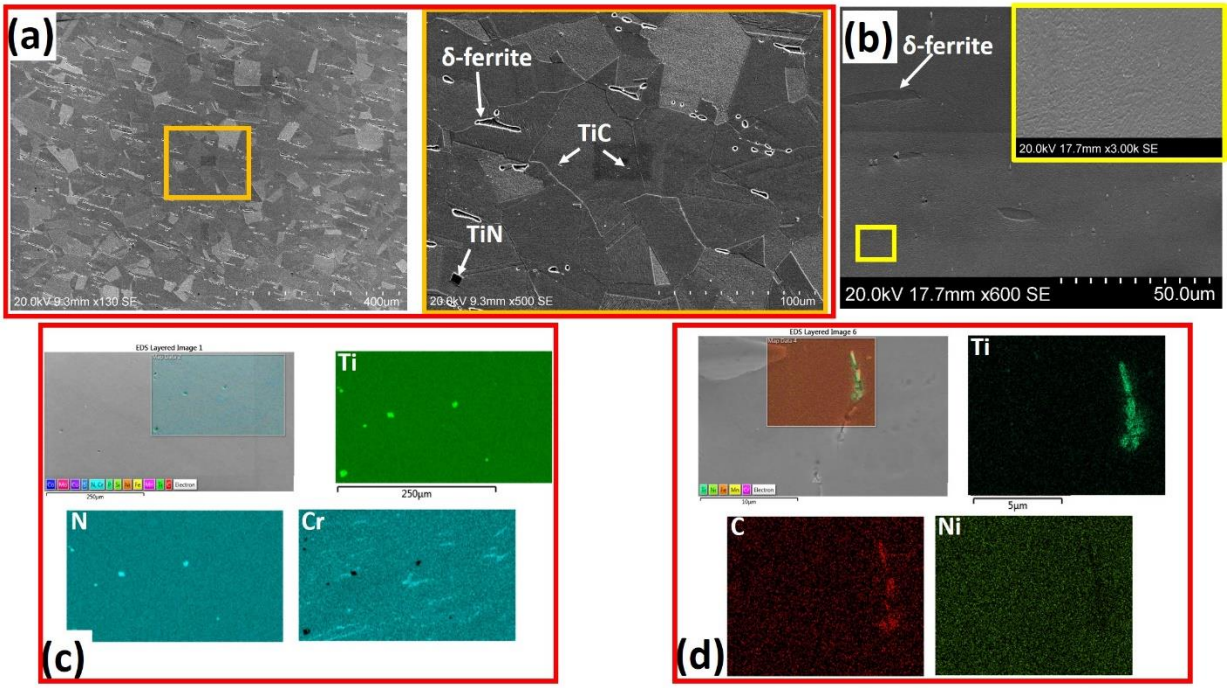


Fig. 11.2. SEM micrographs of (a) CG and (b) UFG undeformed specimens. EDS maps showing the presence of (c) TiN particles and δ-ferrite, and (d) TiC particles in the undeformed specimen.

The selected X-ray diffractometry (XRD) orientation distribution function (ODF) ϕ2 sections show that the undeformed UFG specimen is significantly textured around C {001}<100>

orientation (Fig. 11.3a). The development of R-C {001}<110>, Cu {112}<111>, X {112}<012>, Y {332}<123> and Z {123}<013> orientations are recorded in undeformed FG specimen (Fig. 11.3b). The intensities of these orientations decrease as the grain size increases from fine to coarse (Fig. 11.3c). Figure 11.3d shows the EBSD IPF color map that reveals random orientation of the undeformed CG specimen and its corresponding very low Kernel average misorientation (KAM) value map (Fig. 11.3e), typical of the KAM of UFG and FG specimens. All electrochemical corrosion tests were conducted as described in Section 3.4.

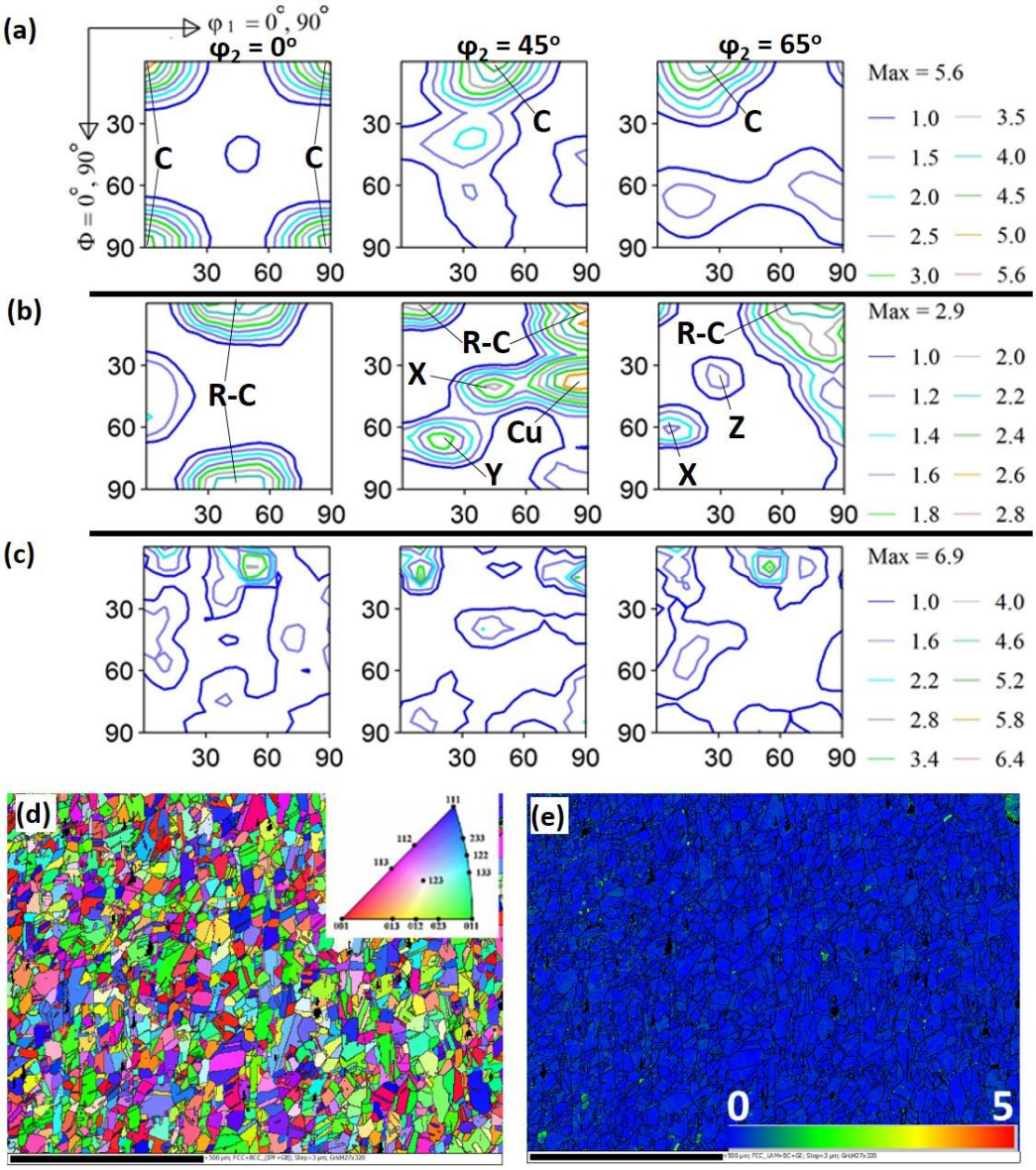


Fig. 11.3. Selected ODF $\phi_2$ sections from the XRD measurement of the undeformed (a) UFG, (b) FG and (c) CG: C {001}<100>, R-C {001}<110>, Cu {112}<111>, X {112}<012>, Y {332}<123>, Z {123}<013>. EBSD (d) IPF and (e) KAM maps of undeformed CG specimen.

## 11.3 Results and discussion

### 11.3.1 Mechanical (dynamic and quasi-static) behavior of AISI 321 austenitic steel

True stress-strain curves depicting the dynamic impact response (8.8 x $10^3$ $s^{-1}$) and the quasi-static compressive behavior (4.4 x $10^{-3}$ $s^{-1}$) of AISI 321 steel are presented in Figs. 11.4a and b, respectively. At both strain rates, the magnitude of yield strength increases as the grain size decreases. However, a significant difference between the dynamic and quasi-static stress-strain curves exist in the deformation process in the plastic region. At the start of the plastic region, the dynamic curve (Fig. 11.4a) falls; it rises to the maximum flow stress and fall again. This trend could be attributed to the rigorous competition between the strain-hardening (rising) and thermal softening (falling) of the impacted specimens. The strain hardening could be attributed to activation of different deformation and/or strengthening mechanisms. Meanwhile, thermal softening leads to thermo-mechanical instability and loss of load-carrying capability as the temperature of the specimen is raised during the dynamic deformation process. The temperature rise in the specimen is due to the conversion of the 90 % of the kinetic energy of projectile to thermal energy during high strain rate [75]. On the other hand, the quasi-static curves in Fig. 11.4b shows a consistent rise (strain-hardening) up to the final deformation true strain of ~0.86.

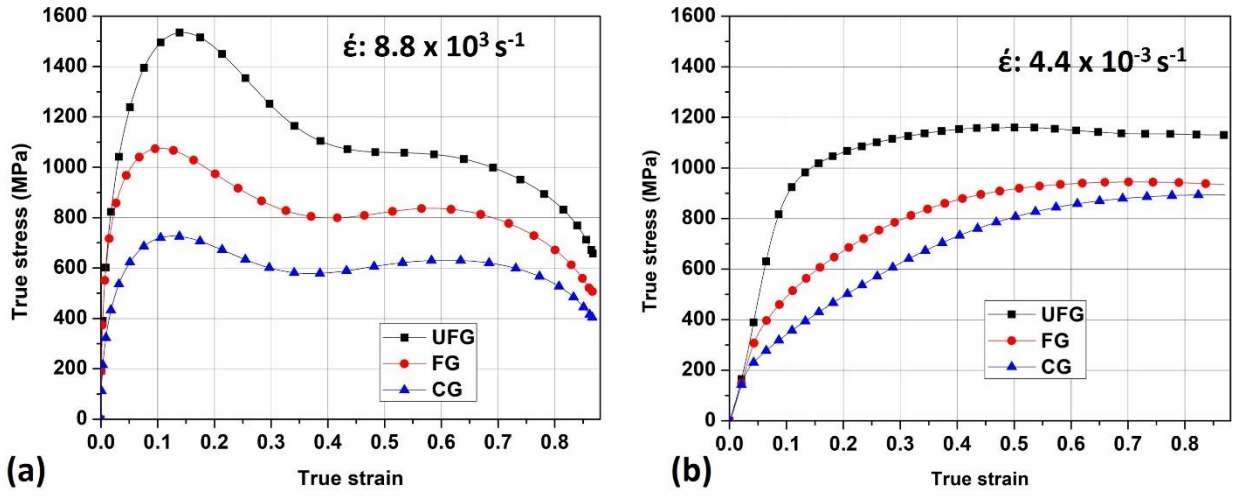


Fig. 11.4. True stress-strain curves of specimens deformed under (a) dynamic and (b) quasi-static loading conditions.

### 11.3.2 Microstructural evaluation before corrosion test

#### 11.3.2.1 Operational deformation mechanisms and macrotexture evaluation

The EBSD band contrast and twin maps in Fig. 11.5 confirms the occurrence of deformation twinning and also the role of grain size and strain rate on twinning activity. These maps reveal near-absence of twins in UFG specimens and its fraction increases with increase in grain size. Similarly, relatively lower twin area fraction is recorded in specimens deformed under dynamic loading conditions (Figs. 11.5a, c, e) than those compressed under quasi-static condition (Figs. 11.5b, d, f). This implies that both coarse grain size and low strain rate favors more twinning activities. Under tensile load, Ueji et al. [80] observed that the evolution of deformation twinning becomes more difficult as the grain size decreases in a high Mn austenitic TWIP steel. A similar result was also observed in the finite element simulation of AISI 304 ASS under uniaxial tension [81].

The EBSD phase maps in Fig. 11.6 (a, c, e, g, i, k) also indicate the occurrence of deformation-induced martensitic transformation and its variability with grain size and strain-rate. At both high (a, e, i) and low (c, g, k) strain-rates, the area fraction of α′-martensite (blue) decreases with an increase in grain size. The higher fraction of α′ in UFG specimen could be largely due to the presence of higher triple junctions (a potential α′ nucleation sites) than those of fine and coarse specimens. The formation of DIM at triple junction of grain boundaries are also reported in deformed AISI 304LN austenitic stainless steel, a derivative of AISI 321 [290]. The dependence of martensitic phase transformation on grain size is also reported in another previous work [290]. Similarly, a higher fraction of α′ martensite was recorded in specimens deformed under quasi-static compressive load than their dynamic-impacted counterpart. The lower fraction of α′ in the specimen under dynamic impact loading is due to temperature rise in the specimen that suppresses phase transformation. The corresponding IPF maps of the phase maps are presented in Fig. 11.6 (b, d, f, h, j, l). While the stable end-orientation of the deformed austenite phase is CD||[110] with a minor spread near CD||[111] fibre texture, that of the DIM is near CD||[100]. Similar texture results have been reported in a cold-rolled AISI 304L stainless steel [314].

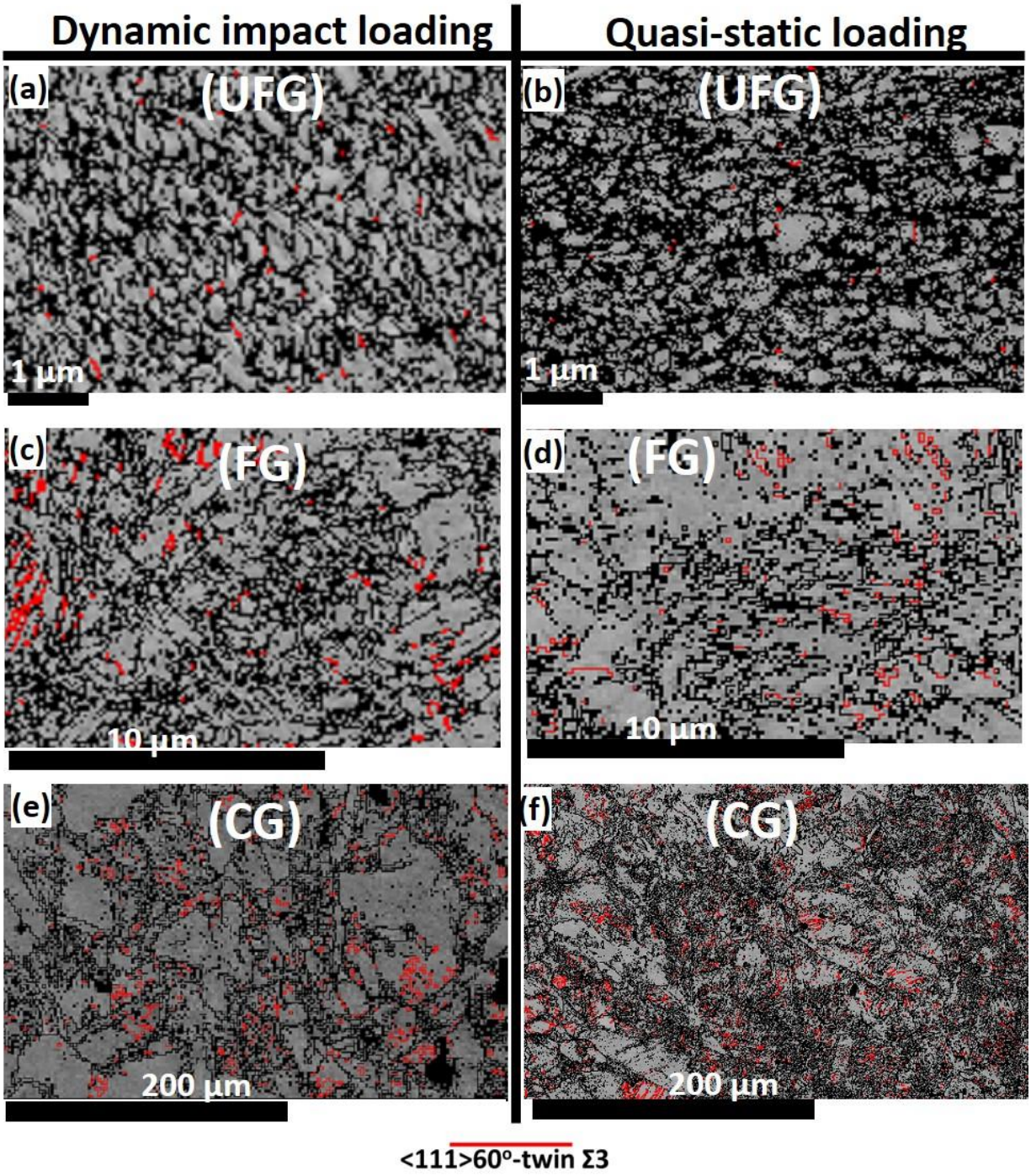


Fig. 11.5. EBSD band contrast and twin maps for specimens subjected to (a, c, e) dynamic and (b, d, f) quasi-static loading conditions.

The activated deformation mechanisms earlier observed using the EBSD technique are further verified by the TEM results in Fig. 11.7. For brevity, only the TEM micrographs of the UFG (Fig. 11.7a and d) and CG (Fig. 11.7b, c, e and f) specimens are presented. Under both dynamic and quasi-static loading conditions, TEM micrographs affirm near-absence of deformation twin in the

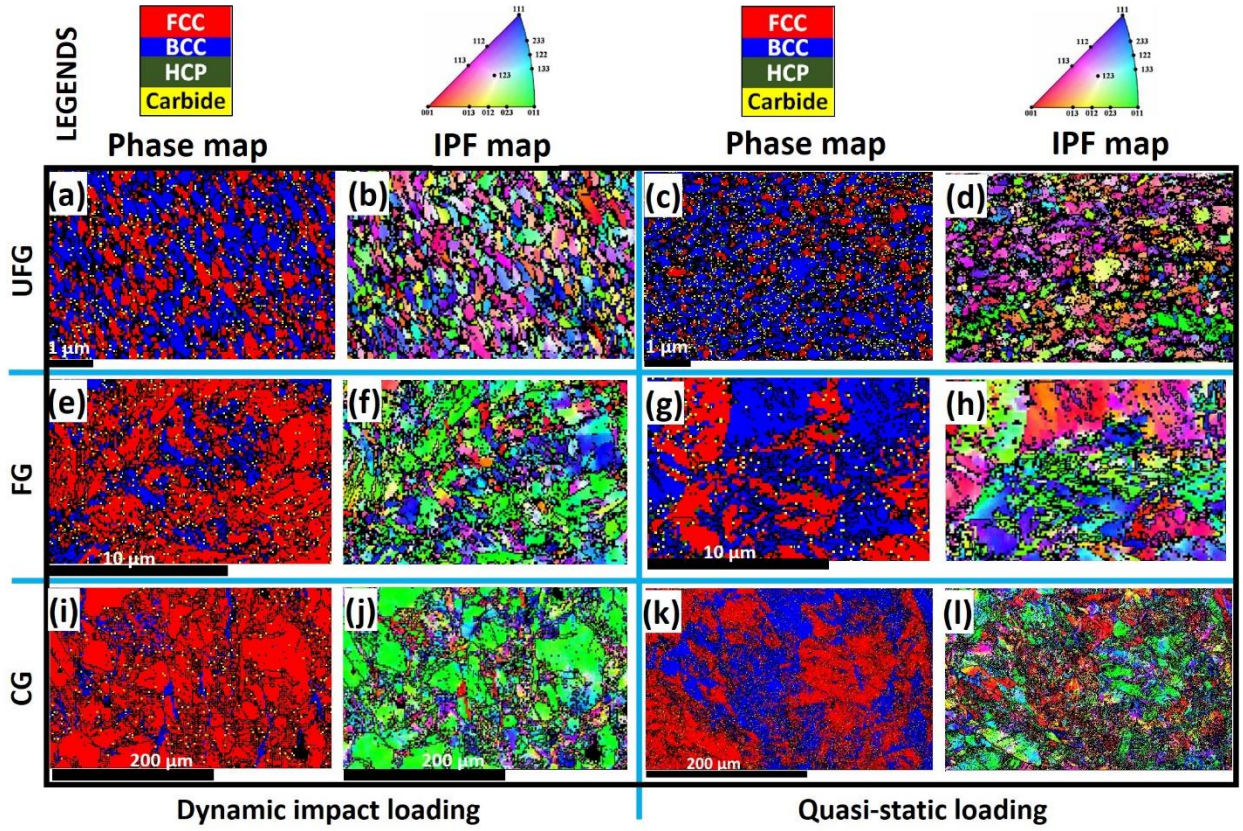


Fig. 11.6. EBSD (a, c, e, g, i, k) phase and (b, d, f, h, j, l) IPF maps for specimens deformed under dynamic and quasi-static loading.

UFG specimens. The TEM micrographs of the CG specimens under dynamic loading condition reveal the formation of deformation twin from the grain boundaries (Figs. 11.7b and c) and within the grain (inset in Fig. 11.7c) at regions of high dislocation densities or networks. Meanwhile, CG specimens compressed under quasi-static condition exhibit massive deformation-induced martensitic transformation (Fig. 11.7e) in addition to deformation twinning and slip (Fig. 11.7f). The results of the feritscope measurement of α′ fraction in the deformed specimens affirm that the decrease in both grain size and strain rate leads to an increase in α′ fraction (Fig. 11.8a) and to a corresponding increase in hardness (Fig. 11.8b). From these observations, it can therefore, be safely concluded that hardening in metastable AISI 321 stainless steel originates from multiple sources. In addition to grain boundary strengthening, hardening in AISI 321 steel is attributed to the occurrence of deformation twinning acting as barrier to dislocation motion, deformation-induced martensitic transformation, dislocation multiplication during slip, and precipitation of carbides that act as barriers to dislocation motion during plastic deformation.

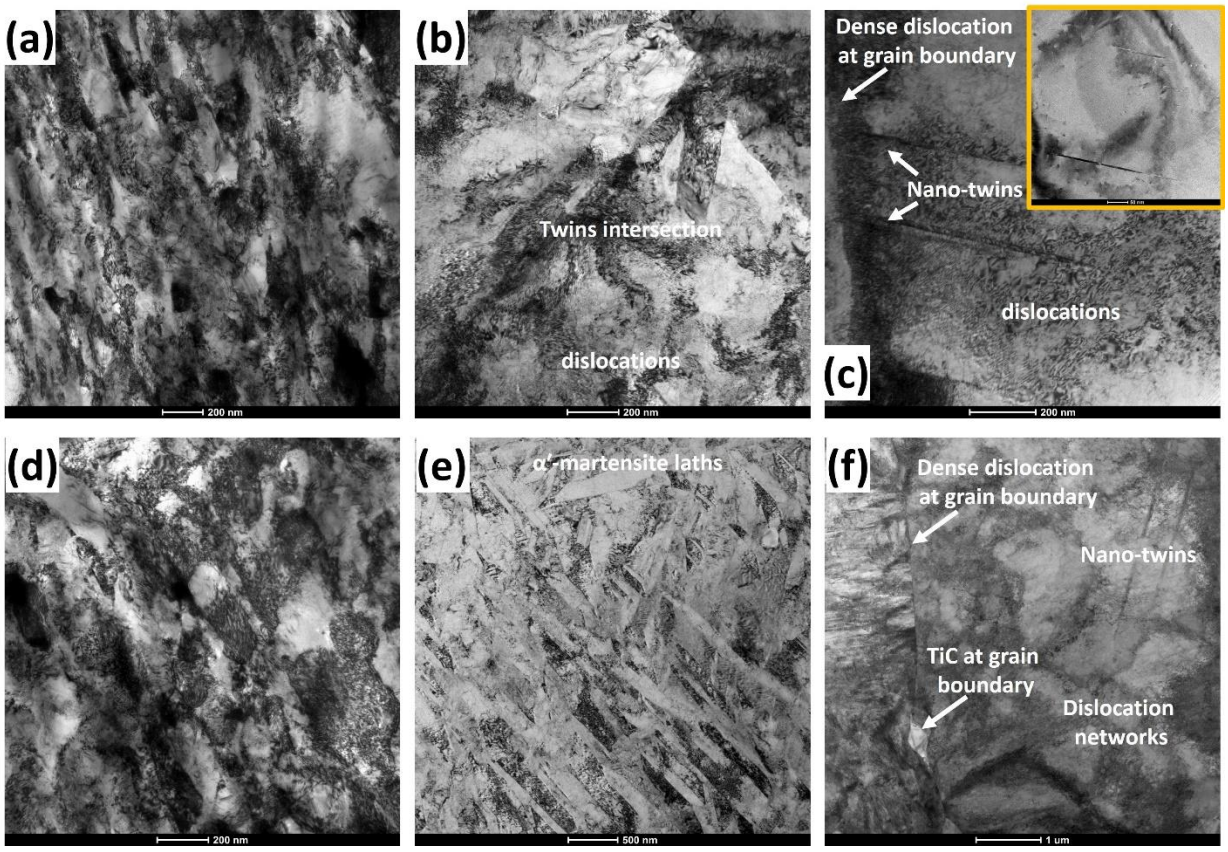


Fig. 11.7. TEM bright field micrographs of specimens subjected to (a-c) dynamic and (d-f) quasi-static loading: (a, d) UFG and (b, c, e, f) CG specimens.

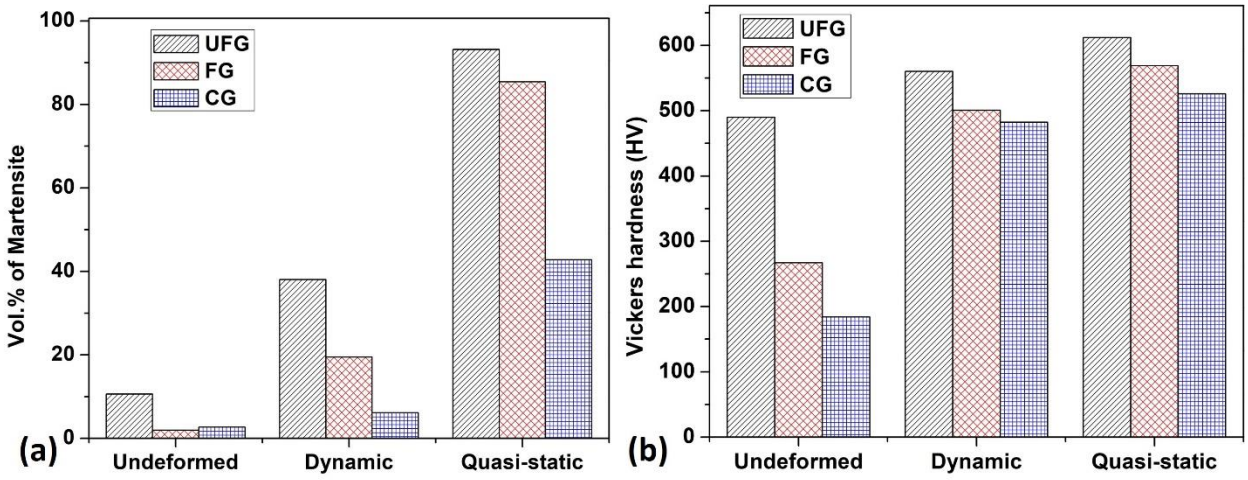


Fig. 11.8. (a) Volume % of deformation-induced martensite and (b) Vickers hardness of undeformed and deformed specimens.

#### 11.3.2.2 Plausible effect of grain size and strain rate on stacking fault energy

The plausible variation of stacking fault energy (SFE) with grain size and strain rate can be proposed from the mechanical behavior and microstructural evolution in the deformed UFG, FG and CG specimens. Generally, the operational deformation mechanisms in a metal are strongly influenced by SFE [66] and are partitioned in such a manner that martensitic phase transformation, twinning, and slip dominates when the SFE are <18 $mJm^{-2}$, in the 18-35 $mJm^{-2}$ range and above 35 $mJm^{-2}$, respectively [54], as schematically shown in Fig. 11.9a. However, regardless of the activated deformation mechanisms, plastic deformation occurs by slip [67]. Although $\gamma$-SFE depend on factors such as chemical composition and temperature [50], the existing compositional equations (Eqns. 2.6-2.8) for estimating SFE does not take into consideration the role of grain size. However, our experimental result suggests a possible variation with grain size. The estimation of SFE for AISI 321 from these equations (Eqn. 1: 21 $mJm^{-2}$, Eqn. 2: 25 $mJm^{-2}$ and Eqn. 3: 34 $mJm^{-2}$) could therefore, be assumed for the undeformed CG sample as indicated in Fig. 11.9a. Since both deformation induced martensitic transformation and twinning can readily occur in AISI 321 steel, it is suggested that Brofman and Ansell equation gives a better approximation (~21 $mJm^{-2}$) of SFE for CG AISI 321 steel, though, the equations do not consider all elements. This is simply because at ~21 $mJm^{-2}$, DIM and twinning can still operate jointly, as it can be observed in Figs. 11.5-11.7. This was also reported in AISI 304 austenitic stainless steel which is an intermediate SFE metal [60]. It should be noted that AISI 304 is a derivative of the investigated AISI 321 in the current study. Elsewhere [19], Brofman and Ansell equation has been reported and confirmed to show the best correlation with experimental results in metastable austenitic stainless steel.

The variation of dominant deformation mechanisms that is largely due to the effect of grain size and strain rate (Figs. 11.5-11.7) however suggests that the SFE of AISI 321 steel possibly deviates from the estimated value of 21 $mJm^{-2}$. In a metastable stainless steel, Galindo-Nava and Rivera-Díaz-del-Castillo [60] established the variation of SFE with strain at a fixed strain rate of $10^{-3}$ $s^{-1}$ as presented in Figs. 11.9b and c. However, it is thought that SFE possibly shifts slightly to the left (i.e. decreases) due to compressive loading at low strain rate and a shift to the right (i.e. increases) at high strain rate. This is premised on the observed substantial promotion and suppression of DIM formation at low and high strain rates, respectively. The suppression of DIM at high strain rates is due to adiabatic heating during deformation. Adiabatic heating has been

reported to result in increased SFE [87]. Similarly, the refinement of CG specimen to UFG structure possibly led to a decrease in SFE as DIM was highly promoted and twinning was highly suppressed in compressed UFG specimens as indicated in Fig. 11.9c. For instance, UFG specimen (Fig. 11.6) underwent extensive deformation-induced martensitic phase transformation that is characteristic of alloys with SFE below 18 $mJm^{-2}$ than those of CG specimens. On the other hand, the deformation-induced twinning occurred more readily in CG specimens (Fig. 11.5), which is characteristic of alloys with SFE in the 18-35 $mJm^{-2}$ range, than those of UFG specimens.

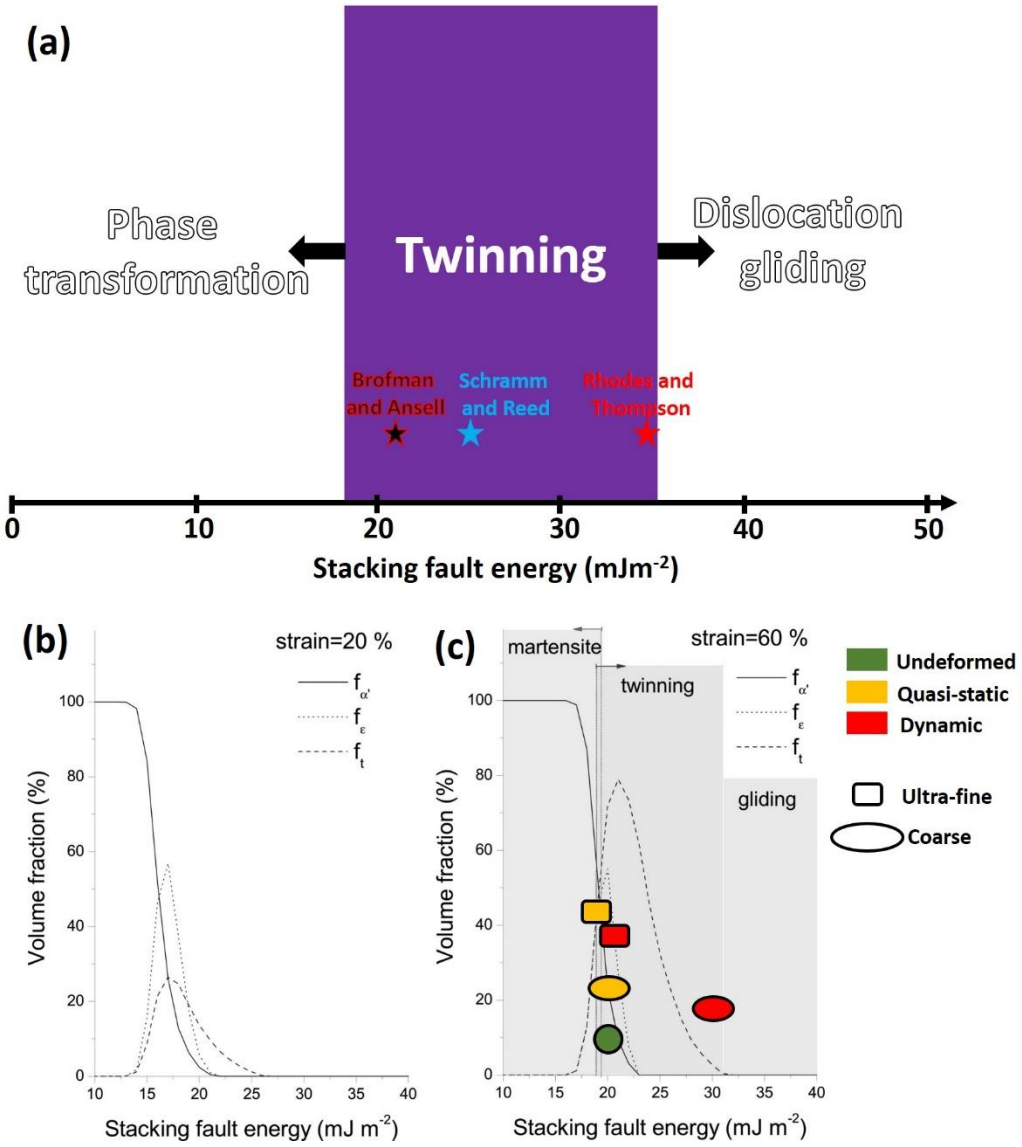


Fig. 11.9. (a) Schematic showing partitioned SFE and their corresponding activated deformation mechanism, (b, c) effect of strain on the volume fraction of DIM and twinning for different stacking fault energies [60].

### 11.3.3 Corrosion tests result

The corrosion behaviors of both undeformed and deformed (dynamic and quasi-static) specimens with different grain sizes were investigated using corrosion electrochemistry and surface analysis after exposure to 3.5 wt.% NaCl solution. The change in corrosion resistance of this Ti-stabilized AISI 321 austenitic stainless steel after the enhancement of its mechanical properties via grain refinement is discussed in this section.

#### 11.3.3.1 Effect of grain size on corrosion resistance

Since electrochemical tests are conducted at open circuit potential ($E_{oc}$), the $E_{oc}$ vs. time curves for the specimen in NaCl were generated (Fig. 11.10). The $E_{oc}$ results in Fig. 11.10 are independent of the grain size and strain rate (dynamic or quasi-static) within the duration of the test. The $E_{oc}$ vs. time curves for the CG and FG specimens deformed under quasi-static condition show a steady rise in $E_{oc}$ between 0 and 400 seconds, then normalized afterward at -0.30 and -0.35 V, respectively. Except for the FG specimens, the CG and UFG specimens reveal more positive $E_{oc}$ values under dynamic loading condition, especially between the mid and end of the test. For CG and FG specimens, the $E_{oc}$ vs. time curves for undeformed and deformed (high strain rates only), are parallel to each other between 0.10 and -0.20 V and between -0.35 and -0.40, respectively. The trend in the magnitude of $E_{oc}$ suggest different electrochemical behaviors for specimens deformed at both strain rates under compression, independent of their grain sizes. These curves indicate significant surface responses within the duration of the test, denoting that 30 mins is sufficient to attain a steady-state condition with few fluctuations in the media.

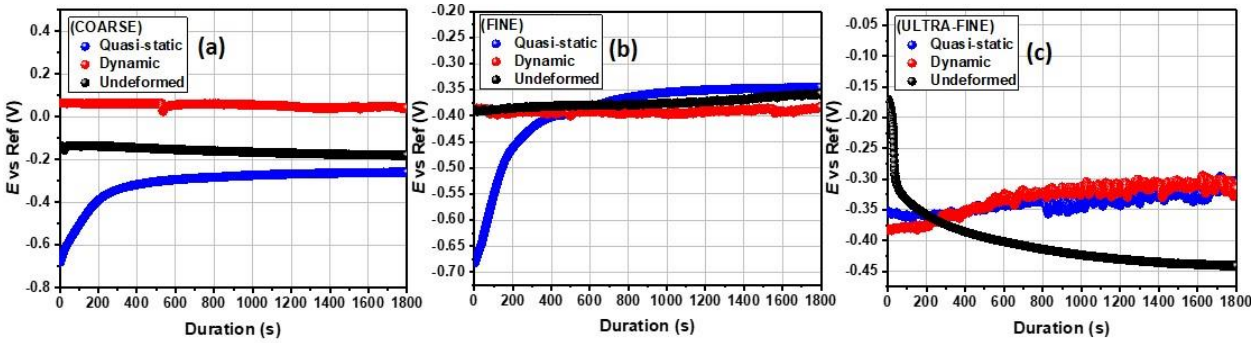


Fig. 11.10. $E_{oc}$ variation with time for undeformed and deformed (under dynamic and quasi-static loading conditions) specimens with varying grain sizes in 3.5 wt.% NaCl solution at room temperature.

The electrochemical impedance spectroscopy (EIS) was used to determine the corrosion resistance of these specimens directly by measuring the electrical parameters related to the resistance against chloride ion ingressions. The results from this test provide data about the electrode processes based on the electrochemical responses. Fig. 11.11a-c presents the Nyquist spectra for both undeformed and deformed specimens with varying grain sizes exposed to 3.5 wt.% NaCl solution. These impedance curves reveal similar corrosion pattern for all specimens since their electrochemical features are relatively similar. At high frequencies, these curves are characterized with single capacitive loops due to inherent charge transfer processes controlling the corrosion reactions [315]. The presence of some unresolved inductive-type loops is also conspicuous at lower frequencies due to relaxation of diffused or adsorbed species.

The observed unevenness in the impedance curves could be linked to the consequence of corrosive attack upon exposure of the metal surfaces to corrosive ions and molecules within the saline media. This could also be associated with other phenomena leading to the prevalence of micro-roughness and surface heterogeneities on the stainless-steel electrodes [315,316]. Since the corrosion resistance of these specimens could be a function of the size of impedance capacitive loops [317],

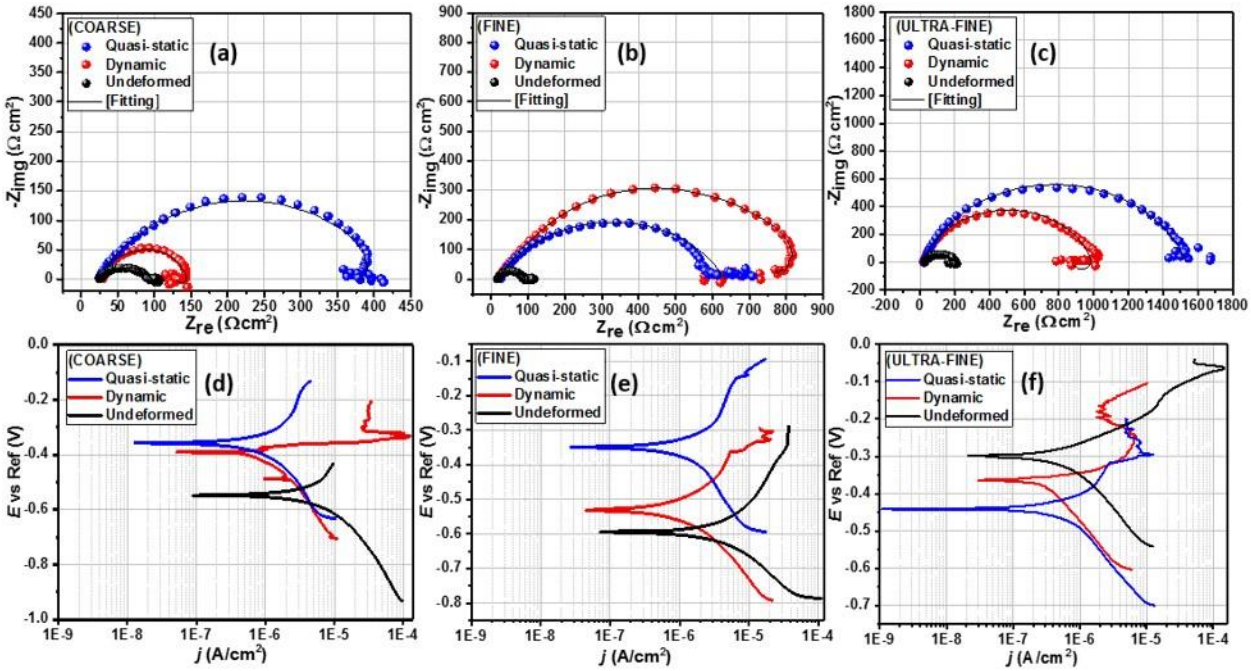


Fig. 11.11. Nyquist (a-c) and Tafel polarization (d-f) curves for stainless-steel substrates with coarse, fine and ultra-fine grain sizes under deformation at different strain rates as well as their undeformed counterpart exposed to 3.5 wt.% NaCl solution at room temperature.

we then could deduce that specimens corresponding to wider Nyquist curve diameters are more resistant to chloride-induced corrosion. By physical inspection, it could be inferred that both deformed and undeformed UFG specimens are more resistant to corrosion than those of the FG and CG specimens. By far, CG specimens trail behind as one with the least resistance to corrosion, whether deformed or not. Experimental impedance data were fitted into an appropriate equivalent circuit model as shown in Fig. 11.12. The electrochemical parameters extracted from this theoretical operation are presented in Table 11.1. Good fittings were achieved with relatively small chi ($\chi^2$) square values to support this claim. The circuit model consists of elements representing solution resistance ($R_{soln}$), charge transfer resistance ($R_{ct}$), inductive resistance ($R_L$), double layer capacitance ($Q_{dl}$) and an inductor ($L$). The observed magnitude of $R_{ct}$ in Table 11.1 follows the order: UFG > FG > CG, for both undeformed and deformed specimens. $R_{ct}$ values for CG specimens are determined to be the least, and are 83, 125, 401 Ω for the undeformed, dynamic and quasi-static deformed specimens, respectively. The values of this parameter increased markedly for those with ultra-fine grains and are 175 Ω (undeformed), 1081 Ω (dynamic), 1509 Ω (quasi-static). Since charge transfer resistance ($R_{ct}$) represents the opposition to the flow of ionic currents, the trend in this parameter for AISI 321 stainless steel with the three grain sizes under study suggests the formation of a more stable adsorbed passive film for UFG specimens.

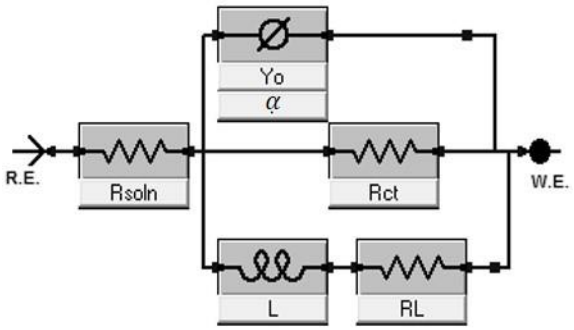


Fig. 11.12. Equivalent circuit model utilized in fitting the experimental impedance data for both undeformed and deformed stainless-steel substrates with varying grain sizes.

In all, more enhanced corrosion resistance was observed for UFG specimens under quasi-static loading condition while the CG specimen corroded more compared to the rest of the specimens. The magnitude of capacitive ($Q_{dl}$) can account for water uptake within the duration of the corrosion test. The trend of its values is the reverse of that of $R_{ct}$ for the three grain sizes investigated; higher values were obtained for undeformed CG specimens. $Q_{dl}$ values for undeformed CG, FG and UFG

specimens are 68.1, 36.3 and 48.4 μF $cm^{-2}$ $s^{-(1-\alpha c)}$, respectively. Lower values of $Q_{dl}$ denotes reduced water uptake by the adsorbed passive film and markedly describes the barrier performance of the film. The capacitive element within the circuit design is constant phase elements (CPE, $Q$) deployed to ensure precise fitting results while also accounting for inherent metal surface inhomogeneity. The impedance of CPE could be defined as expressed in Eqn. 11.1. In this equation, $Y_o$ and $\alpha$ represent the frequency independent factors while $\omega$ is the angular frequency ($2\pi$f, measured in rad/sec) of the ac voltage applied to the electrolytic cell. The magnitude of $\alpha$ is affected by surface inhomogeneities and gross roughness. For an ideal surface, this quantity reaches unity (1) when $Z_{CPE}$ is considered a pure capacitor. In this work, values of $\alpha$ are close to unity.

$$Z_{CPE} = [Y_o(j\omega)^{\alpha}]^{-1} \quad \ldots 11.1$$

Table 11.1. Electrochemical parameters for stainless-steel substrates with coarse, fine and ultra-fine grain sizes subjected to deformation at different strain rates as well their undeformed counterpart exposed to 3.5 wt.% NaCl solution at room temperature.

| Grain structure | Deformation condition | Potentiodynamic polarization technique | | | | Electrochemical impedance spectroscopy | | | | | |
|---|---|---|---|---|---|---|---|---|---|---|---|
| | | $\beta_a$ (mV/dec) | $\beta_c$ (mV/dec) | $j_{corr}$ (μA/cm$^2$) | -$E_{corr}$ (V vs SCE) | $R_{soln}$ (Ω cm$^2$) | $Q_{dl}$, $Y_o$ (μF cm$^{-2}$ s$^{-(1-\alpha c)}$) | $R_{ct}$ (Ω cm$^2$) | $R_L$ (Ω cm$^2$) | L (H) | $\chi^2 \times 10^{-4}$ |
| COARSE | Quasi-static | 373.70 | 4.40 | 0.43 | 0.35 | 23.60 | 24.70 | 401.10 | 3642.0 | 152.50 | 745.500 |
| | **Dynamic** | **65.30** | **15.80** | **16.60** | **0.39** | **29.20** | **41.50** | **124.60** | **838.7** | **41.60** | **20.500** |
| | Undeformed | 73.90 | 706.80 | 142.90 | 0.60 | 23.50 | 68.10 | 83.10 | 0.015 | 35990.00 | 0.161 |
| FINE | Quasi-static | 461.80 | 298.90 | 0.39 | 0.35 | 24.70 | 24.20 | 609.20 | 646.1 | 12330.00 | 0.146 |
| | **Dynamic** | **284.10** | **244.20** | **2.95** | **0.53** | **21.10** | **26.50** | **822.40** | **2614** | **2195.00** | **0.411** |
| | Undeformed | 132.80 | 111.20 | 129.70 | 0.59 | 27.10 | 36.30 | 90.80 | 658 | 1331.20 | 0.359 |
| ULTRA-FINE | Quasi-static | 113.90 | 169.40 | 0.29 | 0.45 | 21.30 | 18.40 | 1509.00 | 5624 | 1.82 | 0.894 |
| | **Dynamic** | **28.80** | **249.50** | **0.59** | **0.36** | **25.40** | **23.70** | **1081.10** | **2896** | **24990.00** | **16.100** |
| | Undeformed | 40.30 | 55.50 | 16.30 | 0.29 | 27.30 | 48.40 | 175.00 | 856 | 465.80 | 0.251 |

Corrosion studies with EIS technique were complemented by Tafel polarization test in the same saline solution. Polarization curves for these specimens with varying grain sizes under different strain rates as well as those of their undeformed counterparts are presented in Fig. 11.11 (d-f). After curve fitting, the polarization parameters were derived by extrapolation of the linear portions of the anodic and cathodic sections of the curves and listed in Table 11.1. These parameters consist of corrosion current density ($j_{corr}$), corrosion potential ($E_{corr}$), anodic ($\beta_a$) and cathodic ($\beta_c$) Tafel slopes. The dissolution of the alloy specimens is characterized by changes in the values of $E_{corr}$ and $j_{corr}$. Evidence of passivation is observed for corrosion resistant specimens due to the formation

of adsorbed stable passive films consistent with Ti-stabilized austenitic stainless steel. This is conspicuous for UFG specimens irrespective of the deformation mode. The prior deformation at low and high strain rate resulted in passivation at an $E_{passivation}$ of -0.30 V (both strain rate) for UFG specimens while that of the FG specimens were recorded at -0.15 V (low strain rate) and -0.35 V (high strain rate), respectively, and -0.3 V (both strain rate) for the CG specimens. The observed surface passivation is also consistent with decreasing magnitude of $j_{corr}$ for FG specimens compared to those with coarse grains. The magnitudes of $j_{corr}$ for ultra-fine specimens under quasi-static, dynamic, and undeformed conditions in NaCl solution are the lowest, and are 0.29, 0.59, and 16.30 μA/cm$^2$, respectively. Higher values of $j_{corr}$ were obtained for CG specimens independent of the rate of deformation. These were determined to be 0.43, 16.6, and 142.9 μA/cm$^2$ for specimens deformed under quasi-static and dynamic loading conditions and for undeformed specimen, respectively.

In the undeformed and dynamic loading conditions, the magnitudes of $E_{corr}$ for the FG and CG specimens are more negative compared to those of UFG specimens. For instance, the $E_{corr}$ values for both FG and CG specimens deformed under dynamic loading condition were -0.53 and -0.39 V, respectively, while -0.36 V was recorded for UFG specimen. On the other hand, -0.35 V was recorded for both FG and CG specimens deformed under quasi-static condition. The improvement in the corrosion resistance of stainless steels due to stronger stability, more compactness, lower defect density and higher chromium content of passive films developed on the nano-crystalline structure in different corrosive media compared to the conventional coarse grain structure has been reported elsewhere [8]. Miyamoto [318] also reported that UFG structure exhibits lower passive current and higher breakdown potential in chloride-containing media, which translates to higher corrosion resistance. Ralston et. al. [319] revealed the existence of a relationship between corrosion rate and grain size (Eqn. 11.2) that is analogous to the classical Hall-Petch relation as follows:

$$j_{corr} = (A) + (B)gs^{-0.5} \quad \ldots 11.2$$

where A is a constant and a function of the environment (corrosive media). B represents a material constant, which depend on the composition or impurity level of the material. Ralston et al. concluded that UFG structures would be more corrosion resistance if the grain boundary density

dictates oxide-film conduction rate on substrate's surface of low to passive corrosion rates (i.e. $j_{corr}$ < 10 μAcm$^{-2}$). However, when the dissolution rates are higher than 10 μAcm$^{-2}$ (i.e. in the absence of oxide film), increase in grain boundary densities (grain refinement) will enhance the overall surface reactivity and in turn, increase corrosion rate.

Although corrosion resistance of stainless steels is improved by grain refinement to nano-structures, processing routes and parameters used to fabricate these nanocrystalline structures have a strong effect on their corrosion behavior [8]. UFG/Nanocrystalline structures produced by techniques such as sputtering, thermomechanical processing (cold-rolling and annealing), equal channel angular pressing (ECAP) and surface mechanical attrition treatment (SMAT) have been reported to be more corrosion resistance than their coarse-grained counterpart [8,319]. This work, therefore, confirms that the development of UFG via thermomechanical processing (cryo-rolling and annealing) improves corrosion resistance.

#### 11.3.3.2 Effect of prior deformation rate on corrosion resistance

Since grain refinement has also enhanced the mechanical properties of AISI 321 MASS, the extent to which prior deformation and the rate at which the deformation occurred has affected corrosion resistance will also be examined. To accomplish this, the Nyquist curves in Fig. 11.11 were rearranged to highlight only the effect of strain rates under compression for individual specimen. Figure 11.13 depicts the Nyquist curves for specimen deformed under dynamic and quasi-static loading conditions compared to their undeformed counterpart. The sizes of the Nyquist semi-circle diameters are wider for more resistive systems. The specimens deformed under quasi-static loading condition are more resistant to corrosion compared to those subjected to dynamic loading condition. By inspection, it could also be inferred that undeformed specimens are less resistant to corrosion; significant amount of corrosion occurs independent of the grain size. $R_{ct}$ values for UFG, FG and CG specimens under low strain rate are 1509, 609, 401 Ω, respectively, while those deformed at high strain rate are 1081 Ω (UFG), 822 Ω (FG), 125 Ω (CG). The values of this parameter decrease markedly for undeformed specimens: 175, 91, 83 Ω, in similar order. This implies that the magnitude of $R_{ct}$ values for this Ti-stabilized AISI 321 austenitic stainless-steel follows the order: quasi-static > dynamic > undeformed, for all grain sizes, except for FG specimens.

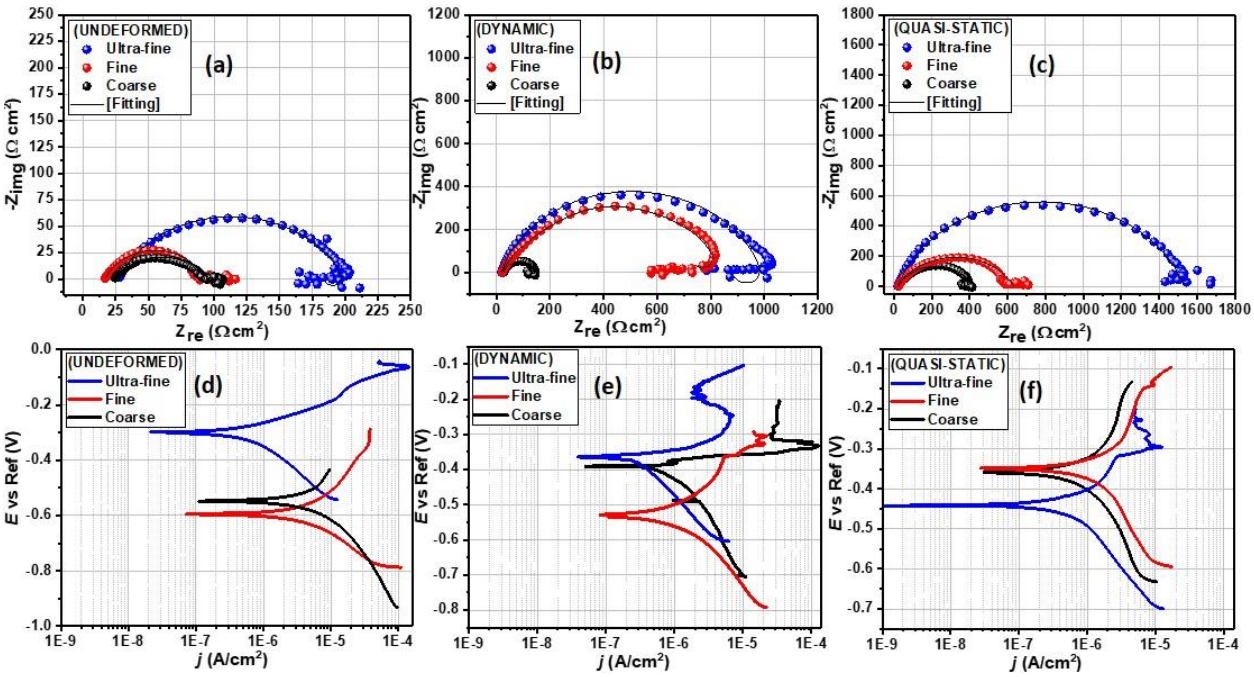


Fig. 11.13. Nyquist (a-c) and Tafel polarization (d-f) curves for both undeformed and deformed stainless-steel substrates with varying grain sizes exposed to 3.5 wt.% NaCl solution at room temperature.

More corrosion-resistant metallic systems continue to show distinct passivation and lower corrosion currents in the polarization curves (Fig. 11.13d-f). Deformed specimens at low strain rates are characterized by low rate of dissolution in the saline NaCl solution. Lower values of $j_{corr}$ are consistent with the formation of stable passive films on the corrosion-resistant steel specimen, especially the deformed UFG specimens. The $j_{corr}$ values for the undeformed specimens are consistently higher than those of the deformed specimens. This is a strong indication that prior deformation contributed to the corrosion resistance. For any given grain size, the jcorr values of the specimens deformed under quasi-static loading condition are the least. For instance, the jcorr values for UFG specimens are 16.3 μA/cm$^2$ (undeformed), 0.59 μA/cm$^2$ (dynamic), and 0.29 μA/cm$^2$ (quasi-static). This implies that corrosion resistance follows the trend quasi-static > dynamic > undeformed for all grain sizes. The magnitudes of $E_{corr}$ for undeformed and deformed (under dynamic loading conditions alone) UFG specimens are more positive and significantly higher; -0.29 and -0.36V, respectively. In this work, it could be further concluded that deformed specimens (under compression) are resistant to chloride-induced corrosion at ambient temperature compared to the undeformed specimens, a similar observation is reported in Ref. [320]. These results suggest that corrosion resistance by surface passivation was enhanced by bulk deformation

[321] mostly at low strain rates which will be further explained by surface analysis using SEM. During the sanding and brushing treatments of AISI 316L, other authors [322] have also reported an improved corrosion resistance via plastic deformation and compressive residual stress. Phadnis et al. [323] also reported that plastic deformation played a significant role on the thickness of protective oxide film in a cold-rolled AISI 304 austenitic stainless steel in de-aerated 3.5% NaCl solution. These authors found cold-rolling to be beneficial to forming thicker oxide film with higher Cr/Fe ratio on cold-rolled specimen than the unrolled specimen.

Despite the evolution of deformation-induced martensite (DIM), the plausible reason for higher corrosion resistance in deformed specimens (compared to the undeformed) could be texture-related. While the austenite phase in the as-received undeformed specimen has random orientations, the phases in the deformed specimens are significantly textured. As discussed in section 3.2 (Fig. 11.6), both the deformed austenite phase and the DIM possesses stable-end orientations (e.g. CD||[110] in the former and CD||[100] in the later) that could be more resistant to corrosion in saline media as also observed in another study [324]. Because CD||[110] is the stable end-orientations for compressed FCC metal [142], it is believed that the stable end-orientation in uniaxial-compressed BCC metals (CD||[111] and [100] [142]) could also be more corrosion resistant than other orientations. Hence, the close-packed crystallographic planes (CD||[110] for austenite and CD||[100] for martensite) nullifies the adverse effect of DIM on the passivation and repassivation features of AISI 321 steel. This is in agreement with observations in a previous study on AISI 304L stainless steel [314].

A number of reasons could also be responsible for higher corrosion resistance in specimens subjected to quasi-static compressive load than those deformed under dynamic loading condition. It is clear, as earlier stated, that there is a significant temperature rise in specimens subjected to dynamic impact loading that could influence the intrinsic property of the metal in a way that is different from those subjected to quasi-static loading, which has a negligible temperature rise. From the critical stress for mechanical twinning's ($\sigma_{twin}$) point of view, i.e. $\sigma_{twin} = 6.14\ (\Gamma/b)$, where $\Gamma$ is the SFE and b is the Burgers vector of the Shockley partials [72], higher material's SFE results in higher $\sigma_{twin}$ and a lower tendency for twinning, and vice-versa. As described in Fig. 11.9, the increase in temperature of specimen subjected to dynamic loading could result in an increase in SFE. Therefore, from the $\sigma_{twin}$ expression (also confirmed in Fig. 11.5), the

deformation twinning will be more favored in specimens deformed under quasi-static compression and less favored in specimens subjected to dynamic-impact load due to an increase in SFE as a result of temperature rise [146]. Evolution of more deformation twin could therefore, be one of the possible reasons for the better corrosion resistance of specimens deformed under quasi-static condition in comparison with specimen subjected to dynamic impact loading. This is in agreement with the findings of Chen et al. [321], who reported that low-energy twins within the austenite grain of AISI 304 stainless steel suppresses chromium depletion at the grain boundaries and promotes passive film formation. Wang et al. [325] also reported a remarkable decrease in the corrosion rate of Mg-3Al-1Zn due to the activation of high density twins. While deformation twinning is beneficial to improving corrosion resistance, it is necessary to highlight that near absence of twins were observed in both undeformed and deformed UFG specimens. In this case, other factors such as the combined presence of close-packed crystallographic planes in both deformed austenite and DIM (highest in deformed UFG specimens), and the dominance of higher grain boundary density over oxide film conduction rate could be beneficial to improving corrosion resistance in undeformed and deformed UFG specimens.

### 11.3.4 Surface morphology

The results of electrochemical corrosion investigations of CG, FG, and UFG specimens (deformed and undeformed) have also been corroborated by surface analyses after corrosion test. The SEM micrographs of the corroded surface are presented in Fig. 11.14 after a continuous 3-month immersion period in aerated saline solution. The corrosion resistance of stainless steel stem from its ability to readily passivate, forming protective films due to the presence of alloying elements (e.g. chromium and nickel) [8]. However, in chloride-enriched media, stainless-steel suffer corrosion due to unrestricted attack by aggressive chloride ions. Physical examination of the specimens' surface after the 3-month exposure to saline solution revealed the occurrence of pitting corrosion since inherent defects in the passive layers allow for further dissolution of the material. The observed pits are localized at sites that are susceptible to chloride ion attack, especially if the anodic sites are widened. The observed extent of pitting corrosion varied, depending on the grain size of the steel as well as the rate of the prior-deformation (Fig. 11.14).

The results of the current study suggest that grain refinement has a significant influence on the mechanical strength and corrosion behavior of AISI 321 stainless steel (Figs. 11.11 and 11.13). This is in agreement with the results obtained by other researchers [326-329]. The research findings in this study also align with those of another previous study on nanocrystalline structures [326]. Previous studies have also attributed the corrosion resistant of nanocrystalline stainless-steel structures to greater Cr diffusion/ Cr-oxide layer [330-332] and other factors associated with their enhanced mechanical properties [331-333] rather than to the presence of coarse grains and alloying elements [8]. Factors associated with ultra-fine grain sizes and structural defects such as grain boundaries and triple points [334,335], are considered in explaining the excellent corrosion resistance of nanocrystalline materials. The distribution of pits is relatively uneven and very localized while the passive films disallow further dissolution of the base metal. The morphology of pits varies depending on the grain size of the alloy. For the CG specimen that was deformed under quasi-static loading condition, pits are scattered in no definite pattern (Fig. 11.14c). The metastable pitting rate of the CG specimen must have significantly exceeded its repassivation ability, leading to the observed corrosion features.

Surface pitting are deeper for the FG specimens (Fig. 11.14 b, e, h) compared to its ultra-fine counterpart (Fig. 11.14 a, d, g) especially along the TiN site. Also localized, the pit buildup is concentrated around the vicinity of TiN second-phase particles in the metal surface due to reduced chromium threshold concentration [336]. Across the fine matrix (also observed in UFG and CG structures), some of the TiN cubic particles are crushed, probably due to plastic deformation. It is also possible that the prolonged exposure of the specimens to the NaCl solution could be responsible for the crushed TiN cubic particles. Few pits observed along the δ-ferrite site (red arrows in Fig. 11.14). Fewer pitting sites and sizes are observed in the UFG specimens relative to the FG specimens. Corrosion is severe for the CG specimens compared to the FG specimens. According to Gupta and Birbilis [8], increased metastable pitting rate could be attributed to elemental distribution (e.g. Mn and S) within the material and higher activity of nanocrystalline surface. The possibilities for metastable-stable pit's transition in nanocrystalline stainless-steel materials is lower, hence, their rapid repassivation rate. The results obtained in this study reveal changes in electrochemical behaviour of metal due to grain refinement as a consequence of changing grain boundary densities [337].

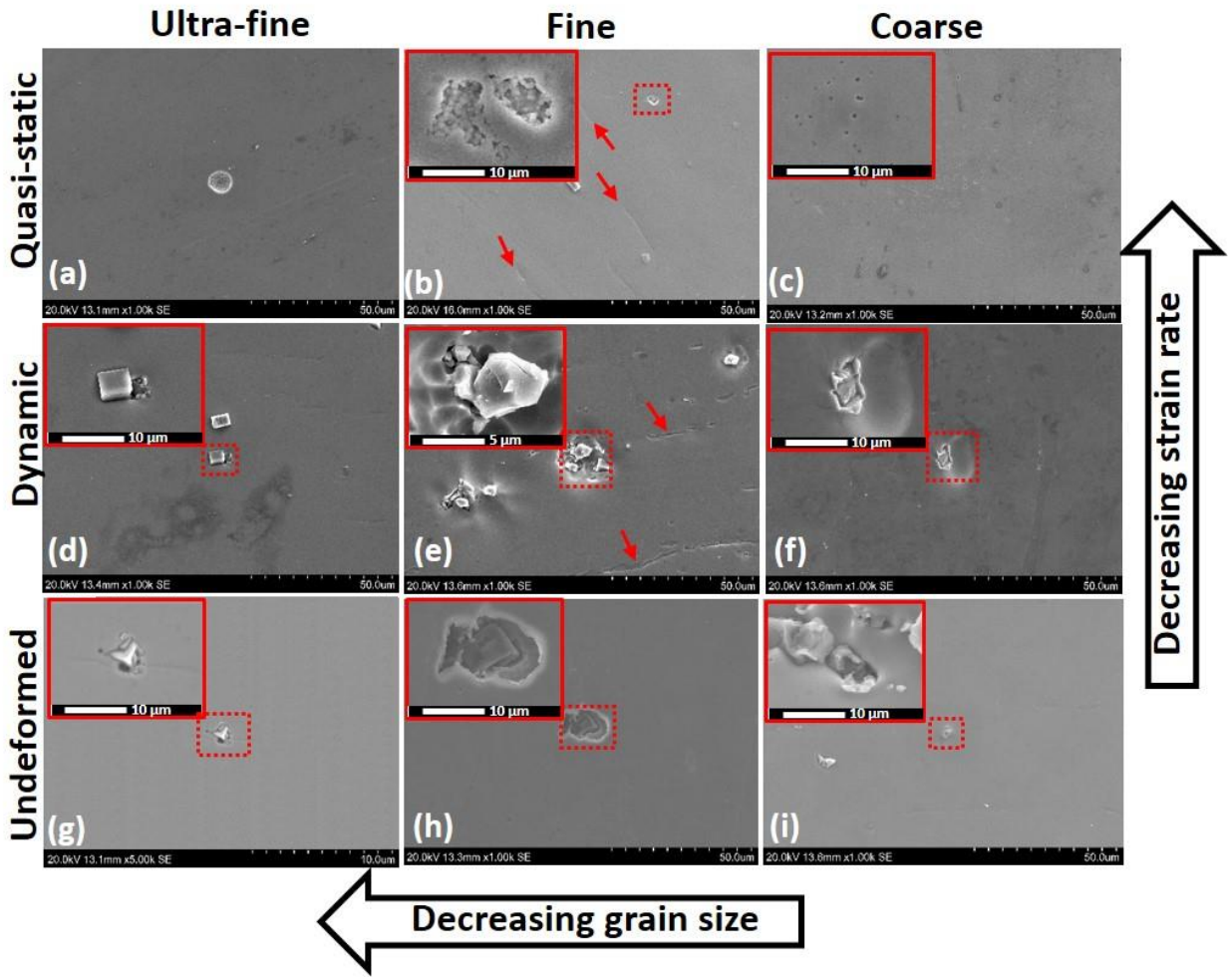


Fig. 11.14. SEM micrographs of stainless-steel substrates with different grain sizes under deformation at different strain rates as well as their undeformed counterpart exposed to 3.5 wt.% NaCl solution at room temperature.

### 11.3.5 Proposed pitting mechanisms for stainless-steel specimen in NaCl

The pitting patterns in deformed and undeformed specimens are schematically presented in Fig. 11.15a. It is worthy of note that these metal samples exhibit varying corrosion behaviors, leading to rather complicated degradation mechanisms. Like most stainless-steel grades, the most prominent form of corrosion observed from SEM is pitting corrosion with clear evidence of corrosion surface pits. Combined actions of corrosive chloride ions and dissolved oxygen initiate these pits. Pitting persists when the rate of re-passivation is significantly slow, and the passivating films (cathodic) continuously leach out dissolved Fe ions from anodic metal surfaces (Fig. 11.15 a). Subsurface pits are observed on undeformed UFG samples with shallow morphologies (Fig. 11.15 b). Irregular elliptical-shaped pits are also observed on surfaces of UFG specimen that was

previously subjected to quasi-static loading quasi-static condition (Fig. 11.15c), upon exposure to the corrosive medium. For UFG specimens, the influence of grain refinement on corrosion resistance could be linked to the metal's ability to readily passivate, especially in environments to which passivity could be established [8,326]. The FG specimen that experienced dynamic loading condition before corrosion test exhibited undercutting pits that are observed at δ-ferrite site (Fig. 11.15d). The depassivation of these areas leads to intergranular corrosion due to insufficient chromium content. This work also confirms the non-detrimental effect of TiC particles to corrosion. SEM micrographs show that no pitting (or galvanic effect) occurred around TiC particles in the matrix and grain boundaries (Fig. 11.15c), and those forming necklace around the stringer ferrite (Fig. 11.15d).

Generally, austenitic stainless steels could be susceptible to thermal residual stress and sensitization. Sensitization defines the precipitation of chromium carbides around grain boundaries, leading to intergranular corrosion, and this is one of the foremost challenges encountered in welding of austenitic stainless steel apart from its low thermal conductivity. The introduction of carbide-formers (e.g. Ti) within AISI 321 creates a strong affinity for carbon (compared to Cr). This results in the formation of more stable solid TiC phases and leaves Cr in solution for corrosion protection [338]. The presence of secondary TiN phase is also recorded in the investigated AISI 321 stainless steel. Contrary to the type of pits presented in Fig. 11.15, the presence of TiN alters the corrosion dynamics. The morphologies of the TiN crystals embedded within the steel sample matrix could reasonably differ depending on the duration of the corrosion test as well as the type of pretreatment procedures utilized before imaging. Pit deepening are observed only around TiN sites for undeformed CG specimens compared to their ultra-fine counterpart (Fig. 11.16b). This could be attributed to the unrestricted chloride-induced corrosion attacks around these particles, especially where the threshold chromium concentrations are significantly low [336]. The dissolution of these TiN particles appears to be a gradual process. In Fig. 11.16, a previously smooth TiN particle within the bulk of the material now shows a pit around its nucleus (Fig. 11.16c). Another TiN site showing the onset of pitting is shown in Fig. 11.16d. Pit nucleation begins in a later formative stage and deepens to the subsurface. However, if the TiN particle falls off at the early stage nucleation, perhaps, due to ultrasonic cleaning, the aggressive progression of pitting corrosion ceases as shown in Fig. 11.16e. This confirms that a galvanic

coupling is usually set up between the TiN particle and its surrounding matrix [320] and hence, resulting in the observed detrimental effect of TiN to pitting corrosion resistance, unlike the TiC particle. The corrosion resistance of AISI 321 stainless steel is therefore, not determined only by the ability to passivate, the presence of secondary stable phases can affect the rate of pitting corrosion.

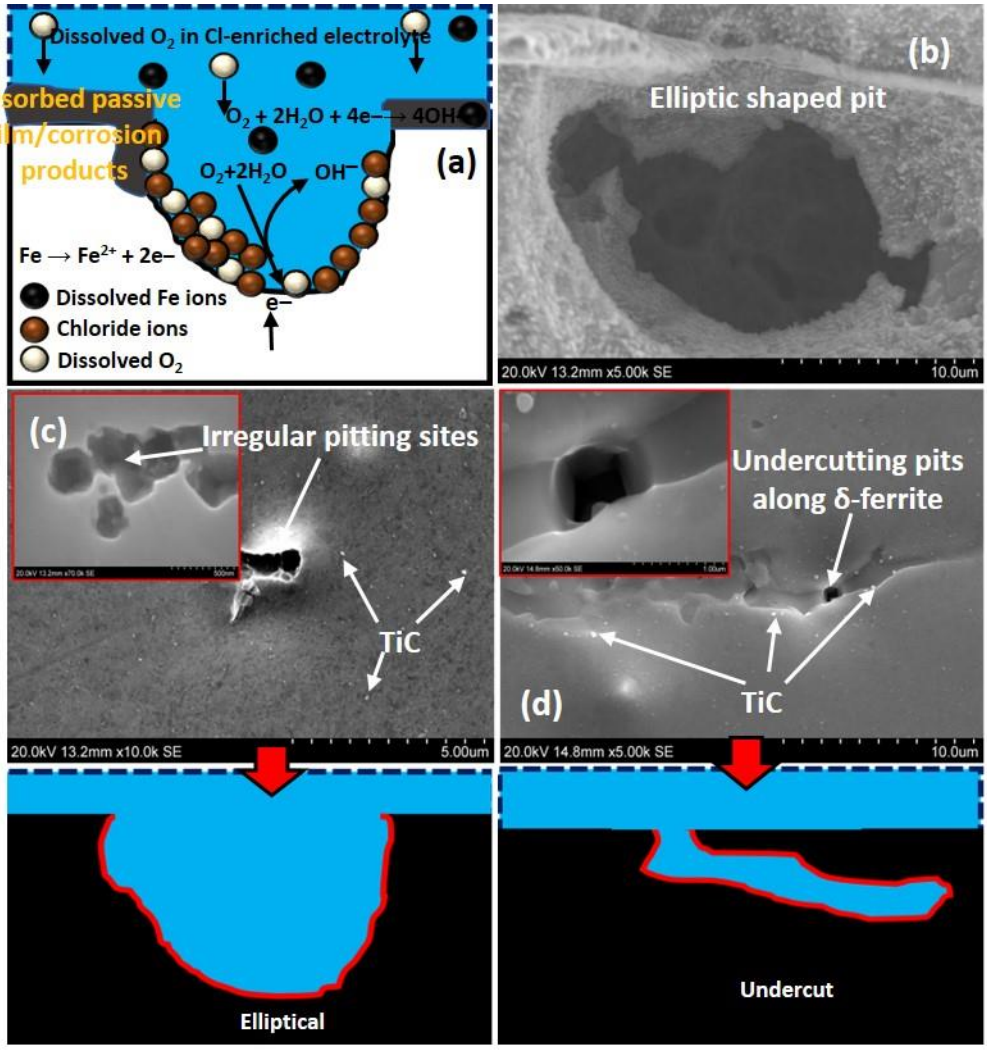


Fig. 11.15. Pitting pattern at TiN sites of stainless-steel samples exposure to NaCl medium. This corrosion pattern is uniform for all samples studied in this work

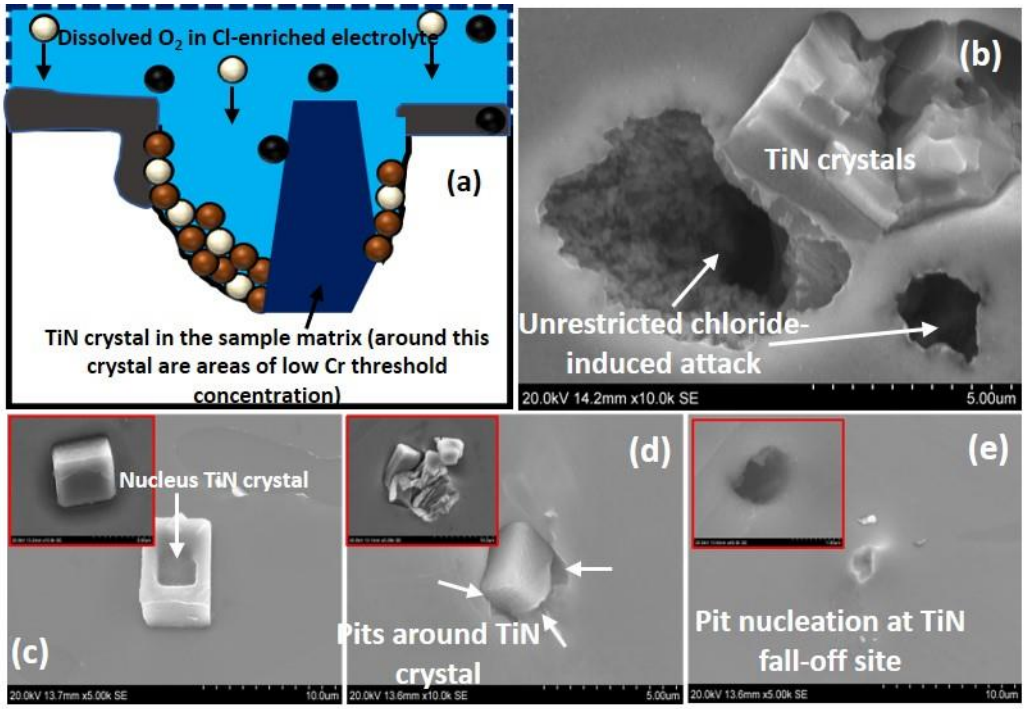


Fig. 11.16. (a) Pitting pattern at TiN sites of stainless-steel samples exposure to NaCl medium, (b) Pit deepening around TiN sites due to reduced threshold chromium concentrations, (c) Smooth crystal showing some form of depression on its nucleus, (d) pit nucleation around TiN and (e) the early stages of pitting corrosion at the TiN fall-off site. This corrosion pattern is the same for all samples studied in this work; only the response of steel sample with coarse grains is presented. Micrographs of coarse grain specimens deformed under quasi-static condition.

## 11.4 Conclusions

The effect of grain size, prior deformation and deformation rate on the corrosion behavior of AISI 321 austenitic stainless steel in 3.5 wt.% NaCl solution was determined. The as-received coarse-grained alloy (~37 µm grain size) was subjected to thermomechanical processing to develop fine (~3 µm grain size) and ultrafine (~0.24 µm grain size) grained structure. The coarse, fine and ultrafine grained specimens were deformed under dynamic (8.8 x $10^3$ $s^{-1}$) and quasi-static (4.4 x $10^{-3}$ $s^{-1}$) loading conditions to the same true strain of ~0.86 using a split Hopkinson pressure bar and Instron R5500 mechanical testing systems, respectively. Using XRD, SEM, TEM, EBSD, and EDS characterization techniques to investigate the steel specimens, the following conclusions are drawn;

(a) Corrosion resistance is highest in the UFG specimens, followed by FG and CG specimens, in that order, in saline media. This is due to the formation of a more stable adsorbed passive film in UFG specimens.

(b) The corrosion resistance of AISI 321 austenitic stainless steel follows the order: quasi-static > dynamic > undeformed, for all grain sizes. This could be due to the evolution of close-packed crystallographic planes (CD||[110] for austenite and CD||[100] for martensite) that nullifies the adverse effect of DIM on the passivation and repassivation characteristics of AISI 321 steel compressed under quasi-static condition.

(c) The presence of TiC particles is not detrimental to the corrosion resistance of AISI 321 steel, whereas, galvanic coupling exist between TiN particles and their surrounding matrix leading to the pitting corrosion around TiN particles.

(d) Overall, the corrosion resistance of AISI 321 austenitic stainless steel is not determined only by the ability to passivate, the presence of secondary stable phases can affect the rate of pitting corrosion.

# Chapter 12

## Summary, Conclusions and Recommendations

### 12.1 Summary

In this study, mechanical behavior, microstructure, texture, and corrosion behavior of as-received and grain-refined AISI 321 austenitic stainless steel was investigated. This alloy has excellent corrosion resistance, but relatively low yield strength. First, the variability in the mechanical behavior of the steel, as well as texture and microstructure across the as-received 25.4 mm-thick steel plate in hot-rolled condition was determined. This was followed by thermomechanical processing of the as-received alloy to obtain an ultrafine grain (UFG) microstructure. Both quasi-static and dynamic deformation behavior of the as-received, coarse-grained, and fine-grained structures were investigated. Microstructural characterization techniques such as OM, SEM, XRD, EDS, EBSD, and TEM were used to understand the activated and operational deformation mechanisms and how they are affected by grain size and crystallographic texture. The effect of initial texture and grain size on the thermal and mechanical stability of austenite phase was also investigated. The effect of grain size on the corrosion resistance of AISI 321 steel in chloride solution was also studied.

### 12.2 Conclusions

The following conclusions are drawn from the research findings obtained in this study:

A. In the 25.4 mm-thick as-received AISI 321 plate, the texture, and the amount of stored energy at the center are different from those in other regions across the thickness of the plate. The stored energy is higher at the centre of the plate. The centre of the plate has the lowest yield strength and the highest strain hardening capability compared to other regions under the dynamic impact loading condition.

B. The optimum thermo-mechanical processing conditions for developing UFG structure are, annealing at 923 K (650 ℃) for approximately 28800 s (480 minutes) resulting in ~0.22 μm grain size and annealing at 1023 K (750 ℃) for 600 s (10 minutes) leading to ~0.31 μm grain size, with {110}<uvw> as the major texture component. The development of UFG structure by annealing the cryo-rolled alloy at 1023 K (750 ℃) is considered the better option since the volume fraction of carbides in the specimen are less than in the specimens

annealed at 923 K (650 ℃). The energy required to achieve UFG structure at 923 K (650 ℃) is higher due to low reversion rate. The hardness of the as-received alloy increased by about 195% as a result of grain refinement to 0.31 μm size. The activation energy (Q) required for the reversion of α′ to γ in AISI 321 ASS is estimated to be 80 $kJmol^{-1}$.

C. The UFG alloy has strong intensity of ζ-fibre ({110}<uvw>) texture, which is is attributed to pseudo-texture memory effect in the investigated AISI 321stainless steel. This indicates the ability of the steel to memorize the crystallographic orientation of the deformed austenite, rather than that of austenite phase in the as-received alloy that is random. The intensity of ζ-fibre decreases with increase in temperature.

D. Under dynamic impact loading, the UFG (0.24 μm) AISI 321 stainless steel shows higher compressive strength than the CG (37 μm) steel specimens while the CG specimens possess higher strain hardenability. Slip and twinning are the active deformation mechanisms in the CG specimens and they are highly suppressed in UFG specimens due to spatial restriction effect. The co-existence of martensitic phase transformation paths with and without an intermediate phase (HCP ε-martensite) during dynamic plastic deformation is confirmed in AISI 321 steel; although temperature rise in specimen and grain size could influence the transformation path. The stable end-orientation of the austenite phase in compression is [110]||CD texture while that of the martensitic phase is [100]||CD with spread towards [111]||CD texture. UFG specimens exhibit lower critical strain and strain rate at which shear strain localization leading to formation of adiabatic shear bands (ASB) occurs. UFG AISI 321 steel specimens are therefore more susceptible to ASB formation than CG specimens. EBSD analysis of areas inside transformed shear bands, outside these bands, and the interface region revealed the development of equiaxed ultra-fine grain structure (average grain sizes of ~0.17 μm in CG and ~0.14 μm in UFG specimens) inside the TSB by rotational dynamic recrystallization mechanism.

E. When subjected to impact loading, a change in strain rate sensitivity (SRS) with increasing true strain rate ($\dot{\varepsilon}_T$) occurred only in fine (3 μm) and coarse-grained specimens. This change occurs at a critical true strain rate ($\dot{\varepsilon}_{Tc}$) of ~5900 and 6800 $s^{-1}$, for FG and CG specimens, respectively. While the SRS of UFG remains unchanged at 0.101 irrespective

of strain rate, those of FG and CG specimens changed from 0.094 to 0.326 and 0.091 to 0.634, respectively, as the strain rate increased beyond the $\dot{\varepsilon}_{Tc}$ value. The complexities in the deformation mechanisms such as simultaneous occurrence of slip, twinning and α' phase transformation in FG and CG metastable AISI 321 stainless steel leads to a change in $\dot{\varepsilon}_{Tc}$. The constant SRS in UFG specimen suggests no change in operational deformation mechanisms at all investigated strain rates.

F. Five strengthening sources that contribute to strain hardening in the AISI 321 steel are identified. They are: (a) grain boundary strengthening, which is most beneficial to UFG specimens, (b) deformation-induced martensite transformation that is most beneficial to UFG specimen, (c) deformation twinning acting as barrier to dislocation motion, which is most beneficial to CG specimens, (d) dislocation-dislocation, which is most most beneficial to CG specimens, and (e) dislocation interaction with titanium carbides, which is most beneficial to CG specimen. However, the synergetic effect of these sources is lower under dynamic impact loading condition due to temperature rise in the specimens.

G. Under quasi-static compressive loading condition, the yield strength ($\sigma_y$) of CG and UFG specimens are ~0.2 and ~1 GPa, respectively. Regions characterized by high dislocation densities, e.g., slip bands and regions close to the grain boundary, are HCP ε-martensite, BCC α′ and deformation twin nucleation sites in CG specimen. While grain boundaries and triple junctions serve as the nucleation sites for martensite in UFG specimens, twinning was not observed in UFG specimens due to space restriction effect. Irrespective of grain size, Shoji-Nishiyama, Kurdjumov-Sachs and Burgers orientation relationships exist between the γ & ε, γ & α′, and ε & α′ phases, respectively. These confirm that the phase transformation sequence follows both FCC γ → BCC α′ and FCC γ → HCP ε→ BCC α′ under quasi-static loading condition. The experimental results agree well with the VPSC simulation that was used to identify the role of deformation mechanisms in macroscopic stress-strain response and texture evolution during quasi-static uniaxial compression test.

H. On the roles of grain size, texture, strain and strain rate on the thermal and mechanical stability of austenite in AISI 321 metastable austenitic stainless steel, fraction of thermally-induced α'-martensite was observed at an incumbent time. This suggests the occurrence of

an isothermal martensitic transformation and its volume fracion increases with increase in grain size. Meanwhile, the fraction of mechanically-induced α' decreases with increase in grain size. Irrespective of grain size, the fraction of mechanically-induced α' also increases with increase in strain and decrease in strain rate. In the event of ASB formation in specimens deformed at high-strain rate, fraction of mechanically-induced α' decreases as the ASB is approached due to the significant temperature rise in the ASB region. EBSD examination revealed that the evolution of both thermal- and deformation-induced martensite is orientation-dependent in both FG and CG specimens. The thermal and mechanical instability of the austenite phase was observed to be highest in the RD/CD||[100]-oriented grains, followed by grains oriented near RD/CD||[110] and RD/CD||[111], in that order.

I. Corrosion resistance is highest in the UFG specimens, followed by FG and CG specimens, in that order, in saline media. This is due to the formation of a more stable adsorbed passive film in UFG specimens. Similarly, on the role of strain and strain rate, the corrosion resistance of AISI 321 austenitic stainless steel follows the order: quasi-static > dynamic > undeformed, for all grain sizes. Whereas the presence of TiC particles in AISI 321 steel is non-detrimental to its (AISI 321) corrosion, TiN particles promote pitting corrosion in the steel due to the galvanic coupling that exists between the particles and their surrounding matrix.

## 12.3 Recommendations for future work

I. This study only focused on the compressive behavior of AISI 321 stainless steel of different grain sizes under quasi-static and dynamic impact responses; hence, torsional and tensile testings under both loading conditions would be of great interest.

II. From Chapter 10, it was observed that the fraction of thermally-induced α'-martensite increases with increase in grain size. Hence, just as the $Md_{30/50}$ (Eqn. 2.5), the $M_s$ (Eqn. 2.3) should be modified to take into consideration, the effect of grain size.

III. The corrosion behavior of UFG, FG and CG AISI 321 steel have only been studied in chloride media, it will be of interest to determine the effects of grain refinement on the resistance of AISI 321 stainless steel to irradiation damage. This is because AISI 321 stainless steel is a choice material in the fabrication of nuclear plants.

## References


[1] D. T. Llewellyn and R. C. Hudd, “Stainless steels,” in *STEELS-Metallurgy and Applications*, Third., Oxford, UK: Reed Educational and Professional Publishing Ltd, 1998, pp. 291–379.

[2] M. Bock, I. Arrayago, and E. Real, “Experiments on cold-formed ferritic stainless steel slender sections,” *J. Constr. Steel Res.*, vol. 109, pp. 13–23, 2015.

[3] J. Wang, Y. Lin, J. Yan, D. Zen, Q. Zhang, R. Huang, and H. Fan, “Influence of time on the microstructure of AISI 321 austenitic stainless steel in salt bath nitriding,” *Surf. Coatings Technol.*, vol. 206, no. 15, pp. 3399–3404, 2012.

[4] A. D. Warren, R. L. Harniman, A. M. Collins, S. A. Davis, C. M. Younes, P. E. J. Flewitt, and T. B. Scott, “Comparison between magnetic force microscopy and electron back-scatter diffraction for ferrite quantification in type 321 stainless steel,” *Ultramicroscopy*, vol. 148, pp. 1–9, 2015.

[5] A. F. Padilha and R. L. Plaut, “Stainless steel heat treatment,” in *Steel Heat Treatment: Metallurgy and Technologies*, 2nd ed., G. E. Totten, Ed. New York: Taylor & Francis Group, 2006, pp. 695–735.

[6] H. F. G. De Abreu, S. S. De Carvalho, P. De Lima Neto, R. P. Dos Santos, V. N. Freire, P. M. D. O. Silva, and S. S. M. Tavares, “Deformation induced martensite in an AISI 301LN stainless steel: characterization and influence on pitting corrosion resistance,” *Mater. Res.*, vol. 10, no. 4, pp. 359–366, 2007.

[7] J. Fu, W. Qiu, Q. Nie, and Y. Wu, “Precipitation of TiN during solidi fi cation of AISI 439 stainless steel,” *J. Alloys Compd.*, vol. 699, pp. 938–946, 2017.

[8] R. K. Gupta and N. Birbilis, “The influence of nanocrystalline structure and processing route on corrosion of stainless steel: A review,” *Corros. Sci.*, vol. 92, pp. 1–15, 2015.

[9] K. H. Lo, C. H. Shek, and J. K. L. Lai, “Recent developments in stainless steels,” *Mater. Sci. Eng. R Reports*, vol. 65, no. 4–6, pp. 39–104, 2009.

[10] F. Borgioli, E. Galvanetto, and T. Bacci, “Low temperature nitriding of AISI 300 and 200 series austenitic stainless steels,” *Vaccum*, vol. 127, pp. 51–60, 2016.

[11] M. Corradi, A. Di Schino, A. Borri, and R. Rufini, “A review of the use of stainless steel for masonry repair and reinforcement,” *Constr. Build. Mater.*, vol. 181, pp. 335–346, 2018.

[12] Y. Sun and T. Bell, “Low Temperature Plasma Nitriding Characteristics of Precipitation Hardening Stainless Steel,” *Surf. Eng.*, vol. 19, no. 5, pp. 331–336, 2004.

[13] D. H. Ping, M. Ohnuma, Y. Hirakawa, Y. Kadoya, and K. Hono, “Microstructural evolution in 13Cr-8Ni-2.5Mo-2Al martensitic precipitation-hardened stainless steel,” *Mater. Sci. Eng. A*, vol. 394, no. 1–2, pp. 285–295, 2005.

[14] A. L. SCHAEFFLER, “Constitution Diagram for Stainless Steel Weld Metal,” *Met. Prog.*, vol. 56, p. 680, 1949.

[15] P. Guiraldenq and O. H. Duparc, “The genesis of the Schaeffler diagram in the history of stainless steel,” *Met. Res. Technol.*, vol. 114, p. 613, 2017.

[16] H. Schneider, “A modified constitution diagram for stainless steels,” *Foundry Trade J.*, vol. 108, pp. 562–571, 1960.

[17] R. L. Klueh, P. J. Maziasz, and E. H. Lee, “Manganese as an Austenite Stabilizer in Fe-Cr-Mn-C Steels,” vol. Materials, pp. 115–124, 1988.

[18] M. Eskandari, a Kermanpur, and a Najafizadeh, “Formation of Nanocrystalline Structure in 301 Stainless Steel Produced by Martensite Treatment,” *Metall. Mater. Trans. A*, vol. 40, no. September, pp. 2241–2249, 2009.

[19] J. Talonen and H. Hänninen, “Formation of shear bands and strain-induced martensite during plastic deformation of metastable austenitic stainless steels,” *Acta Mater.*, vol. 55, pp. 6108–6118, 2007.

[20] W. Zhang, J. Wu, Y. Wen, J. Ye, and N. Li, “Characterization of different work hardening behavior in AISI 321 stainless steel and Hadfield steel,” *J. Mater. Sci.*, vol. 45, pp. 3433–

3437, 2010.

[21] J. P. Liang, Y. L. Gao, R. X. Li, and Q. J. Zhai, “Phase evolution of AISI 321 stainless steel during directional solidification,” *Ironmak. Steelmak.*, vol. 36, no. 8, pp. 603–609, 2009.

[22] J. Cairney, S. Miller, P. Trimby, H.-W. Yen, S. Moody, A. La Fontaine, S. Ringer, and M. Chensee, “Martensitic transformation in an intergranular corrosion area of austenitic stainless steel during thermal cycling,” *Corros. Sci.*, vol. 85, pp. 1–6, 2014.

[23] M. Laleh and F. Kargar, “Suppression of chromium depletion and sensitization in austenitic stainless steel by surface mechanical attrition treatment,” *Mater. Lett.*, vol. 65, no. 12, pp. 1935–1937, 2011.

[24] R. Jones and V. Randle, “Sensitisation behaviour of grain boundary engineered austenitic stainless steel,” *Mater. Sci. Eng. A*, vol. 527, no. 16–17, pp. 4275–4280, 2010.

[25] S. a. a. Akbari Mousavi and a. R. Sufizadeh, “Metallurgical investigations of pulsed Nd:YAG laser welding of AISI 321 and AISI 630 stainless steels,” *Mater. Des.*, vol. 30, no. 8, pp. 3150–3157, 2009.

[26] V. Moura, A. Y. Kina, S. S. M. Tavares, L. D. Lima, and F. B. Mainier, “Influence of stabilization heat treatments on microstructure, hardness and intergranular corrosion resistance of the AISI 321 stainless steel,” *J. Mater. Sci.*, vol. 43, no. 2, pp. 536–540, 2008.

[27] Y. Y. Chen, Y. M. Liou, and H. C. Shih, “Stress corrosion cracking of type 321 stainless steels in simulated petrochemical process environments containing hydrogen sulfide and chloride,” *Mater. Sci. Eng. A*, vol. 407, pp. 114–126, 2005.

[28] K. Guan, X. Xu, H. Xu, and Z. Wang, “Effect of aging at 700°C on precipitation and toughness of AISI 321 and AISI 347 austenitic stainless steel Awelds,” *Nucl. Eng. Des.*, vol. 235, pp. 2485–2494, 2005.

[29] R. K. C. Nkhoma, C. W. Siyasiya, and W. E. Stumpf, “Hot workability of AISI 321 and AISI 304 austenitic stainless steels,” *J. Alloys Compd.*, vol. 595, pp. 103–112, 2014.

[30] M. B. Leban and R. Tisu, “The effect of TiN inclusions and deformation-induced martensite on the corrosion properties of AISI 321 stainless steel,” *Eng. Fail. Anal.*, vol. 33, pp. 430–438, 2013.

[31] G. Sayiram and N. Arivazhagan, “Microstructural characterization of dissimilar welds between Incoloy 800H and 321 Austenitic Stainless Steel,” *Mater. Charact.*, vol. 102, pp. 180–188, 2015.

[32] P. Cunat, “Alloying elements in stainless steel and other chromium-containing alloys.” Euro Inox, Paris, pp. 1–24, 2004.

[33] G. J. Eichelmann and F. C. Hull, “The effect of composition of spontaneous transformation of austenite to martensite in 18–8-type stainless steel,” *Trans. ASM*, vol. 45, pp. 77–104, 1953.

[34] H. K. D. H. Bhadeshia and R. W. K. Honeycombe, “Formation of Martensite,” in *Steels: Microstructure and Properties*, Third., Butterworth-Heinemann, 2006, pp. 95–128.

[35] M. Eskandari, A. Zarei-Hazanki, M. A. Mohtadi-Bonab, A. G. Odeshi, and J. A. Szpunar, “Microstructure and texture evolution in 21Mn–2.5Si–1.6Al–Ti steel subjected to dynamic impact loading,” *Mater. Sci. Eng. A*, vol. 622, pp. 160–167, 2015.

[36] E. P. Butler and M.G.Burke, “Chromium depletion and martensite formation at grain boundaries in sensitised austenitic stainless steels,” *Acta Metall.*, vol. 34, no. 3, pp. 557–570, 1986.

[37] Y. Matsuoka, T. Iwasaki, N. Nakada, and T. Tsuchiyama, “Effect of Grain Size on Thermal and Mechanical Stability of Austenite in Metastable Austenitic Stainless Steel,” *ISIJ Int.*, vol. 53, no. 7, pp. 1224–1230, 2013.

[38] H. Zheng, W. Wang, D. Wu, S. Xue, Q. Zhai, J. Frenzel, and Z. Luo, “Athermal nature of the martensitic transformation in Heusler alloy Ni-Mn-Sn,” *Intermetallics*, vol. 36, pp. 90–95, 2013.

[39] E. Yasar, E. Güler, H. Güngünes, and T. N. Durlu, “Some characteristics of thermally

induced martensite in Fe-30%Ni-3.6%Mo alloy," *Mater. Charact.*, vol. 59, no. 6, pp. 769–772, 2008.

[40] T. Kakeshita, K. Kuroiwa, K. Shimizu, T. Ikeda, A. Yamagishi, and M. Date, "A New Model Explainable for Both the Athermal and Isothermal Natures of Martensitic Transformations in Fe–Ni–Mn Alloys," *Mater. Trans. JIM*, vol. 34, pp. 423–428, 1993.

[41] D. E. Laughlin, N. J. Jones, A. J. Schwartz, and T. B. Massalski, "Thermally Activated Martensite: Its Relationship to Non-Thermally Activated (Athermal) Martensite," *Int. Conf. Martensitic Transform. 2008*, pp. 141–144, 2013.

[42] D. P. Koistinen and R. E. Marburger, "A general equation prescribing the extent of the austenite-martensite transformation in pure iron-carbon alloys and plain carbon steels," *Acta Metall.*, vol. 7, pp. 59–60, 1959.

[43] P. Hedström, "Deformation induced martensitic transformation of metastable stainless steel AISI 301," 2005.

[44] J. M. Nam, T. Terai, and T. Kakeshita, "Effects of particle and grain sizes on martensitic transformation in an Fe-30.5 at.%Ni alloy," *J. Alloys Compd.*, vol. 577, no. SUPPL. 1, pp. S348–S352, 2013.

[45] I. Y. Georgieva; and I. I. Nikitina, "Isothermal and athermal martensitic transformations," vol. 5, pp. 68–72, 1972.

[46] D. Z. Yang and C. M. Wayman, "Lath martensitic transformation with a plate component in an Fe21Ni4Mn alloy," *Scr. Metall.*, vol. 17, no. 11, pp. 1377–1379, 1983.

[47] M. Zhang, L. Li, R. Y. Fu, D. Krizan, and B. C. De Cooman, "Continuous cooling transformation diagrams and properties of micro-alloyed TRIP steels," *Mater. Sci. Eng. A*, vol. 438–440, no. SPEC. ISS., pp. 296–299, 2006.

[48] N. Nohara, K., Ono, Y., Ohashi, "Composition and grain-size dependencies," *J. Iron Steel Inst. Japan*, vol. 63, pp. 212–222, 1977.

[49] M. G. Shahri, S. R. Hosseini, and M. Salehi, “Formation of Nano/Ultrafine Grains in AISI 321 Stainless Steel Using Advanced Thermo-Mechanical Process,” *Acta Metall. Sin. (English Lett.*, vol. 28, no. 4, pp. 499–504, 2015.

[50] C. Herrera, D. Ponge, and D. Raabe, “Design of a novel Mn-based 1 GPa duplex stainless TRIP steel with 60% ductility by a reduction of austenite stability,” *Acta Mater.*, vol. 59, no. 11, pp. 4653–4664, 2011.

[51] P. J. Brofman and G. S. Ansell, “On the Effect of Carbon on the Stacking Fault Energy of Austenitic Stainless Steels,” *Metall. Trans. A*, vol. 9, no. 6, pp. 879–880, 1978.

[52] R. E. Schramm and R. P. Reed, “Stacking fault energies of seven commercial austenitic stainless steels,” *Metall. Trans. A*, vol. 6, no. 7, pp. 1345–1351, 1975.

[53] C. G. Rhodes and A. W. Thompson, “The composition dependence of stacking fault energy in austenitic stainless steels,” *Metall. Trans. A*, vol. 8, no. 12, pp. 1901–1906, 1977.

[54] S. S. F. de Dafé, F. L. Sicupira, F. C. S. Matos, N. S. Cruz, D. R. Moreira, and D. B. Santos, “Effect of cooling rate on (ε, α’) martensite formation in twinning/transformation-induced plasticity Fe-17Mn-0.06C steel,” *Mater. Res.*, vol. 16, no. 6, pp. 1229–1236, 2013.

[55] J. R. Patel and M. Cohen, “Criterion for the action of applied stress in the martensitic transformation,” *Acta Metall.*, vol. 1, no. 5, pp. 531–538, 1953.

[56] Y. Xu, J. Zhang, Y. Bai, and M. A. Meyers, “Shear Localization in Dynamic Deformation: Microstructural Evolution,” *Metall. Mater. Trans. A*, vol. 39, no. 4, pp. 811–843, Feb. 2008.

[57] M. Eskandari, A. Zarei-Hanzaki, J. A. Szpunar, M. A. Mohtadi-Bonab, A. R. Kamali, and M. Nazarian-Samani, “Microstructure evolution and mechanical behavior of a new microalloyed high Mn austenitic steel during compressive deformation,” *Mater. Sci. Eng. A*, vol. 615, pp. 424–435, 2014.

[58] G. B. Olson and M. Cohen, “A mechanism for the strain-induced nucleation of martensitic transformation,” *J. Less-Common Met.*, vol. 28, pp. 107–118, 1972.

[59] H. Yen, S. W. Ooi, M. Eizadjou, A. Breen, C. Huang, H. K. D. H. Bhadeshia, and S. P. Ringer, “Role of stress-assisted martensite in the design of strong ultrafine-grained duplex steels,” *Acta Mater.*, vol. 82, pp. 100–114, 2015.

[60] E. I. Galindo-Nava and P. E. J. Rivera-Díaz-del-Castillo, “Understanding martensite and twin formation in austenitic steels: A model describing TRIP and TWIP effects,” *Acta Mater.*, vol. 128, pp. 120–134, 2017.

[61] H. W. Yen, S. W. Ooi, M. Eizadjou, A. Breen, C. Y. Huang, H. K. D. H. Bhadeshia, and S. P. Ringer, “Role of stress-assisted martensite in the design of strong ultrafine-grained duplex steels,” *Acta Mater.*, vol. 82, pp. 100–114, 2015.

[62] S. J. McCormack, W. Wen, E. V. Pereloma, C. N. Tomé, A. A. Gazder, and A. A. Saleh, “On the first direct observation of de-twinning in a twinning-induced plasticity steel,” *Acta Mater.*, no. June, 2018.

[63] O. Bouaziz, S. Allain, C. P. Scott, P. Cugy, and D. Barbier, “High manganese austenitic twinning induced plasticity steels: A review of the microstructure properties relationships,” *Curr. Opin. Solid State Mater. Sci.*, vol. 15, no. 4, pp. 141–168, 2011.

[64] B. C. De Cooman, Y. Estrin, and S. K. Kim, “Twinning-induced plasticity (TWIP) steels,” *Acta Mater.*, vol. 142, pp. 283–362, 2018.

[65] K. M. Rahman, V. A. Vorontsov, and D. Dye, “The effect of grain size on the twin initiation stress in a TWIP steel,” *Acta Mater.*, vol. 89, pp. 247–257, 2015.

[66] J.-Y. Choi and W. Jin, “Strain induced martensite formation and its effect on strain hardening behavior in the cold drawn 304 austenitic stainless steels,” *Scr. Mater.*, vol. 36, no. 1, pp. 99–104, 1997.

[67] L. Bracke, K. Verbeken, L. Kestens, and J. Penning, “Microstructure and texture evolution during cold rolling and annealing of a high Mn TWIP steel,” *Acta Mater.*, vol. 57, no. 5, pp. 1512–1524, 2009.

[68] S. Curtze and V. T. Kuokkala, “Dependence of tensile deformation behavior of TWIP steels

on stacking fault energy, temperature and strain rate," *Acta Mater.*, vol. 58, no. 15, pp. 5129–5141, 2010.

[69] H. Idrissi, K. Renard, L. Ryelandt, D. Schryvers, and P. J. Jacques, "On the mechanism of twin formation in Fe-Mn-C TWIP steels," *Acta Mater.*, vol. 58, no. 7, pp. 2464–2476, 2010.

[70] J. W. Christian and S. Mahajan, "Deformation twinning," *Prog. Mater. Sci.*, vol. 39, no. 1–2, pp. 1–157, 1995.

[71] O. Bouaziz, S. Allain, and C. Scott, "Effect of grain and twin boundaries on the hardening mechanisms of twinning-induced plasticity steels," *Scr. Mater.*, vol. 58, no. 6, pp. 484–487, 2008.

[72] T. S. Byun, "On the stress dependence of partial dislocation separation and deformation microstructure in austenitic stainless steels," *Acta Mater.*, vol. 51, no. 11, pp. 3063–3071, 2003.

[73] K. T. Ramesh, "High Rates and Impact Experiments," in *Springer Handbook of Experimental Solid Mechanics. Springer Handbooks*, First., S. W., Ed. Springer, Boston, MA, 2008, pp. 929–960.

[74] J. Luo and M. Q. Li, "Strain rate sensitivity and strain hardening exponent during the isothermal compression of Ti60 alloy," *Mater. Sci. Eng. A*, vol. 538, pp. 156–163, 2012.

[75] S. Nemat-Naser, "Introduction to high strain-rate testing, high strain rate tension and compression tests," in *ASM Handbook Vol 8*, 2000, pp. 942–955.

[76] A. Khosravifard, M. M. Moshksar, and R. Ebrahimi, "High strain rate torsional testing of a high manganese steel: Design and simulation," *Mater. Des.*, vol. 52, pp. 495–503, 2013.

[77] S. E. Schoenfeld and T. W. Wright, "A failure criterion based on material instability," *Int. J. Solids Struct.*, vol. 40, no. 12, pp. 3021–3037, Jun. 2003.

[78] H. Wang, Y. Jeong, B. Clausen, Y. Liu, R. J. Mccabe, F. Barlat, and C. N. Tomé, "Effect of martensitic phase transformation on the behavior of 304 austenitic stainless steel under

tension," *Mater. Sci. Eng. A*, vol. 649, pp. 174–183, 2015.

[79] W. S. Park, S. W. Yoo, M. H. Kim, and J. M. Lee, "Strain-rate effects on the mechanical behavior of the AISI 300 series of austenitic stainless steel under cryogenic environments," *Mater. Des.*, vol. 31, no. 8, pp. 3630–3640, 2010.

[80] R. Ueji, N. Tsuchida, D. Terada, N. Tsuji, Y. Tanaka, A. Takemura, and K. Kunishige, "Tensile properties and twinning behavior of high manganese austenitic steel with fine-grained structure," *Scr. Mater.*, vol. 59, no. 9, pp. 963–966, 2008.

[81] Y. F. Shen, N. Jia, Y. D. Wang, X. Sun, L. Zuo, and D. Raabe, "Suppression of twinning and phase transformation in an ultrafine grained 2 GPa strong metastable austenitic steel: Experiment and simulation," *Acta Mater.*, vol. 97, pp. 305–315, 2015.

[82] I. Gutierrez-Urrutia, S. Zaefferer, and D. Raabe, "The effect of grain size and grain orientation on deformation twinning in a Fe – 22 wt.% Mn–0 .6 wt.% C TWIP steel," *Mater. Sci. Eng. A*, vol. 527, no. 15, pp. 3552–3560, 2010.

[83] P. Sahu, S. Curtze, A. Das, B. Mahato, V. T. Kuokkala, and S. G. Chowdhury, "Stability of austenite and quasi-adiabatic heating during high-strain-rate deformation of twinning-induced plasticity steels," *Scr. Mater.*, vol. 62, no. 1, pp. 5–8, 2010.

[84] S. S. Hecker, M. G. Stout, K. P. Staudhammer, and J. L. Smith, "Effects of Strain State and Strain Rate on Deformation-Induced Transformation in 304 Stainless Steel: Part I. Magnetic Measurements and Mechanical Behavior," *Metall. Trans. A*, vol. 13, no. 4, pp. 619–626, 1982.

[85] R. Zaera, J. A. Rodríguez-martínez, and D. Rittel, "On the Taylor – Quinney coefficient in dynamically phase transforming materials . Application to 304 stainless steel," *Int. J. Plast.*, vol. 40, pp. 185–201, 2013.

[86] B. F. Wang, Z. L. Liu, X. Y. Wang, and Z. Z. Li, "An EBSD investigation on deformation-induced shear bands in a low nickel austenitic stainless steel under controlled shock-loading conditions," *Mater. Sci. Eng. A*, vol. 610, pp. 301–308, 2014.

[87] S. Woo, J. Hoon, and K. Park, “Effects of Al addition on high strain rate deformation of fully austenitic high Mn steels,” *Mater. Sci. Eng. A*, vol. 528, no. 24, pp. 7267–7275, 2011.

[88] M. Eskandari, M. A. Mohtadi-Bonab, M. Yeganeh, J. A. Szpunar, and A. G. Odeshi, “High-strain-rate deformation behaviour of new high-Mn austenitic steel during impact shock-loading,” *Mater. Sci. Technol. (United Kingdom)*, vol. 35, no. 1, pp. 77–88, 2019.

[89] H. Zhan, W. Zeng, G. Wang, D. Kent, and M. Dargusch, “Microstructural characteristics of adiabatic shear localization in a metastable beta titanium alloy deformed at high strain rate and elevated temperatures,” *Mater. Charact.*, vol. 102, pp. 103–113, 2015.

[90] J. Peirs, W. Tirry, B. Amin-Ahmadi, F. Coghe, P. Verleysen, L. Rabet, D. Schryvers, and J. Degrieck, “Microstructure of adiabatic shear bands in Ti6Al4V,” *Mater. Charact.*, vol. 75, pp. 79–92, Jan. 2013.

[91] C. Zener and J. H. Holloman, “Effects of strain rates upon plastic flow of steel,” *J. Appl. Phys.*, no. 15, pp. 22–32, 1944.

[92] D. H. Li, Y. Yang, T. Xu, H. G. Zheng, Q. S. Zhu, and Q. M. Zhang, “Observation of the microstructure in the adiabatic shear band of 7075 aluminum alloy,” *Mater. Sci. Eng. A*, vol. 527, no. 15, pp. 3529–3535, Jun. 2010.

[93] E. K. Cerreta, J. F. Bingert, G. T. Gray, C. P. Trujillo, M. F. Lopez, C. A. Bronkhorst, and B. L. Hansen, “Microstructural examination of quasi-static and dynamic shear in high-purity iron,” *Int. J. Plast.*, vol. 40, pp. 23–38, 2013.

[94] C. Z. Duan and L. C. Zhang, “Adiabatic shear banding in AISI 1045 steel during high speed machining: Mechanisms of microstructural evolution,” *Mater. Sci. Eng. A*, vol. 532, pp. 111–119, Jan. 2012.

[95] D. L. Zou, B. F. Luan, Q. Liu, L. J. Chai, and J. W. Chen, “Characterization of adiabatic shear bands in the zirconium alloy impacted by split Hopkinson pressure bar at a strain rate of 6000s−1,” *Mater. Sci. Eng. A*, vol. 558, pp. 517–524, Dec. 2012.

[96] Y. Yang, F. Jiang, B. M. Zhou, X. M. Li, H. G. Zheng, and Q. M. Zhang, “Microstructural

characterization and evolution mechanism of adiabatic shear band in a near beta-Ti alloy," *Mater. Sci. Eng. A*, vol. 528, no. 6, pp. 2787–2794, Mar. 2011.

[97] V. F. Nesterenko, M. a. Meyers, and T. W. Wright, "Self-organization in the initiation of adiabatic shear bands," *Acta Mater.*, vol. 46, no. 1, pp. 327–340, Dec. 1998.

[98] D. Peirce, R. J. Asaro, and A. Needleman, "Material rate dependence and localized deformation in crystalline solids," *Acta Metall.*, vol. 31, no. 12, pp. 1951–1976, Dec. 1983.

[99] L. Anand and S. R. Kalidindi, "The process of shear band formation in plane strain compression of fcc metals: Effects of crystallographic texture," *Mech. Mater.*, vol. 17, no. 2–3, pp. 223–243, Mar. 1994.

[100] R. W. Armstrong and F. J. Zerilli, "Dislocation mechanics aspects of plastic instability and shear banding," *Mech. Mater.*, vol. 17, no. 2–3, pp. 319–327, Mar. 1994.

[101] S. Medyanik, W. Liu, and S. Li, "On criteria for dynamic adiabatic shear band propagation," *J. Mech. Phys. Solids*, vol. 55, no. 7, pp. 1439–1461, Jul. 2007.

[102] D. L. Zou, L. Zhen, C. Y. Xu, and W. Z. Shao, "Characterization of adiabatic shear bands in AM60B magnesium alloy under ballistic impact," *Mater. Charact.*, vol. 62, no. 5, pp. 496–502, May 2011.

[103] L. Zhen, D. L. Zou, C. Y. Xu, W. Z. Shao, L. Zhen, C. Y. Xu, and W. Z. Shao, "Microstructure evolution of adiabatic shear bands in AM60B magnesium alloy under ballistic impact," *Mater. Charact.*, vol. 527, no. 5, pp. 5728–5733, May 2010.

[104] Z. P. Wan, Y. E. Zhu, H. W. Liu, and Y. Tang, "Microstructure evolution of adiabatic shear bands and mechanisms of saw-tooth chip formation in machining Ti6Al4V," *Mater. Sci. Eng. A*, vol. 531, pp. 155–163, Jan. 2012.

[105] A. A. Tiamiyu, M. Eskandari, M. Sanayei, A. G. Odeshi, and J. A. Szpunar, "Mechanical behavior and high-resolution EBSD investigation of the microstructural evolution in AISI 321 stainless steel under dynamic loading condition," *Mater. Sci. Eng. A*, vol. 673, pp. 400–416, 2016.

[106] B. Wang, J. Sun, X. Wang, and A. Fu, “Adiabatic shear localization in a near beta Ti–5Al–5Mo–5 V–1Cr–1Fe alloy,” *Mater. Sci. Eng. A*, vol. 639, no. December, pp. 526–533, 2015.

[107] M. A. Meyers, Y. B. Xu, Q. Xue, M. T. Pérez-Prado, and T. R. McNelley, “Microstructural evolution in adiabatic shear localization in stainless steel,” *Acta Mater.*, vol. 51, no. 5, pp. 1307–1325, Mar. 2003.

[108] S. Boakye-Yiadom, A. K. Khan, and N. Bassim, “Deformation Mapping and the Role of Carbides on the Microstructure and Properties of Evolved Adiabatic Shear Bands,” *Metall. Mater. Trans. A*, vol. 45, no. 12, pp. 5379–5396, 2014.

[109] J. F. C. Lins, H. R. Z. Sandim, H.-J. Kestenbach, D. Raabe, and K. S. Vecchio, “A microstructural investigation of adiabatic shear bands in an interstitial free steel,” *Mater. Sci. Eng. A*, vol. 457, no. 1–2, pp. 205–218, May 2007.

[110] J. Hines, K. Vecchio, and S. Ahzi, “A model for microstructure evolution in adiabatic shear bands,” *Metall. Mater. Trans. A*, vol. 29, no. January 1998, 1998.

[111] B. Derby, “The dependence of grain size on stress during dynamic recrystallisation,” *Acta Metall. Mater.*, vol. 39, no. 5, pp. 955–962, May 1991.

[112] V. F. Nesterenko, M. a. Meyers, J. C. LaSalvia, M. P. Bondar, Y. J. Chen, and Y. L. Lukyanov, “Shear localization and recrystallization in high-strain, high-strain-rate deformation of tantalum,” *Mater. Sci. Eng. A*, vol. 229, no. 1–2, pp. 23–41, Jun. 1997.

[113] B. Verlinden, J. Driver, I. Samajdar, and R. D. Doherty, *Thermo-Mechanical Processing of metallic materials*, First. Oxford, UK: Elsevier Ltd, 2007.

[114] X. Teng, T. Wierzbicki, and H. Couque, “On the transition from adiabatic shear banding to fracture,” *Mech. Mater.*, vol. 39, no. 2, pp. 107–125, Feb. 2007.

[115] S. Boakye-Yiadom and M. N. Bassim, “Effect of prior heat treatment on the dynamic impact behavior of 4340 steel and formation of adiabatic shear bands,” *Mater. Sci. Eng. A*, vol. 528, no. 29–30, pp. 8700–8708, Nov. 2011.

[116] A. G. Odeshi, A. O. Adesola, and A. Y. Badmos, “Failure of AA 6061 and 2099 aluminum alloys under dynamic shock loading,” *Eng. Fail. Anal.*, vol. 35, pp. 302–314, Dec. 2013.

[117] A. G. Odeshi, M. N. Bassim, S. Al-Ameeri, and and Q. Li, “Dynamic shear band propagation and failure in AISI 4340 steel,” *J. Mater. Process. Technol.*, vol. 169, no. 2, pp. 150–155.

[118] A. A. Tiamiyu, A. Y. Badmos, and A. G. Odeshi, “Effects of temper condition on high strain-rate deformation of AA 2017 aluminum alloy in compression,” *Mater. Des.*, vol. 89, pp. 872–883, 2016.

[119] A. G. Odeshi and M. N. Bassim, “High strain-rate fracture and failure of a high strength low alloy steel in compression,” *Mater. Sci. Eng. A*, vol. 525, no. 1–2, pp. 96–101, Nov. 2009.

[120] M. N. Bassim and A. G. Odeshi, “Shear strain localisation and fracture in high strength structural materials,” *Arch. Mater. Sci. Eng.*, vol. 31, no. 2, pp. 69–74, 2008.

[121] H. Ma, L. Huang, Y. Tian, and J. Li, “Effects of strain rate on dynamic mechanical behavior and microstructure evolution of 5A02-O aluminum alloy,” *Mater. Sci. Eng. A*, vol. 606, pp. 233–239, Jun. 2014.

[122] T. Michler, “Formation of martensite in 304 grade stainless steels and their welds,” *Materwiss. Werksttech.*, vol. 38, no. 1, pp. 32–35, 2007.

[123] M. Eskandari, A. Kermanpur, and A. Najafizadeh, “Formation of nano-grained structure in a 301 stainless steel using a repetitive thermo-mechanical treatment,” *Mater. Lett.*, vol. 63, pp. 1442–1444, 2009.

[124] A. A. Tiamiyu, “Deformation and damage mechanisms in selected 2000 series aluminum alloys under both quasi-static and dynamic impact loading conditions,” University of Saskatchewan, 2015.

[125] C. Weinong and S. Bo, *Split Hopkinson (Kolsky) Bar: Design, Testing and Applications (Mechanical Engineering Series)*, Illustrate. New York: Springer Science & Business

Media, 2010.

[126] J. William N. Sharpe, Ed., *Springer Handbook of Experimental Solid Mechanics*, Second. New York: Springer US, 2008.

[127] P. J. Nunez, E. Garcia-Plaza, M. Hernando, and R. Trujillo, "Characterization of surface finish of electropolished stainless steel AISI 316L with varying electrolyte concentrations," *Procedia Eng.*, vol. 63, pp. 771–778, 2013.

[128] S. J. Lee and J. J. Lai, "The effects of electropolishing (EP) process parameters on corrosion resistance of 316L stainless steel," *J. Mater. Process. Technol.*, vol. 140, no. 1–3 SPEC., pp. 206–210, 2003.

[129] T. Kozmel, M. Vural, and S. Tin, "EBSD analysis of high strain rate application Al–Cu based alloys," *Mater. Sci. Eng. A*, vol. 630, pp. 99–106, 2015.

[130] J. Talonen, P. Aspegren, and H. Hänninen, "Comparison of different methods for measuring strain induced α-martensite content in austenitic steels," *Mater. Sci. Technol.*, vol. 20, no. 12, pp. 1506–1512, 2004.

[131] A. M. A. El-Rahman, "An investigation on the microstructure, tribological and corrosion performance of AISI 321 stainless steel carbonitrided by RF plasma process," *Surf. Coatings Technol.*, vol. 205, no. 2, pp. 674–681, 2010.

[132] D. Mohr and J. Jacquemin, "Large deformation of anisotropic austenitic stainless steel sheets at room temperature: Multi-axial experiments and phenomenological modeling," *J. Mech. Phys. Solids*, vol. 56, no. 10, pp. 2935–2956, 2008.

[133] D. Yang, Y. An, P. Cizek, and P. Hodgson, "Development of adiabatic shear band in cold-rolled titanium," *Mater. Sci. Eng. A*, vol. 528, no. 12, pp. 3990–3997, May 2011.

[134] C. K. Syn, D. R. Lesuer, and O. D. Sherby, "Microstructure in adiabatic shear bands in a pearlitic ultrahigh carbon steel," *Mater. Sci. Technol.*, vol. 21, no. 3, pp. 317–324, 2005.

[135] D. R. Lesuer, C. K. Syn, and O. D. Sherby, "Severe plastic deformation through adiabatic

shear banding in Fe-C steels," *Mater. Sci. Eng. A*, vol. 410–411, pp. 222–225, 2005.

[136] F. Yuan, P. Jiang, and X. Wu, "Annealing effect on the evolution of adiabatic shear band under dynamic shear loading in ultra-fine-grained iron," *Int. J. Impact Eng.*, vol. 50, pp. 1–8, Dec. 2012.

[137] M. Eskandari, M. A. Mohtadi-Bonab, A. Zarei-Hanzaki, A. G. Odeshi, and J. A. Szpunar, "High-Resolution EBSD Study of Adiabatic Shear Band and Neighboring Grains After Dynamic Impact Loading of Mn-Steel Used in Vehicle Structure," *J. Mater. Eng. Perform.*, 2016.

[138] A. Fattah-alhosseini, "Passivity of AISI 321 stainless steel in 0.5M H2SO4 solution studied by Mott–Schottky analysis in conjunction with the point defect model," *Arab. J. Chem.*, pp. 0–6, 2012.

[139] A. Pardo, M. C. Merino, A. E. Coy, F. Viejo, M. Carboneras, and R. Arrabal, "Influence of Ti, C and N concentration on the intergranular corrosion behaviour of AISI 316Ti and 321 stainless steels," *Acta Mater.*, vol. 55, pp. 2239–2251, 2007.

[140] K. S. Min, S. C. Lee, and S. W. Nam, "Effects of TiC and Cr23C6 Carbides on Creep-Fatigue Properties in AISI 321 Stainless Steel.," *Mater. Trans.*, vol. 43, no. 11, pp. 2808–2812, 2002.

[141] P. Behjati, A. Kermanpur, A. Najafizadeh, H. Samaei Baghbadorani, J. G. Jung, and Y. K. Lee, "Enhanced mechanical properties in a high-manganese austenitic steel through formation of nano grains, nanotwinned austenite grains, nano carbides and TRIP," *Mater. Sci. Eng. A*, vol. 610, pp. 273–278, 2014.

[142] H. Hu, "Texture of Metals," *Texture*, vol. 1, no. 4, pp. 233–258, 1974.

[143] N. Nakada, T. Tsuchiyama, S. Takaki, and S. Hashizume, "Variant Selection of Reversed Austenite in Lath Martensite," *ISIJ Int.*, vol. 47, no. 10, pp. 1527–1532, 2007.

[144] M. Nezakat, H. Akhiani, M. Hoseini, and J. Szpunar, "Effect of thermo-mechanical processing on texture evolution in austenitic stainless steel 316L," *Mater. Charact.*, vol. 98,

pp. 10–17, 2014.

[145] B. R. Kumar, A. K. Singh, B. Mahato, P. K. De, N. R. Bandyopadhyay, and D. K. Bhattacharya, “Deformation-induced transformation textures in metastable austenitic stainless steel,” *Mater. Sci. Eng. A*, vol. 429, pp. 205–211, 2006.

[146] K. T. Park, S. W. Hwang, J. H. Ji, and C. S. Lee, “Static and dynamic deformation of fully austenitic high Mn steels,” *Procedia Eng.*, vol. 10, pp. 1002–1006, 2011.

[147] H. Ding, Z. Y. Tang, W. Li, M. Wang, and D. Song, “Microstructures and Mechanical Properties of Fe-Mn-(Al, Si) TRIP/TWIP Steels,” *J. Iron Steel Res. Int.*, vol. 13, no. 6, pp. 66–70, 2006.

[148] M. T. Pérez-Prado, J. a. Hines, and K. S. Vecchio, “Microstructural evolution in adiabatic shear bands in Ta and Ta-W alloys,” *Acta Mater.*, vol. 49, pp. 2905–2917, 2001.

[149] M. Chabaud-Reytier, L. Allais, C. Caes, P. Dubuisson, and A. Pineau, “Mechanisms of stress relief cracking in titanium stabilised austenitic stainless steel,” *J. Nucl. Mater.*, vol. 323, no. 1, pp. 123–137, 2003.

[150] H. Kitahara, R. Ueji, M. Ueda, N. Tsuji, and Y. Minamino, “Crystallographic analysis of plate martensite in Fe-28.5 at.% Ni by FE-SEM/EBSD,” *Mater. Charact.*, vol. 54, no. 4–5, pp. 378–386, 2005.

[151] L. Tang, Z. Chen, C. Zhan, X. Yang, C. Liu, and H. Cai, “Microstructural evolution in adiabatic shear bands of copper at high strain rates: Electron backscatter diffraction characterization,” *Mater. Charact.*, vol. 64, pp. 21–26, Feb. 2012.

[152] Y. B. Chun and C. H. J. Davies, “Texture effects on development of shear bands in rolled AZ31 alloy,” *Mater. Sci. Eng. A*, vol. 556, pp. 253–259, Oct. 2012.

[153] W. C. Liu ‖, T. Zhai, C.-S. Man, B. Radhakrishnan, and J. G. Morris, “Effect of initial texture on texture evolution in cold-rolled AA 5182 aluminium alloy,” *Philos. Mag.*, vol. 84, no. 31, pp. 3305–3321, Nov. 2004.

[154] J. A. H. and K. S. Vecchio, J. A. Hines, and K. S. Vecchio, “Recrystallization kinetics within adiabatic shear bands,” *Acta Mater.*, vol. 45, no. 2, pp. 635–649, 1997.

[155] H. Paul, P. Uliasz, M. Miszczyk, W. Skuza, and T. Knych, “An Sem/Ebsd Study of Shear Bands Formation in Al-0.23%wt.Zr Alloy Deformed in Plane Strain Compression / Krystalograficzne Aspekty Formowania Sie Pasm Scinania W Stopie Al-0.23%Wag.Zr Odkształcanym W Próbie Nieswobodnego Sciskania,” *Arch. Metall. Mater.*, vol. 58, no. 1, Jan. 2013.

[156] M. Eskandari, A. Najafizadeh, and A. Kermanpur, “Effect of strain-induced martensite on the formation of nanocrystalline 316L stainless steel after cold rolling and annealing,” *Mater. Sci. Eng. A*, vol. 519, pp. 46–50, 2009.

[157] A Di Schino, M Barteri, and J M Kenny, “Development of ultrafine structure by martensite reversion in stainless steel,” *J Mater Sci Lett*, vol. 21, pp. 751–753, 2002.

[158] D. L. Johannsen, A. Kyrolainen, and P. J. Ferreira, “Influence of Annealing Treatment on the Formation of Nano / Submicron Grain Size AISI 301 Austenitic Stainless Steels,” *Metall. Mater. Trans. A*, vol. 37A, pp. 2325–2338, 2005.

[159] R. Song, D. Ponge, D. Raabe, J. G. Speer, and D. K. Matlock, “Overview of processing, microstructure and mechanical properties of ultrafine grained bcc steels,” *Mater. Sci. Eng. A*, vol. 441, no. 1–2, pp. 1–17, 2006.

[160] T. J. Angel, “Formation of martensite in austenitic stainless steels,” *J. Iron Steel Inst.*, vol. 177, pp. 165–174, 1954.

[161] M. Eskandari, A. Najafizadeh, A. Kermanpur, and M. Karimi, “Potential application of nanocrystalline 301 austenitic stainless steel in lightweight vehicle structures,” *Mater. Des.*, vol. 30, no. 9, pp. 3869–3872, 2009.

[162] R. D. K. Misra, S. Nayak, S. A. Mali, J. S. Shah, M. C. Somani, and L. P. Karjalainen, “On the Significance of Nature of Strain-Induced Martensite on Phase-Reversion-Induced Nanograined/Ultrafine-Grained Austenitic Stainless Steel,” *Met. Mater. Trans. A*, vol. 41, no. January, pp. 3–12, 2010.

[163] R. D. K. Misra, Z. Zhang, P. K. C. Venkatasurya, M. C. Somani, and L. P. Karjalainen, "Martensite shear phase reversion-induced nanograined/ultrafine-grained Fe-16Cr-10Ni alloy: The effect of interstitial alloying elements and degree of austenite stability on phase reversion," *Mater. Sci. Eng. A*, vol. 527, no. 29–30, pp. 7779–7792, 2010.

[164] S. Rajasekhara and P. J. Ferreira, "Martensite ??? austenite phase transformation kinetics in an ultrafine-grained metastable austenitic stainless steel," *Acta Mater.*, vol. 59, no. 2, pp. 738–748, 2011.

[165] A. Das, S. Sivaprasad, M. Ghosh, P. C. Chakraborti, and S. Tarafder, "Morphologies and characteristics of deformation induced martensite during tensile deformation of 304 LN stainless steel," *Mater. Sci. Eng. A*, vol. 486, pp. 283–286, 2008.

[166] A. K. De, D. C. Murdock, M. C. Mataya, J. G. Speer, and D. K. Matlock, "Quantitative measurement of deformation-induced martensite in 304 stainless steel by X-ray diffraction," *Scr. Mater.*, vol. 50, no. 12, pp. 1445–1449, 2004.

[167] K. Tomimura, S. Takaki, and Y. Tokunaga, "Reversion Mechanism from Deformation Induced Martensite to Austenite in Metastable Austenitic Stainless Steels.," *ISIJ Int.*, vol. 31, no. 12, pp. 1431–1437, 1991.

[168] T. Tsuchiyama, Y. Nakamura, H. Hidaka, and S. Takaki, "Effect of Initial Microstructure on Superplasticity in Ultrafine Grained 18Cr-9Ni Stainless Steel," *Mater. Trans.*, vol. 45, no. 7, pp. 2259–2263, 2004.

[169] M. C. Somani, P. Juntunen, L. P. Karjalainen, and R. D. K. Misra, "Enhanced Mechanical Properties through Reversion in Metastable Austenitic Stainless Steels," *Metall. Mater. Trans. A*, vol. 40, pp. 729–744, 2009.

[170] C. Celada-casero, B. M. Huang, M. M. Aranda, J. Yang, and D. S. Martin, "Mechanisms of ultra fi ne-grained austenite formation under different isochronal conditions in a cold-rolled metastable stainless steel," *Mater. Charact.*, vol. 118, pp. 129–141, 2016.

[171] L. Kaufman, E. V. Clougherty, and R. J. Weiss, "The lattice stability of metals-III. Iron," *Acta Metall.*, vol. 11, no. 5, pp. 323–335, 1963.

[172] C. S. Yoo, Y. M. Park, Y. S. Jung, and Y. K. Lee, “Effect of grain size on transformation-induced plasticity in an ultrafine-grained metastable austenitic steel,” *Scr. Mater.*, vol. 59, no. 1, pp. 71–74, 2008.

[173] T. Tomida, M. Wakita, M. Yasuyama, S. Sugaya, Y. Tomota, and S. C. Vogel, “Memory effects of transformation textures in steel and its prediction by the double Kurdjumov-Sachs relation,” *Acta Mater.*, vol. 61, no. 8, pp. 2828–2839, 2013.

[174] A. Poulon-quintin, S. Brochet, J. Vogt, and J. Glez, “Fine Grained Austenitic Stainless Steels : The Role of Strain Induced a ˜Martensite and the Reversion Mechanism Limitations,” *ISIJ Int.*, vol. 49, no. 2, pp. 293–301, 2009.

[175] E. A. Wilson, *Worked Examples in the Kinetics and Thermodynamics of Phase Transformations*. London: The Institution of Metallurgists, 1983.

[176] W. D.Callister and D. G. Rethwisch, *Materials science and engineering*, 9th ed. United States: wiley, 2014.

[177] E. Lee, R. Banerjee, S. Kar, D. Bhattacharyya, and H. L. Fraser, “Selection of α variants during microstructural evolution in α/β titanium alloys,” *Philos. Mag.*, vol. 87, no. 24, pp. 3615–3627, 2007.

[178] D. A. Porter, K. E. Easterling, and M. Y. Sherif, *Phase Transformation in Metals and Alloys*, 3rd ed. FL, USA: CRC Press, 2009.

[179] M. Moallemi, A. Najafizadeh, A. Kermanpur, and A. Rezaee, “Effect of reversion annealing on the formation of nano / ultrafine grained structure in 201 austenitic stainless steel,” *Mater. Sci. Eng. A*, vol. 530, pp. 378–381, 2011.

[180] C. A. Apple and G. Krauss, “The effect of heating rate on themartensite to austenite transformation in Fe-Ni-C alloys,” *Acta Met.*, vol. 20, pp. 849–856, 1972.

[181] A. K. Jena and M. C. Chaturvedi, *Phase Transformation in Materials*. New Jersey: Prentice Hall, 1992.

[182] S. Rajasekhara, L. P. Karjalainen, A. Kyröläinen, and P. J. Ferreira, "Microstructure evolution in nano / submicron grained AISI 301LN stainless steel," *Mater. Sci. Eng. A*, vol. 527, pp. 1986–1996, 2010.

[183] K. S. Min, K. J. Kim, and S. W. Nam, "Investigation of the effect of the types and densities of grain boundary carbides on grain boundary cavitation resistance of AISI 321 stainless steel under creep–fatigue interaction," *J. Alloys Compd.*, vol. 370, pp. 223–229, 2004.

[184] S. Xu, X. Q. Wu, E. H. Han, W. Ke, and Y. Katada, "Crack initiation mechanisms for low cycle fatigue of type 316Ti stainless steel in high temperature water," *Mater. Sci. Eng. A*, vol. 490, no. 1–2, pp. 16–25, 2008.

[185] B. Hutchinson and L. A. I. Kestens, "Origins of texture memory in steels," in *Applications of texture analysis*, no. November 2008, Rollett AD, Ed. New Jersey: John Wiley Sons Inc, 2008, pp. 281–290.

[186] T. Tomida, M. Wakita, M. Yasuyama, S. Sugaya, Y. Tomota, and S. C. Vogel, "Memory effects of transformation textures in steel and its prediction by the double Kurdjumov – Sachs relation," *Acta Mater.*, vol. 61, no. 8, pp. 2828–2839, 2013.

[187] N. Yoshinaga, H. Inoue, K. Kawasaki, L. Kestens, and B. C. De Cooman, "Factors Affecting Texture Memory Appearing $\alpha \rightarrow \gamma \rightarrow \alpha$ through Transformation in IF Steels," *Mater. Trans.*, vol. 48, no. 8, pp. 2036–2042, 2007.

[188] H. Beladi, Q. Chao, and G. S. Rohrer, "Direct Variant selection and intervariant crystallographic planes distribution in martensite in a Ti – 6Al – 4V alloy," *ACTA Mater.*, vol. 80, pp. 478–489, 2014.

[189] J. Romero, M. Preuss, and J. Q. Fonseca, "Texture memory and variant selection during phase transformation of a zirconium alloy," *Acta Mater.*, vol. 57, pp. 5501–5511, 2009.

[190] M. Humbert, B. Petit, B. Bolle, and N. Gey, "Analysis of the γ-ε-α′ variant selection induced by 10 % plastic deformation in 304 stainless steel at − 60 ◦ C," *Mater. Sci. Eng. A*, vol. 454–455, pp. 508–517, 2007.

[191] X. F. Zhang, H. Terasaki, and Y. Komizo, “Correlation of delta-ferrite precipitation with austenite grain growth during annealing of steels,” *Philos. Mag. Lett.*, vol. 91, no. 7, pp. 491–497, 2011.

[192] Y. B. Xu, W. L. Zhong, Y. J. Chen, L. T. Shen, Q. Liu, Y. L. Bai, and M. a. Meyers, “Shear localization and recrystallization in dynamic deformation of 8090 Al–Li alloy,” *Mater. Sci. Eng. A*, vol. 299, no. 1–2, pp. 287–295, Feb. 2001.

[193] H. M. Ghomi and A. G. Odeshi, “The effects of microstructure, strain rates and geometry on dynamic impact response of a carbon–manganese steel,” *Mater. Sci. Eng. A*, vol. 532, pp. 308–315, Jan. 2012.

[194] M. N. Bassim, “Study of the formation of adiabatic shear bands in steels,” *J. Mater. Process. Technol.*, vol. 119, no. 1–3, pp. 234–236, Dec. 2001.

[195] J. Li, J. Yu, and Z. Wei, “Influence of specimen geometry on adiabatic shear instability of tungsten heavy alloys,” *Int. J. Impact Eng.*, vol. 28, no. 3, pp. 303–314, Mar. 2003.

[196] K. M. Roessig and J. J. Mason, “Adiabatic shear localization in the impact of edge-notched specimens,” *Exp. Mech.*, vol. 38, no. 3, pp. 196–203, Sep. 1998.

[197] S. Boakye-Yiadom and N. Bassim, “Effect of heat treatment on stability of impact-induced adiabatic shear bands in 4340 steel,” *Mater. Sci. Eng. A*, vol. 546, pp. 223–232, Jun. 2012.

[198] A. A. Tiamiyu, A. Y. Badmos, A. G. Odeshi, and J. A. Szpunar, “The influence of temper condition on adiabatic shear failure of AA 2024 aluminum alloy,” *Mater. Sci. Eng. A*, vol. 708, 2017.

[199] T. Kamijo, A. Fujiwara, and H. Inagaki, “SHEAR BANDS IN HIGH PURITY Al,” *Scr. Met. Mater.*, vol. 25, pp. 949–954, 1991.

[200] W. B. Lee and K. C. Chan, “A microplasticity analysis of shear band cracks in rolled 2024 aluminum alloy,” *Int. J. Fract.*, vol. 52, pp. 207–221, 1991.

[201] Q. Xue and G. T. Gray, “Development of Adiabatic Shear Bands in Annealed 316L

Stainless Steel : Part II . TEM Studies of the Evolution of Microstructure during Deformation Localization," *Met. Mater. Trans. A*, vol. 37, pp. 2447–2458, 2006.

[202] W. Lee, C. Lin, and T. Liu, "Impact and fracture response of sintered 316L stainless steel subjected to high strain rate loading," *Mater. Charact.*, vol. 58, pp. 363–370, 2007.

[203] L. Zezhou, B. Wang, S. Zhao, R. Z. Valiev, K. S. Vecchio, and M. A. Meyers, "Dynamic deformation and failure of ultrafine- grained titanium," *Acta Mater.*, no. November, p. 210e218 Contents, 2016.

[204] G. M. Owolabi, D. T. Bolling, A. A. Tiamiyu, R. Abu, A. G. Odeshi, and H. A. Whitworth, "Shear strain localization in AA 2219-T8 aluminum alloy at high strain rates," *Mater. Sci. Eng. A*, vol. 655, pp. 212–220, 2016.

[205] K. Yvell, T. M. Grehk, and G. Engberg, "Microstructure characterization of 316L deformed at high strain rates using EBSD," *Mater. Charact.*, vol. 122, pp. 14–21, 2016.

[206] B. M. Morrow, R. A. Lebensohn, C. P. Trujillo, D. T. Martinez, F. L. Addessio, C. A. Bronkhorst, T. Lookman, and E. K. Cerreta, "Characterization and modeling of mechanical behavior of single crystal titanium deformed by split-Hopkinson pressure bar," *Int. J. Plast.*, vol. 82, pp. 225–240, 2016.

[207] A. A. Tiamiyu, J. A. Szpunar, A. G. Odeshi, I. Oguocha, and M. Eskandari, "Development of Ultra-Fine-Grained Structure in AISI 321 Austenitic Stainless Steel," *Metall. Mater. Trans. A Phys. Metall. Mater. Sci.*, vol. 48A, pp. 5990–6012, 2017.

[208] A. A. Tiamiyu, A. G. Odeshi, and J. A. Szpunar, "Multiple strengthening sources and adiabatic shear banding during high strain-rate deformation of AISI 321 austenitic stainless steel : Effects of grain size and strain rate," *Mater. Sci. Eng. A*, vol. 711, pp. 233–249, 2018.

[209] W. Lee and C. Lin, "Comparative Study of the Impact Response and Microstructure of 304L Stainless Steel with and without Prestrain," *Metall. Mater. Trans. A*, vol. 33, pp. 2801–2810, 2002.

[210] E. O. Hall, "The deformation and ageing of mild steel : III Discussion of Results," *Phys.*

*Soc. Lond.*, vol. 64, pp. 747– 753, 1951.

[211] N. J. Petch, "The cleavage strength of polycrystals," *J. Iron Steel Inst.*, vol. 174, pp. 25–28, 1953.

[212] D. L. Zou, L. Zhen, Y. Zhu, C. Y. Xu, W. Z. Shao, and B. J. Pang, "Deformed microstructure evolution in AM60B Mg alloy under hypervelocity impact at a velocity of 5kms-1," *Mater. Des.*, vol. 31, no. 8, pp. 3708–3715, 2010.

[213] S. P. Timothy, "The structure of adiabatic shear bands in metals: A critical review," *Acta Metall.*, vol. 35, no. 2, pp. 301–306, 1987.

[214] S. M. Walley, "Shear Localization : A Historical Overview," *Metall. Mater. Trans. A*, vol. 38, no. November, pp. 2629–2654, 2007.

[215] S. S. Hecker, M. G. Stout, K. P. Staudhammer, and J. L. Smith, "Effects of Strain State and Strain Rate on Deformation-Induced Transformation in 304 Stainless Steel: Part I. Magnetic Measurements and Mechanical Behavior," *Metall. Trans. A*, no. April, pp. 619–626, 1982.

[216] J. R. C. Guimar??es and P. R. Rios, "The mechanical-induced martensite transformation in Fe-Ni-C alloys," *Acta Mater.*, vol. 84, pp. 436–442, 2015.

[217] C. U. Jeong, Y. U. Heo, J. Y. Choi, W. Woo, and S. H. Choi, "A study on the micromechanical behaviors of duplex stainless steel under uniaxial tension using ex-situ experimentation and the crystal plasticity fi nite element method," *Int. J. Plast.*, vol. 75, pp. 22–38, 2015.

[218] B. Petit, "Deformation behavior and microstructure / texture evolution of an annealed 304 AISI stainless steel sheet . Experimental and micromechanical modeling," *Int. J. Plast.*, vol. 23, pp. 323–341, 2007.

[219] B. B. He, H. W. Luo, and M. X. Huang, "Experimental investigation on a novel medium Mn steel combining transformation-induced plasticity and twinning-induced plasticity effects," *Int. J. Plast.*, vol. 78, pp. 173–186, 2016.

[220] O. Grässel, L. Krüger, G. Frommeyer, and L. W. Meyer, “High strength Fe-Mn-(Al, Si) TRIP/TWIP steels development - properties - application,” *Int. J. Plast.*, vol. 16, no. 10, pp. 1391–1409, 2000.

[221] F. H. G. de Abreu, Marcelo José Gomes da Silva, L. F. G. Herculano, and H. Bhadeshia, “Texture Analysis of Deformation Induced Martensite in an AISI 301L Stainless Steel : Microtexture and Macrotexture Aspects,” *Mater. Res.*, vol. 12, no. 3, pp. 291–297, 2009.

[222] M. Eskandari, A. Zarei-hanzaki, M. A. Mohtadi-bonab, Y. Onuki, R. Basu, and A. Asghari, “Materials Science & Engineering A a super-high-strength , high ductility austenitic Mn-steel,” *Mater. Sci. Eng. A*, vol. 674, pp. 514–528, 2016.

[223] Y. Li, W. Li, J. Cheng, H. Mei, and X. Jun, “Compatible strain evolution in two phases due to epsilon martensite transformation in duplex TRIP-assisted stainless steels with high hydrogen embrittlement resistance,” *Int. J. Plast.*, vol. 88, pp. 53–69, 2017.

[224] K. M. Rahman, V. A. Vorontsov, and D. Dye, “The effect of grain size on the twin initiation stress in a TWIP steel,” *Acta Mater.*, vol. 89, pp. 247–257, 2015.

[225] A. Ghaderi and M. R. Barnett, “Sensitivity of deformation twinning to grain size in titanium and magnesium,” *Acta Mater.*, vol. 59, pp. 7824–7839, 2011.

[226] C. E. Carlton and P. J. Ferreira, “What is behind the inverse Hall – Petch effect in nanocrystalline materials ?,” *Acta Mater.*, vol. 55, pp. 3749–3756, 2007.

[227] U. F. Kocks, “The Relation Between Polycrystal Deformation and Single-Crystal Deformation,” *Metall. Mater. Trans. B*, vol. 1, pp. 1121–1143, 1970.

[228] K. Spencer, J. D. Embury, K. T. Conlon, M. Véron, and Y. Bréchet, “Strengthening via the formation of strain-induced martensite in stainless steels,” *Mater. Sci. Eng. A*, vol. 387–389, pp. 873–881, 2004.

[229] H. Frost and M. Ashby, *Deformation mechanism maps: the plasticity and creep of metals and ceramics*, 1st ed. New York: Oxford: Pergamon, 1982.

[230] P. Longère, “Respective / combined roles of thermal softening and dynamic recrystallization in adiabatic shear banding initiation,” *Mech. Mater.*, vol. 117, no. October 2017, pp. 81–90, 2018.

[231] Q. Xue, M. A. Meyers, and V. F. Nesterenko, “Self organization of shear bands in stainless steel,” *Mater. Sci. Eng. A*, vol. 384, no. 1–2, pp. 35–46, Oct. 2004.

[232] Q. Xue, M. A. Meyers, and V. F. Nesterenko, “Self-organization of shear bands in titanium and Ti-6Al-4V alloy,” *Acta Mater.*, vol. 50, pp. 575–596, 2002.

[233] Y. Yang, H. G. Zheng, Z. J. Shi, and Q. M. Zhang, “Effect of orientation on self-organization of shear bands in 7075 aluminum alloy,” *Mater. Sci. Eng. A*, vol. 528, no. 6, pp. 2446–2453, Mar. 2011.

[234] Y. Yang, H. G. Zheng, Z. D. Zhao, Q. Zhang, Q. M. Zhang, F. Jiang, and X. M. Li, “Effect of phase composition on self-organization of shear bands in Ti-1300 titanium alloy,” *Mater. Sci. Eng. A*, vol. 528, no. 25–26, pp. 7506–7513, Sep. 2011.

[235] Y. Yang, L. Jiang, Z. Xu, and Z. Wang, “An examination of adiabatic shearing behavior in ZK60 alloy with different states of heat treatment,” *Mater. Sci. Eng. A*, vol. 685, no. December 2016, pp. 57–64, 2017.

[236] Y. Yang, D. H. Li, H. G. Zheng, X. M. Li, and F. Jiang, “Self-organization behaviors of shear bands in 7075 T73 and annealed aluminum alloy,” *Mater. Sci. Eng. A*, vol. 527, no. 1–2, pp. 344–354, Dec. 2009.

[237] F. Zhou, T. W. Wright, and K. T. Ramesh, “The formation of multiple adiabatic shear bands,” *J. Mech. Phys. Solids*, vol. 54, no. 7, pp. 1376–1400, 2006.

[238] J. Liu, Q. Fan, H. Cai, and F. Wang, “Underlying mechanism of periodical adiabatic shear bands generated in Ti–6Al–4V target by projectile impact,” *Mater. Des.*, vol. 87, pp. 231–237, 2015.

[239] Y. Yang, Y. Zeng, D. H. Li, and M. Li, “Damage and fracture mechanism of aluminium alloy thick-walled cylinder under external explosive loading,” *Mater. Sci. Eng. A*, vol. 490,

no. 1–2, pp. 378–384, Aug. 2008.

[240] N. L. Okamoto, D. Kashioka, T. Hirato, and H. Inui, “Specimen- and grain-size dependence of compression deformation behavior in nanocrystalline copper,” *Int. J. Plast.*, vol. 56, pp. 173–183, 2014.

[241] R. D. K. Misra, V. S. A. Challa, P. K. C. Venkatsurya, Y. F. Shen, M. C. Somani, and L. P. Karjalainen, “Interplay between grain structure, deformation mechanisms and austenite stability in phase-reversion-induced nanograined/ultrafine-grained austenitic ferrous alloy,” *Acta Mater.*, vol. 84, pp. 339–348, 2015.

[242] Y. F. Shen, X. X. Li, X. Sun, Y. D. Wang, and L. Zuo, “Twinning and martensite in a 304 austenitic stainless steel,” *Mater. Sci. Eng. A*, vol. 552, pp. 514–522, 2012.

[243] R. A. Lebensohn and C. N. Tomé, “A self-consistent anisotropic approach for the simulation of plastic deformation and texture development of polycrystals: Application to zirconium alloys,” *Acta Metall. Mater.*, vol. 41, no. 9, pp. 2611–2624, 1993.

[244] C. Tome, G. R. Canova, U. F. Kocks, N. Christodoulou, and J. J. Jonas, “The relation between macroscopic and microscopic strain hardening in F.C.C. polycrystals,” *Acta Metall.*, vol. 32, no. 10, pp. 1637–1653, 1984.

[245] I. Gutierrez-Urrutia and D. Raabe, “Grain size effect on strain hardening in twinning-induced plasticity steels,” *Scr. Mater.*, vol. 66, no. 12, pp. 992–996, 2012.

[246] H. Beladi, I. B. Timokhina, Y. Estrin, J. Kim, B. C. De Cooman, and S. K. Kim, “Orientation dependence of twinning and strain hardening behaviour of a high manganese twinning induced plasticity steel with polycrystalline structure,” *Acta Mater.*, vol. 59, pp. 7787–7799, 2011.

[247] F. Di Gioacchino and J. Q. da Fonseca, “An experimental study of the polycrystalline plasticity of austenitic stainless steel,” *Int. J. pl*, vol. 74, pp. 92–109, 2015.

[248] S. Cui, Y. Cui, J. Wan, Y. Rong, and J. Zhang, “Grain size dependence of the martensite morphology – A phase-field study,” *Comput. Mater. Sci.*, vol. 121, pp. 131–142, 2016.

[249] E. El-Danaf, S. R. Kalidindi, R. D. Doherty, and C. Necker, “Deformation texture transition in brass: critical role of micro-scale shear bands,” *Acta Mater.*, vol. 48, no. 10, pp. 2665–2673, Jun. 2000.

[250] R. D. K. Misra, V. S. A. Challa, P. K. C. Venkatsurya, Y. F. Shen, M. C. Somani, and L. P. Karjalainen, “Interplay between grain structure , deformation mechanisms and austenite stability in phase-reversion-induced nanograined / ultrafine-grained austenitic ferrous alloy,” *Acta Mater.*, vol. 84, pp. 339–348, 2015.

[251] E. El-Danaf, S. R. Kalidindi, and R. D. Doherty, “Influence of deformation path on the strain hardening behavior and microstructure evolution in low SFE FCC metals,” *Int. J. Plast.*, vol. 17, pp. 1245–1265, 2001.

[252] A. S. Khan, A. Pandey, T. Gnäupel-Herold, and R. K. Mishra, “Mechanical response and texture evolution of AZ31 alloy at large strains for different strain rates and temperatures,” *Int. J. Plast.*, vol. 27, no. 5, pp. 688–706, 2011.

[253] I. Kazunorl Sato, M. Ichinose, and Y. Inoue, “Effects of Deformation Induced Phase Transformation and the Mechanical Properties of Austenitic Fe-Mn-AI Alloys Twinning on ;I,” *ISIJ Int.*, vol. 29, no. lO, pp. 868–877, 1989.

[254] A. A. Saleh, E. V. Pereloma, and A. A. Gazder, “Microstructure and texture evolution in a twinning-induced-plasticity steel during uniaxial tension,” *Acta Mater.*, vol. 61, no. 7, pp. 2671–2691, 2013.

[255] A. Kundu and P. C. Chakraborti, “Effect of strain rate on quasistatic tensile flow behaviour of solution annealed 304 austenitic stainless steel at room temperature,” *J. Mater. Sci.*, vol. 45, no. 20, pp. 5482–5489, 2010.

[256] C. Duhamel, Y. Brechet, and Y. Champion, “Activation volume and deviation from Cottrell-Stokes law at small grain size,” *Int. J. Plast.*, vol. 26, no. 5, pp. 747–757, 2010.

[257] H. Wang, P. Wu, S. Kurukuri, M. J. Worswick, Y. Peng, D. Tang, and D. Li, “Strain rate sensitivities of deformation mechanisms in magnesium alloys,” *Int. J. Plast.*, p. in press, 2018.

[258] W. D. MacDonald, G. J. C. Carpenter, and S. Saimoto, “Using strain rate sensitivity measurements to determine phase relations in A430 stainless steel,” *Mater. Sci. Eng. A*, vol. 190, no. 1–2, pp. 33–42, 1995.

[259] A. S. Khan and H. Liu, “Variable strain rate sensitivity in an aluminum alloy: Response and constitutive modeling,” *Int. J. Plast.*, vol. 36, pp. 1–14, Sep. 2012.

[260] Q. Wei, S. Cheng, K. T. Ramesh, and E. Ma, “Effect of nanocrystalline and ultrafine grain sizes on the strain rate sensitivity and activation volume: Fcc versus bcc metals,” *Mater. Sci. Eng. A*, vol. 381, no. 1–2, pp. 71–79, 2004.

[261] W. Lee and C. Lin, “Comparative study of the impact response and microstructure of 304L stainless steel with and without prestrain,” *Metall. Mater. Trans. A*, vol. 33, no. 9, pp. 2801–2810, 2002.

[262] J. A. Lichtenfeld, M. C. Mataya, and C. J. Van Tyne, “Effect of Strain Rate on Stress-Strain Behaviour of Alloy 309 and 304L{} Austenitic Stainless Steel,” *Metall. Mater. Trans. A*, vol. 37, no. January, pp. 147–161, 2006.

[263] N. Ahmed and A. Hartmaier, “Mechanisms of grain boundary softening and strain-rate sensitivity in deformation of ultrafine-grained metals at high temperatures,” *Acta Mater.*, vol. 59, no. 11, pp. 4323–4334, 2011.

[264] W.-S. Lee and Y.-C. Huang, “Mechanical Properties and Dislocation Substructure of 6061-T6 Aluminum Alloy Impacted at Cryogenic Temperatures,” *Mater. Trans.*, vol. 57, no. 3, pp. 344–350, 2016.

[265] M. S. Mohebbi and A. Akbarzadeh, “Development of equations for strain rate sensitivity of UFG aluminum as a function of strain rate,” *Int. J. Plast.*, vol. 90, pp. 167–176, 2017.

[266] W. G. Ferguson, A. Kumar, and J. E. Dorn, “Dislocation damping in aluminum at high strain rates,” *J. Appl. Phys.*, vol. 38, no. 4, pp. 1863–1869, 1967.

[267] A. Kumar, F. E. Hauser, and J. E. Dorn, “Viscous drag on dislocations in aluminum at high strain rates,” *Acta Metall.*, vol. 16, no. 9, pp. 1189–1197, 1968.

[268] K. Sakino, “Strain Rate Sensitivity of Dynamic Flow Stress of FCC Metals at Very High Strain Rates,” *Japan Soc. Mater. Sci.*, vol. 63, pp. 939–944, 1997.

[269] H. Couque, “The use of the direct impact Hopkinson pressure bar technique to describe thermally activated and viscous regimes of metallic materials,” *Philos. Trans. R. Soc. A Math. Phys. Eng. Sci.*, vol. 372, no. 2023, pp. 20130218–20130218, 2014.

[270] J. W. Cahn and F. R. . N. Nabarro, “Thermal activation under shear,” *Philos. Mag.*, vol. 81, pp. 1409–1426, 2001.

[271] J. Gubicza, L. Farbaniec, G. Csiszár, T. Sadat, H. Couque, and G. Dirras, “Microstructure and strength of nickel subjected to large plastic deformation at very high strain rate,” *Mater. Sci. Eng. A*, vol. 662, pp. 9–15, 2016.

[272] B. Gurrutxaga-Lerma, D. S. Balint, D. Dini, and A. P. Sutton, “The mechanisms governing the activation of dislocation sources in aluminum at different strain rates,” *J. Mech. Phys. Solids*, vol. 84, pp. 273–292, 2015.

[273] A. Ghosh, A. Adesola, J. A. Szpunar, A. G. Odeshi, and N. P. Gurao, “Effect of tempering conditions on dynamic deformation behaviour of an aluminium–lithium alloy,” *Mater. Des.*, vol. 81, pp. 1–10, 2015.

[274] W. A. Counts, M. V. Braginsky, C. C. Battaile, and E. A. Holm, “Predicting the Hall-Petch effect in fcc metals using non-local crystal plasticity,” *Int. J. Plast.*, vol. 24, no. 7, pp. 1243–1263, 2008.

[275] T. Iwamoto, T. Sawa, and M. Cherkaoui, “A Study on Impact Deformation and Transformation Behavior of Trip Steel By Finite Element Simulation and Experiment,” *Int. J. Mod. Phys. B*, vol. 22, pp. 5985–5990, 2008.

[276] J. Talonen, H. Hänninen, P. Nenonen, and G. Pape, “Effect of strain rate on the strain-induced $\gamma \rightarrow \alpha'$-martensite transformation and mechanical properties of austenitic stainless steels,” *Metall. Mater. Trans. A*, vol. 36, no. 2, pp. 421–432, 2005.

[277] A. A. Tiamiyu, A. G. Odeshi, and J. A. Szpunar, “Multiple strengthening sources and

adiabatic shear banding during high strain-rate deformation of AISI 321 austenitic stainless steel: Effects of grain size and strain rate," *Mater. Sci. Eng. A*, vol. 711, no. August 2017, pp. 233–249, 2018.

[278] S. Lee and Y. Lee, "Effect of Austenite Grain Size on Martensitic Transformation of a Low Alloy Steel," *Mater. Sci. Forum*, vol. 475–479, pp. 3169–3172, 2005.

[279] F. Kabirian, A. S. Khan, and A. Pandey, "Negative to positive strain rate sensitivity in 5xxx series aluminum alloys: Experiment and constitutive modeling," *Int. J. Plast.*, vol. 55, pp. 232–246, 2014.

[280] L. Hollang, E. Hieckmann, D. Brunner, C. Holste, and W. Skrotzki, "Scaling effects in the plasticity of nickel," *Mater. Sci. Eng. A*, vol. 424, no. 1–2, pp. 138–153, 2006.

[281] Z. Budrovic, H. Van Swygenhoven, P. M. Derlet, S. Van Petegem, and B. Schmitt, "Plastic Deformation with Reversible Peak Broadening in Nanocrystalline Nickel," *Science (80-. ).*, vol. 304, pp. 273–275, 2004.

[282] S. P. Tsai, Y. T. Tsai, Y. W. Chen, P. J. Chen, P. H. Chiu, C. Y. Chen, W. S. Lee, J. W. Yeh, and J. R. Yang, "High-entropy CoCrFeMnNi alloy subjected to high-strain-rate compressive deformation," *Mater. Charact.*, vol. 147, no. October 2018, pp. 193–198, 2019.

[283] H. Frost and M. Ashby, "Deformation mechanism maps: the plasticity and creep of metals and ceramics," 1st ed., New York: Oxford: Pergamon, 1982.

[284] Z. Li, B. Wang, S. Zhao, R. Z. Valiev, K. S. Vecchio, and M. A. Meyers, "Dynamic deformation and failure of ultrafine-grained titanium," *Acta Mater.*, vol. 125, no. December, pp. 210–218, 2017.

[285] B. Mahato, T. Sahu, S. K. Shee, P. Sahu, T. Sawaguchi, J. Komi, and L. P. Karjalainen, "Simultaneous twinning nucleation mechanisms in an Fe - Mn - Si - Al twinning induced plasticity steel," *Acta Mater.*, vol. 132, pp. 264–275, 2017.

[286] S. S. F. De Dafé, F. L. Sicupira, F. C. S. Matos, N. S. Cruz, D. R. Moreira, and D. B. Santos,

"Effect of cooling rate on martensite formation in twinning/transformation-induced plasticity Fe-17Mn-0.06C steel ," *Mater. Res.*, vol. 16, no. 6, pp. 1229–1236, 2013.

[287] L. Wang, J. C. E, Y. Cai, F. Zhao, D. Fan, and S. N. Luo, "Shock-induced deformation of nanocrystalline Al: Characterization with orientation mapping and selected area electron diffraction," *J. Appl. Phys.*, vol. 117, no. 8, 2015.

[288] D. Wolf, V. Yamakov, S. R. Phillpot, A. Mukherjee, and H. Gleiter, "Deformation of nanocrystalline materials by molecular-dynamics simulation: Relationship to experiments?," *Acta Mater.*, vol. 53, no. 1, pp. 1–40, 2005.

[289] A. A. Tiamiyu, V. Tari, J. A. Szpunar, A. G. Odeshi, and A. K. Khan, "Effects of grain refinement on the quasi-static compressive behavior of AISI 321 austenitic stainless steel: EBSD, TEM, and XRD studies," *Int. J. Plast.*, vol. 107, no. April, pp. 79–99, 2018.

[290] A. Das and S. Tarafder, "Experimental investigation on martensitic transformation and fracture morphologies of austenitic stainless steel," *Int. J. Plast.*, vol. 25, no. 11, pp. 2222–2247, 2009.

[291] E. N. Hahn and M. A. Meyers, "Grain-size dependent mechanical behavior of nanocrystalline metals," *Mater. Sci. Eng. A*, vol. 646, pp. 101–134, 2015.

[292] W. Q. Song, S. Sun, S. Zhu, G. Wang, J. Wang, and M. S. Dargusch, "Compressive deformation behavior of a near-beta titanium alloy," *Mater. Des.*, vol. 34, pp. 739–745, 2012.

[293] C. Mondal, B. Mishra, P. K. Jena, K. Siva Kumar, and T. B. Bhat, "Effect of heat treatment on the behavior of an AA7055 aluminum alloy during ballistic impact," *Int. J. Impact Eng.*, vol. 38, no. 8–9, pp. 745–754, Aug. 2011.

[294] J. Y. Choi, T. Fukuda, and T. Kakeshita, "Isothermal Martensitic Transformation in a Sensitized SUS304 Stainless Steel under Magnetic Field," *Mater. Sci. Forum*, vol. 654–656, no. 3, pp. 130–133, 2010.

[295] P. R. Rios and J. R. C. Guimarães, "Athermal Martensite Transformation Curve," *Mater.*

*Res.*, vol. 19, no. 2, pp. 490–495, 2016.

[296] T. Kakeshita, T. Saburi, and K. Shimizu, "Kinetics of martensitic transformations in some ferrous and non-ferrous alloys," *Philos. Mag. B Phys. Condens. Matter; Stat. Mech. Electron. Opt. Magn. Prop.*, vol. 80, no. 2, pp. 171–181, 2000.

[297] P. R. Rios, G. da Silva Drumond, T. Neves, and J. R. C. Guimarães, "Martensite Spread: Analytical Modeling and Computer Simulation," *Mater. Sci. Forum*, vol. 783–786, no. September 2015, pp. 2182–2187, 2014.

[298] Y. L. Chang, P. Y. Chen, Y. T. Tsai, and J. R. Yang, "Crystallographic analysis of lenticular martensite in Fe-1.0C-17Cr stainless steel by electron backscatter diffraction," *Mater. Charact.*, vol. 113, pp. 17–25, 2016.

[299] H. Y. Lee, H. W. Yen, H. T. Chang, and J. R. Yang, "Substructures of martensite in Fe-1C-17Cr stainless steel," *Scr. Mater.*, vol. 62, no. 9, pp. 670–673, 2010.

[300] T. Maki, "Morphology and substructure of martensite in steels," in *Phase transformations in steels*, Woodhead Publishing, 2012, pp. 34–58.

[301] M. Umemoto, E. Yoshitake, and I. Tamura, "The Morphology of Martensite in Iron-5% Nickel Alloys.pdf," *J. Mater. Sci.*, vol. 18, pp. 2893–2904, 1983.

[302] A. Shibata, T. Murakami, S. Morito, T. Furuhara, and T. Maki, "The origin of midrib in lenticular martensite," *Mater. Trans.*, vol. 49, pp. 1242–1248, 2008.

[303] S. Kajiwara and W. S. Owen, "The martensite-austenite interface and the thickness of twins in martensite in Fe3Pt," *Scr. Metall.*, vol. 11, no. 2, pp. 137–142, 1977.

[304] N. N. Thadhani and M. A. Meyers, "Kinetics of isothermal martensitic transformation," *Prog. Mater. Sci.*, vol. 30, pp. 1–37, 1986.

[305] W. S. Choi, S. Sandlöbes, N. V. Malyar, C. Kirchlechner, S. Korte-Kerzel, G. Dehm, B. C. De Cooman, and D. Raabe, "Dislocation interaction and twinning-induced plasticity in face-centered cubic Fe-Mn-C micro-pillars," *Acta Mater.*, vol. 132, no. April, pp. 162–173, 2017.

[306] M. Karlsen, Ø. Grong, M. Søfferud, J. Hjelen, G. Rørvik, and R. Chiron, "Scanning electron microscopy/electron backscatter diffraction - Based observations of martensite variant selection and slip plane activity in supermartensitic stainless steels during plastic deformation at elevated, ambient, and subzero temperatures," *Metall. Mater. Trans. A Phys. Metall. Mater. Sci.*, vol. 40, no. 2, pp. 310–320, 2009.

[307] C. Boonruang, A. Thong-On, and P. Kidkhunthod, "Effect of nanograin-boundary networks generation on corrosion of carburized martensitic stainless steel," *Sci. Rep.*, vol. 8, no. 1, pp. 1–10, 2018.

[308] J. Lv and H. Luo, "The effect of low temperature sensitization on corrosion resistance of ultrafine-grained type 321 stainless steels," *J. Mater. Eng. Perform.*, vol. 23, no. 1, pp. 262–267, 2014.

[309] L. Jinlong and L. Hongyun, "Comparison of corrosion properties of passive films formed on phase reversion induced nano/ultrafine-grained 321 stainless steel," *Appl. Surf. Sci.*, vol. 280, pp. 124–131, 2013.

[310] Y. Huang, "Stress corrosion cracking of AISI 321 stainless steel in acidic chloride solution," *Bull. Mater. Sci.*, vol. 25, no. 1, pp. 47–51, 2002.

[311] B. N. Mordyuk, G. I. Prokopenko, M. A. Vasylyev, and M. O. Iefimov, "Effect of structure evolution induced by ultrasonic peening on the corrosion behavior of AISI-321 stainless steel," *Mater. Sci. Eng. A*, vol. 458, pp. 253–261, 2007.

[312] W. Shi, S. Yang, and J. Li, "Correlation between evolution of inclusions and pitting corrosion in 304 stainless steel with yttrium addition," *Sci. Rep.*, vol. 8, no. 1, pp. 1–9, 2018.

[313] H. Li, E. Zhou, D. Zhang, D. Xu, J. Xia, C. Yang, H. Feng, Z. Jiang, X. Li, T. Gu, and K. Yang, "Microbiologically Influenced Corrosion of 2707 Hyper-Duplex Stainless Steel by Marine Pseudomonas aeruginosa Biofilm," *Sci. Rep.*, vol. 6, no. July 2015, pp. 1–12, 2016.

[314] B. R. Kumar, R. Singh, B. Mahato, P. K. De, N. R. Bandyopadhyay, and D. K. Bhattacharya, "Effect of texture on corrosion behavior of AISI 304L stainless steel," *Mater. Charact.*, vol. 54, no. 2, pp. 141–147, 2005.

[315] S. Banerjee, V. Srivastava, and M. M. Singh, “Chemically modified natural polysaccharide as green corrosion inhibitor for mild steel in acidic medium OH,” *Corros. Sci.*, vol. 59, pp. 35–41, 2012.

[316] K. C. Emregül and M. Hayvalı, “Studies on the effect of vanillin and protocatechualdehyde on the corrosion of steel in hydrochloric acid,” *Mater. Chem. Phys.*, vol. 83, pp. 209–216, 2004.

[317] S. Masroor, M. Mobin, M. J. Alam, and S. Ahmad, “RSC Advances The novel iminium surfactant p -benzylidene benzyldodecyl iminium chloride as a corrosion inhibitor for plain carbon steel in 1 M HCl : electrochemical and DFT evaluation †,” *RSC Adv.*, vol. 7, no. 1, pp. 23182–23196, 2017.

[318] H. Miyamoto, “Corrosion of Ultrafine Grained Materials by Severe Plastic Deformation, an Overview,” *Mater. Trans.*, vol. 57, no. 5, pp. 559–572, 2016.

[319] K. D. Ralston, N. Birbilis, and C. H. J. Davies, “Revealing the relationship between grain size and corrosion rate of metals,” *Scr. Mater.*, vol. 63, no. 12, pp. 1201–1204, 2010.

[320] A. A. Tiamiyu, U. Eduok, A. G. Odeshi, and J. A. Szpunar, “Effect of prior plastic deformation and deformation rate on the corrosion resistance of AISI 321 austenitic stainless steel,” *Mater. Sci. Eng. A*, vol. 745, no. December 2018, pp. 1–9, 2019.

[321] A. Y. Chen, W. F. Hu, D. Wang, Y. K. Zhu, P. Wang, J. H. Yang, X. Y. Wang, J. F. Gu, and J. Lu, “Improving the intergranular corrosion resistance of austenitic stainless steel by high density twinned structure,” *Scr. Mater.*, vol. 130, pp. 264–268, 2017.

[322] A. Ben Rhouma, C. Braham, M. E. Fitzpatrick, J. Ledion, and H. Sidhom, “Effects of surface preparation on pitting resistance, residual stress, and stress corrosion cracking in austenitic stainless steels,” *J. Mater. Eng. Perform.*, vol. 10, no. 5, pp. 507–514, 2001.

[323] S. V. Phadnis, A. K. Satpati, K. P. Muthe, J. C. Vyas, and R. I. Sundaresan, “Comparison of rolled and heat treated SS304 in chloride solution using electrochemical and XPS techniques,” *Corros. Sci.*, vol. 45, no. 11, pp. 2467–2483, 2003.

[324] L. Zhang, J. A. Szpunar, R. Basu, J. Dong, and M. Zhang, “Influence of cold deformation on the corrosion behavior of Ni-Fe-Cr alloy 028,” *J. Alloys Compd.*, vol. 616, pp. 235–242, 2014.

[325] B. J. Wang, D. K. Xu, Y. C. Xin, L. Y. Sheng, and E. H. Han, “High corrosion resistance and weak corrosion anisotropy of an as-rolled Mg-3Al-1Zn (in wt.%) alloy with strong crystallographic texture,” *Sci. Rep.*, vol. 7, no. 1, pp. 1–14, 2017.

[326] K. H. Lo, C. H. Shek, and J. K. L. Lai, “Recent developments in stainless steels,” *Mater. Sci. Eng. R*, vol. 65, pp. 39–104, 2009.

[327] B. R. Kumar, S. Sharma, and B. Mahato, “Formation of ultrafine grained microstructure in the austenitic stainless steel and its impact on tensile properties,” *Mater. Sci. Eng. A*, vol. 528, no. 6, pp. 2209–2216, 2011.

[328] L. I. Hua-bing, Z. Jiang, Z. Zhang, and Y. Yang, “Effect of Grain Size on Mechanical Properties of Nickel-Free High Nitrogen Austenitic Stainless Steel,” *J. Iron Steel Res. Int.*, vol. 16, no. 1, pp. 58–61, 2009.

[329] A. D. I. Schino, C. S. Materiali, and V. B. Brin, “Effects of grain size on the properties of a low nickel austenitic stainless steel,” *J. Mater. Sci.*, vol. 8, pp. 4725–4733, 2003.

[330] S. G. Wang, M. Sun, H. B. Han, K. Long, and Z. D. Zhang, “The high-temperature oxidation of bulk nanocrystalline 304 stainless steel in air,” *Corros. Sci.*, vol. 72, pp. 64–72, 2013.

[331] X. H. Chen, J. Lu, L. Lu, and K. Lu, “Tensile properties of a nanocrystalline 316L austenitic stainless steel,” *Scr. Mater.*, vol. 52, pp. 1039–1044, 2005.

[332] R. K. Gupta and K. S. Darling, “Synthesis , characterization and mechanical behaviour of an in situ consolidated nanocrystalline FeCrNi alloy,” *J. Mater. Sci.*, vol. 47, pp. 1562–1566, 2012.

[333] M. Tikhonova, Y. Kuzminova, A. Belyakov, and R. Kaibyshev, “Nanocrystalline S304H austenitic stainless steel processed by multiple forging,” *Rev. Adv. Mater. Sci.*, vol. 31, pp. 68–73, 2012.

[334] G. Palumbo, S. J. Thorpe, and K. T. Aust, “On the contribution of triple junctions to the structure and properties of nanocrystalline materials,” *Scr. Metall. Mater.*, vol. 24, no. 1, pp. 1347–1350, 1990.

[335] R. Birringer, H. Gleiter, H. Klein, and P. Marquardt, “Nanocrystalline materials an approach to a novel solid structure with gas-like disorder?,” *Phys. Lett.*, vol. 102, no. 8, pp. 365–369, 1984.

[336] J. A. Syed, S. Tang, H. Lu, and X. Meng, “Water-soluble polyaniline-polyacrylic acid composites as efficient corrosion inhibitors for 316ss,” *Ind. Eng. Chem. Res.*, vol. 54, no. 11, pp. 2950–2959, 2015.

[337] A. Abbasi Aghuy, M. Zakeri, M. H. Moayed, and M. Mazinani, “Effect of grain size on pitting corrosion of 304L austenitic stainless steel,” *Corros. Sci.*, vol. 94, pp. 368–376, 2015.

[338] K. Devendranath Ramkumar, B. Pavan, and V. Chandrasekar, “Development of improved microstructural traits and mechanical integrity of stabilized stainless steel joints of AISI 321,” *J. Manuf. Process.*, vol. 32, no. March, pp. 582–594, 2018.

## Appendix A

List of publications from this study

A. Peer-review journal publications

1 **A. A. Tiamiyu**, Ubong Eduok, J. A. Szpunar, and A. G. Odeshi (2019). Corrosion behavior of metastable AISI 321 austenitic stainless steel: Investigating the effect of grain size and prior plastic deformation on its degradation pattern in saline media. *Scientific Report*. **Accepted**.

2 **A. A. Tiamiyu**, Shiteng Zhao, Zezhou Li, A.G. Odeshi, J.A. Szpunar (2019). Thermal and mechanical stability of austenite in metastable austenitic stainless steel. *Metall. Mater. Trans. A Phys. Metall. Mater. Sci.*, **Accepted**.

3 **Tiamiyu**, **A. A.,** Szpunar, J. A., and Odeshi, A. G. (2019). Strain rate sensitivity and activation volume of AISI 321 stainless steel under dynamic impact loading: grain size effect. *Materials Characterization*. **154**:7–19.

4 **Tiamiyu**, **A. A.,** Eduok, U., Odeshi, A. G., and Szpunar, J. A. (2019). Effect of strain rate on the corrosion resistance of AISI 321 austenitic stainless steel under compression. *Materials and Engineering A*. **745**:1–9.

**5** **Tiamiyu**, **A. A.,** Odeshi, A. G., and Szpunar, J. A. (2018). Characterization of coarse and ultrafine-grained austenitic stainless steel subjected to dynamic impact load: XRD, SEM, TEM and EBSD analyses. *Materialia*. **4**:81–98.

6 **Tiamiyu, A. A**., Vahid, T., Szpunar, J. A., Odeshi, A. G., and Khan, A. K. (2018). Effects of Grain Refinement on the Quasi-Static Compressive Behavior of AISI 321 Austenitic Stainless Steel: EBSD, TEM, and XRD Studies. *International Journal of Plasticity*. **107**:79–99.

7 **Tiamiyu, A. A**., Odeshi, A. G., and Szpunar, J. A. (2018). Multiple Strengthening Sources and Adiabatic Shear Banding during High Strain-Rate Deformation of AISI 321 Austenitic Stainless Steel: Effects of Grain Size and Strain Rate. *Materials Science and Engineering A.* **711**:233–49.

8 **Tiamiyu, A. A**., Odeshi, A. G., and Szpunar, J. A. (2018). Austenitic Reversion of Cryo-Rolled Ti-Stabilized Austenitic Stainless Steel: High-Resolution EBSD Investigation. *Journal of Materials Engineering and Performance*. **27**:889–904.

9 **Tiamiyu, A. A**., Szpunar, J. A., Odeshi, A. G., Oguocha, I., and Eskandari, M.(2017).

Development of Ultra-Fine-Grained Structure in AISI 321 Austenitic Stainless Steel. *Metallurgical and Materials Transactions A: Physical Metallurgy and Materials Science.* **48A**:5990–6012.

10 **Tiamiyu, A. A**., Eskandari, M., Nezakat, M., Wang, X., Szpunar, J. A., and Odeshi, A. G. (2016). A Comparative Study of the Compressive Behaviour of AISI 321 Austenitic Stainless Steel under Quasi-Static and Dynamic Shock Loading. *Materials and Design.* **112**:309–19.

11 **Tiamiyu, A. A**., Eskandari, M., Sanayei, M., Odeshi, A. G., and Szpunar, J. A. (2016). Mechanical Behavior and High-Resolution EBSD Investigation of the Microstructural Evolution in AISI 321 Stainless Steel under Dynamic Loading Condition. *Materials Science & Engineering A*. **673**:400–416.

B. Conference publications

1 **A A Tiamiyu**, A G Odeshi, J A Szpunar. (2018). Dynamic Hall-Petch effect in AISI 321 austenitic stainless steel: role of grain size and deformation mode. *Materials Science and Technology 2018*, Columbus, United States.

2 **A A Tiamiyu**, J A Szpunar, A G Odeshi. (2017). Pseudo-texture memory in AISI 321 austenitic stainless steel. IOP Conference series. *ICOTOM 2017*, St George, Utah, U.S.A.

3 **Tiamiyu A**, Odeshi A, Szpunar J. (2017). Deformation and Strengthening Mechanisms in AISI 321 Austenitic Stainless Steel under both Dynamic and Quasi-static Loading Conditions. *TMS 2017*, San Diego, United States

## Appendix B

Packing list and certified material test reports for ordered AISI 321 austenitic stainless steel

**PACKING LIST** SSC ORDER NO. 88539

**SANDMEYER STEEL COMPANY**

(Incorporated)

ONE SANDMEYER LANE • PHILADELPHIA, PA 19116-3598

800-523-3663 • FAX 215-677-1430 • www.SandmeyerSteel.com

*Family Owned and Managed —*
*Making Stainless Steel and Nickel Alloy Plate Products*
*Since 1952*

BILL TO
UNIVERSITY OF SASKATCHEWAN
57 CAMPUS DRIVE
ROOM 3B48 MECHANICAL ENGR
SASKATOON SK
CANADA S7N 5A9

SHIP TO
SAME

| DATE | CUSTOMER ORDER NO. | MARKINGS | COMPLETE | PARTIAL |
|---|---|---|---|---|
| 10/13/15 | AHMED 10-2-2015 | | X | |

| SHIPPED VIA | TERMS OF SALE |
|---|---|
| U.P.S. | FOB Origin, Freight Prepaid & Allow |

| PIECES | WEIGHT | DESCRIPTION |
|---|---|---|
| | | SSC TYPE 321 UNS S32100 PLATE<br>ASME SA240 2004 ED |
| 6 | 28 | 1" X 4" X 4"<br>PLATE # 200677 HT 289407 |
| * | 28 * | |

NOTICE: THE CARRIER IS RESPONSIBLE FOR THIS SHIPMENT. If you fail to receive the full number of pieces or other items shown heron, contact the carrier immediately and file a claim if necessary. If any question arises regarding the amount or type of the goods shipped, which does not involve the carrier, you must make a claim with Sandmeyer Steel Company within 72 hours of delivery.

**CERTIFIED MATERIAL TEST REPORT** SSC ORDER NO. 88539

# SANDMEYER STEEL COMPANY

(Incorporated)

ONE SANDMEYER LANE • PHILADELPHIA, PA 19116-3598
800-523-3663 • FAX 215-677-1430 • www.SandmeyerSteel.com

*Family Owned and Managed —*
*Making Stainless Steel and Nickel Alloy Plate Products*
*Since 1952*

BILL TO

UNIVERSITY OF SASKATCHEWAN
57 CAMPUS DRIVE
ROOM 3B48 MECHANICAL ENGR
SASKATOON SK
CANADA S7N 5A9

CERTIFICATE OF TEST

WE CERTIFY THAT THE CHEMICAL ANALYSIS AND MECHANICAL TEST RESULTS APPEARING IN THIS CERTIFICATE ARE CORRECT AND ACCURATE AS REPORTED BY THE MANUFACTURER.

CUSTOMER ORDER NO. AHMED 10-2-2015

DATE: 10/13/2015

TERRILL BOHNSACK, SANDMEYER STEEL COMPANY
MANAGER - QUALITY ASSURANCE AND ENGINEERING

| PIECES | DESCRIPTION |
|---|---|
| | SSC TYPE 321 (UNS S32100) PLATE<br>ASME SA240 2004 ED |
| 6 | 1" X 4" X 4" PLATE NO. 200677 |

| HEAT NO. | C | Mn | P | S | Si | Ni | Cr | N |
|---|---|---|---|---|---|---|---|---|
| 289407 | 0.044 | 1.560 | 0.040 | 0.00100 | 0.400 | 9.170 | 17.610 | 0.012 |
| PC# | Ti | | | | | | | |
| 64024 | 0.360 | | | | | | | |

| HEAT NO. | Yield * | Tensile * | Elong | Red | Hardness | Grain Size |
|---|---|---|---|---|---|---|
| 289407 | 35,090 | 80,330 | 47% IN 2" | 64% | RB 80 | 6 |
| | Inter Gran | | | | | |
| | A-262 E | | | | | |

RECORDS OF ALL TESTS ARE MAINTAINED AT SANDMEYER STEEL COMPANY

* LBS/IN2

MATERIAL PRODUCED BY Acroni
THIS MATERIAL IS FREE FROM MERCURY CONTAMINATION

ACRONI

ACRONI d.o.o., Cesta Borisa Kidriča 44, SI-4270 Jesenice

Izdajatelj certifikata / Aussteller der Bescheinigung / Originator of the document

KONTROLA KAKOVOSTI
Telefon: +386 4 584 10 40
Telefax: +386 4 584 10 68
http://www.acroni.si
E-mail:mirjam.pirnat@acroni.si

# Potrdilo o prevzemu 3.1/ Abnahmeprufzeugnis 3.1/ Inspection certificate 3.1

Stran/Seite/Page 1 / 2
St. / Nr. / No.

EN 10 204 3.1
Datum / Datum / Date

310085191-3 11.07.2014

Narocnik / Kunde / Customer

SANDMEYER STEEL COMPANY

ONE SANDMEYER LANE
PA19116 PHILADELPHIA

UNITED STATES

Narocilo / Bestellung Nr. / Order No.
62833 disp.39777

Dobavni list / Lieferschein / Despatch note
310085191 z/vom/from 11.07.2014

Izdelek / Erzeugnis / Product
Hot Rolled Annealed andPickled

Vrsta peci / Erschmelzunsart / Melting furnace
E+VOD

Znak izvedenca TK / Zeichen des sachverstandigen / Inspectors' stamp

Znak proizvajalca / Zeichen des Herstellewerks / Mark of the Manufacturer

| Specifikacije / Vorschriften / Specifications | Tip / W.nr. / Type | Pov./ Flache / Finish | Koroz. test / Int.krist.korr. / Corrosion test |
|---|---|---|---|
| ASTM A240 Ed.2011 | 321H/321 | No.1 | ASTM A262 PRACTICE E:OK |
| ASME SA240/240M,BPVC,Sec.II,PartA,Ed10,Add11a | 321H/321 | No.:1 | |
| QQ-S-766D | | | |
| | S32109/S32100 | | |
| AMS 5510S | SAE 30321 | | |
| EN 10028-7/ED.2007 | X6CrNiTi 18/10 | 1D | EN ISO 3651-2Method A:OK |
| | W.Nr.:14541 | | |
| PED/97/23/EC | | | NACE MR 0103-2012 |
| | | | NACE MR 0175-2012 |

## Obseg dobave / Umfang der Lieferung / Extent of material delivery

| Poz. / Pos. / Item | St. sarze / Schmelzen Nr. / Heat No. | St. plosce / Waltztafel / Plate No. | | Teza neto / Gewicht / Weight kg | Dimenzije / Abmessungen / Dimensions inch | St. kom. / Stuckzahl / Quantity | St. vzorca / Probe Nr. / Sample No. |
|---|---|---|---|---|---|---|---|
| 20 | 289407 | 64024 | 200676 | 3020 | 1.00 / 96 / 240 | 1 | 64024 T |
| 20 | 289407 | 64024 | 200677 | 3020 | 1.00 / 96 / 240 | 1 | 64024 T |

## Mehanske lastnosti / Mechanische Eigenschaften / Mechanical properties

| St.vzorca / Probe Nr. / Sample No. | Smer vzorca / Proben lage / Position | Nap.tecenja / Dehn grenze / Yield 0,2% KSI | Nap.tecenja / Dehn grenze / Yield 1% KSI | Nat.trdnost / Zugfestigkeit / Tensile str. KSI | Raztezek / Bruchdehnung / Elongation A5 % | Zn % | A80 % | Kontrakc. / Einschnurun / Z | % | Trdota / Harte / Hardness HRcB | Zilavost / Kerbschlag / Impact pri /smer bei /lage Pt.b | at/posit. °F |
|---|---|---|---|---|---|---|---|---|---|---|---|---|
| Zahteve / Anforderung. | MIN | 30 | | 75 | | 40 | | | | | | |
| | MAX | | | | | | | | | 95 | | |
| 64024 T | P | 35,09 | | 80,33 | | 47.0 | | 64 | | 80 | 210 218 214 | 68 |

G - Glava / Kopf / Top N - Noga / Fuss / Bottom V - Vzdolzno / Langs / Longitudinal P - Precno / Quer / Transverse Upogib / Biege / Bend :

ACRONI
ACRONI d.o.o., Cesta Borisa Kidriča 44, SI-4270 Jesenice

Izdajatelj certifikata
Aussteller der Bescheinigung
Originator of the document

KONTROLA KAKOVOSTI
Telefon: +386 4 584 10 40
Telefax: +386 4 584 10 68
http://www.acroni.si
E-mail:miran.pirnat@acroni.si

# Potrdilo o prevzemu 3.1/ Abnahmeprufzeugnis 3.1/ Inspection certificate 3.1

St./Nr./No. 310085191-3



## Kemicna analiza / Chemische Zusammensetzung / Chemical Composition

| Sarza/Schmelzen Nr./ | %C | %Si | %Mn | %P | %S | %Cr | %Ni | %Cu | %Mo | %Co | %N | %Nb | %Ti | Ferrite |
|---|---|---|---|---|---|---|---|---|---|---|---|---|---|---|
| 289407 | 0.044 | 0.40 | 1.56 | 0.040 | 0.001 | 17.61 | 9.17 | 0.30 | 0.42 | 0.15 | 0.0117 | 0.008 | 0.360 | |

Opombe / Bemerkungen / Remarks

GRAIN SIZE ACC. ASTM E 112 Ed 96 (Reapp04): 6,0
DIMENSIONAL INSPECTION ACCORDING ASTM A 480 / ASME SA 480: OK
FREE FROM KNOWN CONTAMINATION WITH MERCURY
NO WELD REPAIR
HEAT TRETAMENT: SOLUTION ANNEALED AT min. 1925°F WATER QUENCHED
POSITIVE MATERIAL IDENTIFICATION (PMI TEST): OK
FREE FROM RADIACTIVE CONTAMINATION
Certified acc. Pressure Equipment Directive (97/23/EC)
by TÜV-CERT-Certification body for pressure equipment of the
TÜV Industrie Service G.m.b.H TÜV Süd Gruppe.
COUNTRY OF ORIGIN = COUNTRY OF MELT = COUNTRY OF SLAB: SLOVENIA - EU
MATERIAL FULLY COMPLY WITH RoHS DIRECTIVE, Details on: http://www.acroni.si/en/data/files/1370588262.pdf
We confirm herewith that the delivered material complies with the terms of the order.

## Appendix C

Copy Right Permissions

**Chapter 2, Figures 2.1, 2.2 and 2.3a**

This Agreement between Ahmed Tiamiyu ("You") and Elsevier ("Elsevier") consists of your license details and the terms and conditions provided by Elsevier and Copyright Clearance Center.

| | |
|---|---|
| License Number | 4541600497412 |
| License date | Mar 03, 2019 |
| Licensed Content Publisher | Elsevier |
| Licensed Content Publication | Elsevier Books |
| Licensed Content Title | Steels |
| Licensed Content Author | D.T. Llewellyn,R.C. Hudd |
| Licensed Content Date | Jan 1, 1998 |
| Licensed Content Pages | 89 |
| Start Page | 291 |
| End Page | 379 |
| Type of Use | reuse in a thesis/dissertation |
| Intended publisher of new work | other |
| Portion | figures/tables/illustrations |
| Number of figures/tables/illustrations | 6 |
| Format | both print and electronic |
| Are you the author of this Elsevier chapter? | No |
| Will you be translating? | No |
| Original figure numbers | Figures 4.1, 4.2, 4.3, 4.4, 4.5 and 4.7 |
| Title of your thesis/dissertation | DYNAMIC IMPACT RESPONSE AND CORROSION BEHAVIOR OF AISI 321 AUSTENITIC STAINLESS STEEL |
| Publisher of new work | University of Saskatchewan |
| Expected completion date | Aug 2019 |
| Estimated size (number of pages) | 1 |
| Requestor Location | Ahmed Tiamiyu<br>57, College drive |

| | |
|---|---|
| | Saskatoon, SK S7N 5A9<br>Canada<br>Attn: Ahmed Tiamiyu |
| Publisher Tax ID | GB 494 6272 12 |
| Total | 0.0 USD<br>1.0 |

Terms and Conditions

**INTRODUCTION**

1. The publisher for this copyrighted material is Elsevier. By clicking "accept" in connection with completing this licensing transaction, you agree that the following terms and conditions apply to this transaction (along with the Billing and Payment terms and conditions established by Copyright Clearance Center, Inc. ("CCC"), at the time that you opened your Rightslink account and that are available at any time at http://myaccount.copyright.com).

**GENERAL TERMS**

2. Elsevier hereby grants you permission to reproduce the aforementioned material subject to the terms and conditions indicated.

3. Acknowledgement: If any part of the material to be used (for example, figures) has appeared in our publication with credit or acknowledgement to another source, permission must also be sought from that source. If such permission is not obtained then that material may not be included in your publication/copies. Suitable acknowledgement to the source must be made, either as a footnote or in a reference list at the end of your publication, as follows:

"Reprinted from Publication title, Vol /edition number, Author(s), Title of article / title of chapter, Pages No., Copyright (Year), with permission from Elsevier [OR APPLICABLE SOCIETY COPYRIGHT OWNER]." Also Lancet special credit - "Reprinted from The Lancet, Vol. number, Author(s), Title of article, Pages No., Copyright (Year), with permission from Elsevier."

4. Reproduction of this material is confined to the purpose and/or media for which permission is hereby given.

5. Altering/Modifying Material: Not Permitted. However figures and illustrations may be altered/adapted minimally to serve your work. Any other abbreviations, additions, deletions and/or any other alterations shall be made only with prior written authorization of Elsevier Ltd. (Please contact Elsevier at permissions@elsevier.com). No modifications can be made to any Lancet figures/tables and they must be reproduced in full.

6. If the permission fee for the requested use of our material is waived in this instance, please be advised that your future requests for Elsevier materials may attract a fee.

7. Reservation of Rights: Publisher reserves all rights not specifically granted in the combination of (i) the license details provided by you and accepted in the course of this licensing transaction, (ii) these terms and conditions and (iii) CCC's Billing and Payment terms and conditions.

8. License Contingent Upon Payment: While you may exercise the rights licensed immediately upon issuance of the license at the end of the licensing process for the

transaction, provided that you have disclosed complete and accurate details of your proposed use, no license is finally effective unless and until full payment is received from you (either by publisher or by CCC) as provided in CCC's Billing and Payment terms and conditions. If full payment is not received on a timely basis, then any license preliminarily granted shall be deemed automatically revoked and shall be void as if never granted. Further, in the event that you breach any of these terms and conditions or any of CCC's Billing and Payment terms and conditions, the license is automatically revoked and shall be void as if never granted. Use of materials as described in a revoked license, as well as any use of the materials beyond the scope of an unrevoked license, may constitute copyright infringement and publisher reserves the right to take any and all action to protect its copyright in the materials.

9. Warranties: Publisher makes no representations or warranties with respect to the licensed material.

10. Indemnity: You hereby indemnify and agree to hold harmless publisher and CCC, and their respective officers, directors, employees and agents, from and against any and all claims arising out of your use of the licensed material other than as specifically authorized pursuant to this license.

11. No Transfer of License: This license is personal to you and may not be sublicensed, assigned, or transferred by you to any other person without publisher's written permission.

12. No Amendment Except in Writing: This license may not be amended except in a writing signed by both parties (or, in the case of publisher, by CCC on publisher's behalf).

13. Objection to Contrary Terms: Publisher hereby objects to any terms contained in any purchase order, acknowledgment, check endorsement or other writing prepared by you, which terms are inconsistent with these terms and conditions or CCC's Billing and Payment terms and conditions. These terms and conditions, together with CCC's Billing and Payment terms and conditions (which are incorporated herein), comprise the entire agreement between you and publisher (and CCC) concerning this licensing transaction. In the event of any conflict between your obligations established by these terms and conditions and those established by CCC's Billing and Payment terms and conditions, these terms and conditions shall control.

14. Revocation: Elsevier or Copyright Clearance Center may deny the permissions described in this License at their sole discretion, for any reason or no reason, with a full refund payable to you. Notice of such denial will be made using the contact information provided by you. Failure to receive such notice will not alter or invalidate the denial. In no event will Elsevier or Copyright Clearance Center be responsible or liable for any costs, expenses or damage incurred by you as a result of a denial of your permission request, other than a refund of the amount(s) paid by you to Elsevier and/or Copyright Clearance Center for denied permissions.

**LIMITED LICENSE**

The following terms and conditions apply only to specific license types:

15. **Translation**: This permission is granted for non-exclusive world **English** rights only unless your license was granted for translation rights. If you licensed translation rights you may only translate this content into the languages you requested. A professional translator must perform all translations and reproduce the content word for word preserving the integrity of the article.

16. **Posting licensed content on any Website**: The following terms and conditions apply as follows: Licensing material from an Elsevier journal: All content posted to the web site must maintain the copyright information line on the bottom of each image; A hyper-text must be included to the Homepage of the journal from which you are licensing at http://www.sciencedirect.com/science/journal/xxxxx or the Elsevier homepage for books at http://www.elsevier.com; Central Storage: This license does not include permission for a scanned version of the material to be stored in a central repository such as that provided by Heron/XanEdu.
Licensing material from an Elsevier book: A hyper-text link must be included to the Elsevier homepage at http://www.elsevier.com . All content posted to the web site must maintain the copyright information line on the bottom of each image.

**Posting licensed content on Electronic reserve**: In addition to the above the following clauses are applicable: The web site must be password-protected and made available only to bona fide students registered on a relevant course. This permission is granted for 1 year only. You may obtain a new license for future website posting.
17. **For journal authors:** the following clauses are applicable in addition to the above:
**Preprints:**
A preprint is an author's own write-up of research results and analysis, it has not been peer-reviewed, nor has it had any other value added to it by a publisher (such as formatting, copyright, technical enhancement etc.).
Authors can share their preprints anywhere at any time. Preprints should not be added to or enhanced in any way in order to appear more like, or to substitute for, the final versions of articles however authors can update their preprints on arXiv or RePEc with their Accepted Author Manuscript (see below).
If accepted for publication, we encourage authors to link from the preprint to their formal publication via its DOI. Millions of researchers have access to the formal publications on ScienceDirect, and so links will help users to find, access, cite and use the best available version. Please note that Cell Press, The Lancet and some society-owned have different preprint policies. Information on these policies is available on the journal homepage.
**Accepted Author Manuscripts:** An accepted author manuscript is the manuscript of an article that has been accepted for publication and which typically includes author-incorporated changes suggested during submission, peer review and editor-author communications.
Authors can share their accepted author manuscript:

- immediately
    - via their non-commercial person homepage or blog
    - by updating a preprint in arXiv or RePEc with the accepted manuscript
    - via their research institute or institutional repository for internal institutional uses or as part of an invitation-only research collaboration work-group
    - directly by providing copies to their students or to research collaborators for their personal use
    - for private scholarly sharing as part of an invitation-only work group on commercial sites with which Elsevier has an agreement
- After the embargo period

- via non-commercial hosting platforms such as their institutional repository
- via commercial sites with which Elsevier has an agreement

In all cases accepted manuscripts should:

- link to the formal publication via its DOI
- bear a CC-BY-NC-ND license - this is easy to do
- if aggregated with other manuscripts, for example in a repository or other site, be shared in alignment with our hosting policy not be added to or enhanced in any way to appear more like, or to substitute for, the published journal article.

**Published journal article (JPA):** A published journal article (PJA) is the definitive final record of published research that appears or will appear in the journal and embodies all value-adding publishing activities including peer review co-ordination, copy-editing, formatting, (if relevant) pagination and online enrichment.
Policies for sharing publishing journal articles differ for subscription and gold open access articles:
**Subscription Articles:** If you are an author, please share a link to your article rather than the full-text. Millions of researchers have access to the formal publications on ScienceDirect, and so links will help your users to find, access, cite, and use the best available version.
Theses and dissertations which contain embedded PJAs as part of the formal submission can be posted publicly by the awarding institution with DOI links back to the formal publications on ScienceDirect.
If you are affiliated with a library that subscribes to ScienceDirect you have additional private sharing rights for others' research accessed under that agreement. This includes use for classroom teaching and internal training at the institution (including use in course packs and courseware programs), and inclusion of the article for grant funding purposes.
**Gold Open Access Articles:** May be shared according to the author-selected end-user license and should contain a CrossMark logo, the end user license, and a DOI link to the formal publication on ScienceDirect.
Please refer to Elsevier's posting policy for further information.
18. **For book authors** the following clauses are applicable in addition to the above: Authors are permitted to place a brief summary of their work online only. You are not allowed to download and post the published electronic version of your chapter, nor may you scan the printed edition to create an electronic version. **Posting to a repository:** Authors are permitted to post a summary of their chapter only in their institution's repository.
19. **Thesis/Dissertation**: If your license is for use in a thesis/dissertation your thesis may be submitted to your institution in either print or electronic form. Should your thesis be published commercially, please reapply for permission. These requirements include permission for the Library and Archives of Canada to supply single copies, on demand, of the complete thesis and include permission for Proquest/UMI to supply single copies, on demand, of the complete thesis. Should your thesis be published commercially, please reapply for permission. Theses and dissertations which contain embedded PJAs as part of the formal submission can be posted publicly by the awarding institution with DOI links back to the formal publications on ScienceDirect.

20. **Other Conditions**:

v1.9

**Questions? customercare@copyright.com or +1-855-239-3415 (toll free in the US) or +1-978-646-2777.**

**Chapter 2, Figures 2.3b**

This Agreement between Ahmed Tiamiyu ("You") and Elsevier ("Elsevier") consists of your license details and the terms and conditions provided by Elsevier and Copyright Clearance Center.

| | |
|---|---|
| License Number | 4533830645385 |
| License date | Feb 21, 2019 |
| Licensed Content Publisher | Elsevier |
| Licensed Content Publication | Materials Science and Engineering: A |
| Licensed Content Title | Manganese as an austenite stabilizer in Fe□Cr□Mn□C steels |
| Licensed Content Author | R.L. Klueh,P.J. Maziasz,E.H. Lee |
| Licensed Content Date | Jun 1, 1988 |
| Licensed Content Volume | 102 |
| Licensed Content Issue | 1 |
| Licensed Content Pages | 10 |
| Start Page | 115 |
| End Page | 124 |
| Type of Use | reuse in a thesis/dissertation |
| Intended publisher of new work | other |
| Portion | figures/tables/illustrations |
| Number of figures/tables/illustrations | 1 |
| Format | both print and electronic |
| Are you the author of this Elsevier article? | No |
| Will you be translating? | No |
| Original figure numbers | Fig. 9 |

| | |
|---|---|
| Title of your thesis/dissertation | DYNAMIC IMPACT RESPONSE AND CORROSION BEHAVIOR OF AISI 321 AUSTENITIC STAINLESS STEEL |
| Publisher of new work | University of Saskatchewan |
| Expected completion date | Aug 2019 |
| Estimated size (number of pages) | 1 |
| Requestor Location | Ahmed Tiamiyu<br>57, College drive<br><br>Saskatoon, SK S7N 5A9<br>Canada<br>Attn: Ahmed Tiamiyu |
| Publisher Tax ID | GB 494 6272 12 |
| Total | 0.00 USD |
| Terms and Conditions | |

**Chapter 2, Figures 2.4**

This Agreement between Ahmed Tiamiyu ("You") and Elsevier ("Elsevier") consists of your license details and the terms and conditions provided by Elsevier and Copyright Clearance Center.

| | |
|---|---|
| License Number | 4536290886306 |
| License date | Feb 26, 2019 |
| Licensed Content Publisher | Elsevier |
| Licensed Content Publication | Acta Materialia |
| Licensed Content Title | Understanding martensite and twin formation in austenitic steels: A model describing TRIP and TWIP effects |
| Licensed Content Author | E.I. Galindo-Nava,P.E.J. Rivera-Díaz-del-Castillo |
| Licensed Content Date | Apr 15, 2017 |
| Licensed Content Volume | 128 |
| Licensed Content Issue | n/a |
| Licensed Content Pages | 15 |

| | |
|---|---|
| Start Page | 120 |
| End Page | 134 |
| Type of Use | reuse in a thesis/dissertation |
| Intended publisher of new work | other |
| Portion | figures/tables/illustrations |
| Number of figures/tables/illustrations | 1 |
| Format | both print and electronic |
| Are you the author of this Elsevier article? | No |
| Will you be translating? | No |
| Original figure numbers | Fig. 1 |
| Title of your thesis/dissertation | DYNAMIC IMPACT RESPONSE AND CORROSION BEHAVIOR OF AISI 321 AUSTENITIC STAINLESS STEEL |
| Publisher of new work | University of Saskatchewan |
| Expected completion date | Aug 2019 |
| Estimated size (number of pages) | 1 |
| Requestor Location | Ahmed Tiamiyu<br>57, College drive<br><br>Saskatoon, SK S7N 5A9<br>Canada<br>Attn: Ahmed Tiamiyu |
| Publisher Tax ID | GB 494 6272 12 |
| Total | 0.00 USD |
| Terms and Conditions | |

**Chapter 2, Figures 2.5**

This Agreement between Ahmed Tiamiyu ("You") and Elsevier ("Elsevier") consists of your license details and the terms and conditions provided by Elsevier and Copyright Clearance Center.

| | |
|---|---|
| License Number | 4536121459748 |
| License date | Feb 25, 2019 |
| Licensed Content Publisher | Elsevier |

| | |
|---|---|
| Licensed Content Publication | Acta Materialia |
| Licensed Content Title | Role of stress-assisted martensite in the design of strong ultrafine-grained duplex steels |
| Licensed Content Author | Hung-Wei Yen,Steve Woei Ooi,Mehdi Eizadjou,Andrew Breen,Ching-Yuan Huang,H.K.D.H. Bhadeshia,Simon P. Ringer |
| Licensed Content Date | Jan 1, 2015 |
| Licensed Content Volume | 82 |
| Licensed Content Issue | n/a |
| Licensed Content Pages | 15 |
| Start Page | 100 |
| End Page | 114 |
| Type of Use | reuse in a thesis/dissertation |
| Intended publisher of new work | other |
| Portion | figures/tables/illustrations |
| Number of figures/tables/illustrations | 1 |
| Format | both print and electronic |
| Are you the author of this Elsevier article? | No |
| Will you be translating? | No |
| Original figure numbers | Fig. 11 |
| Title of your thesis/dissertation | DYNAMIC IMPACT RESPONSE AND CORROSION BEHAVIOR OF AISI 321 AUSTENITIC STAINLESS STEEL |
| Publisher of new work | University of Saskatchewan |
| Expected completion date | Aug 2019 |
| Estimated size (number of pages) | 1 |
| Requestor Location | Ahmed Tiamiyu<br>57, College drive<br><br>Saskatoon, SK S7N 5A9<br>Canada<br>Attn: Ahmed Tiamiyu |
| Publisher Tax ID | GB 494 6272 12 |
| Total | 0.00 USD |

Terms and Conditions

**Chapter 2, Figures 2.7**

This Agreement between Ahmed Tiamiyu ("You") and Elsevier ("Elsevier") consists of your license details and the terms and conditions provided by Elsevier and Copyright Clearance Center.

| | |
|---|---|
| License Number | 4540400969029 |
| License date | Mar 01, 2019 |
| Licensed Content Publisher | Elsevier |
| Licensed Content Publication | Acta Materialia |
| Licensed Content Title | Self-organization in the initiation of adiabatic shear bands |
| Licensed Content Author | V.F. Nesterenko,M.A. Meyers,T.W. Wright |
| Licensed Content Date | Dec 19, 1998 |
| Licensed Content Volume | 46 |
| Licensed Content Issue | 1 |
| Licensed Content Pages | 14 |
| Start Page | 327 |
| End Page | 340 |
| Type of Use | reuse in a thesis/dissertation |
| Intended publisher of new work | other |
| Portion | figures/tables/illustrations |
| Number of figures/tables/illustrations | 1 |
| Format | both print and electronic |
| Are you the author of this Elsevier article? | No |
| Will you be translating? | No |
| Original figure numbers | Fig. 13 |

| | |
|---|---|
| Title of your thesis/dissertation | DYNAMIC IMPACT RESPONSE AND CORROSION BEHAVIOR OF AISI 321 AUSTENITIC STAINLESS STEEL |
| Publisher of new work | University of Saskatchewan |
| Expected completion date | Aug 2019 |
| Estimated size (number of pages) | 1 |
| Requestor Location | Ahmed Tiamiyu<br>57, College drive<br><br>Saskatoon, SK S7N 5A9<br>Canada<br>Attn: Ahmed Tiamiyu |
| Publisher Tax ID | GB 494 6272 12 |
| Total | 0.00 USD |

**Chapter 2, Figures 2.8b**

This Agreement between Ahmed Tiamiyu ("You") and Elsevier ("Elsevier") consists of your license details and the terms and conditions provided by Elsevier and Copyright Clearance Center.

| | |
|---|---|
| License Number | 4540980647090 |
| License date | Mar 02, 2019 |
| Licensed Content Publisher | Elsevier |
| Licensed Content Publication | Materials Science and Engineering: A |
| Licensed Content Title | Shear localization and recrystallization in high-strain, high-strain-rate deformation of tantalum |
| Licensed Content Author | V.F. Nesterenko,M.A. Meyers,J.C. LaSalvia,M.P. Bondar,Y.J. Chen,Y.L. Lukyanov |
| Licensed Content Date | Jun 30, 1997 |
| Licensed Content Volume | 229 |
| Licensed Content Issue | 1-2 |
| Licensed Content Pages | 19 |
| Start Page | 23 |

| | |
|---|---|
| End Page | 41 |
| Type of Use | reuse in a thesis/dissertation |
| Intended publisher of new work | other |
| Portion | figures/tables/illustrations |
| Number of figures/tables/illustrations | 1 |
| Format | both print and electronic |
| Are you the author of this Elsevier article? | No |
| Will you be translating? | No |
| Original figure numbers | Fig. 19 |
| Title of your thesis/dissertation | DYNAMIC IMPACT RESPONSE AND CORROSION BEHAVIOR OF AISI 321 AUSTENITIC STAINLESS STEEL |
| Publisher of new work | University of Saskatchewan |
| Expected completion date | Aug 2019 |
| Estimated size (number of pages) | 1 |
| Requestor Location | Ahmed Tiamiyu<br>57, College drive<br><br>Saskatoon, SK S7N 5A9<br>Canada<br>Attn: Ahmed Tiamiyu |
| Publisher Tax ID | GB 494 6272 12 |
| Total | 0.00 USD |

**Chapter 2, Figures 2.9**

Copyright Clearance Center RightsLink®

Home | Account Info | Hel

ELSEVIER

**Title:** Effects of temper condition on high strain-rate deformation of AA 2017 aluminum alloy in compression

**Author:** A.A. Tiamiyu,A.Y. Badmos,A.G. Odeshi

**Publication:** Materials & Design

**Publisher:** Elsevier

**Date:** 5 January 2016

Copyright © 2015 Elsevier Ltd. Published by Elsevier Ltd. All rights reserved.

Logged in as:
Ahmed Tiamiyu
Account #:
3000896829

LOGOUT

Please note that, as the author of this Elsevier article, you retain the right to include it in a thesis or dissertation, provided it is not published commercially. Permission is not required, but please ensure that you reference the journal as the original source. For more information on this and on your other retained rights, please visit: https://www.elsevier.com/about/our-business/policies/copyright#Author rights

BACK | CLOSE WINDOW

Copyright © 2019 Copyright Clearance Center, Inc. All Rights Reserved. Privacy statement. Terms and Conditions.
Comments? We would like to hear from you. E-mail us at customercare@copyright.com

**Chapter 4**

Copyright Clearance Center RightsLink®

Home | Account Info | Help

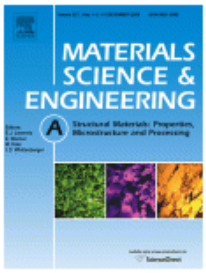

**Title:** Mechanical behavior and high-resolution EBSD investigation of the microstructural evolution in AISI 321 stainless steel under dynamic loading condition

**Author:** A.A. Tiamiyu,M. Eskandari,Mohsen Sanayei,A.G. Odeshi,J.A. Szpunar

**Publication:** Materials Science and Engineering: A

**Publisher:** Elsevier

**Date:** 15 September 2016



Logged in as:
Ahmed Tiamiyu
Account #:
3000896829
LOGOUT



BACK | CLOSE WINDOW



**Chapter 5**

This Agreement between Ahmed Tiamiyu ("You") and Springer Nature ("Springer Nature") consists of your license details and the terms and conditions provided by Springer Nature and Copyright Clearance Center.

| | |
|---|---|
| License Number | 4526691269506 |
| License date | Feb 12, 2019 |
| Licensed Content Publisher | Springer Nature |
| Licensed Content Publication | Metallurgical and Materials Transactions A |
| Licensed Content Title | Development of Ultra-Fine-Grained Structure in AISI 321 Austenitic Stainless Steel |
| Licensed Content Author | A. A. Tiamiyu, J. A. Szpunar, A. G. Odeshi et al |
| Licensed Content Date | Jan 1, 2017 |
| Licensed Content Volume | 48 |

| | |
|---|---|
| Licensed Content Issue | 12 |
| Type of Use | Thesis/Dissertation |
| Requestor type | academic/university or research institute |
| Format | print and electronic |
| Portion | full article/chapter |
| Will you be translating? | no |
| Circulation/distribution | >50,000 |
| Author of this Springer Nature content | yes |
| Title | DYNAMIC IMPACT RESPONSE AND CORROSION BEHAVIOR OF AISI 321 AUSTENITIC STAINLESS STEEL |
| Institution name | University of Saskatchewan |
| Expected presentation date | Aug 2019 |
| Requestor Location | Ahmed Tiamiyu<br>57, College drive<br><br>Saskatoon, SK S7N 5A9<br>Canada<br>Attn: Ahmed Tiamiyu |
| Billing Type | Invoice |
| Billing Address | Ahmed Tiamiyu<br>57, College drive<br><br>Saskatoon, SK S7N 5A9<br>Canada<br>Attn: Ahmed Tiamiyu |
| Total | 0.00 USD |

Terms and Conditions

**Springer Nature Terms and Conditions for RightsLink Permissions**
**Springer Nature Customer Service Centre GmbH (the Licensor)** hereby grants you a non-exclusive, world-wide licence to reproduce the material and for the purpose and requirements specified in the attached copy of your order form, and for no other use, subject to the conditions below:

1. The Licensor warrants that it has, to the best of its knowledge, the rights to license reuse of this material. However, you should ensure that the material you are requesting is original to the Licensor and does not carry the copyright of another entity (as credited in

the published version).

If the credit line on any part of the material you have requested indicates that it was reprinted or adapted with permission from another source, then you should also seek permission from that source to reuse the material.

2. Where **print only** permission has been granted for a fee, separate permission must be obtained for any additional electronic re-use.
3. Permission granted **free of charge** for material in print is also usually granted for any electronic version of that work, provided that the material is incidental to your work as a whole and that the electronic version is essentially equivalent to, or substitutes for, the print version.
4. A licence for 'post on a website' is valid for 12 months from the licence date. This licence does not cover use of full text articles on websites.
5. Where **'reuse in a dissertation/thesis'** has been selected the following terms apply: Print rights of the final author's accepted manuscript (for clarity, NOT the published version) for up to 100 copies, electronic rights for use only on a personal website or institutional repository as defined by the Sherpa guideline (www.sherpa.ac.uk/romeo/).
6. Permission granted for books and journals is granted for the lifetime of the first edition and does not apply to second and subsequent editions (except where the first edition permission was granted free of charge or for signatories to the STM Permissions Guidelines http://www.stm-assoc.org/copyright-legal-affairs/permissions/permissions-guidelines/), and does not apply for editions in other languages unless additional translation rights have been granted separately in the licence.
7. Rights for additional components such as custom editions and derivatives require additional permission and may be subject to an additional fee. Please apply to Journalpermissions@springernature.com/bookpermissions@springernature.com for these rights.
8. The Licensor's permission must be acknowledged next to the licensed material in print. In electronic form, this acknowledgement must be visible at the same time as the figures/tables/illustrations or abstract, and must be hyperlinked to the journal/book's homepage. Our required acknowledgement format is in the Appendix below.
9. Use of the material for incidental promotional use, minor editing privileges (this does not include cropping, adapting, omitting material or any other changes that affect the meaning, intention or moral rights of the author) and copies for the disabled are permitted under this licence.
10. Minor adaptations of single figures (changes of format, colour and style) do not require the Licensor's approval. However, the adaptation should be credited as shown in Appendix below.

**Appendix — Acknowledgements:**

**For Journal Content:**

Reprinted by permission from [**the Licensor**]: [**Journal Publisher** (e.g. Nature/Springer/Palgrave)] [**JOURNAL NAME**] [**REFERENCE CITATION**(Article name, Author(s) Name), [**COPYRIGHT**] (year of publication)

For **Advance Online Publication papers:**

Reprinted by permission from [**the Licensor**]: [**Journal Publisher** (e.g.

Nature/Springer/Palgrave)] [**JOURNAL NAME**] [**REFERENCE CITATION**(Article name, Author(s) Name), [**COPYRIGHT**] (year of publication), advance online publication, day month year (doi: 10.1038/sj.[JOURNAL ACRONYM].)

**For Adaptations/Translations:**

Adapted/Translated by permission from [**the Licensor**]: [**Journal Publisher** (e.g. Nature/Springer/Palgrave)] [**JOURNAL NAME**] [**REFERENCE CITATION**(Article name, Author(s) Name), [**COPYRIGHT**] (year of publication)

**Note: For any republication from the British Journal of Cancer, the following credit line style applies:**

Reprinted/adapted/translated by permission from [**the Licensor**]: on behalf of Cancer Research UK: : [**Journal Publisher** (e.g. Nature/Springer/Palgrave)] [**JOURNAL NAME**] [**REFERENCE CITATION** (Article name, Author(s) Name), [**COPYRIGHT]** (year of publication)

For **Advance Online Publication** papers:

Reprinted by permission from The [**the Licensor**]: on behalf of Cancer Research UK: [**Journal Publisher** (e.g. Nature/Springer/Palgrave)] [**JOURNAL NAME**] [**REFERENCE CITATION** (Article name, Author(s) Name), [**COPYRIGHT**] (year of publication), advance online publication, day month year (doi: 10.1038/sj.[JOURNAL ACRONYM])

**For Book content:**

Reprinted/adapted by permission from [**the Licensor**]: [**Book Publisher** (e.g. Palgrave Macmillan, Springer etc) [**Book Title**] by [**Book author**(s)] [**COPYRIGHT**] (year of publication)

**Other Conditions**:

Version 1.1

**Questions? customercare@copyright.com or +1-855-239-3415 (toll free in the US) or +1-978-646-2777.**

# Chapter 7

LR Lingayath, Roopa (ELS-CHN) <r.lingayath@elsevier.com>
Thu 3/21, 1:26 AM
Tiamiyu, Ahmed

Reply all

Inbox

ELSEVIER

Dear Tiamiyu,
We hereby grant you permission to reproduce the material detailed below in **print and electronic format** at no charge subject to the following conditions:

**RE: Tiamiyu, A. A., Odeshi, A. G., and Szpunar, J. A. (2018). Characterization of coarse and ultrafine-grained austenitic stainless steel subjected to dynamic impact load: XRD, SEM, TEM and EBSD analyses. Materialia. 4:81-98**

1. If any part of the material to be used (for example, figures) has appeared in our publication with credit or acknowledgement to another source, permission must also be sought from that source. If such permission is not obtained then that material may not be included in your publication/copies.

2. Suitable acknowledgement to the source must be made, either as a footnote or in a reference list at the end of your publication, as follows:

   "This article was published in Publication title, Vol number, Author(s), Title of article, Page Nos, Copyright Elsevier (or appropriate Society name) (Year)."

3. This permission is granted for non-exclusive world rights in all languages.

4. Reproduction of this material is granted for the purpose for which permission is hereby given, and includes use in any future editions.

Yours sincerely,
Roopa

**Thanks & Regards,**
**Roopa Lingayath**
Sr Copyrights Coordinator – Global Rights | Global Book Production
**Elsevier**
**(A division of Reed Elsevier India Pvt. Ltd.)**

International Tech Park | Crest – 5th Floor | CSIR Road | Taramani | Chennai 600 113 | India
Tel: +91 44 3378 4167 | Fax: +91 44 4299 4568
E-mail: r.lingayath@elsevier.com | url: www.elsevier.com

**From:** Tiamiyu, Ahmed <ahmed.tiamiyu@usask.ca>
**Sent:** 14 February 2019 01:35
**To:** Rights and Permissions (ELS) <Permissions@elsevier.com>
**Subject:** Permission to use

*** External email: use caution ***

Hi,

My name is Ahmed Tiamiyu, a PhD student at the University of Saskatchewan, Canada. I write to request your permission to use the full manuscript (**Tiamiyu, A. A.,** Odeshi, A. G., and Szpunar, J. A. (2018). Characterization of coarse and ultrafine-grained austenitic stainless steel subjected to dynamic impact load: XRD, SEM, TEM and EBSD analyses. Materialia. 4:81-98) as part of my PhD thesis.

Thanks as I await your response.

**Chapter 8**

**Chapter 9**

Copyright Clearance Center RightsLink®

Home | Account Info | Help

**Title:** Strain rate sensitivity and activation volume of AISI 321 stainless steel under dynamic impact loading: Grain size effect

**Author:** A.A. Tiamiyu,J.A. Szpunar,A.G. Odeshi

**Publication:** Materials Characterization

**Publisher:** Elsevier

**Date:** August 2019



Logged in as:
Ahmed Tiamiyu
Account #:
3000896829
LOGOUT

Please note that, as the author of this Elsevier article, you retain the right to include it in a thesis or dissertation, provided it is not published commercially. Permission is not required, but please ensure that you reference the journal as the original source. For more information on this and on your other retained rights, please visit: https://www.elsevier.com/about/our-business/policies/copyright#Author-rights

BACK | CLOSE WINDOW



**Chapter 10**

This Agreement between Ahmed Tiamiyu ("You") and Springer Nature ("Springer Nature") consists of your license details and the terms and conditions provided by Springer Nature and Copyright Clearance Center.

Your confirmation email will contain your order number for future reference.

printable details

| | |
|---|---|
| License Number | 4625700410737 |
| License date | Jul 10, 2019 |
| Licensed Content Publisher | Springer Nature |
| Licensed Content Publication | Metallurgical and Materials Transactions A |

| | |
|---|---|
| Licensed Content Title | Thermal and Mechanical Stability of Austenite in Metastable Austenitic Stainless Steel |
| Licensed Content Author | A. A. Tiamiyu, Shiteng Zhao, Zezhou Li et al |
| Licensed Content Date | Jan 1, 2019 |
| Type of Use | Thesis/Dissertation |
| Requestor type | academic/university or research institute |
| Format | print and electronic |
| Portion | full article/chapter |
| Will you be translating? | no |
| Circulation/distribution | >50,000 |
| Author of this Springer Nature content | yes |
| Title | DYNAMIC IMPACT RESPONSE AND CORROSION BEHAVIOR OF AISI 321 AUSTENITIC STAINLESS STEEL |
| Institution name | University of Saskatchewan |
| Expected presentation date | Aug 2019 |
| Requestor Location | Ahmed Tiamiyu<br>57, College drive<br><br>Saskatoon, SK S7N 5A9<br>Canada<br>Attn: Ahmed Tiamiyu |
| Total | 0.00 USD |